The application of nuclear quadrupole resonance to pharmaceutical analysis

Tate, Elizabeth Alice Kate

The Application of Nuclear Quadrupole Resonance to Pharmaceutical Analysis

Elizabeth A. K. Tate

Thesis submitted in partial fulfilment of the requirements for the degree of Doctor of Philosophy.

King's College
University of London

March 2007

DECLARATION

I DECLARE THAT THE WORK PRESENTED IN THIS THESIS IS MY OWN

ELIZABETH A. K. TATE

ACKNOWLEDGEMENTS

Firstly I would like to thank Professor John Smith for his supervision, advice, patience, optimism and encouragement over the years of this work. Thanks also to Dr. David Malcolme-Lawes for his supervision over my many years at King's, and to the other members of the NQR research group; Anna D'Aloya, Samuel Somasundaram, Drs. Michael Rowe, Jamie Barras, Iain Poplett and Neil Peirson have all helped me immensely with practical advice and support as well as company in an ever decreasing chemistry department.

My friends in London, Reading and Liverpool have all kept me entertained and listened to me talk about science over the years, so my appreciation goes to them also, particularly Nawaf Aldiwan for making completing a thesis not seem like an impossibility.

My gratitude also goes to my sponsors - Gareth Pearce at Merck Sharp and Dohme and Stephen Wren at AstraZeneca particularly for their support and input, as well as the industrial financial support from their companies, and also from EPSRC. For provision of equipment and materials I would also like to thank the Defence Science and Technology Laboratory at Fort Halstead.

Thanks also to those who have assisted and collaborated with me in parts of this work including David Apperley, Michael Bearpark, Anthony Horsewill, Fraser Markwell, Jonathon Steed and David Stephenson.

Finally I thank my parents and my husband, Justin, for their love, support, guidance and encouragement.

ABSTRACT

Research was conducted using nuclear quadrupole resonance (NQR) to investigate its potential application to pharmaceutical analysis. 14-nitrogen and 35-chlorine quadrupole resonance frequencies between 1 and 37 MHz have been established and characterised for a number of materials of pharmaceutical and chemical interest with a view to applying the technique of NQR to pharmaceutical analysis, possibly on an industrial scale. Background information and the theory of nuclear quadrupole resonance are discussed, together with the experimental hardware used, personal instrumental modifications made, pulse sequences and data processing methods.

The characterisation of materials by other methods currently used in analysis, such as infrared and X-ray spectroscopy, thermogravimetric analysis and differential scanning calorimetry, are described and the limits of such techniques compared to those of NQR. Furosemide, heroin hydrochloride monohydrate, heroin, triazole, histidine, chloroquine diphosphate, dipicolinic acid and 4-methylimidazole have all been studied and characterised to varying degrees with their NQR frequencies, line widths, temperature coefficients, and relaxation rates having been found experimentally.

The ability to distinguish between polymorphs has been shown in furosemide – an important consideration in the manufacture of medicines. Quantification using both 14-N and 35-Cl signals has been demonstrated, with mass of material being predicted to within 5 % in triazole and furosemide, using free induction decay and pulse-spin locking echo signals respectively. Quantification of two materials within the same container has been combined with signal processing techniques in the study of histidine and 4-methylimidazole. The ability to predict quadrupolar parameters by theoretical calculation has been shown to be feasible in the case of 14-N nuclei within heroin hydrochloride monohydrate by modelling. Finally, future perspectives are discussed and the possibilities and potential of industrial application considered.

TABLE OF CONTENTS

TABLE OF FIGURES

TABLE OF TABLES

TABLE OF ABBREVIATIONS

°	Degree
90_{eff}	90 degree effective pulse
A	Ampere
Å	Angstrom
AML	Approximative maximum likelihood
API	Active pharmaceutical ingredient
C	Celsius
Calc.	Calculated
CCD	Charge-coupled device
cm	Centimetre
CP-MAS	Cross polarised, magic angle spun
CR	Cross relaxation
d.c.	Direct current
dB	Decibel
DMF	Dimethylformamide
DRLC	Double resonance by level crossing
DSC	Differential scanning calorimetry
DSTL	Defence Science and Technology Laboratory
DTA	Differential thermal analysis
EFG	Electric field gradient
FID	Free induction decay
FT	Fourier transformed
g	Gram
GRLT	Generalised likelihood ratio test
HF	Hartree-Fock
HMX	High melting point explosive
Hz	Hertz
IR	Infrared
K	Kelvin
kHz	Kilohertz

kV	Kilovolt
kΩ	Kiloohm
L	Litre
m	Metre
mA	Milliampere
mB	Millibarn
MDMA	3,4-methylenedioxy-N-methylamphetamine
mg	Milligram
MHz	Megahertz
min	Minute
ml	Millilitre
mm	Millimetre
ms	Millisecond
mT	Millitesla
mV	Millivolt
nF	Nanofarad
NMR	Nuclear magnetic resonance
NQR	Nuclear quadrupole resonance
ns	Nanosecond
PE-NQR	Polarisation enhanced nuclear quadrupole resonance
pF	Picofarad
ppm	Parts per million
PSL	Pulse spin locking
PTFE	Polytetrafluoroethylene
Q (factor)	Quality (factor)
QCC	Quadrupole coupling constant
RDX	Cyclotrimethylenetrinitramine
RF	Radiofrequency
s	Second
SCF	Self consistent field
SNR	Signal-to-noise ratio

SPA	Sulfapyridine recrystallised from acetone
SPE	Sulfapyridine recrystallised from ethanol
SSNMR	Solid state nuclear magnetic resonance
SSS	Steady state sequence
T	Tesla
TGA	Thermogravimetric analysis
TNT	Trinitrotoluene
V	Volt
W	Watt
w.r.t.	With respect to
XRPD	X-ray powder diffraction
Ω	Ohm
μF	Microfarad
μH	Microhenry
μm	Micrometre
μs	Microsecond
μV	Microvolt

1 Introduction and outline

1.1 Introduction

Nuclear quadrupole resonance (NQR) is a radiofrequency (RF) spectroscopic technique used to detect signals from quadrupolar nuclei present in solids or solid-like materials. It is a non-destructive, non-invasive and highly sensitive analytical technique for which little sample preparation is required. Unlike the closely related technique of nuclear magnetic resonance (NMR), no magnetic field is required, making NQR probes relatively cheap and portable. Indeed, current uses include the detection of land-mines[1] and other explosives such as HMX[2,3,4,5] (**1**), TNT[3,5] (**2**) and RDX[3,5] (**3**), and also in narcotics such as MDMA[6] (**4**), cocaine[7,8] (**5**) and heroin[2,9,10] (**6**).

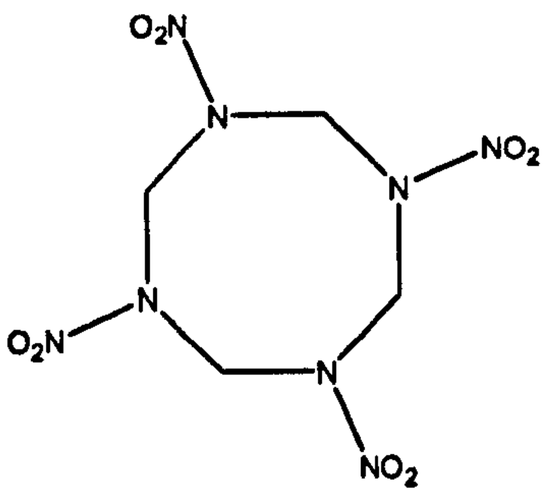

1

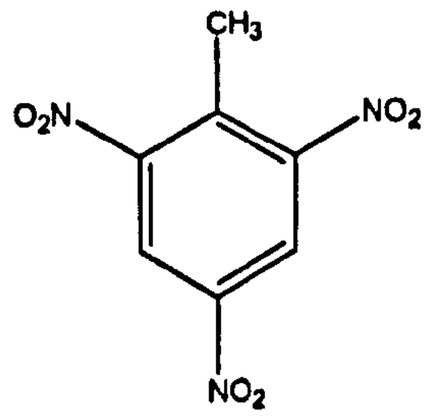

2

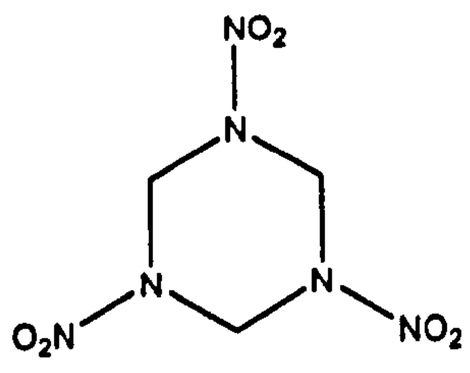

3

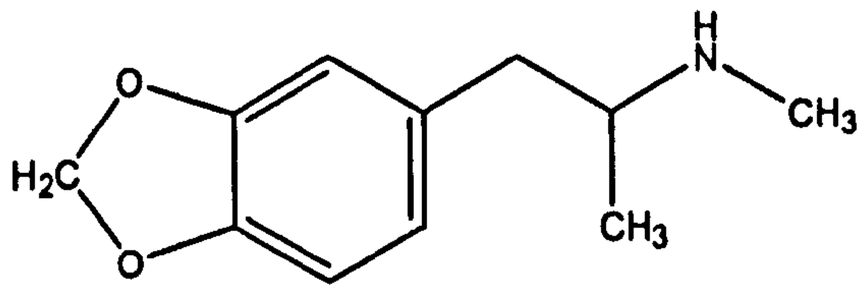

4

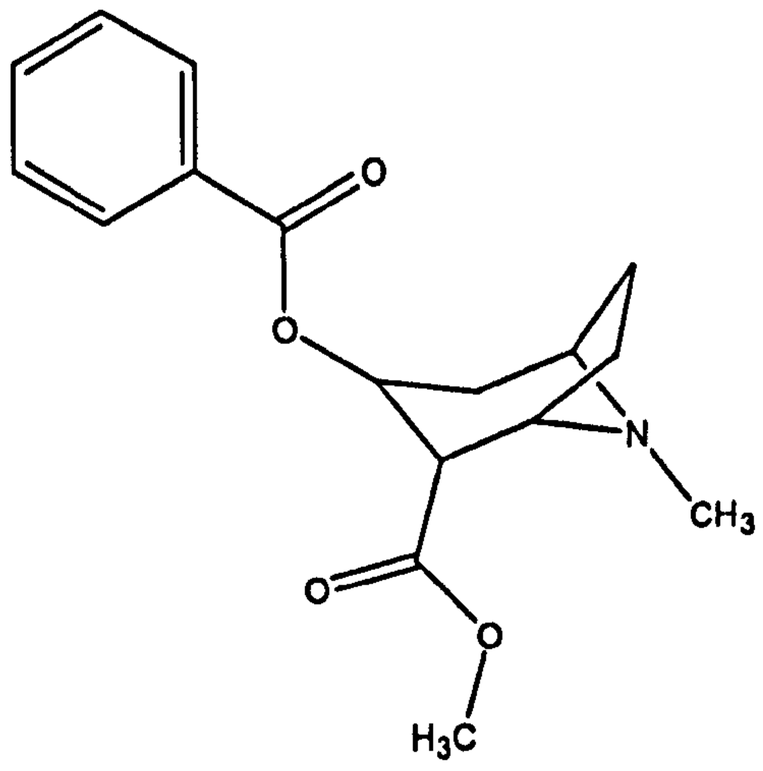

5

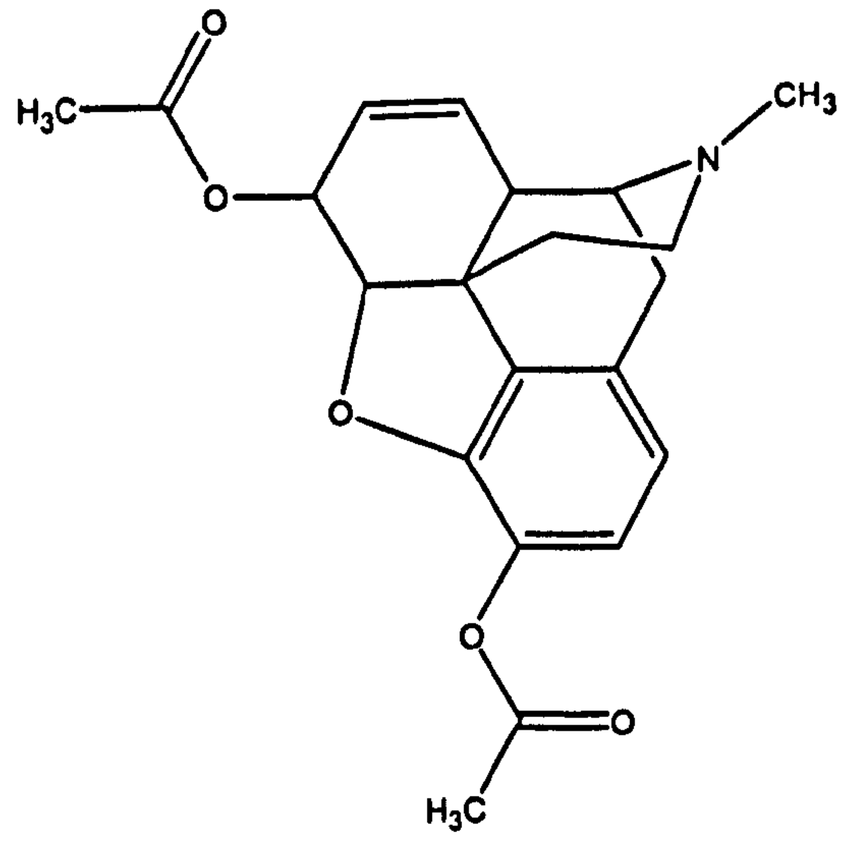

6

In the cases above, ^{14}N nuclei have been studied; it is found in many explosives and narcotics, has spin quantum number $I = 1$ and a natural abundance of 99.634 %[11]. It is a widely studied nucleus in NQR generating signals in the low RF frequency range between 0.4 and 6 MHz. ^{35}Cl is another widely studied nucleus; it has $I = {}^3/_2$ and a natural abundance of 75.77 %[11] but often having much higher NQR frequencies – up to around 40 MHz – and although less naturally abundant, its presence in many pharmaceuticals and ability to produce strong signals make it an attractive option in NQR analysis.

Until recently, NQR as an analytical tool has been mainly used for detection of explosives and narcotics in security applications, such as airport and aircraft safety, and as a measure against illegal drug trafficking, with marketable probes being made and tested[12,13]. However, the technique lends itself particularly well to pharmaceutical analysis – an area which has not been greatly explored although there have been recent publications[14,15] highlighting the possibilities of NQR – for a number of reasons, with potential for use in detection, analysis, and quality control of pharmaceuticals at all stages of manufacture.

Firstly, NQR is a solid-state analytical technique; approximately 90 % of commercially available pharmaceutical products are in the solid form[16] and can therefore be studied as both the bulk powder form of the material under investigation and as tablets. A wide range of volumes can be studied by NQR methods – probes can be designed to fit the sample, unlike NMR, with signals having been observed from a single 20 mg tablet to samples in large volumes of up to 8000 L[17]. Secondly, NQR is highly specific (in more than 12 000 compounds studied so far, each has had a unique set of frequencies and relaxation rates assigned to them[18]); any signal from the active pharmaceutical ingredient (API) can be easily distinguished from excipients in tablets or contaminants and impurities present in the material under examination. Finally, the non-destructive and non-invasive nature of the analysis makes it unnecessary to even remove the materials from their containers in most circumstances; there is even the possibility of examining tablets in blister packs. This property of NQR also allows remote testing, introducing the possibility of at-line testing, that is, at the point of manufacture, without the need for removal to a laboratory environment and without contamination of sealed products.

Chemical analysis is necessary in all areas of pharmaceutical manufacture, from the initial research and development of new drugs through to ongoing quality control work in the final marketable product. By using NQR spectroscopic analysis, development times could be reduced, along with manufacturing costs, while the quality of the pharmaceutical could be increased, together with our knowledge of the product, through further characterisation using NQR. NQR would be complementary to the range of analytical techniques used currently – many are solution-based (for example solution nuclear magnetic resonance, high performance liquid chromatography and electrospray mass spectrometry) techniques which cannot give direct information on the solid state and require sample preparation, as well as clearly being destructive in nature. Solid-state techniques such as solid-state NMR, infrared spectroscopy, X-ray diffraction, differential scanning calorimetry and thermogravimetric analysis are also commonly used and their limitations and advantages in comparison to NQR are discussed in chapter 4 of this thesis.

1.2 Outline and aims

This work was commenced with an aim to further the study of pharmaceutical compounds using NQR and to highlight the potential uses of NQR in pharmaceutical analysis. In order to demonstrate that this spectroscopic technique is a viable option in laboratory and industrial work, we intend to characterise a number of pharmaceutical materials to different degrees of detail. Firstly, the theory of NQR will be explained both classically and quantum mechanically to allow an understanding of the principles and provide an explanation of the resulting NQR data and spectra. As well as pure NQR, double resonance methods will be briefly described, as these can be important in initial studies of a compound. Going on to the NQR instrumentation, the basic hardware is introduced and more importantly, the measures taken to improve the NQR experiment through instrumental modifications are discussed. As NQR is not currently a widely used technique, commercial laboratory instrumentation is not generally available so the individual design and hand-building of NQR probes is a necessary job and skill which was an important part of this work. Another important aim was to show the ability for quantification – a goal that can be facilitated with techniques such as Q-damping and re-design of the NQR solenoid to ensure the sample experiences a more uniform RF field across its volume.

One particular material, furosemide, was studied in great detail; it is a commercially available anti-hypertensive drug known to exist in several different forms and was chosen as a subject for study as it would allow us to investigate polymorphs and determine whether NQR could be used to distinguish between different forms of the same drug – vitally important in pharmaceutical manufacture considering that different polymorphs of the same drug can have different stabilities, dissolution rates and effects upon the user. The most stable form (phase I) was to be fully characterised with ^{14}N and ^{35}Cl signals from both the bulk powder and tablets being investigated, as well as temperature effects. The polymorph assigned to be phase II was also to be characterised to a lesser degree, allowing a comparison of the two phases by solid-state NMR, IR spectroscopy, X-ray diffraction, differential scanning calorimetry, thermogravimetric analysis and microscopy, as well as NQR.

Quantitative analysis was another important objective in this work, as already mentioned, and following instrumental modifications a number of compounds was studied to see if quantification could be realised in the laboratory conditions to a reasonable degree of precision – in particular, we hoped to provide the conditions necessary to yield a linear response with respect to mass. As well as looking at spectra obtained under standard conditions, with the usual data processing of the signal, state-of-the-art maximum likelihood methods were used to enhance the signals observed and possibly allow faster acquisition of spectra and a more accurate measurement of the relative proportions of different polymorphs.

One of the most tedious areas of NQR research is the determination of frequencies of previously unstudied materials. We aimed to use theoretical calculations, together with double resonance methods, to show that an estimate of NQR frequency could be made, lessening the range across which searching would need to be carried out and so reducing the time taken in characterisation of a new substance.

Finally we look at what the future could hold for NQR; up and coming advances in the technique are discussed as well as further experiments which could have been done with the present equipment without the constraints of time. There are many more uses for NQR in pharmaceutical analysis that should be investigated further

and it is hoped that this work can form a basis from which further research can proceed.

1.3 References

[1] Garroway, A. N.; Buess, M. L.; Miller, J. B.; Suits, B. H.; Hibbs, A. H.; Barrall, G. A.; Matthews, R.; Burnett, L. *J. IEEE Trans. Geosci. Rem. Sens.*, **2001**, *39*, 1108 - 1118.

[2] Balchin, E. *"Nuclear Quadrupole Resonance: The Detection of Narcotics and Explosives"*, 4th Year Project, March **2002**, King's College London.

[3] Landers A. G.; Brill, T. B.; Marino, R. A. *J. Phys. Chem.* **1981**, *85*, 2618 - 2623.

[4] Pati, R.; Das, T. P.; Sahoo, N.; Ray, S. N. *J. Phys. Chem.* **1997**, *101*, 6101 - 6106.

[5] Grechishkin, V. S. *J. Struct. Chem.*, **1991**, *32*, 609 - 610.

[6] Rowe, M. D.; Smith, J. A. S. Unpublished results.

[7] Rowe, M. D. "NQR Spectra of Cocaine Hydrochloride and Heroin," NQR Group Report, June **2001**.

[8] Yesinowski, J. P.; Buess, M. L.; Garroway, A. N.; Ziegeweid, M.; Pines, A. *Anal. Chem.* **1995**, *67*, 2256 - 2263.

[9] Grechishkin, V. S.; Ya Sinyavski, N. *Physics Uspekhi*, **1997**, *40 (4)*, 393 - 406.

[10] Pati, R.; Das, T. P.; Sahoo, N.; Ray, S. N. *J. Phys. Chem.* **1998**, *102*, 3209 - 3214.

[11] Emsley, J. *The Elements; 3rd Ed.*, Clarendon Press, Oxford, **1998**, pp 143.

[12] QRX1000, QRSciences, Cannington, WA 6017, Australia.

[13] Quantum Magnetics, 7740 Kenamar Ct., San Diego, CA 92121, USA.

[14] Perez, S.C.; Cerioni, L.; Wolfenson, A. E.; Faudone, S.; Cuffini, S. L., *Int. J. Pharm.*, **2005**, *298*, 143 - 152.

[15] Balchin, E.; Malcolme-Lawes, D. J.; Poplett, I. J. F.; Rowe, M. D.; Smith, J. A. S.; Pearce, G. E. S.; Wren, S. A. C. *Anal. Chem.* **2005**, *77*, 3925 - 3930.

[16] Brittain, H. G. *Physical Characterization of Pharmaceutical Solids*; Marcel Dekker Inc.; New York, **1995**, pp 57 and 94.

[17] Barras, J.; Gaskell, M. J.; Hunt, N.; Jenkinson, R. I.; Pedder, D. A. G.; Shilstone, G. N.; Smith, J. A. S. *Appl. Magn. Res.* **2004**, *25*, 411 - 437.

[18] *NQR Database.* Japan Association of International Chemical Information (JAICA): Nakai Building, 6-25-4 Henkomagome, Bunkyo-ku, Tokyo 113, Japan.

2 The theory of nuclear quadrupole resonance

2.1 An introduction to nuclear magnetic resonance

It is well known that in nuclear magnetic resonance an externally applied magnetic field induces precession as the magnetic moment μ experiences a torque. Precession about the applied magnetic field B_0 occurs at the Larmor frequency, ν

$$\nu = \left|\frac{\gamma}{2\pi}\right| B_0 \qquad (2.1)$$

where γ is the gyromagnetic ratio and can be visualized as figure 2.1.

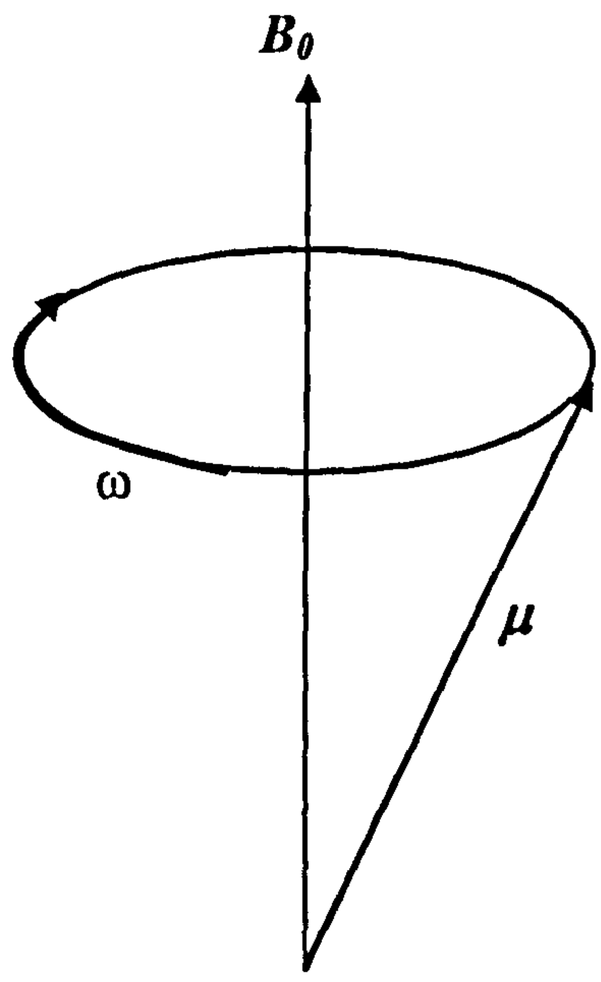

Figure 2.1: Precession of a magnetic moment μ about the axis of an applied magnetic field, B_0.

Nuclei with spin quantum number $I \geq ½$ have a magnetic dipole moment, μ. This dipole moment is a vector quantity, dependent on the gyromagnetic ratio and the nuclear spin angular momentum, P

$$\mu = \gamma . P \qquad (2.2)$$

where

$$P = I\hbar \qquad (2.3)$$

and I is the angular momentum operator with I^2 having $I(I+1)$ eigenvalues.

The magnetic dipole moment interacts with the applied magnetic field, B, with a classical energy defined as

$$U = -\mu.B \tag{2.4}$$

Quantum mechanically the Hamiltonian which defines this interaction is

$$\mathcal{H} = -\mu B_0 \tag{2.5}$$

If the magnetic field is aligned along the z-axis in the laboratory frame we see

$$\mathcal{H} = -\gamma \hbar I_z B_0 \tag{2.6}$$

where I_z is the nuclear spin operator component along the z-axis. The solutions of this Hamiltonian are multiples of the I_z eigenvalues and give $(2I+1)$ energy levels, calculated to be

$$E_m = \gamma \hbar B_0 m_I \tag{2.7}$$

where $m_I = -I, -I+1 \ldots . I-1, I$, with I being the nuclear spin quantum number.

The transitions between these energy levels should obey the magnetic selection rule ($\Delta m_I = \pm 1$ in the NMR case of ^{1}H where $I = {}^1/_2$) and can be calculated as

$$\Delta E = h\nu = \gamma \hbar B_0 = \frac{h}{2\pi} \gamma B_0 \tag{2.8}$$

with a rearrangement showing clearly the frequency associated with the transition is as that found classically (2.1).

The nuclear spin energy levels for nuclei in a magnetic field are well known for $I = ½$ and are easily formed for higher values of I.

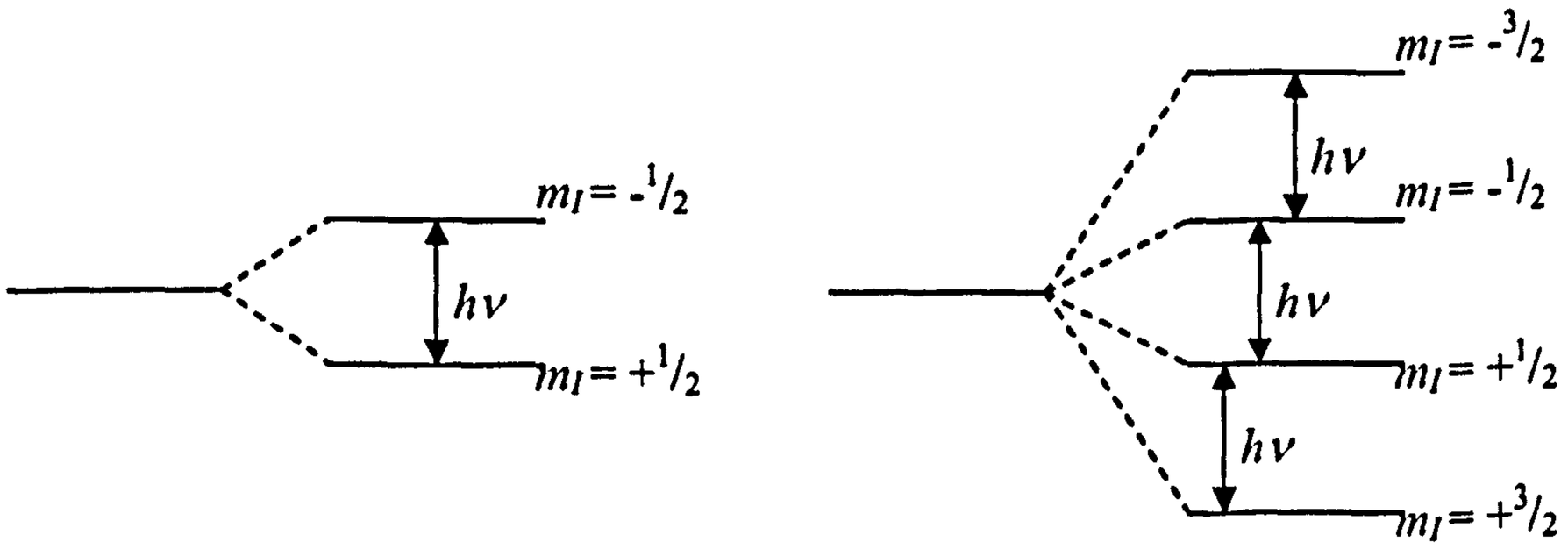

Figures 2.2a and b: Nuclear spin energy levels for nuclei with spin quantum number $I = ½$ and $^3/_2$, with transitions of energy $\gamma \hbar B_0$, and selection rule $\Delta m_I = \pm 1$ in the presence of magnetic field B_0.

The energy levels present due to the external magnetic field allow the detection of nuclei with $I \geq ½$ by the application of radiofrequency (RF) radiation. In NMR there is usually a permanent, static magnetic field applied to generate the splittings and new energy levels. In contrast, with quadrupolar nuclei, the energy levels between which transitions can occur are already present due to the nature of their charge distribution.

2.2 The quadrupolar nucleus

Nuclei with a spin quantum, I, greater than ½ are said to be quadrupolar; the charge distribution can be compared to that of two anti-parallel dipoles as in figure 2.3. The nucleus has an electric quadrupole moment, defined as the scalar quantity Q, which is indicative of the charge distribution. If $Q < 0$ the charge distribution is said to be oblate. If $Q > 0$ it is said to be prolate[1].

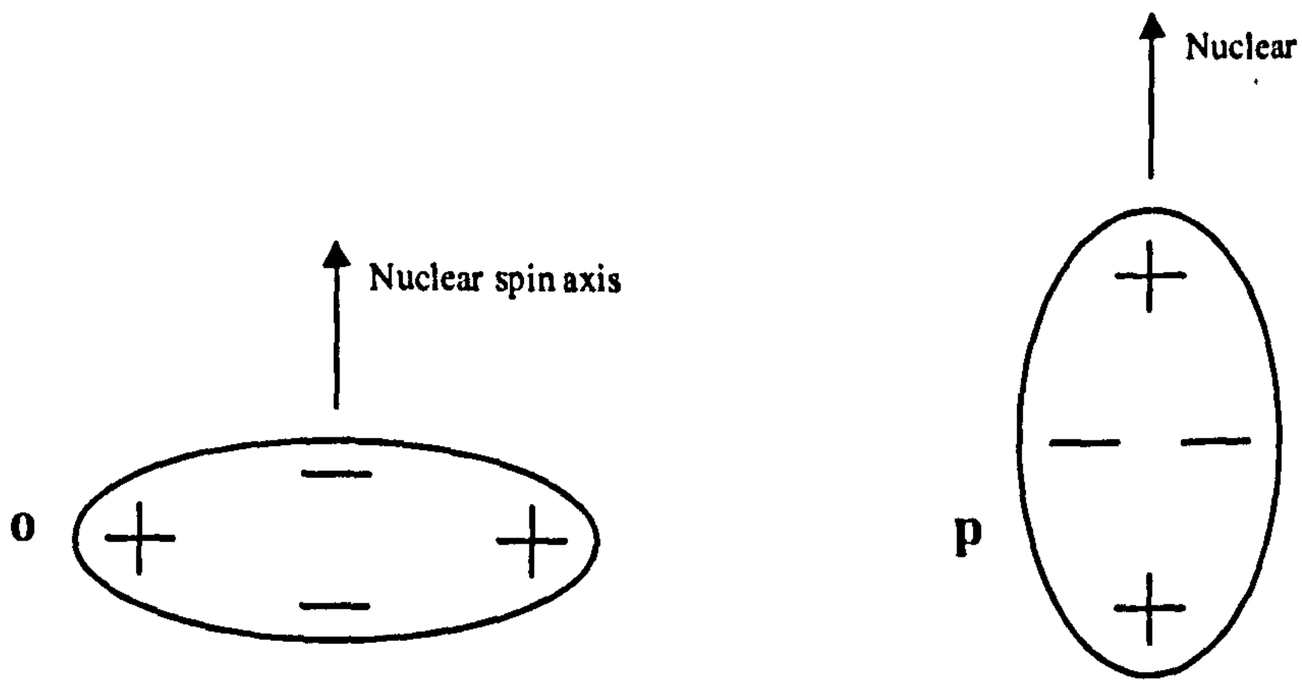

Figure 2.3: Oblate (o) and prolate (p) charge distribution.

Simply and classically viewed, a quadrupole placed in an electric field gradient (EFG) will have different energy levels at different orientations. The torque generated by the electric field gradient acting on the two electric dipoles in figure 2.3 leads to quadrupolar precession about the direction of the maximum electric field gradient, which is analogous to the precession induced by a magnetic field in NMR. The NQR precession has a frequency which is dependent on fixed nuclear conditions and not external parameters, unlike NMR, in which the static external magnetic field B_0 governs the frequencies. The quadrupolar interaction is electrical in nature, as opposed to NMR where it is magnetic, with the quadrupolar Hamiltonian describing the interaction of the charge distribution

with the electric field gradient, the eigenstates of which define the energy levels and the NQR frequencies corresponding to the transitions between these levels.
This chapter will discuss the factors which determine these frequencies and the processes that occur and equations that describe nuclear quadrupole resonance.

The NQR frequencies mainly depend on the quadrupole coupling constant and the asymmetry parameter, η. The quadrupole coupling constant is measured in Hz and is equal to e^2qQ/h where e is the charge on an electron, h is Planck's constant, Q is the nuclear electric quadrupole moment and q is the principal z-component of the electric field gradient tensor, the second derivative of V, the electrostatic potential at the nucleus. q is a tensor with three principal components, q_{xx}, q_{yy} and q_{zz}, along the Cartesian axes and it can be either negative or positive. We shall now present calculations of these NQR parameters and frequencies, for spin-$^3/_2$ and spin-1, being the values of I for ^{35}Cl and ^{14}N respectively - the two nuclei studied in this body of work. In some cases calculations and derivations for spin-$^1/_2$ will be stated for simplicity.

2.3 The quadrupolar Hamiltonian, the quadrupole moment and the electric field gradient

The quadrupolar Hamiltonian $\mathcal{H}_Q$ describes the interaction between the quadrupolar charge distribution and the electronic environment generated by the electric field gradient.

$$\mathcal{H}_Q = \frac{1}{6}\sum_{ij}\hat{V}_{ij}\hat{Q}_{ij} \qquad (2.9)$$

The electric field gradient is determined by the charge distribution about the nucleus being studied with the asymmetry parameter together with the EFG tensor depending on the orbital occupations of adjacent nuclei; the detailed equations relating these influences are discussed elsewhere[2]. The tensor which defines the EFG has nine components of the form

$$V_{ij} = \frac{\partial^2 V}{\partial x_i \partial x_j} = q_{ij} \qquad (2.10)$$

where $x_i, x_j = x, y$ or z and V is the electrostatic potential due to charge at the point (x, y, z), the nucleus being located at the origin. The tensor, q_{ij} has the irreducible components in the principal axis frame of reference,

$$V^0 = \frac{1}{2}eq \tag{2.11}$$

$$V^{\pm 1} = 0 \tag{2.12}$$

$$V^{\pm 2} = \frac{1}{2\sqrt{6}}eq\eta \tag{2.13}$$

These values are subject to the condition $q_{zz} \geq q_{yy} \geq q_{xx}$; q_{zz} is often denoted by q, the maximum principal component. In addition, Laplace's equation holds

$$q_{xx} + q_{yy} + q_{zz} = 0 \tag{2.14}$$

so the electric field gradient experienced at the nucleus is due to external charges only and the quantity

$$(q_{yy} - q_{xx})/q_{zz} = \eta \tag{2.15}$$

may be defined. η is the asymmetry parameter, a positive parameter lying between 0 and 1; it is a measure of the axial asymmetry of the electric field gradient; that is, in the case of axial symmetry, $\eta = 0$. Coupling of the quadrupolar nucleus in its different orientations with respect to the electric field gradient yields different energy levels. As these energy levels are determined by η as well as Q, we can garner information about the surrounding charges, and hence possible structural and electronic information.
The scalar quadrupole moment, Q, can be calculated[3] as

$$eQ = \int \rho_n r_n^2 \left(3\cos^2 \theta_{nI} - 1\right) d\tau_n \tag{2.16}$$

where $-e$ is the charge on an electron, ρ_n the nuclear charge density in volume element τ_n at a distance r_n from the center of the nucleus and θ_{nI} is the angle between the vector r_n and the nuclear spin axis (the axis of cylindrical symmetry in the laboratory frame) and

from which we can see that a spherical charge distribution would yield a quadrupole moment of zero. Q is usually measured in units of Barn (10^{-28} m^2), it being of a suitable order of magnitude to define the values commonly found.

The irreducible components of the traceless, symmetric second rank tensor[4] are

$$Q^0 = \frac{eQ}{I(2I-1)}\frac{1}{2}\left[3I_z^2 - I(I+1)\right] \tag{2.17}$$

$$Q^{\pm 1} = \frac{eQ}{I(2I-1)}\frac{\sqrt{6}}{4}\left[I_z I_\pm + I_z I_\pm\right] \tag{2.18}$$

$$Q^{\pm 2} = \frac{eQ}{I(2I-1)}\frac{\sqrt{6}}{4} I_\pm^2 \tag{2.19}$$

We can now expand (2.9) by use of (2.11 - 2.13) and (2.17 - 2.19) to find

$$\mathcal{H}_Q = \frac{e^2qQ}{4I(2I-1)}\left[3I_z^2 - I(I+1) + \frac{\eta}{2}(I_+^2 + I_-^2)\right] \tag{2.20}$$

in the principal axis frame of reference of the EFG, where I_z, I_+ and I_- are nuclear spin operators, I_+ and I_- being the raising and lowering operators corresponding to $\Delta m_I = +1$ and -1 respectively[4]. The eigenvalues of the Hamiltonian will give us $(2I + 1)$ quantized energy levels[5] from which the allowed transition frequencies can be calculated. Transitions between the energy levels defined by these eigenvalues will have a characteristic frequency for each type of nucleus, highly sensitive to the electronic environment, and measurement of these frequencies can help to identify a material, and in some cases allow calculation of quadrupole coupling constants and asymmetry parameters.

2.4 The matrix elements of the quadrupolar Hamiltonian

2.4.1 Axially symmetric field gradients

In an axially symmetric field gradient the matrix elements of the Hamiltonian[3] are

$$\langle m|\mathcal{H}_Q|m'\rangle = \frac{e^2qQ}{4I(2I-1)}\left[3m^2 - I(I+1)\right]\delta_{mm'} \tag{2.21}$$

where m is the magnetic quantum number with respect to the Z axis and δ is the Krönecker delta so

$$\delta_{mm'} = 0 \text{ when } m \neq m' \text{ and } \delta_{mm'} = 1 \text{ when } m = m' \tag{2.22}$$

Diagonal eigenvalues of I_Z give the energy levels to be

$$E_m = \frac{e^2qQ}{4I(2I-1)}\left[3m^2 - I(I+1)\right] \tag{2.23}$$

However, it is more usual for the EFG not to be axially symmetric, and we will now consider the $\eta \neq 0$ case for spin-$^3/_2$ and spin-1 nuclei.

2.4.2 Non-axially symmetric field gradients

2.4.2.1 Spin-$^3/_2$ nuclei

In the cases of an axially asymmetric field gradient for any half integral spin the matrix elements of $\mathcal{H}_Q$ are

$$\langle m|\mathcal{H}_Q|m\rangle = \frac{e^2qQ}{4I(2I-1)}\left[3m^2 - I(I+1)\right] \tag{2.24}$$

$$\langle m'|\mathcal{H}_Q|m\rangle = \frac{e^2qQ}{4I(2I-1)}\frac{\eta}{2} f_I(\pm m) f_I(\pm m)\delta_{m',m\pm 2} \tag{2.25}$$

where

$$f_I(m) = f_I(-m-1) = \left[(I-m)(I+m+1)\right]^{1/2} \tag{2.26}$$

For spin $I = {}^3/_2$ nuclei the following matrix is derived

$$\mathcal{H}_{3/2} = \frac{e^2qQ}{12}\begin{bmatrix} 3 & 0 & \sqrt{3}\eta & 0 \\ 0 & -3 & 0 & \sqrt{3}\eta \\ \sqrt{3}\eta & 0 & -3 & 0 \\ 0 & \sqrt{3}\eta & 0 & 3 \end{bmatrix} \tag{2.27}$$

It is clear that in the spherical case, where $\eta = 0$, $\mathcal{H}_Q$ is a traceless, diagonal operator in agreement with the easily visualized classical view of the interaction.

In this case where $\eta \neq 0$ there will be mixing of states with $\Delta m = 2$. Now the Hamiltonian matrix consists of two submatrices from which the secular equations can be calculated. For $I = {}^3/_2$ the secular equation is found[3]

$$E^2 - 3\eta^2 - 9 = 0 \tag{2.28}$$

where E is in units of A, where

$$A = \frac{e^2 qQ}{4I(2I-1)} \tag{2.29}$$

and the eigenvalues for $I = {}^3/_2$ are found to be

$$E_{\pm 1/2} = 3A\left(1+\frac{\eta}{3}\right)^{1/2} \tag{2.30}$$

and

$$E_{\pm 1/2} = -3A\left(1+\frac{\eta}{3}\right)^{1/2} \tag{2.31}$$

Secular equations for further half integer spin values can be similarly calculated and are detailed elsewhere[3,6].

The frequency of a transition is calculated as

$$\nu_Q(m \rightarrow m') = \frac{E_m - E_{m'}}{h} \tag{2.32}$$

so for spin-${}^3/_2$ nuclei, such as ^{35}Cl,

$$\nu_Q = \frac{1}{2}\frac{e^2 qQ}{h}\left(1+\frac{\eta^2}{3}\right)^{1/2} \tag{2.33}$$

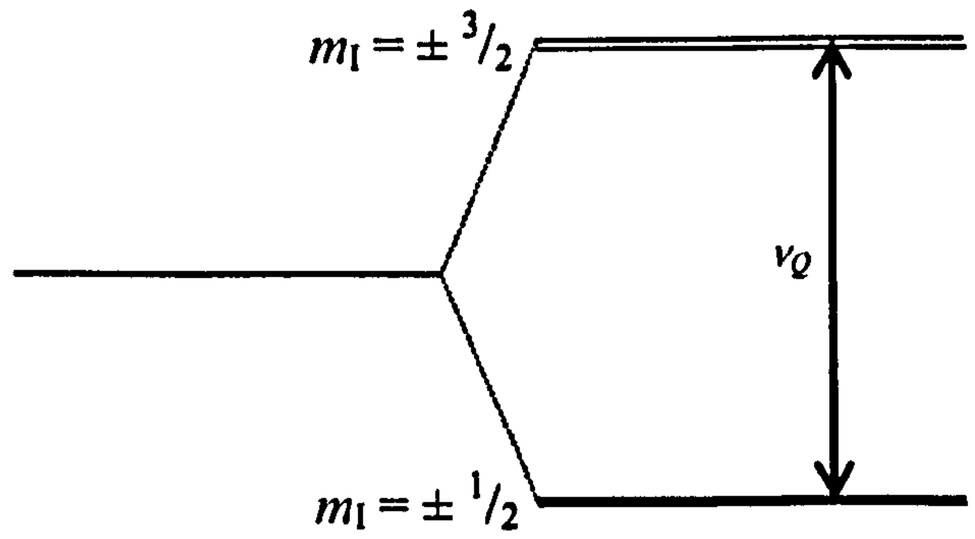

Figure 2.4: Energy levels for a spin-${}^3/_2$ nucleus.

Only one quadrupolar frequency, ν_Q, is observed, corresponding to a transition between the doubly degenerate energy levels. This single transition means that a pure zero field

NQR experiment alone cannot yield both the asymmetry parameter and quadrupole coupling constant. The application of a second field however, can solve this problem.

2.4.2.2. Zeeman splitting

Kramer observed that the degeneracy[3] of half integral spin systems cannot simply be lifted by the presence of an electric field. However, the presence of a weak magnetic field will lift the degeneracy, bringing about a Zeeman splitting. The influence of the applied magnetic field removes the so called Kramers degeneracy, giving four energy levels in the case of spin-$^3/_2$. This allows determination of the asymmetry parameter and the quadrupole coupling constant which was previously unobtainable from experimental frequency measurements.

If the electric field gradient is axially symmetric the application of a magnetic field, B_0, with θ and ϕ angles describing its position with relative to the principal axis system, there is an additional term to the quadrupolar Hamiltonian due to the interaction of the magnetic dipole moment, the energy of which is given[3] by

$$\mathcal{H}_M = -\hbar\gamma B_0\left(I_z\cos\theta + I_x\sin\theta\cos\phi + I_y\sin\theta\sin\phi\right) \tag{2.34}$$

with the assumption that $\hbar\gamma B_0 << e^2qQ$ so that the net Hamiltonian is

$$\mathcal{H} = \mathcal{H}_Q + \mathcal{H}_M \tag{2.35}$$

Each degenerate pair is split into two energy levels

$$E_{\pm m} = A[3m^2 - I(I+1)] \mp m\hbar\gamma B_0\cos\theta \tag{2.36}$$

so there are now 4 energy levels for a spin-$^3/_2$ nucleus with $\eta = 0$ in a constant magnetic field. The frequencies which can now be observed can be calculated as

$$\nu_m^{\pm} = \frac{3A}{h}\left(2|m|+1\right) \pm \gamma B_0\cos\theta \tag{2.37}$$

When $\eta \neq 0$ the equations become more complex and will not be utilized or discussed within this work; they are detailed elsewhere[3]. The secular equations and energy levels for higher half integral spin nuclei have been solved for a number of values of η, together with the intensities and Zeeman splittings[3,6].

2.4.2.3 Spin-1 nuclei

For nuclei with $I = 1$, the quadrupolar Hamiltonian in the principal axis frame of reference can be defined as

$$\mathcal{H} = I_x^2 A' + I_y^2 B' + I_z^2 C' \tag{2.38}$$

$$A' = \frac{eQ}{2I(2I-1)} V_{zz} = 2A \tag{2.39}$$

$$B' = \frac{eQ}{2I(2I-1)} V_{YY} = -A(1-\eta) \tag{2.40}$$

$$C' = \frac{eQ}{2I(2I-1)} V_{XX} = -A(1+\eta) \tag{2.41}$$

where A is as defined in equation (2.29).

The following matrix describes the $I = 1$ states

$$\mathcal{H}_1 = \frac{e^2 qQ}{4} \begin{bmatrix} 1 & 0 & \eta \\ 0 & -2 & 0 \\ \eta & 0 & 1 \end{bmatrix} \tag{2.42}$$

In order to diagonalise the Hamiltonian we select linear combinations of the magnetic spin wavefunctions

$$\Psi_+ = \Psi_y = \frac{1}{\sqrt{2}} (|+1\rangle + |-1\rangle) \tag{2.43}$$

$$\Psi_- = \Psi_x = \frac{1}{\sqrt{2}} (|+1\rangle - |-1\rangle) \tag{2.44}$$

$$\Psi_0 = \Psi_z = |0\rangle \tag{2.45}$$

with application of the Hamiltonian (2.20) giving the three energy levels of the states

$$E_+ = \frac{\langle \Psi_+ | \mathcal{H}_Q | \Psi_+ \rangle}{\langle \Psi_+ | \Psi_+ \rangle}$$

$$= \frac{e^2 qQ}{4} \frac{1}{2} \left(\langle + | \mathcal{H}_Q | + \rangle + \langle - | \mathcal{H}_Q | - \rangle + \langle + | \mathcal{H}_Q | - \rangle + \langle - | \mathcal{H}_Q | + \rangle \right)$$

$$= \frac{e^2 qQ}{4} \frac{1}{2} \left(3\langle + | I_z^2 | + \rangle + 3\langle - | I_z^2 | - \rangle - 2 - 2 + \frac{1}{2}\eta \left[\langle + | I_+^2 | - \rangle + 3\langle - | I_-^2 | + \rangle \right] \right) \quad (2.46)$$

$$= \frac{e^2 qQ}{4} \frac{1}{2} \left(3 + 3 - 4 + \frac{1}{2}\eta \left[\sqrt{2}\langle + | I_+ | 0 \rangle + \sqrt{2}\langle - | I_- | 0 \rangle \right] \right)$$

$$= \frac{e^2 qQ}{4} \frac{1}{2} \left(2 + \frac{1}{2}\eta [2 + 2] \right)$$

$$= \frac{e^2 qQ}{4} (1 + \eta)$$

$$E_- = \frac{\langle \Psi_- | \mathcal{H}_Q | \Psi_- \rangle}{\langle \Psi_- | \Psi_- \rangle}$$

$$= \frac{e^2 qQ}{4} \frac{1}{2} \left(\langle + | \mathcal{H}_Q | + \rangle + \langle - | \mathcal{H}_Q | - \rangle - \langle + | \mathcal{H}_Q | - \rangle + \langle - | \mathcal{H}_Q | + \rangle \right)$$

$$= \frac{e^2 qQ}{4} \frac{1}{2} \left(3\langle + | I_z^2 | + \rangle + 3\langle - | I_z^2 | - \rangle - 2 - 2 - \frac{1}{2}\eta \left[\langle + | I_+^2 | - \rangle + 3\langle - | I_-^2 | + \rangle \right] \right) \quad (2.47)$$

$$= \frac{e^2 qQ}{4} \frac{1}{2} \left(3 + 3 - 4 - \frac{1}{2}\eta \left[\sqrt{2}\langle + | I_+ | 0 \rangle + \sqrt{2}\langle - | I_- | 0 \rangle \right] \right)$$

$$= \frac{e^2 qQ}{4} \frac{1}{2} \left(2 - \frac{1}{2}\eta [2 + 2] \right)$$

$$= \frac{e^2 qQ}{4} (1 - \eta)$$

$$E_0 = \frac{\langle \Psi_0 | \mathcal{H}_Q | \Psi_0 \rangle}{\langle \Psi_0 | \Psi_0 \rangle}$$

$$= \frac{e^2 qQ}{4} \left(\langle 0 | \mathcal{H}_Q | 0 \rangle \right)$$

$$= \frac{e^2 qQ}{4} \left(3\langle 0 | I_z^2 | 0 \rangle - 2 - \frac{1}{2}\eta \left[\langle 0 | I_+^2 | 0 \rangle + \langle 0 | I_-^2 | 0 \rangle \right] \right) \quad (2.48)$$

$$= \frac{e^2 qQ}{4} \left(-2 - \frac{1}{2}\eta \left[\sqrt{2}\langle 0 | I_+ | + \rangle + \sqrt{2}\langle 0 | I_- | - \rangle \right] \right)$$

$$= \frac{e^2 qQ}{4} (-2 - 0)$$

$$= -\frac{e^2 qQ}{2}$$

An RF pulse applied on resonance can induce the three following transitions between the energy levels yielding the well known NQR frequencies

$$E_{+} \; E_{-} \quad \nu_0 = \frac{1}{2}\frac{e^2qQ}{h}\eta \tag{2.49}$$

$$E_{+} \; E_0 \quad \nu_+ = \frac{3}{4}\frac{e^2qQ}{h}\left(1+\frac{\eta}{3}\right) \tag{2.50}$$

$$E_{-} \; E_0 \quad \nu_- = \frac{3}{4}\frac{e^2qQ}{h}\left(1-\frac{\eta}{3}\right) \tag{2.51}$$

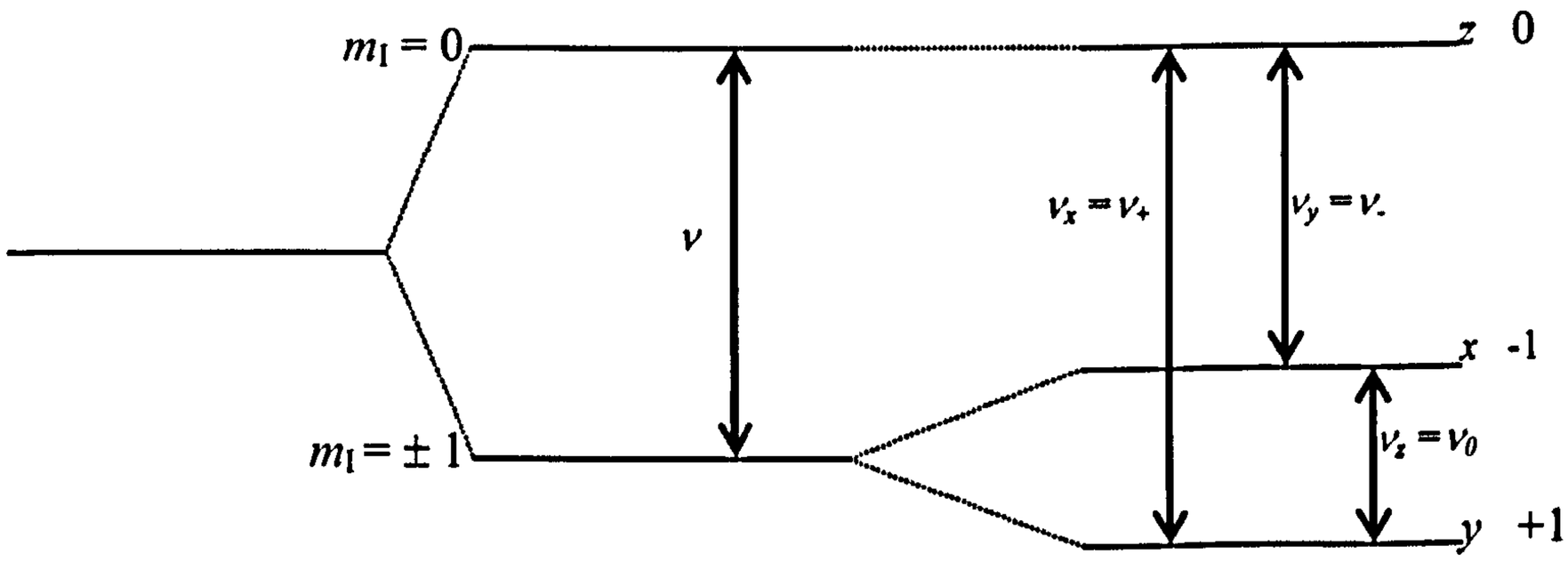

Figure 2.5: Energy levels and transitions in various environments when $I = 1$.

When there is axial symmetry and $\eta = 0$, $\nu_x = \nu_y$, there is no splitting of the $m_I = \pm 1$ energy level and only one allowed transition. In the general case of a quadrupolar nucleus such as ^{14}N, this level is usually split and three energy levels are present (figure 2.5) and three possible transitions are observed.

Three transitions are therefore commonly observed in NQR for each non-equivalent $I = 1$ nucleus generating three frequencies, ν_+, ν_- and ν_0; with the latter being at a low RF frequency and often difficult to observe; it corresponds to a transition of $\Delta m = 2$, a previously forbidden mixing of states. However, observation of the two upper lines

enables deduction of the lower frequency ν_0 line as well as the asymmetry parameter, η, and the quadrupole coupling constant from equations (2.50) and (2.51). These NQR parameters can also be calculated theoretically, as shown in chapter 7, and the QCC can also be found from solid state NMR spectra in cases where the quadrupole splitting value is observable. How the radiofrequency radiation excites the transitions between energy levels and the process by which they are measured is discussed in the next section.

2.5 The effect of radiofrequency

In order to observe the transition frequencies the nuclei must first be perturbed from their equilibrium state. The pulses of RF radiation applied are similar to those in NMR and similar equations corresponding to the processes which occur can be derived although they are somewhat more complicated in NQR, particularly for the higher spin nuclei. We will first look at the classical view and then go on to quantum mechanical derivations for various conditions.

2.5.1 The rotating frame and the classical view

In order to simplify and better understand the effects of RF on nuclei, the rotating frame vector model must be introduced. Let the Cartesian axes of the principal components of the EFG in the stationary laboratory frame be as below, the z component is vertical and x and y are perpendicular to it. The rotating frame axes are denoted x', y' and z', with z' in the same direction as z and x' and y' perpendicular to each other, rotating about the z' axis (figure 2.6).

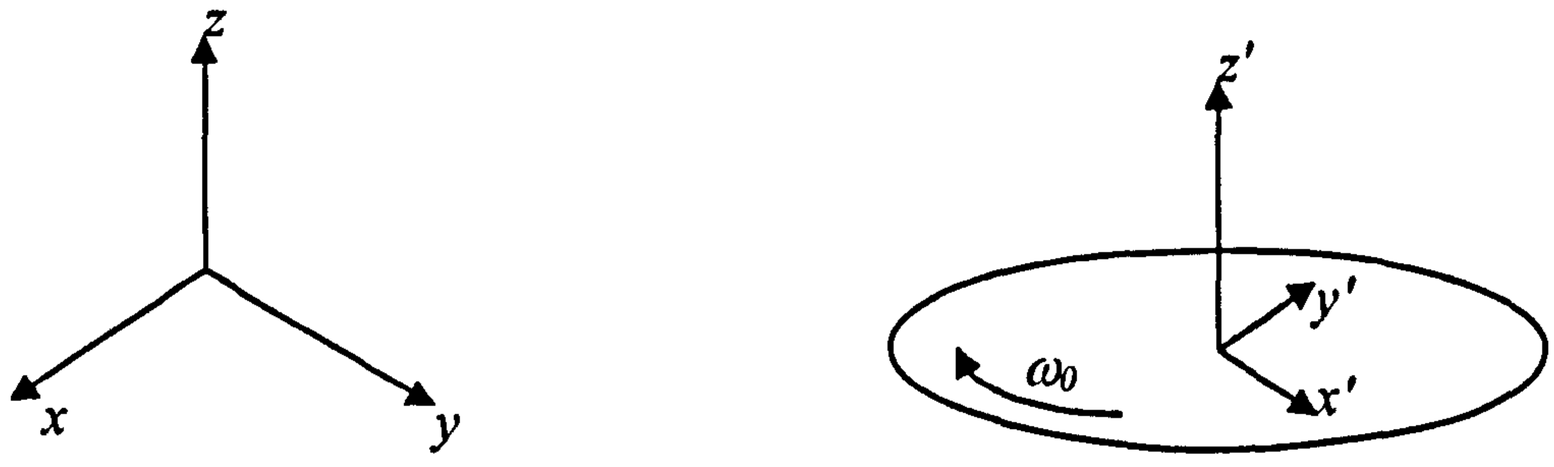

Figure 2.6: The stationary Cartesian axes, x, y and z and the rotating frame with axes x', y' and z'.

In a frame of reference rotating about the z axis at the excitation frequency, ω_0, the effective frequency 'seen' by the spins in this rotating frame is $\omega_0 - \omega_Q$, where ω_Q is the NQR frequency. At resonance $\omega_0 = \omega_Q$, and the resultant magnetisation, M, appears stationary.

If an RF field, B_1, rotating about the z axis is now applied at resonance, we can represent this in the rotating frame as a vector along (say) x; the effective field experienced by M is now B_1 about which it precesses at an angular frequency, ω_1, known as the nutation frequency, so changing the angle between the z axis and M. Hence

$$\omega_1 = \gamma B_1 \tag{2.52}$$

where γ is the gyromagnetic ratio for the nucleus[7].

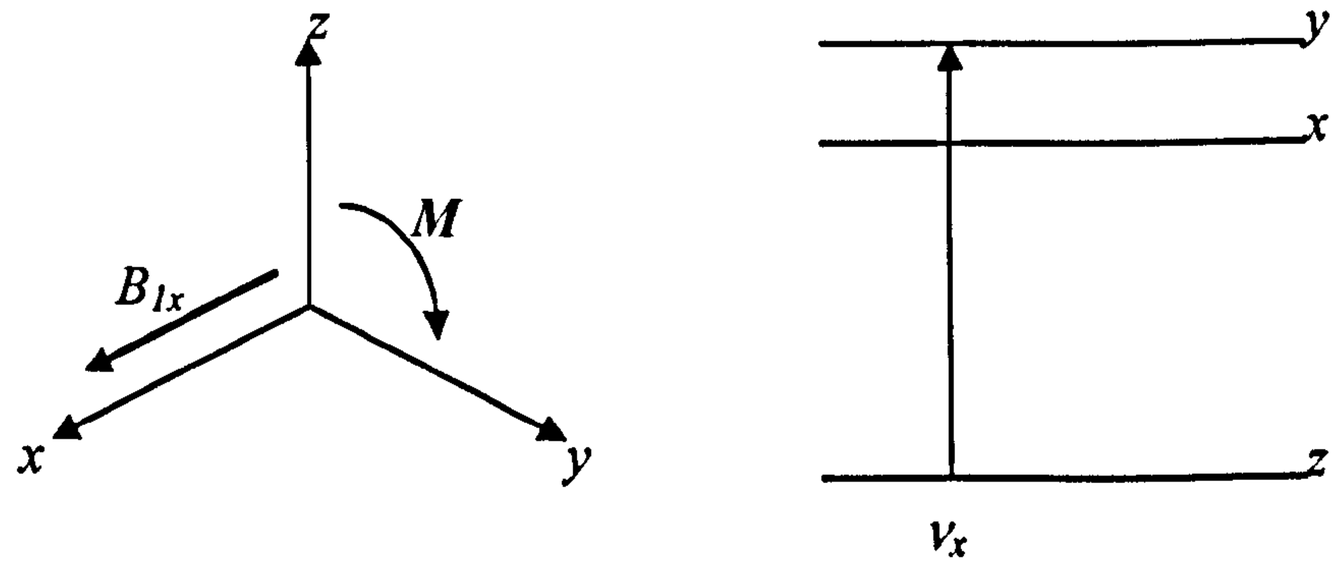

Figure 2.7: An RF field applied along the x axis rotates M from z to y, corresponding to the ν_+ (ν_x) transition of a spin-1 nucleus.

This is a classical model for the process. A quantum mechanical model begins by assuming that before a pulse is applied, the spins occupy their energy levels according to the Boltzmann distribution so that at moderate temperatures there are more in the lower energy level. When the resonant B_1 field is applied along one axis (figure 2.7), spins can absorb energy and jump to the higher level, corresponding to the applied frequency, and on removal of the B_1 pulse they return back to thermal equilibrium by a process known as spin-lattice relaxation.

This view is analogous to that of NMR, where a transition between the $m_I = +^1/_2$ and $-^1/_2$ energy levels, induced by a static magnetic field, occurs. We now detail this effect of the RF pulse in an NMR experiment.

2.5.2 The interaction of spins with the rotating RF field, $I = ½$ - the NMR case

In a rotating field, the total magnetic field, $B(t)$, rotating with angular velocity ω_z is

$$B(t) = iB_1 \cos\omega_z t + jB_1 \sin\omega_z t + kB_0 \tag{2.53}$$

where B_1 is the applied field and B_0 is any static field present and i, j, and k are the unit vectors corresponding the x, y and z axes respectively. The time-dependent Schrödinger equation[8] is found to be

$$-\frac{\hbar}{i}\frac{\partial\Psi}{\partial t} = -\mu.B\Psi = -\gamma\hbar\left[B_0 I_z + B_1\left(I_x \cos\omega_z t + I_y \sin\omega_z t\right)\right]\Psi \tag{2.54}$$

Using the relationships

$$I_{x'} \equiv e^{-iI_z\theta} I_x e^{iI_z\theta} = I_x \cos\theta + I_y \sin\theta \tag{2.55}$$

$$I_{y'} \equiv e^{-iI_z\theta} I_x e^{iI_z\theta} = -I_x \sin\theta + I_y \cos\theta \tag{2.56}$$

$$I_{z'} \equiv e^{-iI_z\theta} I_x e^{iI_z\theta} = I_z \tag{2.57}$$

the Hamiltonian can be expressed as

$$\mathcal{H} = -\gamma\hbar\left(B_0 I_z + B_1 e^{-i\omega_z t I_z} I_x e^{i\omega_z t I_z}\right) \tag{2.58}$$

We separate I_x from the operator containing the I_z to let it act on Ψ by setting

$$\Psi' = e^{i\omega_z t I_z}\Psi \text{ or } \Psi = e^{-i\omega_z t I_z}\Psi' \tag{2.59}$$

indicating the rotation of Ψ through to Ψ' by an angle of $\omega_z t$. So,

$$\frac{\partial\Psi}{\partial t} = -i\omega_z I_z e^{-i\omega_z t I_z}\Psi' + e^{-i\omega_z t I_z}\frac{\partial\Psi'}{\partial t} \tag{2.60}$$

Substitution of these terms into the original Schrödinger equation and multiplication by $\exp(i\omega_z t I_z)$ gives

$$-\frac{\hbar}{i}\frac{\partial\Psi}{\partial t} = -\left[\hbar\left(\omega_z + \gamma B_0\right)I_z + \gamma\hbar B_1 I_x\right]\Psi' \tag{2.61}$$

removing the time dependence of $B_1(t)$.

At resonance, $\omega_z \approx -\gamma B_0$. The rotationally transformed Hamiltonian $\mathcal{H}'$ is defined as

$$\mathcal{H}' = -\left[\left(\hbar\omega_z + \gamma\hbar B_0\right) I_z + \gamma\hbar B_1 I_x\right] \tag{2.62}$$

so we can solve the rotationally transformed Schrödinger equation (2.61)

$$\Psi'(t) = e^{-(i/\hbar)\mathcal{H}'t}\Psi'(0) \tag{2.63}$$

and by use of (2.59) we achieve a solution of the original Schrödinger equation in the presence of a rotating field

$$\Psi = e^{-i\omega_z t I_z} e^{-(i/\hbar)\mathcal{H}'t}\Psi'(0) \tag{2.64}$$

and we see that at $t = 0$ $\Psi(0) = \Psi'(0)$.

We can now calculate the time dependence of the expectation value of the x-component of the magnetic moment, $\langle\mu_x\rangle$. Assuming B_1 is on resonance, we can say

$$\mathcal{H}' = -\gamma\hbar B_1 I_x \tag{2.65}$$

By use of 2.64 in 2.65 we find

$$\begin{aligned} \langle\mu_z(t)\rangle &= \int\Psi^*(t)\mu_z\Psi(t)d\tau \\ \langle\mu_z(t)\rangle &= \gamma\hbar\int\left[e^{-i\omega_z t I_z} e^{i\gamma B_1 I_x t}\Psi(0)\right]^* I_z\left[e^{-i\omega_z t I_z} e^{i\gamma B_1 I_x t}\Psi(0)\right]d\tau \end{aligned} \tag{2.66}$$

If

$$\omega_1 \equiv \gamma B_1 \tag{2.67}$$

and I_x and I_z are Hermitian

$$\begin{aligned} \langle\mu_z(t)\rangle &= \gamma\hbar\int\Psi^*(0)e^{-i\omega_1 t I_x} e^{i\omega_z t I_z} I_z e^{-i\omega_z t I_z} e^{i\omega_1 t I_x}\Psi d\tau \\ \langle\mu_z(t)\rangle &= \gamma\hbar\int\Psi^*(0)e^{-i\omega_1 t I_x} I_z e^{i\omega_1 t I_x}\Psi d\tau \end{aligned} \tag{2.68}$$

by use of 2.55 - 2.57 we find

$$e^{-i\omega_1 t I_x} I_z e^{i\omega_1 t I_x} = -I_y \sin\omega_1 t + I_z \cos\omega_1 t \tag{2.69}$$

Substitution of 2.68 gives

$$\langle\mu_z(t)\rangle = -\langle\mu_y(0)\rangle\sin\omega_1 t + \langle\mu_z(0)\rangle\cos\omega_1 t \tag{2.70}$$

When at time $t = 0$ the magnetization lies along the z-axis, $\langle\mu_y(0)\rangle = 0$ and so

$$\langle\mu_z(t)\rangle = \langle\mu_z(0)\rangle\cos\gamma B_1 t \tag{2.71}$$

So this fits the classical picture of the oscillation of magnetization in time, precessing about B_1. However, this calculation does yield an indefinite oscillation as it does not include spin-spin or spin-lattice interactions leading to relaxation.

2.5.3 The interaction of spins with the rotating RF field, $I > {}^1/_2$ - the NQR case

2.5.3.1 The axially symmetric field gradient general case

The interaction of the quadrupolar nucleus with the applied RF field is given by the time dependent Hamiltonian

$$\mathcal{H}_M(t) = -\gamma\hbar[B_X(t)I_X + B_Y(t)I_Y + B_Z(t)I_Z] \tag{2.72}$$

$B_X(t)$, $B_Y(t)$, $B_Z(t)$ are the components of the RF magnetic field $2B_1\cos\omega t$ in the principal axis frame of reference. The matrix elements of the spin angular momentum are described by

$$\langle m|I_Z|m'\rangle = m\delta_{mm'} \tag{2.73}$$

$$\langle m|I_X \pm iI_Y|m'\rangle = \left[(I \pm m)(I \mp m+1)\right]^{1/2}\delta_{m\mp1,m'} \tag{2.74}$$

The X and Y components of the RF field induce $\Delta m = \pm 1$ transitions, whilst $\Delta m = 0$ transitions, corresponding to no change in energy, are induced by the Z component. In this case of axial symmetry, there are $(I - ½)$ transitions observed for half integral spins, meaning that one transition would be observed for nuclei with $I = {}^3/_2$ whilst a spin-${}^1/_2$ nucleus would yield no NQR frequency. Integral spins can produce I transition frequencies.

2.5.3.2 The response of quadrupolar nuclei

We shall now consider the response to pulses of RF radiation in the case of spin-${}^3/_2$ nuclei when $\eta = 0$. We can say that a Gaussian distribution, $g(\omega_0')$ of frequencies ω_0' is assumed[3] so that

$$g(\omega_Q') = \frac{\delta}{\sqrt{2\pi}}\exp\left[-\frac{(\omega_Q' - \omega_Q)^2}{2\delta^2}\right] \tag{2.75}$$

where ω_Q is the frequency, given by

$$\omega_m = \frac{3A}{\hbar}(2|m|+1) \tag{2.76}$$

and δ is the root mean square width, taking into account line broadening, which will be discussed later. Relaxation effects are neglected. With the radiofrequency field

generated by the pulses perpendicular to the symmetry axis, we find the terms in (2.72) to be

$$B_X = 2B_1 \cos \omega_Q t \tag{2.77}$$

$$B_Y = 0 \tag{2.78}$$

$$B_Z = 0 \tag{2.79}$$

where the amplitude of the field is B_1 and its frequency ω_Q. We shall set the conditions to be

$$t_w << \frac{1}{\delta} \tag{2.80}$$

and

$$\tau >> \frac{1}{\delta} \tag{2.81}$$

where t_w is the pulse width and t the time between pulses (which are of equal length) with all nuclear spins behaving identically during the pulse. We can write the wavefunction at time t for a given spin as

$$\psi = \sum_{m=-3/2}^{3/2} C_m(t)\psi_m e^{-iE_m t/\hbar} \tag{2.82}$$

where

$$\sum_{-3/2}^{3/2} |C_m(t)|^2 = 1 \tag{2.83}$$

and the wavefunctions ψ_m correspond to the eigenstates of equation 2.21 and the energy levels calculated in 2.23. Preceding the first pulse, at $t = 0$, there is thermal equilibrium and

$$\left|C_{3/2}(0)\right|^2 = \left|C_{-3/2}(0)\right|^2 = \frac{1}{4} e^{-\hbar\omega_Q/2kT} \tag{2.84}$$

$$\left|C_{1/2}(0)\right|^2 = \left|C_{-1/2}(0)\right|^2 = \frac{1}{4} e^{+\hbar\omega_Q/2kT} \tag{2.85}$$

We write the time dependent Schrödinger equation as

$$i\hbar\dot{\psi} = \mathcal{H}\psi = (\mathcal{H}_0 + \mathcal{H}_1)\psi \tag{2.86}$$

where

$$\mathcal{H}_0 = \frac{\hbar\omega_Q'}{2}(3I_z^2 - \mathbf{I}^2) \tag{2.87}$$

where ω_Q' is the resonance frequency and

$$\mathcal{H}_1 = -2\gamma\hbar I_x B_1 \cos\omega_Q t \tag{2.88}$$

Removal of the RF perturbation gives

$$i\hbar\psi = \mathcal{H}_0\psi \tag{2.89}$$

We can now solve the Hamiltonian both in the presence of the pulse and following its removal

$$\psi(t+t_0) = \sum_{m=-3/2}^{3/2} \psi_m C_m(t_0) e^{-iE_m t/\hbar} \tag{2.90}$$

$$\psi(t+t_0) = \sum_{m=-3/2}^{3/2} \psi_m C_m(t_0+t) e^{-iE_m t/\hbar} \tag{2.91}$$

with

$$E_{\pm 3/2} = -\frac{\hbar\omega_Q'}{2} \tag{2.92}$$

and

$$E_{\pm 3/2} = +\frac{\hbar\omega_Q'}{2} \tag{2.93}$$

The relation between the two events holds

$$C_m(t_0+t) = RC_m(t_0) \tag{2.94}$$

with the matrix

$$R = \begin{vmatrix} \cos\frac{\sqrt{3}\omega_1 t}{2} & 0 & i\sin\frac{\sqrt{3}\omega_1 t}{2} & 0 \\ 0 & \cos\frac{\sqrt{3}\omega_1 t}{2} & 0 & i\sin\frac{\sqrt{3}\omega_1 t}{2} \\ i\sin\frac{\sqrt{3}\omega_1 t}{2} & 0 & \cos\frac{\sqrt{3}\omega_1 t}{2} & 0 \\ 0 & i\sin\frac{\sqrt{3}\omega_1 t}{2} & 0 & \cos\frac{\sqrt{3}\omega_1 t}{2} \end{vmatrix} \tag{2.95}$$

Assuming a uniform RF field across the sample, for simplicity, we can set

$$\sqrt{3}\omega_1 t_w = \xi \tag{2.96}$$

for a given pulse width, t_w.

We can now calculate the expectation values of the magnetization in each direction and at time $t > t_w$ we find

$$< I_x >= \sqrt{3}\omega_Q' \hbar \sin\xi \sin\omega_Q' t \tag{2.97}$$

$$< I_y >= 0 \tag{2.98}$$

$$< I_z >= 0 \tag{2.99}$$

As would be expected there is only magnetization in the x-direction, found with use of (2.75) to be

$$M_x = \frac{\sqrt{3}N\omega_Q \hbar^2 \gamma}{4kT} \sin\xi e^{-\delta^2 t^2/2} \sin\omega_Q t \tag{2.100}$$

For a sample containing N spins we can find the voltage induced in the NQR solenoid following a pulse to be

$$\Delta V_x = An\frac{dM_x}{dt} = \frac{\sqrt{3}AnN\omega_Q \hbar^2 \gamma}{4kT} \sin\xi \cos\omega_Q t e^{-\delta^2 t^2/2} \tag{2.101}$$

where A is the cross-sectional area of the cylindrical solenoid and n is the number of turns. In a two pulse sequence the voltage induced can be calculated as

$$\Delta V_x = \frac{\sqrt{3}AnN\omega_Q \hbar^2 \gamma}{4kT} \left[\begin{array}{l} \sin\xi \cos^2\frac{\xi}{2} \cos\omega_Q t e^{-\delta^2 t^2/2} + \\ \sin\xi \cos\xi \cos\omega_Q (t-\tau) e^{-\delta^2 (t-\tau)^2/2} \\ -\sin\xi \sin^2\frac{\xi}{2} \cos\omega_Q (t-2\tau) e^{-\delta^2 (t-2\tau)^2/2} \end{array} \right] \tag{2.102}$$

giving a maximum echo signal at $t = 2\tau$ corresponding to the third term in the above equation and in agreement with the classical model. These voltage calculations can be applied to quadrupolar nuclei of any spin by substitution of the $\sqrt{3}$ term by $\left[(I-|m|)(I+|m|+1)\right]^{1/2}$ in equation (2.95) onwards provided that $\eta = 0$. Similar equations for the nuclear response in a small magnetic field are detailed elsewhere[9].

2.6 Transition probabilities

Having determined the energy levels between which transitions can occur and the effects of RF pulses on the nuclei, we must now discuss the probabilities of these transitions occurring. We will first consider the simple NMR case for spin-$^1/_2$.

2.6.1 A simple 2 level system

In a sample of certain mass there will be a total of N spins, which can be found in the $m = +^1/_2$ or $m = -^1/_2$ states, which will have N_+ and N_- spins in each state respectively. On the application of an RF pulse a transition may be induced, changing the populations of each state. The probability per second of inducing a transition from state i to state j is denoted as W_{ij}.

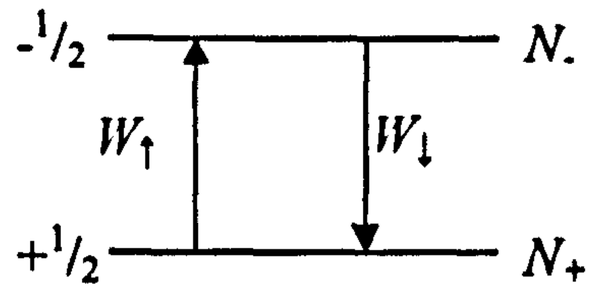

Figure 2.8: Transitions between states +½ and -½ with their associated populations and transition probabilities.

The rate of change of the population N_+ is

$$\frac{dN_+}{dt} = N_-W_\downarrow - N_+W_\uparrow \tag{2.103}$$

Introducing the well known formula for the probability per second $P_{a\to b}$ of a transition from state a to state b, with energies E_a and E_b respectively, due to a time dependent interaction $V(t)$ we state

$$P_{a\to b} = \frac{2\pi}{\hbar}\left|(b|V|a)\right|^2 \delta(E_a - E_b - \hbar\omega) \tag{2.104}$$

We know that

$$\left|(a|V|b)\right|^2 = \left|(b|V|a)\right|^2 \tag{2.105}$$

so that the rate on population change in each direction is equal and so

$$W_\downarrow = W_\uparrow \equiv W \tag{2.106}$$

We can now write

$$\frac{dN_+}{dt} = W(N_- - N_+) \tag{2.107}$$

We know that the total population is

$$N = N_+ + N_- \tag{2.108}$$

and we introduce the population difference,

$$n = N_- - N_+ \tag{2.109}$$

so we can now say

$$N_+ = \frac{1}{2}(N+n) \tag{2.110}$$

and

$$N_- = \frac{1}{2}(N-n) \tag{2.111}$$

We now find

$$\frac{dn}{dt} = -2Wn \tag{2.112}$$

solved as

$$n = n(0)e^{-2Wt} \tag{2.113}$$

As the populations of each state change due to transitions, the rate of energy absorbed by the system is written as

$$\frac{dE}{dt} = N_+W\hbar\omega - N_-W\hbar\omega = W\hbar\omega n \tag{2.114}$$

We observe that there must be a population difference, i.e. $n \neq 0$, for a net absorption of energy. The above result would indicate that resonant absorption of energy would cease as a zero value of n was reached and a zero probability (with no magnetic field applied) would result in no population change. In reality, once the spins have aligned themselves with the magnetic field, following its application, the populations change but the system must then lose energy as they relax back to equilibrium. The energy is transferred to another system - the lattice. The lattice acts as a spin reservoir, absorbing the energy transferred through molecular motions such as rotations, until equilibrium is reached at

which the relative populations N_+/N_- correspond to the temperature T of the lattice. At this equilibrium point, the relative populations of each state are

$$\frac{N_-^0}{N_+^0} = e^{-\Delta E/kT} = e^{-\gamma\lambda B_0/kT} \qquad (2.115)$$

We now introduce transition probabilities relating to the coupling of spins with the lattice system. If $W_\uparrow$ be the probability per second of a transition from $+^1/_2$ to $-^1/_2$ states and $W_\downarrow$ the reverse then

$$\frac{dN_+}{dt} = W_\downarrow N_- - W_\uparrow N_+ \qquad (2.116)$$

The transitions probabilities are now unequal and as the rate of change of N_+ population is zero at equilibrium, we can state that

$$\frac{N_-^0}{N_+^0} = \frac{W_\uparrow}{W_\downarrow} \qquad (2.117)$$

and find

$$\frac{W_\downarrow}{W_\uparrow} = e^{\gamma\lambda B_0/kT} \qquad (2.118)$$

Now, transitions can only occur when a simultaneous transition occurs in the lattice system, in order to conserve energy (figure 2.9).

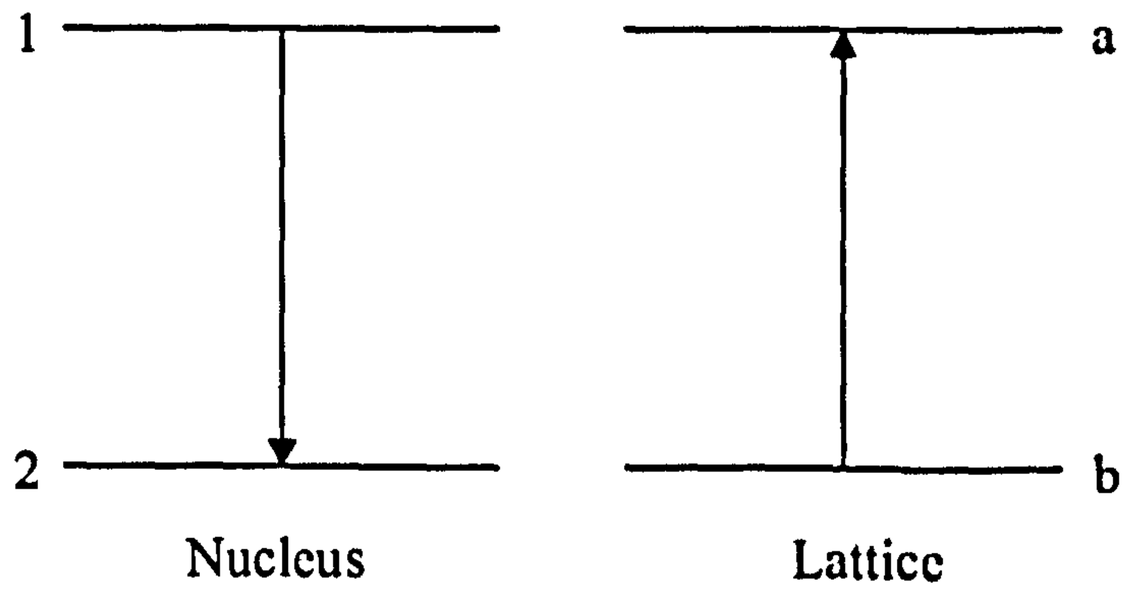

Figure 2.9: An allowed transition event conserving energy within the nuclear spin and lattice systems.

Now we find the number of transitions per second to be

$$N_1 N_b W_{1b\to 2a} \qquad (2.119)$$

with the transition probability $W_{1b\to 2a}$ being that of the allowed condition.

In the steady state

$$N_1 N_b W_{1b\to 2a} = N_2 N_a W_{2a\to 1b} \tag{2.120}$$

and as

$$W_{1b\to 2a} = W_{2a\to 1b} \tag{2.121}$$

at thermal equilibrium

$$\frac{N_1}{N_2} = \frac{N_a}{N_b} \tag{2.122}$$

and we can find

$$W_{\uparrow} = N_a W_{2a\to 1b} \tag{2.123}$$

and

$$W_{\downarrow} = N_b W_{1b\to 2a} = N_b W_{2a\to 1b} \tag{2.124}$$

so it is clear that the two transition probabilities are not equal. Substituting 2.110 and 2.111 into 2.112 we can write

$$\frac{dn}{dt} = N(W_{\downarrow} - W_{\uparrow}) - n(W_{\downarrow} + W_{\uparrow}) \tag{2.125}$$

or

$$\frac{dn}{dt} = \frac{n_0 - n}{T_1} \tag{2.126}$$

when

$$n_0 = N\left(\frac{W_{\downarrow} - W_{\uparrow}}{W_{\downarrow} + W_{\uparrow}}\right) \tag{2.127}$$

and

$$\frac{1}{T_1} = (W_{\downarrow} + W_{\uparrow}) \tag{2.128}$$

Now we find

$$n = n_0\left(Ae^{-t/T_1}\right) \tag{2.129}$$

where A is a constant of integration, n_0 is the population difference at thermal equilibrium and we introduce T_1, the spin-lattice relaxation time - a characteristic value of great importance in NMR and NQR experimental work.

This rate defines the time necessary for magnetization to be established, following an exponential rise to equilibrium from an initial unmagnetized state,

$$n = n_0\left(1 - e^{-t/T_1}\right) \tag{2.130}$$

Bringing together (2.112) and (2.126) we find the transition rate given by thermal processes and the applied magnetic field to be

$$\frac{dn}{dt} = -2Wn + \frac{n_0 - n}{T_1} \tag{2.131}$$

where at steady state

$$n = \frac{n_0}{1 + 2WT_1} \tag{2.132}$$

and on substitution into (2.114)

$$\frac{dE}{dt} = n_0\hbar\omega\frac{W}{1 + 2WT_1} \tag{2.133}$$

We observe that if $2WT_1 << 1$ the populations are not disturbed from their thermal equilibrium values by absorption of the energy of the applied field.

2.6.2 Quadrupolar transition probabilities

The solutions of the rate equations for higher spin nuclei and the corresponding transition probabilities are somewhat more complicated than those stated above for the spin-½ case. Spin-$^3/_2$ nuclei recovery follows an exponential function because the energy levels are equally spaced, similar to the NMR situation. In general, the spin-lattice relaxation rate for spin-$^3/_2$ nuclei can be simply calculated[10] as

$$T_1 = \frac{1}{2(W_1 + W_2)} \tag{2.134}$$

where W_1 and W_2 correspond to the $\Delta m = \pm 1$ and $\Delta m = \pm 2$ transitions.

For spin $I = 1$, there are three NQR transitions possible and hence three transition probabilities - W_{zy}, W_{zx} and W_{xy} - contributing to the spin lattice relaxation rate. The way in which these probabilities can be determined experimentally is detailed by Vega[11]. It is clear that the overall transition probability is now dependent on all three transitions and so we may expect the relaxation to deviate from a single exponential function. Detailed derivations of the transition probabilities will not be given here but a general case will be stated. In the axially symmetric case, use of first order perturbation theory finds the probability from state ψ_m to ψ_{m+1} to be

$$W_{m\to m+1} = \frac{1}{4}\gamma^2 B_1^2 \left|\langle m+1|I_+|m\rangle\right|^2 g(\omega_m) \tag{2.135}$$

where B_1 is the resonant RF field amplitude and $g(\omega)$ is the normalised line shape function.

$$\int_{-\infty}^{\infty} g(\omega)d\omega = 1 \tag{2.136}$$

$$\omega_m = \frac{3A}{\hbar}(2|m|+1) \tag{2.137}$$

The effects of the internal motions of the solid sample on the quadrupolar transition probablilities, $W_{\pm 1}$ and $W_{\pm 2}$ and the factors that determine their values are discussed in further detail elsewhere[3].

At low or zero values of η, only the $\Delta m = \pm 1$ transition is observable. $\Delta m = \pm 2$ transitions may occur in NQR during the restoration of equilibrium via torsional motions. For this case, Woessner and Gutowsky have discussed the transition probabilities for the relaxation of spin-$^3/_2$ nuclei for a number of relaxation mechanisms using first order perturbation theory with the assumption that the nuclei within the molecule exist in discrete torsional oscillation energy levels. Derivations of W_1 and W_2, relating to the $\Delta m = \pm 1$ and $\Delta m = \pm 2$ transitions respectively, were published for the case of harmonic torsional oscillations and also for relaxation by fluctuation in the electric field gradient. The rare case of relaxation vibration in which energy is exchanged directly between the spin system and the lattice phonons is also briefly discussed.

2.7 Bloch's equations

The relaxation of the nuclei back to equilibrium in NMR can be discussed in terms of their magnetisation along the perpendicular axes, governed by the spin-lattice (longitudinal) and spin-spin (transverse) relaxation rates; T_1 and T_2 respectively. Bloch described the rates of change of magnetisation relative to the relaxation rates as

$$\frac{dM_z}{dt} = -\frac{M_z - M_0}{T_1} \tag{2.138}$$

$$\frac{dM_x}{dt} = -\frac{M_x}{T_2} \tag{2.139}$$

$$\frac{dM_y}{dt} = -\frac{M_y}{T_2} \tag{2.140}$$

where M_z is the time dependent magnetisation parallel to the applied field and M_x and M_y are the components of magnetisation perpendicular to the field.

We find that

$$\frac{dM_x}{dt} = -\frac{M_x}{T_2} + M_y\Delta\omega \tag{2.141}$$

$$\frac{dM_y}{dt} = -\frac{M_y}{T_2} + -M_x\Delta\omega + \gamma B_1 M_z \tag{2.142}$$

$$\frac{dM_z}{dt} = -\frac{M_z - M_0}{T_1} - M_y\gamma B_1 \tag{2.143}$$

and in the rotating frame model the steady state solutions taking account of the applied B_1 RF field are found to be

$$M_x = \frac{\Delta\omega\gamma B_1 T_2^2}{1+(\Delta\omega T_2)^2 + \gamma^2 B_1^2 T_1 T_2} M_0 \tag{2.144}$$

$$M_y = \frac{\gamma B_1 T_2}{1+(\Delta\omega T_2)^2 + \gamma^2 B_1^2 T_1 T_2} M_0 \tag{2.145}$$

$$M_z = \frac{1+(\Delta\omega T_2^2)}{1+(\Delta\omega T_2)^2 + \gamma^2 B_1^2 T_1 T_2} M_0 \tag{2.146}$$

2.8 Nuclear relaxation

We have already discussed the equations describing the voltage induced following a pulse or number of pulses of RF radiation in an NQR experiment. We will now take the macroscopic view of some NQR phenomena experimentally observed or utilized in this work.

2.8.1 The free induction decay

Free induction decays (FIDs) are the responses due a single pulse. Following a pulse there must be a 'dead time' during which neither RF is applied nor can data be acquired (figure 2.10) so that the maximum intensity observed is somewhat less than the response

at $t = 0$, usually taken as the centre of the pulse; reception of the signal immediately after the pulse would lead to pulse breakthrough, which is usually much greater than any signal, so saturating the receiver.

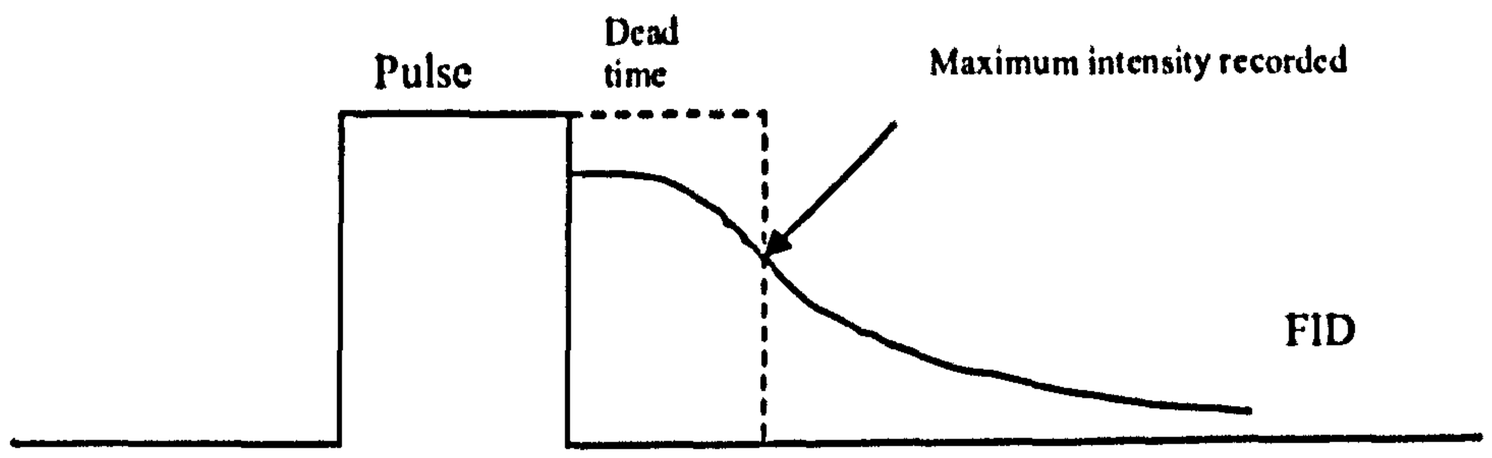

Figure 2.10: Free induction decay signal following a pulse.

We usually assume the FID to be singly exponential with the signal decaying proportionally to $\exp^{-t/T_2^*}$; this being the case, Fourier transformation of the FID would then yield a spectrum following Lorentzian lineshape. Lowe and Norberg[12] give a thorough discussion of free induction decays in solids, the full quantum mechanical terms of which will not be discussed here.

2.8.1.1 Lorentzian and Gaussian lineshapes

A Lorentzian line shape is described by the function[13]

$$L(x) = A\frac{1}{1+M^2(x-x_0)^2} \tag{2.147}$$

with constants A and M, which define the steepness of the slope, and offset x_0, usually the resonance frequency in an NQR experiment. A Lorentzian line has the characteristics of maximum amplitude at $x = x_0$ and full width at half height of

$$\Delta L = \frac{2}{M} \tag{2.148}$$

This is a commonly observed line shape in NQR experiments and can be used to estimate T_2^*, commonly known as the spin-phase memory decay time. T_2^* appears in the above equations as the steepness constant M in the Lorentzian function. A narrow Lorentzian line will be observed when T_2^* is long, and vice versa.

Other line shapes may be observed, depending on the purity of the sample and the presence of internal strains; one such lineshape follows a Gaussian distribution, described by the function

$$G(x) = \exp\left(\frac{-(x-x_0)^2}{N^2}\right) \qquad (2.149)$$

with the constant N defining the steepness of slope with the width at half height found to be

$$\Delta G = 2N\sqrt{\ln 2} \qquad (2.150)$$

and characteristically the Fourier transform of a Gaussian will yield another Gaussian lineshape. Gaussian functions have much smaller 'wings' in comparison to Lorentzian lineshapes (figure 2.11).

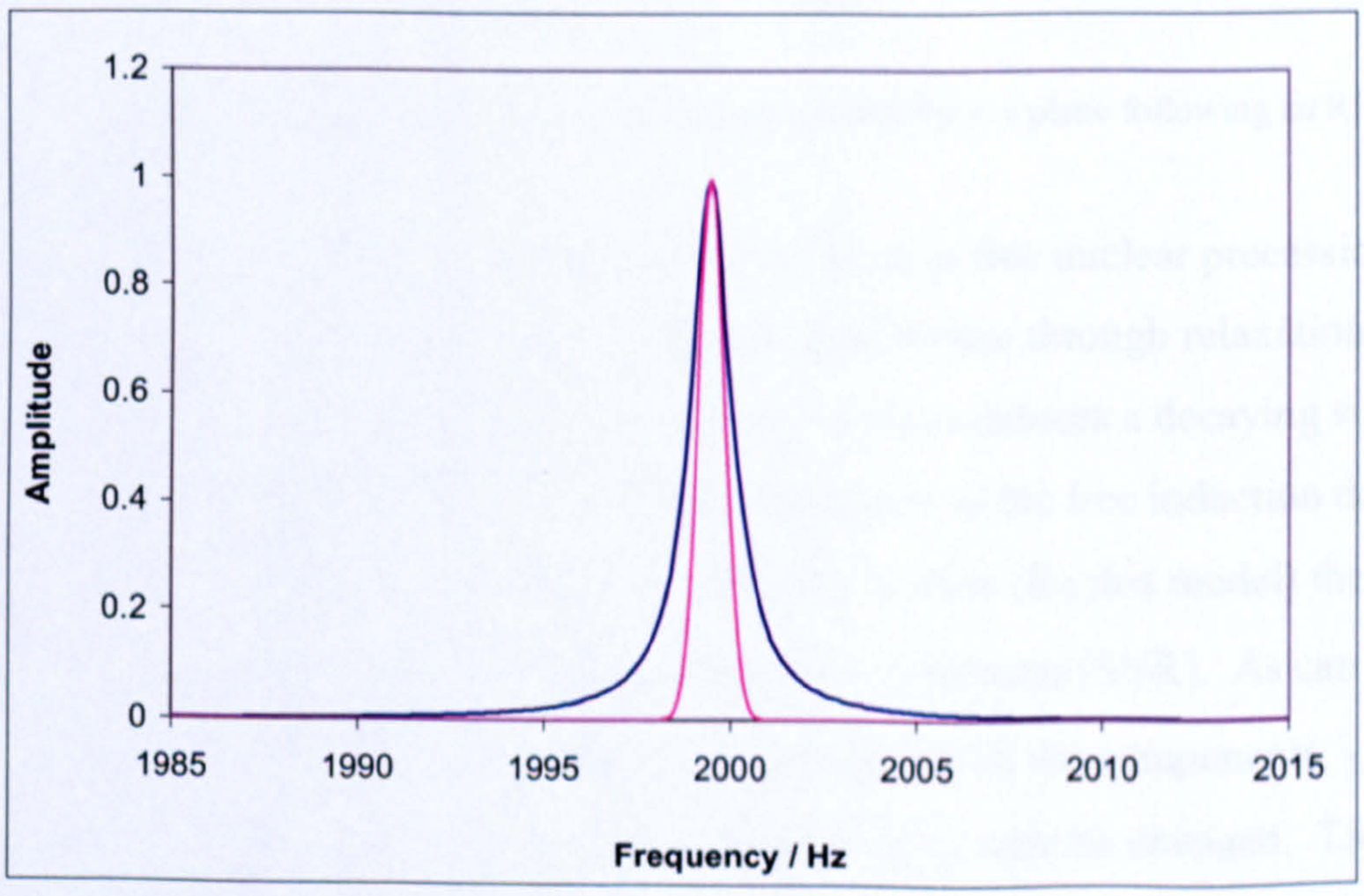

Figure 2.11: Lorentzian (blue) and Gaussian (pink) lineshapes, with M *or* N = 0.5 s and x_0 = 2000 Hz.

If the FID is short, i.e. with broad lines, the maximum FID intensity recorded will be low and the errors in relaxation calculations will be large as there will be fewer points to fit to the function, which can lead to other problems, discussed in the experimental section. Long dead times also diminish the amount of FID electronically recovered; one way of overcoming this problem is to use echoes, which will be discussed.

2.8.1.2 Flip angle

The orientation of the applied field relative to the electric field gradient determines the energy absorbed and therefore the intensity of the signal recovered. To return to the classical model, M rotates about B_1 (figure 2.12) by an angle, α, called the flip angle[14], given by the equation

$$\alpha = \gamma B_1 t_w \qquad (2.151)$$

where B_1 = the amplitude of RF field and t_w = the pulse width.

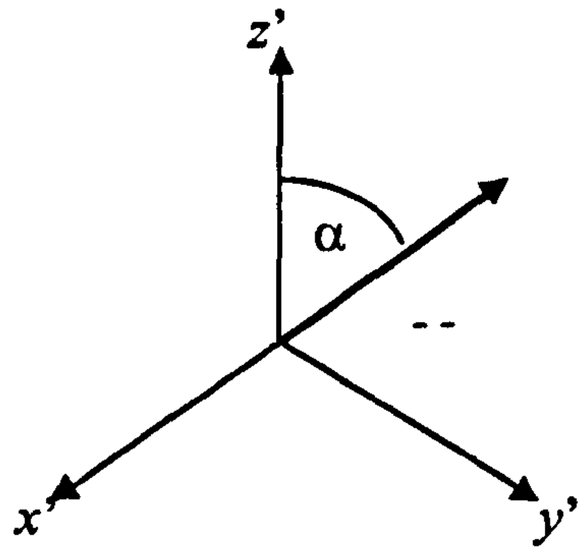

Figure 2.12: The resultant magnetisation, M, tipped towards the x-y plane following an RF pulse.

As we know, once the RF pulse has been removed, there is free nuclear precession at an allowed frequency and the spins return to thermal equilibrium through relaxation processes; as they do so, the magnetisation in the x-y plane induces a decaying signal in the same RF coil which generated the B_1 field, giving rise to the free induction decay. The FID intensity depends on α and so it is desirable to have (for this model) the optimum α value of 90 ° to achieve the best signal-to-noise ratio (SNR). As can be seen from equation (2.151) this could be done by increasing any of the components, γ, B_1 or t_w. However, γ is intrinsic to a specific nucleus and so B_1 or t_w must be changed. The pulse time can be varied and controlled most easily and so by running a number of sequences using different pulse times to generate signals, a periodic function of t_w can be generated in a 2-dimensional scan. The stack plot shows the maximum amplitude of the Fourier transformed FID plotted as a function of the pulse width; in NQR, the peak intensity follows a Bessel function with maxima and minima at certain pulse lengths (except when $\eta = 0$). The Bessel function takes account of the fact that in a solid polycrystalline material the crystal axes can take up all different directions with respect to the B_1

direction. If this were not the case, as in a single crystal, a simple sine function could be used, for example as in NMR.

Assume that

$$< I_x >= \left(\frac{\omega_Q}{kT}\right) \sin\left(2\omega_1 t_w \cos\alpha\right) \qquad (2.152)$$

where $<I_x>$ is the expectation value of the angular momentum operator, I_x, and ω_Q is the NQR frequency. To allow for the crystals being orientated in different directions with respect to B_1, the following equation is used

$$\left(\frac{2\pi \sin\alpha}{4\pi}\right) d\alpha = -\frac{1}{2} d(\cos\alpha) \qquad (2.153)$$

which is the fraction of crystallites with the principal x-axis of the electric field gradient lying between α and $\alpha + d\alpha$ with respect to the coil axis.

By integrating over all α values, combining equations (2.152) and (2.153) and including a *cos* α term (introduced because the induced coil signal is proportional to *cos* α) the following equation for the NQR signal can be derived[15];

$$< \bar{I}_{coil} > \propto -\left(\frac{\omega_Q}{2kT}\right) \cos\alpha \sin\left(\omega_1 t_w \cos\alpha\right) d(\cos\alpha) \qquad (2.154)$$

$$< \bar{I}_{coil} >= \left(\frac{\omega_Q}{kT}\right) \frac{1}{\alpha^2} (\sin\alpha - \cos\alpha) \qquad (2.155)$$

and this function has a maximum at 119 ° not 90 °. However, it is common for a 119 ° flip angle to be referred to as 90_{eff}, or $\pi/2$ pulse in NQR. In all experimental work it is important to analyse the signal response in terms of the above equation to maximise the SNR.

2.8.2 The Hahn echo

It has been observed in section 2.5 that two pulses (which are short compared to T_2), applied time τ apart, will generate an echo signal at a time τ after the second pulse. The echo suffers little or no dead time loss, as it is measured at a time after the pulse sufficient to move most or all of the signal away from the dead time (figure 2.13).

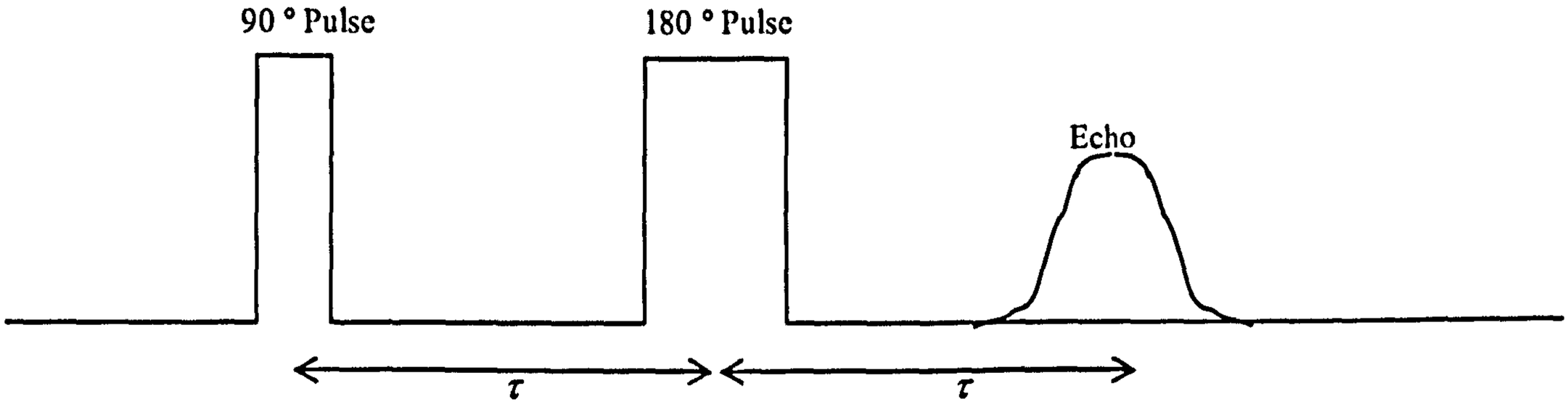

Figure 2.13: Two pulses separated by time, τ, generate an echo time, τ, after the second pulse.

The spin echo, developed in NMR by Hahn[16], arises in terms of the classical vector model when a second π pulse of the same or opposite pulse is applied, at time τ, a 180 ° rotation is then performed on the spins about the x' axis, which had previously fanned out in the $x'y'$ plane following an initial $^{\pi}/_{2}$ pulse at $t = 0$. Following this π pulse the spins are still in the x'-y' plane but the slower spins are now ahead of the y' axis by the same amount as they were behind, and similarly the spins which were ahead are now having to catch up. As they are all precessing at their unchanged NQR frequencies it will take the same amount of time, τ, for all of the isochromats to rephase and get back to parallelism with the y' axis to give a total magnetisation along the $+y'$ or $-y'$ direction (figure 2.14).

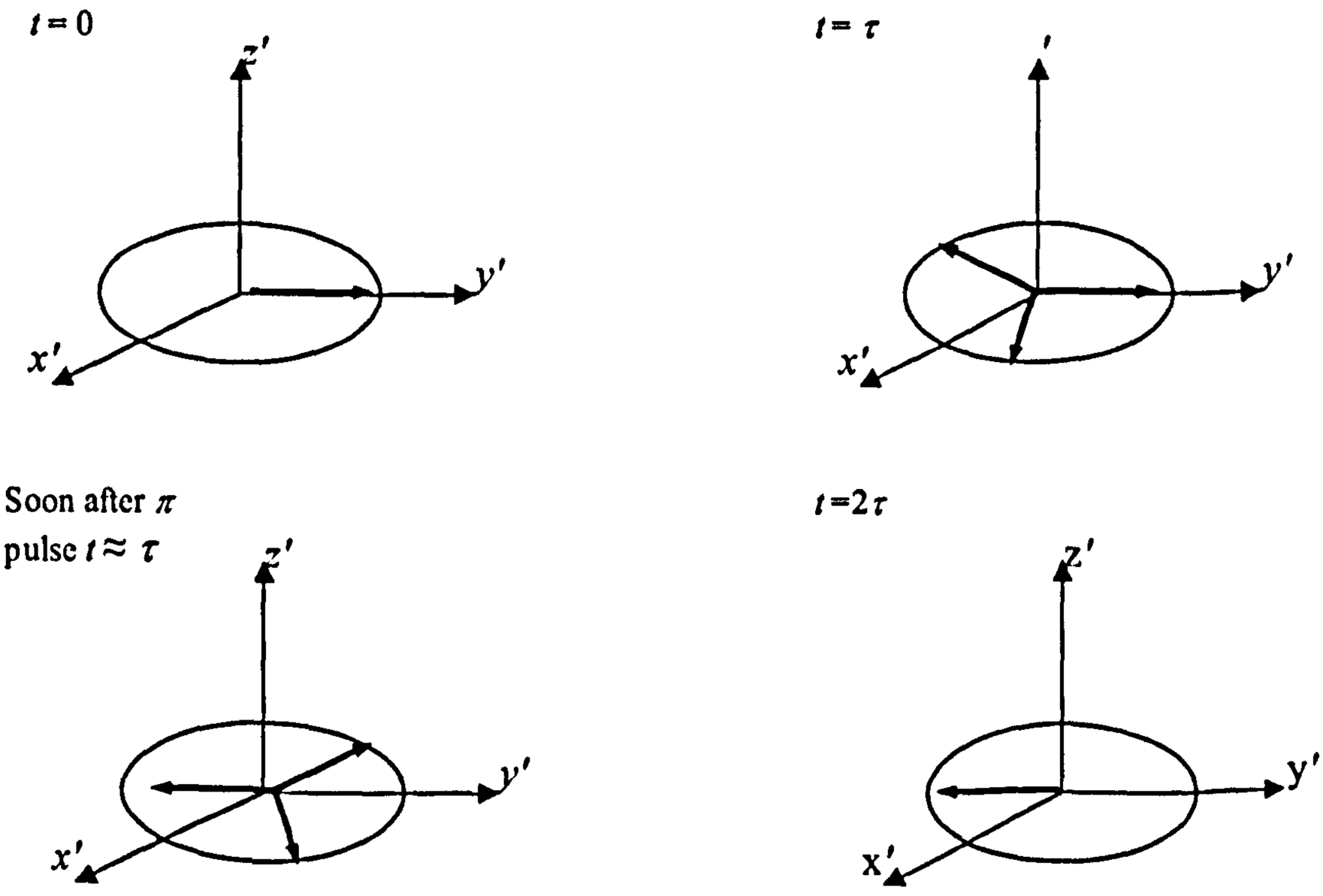

Figure 2.14: Hahn echo refocussing.

Hence, at time 2τ an echo, which is two FIDs back to back, will be observed, as calculated in equation 2.102. Whether the echo is positive or negative depends on the phase of the second pulse, relative to the first. If pulses of the same phase (applied along the same axis) are used, the echo is negative, and if pulses of different phases (one applied along x', the other along y') the echo is positive. When finding relaxation times the peak magnitude is the used value, so the sign is irrelevant.

Through measurement of the signals generated as FIDs and spin echoes, information about relaxation processes can be obtained. The different relaxation times and the pulse programs used to obtain them are described in the next section.

The transient and echo responses and relaxation rates for various pulse sequences will differ slightly in the calculations according to the various pulse combinations used and a number of publications discuss different combinations for both NMR[17], and NQR[18,19,20,21]; in the latter case, η is often set to zero, avoiding the more complex calculations presented in the more usual case of axial asymmetry. The most common and general relaxation rate calculations which are used experimentally will be presented below.

2.8.3 Relaxation rates

We will now discuss further the relaxation rates introduced in the Bloch equations and present the classical view of the processes occurring and some information about the rates.

2.8.3.1 T_1: Spin-lattice relaxation time

The spin-lattice relaxation time is probably the most important relaxation rate in NQR. As discussed in section 2.6, it is dependent on the transition probabilities, W_{ij}, determined by the interactions of the lattice with the spins and the energy level populations; it also determines the rate of change of magnetization (2.138). It is used to characterize a material and is essential knowledge in the identification and analysis of a sample. When RF energy is applied to a set of nuclei and perturbs the equilibrium Boltzmann populations, the spins will relax back to equilibrium by transferring their energy into the

thermal energy of the translations, rotations and vibrations of atoms and molecules in the solid sample. Together these atomic and molecular motions, the thermal degrees of freedom, are referred to as the lattice; hence T_1 is spin-lattice relaxation (it is also referred to as longitudinal relaxation, as in NMR it governs changes of components parallel to B_0).

Quadrupolar and dipolar effects may both contribute to the relaxation and the dependence of T_1 on the lattice motions can give an insight into the molecular or atomic motions in the sample. For example, molecular motion, such as ring buckling in piperazine[22], will change the EFG experienced by the quadrupolar nuclei, producing quadrupolar relaxation. Plotting the spin-lattice relaxation rate against temperature is particularly useful in determining the possible relaxation mechanisms taking place. If an activation energy value can be determined from such a graph, usually across a specific temperature range, this can be compared with known or expected values for thermally activated processes occurring within the molecule under analysis. T_1 is particularly sensitive to hindered rotations and other large amplitude molecular modes which follow an Arrhenius-type equation[23]

$$T_1 = T_1(0)e^{\Delta E^*/RT} \qquad (2.156)$$

If a straight line is observed in a ln T_1 vs $1/T$ plot, the activation energy, ΔE^* for the mode can be calculated from the gradient. It should be noted however, that in different temperature regions different processes will dominate the relaxation rate[24].

The energy exchange occurring during relaxation also changes the temperature of the sample but this is negligible except at very low temperatures (20 K or less).

There are a number of different pulse sequences which can be used to determine T_1, some of which will be discussed here. Since the coil responds to magnetization in the x-y plane and T_1 is a measure of recovery of M in the z direction, to measure T_1 a second pulse must be used, which monitors the recovered magnetisation in the z direction. Relaxation rate equations considering a number of NQR pulse sequence situations have been thoroughly investigated by Vega and Vaughan[25]. We now look at the different techniques and pulse sequences which can be used to measure T_1.

2.8.3.1.1. Inversion-recovery ($\pi - \tau - {}^{\pi}/_{2}$ or 180 ° - τ - 90 °)

The first π pulse is applied at approximately twice the 90_{eff} pulse length, inverting the population of the energy levels; in the rotating frame the spins are rotated through 180 ° and the magnetisation is $-M_0$. The magnetisation then begins to recover through zero, towards a constant positive equilibrium value, when the value of M is equal to $+M_0$. The second pulse, the 90_{eff} pulse, is then applied after a short time, τ, and the z magnetisation recovered at that time rotated into the x-y plane and thus measured by the coil. This sequence, $\pi - \tau - {}^{\pi}/_{2}$, is carried out several times with at least ten different τ values, from τ = 0 to $\tau \geq 5T_1$, between pulses. The Fourier transformed signals can then be brought together in a 2-dimensional plot, or the recovered magnetisation (peak intensity) plotted as a function of τ, when the signal is seen to increase with increasing τ, due to greater recovery at longer values of τ. The recovered FID after the second pulse may be fitted to the equation[14]

$$M_z(t) = M_0\left(1 - 2e^{-\tau/T_1}\right) \qquad (2.157)$$

For spin-1 systems with three levels, as for ^{14}N, the T_1 recoveries are in general bi-exponential but often a single-exponential fit is sufficient to estimate T_1. The time needed for full recovery of magnetisation and return to equilibrium is at least 4 or 5 times T_1, so the time between scans must be sufficient to allow for this. In NQR of a polycrystalline sample a perfect 180 ° pulse cannot be achieved for all spins, which results in the inversion recovery starting at less than its full negative magnitude, $-M_0$; this value is however needed for a T_1 calculation. Hence, when T_1 is calculated using the MacNMR software utilized in this work, a value is given which is a measure of how symmetric the curve is on either side of the baseline; in NQR the final steady state value will always be greater in magnitude than the negative starting value.

2.8.3.1.2. Saturation-recovery (${}^{\pi}/_{2} - \tau - {}^{\pi}/_{2}$ or 90 ° - τ - 90 °)

In this method a fast pulse sequence uses ${}^{\pi}/_{2}$ pulses to saturate the spins, which are then allowed to relax during an 'off' period, τ, before a second ${}^{\pi}/_{2}$ pulse is used to measure the recovered magnetisation. The equation that relates the magnetisation at time τ, $M_z(t,)$ to T_1 for single exponential recovery is

$$M_z(t) = M_0\left(1 - e^{-t/T_1}\right) \qquad (2.158)$$

The time between scans does not need to be long, as in inversion recovery, as the magnetization does not have to recover through $2M_0$, and so this technique is suitable for compounds with a long T_1, although the maximum τ value must be greater than T_1. It is a useful method because it is fast and for a broad spectrum it can produce accurate line intensities, compared to using inversion-recovery, as the preparation pulse is half that for inversion recovery so the frequency excitation width is doubled for a given power and coil set up.

2.8.3.1.3. Steady state sequence

T_1 can also be measured using a steady state sequence (SSS). This is similar to the saturation-recovery sequence above, except in this case there is the same delay between all pulses. A long train of $\pi/2$ pulses, separated by τ, is applied and after a time a steady state is reached. The magnetisation at time τ is the same as in the $\pi/2$-τ-$\pi/2$ sequence (2.158). This is a useful sequence if T_1 is completely unknown, or suspected to be long, as the 2-dimensional plot shows the magnetization still rising if T_1 is longer than estimated. This is advantageous compared to inversion recovery, where the T_1 must not be assumed to be shorter than it is, in order that a sufficient time (at least $5T_1$) is allowed between scans to achieve full recovery and acquire a 'true' plot. According to Vega[11] a steady state sequence can also yield a true exponential recovery for both single crystal and powder experiments.

2.8.3.2 T_2*: Spin-phase memory decay time

T_2* governs the FID time. It is usually shorter than T_2 in NQR and this difference is a measure of how inhomogeneous the system is; this inhomogeneity can be due to defects or impurities in the sample, which disturb the EFG, or it can also be due to fluctuations in the EFG itself. Precession will occur at different rates in different parts of the sample due to impurities or the slight differences in environment and this leads to a dephasing of the signal, thus a shorter T_2* time than might be expected in a homogenous system. As the sample/system becomes more homogeneous T_2* increases until it equals T_2, so in all

cases $T_2^* \leq T_2$. In terms of the vector model, different parts of the sample experience different EFGs, and may have differing magnetisations. Each small section, experiencing a homogenous electric field gradient in its vicinity, is called a spin isochromat. Following a $\pi/2$ pulse, each isochromat precesses at its characteristic NQR frequency, with those experiencing a larger electric field gradient having a greater frequency and vice versa. The spin isochromats will gradually get out of phase with each other in time, some being slower and some faster than average, as the total magnetisation fans out across the x'-y' plane (figure 2.15).

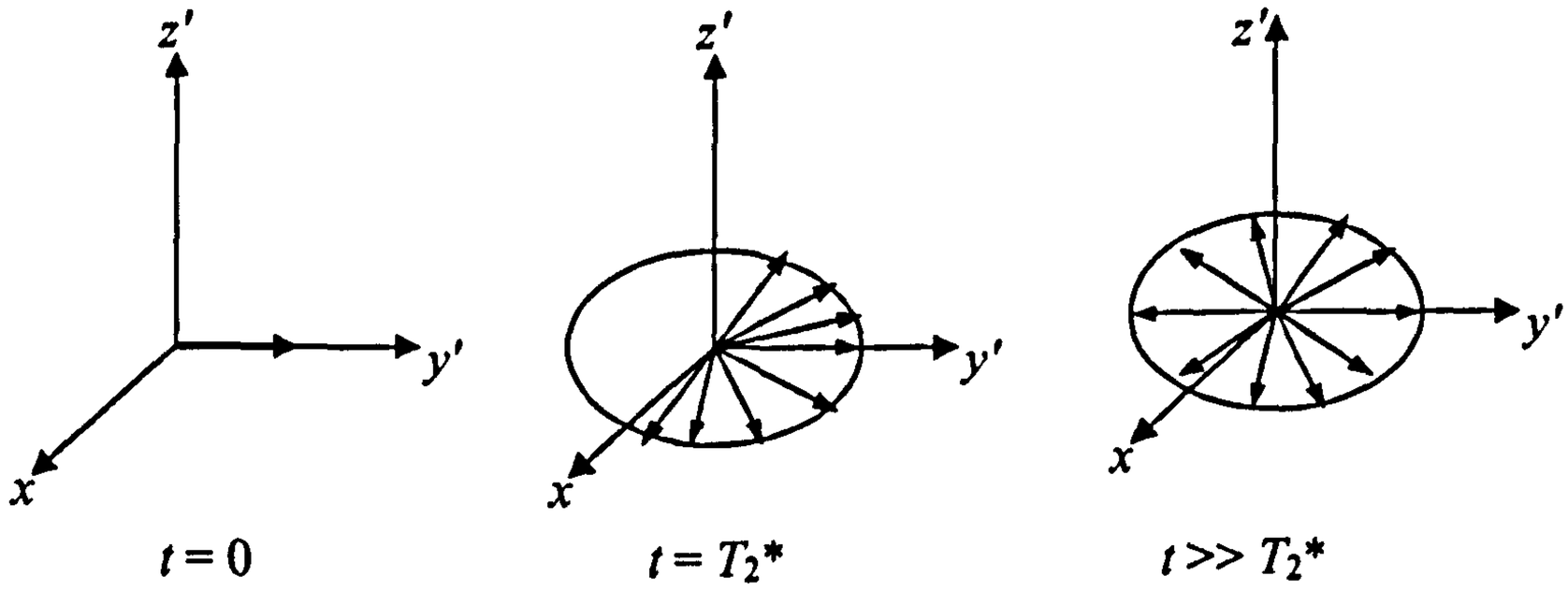

Figure 2.15: Following a $\pi/2$ pulse in the rotating frame, the magnetisation fans out in the x'-y' plane due to inhomogeneity.

This leads to decay in the signal as the magnetisation along the y axis decreases in amplitude, and the voltage decays according to T_2^*. This is the free induction decay seen following a single pulse. Magnetic dipole and electric quadrupolar effects will affect both transverse relaxation rates, leading to line broadening.

2.8.3.3 T_2: Spin-spin relaxation time

This is also known as transverse relaxation and is a measure of the true decay of the x-y plane precession as introduced in the Bloch equations 2.139 and 2.140. As the name suggests, the energy from one spin is transferred to another spin in energy conserving spin-flips. T_2 is determined by molecular diffusion in liquids and is often equal to T_1 but this is rarely the case in NQR. In solids there is much less molecular motion and T_2 is often governed by dipole-dipole interactions. Due to inhomogeneity broadening T_2 cannot be measured directly and so echo sequences must be used.

The fanning out in figure 2.14 is reversible through application of a second pulse along the x' axis as already discussed in section 2.8.2. When the time between pulses, τ, is increased, the intensity of the echo will diminish so a 2-dimensional plot of the intensity as a function of time can be generated, which allows calculation of T_2, by fitting the curve to the following equation

$$M_{echo}(t) = M_0 e^{-2\tau/T_2} \tag{2.159}$$

2.9 Dipolar coupling

As NQR deals with solid samples, the nuclei are usually fixed in rigid positions within the sample and will experience local magnetic fields due to their neighbours which will not be averaged out by rapid molecular motion as occurs in liquids. Line broadening due to the frequency deviations caused by this dipole-dipole interaction has been derived and discussed in terms of its influence on lineshapes obtained from free induction decays and echoes[17]. We calculate here the energy due to this interaction between nuclei.

We first introduce the classical interaction energy between two magnetic moments as

$$E = \frac{\mu_1 \cdot \mu_2}{r^3} - \frac{3(\mu_1 . r)(\mu_2 . r)}{r^5} \tag{2.160}$$

where r is the radius vector between the two magnetic moments μ_1 and μ_2. To treat this interaction quantum mechanically, we first view the magnetic moments as operators

$$\mu_1 = \gamma_1 \hbar I_1 \tag{2.161}$$

$$\mu_2 = \gamma_2 \hbar I_2 \tag{2.162}$$

and the dipolar Hamiltonian can be written as

$$\mathcal{H}_D = \frac{1}{2}\sum_{j=1}^{N}\sum_{k=1}^{N}\left[\frac{\mu_j \cdot \mu_k}{r_{jk}^3} - \frac{3(\mu_j . r_{jk})(\mu_k . r_{jk})}{r_{jk}^5}\right] \tag{2.163}$$

for N spins. For a pair of dipoles this can now be written as

$$\mathcal{H}_D = \frac{\gamma_1 \gamma_2 \hbar^2}{r^3}(A + B + C + D + E + F) \tag{2.164}$$

commonly known as the dipolar alphabet, where

$$A = I_{1z} I_{2z}(1 - 3\cos^2\theta) \tag{2.165}$$

$$B = -\frac{1}{4}\left(I_1^+ I_2^- + I_1^- I_2^+\right)\left(1 - 3\cos^2\theta\right) \tag{2.166}$$

$$C = -\frac{3}{2}\left(I_1^+ I_{2z}^- + I_{1z}^- I_2^+\right)\sin\theta\cos\theta e^{-i\phi} \tag{2.167}$$

$$D = -\frac{3}{2}\left(I_1^- I_{2z} + I_{1z} I_2^-\right)\sin\theta\cos\theta e^{i\phi} \tag{2.168}$$

$$E = -\frac{3}{4}\left(I_1^+ I_2^+\right)\sin^2\theta e^{-2i\phi} \tag{2.169}$$

$$F = -\frac{3}{4}\left(I_1^- I_2^-\right)\sin^2\theta e^{2i\phi} \tag{2.170}$$

where the raising and lowering operators are as standard and θ and ϕ are expressions of the polar coordinates of r. However, as stated earlier, this contribution to the total Hamiltonian is often only a small perturbation and can sometimes be neglected in energy calculations if the electric interaction is many times greater[10].

2.9.1 Multiple pulse echo train sequences

NQR experiments commonly use pulse sequences which generate echo trains and multiple pulse sequences have the advantage that they can remove dipolar broadening, thus narrowing lines. Phase shifting of the pulses applied averages out the dipolar interaction between spins to zero as each nucleus experiences an equal time along the different axes of the system[8].

A well known sequence which generates a train of echoes was developed by Carr and Purcell[26]; this sequence consists of an initial 90_{eff} pulse, followed by a series of 180_{eff} pulses. The first 180_{eff} pulse is applied at time τ after the 90_{eff} pulse, with subsequent pulses spaced 2τ apart. Echoes are formed in between pulses with maxima at $(2n)\tau$ due to the rephrasing described earlier in the Hahn echo treatment. Theoretically, the decay of the maxima of the echo train should follow an exponential loss with constant T_2 but practically relaxation rates shorter than T_2 are found; this relaxation rate is known as T_2e. Use of the standard Carr-Purcell pulse sequence results in the echoes being generated in a series of amplitudes alternating between positive and negative. Often a slightly modified sequence is used in order to generate an echo train consisting only of positive amplitude maxima. In this Meiboom-Gill modification[27] each 180_{eff} pulse is phase shifted by 90

degrees with respect to the first 90_{eff} pulse by use of phase tables in the pulse sequence programming. Marino and Klainer[28] investigated these echo trains in NQR, as opposed to NMR, and found that echo trains could be sustained for lengths of time significantly longer than T_2 if $\tau \leq T_2$. The decay of the echo train was suggested to be the sum of two exponential decays, though usually T_2e is found by fitting the decay of the echo maxima, $M(t)$ at time t, to

$$M(t) = M_0 e^{-t/T_2e} \qquad (2.171)$$

unless the results suggest otherwise.

The value of T_2e is greatly dependent on the spacing between the pulses, τ, with suggested proportionalities of τ^{-5}(Marino *et al.*) and τ^{-2} (Hitrin et al.)[29] in ^{14}N resonance. Generally, this pulse sequence is referred to as pulse spin locking (PSL) or spin-locked spin-echo (SLSE) in NQR and is frequently employed. Further analysis of line-narrowing and models of the magnetisation and spin evolution can be found elsewhere[30,31,32].

2.10 Temperature effects

In most cases studied using NQR, the resonant frequency decreases with temperature, typically above 100 K[22]. This variation in molecular crystals is usually ascribed to the increasing amplitude of molecular vibrations with increasing temperature. These torsional frequencies are much higher than quadrupole resonance frequencies. As the temperature increases the molecular motion induced will reduce the average electric field gradient experienced by the nuclei, so the NQR frequency decreases; - in simple terms, greater molecular motion leads to an averaging of the EFG experienced by the nuclei and in liquids actually averages the electric field gradient to zero. Returning to the solid state, the effect on the asymmetry is found to be slight, unless η is large[3].

The EFG is then dependent on the mean librational amplitude[33], $<\theta^2>$, according to the equation

$$eq = eq_0\left(1-\frac{3}{2}<\theta>\right) \qquad (2.171)$$

For an harmonic librational motion of frequency, ω_l

$$<\theta^2>=\frac{\hbar}{2I_1\omega_1}\coth\left(\frac{\hbar\omega_1}{2kT}\right) \qquad (2.172)$$

where I_l is the relevant moment of inertia[34].

Across narrow temperature ranges it is sometimes convenient to fit a linear temperature coefficient to the NQR frequency; however, over wider ranges a marked curve can be whose theoretical temperature coefficient of the frequency, ω' is given by

$$\frac{1}{\omega_m}\frac{d\omega'}{dT}=-\frac{3\hbar^2}{2kT^2}\left[\frac{e^{\hbar\omega_X/kT}}{A_X\left(e^{\hbar\omega_X/kT}-1\right)^2}+\frac{e^{\hbar\omega_Y/kT}}{A_X\left(e^{\hbar\omega_Y/kT}-1\right)^2}\right] \qquad (2.173)$$

where ω_m is the NQR frequency of the stationary molecule, A_X and A_Y are the moments of inertia which correspond to torsional frequencies about the X and Y axes respectively[3] (there are no contributions from the torsional motion about the Z axis).

The dependence of the NQR frequency on both temperature and pressure was investigated by Kushida[35] et *al.* who, assuming the high frequency contribution is small in comparison to the low frequency contribution, at a given volume found

$$\nu=a\left(1+bT+\frac{c}{T}\right) \qquad (2.175)$$

where

$$a=\nu_0 \qquad (2.176)$$

$$b=-\frac{3}{2}k\sum_1^M\frac{A_i}{\omega_i^2} \qquad (2.177)$$

$$c=-\frac{\hbar^2}{8k}\sum_1^M A_i \qquad (2.178)$$

2.11 References

[1] Harris, R. K. *"Nuclear Magnetic Resonance Spectroscopy,"* Pitman, 1983.

[2] Vega, S. *J. Chem. Phys.*, 1974, *60*, 3884 - 3888.

[3] Das, T. P.; Hahn, E. L.*"Nuclear Quadrupole Resonance Spectroscopy,"* Academic Press, 1958.

[4] Abragam, A. "*The Principals of Nuclear Magnetism*", Oxford, 1961.

[5] Smith, J. A. S. "*Nuclear Quadrupole Resonance in Chemistry*," Inaugural Lecture Queen Elizabeth College.

[6] Cohen. M. H. *Phys. Rev.*, 1954, *96*, 1278 - 1284.

[7] Martin, M. L.; Delpuech, J. J.; Martin, G. J.*"Practical NMR Spectroscopy,"* Heyden, 1980.

[8] Slichter, C. P.*"Principles of Magnetic Resonance,"* Springer-Verlag, 1978.

[9] Bloom, M.; Hahn, E. L.; Herzog, B. *Phys. Rev.*, 1955, *97*, 1699 - 1709.

[10] Woessner, D. E.; Gutowsky, H. S.; *J. Chem. Phys.* 1963, *39*, 440 - 456.

[11] Vega, S. *J. Chem. Phys.*, 1974, *61*, 1093 - 1100.

[12] Lowe, I. J.; Norberg, R. E. *Phys. Rev.*, 1957, *107*, 46 - 61.

[13] Hennel, J. W.; Klinowski, J. *"Fundamentals of Nuclear Magnetic Resonance,"* 2nd Edition, Longman, 1993.

[14] Fukushima, E.; Roeder, S. B. W. *"Experimental Pulse NMR,"* Addison-Wesley, 1981.

[15] Ramamoorthy , A. Narasimhan, P. T.*"NQR Composite Pulses,"* a paper presented at the Xth International Symposium on Nuclear Quadrupole Resonance, Takayama, Japan, August 22-26, 1989.

[16] Hahn, E. L. *Phys. Rev.*, 1950, *80*, 580 - 594.

[17] Herzog, B.; Hahn, E. L. *Phys. Rev.*, 1956, *103*, 148 - 166.

[18] Das, T. P.; Roy. D. K. *Phys. Rev.*, 1955, *98*, 525 - 531.

[19] Krishnan, M. S.; Temme, F. P.; Sanctuary, B. C. *Molec. Phys.* 1993, *78*, 1385 - 1404.

[20] Pratt, J. C. *Molec. Phys.*, 1977, *34*, 539 - 555.

[21] Das, T. P.; Saha, A. K. *Phys. Rev.*, 1955, *98*, 516 - 524.

[22] Tzalmona, A. *J. Chem. Phys.*, 1969, *50*, 366 - 372.

[23] Zussman, A.; Alexander, S.; *J. Chem. Phys.*, 1968, *48*, 3534 - 3539.

[24] Alexander, S.; Tzalmona, A.; *Phys. Rev. A*, 1965, *138*, 845 - 855.

[25] Vega, A. J.; Vaughan, R. W. *J. Chem. Phys.*, 1978, *68*, 1958 - 1966.

[26] Carr, H. Y.; Purcell, E. M., *Phys. Rev.*, 1954, *94*, 7784 - 7785.

[27] Meiboom, S.; Gill, D. *Rev. Sci. Instrum.*, 1958, *29*, 688 - 691.

[28] Marino, R. A.; Klainer, S. M., *J. Chem. Phys. Lett.*, 1977, *67*, 3388 - 3389.

[29] Hitrin, A. K.; Karnaukh, G. E.; Provotorov, B. N., *J. Mol. Struct.*, 1982, *83*, 269 - 275.

[30] Cantor, R. S.; Waugh, J. S., *J. Chem. Phys.*, 1980, *73*, 1054 - 1063.

[31] Ainbinder, N. E.; Volgina, G. A.; Osipenko, A. N.; Furman, G. B.; Shaposhnikov, I. G.; *J. Mol. Sruct.*, **1983**, *111*, 65 - 70.

[32] Pratt, J. C., *J. Mol. Sruct.*, **1983**, *111*, 113 - 118.

[33] Semin, G. K.; Babushkina, T.A.; Yakobson, G. G. *"Nuclear Quadrupole Resonance in Chemistry,"* Halsted Press, **1972**.

[34] Chihara, H.; Nakamura, N. *Adv. NQR*, **1980**, *4*, 1.

[35] Kushida, T.; Benedek, G. B.; Bloembergen, N. *Phys. Rev.*, **1956**, *104*, 1364 - 1377.

3 Experimental methods and techniques

3.1 Introduction

Nuclear quadrupole resonance is a technique relatively rarely used in analysis and detection in industry; as such standard, ready-to-use NQR equipment is not commercially available in the sense that NMR hardware can be purchased. Non-commercial, laboratory-built hardware is needed, particularly for research such as this, where a wide range of samples and environments must be catered for. Much of the work over the course of this research programme involved gaining and using workshop skills, with probes and coils being handmade, using sometimes unorthodox materials, as well as circuit construction being required as necessary, in order to achieve a working apparatus capable of pharmaceutical analysis. This chapter aims to introduce the basic NQR apparatus used in the laboratory as well as highlighting instrumental modifications, which were made in order to improve experimental conditions and to achieve increased performance in areas such as temperature stability, RF field homogeneity and greater acquisition of signal by decreasing dead time.

The manner in which pulse sequences are input and the data processing options available are also described, with the main features of standard spectral analyses also briefly described to give an understanding of the processes which occur in order to achieve the NQR spectra which are finally output, revealing their characteristics and allowing identification, quantification and a greater understanding of the chemical samples under investigation.

Firstly, we present a flow chart of the standard hardware that forms part of the apparatus used together with instrumental details for each section. The basic instrument is the Libra pulsed RF spectrometer made by Tecmag of Houston, Texas.

3.2 The NQR spectrometer

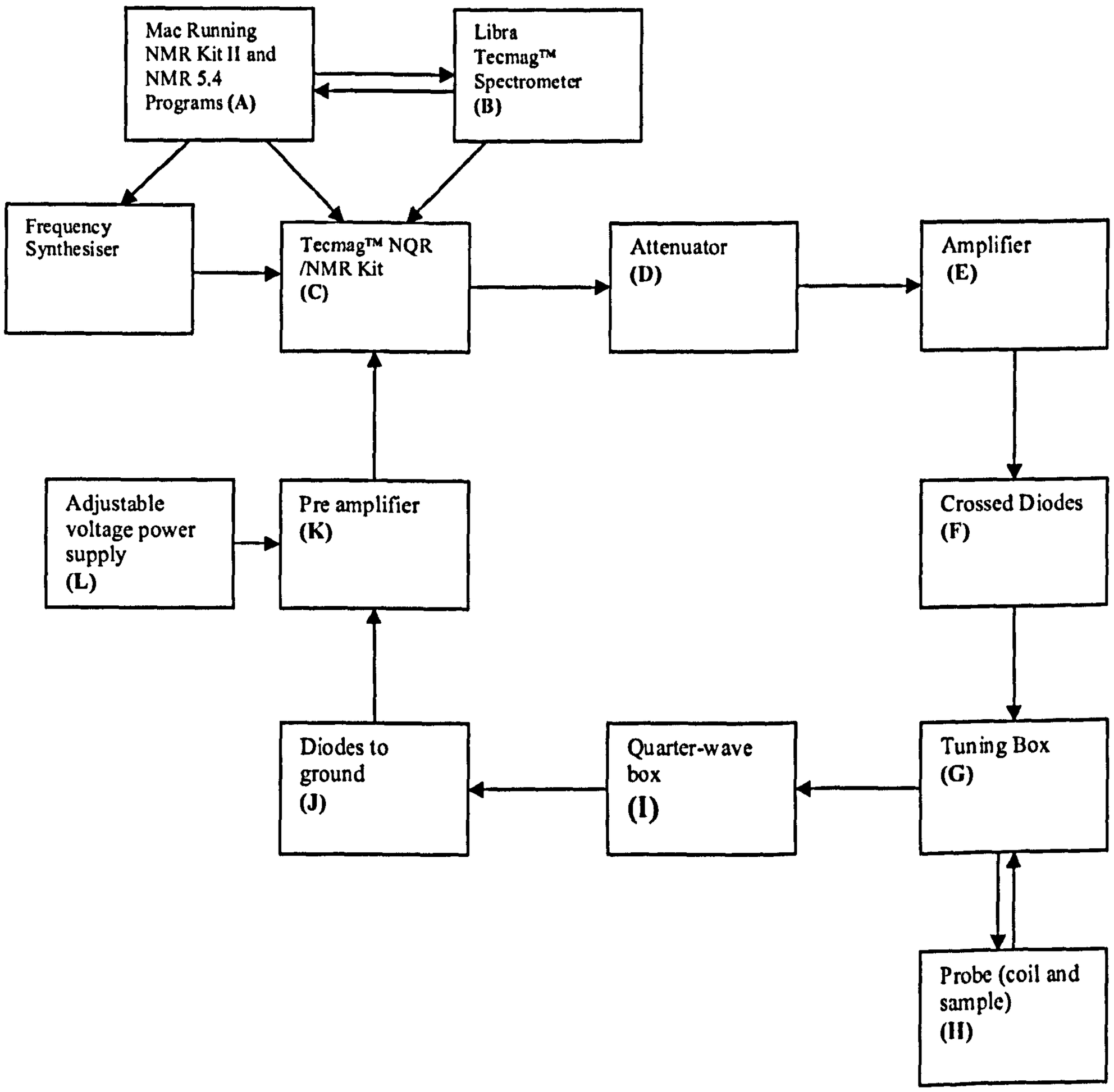

Figure 3.1: NQR hardware flowchart.

A: An Apple Macintosh computer runs the programs which control the spectrometer - NMR Kit II controls the radiofrequency applied and allows filters, extra attenuation and RF gain to be set and varied according to the signal being observed, the temperature and other experimental considerations.

- NMR 5.4 software - used to develop and control pulse sequences, discussed further in section 3.5.1.

B and C: Together with the spectrometer and NQR or NMR kit, they transmit and receive pulses and signals. The spectrometer has a minimum pulse width of 100 ns and a resolution of 10 ns and is controlled by the Macintosh computer when running pulse sequences. The NQR Kit can be used for frequencies up to around 12 MHz. The NMR Kit is used for ^{35}Cl work together with a frequency synthesizer which can generate frequencies between 0.1 and 310 MHz.

D: The attenuator (Pascall manual attenuator, model AC701, 1 – 100 dB, 1 W) allows the power to be attenuated from 1 to 30 decibels, changing the B_1 field generated when all other parameters are held constant. Attenuation at this stage is sometimes necessary to enable variation of pulse widths.

E: The amplifier increases the pulse power. When using the NMR Kit an Amplifier Research (Model 1000LPM9, 200/1000 W, 0.4 - 200 MHz) amplifier is used. When the NQR Kit is used an AmpUK amplifier and driver unit (1500 W, 1.6 – 7 MHz) is used.

F: The blocking diode pairs (5 pairs of 6 V, 1.3 W diodes) only pass current in either direction if it is above a certain threshold, thus reducing noise. When the pulse is being applied there is a low impedance path (there is little resistance to current passing through) and when the pulse is off there is a high impedance, so attenuating noise.

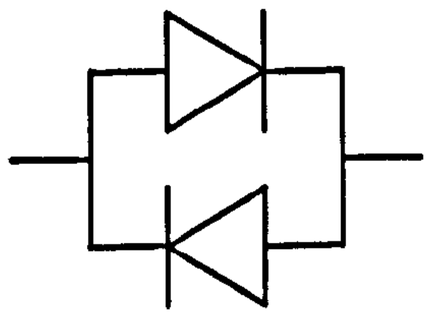

Figure 3.2: Crossed diodes circuitry.

G: The tuning box consists of a variable capacitor in series and a variable capacitor in parallel (Jennings variable vacuum capacitors, of capacitance 5 – 125 pF) and enables the resonance frequency to be varied and impedance of the coil to be matched to the rest of the equipment.

H: The probe contains the coil surrounding the sample which induces the B_1 field. Probes are hand-built and designed around experimental needs and the NQR sample. More details of the probe and solenoid are given in section 3.3.

I: The $\lambda/4$ box acts as a transformer which matches the impedance and protects the pre-amplifier (together with the diodes to ground). Transmission lines have a characteristic

impedance; 50 Ohms in the case of the coaxial cables used in this project. Impedance matching minimizes the reflected power and signal loss. Quarter-wave boxes only tolerate an approximate 10 % variation in frequency around the designated value, making it important to adjust or replace old boxes accordingly for each new material. By allowing current to pass only when the transmitter is off, the pre-amplifier and receiver are not saturated by the pulse and only the desired frequencies can pass. Equation (3.1) allows calculation of the necessary capacitance, C, in designing a quarter wave box to suit the frequencies, ν, being observed.

$$Z = 2\pi\nu L = \frac{1}{2\pi\nu C} \tag{3.1}$$

A 50 Ohm impedance, Z, at 2.9 MHz gives an inductance value of 2.74 μH and 1098 pF capacitance. The solenoid in the circuit is constructed with copper wire and designed using the standard solenoid inductance equations (3.2 – 3.3).

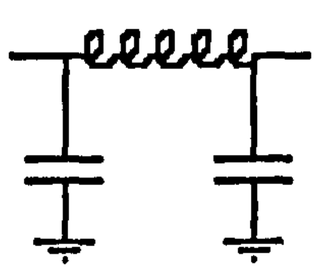

Figure 3.3: Quarter-wave circuitry.

At high frequencies, where the wavelength is shorter, relatively short lengths of co-axial cable must be used instead of the separate solenoid and capacitor tuning box design.

J: The diodes to ground ensure that the current goes to ground when the pulse is on, thus directing the current through the coil but when the pulse is off, the signal current is directed to the pre amplifier to be amplified.

K: The pre-amplifier (Miteq Model AN1054-1103, 1 – 500 MHz, S/N 465251) boosts the signal received form the coil. This is necessary as only a small voltage is generated by the magnetisation of the spins.

L: This is the power supply for the pre-amplifier (EMS adjustable voltage model 2381/10 - 20, 10 – 20 V, 500 mA, set to 15 V).

The Apple Macintosh, the Libra Spectrometer and the NQR Kit were supplied by the Defence Science and Technology Laboratory (DSTL) at Fort Halstead.

To achieve optimum power, the RF probe must be tuned before each experiment using a signal generator and an oscilloscope. The frequency which is to be used to irradiate the sample is output by the signal generator to the probe and the reflected power observed on the oscilloscope monitor. The amplitude of the observed waveform is minimised by adjusting the matching and tuning dials of the probe. These dials adjust capacitors, one set in parallel and one in series, so that they work in combination. Tuning sets the resonance frequency of the RF probe to that of the signal generator and matching sets the impedance of the RF probe to that of the system. A tuned solenoid is achieved when the amplitude of the reflected power is at a minimum for both controls.

3.3 Probe and coil design

NQR probes can be made in a number or forms, the most common being a cylindrical single or multi-turn solenoid or 'bird-cage', with insertion of the sample within the coil, or surface coils, with spiral[1] or meanderline[2] planar antenna. An advantage of NQR over other analytical techniques is the ability to design the probe and coil to fit the sample instead of having to fit the material into a fixed container, for example into fixed volume NMR sample tubes. Planar spiral coils are most often used for applications such as land mine detection or as hand-held scanning devices[3]. The field generated by a spiral coil allows remote detection and can typically reach a depth of 10 – 100 cm but clearly cannot be shielded in the same manner as a contained cylindrical solenoid.

3.3.1 Designing a standard ^{14}N NQR probe

In order to achieve a degree of temperature control, initial experiments were to be carried out using a probe submerged in an oil bath. A suitable hand made probe was designed as follows. A stainless steel lidded canister (12.5 cm diameter, 14 cm height) was used as the main housing and to shield the RF solenoid from external interference, for example from nearby machinery, external radio signals or other equipment. Using a lathe, three 4 mm diameter holes were bored out of the lid of the canister, one in the centre and two 5

cm away from the centre so that all three lay in a straight line. The outer holes were then drilled with a 12 mm bit to increase their diameter. Into one of the larger holes an RS 477 107 Buckhead adapter (co-axial connectors on each side) was placed. Into the other a Greenpar B35H39E010X (co-axial connector on one side, threaded nut on the other) was placed. Each component had the co-axial connection facing out of the lid. These were to be the connectors to the probe for the RF line in and for the induction loop for tuning. The central hole was made to enable the coil to be screwed to the lid (figure 3.4), enabling different solenoids to be used within the probe with ease of exchange.

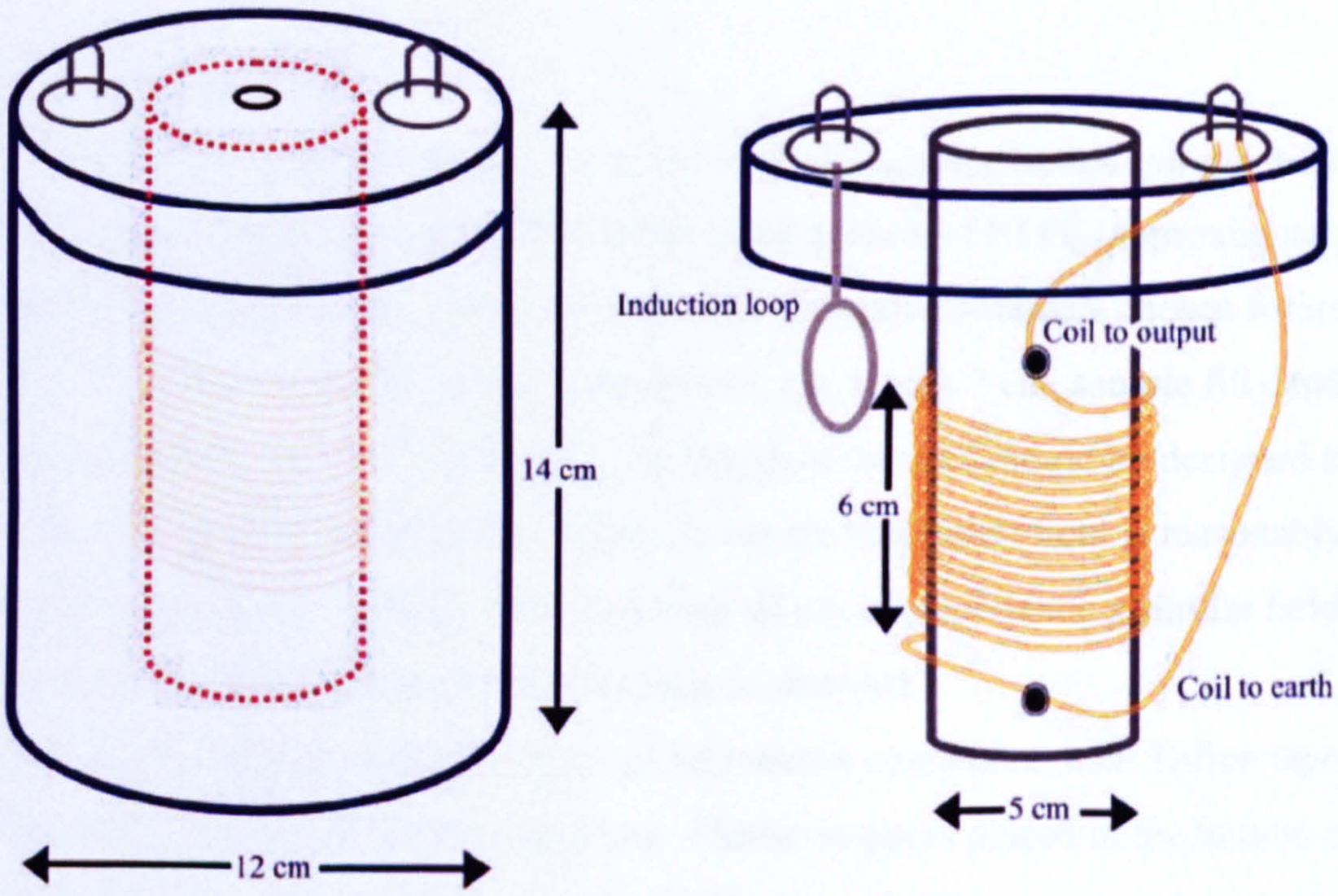

Figure 3.4: Probe 'A' and coil 'A'.

Throughout this research programme only cylindrical solenoids were used. In designing such a coil the number of turns of the coil should be calculated from equation (3.2) so that the inductance is suitable for the intended incident frequencies.

$$L(\mu\mathrm{H}) = r^2 n^2/(9\mathrm{r} + 10l) \qquad (3.2)$$

where L is the inductance (in microhenries)

r is the radius of the coil (in inches)

n is the number of turns of the coil

l is the length of the coil (in inches)

Theoretically, the inductance, L, required for a given frequency, ν, can be calculated from equation (3.3) for a given quality factor, Q, (explained further in section 3.4) and resistance of the system

$$Q = 2\pi\nu\frac{L}{R} \tag{3.3}$$

where R is the resistance.

A 13 cm long, 5 cm internal diameter, 5.5 cm external diameter, hollow plastic drainpipe was used as the coil support and sample holder with a block of PTFE (approximately 5 cm length by 5 cm diameter) held at one end. The standard containers chosen for use in the ^{14}N work were plastic containers of diameter 5 cm, length 7 cm, sample fill depth 5.5 cm giving a sample volume of 108 cm^3. The length of the coil should be designed to be slightly longer than the length of the sample, to ensure that the B_1 field is reasonably homogeneous across the sample, hence ensuring all nuclei experience a similar field strength, and the whole volume of the container is sampled.

The samples were placed in plastic commercial vitamin containers, with Teflon tape used to seal the join between the lid the container. Plastic stoppers placed in the bottom of the pipe ensured the sample was held centrally within the coil. The container was made airtight to ensure that silicon oil from the temperature bath did not enter the sample as this could affect the spectra, due to dissolution or interaction, as well as producing a volume change. Also, the sample would be tedious to dispose of and expensive to replace.

Applying equation (3.2) the number of turns required to give an inductance of 10 μH, calculated for a frequency of 3.56 MHz, was 17. The first coil to be used in this probe (coil A) had been previously built by Dr. Michael Rowe, and consisted of 18 evenly spaced turns of Litz wire, mounted on the PTFE pipe, with a 5 cm diameter and an overall solenoid length of 6 cm. (Litz wire is a multi-strand wire; a number of thin,

insulated wires are woven together to form a wire with a lower resistance than would occur if the wire were a single, thicker uniform strand of metal. It is used to overcome the 'skin effect': an alternating current tends to flow at the edges of a wire, rather than the centre.) The inductance was measured to be 14 μH.

Tin annealed copper wire was used to connect one end of the coil to the co axial connector in the lid and the other end of the coil to earth. It was also used to make the induction loop, and to connect it to the co axial output. An induction loop is a small loop of wire, in this case with an approximate diameter of 15 mm, which allows the RF input to be monitored externally on as oscilloscope. Pulse shapes, widths, and peak-to-peak voltages can all be monitored with an oscilloscope via the induction loop, which can prove particularly useful when diagnosing experimental problems. M4 rings were soldered to the wire for the connections. Tin coated wire can sometimes be problematic in radiofrequency work as the RF flows through the skin, i.e. the tin, instead of through the copper wire, the better, and intended, conductor. The connections were then covered with insulation tape to ensure the wires did not touch the sides of the canister. The lid was then placed on the canister to complete the probe.

3.3.2 Designing a coil of variable pitch

It has been shown that a coil wound with variably spaced turns can give a more homogeneous B_1 field than a comparable coil with even spacing[4]. This is particularly important in quantitative work, where the amount of material in the RF probe has to be determined. A coil of variable pitch was wound, to give increased field homogeneity, based on equations originally given by Leifer[5] which generated a B_1 field with only a 5% peak-to-peak variation. Coil 'A', designed for use around 3.56 MHz, consisted of 18 uniform turns and had an inductance of approximately 14 μH. The dimensions of the coil used by Leifer (5.1 cm diameter, 7.6 cm length) were slightly less than those necessary to hold the preferred sample containers, so a scaled-up version was used.

The 18 turn coil, of length 9 cm, was supported on a length of plastic piping, with external diameter 5.5 cm. A continuous spiral groove, in which the wire would sit, was filed after a guidance line had been etched in; this line was drawn by plotting on graph paper (with ordinates x = coil length and y = circumference) the mid points of the turns at

$+^{2\pi r}/_{2}$ and $-^{2\pi r}/_{2}$, and the turn points along the x-axis, joining the points on the graph to form a series of diagonal lines, wrapping this around the pipe to give a continuous spiral and then cutting along the lines with a Stanley knife. Anchor screws were placed at each end of the coil and 1 mm diameter copper wire was tightly wound onto the pipe along the grooves, with washers and nuts securing the ends at the anchor points. Araldite™ was used to secure the anchor points and varnish was applied over the whole coil to seal it and help to hold the wire in the grooves. The coil was placed in an old probe canister and tuned to 3.563 MHz to enable tests to be carried out. A simple echo sequence was run at room temperature and a ^{14}N signal from furosemide was observed.

The effect of variable pitch on the inductance was of interest: how well would equation (3.2) hold? The inductance across the solenoid was measured using a hand held meter and found to be approximately 9 μH. This is in reasonable agreement with the value of 8.2 μH predicted by the above equation (3.2). Q was found to be approximately 100. To enable a direct comparison and to measure the effect of the variable pitch only, a second solenoid was made, with the same dimensions, materials and construction methods, the only difference being that the turns were equally spaced. For this coil Q = 91 L = 8 μH. In order to measure the field homogeneity a small induction loop, approximately 1 cm diameter, which could be inserted into the solenoid at different positions, was constructed using thin copper wire. The induction loop was mounted on a plastic cylinder and connected to an oscilloscope so that the induced RF signal could be measured. As the loop was moved along the length of the coil in the centre of the solenoid, a repeated RF pulse of 110 μs length was run with the coil tuned to 3.563 MHz, on resonance, and the peak-to-peak voltage measured at intervals of 0.5 cm.

Figure 3.5: Solenoid of variable pitch, 18 turns with an inductance of approximately 9 μH.

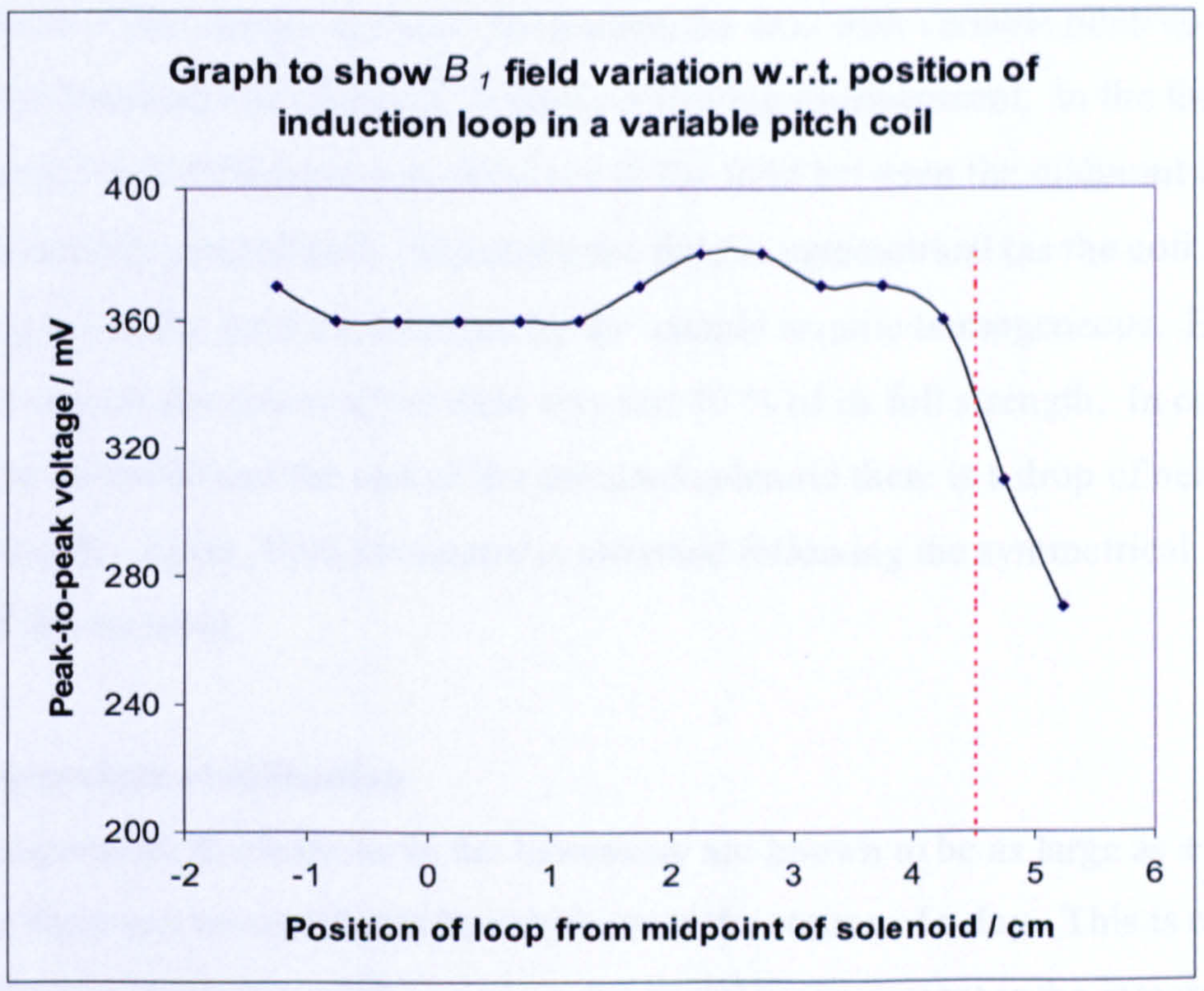

Figure 3.6: Field strength in the variable pitch coil at various points along the coil axis. The end of the solenoid is marked by the red dotted line.

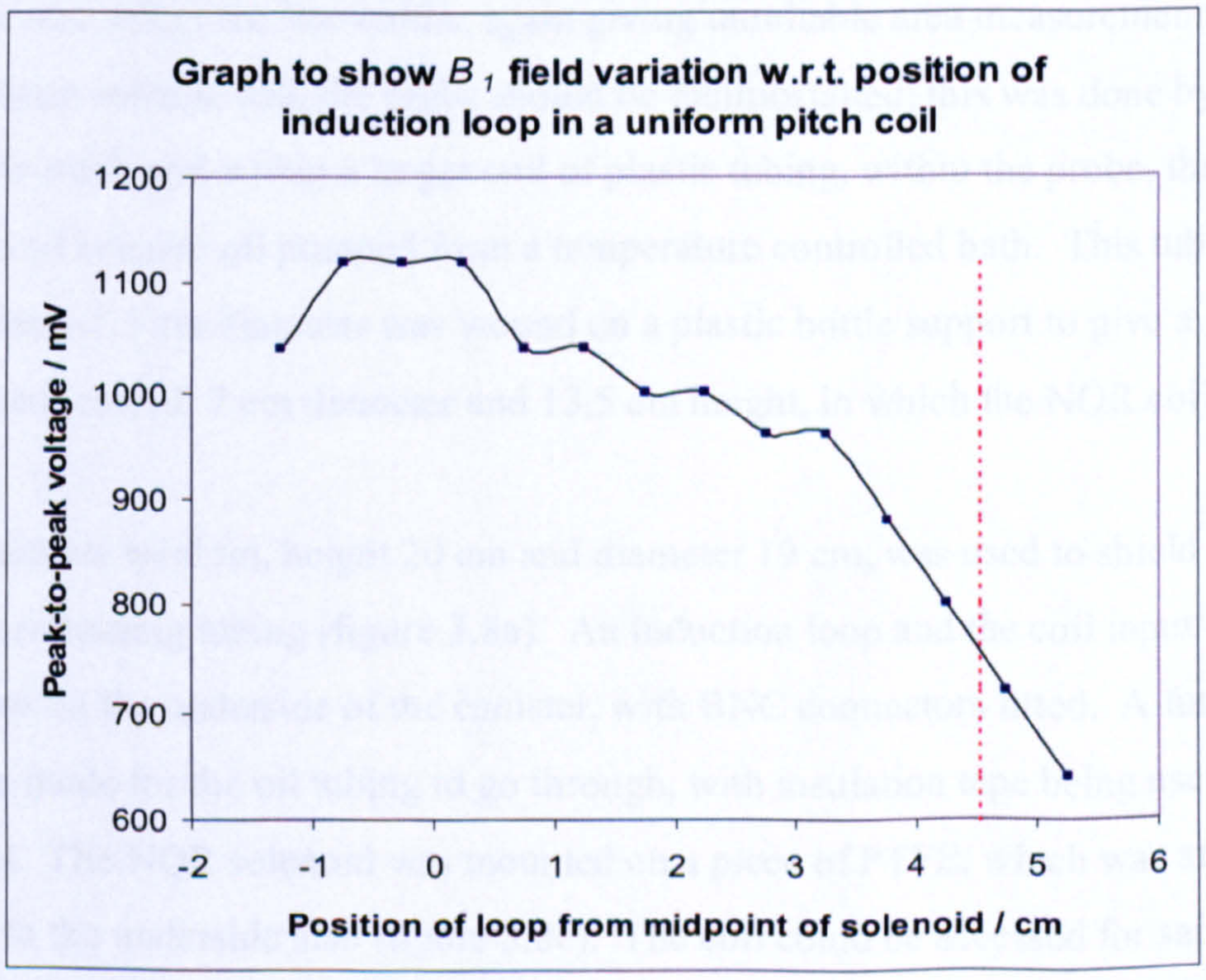

Figure 3.7: Field strength in the standard pitch coil at various points along the coil axis. The end of the solenoid is marked by the red dotted line.

A comparison of the change in the B_1 field along the axis with variable pitch coil (figure 3.6) with the standard coil (figure 3.7) shows a striking improvement. In the former, a range of only 5.3 % difference was observed in the field between the midpoint and the end of the variably pitched coil. Assuming the field is symmetrical (as the coil is, turn and spacing-wise) the field experienced by the sample is quite homogeneous. Even at a point 1 cm outside the solenoid the field was just 70 % of its full strength. In contrast, between the midpoint and the end of the standard solenoid there is a drop of nearly 30 % in field strength. Again, field symmetry is assumed following the symmetrical turn spacing of the solenoid.

3.3.3 Temperature stabilisation

Diurnal temperature fluctuations in the laboratory are known to be as large as ± 5 C and this means there can be significant line shifts over the course of a day. This is especially problematic in quantitative work as one useful signal measurement is the integrated intensity of the peak; with shifting lines it can be difficult to measure the area of the peak as overlapping signals and apparent broadening can occur. Temperature gradients across the sample also affect the linewidths, again giving unreliable area measurements. In order to obtain reliable data the probe should be thermostatted; this was done by setting the variable-pitch coil within a larger coil of plastic tubing, within the probe, through which flowed silicone oil pumped from a temperature controlled bath. This tubing, approximately 1.5 cm diameter was wound on a plastic bottle support to give a thermostatted coil of 7 cm diameter and 13.5 cm height, in which the NQR coil could be contained.

A large stainless steel tin, height 20 cm and diameter 19 cm, was used to shield the NQR coil and surrounding tubing (figure 3.8a). An induction loop and the coil input/output were placed on the underside of the canister, with BNC connectors fitted. A further 2 holes were made for the oil tubing to go through, with insulation tape being used to form a tight seal. The NQR solenoid was mounted on a piece of PTFE, which was attached internally to the underside also (figure 3.8c). The coil could be accessed for sample changing very easily via the lid. The samples were contained within the usual 5 cm by 8.5 cm containers and held in place with a polystyrene stopper. A piece of polystyrene,

approximately 1.5 cm thick was also placed between the end of the coil and the lid, to minimize conduction of heat (figure 3.8d).

The plastic tubing was lagged between the canister and the external connectors of the oil bath, which was set to 25 ± 0.1 C with a constant flow through the tubes for 'room temperature' work. The set up could be used for future higher or lower temperature work with ease.

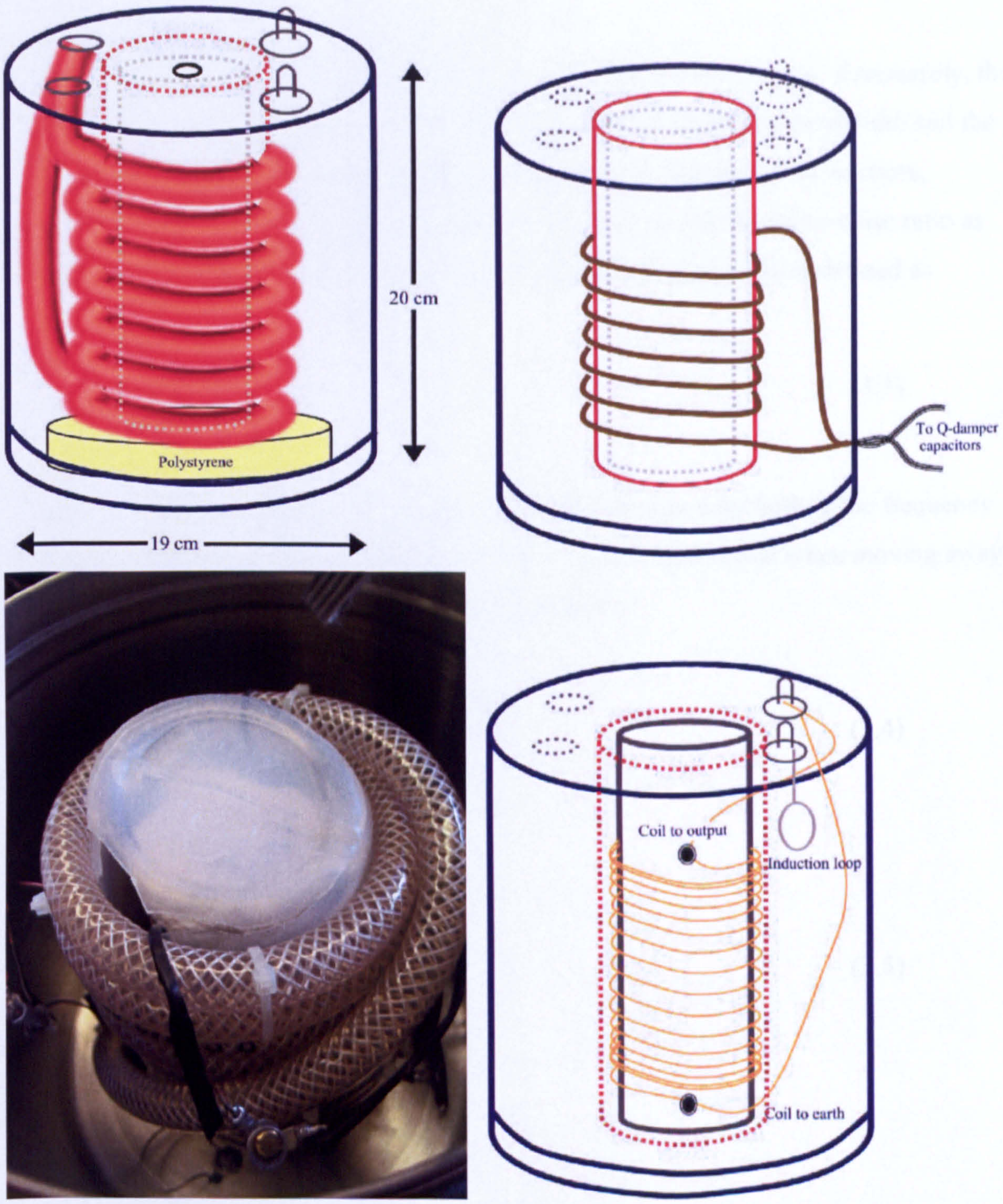

Figure 3.8: The NQR probe and coil 'B', clockwise from top left-; (a) first layer showing the temperature stabilization coil, (b) next the *Q*-damping coil mounted on a plastic cylinder, (c) down to the variable pitch coil mounted on a plastic tube in which the sample in placed. Finally (d) an internal photograph of the probe shows the temperature stabilization coil surrounding the NQR solenoid.

3.4 *Q*-damping

The quality factor (Q) of a coil is a measure of its ability to store energy. Conversely, the lower the Q value, the greater the damping – the wider the frequency bandwidth and the shorter the decay time. In damping Q the excess energy is dissipated by resistors, lessening ringdown and allowing shorter dead times, increasing signal-to-noise ratio as more of the signal can be accumulated. We recall that the Q of a coil is defined as

$$Q = 2\pi\nu\frac{L}{R} \tag{3.3}$$

In practice, once a probe has been set up it is readily measured by finding the frequency range, $\Delta\nu$, over which a voltage greater than $0.7*V_{tuned}$ is maintained when moving away from the tuned frequency, ν_Q, and using the equation

$$Q = \frac{\nu_Q}{\Delta\nu} \tag{3.4}$$

The probe ring down time is

$$\tau_r \approx \frac{Q}{\pi\nu_Q} \tag{3.5}$$

and the dead time is defined by

$$t_d = \frac{Q\ln\left(A_0/A_t\right)}{\pi\nu_Q} = \tau_r \ln\left(A_0/A_t\right) \tag{3.6}$$

Typically at 3.7 MHz, A_0 (the initial voltage) is approximately 10 kV, A_t (the voltage after the dead time) is around 1 μV, so $23\,\tau_r = t_d$ approximately. Following a design by Nigel Hunt at ERA Technology Ltd[6], a Q-damping coil and circuitry (figure 3.9) were

constructed. The main circuitry (figure 3.10a), which can be transferred for use with any Q-damping coil and frequency, and the capacitance and resistance box (figure 3.10b), which can be varied accordingly, were housed in die-cast aluminium boxes, with BNC connectors for ease of use. In the capacitance box, screw-in connector blocks were used to enable the capacitors and resistors to be changed easily.

The capacitances for **C8** and **C9** were calculated using the following equation:

$$\nu = \frac{1}{2\pi\sqrt{LC}} \tag{3.7}$$

The optimum values for resistors **R16** and **R17** were found using a potentiometer: in place of one of the resistors, a shorting link was inserted and a potentiometer was placed across the other. The resistance was adjusted, with the pulse shape monitored on an oscilloscope, until optimum damping was achieved. The potentiometer was then removed and the resistance measured. The value was then divided by two and the resulting values used for **R16** and **R17.**

3.4.1 *Q*-damper circuitry

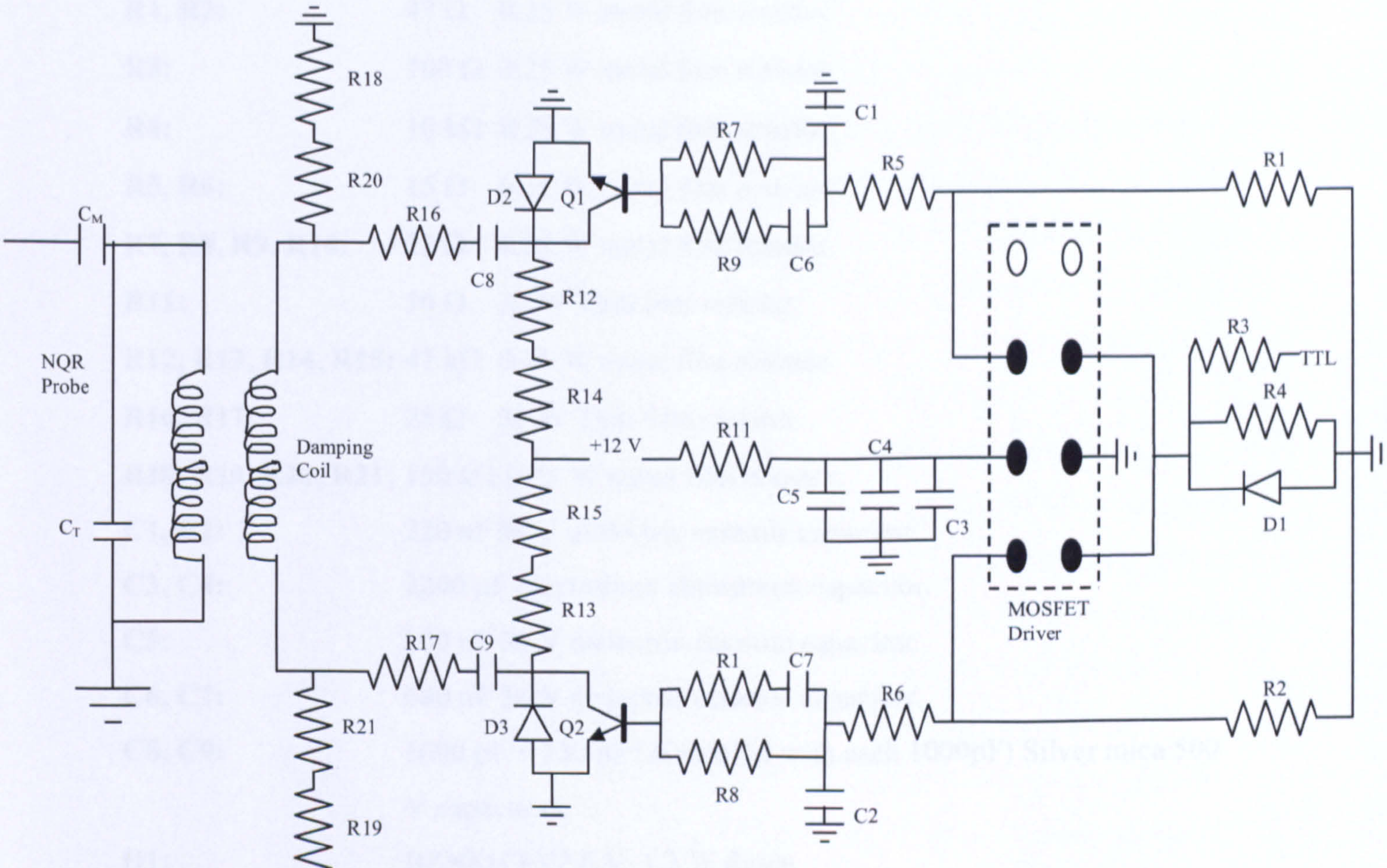

Figure 3.9: *Q*-damper circuit diagram.

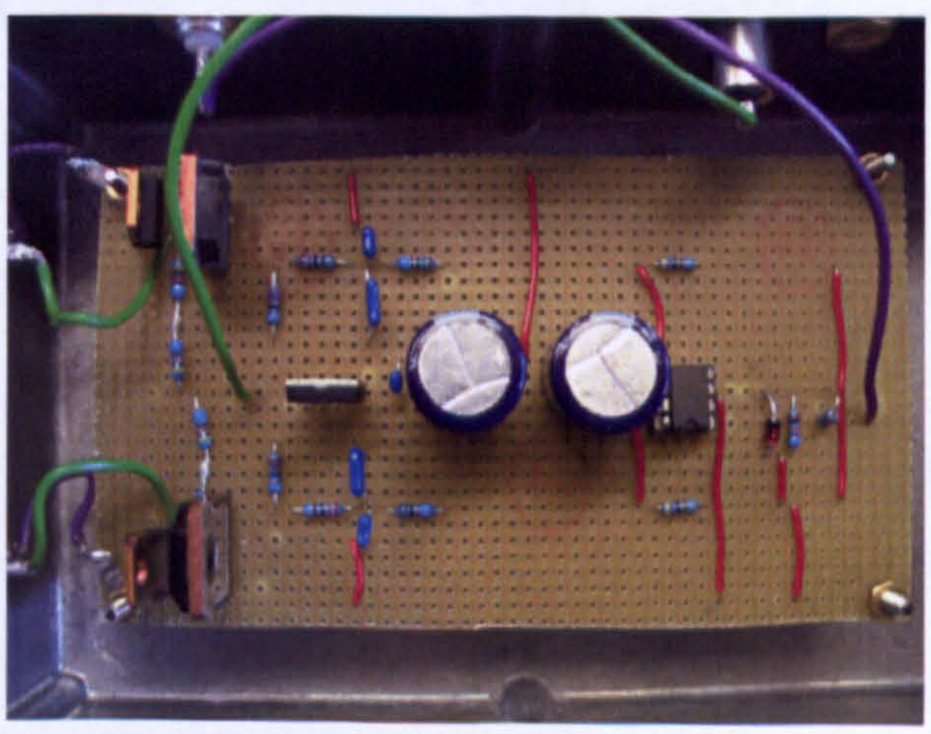

Figure 3.10a: The main *Q*-damping circuitry.

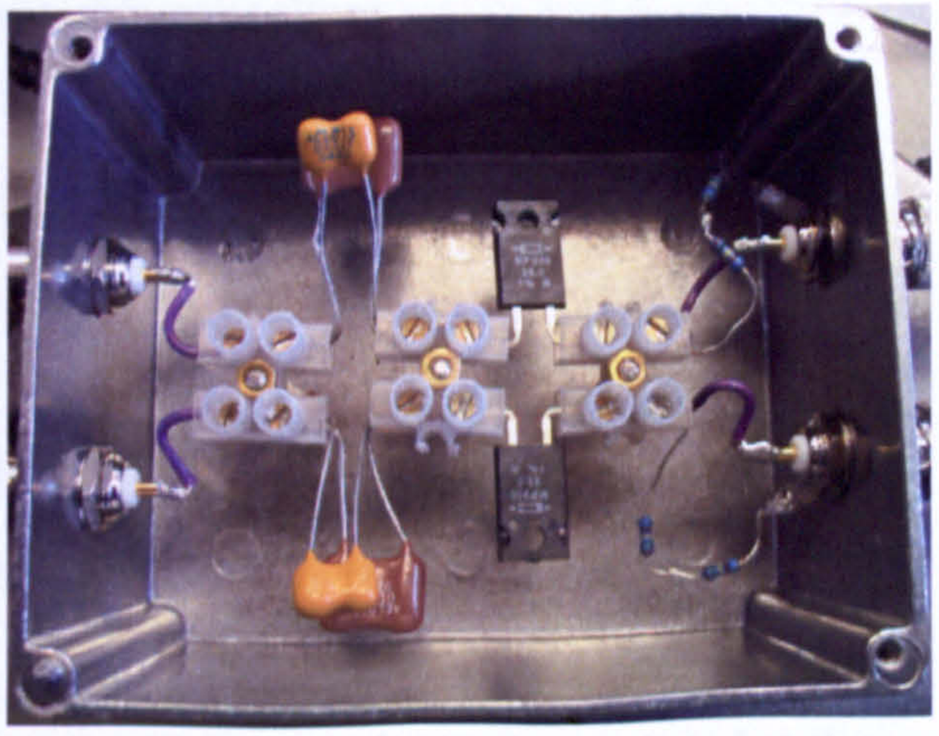

Figure 3.10b: The separate capacitance box (**C8, C9, R16 – R21**).

Key to components

R1, R2:	47 Ω	0.25 W metal film resistor.
R3:	100 Ω	0.25 W metal film resistor.
R4:	10 kΩ	0.25 W metal film resistor.
R5, R6:	15 Ω	0.25 W metal film resistor.
R7, R8, R9, R10:	22 Ω	0.25 W metal film resistor.
R11:	10 Ω	30 W Thin film resistor.
R12, R13, R14, R15:	47 kΩ	0.25 W metal film resistor.
R16, R17:	25 Ω	30 W Thin film resistor.
R18, R19, R20, R21:	150 kΩ	0.25 W metal film resistor.
C1, C2:	220 nF 50 V dielectric ceramic capacitor.	
C3, C4:	2200 μF electrolytic aluminium capacitor.	
C5:	100 nF 50 V dielectric ceramic capacitor.	
C6, C7:	680 nF 50 V dielectric ceramic capacitor.	
C8, C9:	1000 pF + 330 pF (in parallel with each 1000pF) Silver mica 500 V capacitors.	
D1:	BZX85C6V2 6 V, 1.3 W diode.	
D2, D3:	STTA806D TO220 diode.	
Q1, Q2:	BUP35 High voltage NPN transistor.	
C_M, C_T:	Matching and tuning variable capacitors.	
TTL	Trigger: lower BAROUT module from Libra spectrometer.	
+12 V:	Adjustable power supply (10 to 20 V) set at 12 V.	
MOSFET Driver:	MC34152P	

The R1, R8, C7 and C2 (and corresponding R7, R9, C6 and C1) parts of this circuit ensure a smooth restoration of *Q*, decreasing the problem of voltage flares at the 'switch-off' point.

Initially a damping coil of 4 turns (length 8 mm, radius 55 mm) was constructed and mounted on a length of solid plastic, which acted as a 'stopper' at the base of the NQR coil. The damping coil was approximately 20 mm away from the end of the NQR

solenoid. Tuning was checked using a small induction loop placed at the end of the damper coil, and the required capacitance for C8 and C9 was found. Tests to measure the effectiveness of the *Q*-damper were carried out; these included monitoring the pulse shape using a pick up loop, measuring *Q* using a frequency generator and varying the dead time in a simple FID pulse sequence to see when breakthrough occurred. Although there was some effect, the results were not satisfactory: the damping coil may have been too far away from the solenoid field to couple well, a problem aggravated in this case because a variable pitch coil produces a sharper drop in field strength at each end of the solenoid than a standard coil. A *Q*-damping coil which would surround the coil was planned. The probe had been initially designed with temperature control in mind, for which purpose a tube containing silicon oil was mounted on a plastic cylinder, which was placed over the NQR coil. The damping coil was also mounted on this plastic cylinder, with the wire being placed between the turns of the oil tube (figure 3.8b). The damping coil had 7 turns, a length of 3.5 inches and radius 1.25 inches, giving a calculated inductance of 1.66 μH. The damping coil was approximately 10 mm away from the NQR coil. A hole was drilled in the side of the canister, through which *Q*-damping coil wires could exit to join the capacitance box. Greatly enhanced results were seen. Using a simple FID sequence before and after the *Q*-damping, the affect on dead time was impressive and easily observed: using the induction loop to monitor the pulses, the difference was clear between the *Q*-damped pulse and the undamped pulse (figures 3.11a and 3.11b).

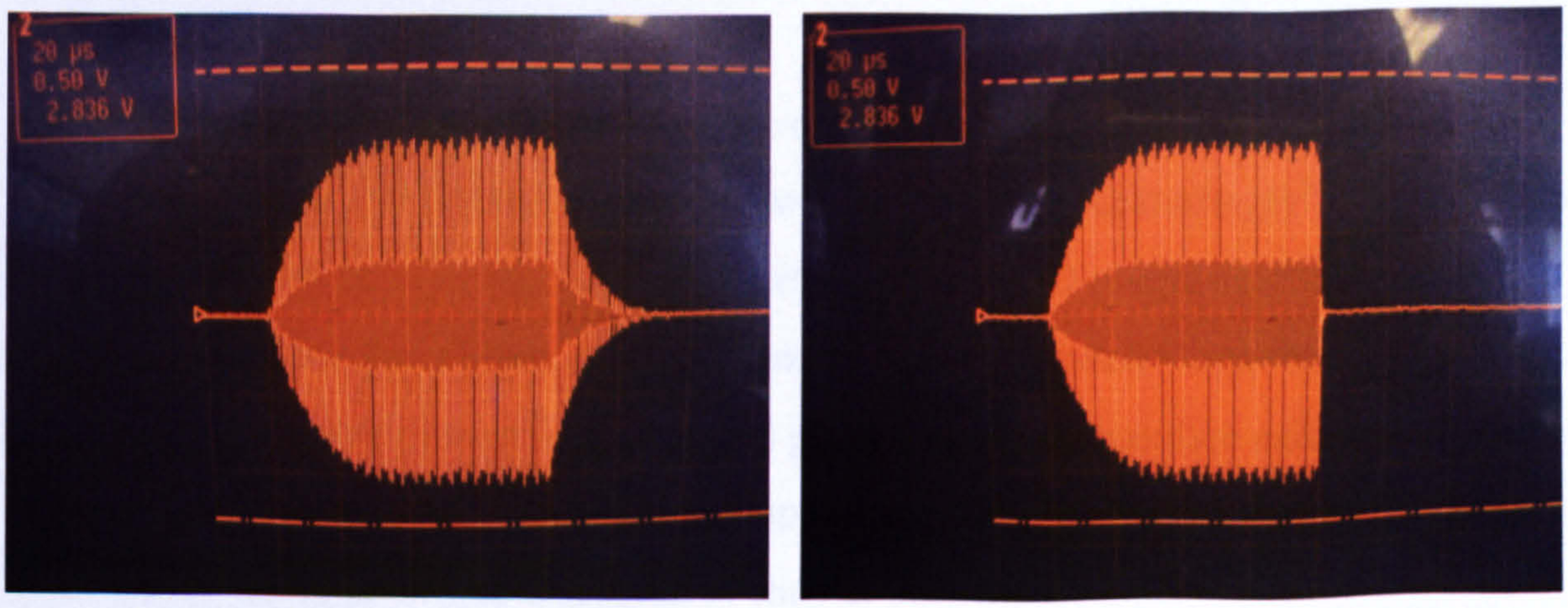

Figures 3.11a and 3.11b: An 80 μs pulse, monitored using an induction loop, (a) pre- and (b) post-damping at 3.787 MHz. Scale: each increment is 20 μs.

Prior to *Q*-damping, a 170 μs dead time was required to give a 'clean' signal at 3.787 MHz with no breakthrough following an 80 μs, 90_{eff} pulse - with damping this was reduced to 20 μs, giving great potential for zero time resolution[7,8] measurements. *Q*-damping enables stronger signals to be observed, as more of the signal can be recorded in a shorter time, especially vital in cases of substances with short decay times.

3.5 Pulse sequences and data processing

Pulse sequence programming is carried out using the Tecmag supplied MacNMR 5.5 software. The layout can be compared to that of a musical score with events numbered from 1 to infinity, like bars in music, and the different actions, such as delays, phase information, loop information, number of acquisition points and their dwell times and pulse lengths are programmed in at different bars. As well as programming the pulse sequence to be carried out, the MacNMR software allows the user to carry out a range of spectral analysis and data processing options, with those used in this research described below.

3.5.1 Spectral analysis

When the NQR signal is recorded the real, imaginary and magnitude intensities of the lines are plotted. Following the acquisition of the signal in the time domain the spectrum undergoes a sequence of processes before analysis.

3.5.1.1 Baseline correction

Firstly, the signal is baseline corrected; this removes any d.c. offset by calculating the mean over the last 12 % of the data and adjusting the spectra accordingly[9]. Badly defined baselines can also be a serious systematic error; the first FID points determine the baseline and an incorrect point, due for example to pulse breakthrough, can lead to a d.c. offset and a number of incorrect points will greatly affect the baseline and lead to 'bowing' or 'rolling'[10]. It is particularly important to ensure a true baseline in quantitative work, as will be discussed in chapter 5.

3.5.1.2 Zero filling and digitisation noise

Zero filling is another method of seemingly enhancing the resolution. If there are N data points in the time domain free induction decay, a further N zero points are added to the spectrum; twice the number of data undergoes Fourier transformation and SNR is increased by a factor of $2^{½}$. This increase in the number of points in the frequency domain improves definition, giving a smoother looking spectrum, the resolution of which is limited by the rate of acquisition of data and the dwell time of which the spectrometer is capable. In order to achieve as good a resolution as practical a short dwell time with respect to the total acquisition time is important. The Tecmag equipment can theoretically achieve 1 μs dwell times, but in practice 3 μs is the minimum used in signal acquisition. The process of converting a continuous analogue signal into discrete data points produces digitisation noise and the spectral resolution, i.e. dwell time, is important in its determination. Having achieved a time domain spectrum with the best possible conditions and applied the necessary signal processing techniques, Fourier transformation is carried out in order to visualise the NQR signal in the frequency domain.

3.5.1.3 Fourier transformation

Fourier transformation is an important tool in NMR and NQR. A wave can be seen graphically in two different ways; as a snapshot in time, viewing amplitude vs. frequency, or as amplitude vs. time - two different views of the same information. Fourier transformation is a function that allows us to translate one form into the other. The FID seen in NQR is directly seen as amplitude vs. time but is a combination of a number of frequencies. As well as the resonance frequencies there are noise frequencies and together all these form an interferogram. It is not easy to identify the dominant frequencies from the FID, so Fourier transformation is used to give us what are often Lorentzian peaks in an amplitude vs. frequency plot, so they can be easily observed.

To convert the time domain data to the frequency domain the following equation is used[11]

$$f(\omega) = \int_{-\infty}^{\infty} F(t) e^{-i\omega t}\, dt \qquad (3.8)$$

To convert information in the frequency domain to the time domain

$$f(t) = \frac{1}{2}\int_{-\infty}^{\infty} F(\omega)e^{i\omega t}d\omega \; f(t) \qquad (3.9)$$

where $f(\omega)$ is the Fourier transform of the time varying function $f(t)$ and ω is angular frequency. Equation (3.9) can be expanded to

$$f(t) = \int_{-\infty}^{\infty} F(\omega)\cos(\omega t)d\omega + \int_{-\infty}^{\infty} F(\omega)\sin(\omega t)d\omega \qquad (3.10)$$

and it becomes clear that the time dependent function can be seen as a sum of a number of functions at varying frequencies, the most dominant of which we hope to be the NQR signal.

A single RF pulse can excite a range of frequencies simultaneously, decreasing the time necessary to achieve an acceptable SNR. This is known as the Fellgett, or multiplex, advantage and the experimental sensitivity gained allows a reduction of $t^{1/2}$ in the acquisition time compared to the use of a single, monochromatic excitation.

Echo Fourier transformation allows Fourier transformation of an echo with the view that an echo is simply two free induction decays back-to-back. The beginning of the FID can be set at any defined point within the time domain signal. The default setting assumes the peak of the echo, and the start of the FID, to be the midpoint of the time domain signal acquisition period, although this can be changed manually, depending on the pulse sequence and conditions. For ease of processing the 1DFT command can be set up to baseline correct, zero fill, Fourier transform and phase adjust in one 'click'.

Fourier transformation does have its disadvantages; it is assumed the data runs to infinity whereas in practice there is a defined end time of acquisition. This is remedied by apodisation which smooths a spectrum that has a defined end point, that is to say, applying an apodisation function essentially lessens the 'sharp edges' at the beginning or end of an event. This can help to reduce noise and give a sharper spectrum by removing the variation of signal on either side of the main peak. However, very weak signals could

be lost, and it is important to ensure that the acquisition time is long enough to record a full response[12]. The apodisation function is carried out automatically as part of the Fourier transformation option in the MacNMR software.

3.5.2 Pulse breakthrough

Pulse breakthrough is an example of systematic noise. It is often due to ringdown but can also be caused by an underlying signal from the spectrometer. The ringdown breakthrough can be removed by lengthening dead time, introducing Q-damping circuitry, or removal of initial points in the time domain spectrum before Fourier transformation. Alternating the phases in the pulse sequence can remove any breakthrough due to current leakage which could otherwise dominate the Fourier transformed frequency domain spectrum.

3.6 Double resonance quadrupole resonance techniques

The apparatus and techniques described above are used for what is known as pure or zero-field NQR. However, there are a number of different double resonance methods which can be utilized in NQR spectroscopy. Double resonance methods are more complicated than 'pure' NQR but can bring advantages not present in zero-field experimentation, in particular because there are at least two spin systems, their interactions can bring enhancements which would not be seen in a single system experiment. Double resonance experiments can be particularly useful when faced with a material of which the NQR frequencies are unknown, especially if the signals are thought to be weak. They provide a easier frequency searching by estimation of the zero field NQR frequency from a fixed frequency high-field NMR spectrum. Double resonance by level crossing (LC) and cross relaxation (CR) NQR are two methods in which the high-field spin-$^1/_2$ ^{1}H signals are measured. They are briefly discussed below, as these techniques were used in this work by Drs. Anthony Horsewill and David Stephenson's research group, polarisation-enhanced NQR (PE-NQR), in which the quadrupolar nuclei signals are measured, will be discussed in chapter 8.

In this field-cycled technique the non-quadrupolar spin-$^1/_2$ (usually ^{1}H) spin system undergoes polarization in a high magnetic field; as the field is cycled to zero, at level

crossing the ^{1}H magnetisation is transferred to the quadrupolar nuclei (e.g. ^{14}N) giving an enhanced NQR signal in zero field. The basic field cycle is illustrated in figure 3.12.

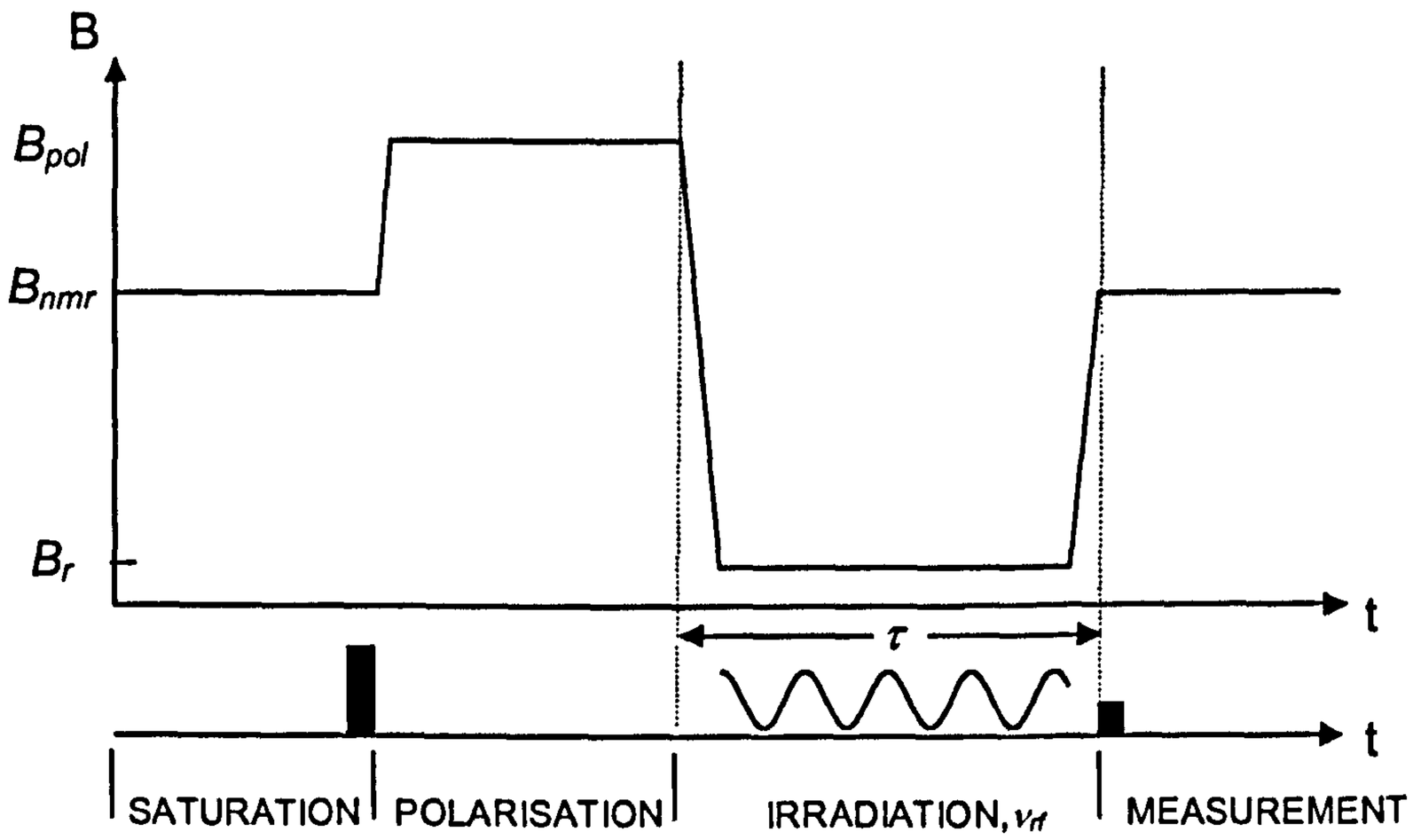

Figure 3.12: NMR sequence used in double resonance experiments.

3.6.1 Double resonance by level crossing

In double resonance by level crossing[13] (DRLC) experiments the sample under investigation is first placed in a large magnetic field; the polarising field B_{pol} is typically around 1 Tesla and polarisation times can be up to a minute or more to allow the ^{1}H spins to reach an equilibrium temperature with the lattice. Level crossing occurs as the sample passes from high to low field where the Zeeman splittings equal the quadrupolar splittings. Following this, the nuclei are irradiated in zero field with RF radiation. Level crossing occurs once more as the sample experiences the increasing field. The proton response is then measured back in high field; the NMR observation field B_{nmr} is set lower than the polarizing field and corresponds to a proton NMR frequency. The presence of quadrupolar nuclei is observed when level crossing has taken place; energy gained by the quadrupolar nuclei in low field is transferred to the protons which results in a loss of signal in high field. As the frequency is swept across the region of interest minima are observed corresponding to quadrupole resonance frequencies in zero field.

3.6.2 Double resonance by cross relaxation

Cross-relaxation[14] (CR) NQR is a non-irradiative technique; in these experiments, B_{nmr} is equal to B_{pol}, both being supplied by a permanent magnet. The sample is polarised in high field, and the ^{1}H NMR signal is then recorded. The sample is then transferred to the cross-relaxation field. At this point the spins reach a common spin temperature during the cross relaxation time. No RF radiation is applied; relaxation occurs at a rate which is influenced by both the proton and quadrupolar spin-lattice relaxation rates. The CR spectrum is achieved by stepping B_{res} between successive ^{1}H NMR signals in the region of interest (the range in which the quadrupolar frequencies are expected to be found). Dips are seen in the cross relaxation spectrum, corresponding to losses in the proton signal. The frequencies at which these dips occur are shifted from the pure, zero field, NQR frequencies due to Zeeman effects, although this can be corrected for, and the lines are also broadened. Sensitivity is increased when the quadrupolar spin-lattice relaxation time is much shorter than that of the protons.

3.7 References

[1] Suits, B. H.; Garroway, A. N.; Miller, J. B.; *J. Magn. Reson.* **1998**, *135*, 373 - 379.

[2] Buess, M. L.; Garroway, A. N.; Miller, J. B.; *J. Magn. Reson.* **1991**, *92*, 348 - 362.

[3] Garroway, A. N.; Buess, M. L.; Miller, J. B.; Suits, B. H.; Hibbs, A. H.; Barrall, G. A.; Matthews, R.; Burnett, L. *IEEE Trans. Geosci. Rem. Sens.*, **2001**, *39*, 1108 - 1118.

[4] Idziak, S.; Haeberlen, U. *J. Magn. Reson.* **1982**, *50*, 281 - 288.

[5] Leifer, M. C. *J. Magn. Reson.* **1993**, *A105*, 1 - 6.

[6] Hunt, N. ERA Technologies, *Personal Communication.*

[7] Singh, M. A.; Armstrong, R. L. *J. Magn. Reson.*, **1988**, *78*, 538 - 554.

[8] Vollmers, K. W.; Lowe, I.J.; Pukkinen, M. *J. Magn. Reson.*, **1978**, *30*, 33 - 50.

[9] MacNMR 5.4 Manual, Tecmag. **1996.**

[10] Freeman, R. *A Handbook of Nuclear Magnetic Resonance*, 2nd Edition. Addison Wesley Longman Ltd, **1997**, pp 116 - 117.

[11] Marshall, A. G.; Verdun, F. R. "*Fourier Transforms in NMR, Optical, and Mass Spectrometry,*" Elsevier Science Publishing Company Inc. **1990.**

[12] Shaw, D. *Fourier Transform NMR Spectroscopy, 2nd Ed.* Elsevier Science publishing company inc., Amsterdam, **1984.**

[13] Edmonds, D. T.; *Phys. Lett. C*, **1977**, *29*, 233 - 290.

[14] Stephenson, D.; Smith, J. A. S. *Proc. R. Soc. London, Ser. A*, 1988, *416*, 149 - 178.

4 Furosemide

4.1 Introduction

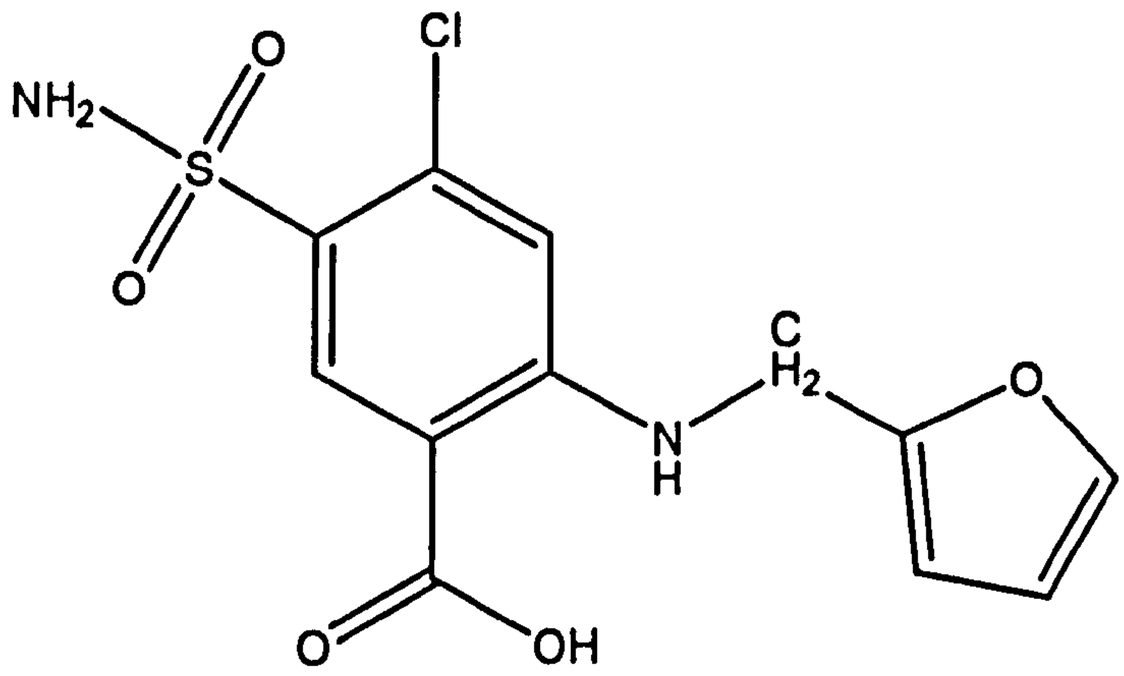

7

Furosemide (7) was chosen as a sample material to be studied as it is a currently produced diuretic widely used in the treatment of hypertension[1]; it exhibits polymorphism, existing in several crystal forms, containing two abundant quadrupolar nuclei, ^{14}N and ^{35}Cl with three quadrupolar environments with potential for analysis within each molecule - a sulfonamide group, a secondary amine and the chlorine atom attached to a benzene ring. Chlorine signals have been reported at 77 K[2] but not extensively studied prior to this work. Furosemide tablets, manufactured by Hoechst Marion Roussel and marketed as Lasix®, are available in 20 mg, 40 mg and 500 mg doses and the pure powder can be purchased from Sigma and generally used without further purification. The objectives of this work were to characterize the ^{14}N and ^{35}Cl signals in furosemide powder; to observe signals from furosemide tablets and record any changes in the corresponding powder signals; to find at least one NQR signal in a polymorph of furosemide and to demonstrate the ability to distinguish between polymorphs using NQR.

4.2 X-Ray crystal structure

Previous publications[3,4] have reported a number of forms of furosemide, four crystal phases, two solvates (DMF and dioxan) and one amorphous form. The X-ray crystal structures have been published for furosemide phases I[5] and II[6,7], although the two phase II structures were found to have seemingly different unit cells. However, when the

triclinic cell dimensions reported in the two papers are properly reduced, to give angles of less than 90 °, both papers have similar values:

	a	*b*	*c*	α	β	γ
[6]:	5.251	8.771	15.038	78.23	89.05	82.43
[7]:	5.234	8.751	14.982	77.43	89.10	84.41

Some structural data can be found in the literature regarding the other forms[3,4].
The form of furosemide used medicinally, and the most stable, is obtained in the laboratory by recrystallisation from acetone and will be referred to as phase I. The triclinic crystals of phase I furosemide have the space group $P\bar{1}$ and $Z = 4$[5] and two sets of ^{14}N signals are expected, one from the secondary amine and the other from the sulfonamide nitrogen, both of which should be doublets.

4.3 ^{14}N Phase I furosemide quadrupole resonance experiments

4.3.1 Cross relaxation

As no ^{14}N NQR data had been published for this material, prior to the start of this work, an initial cross relaxation experiment was carried out by David Stephenson at the University of the West Indies. Approximately 1 gram of phase I furosemide powder was used with the following experimental conditions; room temperature pneumatic transfer from high field (^{1}H frequency of 20.10 MHz - permanent magnet of 0.472 T) to cross-relaxation field stepped from 0 to 4700 kHz in 4.58 kHz increments with time at high field magnet, $\tau_P = 20$ s and time at low field, $\tau_Q = 80$ ms.

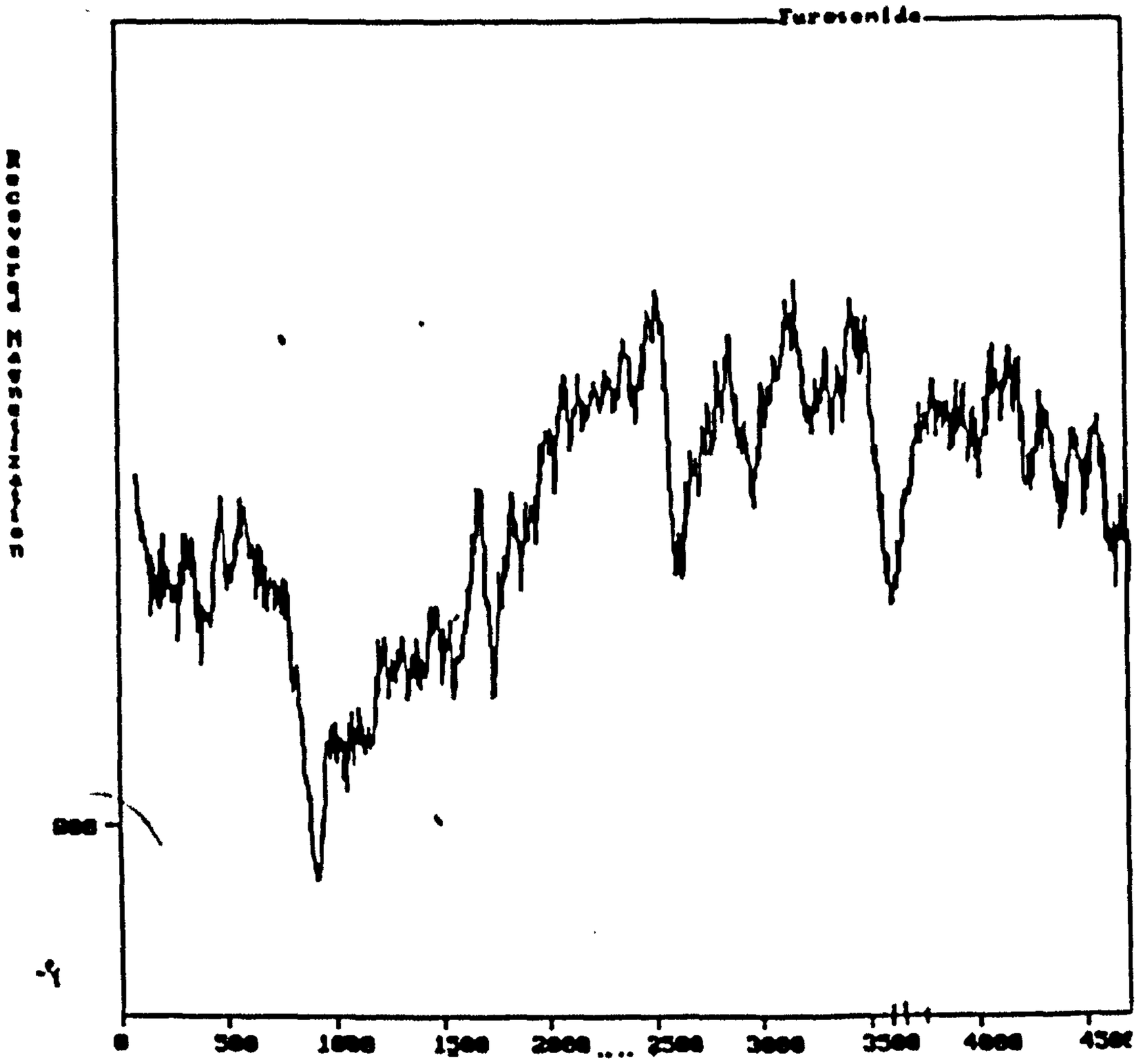

Figure 4.1: Furosemide phase I cross relaxation spectrum, the sum of 7 spectra, with the horizontal axis being approximate frequency (kHz).

The ^{14}N cross relaxation spectrum (figure 4.1) showed some evidence of doubling as expected. The pronounced dip around 3.6 MHz is most likely due to the ^{14}N nuclei of the sulfonamide group. Based on these data a search for the ^{14}N NQR frequency in zero field was conducted around this region.

4.3.2 Furosemide ^{14}N frequency searching.

4.3.2.1 Experimental set-up with HMX as a surrogate material

A pulse spin locking echo (PSL) sequence was run using the explosive HMX (**1**) as a surrogate material, as it has a similar NQR frequency, 3.62 MHz[8], with a strong signal which is usually easily observed. A 170 g sample of HMX was placed in coil A and the

Amplifier Research 1000 Watt amplifier, a *Tecmag* NQRkit and a *Tecmag* Libra-F12 spectrometer were used together with the standard equipment at room temperature.

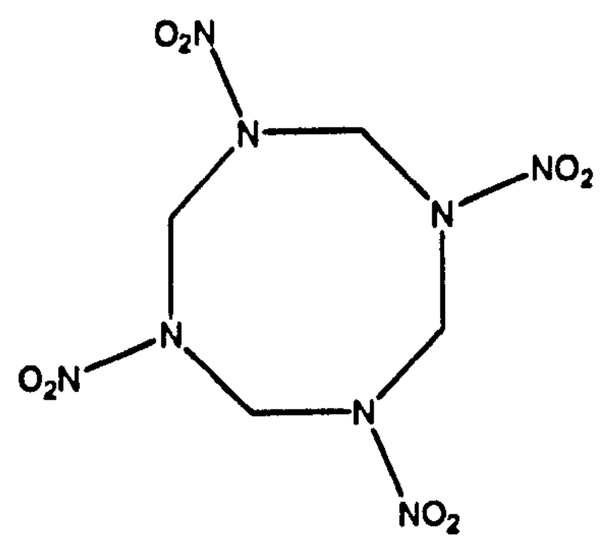

1

Event	
Pulse / μs	40
Acquisition	128 points / 10 μs dwell time
Final Delay / ms	100
No. of scans	5000
Frequency / MHz	Variable

Table 4.1: HMX and Furosemide frequency search PSL pulse sequence.

An echo was observed for HMX using a PSL sequence with the above settings and, following this, furosemide experiments were begun.

4.3.2.2 Search for ^{14}N signal from phase I furosemide around 3.6 MHz

Following the observation of a signal at 3.623 MHz from HMX, the same conditions were to be used to search the radiofrequency range between 3.500 and 3.620 MHz, in steps of 0.005 MHz, with the probe tuned to within 11 kHz. Approximately 56 g of phase I furosemide powder was densely packed into a lidded plastic cylinder, 5 cm in diameter by 7 cm in height, and the sample was placed in the RF coil at room temperature. All apparatus was as used above. The experiment was conducted at room temperature, with a diurnal variation of ± 5 K. The spin-lattice relaxation rate was unknown at this point so a sufficient recovery time between scans was required to allow for a long T_1.

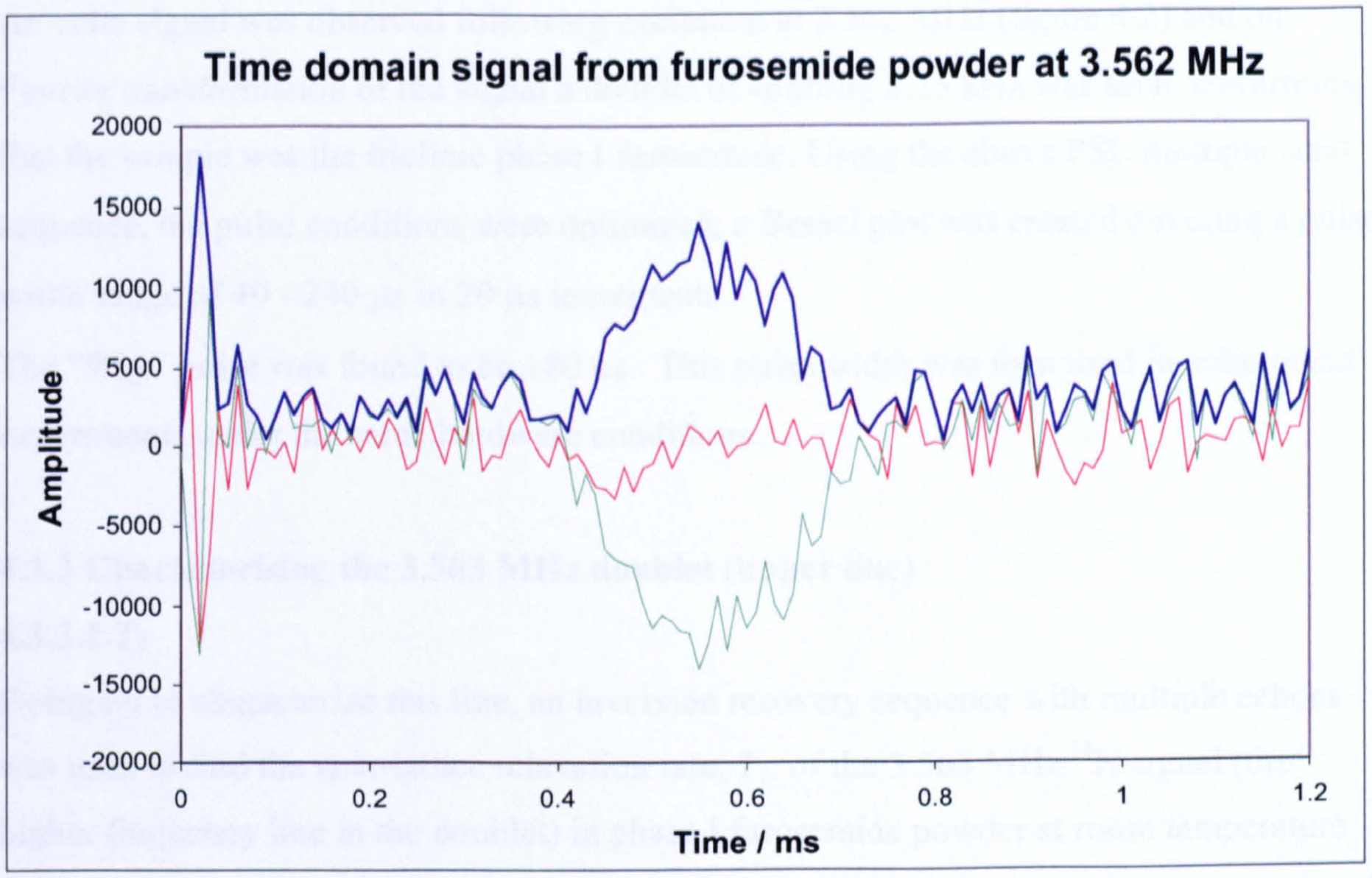

Figure 4.2: Furosemide (Sigma powder) ^{14}N room temperature signal in the time domain; 10 summed echoes in each PSL scan, 10000 scans; 3.562 MHz.

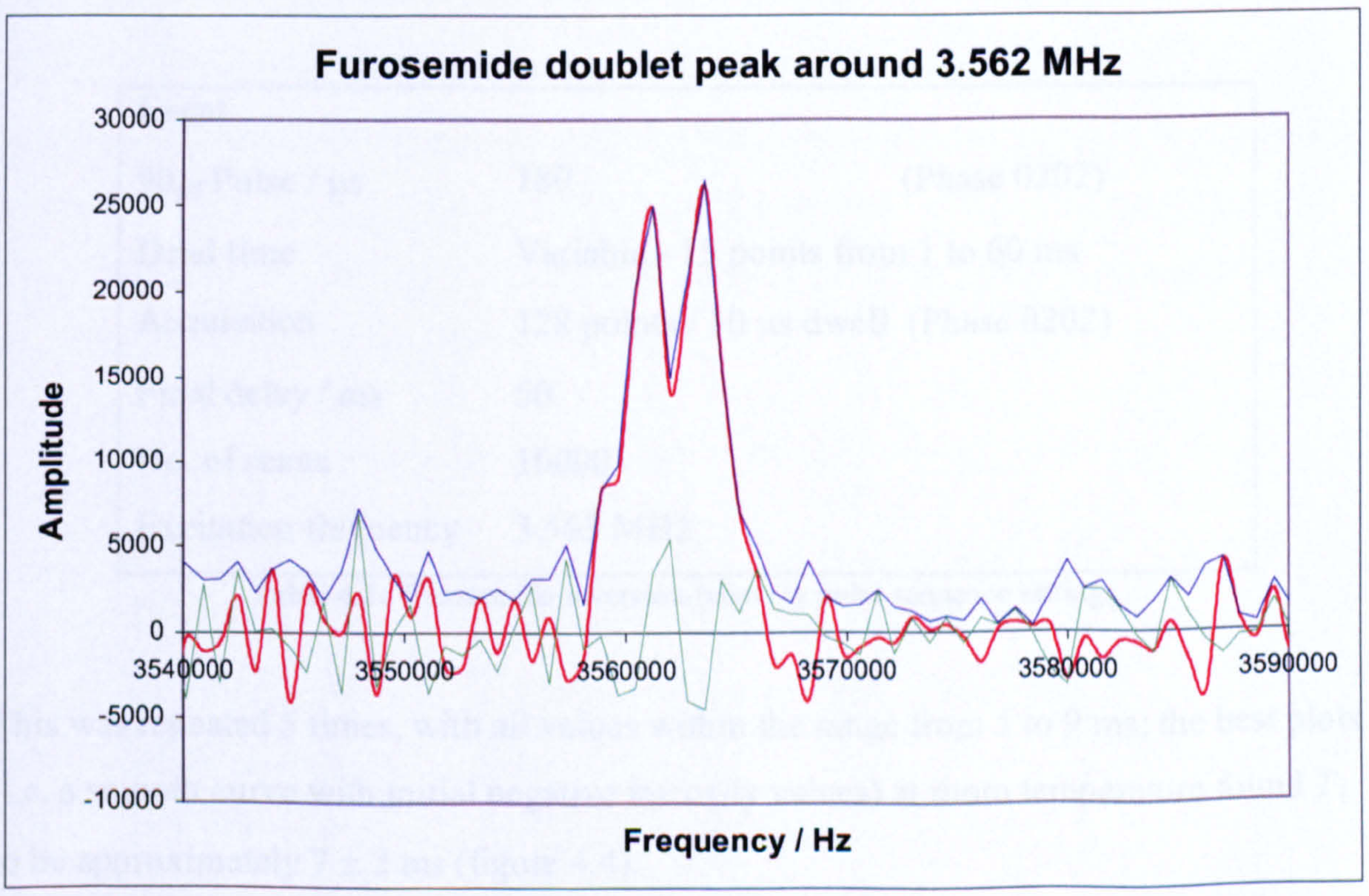

Figure 4.3: Doublet peak from furosemide (Sigma powder); Fourier transform of figure 4.2 with doublet frequencies 3.5636 and 3.5612 MHz, splitting approximately 2350 Hz.

An echo signal was observed following excitation at 3.562 MHz (figure 4.2) and on Fourier transformation of the signal a doublet of splitting 2.35 kHz was seen, confirming that the sample was the triclinic phase I furosemide. Using the above PSL multiple echo sequence, the pulse conditions were optimized; a Bessel plot was created covering a pulse width range of 40 - 240 μs in 20 μs increments.

The "90_{eff}" pulse was found to be 180 μs. This pulse width was then used in subsequent experiments under the same hardware conditions.

4.3.3 Characterising the 3.563 MHz doublet (upper line)

4.3.3.1 T_1

Going on to characterize this line, an inversion recovery sequence with multiple echoes was used to find the spin-lattice relaxation rate, T_1, of the 3.563 MHz ^{14}N signal (the higher frequency line in the doublet) in phase I furosemide powder at room temperature under with the following conditions. Determining T_1 would allow the optimum setting of the time between scans, ensuring that no signal was loss due to insufficient recovery time and excessive experimental times were not used from over estimation of recovery time.

Event		
90_{eff} Pulse / μs	180	(Phase 0202)
Dead time	Variable - 15 points from 1 to 60 ms	
Acquisition	128 points / 10 μs dwell	(Phase 0202)
Final delay / ms	50	
No. of scans	10000	
Excitation frequency	3.563 MHz	

Table 4.2: Furosemide inversion-recovery pulse sequence settings.

This was repeated 5 times, with all values within the range from 5 to 9 ms; the best plots (i.e. a smooth curve with initial negative intensity values) at room temperature found T_1 to be approximately 7 ± 2 ms (figure 4.4).

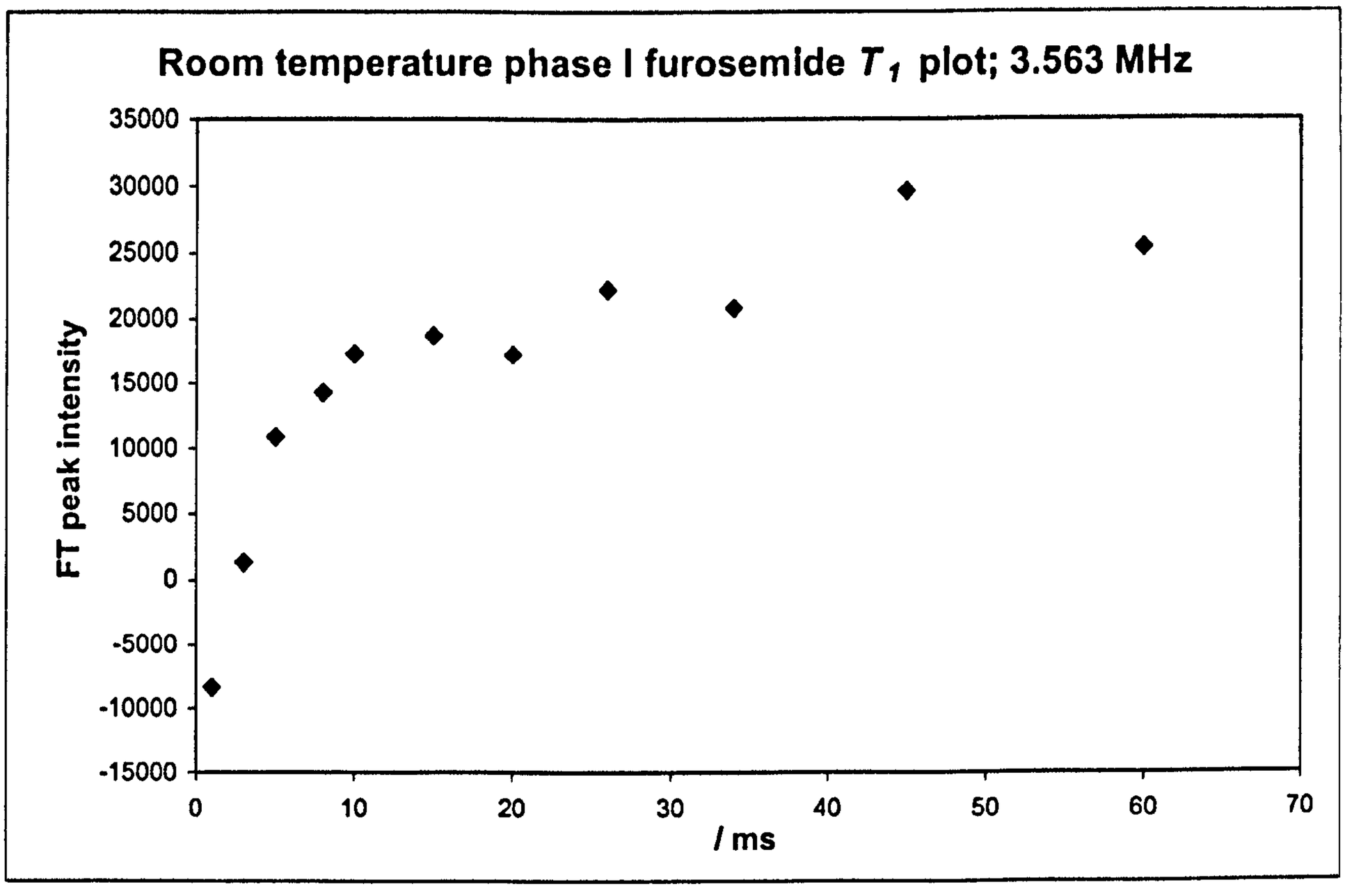

Figure 4.4: Furosemide (Sigma powder) T_1 plot at 25°C; 3.563 MHz.

4.3.3.2 T_2

T_2, the spin-spin relaxation time, was found using a Hahn echo sequence. Following a Bessel plot to determine 90_{eff} pulse width the subsequent pulse sequence was conducted using the *Tecmag* NQRkit, the *Tecmag* Libra-FTR spectrometer, a 150 Watt *Amp UK* driver unit supplying a 1500 Watt *Amp UK* linear amplifier at room temperature with an incident frequency of 3.563 MHz:

Event		
Pulse / μs	130	(Phase 0202)
Dead time	Variable - 15 points from 1 to 10 ms	
Acquisition	128 points / 10 μs dwell (Phase 0202)	
Final delay / ms	60	
No. of scans	80000	
Excitation frequency	3.563 MHz	

Table 4.3: Furosemide Hahn echo pulse sequence settings.

T_2 values were found to be short, the mean value was 1.95 ± 0.32 ms (figure 4.5).

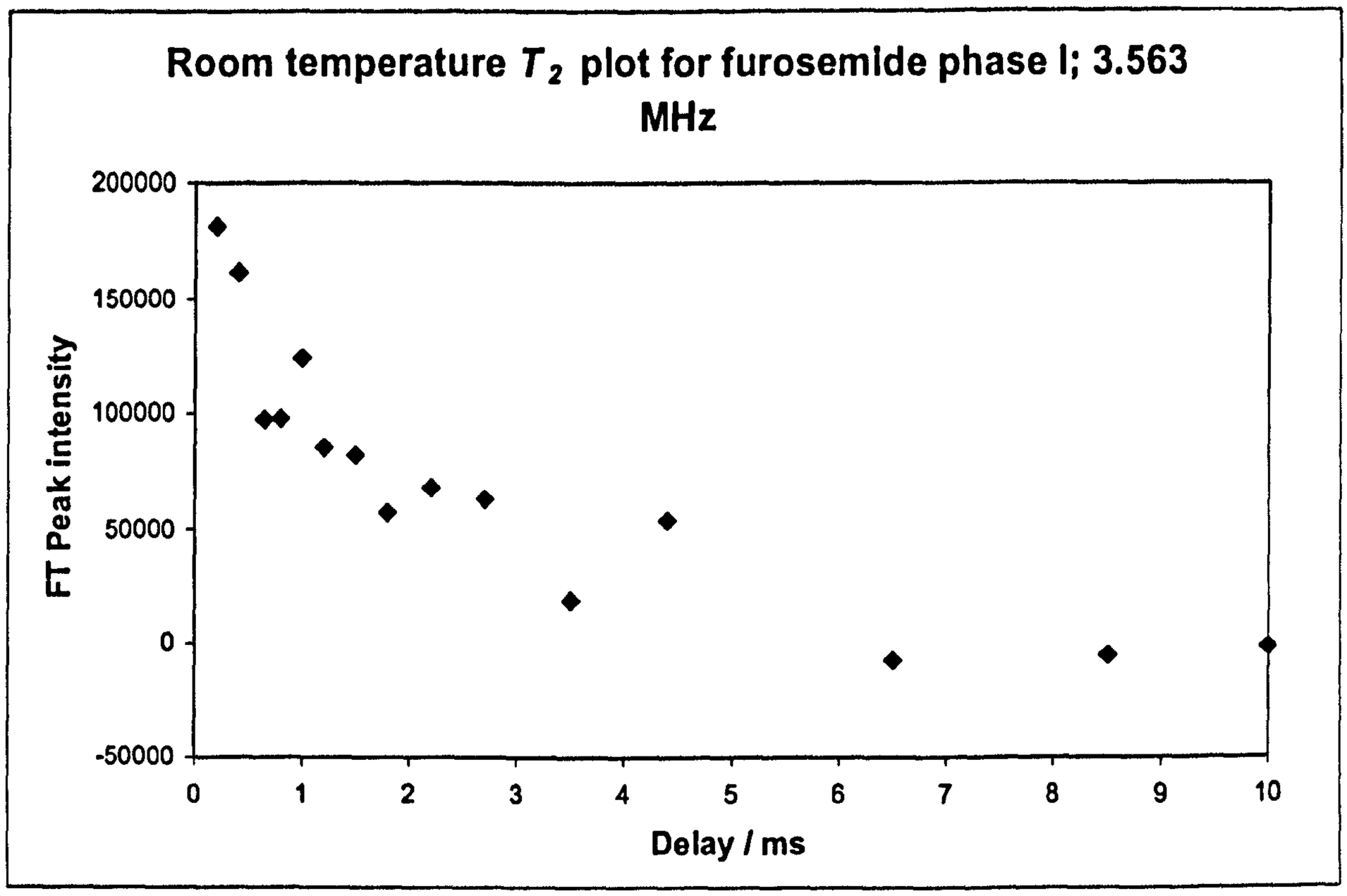

Figure 4.5: Phase I furosemide room temperature T_2 plot; T_2 = 1.95 ± 0.32 ms.

4.3.3.3 T_2e

The T_2e values were calculated to give an idea of the sustainability of the echo train, an important factor in the feasibility of real life applications. The experiment was carried out 3 times using the following PSL sequence at room temperature at 3.563 MHz

Event	2τ = 1.49 ms
Pulse / μs	110
Acquisition	128 points / 10 μs dwell time
Final Delay / ms	100
No. of scans	5000
Frequency / MHz	3.563

Table 4.4: Furosemide 2τ = 1.49 ms T_2e pulse sequence settings.

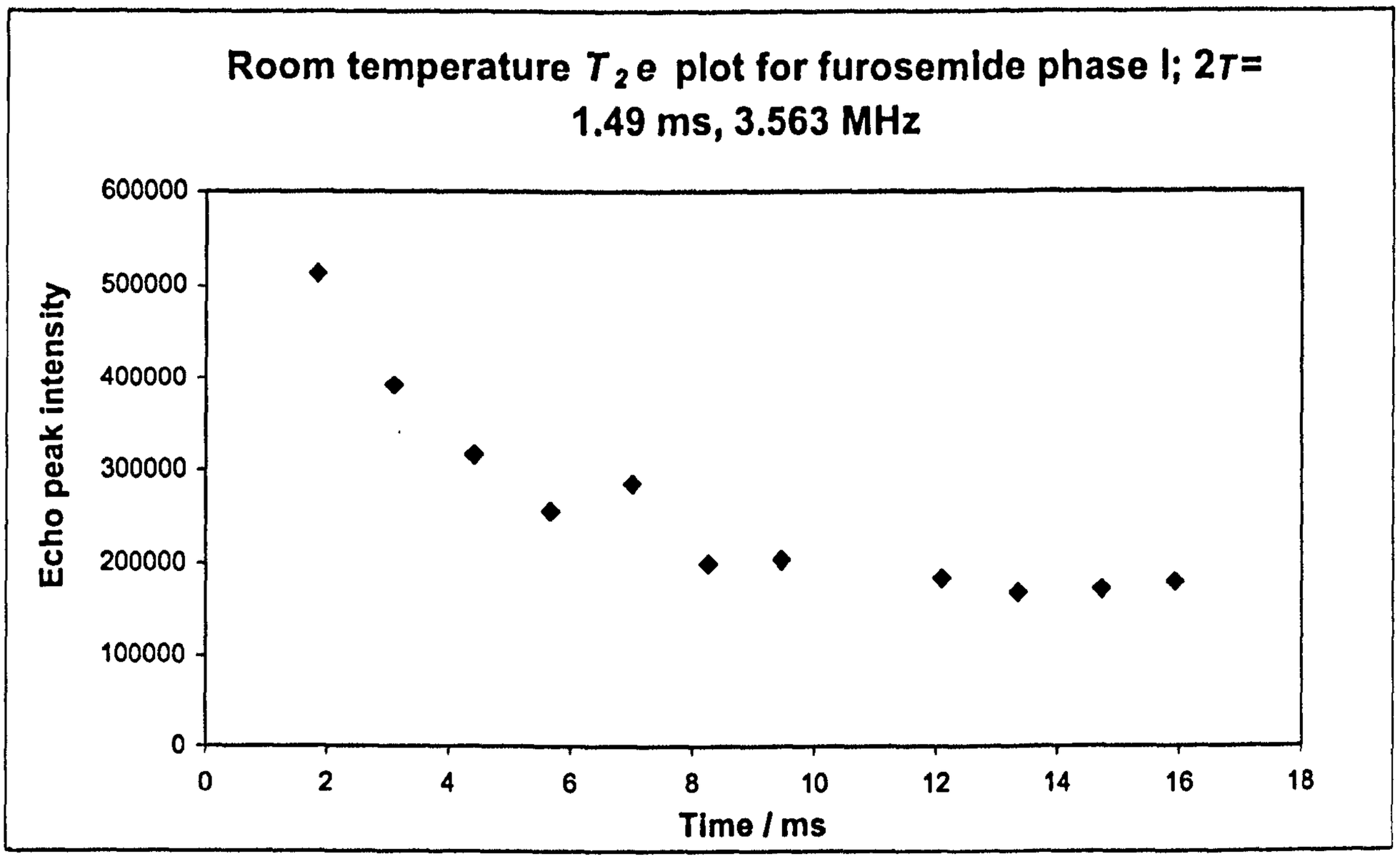

Figure 4.6: Furosemide Phase I; 3.563 MHz line echo peak magnitude points for 2τ=1.49 ms T_2e = 11.30 ± 0.10 ms, fitted to an offset single exponential plot as the curve does not tend to zero.

Only a short echo train - 5 echoes - could be sustained (figure 4.6) before the signal was drowned by noise. A good exponential fit ideally requires more points, though a rough fit could still be applied - T_2e was found to be 11.30 ± 0.10 ms for a 2τ value of 1.49 ms. In these cases the errors are calculated to indicate the T_2e range from 3 experiments. As the plot did not tend to zero; an offset was present, which may be due to very short relaxation times, and so an offset exponential curve was fitted.

4.3.3.4 T_2*

T_2* was also calculated for phase I at room temperature by fitting half an echo, obtained by a PSL sequence, to an exponential curve with the equation

$$M = \exp(^{-t}/T_2^*) \qquad (4.1)$$

The PSL pulse sequence settings were as follows:

Event	
Pulse / μs	110
Acquisition	128 points / 10 μs dwell time
Final Delay / ms	100
No. of scans	30000
Frequency / MHz	3.563

Table 4.5: Furosemide T_2* pulse sequence settings.

The time domain plot was then exported as a text file and the second half of the echo was plotted in Excel before equation (4.1) was fitted.

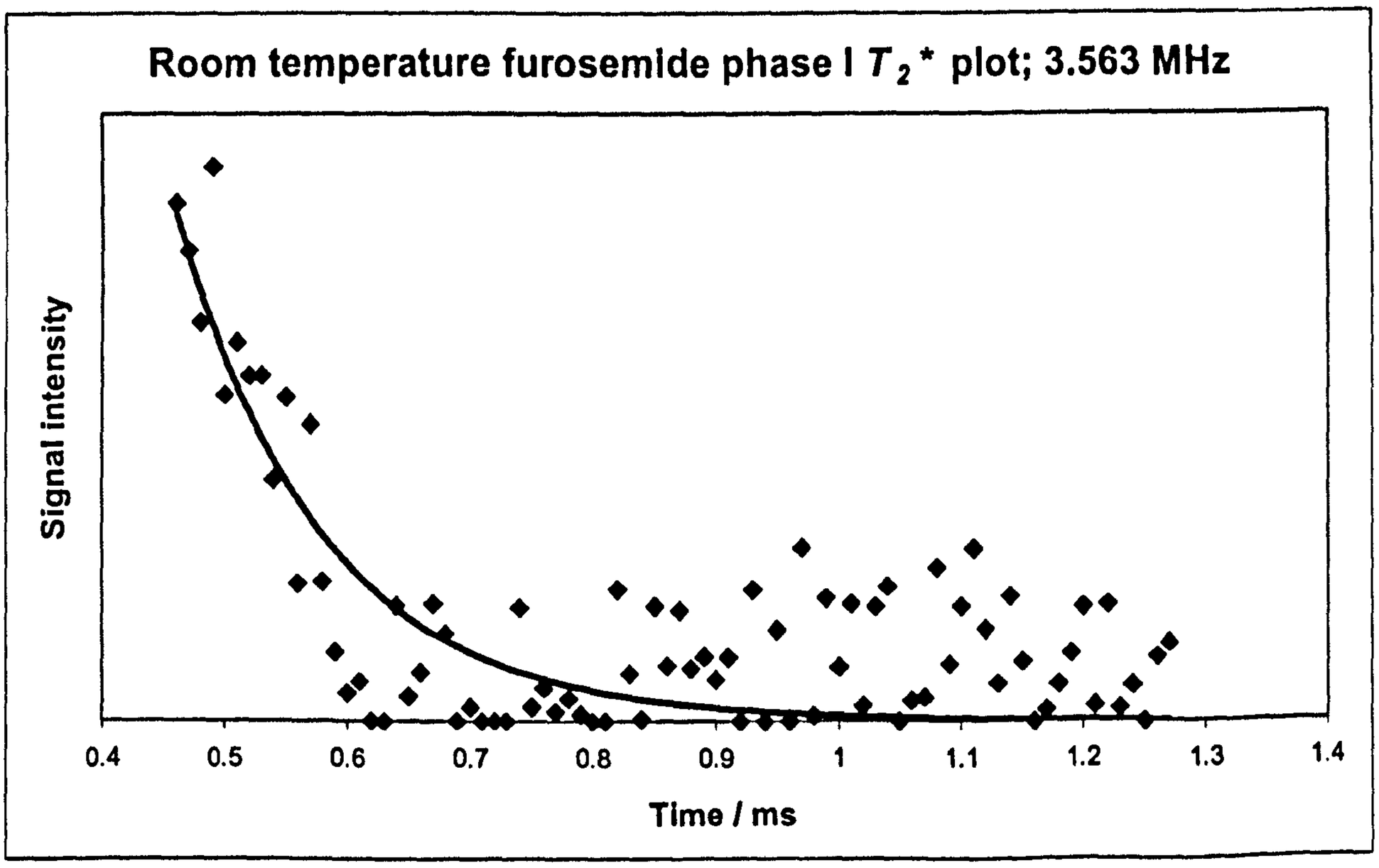

Figure 4.7: T_2* exponential curve for room temperature phase I furosemide; T_2* = 0.10 ± 0.02 ms; 3.563 MHz.

T_2* was found to be 0.10 ± 0.02 ms (mean) for phase I of furosemide (figure 4.7). The error was calculated from the results of 3 experiments.

4.3.4 Observation of ^{14}N signals in furosemide tablets

Furosemide tablets, manufactured by Hoechst Marion Roussel, were provided by Dr. Gareth Pearce, of Merck Sharp and Dohme. The 20 mg and 40 mg Lasix® tablets each consist of approximately 25 % furosemide by weight, the other ingredients being lactose, maize starch, talc, magnesium stearate and colloidal silicon dioxide[9,10]. The 500 mg tablets contain approximately 71 % furosemide by weight, the other ingredients being maize starch, lactose, colloidal silicon dioxide, ultraamyl pectin, talc, eleema, magnesium stearate and quinoline yellow[11]. The tablets to be tested were placed in lidded plastic cylinders, 5 cm in diameter by 7 cm in height, with a sample fill depth of 5.5 cm. There was an insufficient quantity of the 20 mg and 40 mg tablets to fill a container and as they contain the same percentage of furosemide, were tested together. 559 20 mg and 395 40 mg tablets were used in one sample cylinder, with the overall mass of furosemide present being 26.98 g. 146 500 mg tablets filled a plastic cylinder of the same dimensions with the total furosemide mass being 73.00 g.

A multiple echo pulse spin-locking (PSL) sequence was used, as previously, to observe echo signals in tablets. The following settings were used with the *Tecmag* NQRkit, the *Tecmag* Libra-FTR spectrometer, a 150 Watt *Amp UK* driver unit supplying a 1500 Watt *Amp UK* linear amplifier:

Event	
Pulse / μs	110
Acquisition	128 points / 10 μs dwell time
Final Delay / ms	50
No. of scans (20 + 40 mg/ 500 mg)	100000 / 50000
Frequency / MHz	3.563

Table 4.6: Furosemide tablets PSL pulse sequence settings.

The echoes generated were baseline corrected, phase adjusted and echo Fourier transformed to give signals in the frequency domain (figures 4.8, 4.9). The doublet structure can be seen in each case with no change in the peak frequencies or splittings, and in good agreement with the powder sample spectrum (figure 4.3) with the doublet

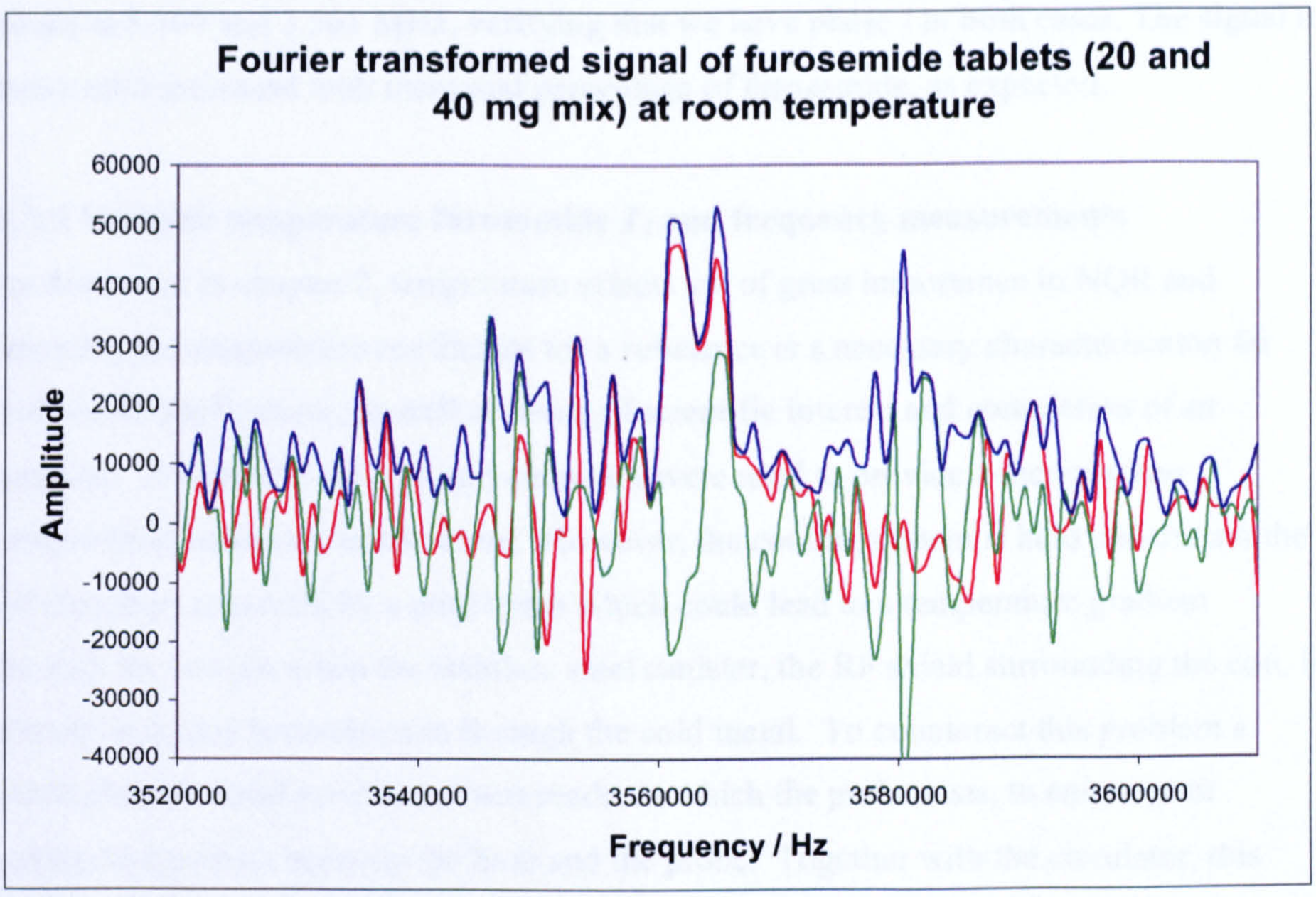

Figure 4.8: Fourier transformed ^{14}N signal from phase I furosemide; 559 20 mg and 395 40 mg tablets at room temperature with doublet frequencies 3.565 and 3.562 MHz.

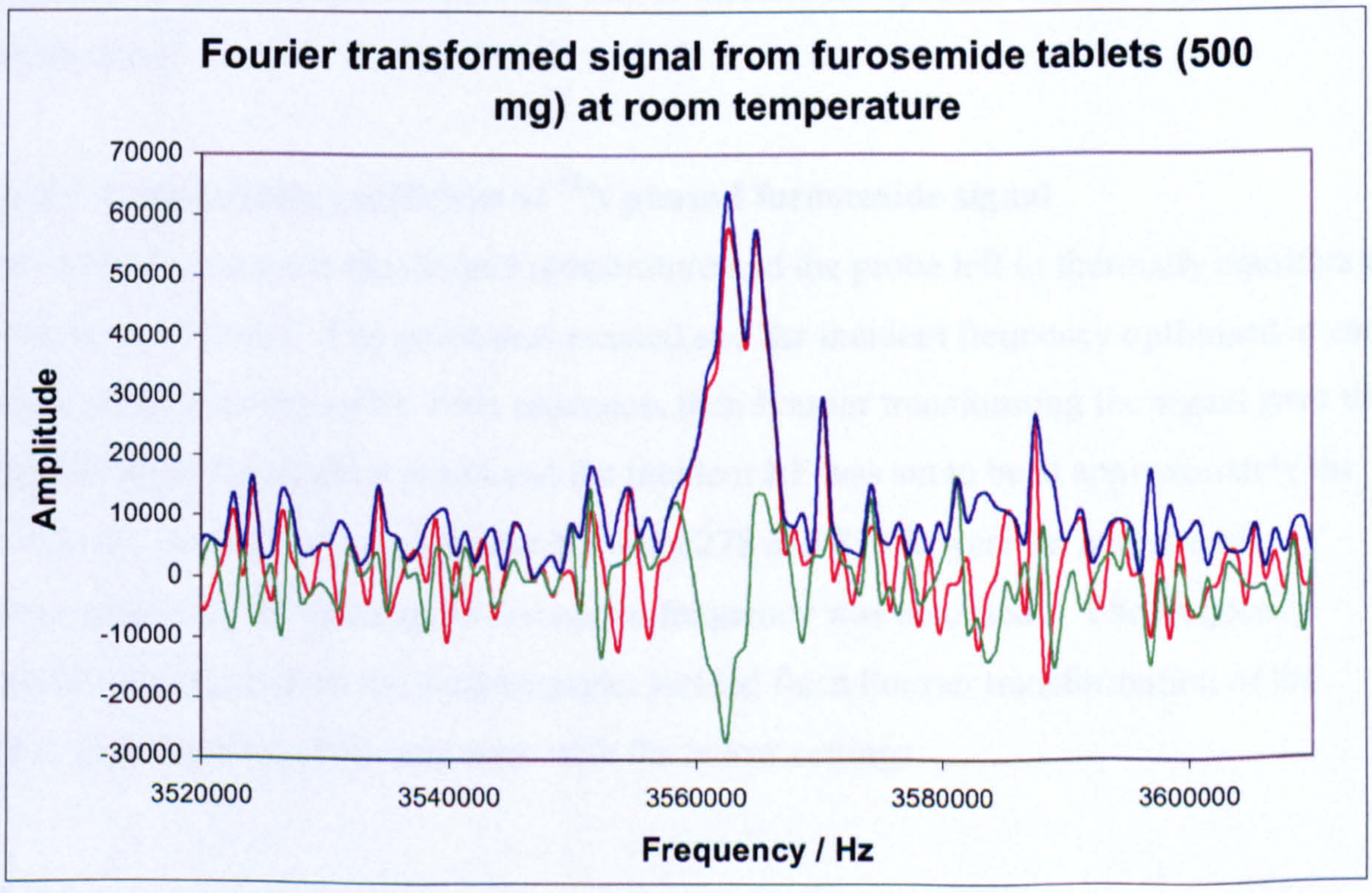

Figure 4.9: Fourier transformed ^{14}N signal from phase I furosemide; 146 500 mg tablets at room temperature with doublet frequencies 3.565 and 3.562 MHz.

peaks at 3.564 and 3.561 MHz, verifying that we have phase I in both cases. The signal to noise ratio increased with increased percentage of furosemide, as expected.

4.3.5 Variable temperature furosemide T_1 and frequency measurements

As discussed in chapter 2, temperature effects are of great importance in NQR and knowing the temperature coefficient for a substance is a necessary characterization for real-world applications, as well as being of scientific interest and completion of an analysis. A Julabo™ oil bath and circulator were used to provide a thermostatic environment at known temperature. However, the cooling system is held underneath the oil chamber, separated by a metal base which could lead to a temperature gradient through the sample when the stainless steel canister, the RF shield surrounding the coil, is placed on it, due to conduction through the cold metal. To counteract this problem a small plastic coated mesh stand was made on which the probe rests, to ensure poor conducting contact between the base and the probe. Together with the circulator, this should ensure a more even temperature throughout the oil bath and less temperature gradient across the sample and therefore less broadening of the signal. A one inch thick polystyrene 'lid' was placed over the bath to insulate the system from the surrounding environment.

4.3.5.1 Temperature coefficient of ^{14}N phase I furosemide signal

The oil bath was set to the desired temperature and the probe left to thermally equilibrate for at least 15 hours. The probe was retuned and the incident frequency optimised at each temperature; running a PSL echo sequence, then Fourier transforming the signal gave the frequencies of the doublet peaks and the incident RF was set to be at approximately the mid point. A range of temperatures between 278 and 318 K were set and at each temperature the ^{14}N quadrupole resonance frequency was recorded. The frequency values were taken from the doublet peaks yielded from Fourier transformation of the echo, generated by a PSL sequence with the below settings:

Event	
Pulse / μs	130
Acquisition	128 points / 10 μs dwell time
Final Delay / ms	Variable; dependent on temperature.
No. of scans	Variable; dependent on temperature.
Frequency / MHz	Variable; dependent on temperature.

Table 4.7: Furosemide PSL pulse sequence (determination of temperature coefficient).

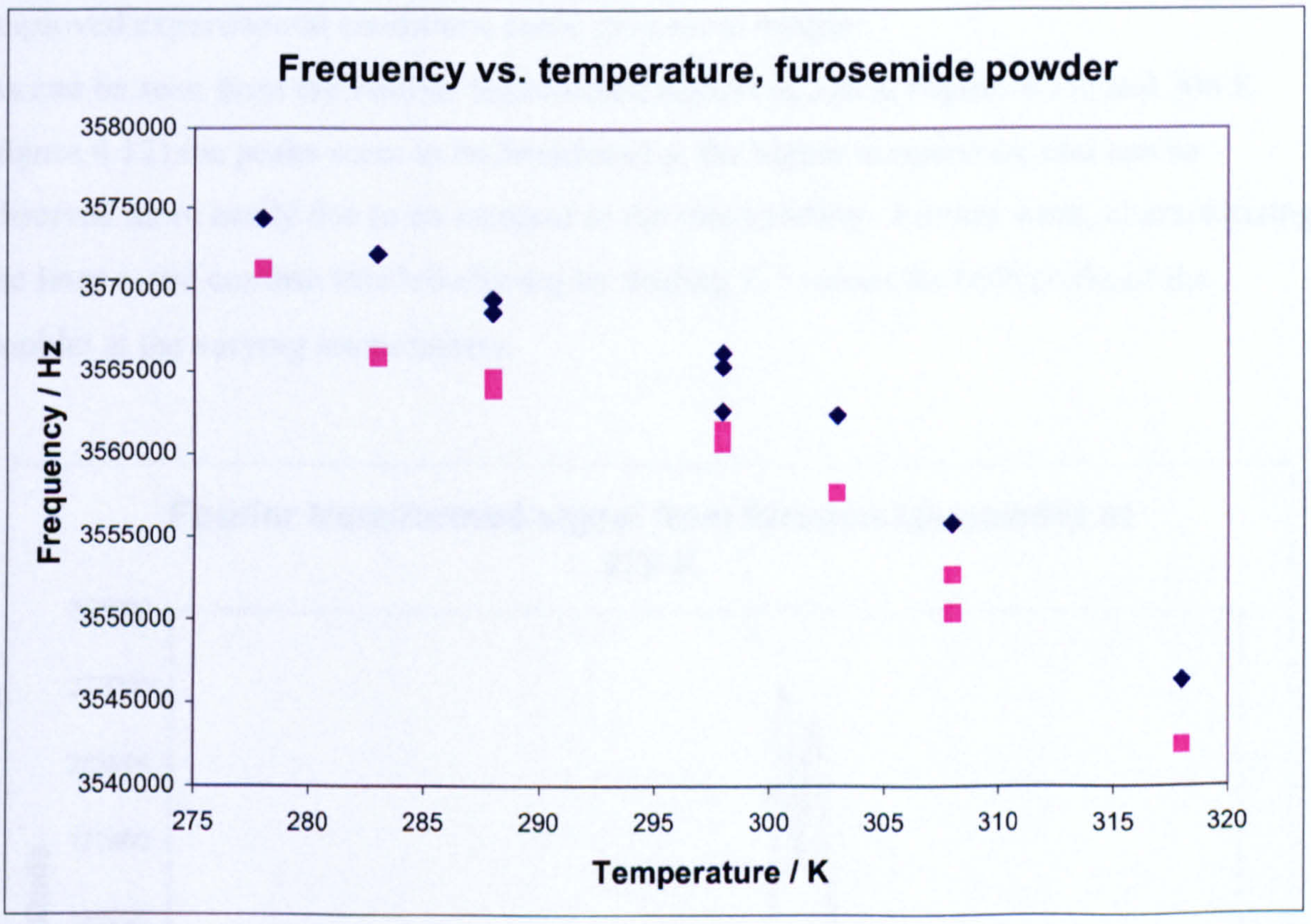

Figure 4.10: Frequency (Hz) vs. temperature (K) graph from the ^{14}N signal in phase I furosemide (Sigma) powder where the blue points and purple points are the higher and lower frequency peaks of the doublet respectively.

Figure 4.10 shows the peak frequency clearly decreasing with increasing temperature. The correlation is linear above 298 K, with a temperature coefficient of approximately 0.9 kHz K^{-1} between 298 and 318 K for both lines. At lower temperatures, where the oil bath was not so reliable, the gradient decreases; however, the trend towards increasing frequency with lowering temperature is still clear. However, these points do not

convincingly show a linear correlation across this range of frequency with temperature. Ideally, these experiments could be repeated over a wider range with a better temperature control system than that which was used (Probe A submerged in an oil bath - it was later found that low temperature values, 278 and 288 K, may not be reliable as it was subsequently realized that the oil bath used was unable to maintain a constant even temperature below room temperature, with fluctuations of up to 15 °). Such results could confirm a linear or quadratic relationship. Also, the splitting of the doublet varies across the temperature range and perhaps higher frequency resolution spectra together with improved experimental conditions could give more insight.

As can be seen from the Fourier transformed signals at 278 K (figure 4.11) and 308 K (figure 4.12) the peaks seem to be broadened at the higher temperature and can be observed more easily due to an increase in the line splitting. Further work, characterizing the lines could confirm this broadening by finding T_2* values for both peaks of the doublet at the varying temperatures.

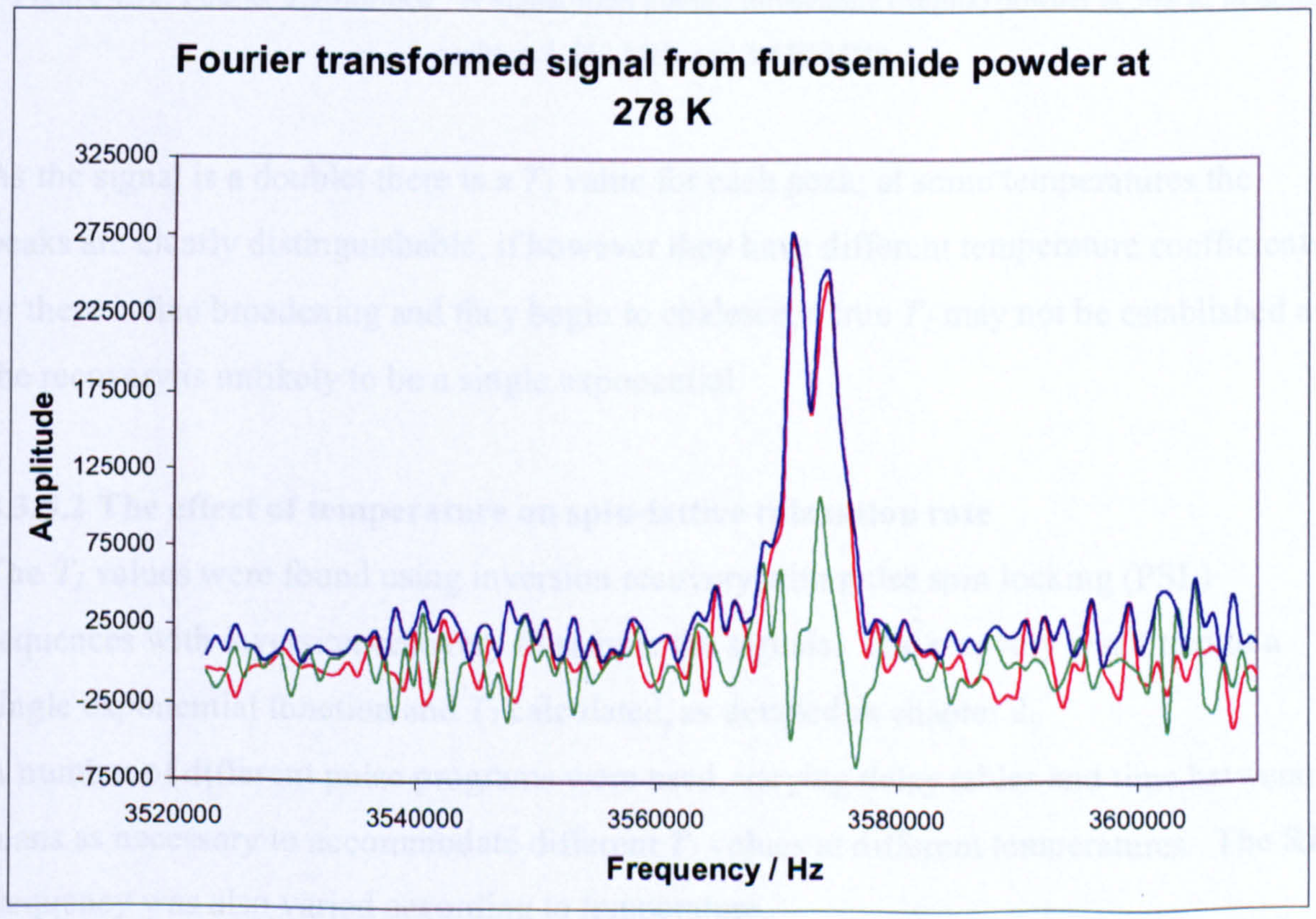

Figure 4.11: Fourier transformed ^{14}N signal from phase I furosemide (Sigma) powder at 278 K; doublet peaks at 3.574 MHz and 3.571 MHz.

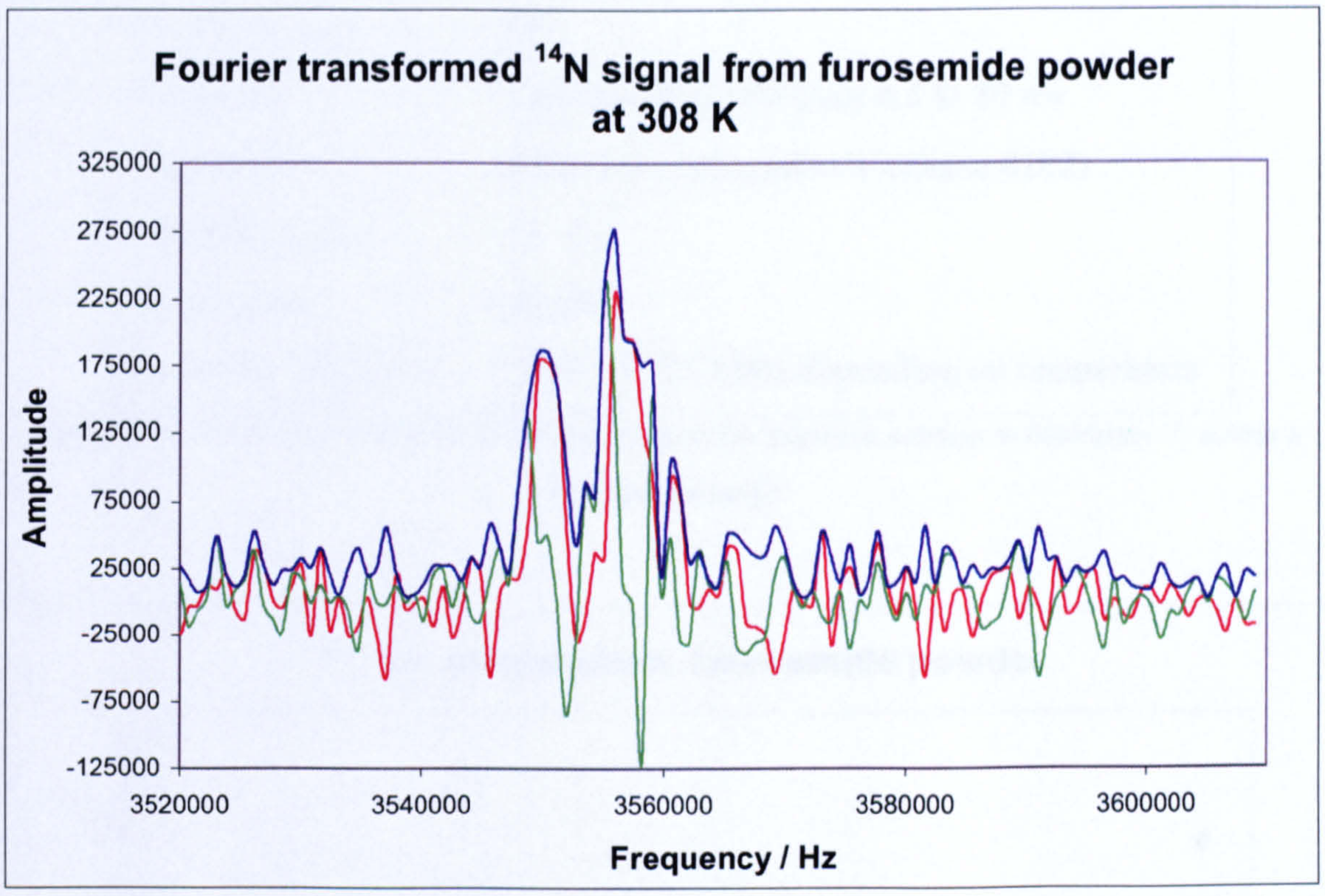

Figure 4.12: Fourier transformed ^{14}N signal from phase I furosemide (Sigma) powder at 308 K; doublet peaks at 3.556 MHz and 3.550 MHz.

As the signal is a doublet there is a T_1 value for each peak; at some temperatures the peaks are clearly distinguishable, if however they have different temperature coefficients or there is line broadening and they begin to coalesce, a true T_1 may not be established as the recovery is unlikely to be a single exponential.

4.3.5.2 The effect of temperature on spin-lattice relaxation rate

The T_1 values were found using inversion recovery with pulse spin locking (PSL) sequences with inversion-recovery to sample the signals. The recovery was fitted to a single exponential function and T_1 calculated, as detailed in chapter 2.

A number of different pulse programs were used, varying delay tables and time between scans as necessary to accommodate different T_1 values at different temperatures. The RF frequency was also varied according to temperature.

The following settings were used:

Event	
90_{eff} Pulse / μs	130
Dead time	Variable 15 points from 0.2 to 80 ms
Acquisition	128 points / 10 μs dwell (Phase 0202)
Final delay / ms	60 - 80
No. of scans	80000
Excitation frequency	3.540 - 3.575 MHz depending on temperature

Table 4.8: Furosemide tablets inversion-recovery pulse sequence settings to determine T_1 across a temperature range.

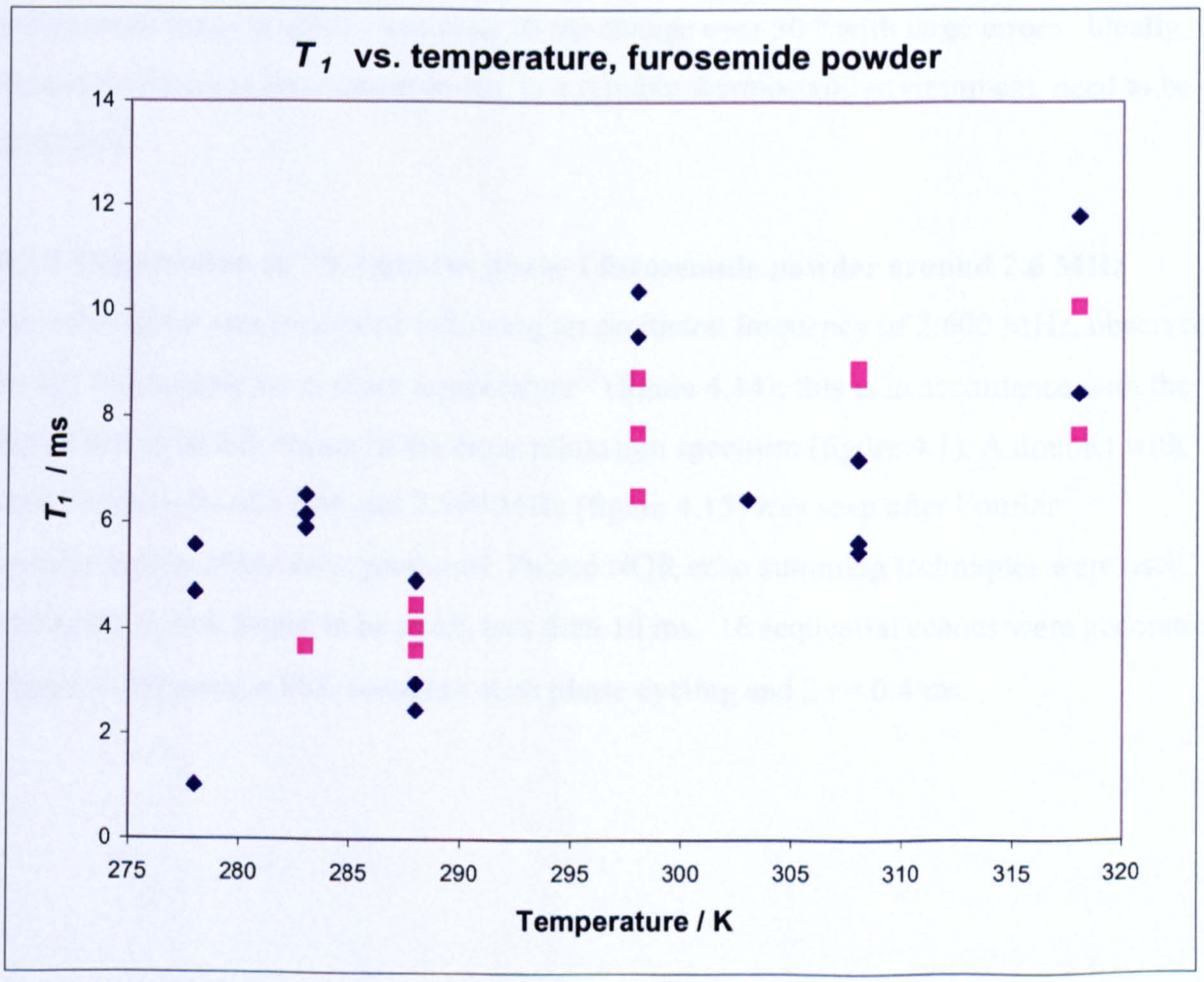

Figure 4.13: T_1 (ms) vs. Temperature (K) graph from the ^{14}N signal in phase I furosemide (Sigma) powder; the blue diamonds and the pink squares are the higher and lower frequency peaks of the doublet respectively.

Figure 4.13 shows how T_1 changes with temperature over the range of 278 to 318 K. There is not a clear linearity to the graph, although T_1 does seem to increase with increasing temperature with a small temperature coefficient. T_1 may have a minimum around 280 K although this is not clear. Further study with a better temperature controlled system is needed.

The shape of the T_1 vs. temperature graph can give an indication of the relaxation mechanisms occurring within the material; the drop in T_1 with decreasing temperature suggests a dipolar relaxation mechanism and the observation of a minimum, if verified, together with an activation energy, would enable a more specific assignment of the relaxation mechanism to be made. Unfortunately there was little change in T_1 over the temperature range studied - less than 10 ms change over 30 ° with large errors. Ideally, further T_1 values at low temperatures, in a reliable thermostatic environment, need to be measured.

4.3.6 Observation of ^{14}N signal in phase I furosemide powder around 2.6 MHz

An echo signal was generated following an excitation frequency of 2.600 MHz, observed by Dr. Michael Rowe at room temperature[12] (figure 4.14); this is in accordance with the dip observed in this region in the cross relaxation spectrum (figure 4.1). A doublet with peak frequencies of 2.604 and 2.599 MHz (figure 4.15) was seen after Fourier transformation of the echo produced. Pulsed NQR echo summing techniques were used and again T_1 was found to be short, less than 10 ms. 16 sequential echoes were generated (figure 4.16) using a PSL sequence with phase cycling and $2\tau = 0.4$ ms.

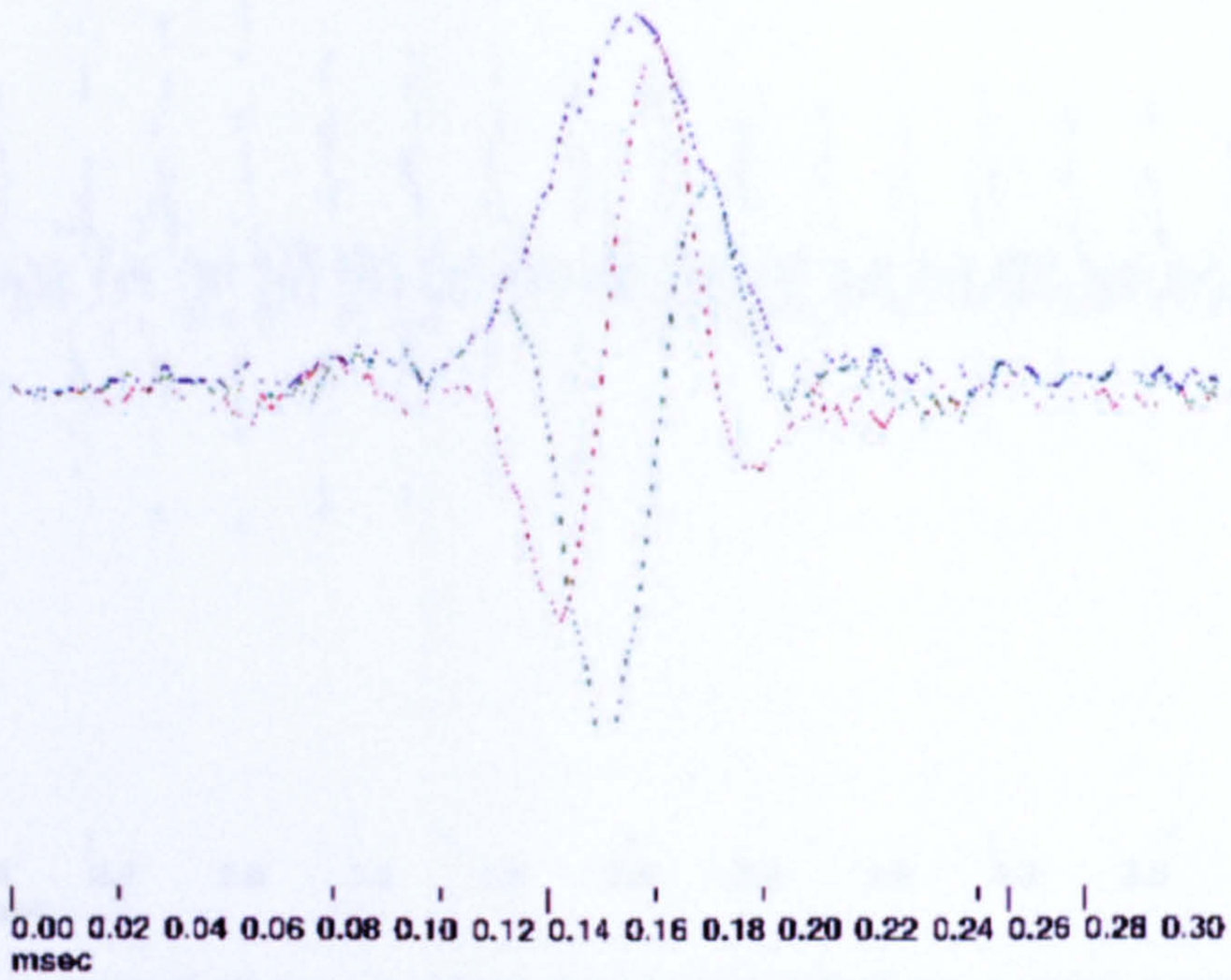

Figure 4.14: 32 Summed phase I furosemide (Sigma powder) echoes at room temperature, 2.600 MHz excitation frequency.

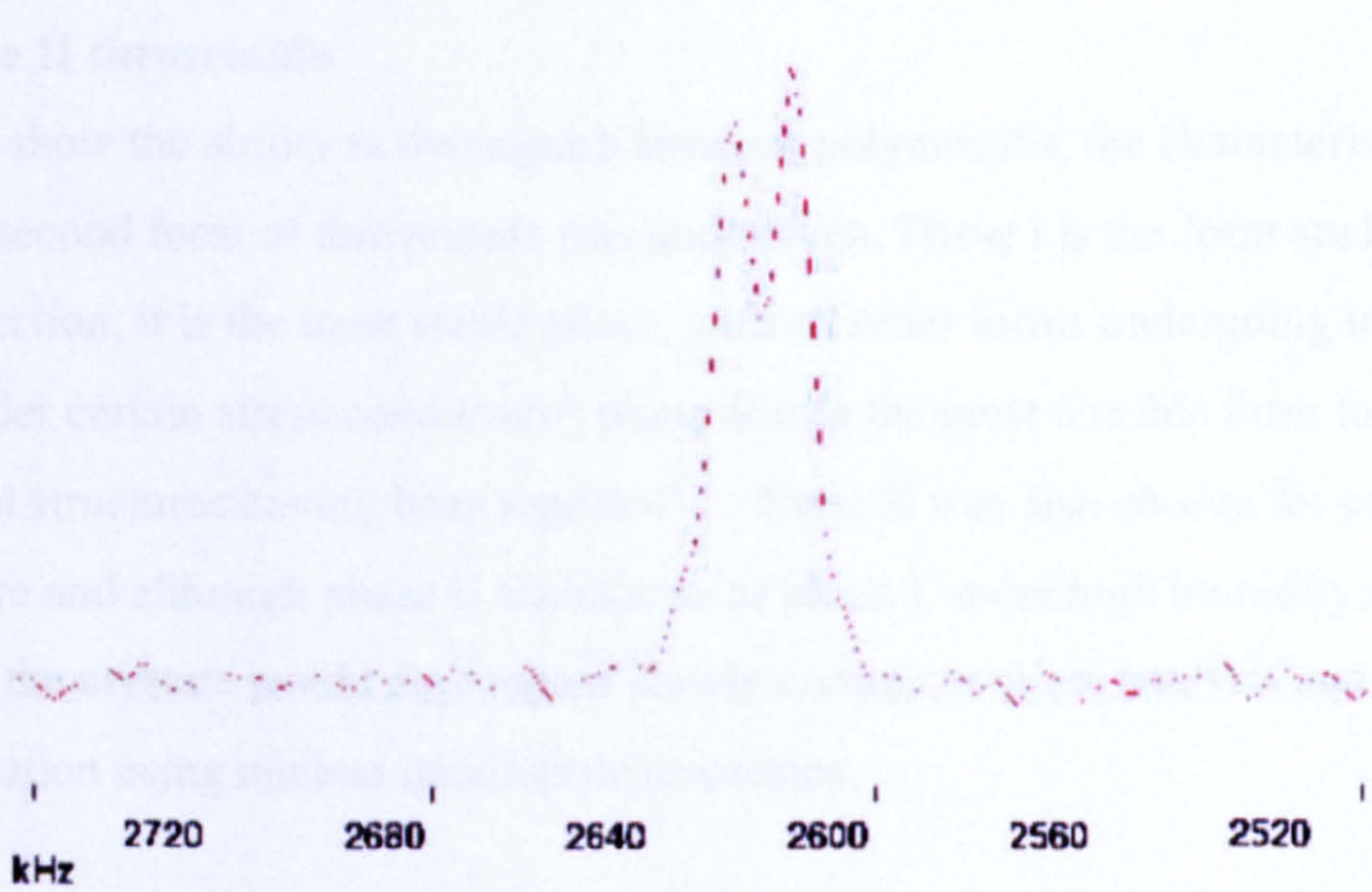

Figure 4.15: Phase I furosemide (Sigma) powder signal in the frequency domain. Doublet observed with peak frequencies 2.604 and 2.599 MHz; room temperature, 2.600 MHz excitation frequency.

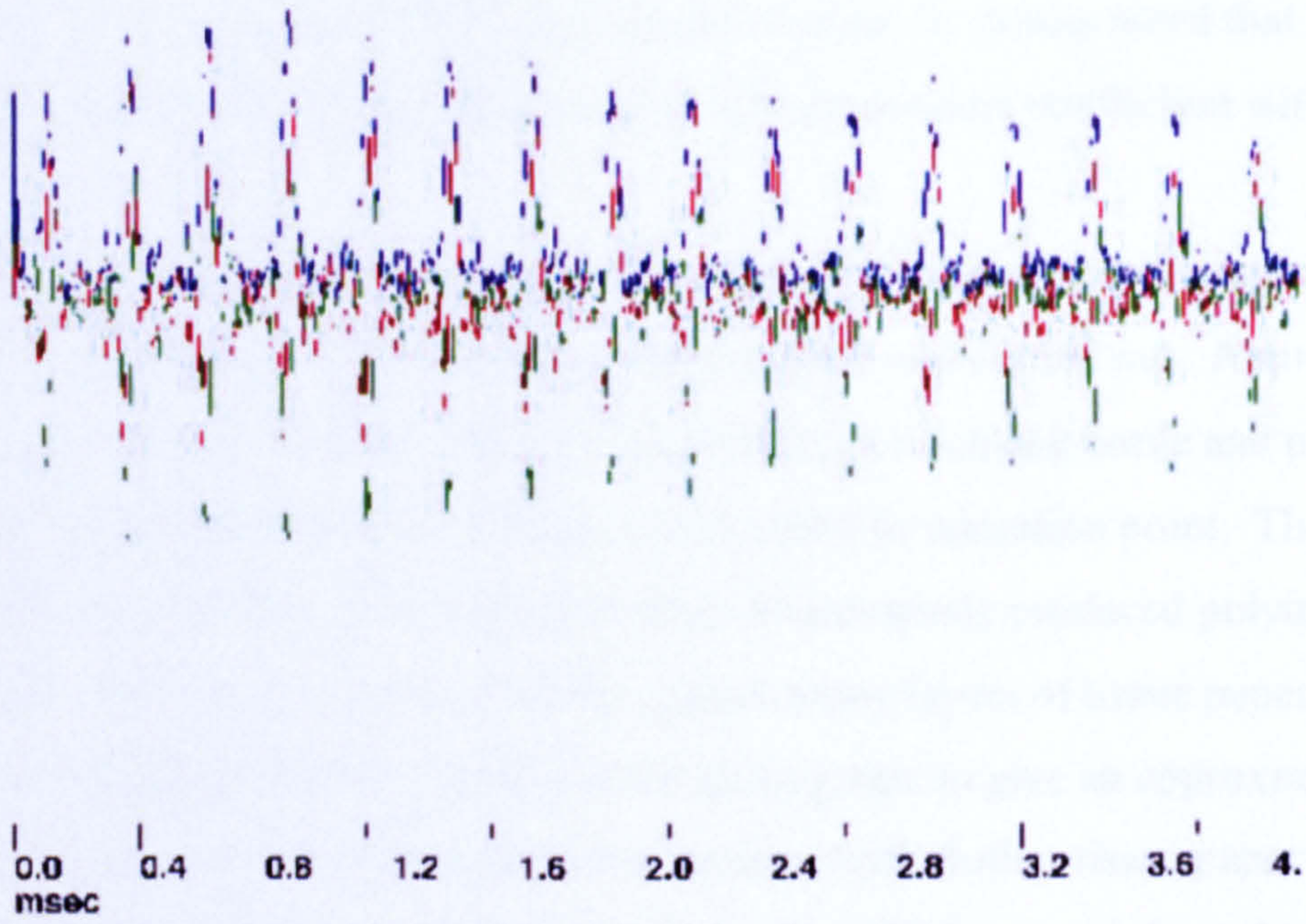

Figure 4.16: 16 sequential echoes; signal from phase I furosemide (Sigma powder) at room temperature; 2.610 MHz excitation frequency, 70252 scans, $2\tau = 0.4$ ms.

4.4 Investigating a second phase of furosemide

4.4.1 Phase II furosemide

In order to show the ability to distinguish between polymorphs, the characterisation and study of a second form of furosemide was undertaken. Phase I is the form studied in the previous section; it is the most stable phase, with all other forms undergoing transitions to phase I under certain stress conditions[3]; phase II was the most feasible form for study with crystal structures having been reported[6,7]. Phase II was also chosen for ease of manufacture and although phase II transforms to phase I under high humidity it was hoped that the crystals would decompose slowly enough to allow analysis and characterization using nuclear quadrupole resonance.

4.4.2 Preparation of phase II furosemide

The method of slow recrystallisation was used to produce forms (I) and (II), as named and prepared by Matsuda and Tatsumi[3], using acetone and 1-butanol respectively. Forms (I) and (II) prepared by Matsuda and Tatsumi were clearly distinguishable by crystal morphology with form (I) being hexagonal tabular crystals, whilst form (II) is characterised by long needle-like crystals. Initial rough recrystallisations produced a

powder-like phase I and small fibre like crystals of phase II. It was noted that in both acetone and butanol, furosemide powder has a low temperature coefficient with regard to solubility.

In order to obtain a crystal large enough to be studied by X-ray crystallographic techniques, a small-scale, slow-cooled, recrystallisation was carried out. Approximately 60 cm^3 butan-1-ol was heated to approximately 70°C in a Schlenk bottle and phase I furosemide powder, purchased from Sigma, was added to saturation point. The mixture was seeded by the addition of two small crystals of previously produced polymorph (II) and the bottle was wrapped in an insulation jacket; many layers of tissue paper were shaped into a cylinder and held together with sticking tape to give an approximate thickness of 1 cm. The top of the jacket was covered with further tissue paper and a polystyrene cover was placed over the apparatus. The solution was left on the heating plate at 35- 40 °C for 3 hours, then left on the turned-off plate overnight. The heating plate was turned on at 35 °C for a further 7 hours, then off for 22 hours, then on for 3 hours, then off for 16 hours before the liquid was decanted off and the crystals left to dry in air on filter paper. The fine strands produced were approximately 1 mm in diameter and varied in length between 1 and 2 cm. The long strands grew dendritically, from the base of the flask, to give a spiky cluster (figure 4.17).

Figure 4.17: A cluster of furosemide phase II crystals, recrystallised from butanol.

Although the long needles appeared to be single crystals, on microscopic inspection it could be seen that most were bundles of two or more very fine needles. In order to

ascertain whether they would be suitable for further structural study they were viewed under a polarising microscope; the refracted light from a true single crystal varies in intensity between very strong and zero when rotated between crossed Polaroid filters. Once a suitable single crystal had been found and isolated it was given to Professor Stanley Nyburg at King's College for X-ray analysis.

The two publications[6,7] reporting furosemide structures different to that characterised by Lamotte[5] were reduced to standard angles, as demonstrated earlier, and both report the space group to be $P\bar{1}$ and $Z = 2$, hence the two molecules are equivalent, related through a centre of symmetry, and a singlet peak ^{14}N NQR signal would be expected. This published data is in agreement with the X-ray work performed by Professor Stanley Nyburg at King's College London, on the above single crystal of phase II furosemide. The phase I polymorph also has the same space group $P\bar{1}$ but with $Z = 4$ and two molecules in the repeat unit yields doublets in NQR, giving us a clearly defined and attributable method of distinguishing between the two polymorphs. The only problem in this method is that in some conditions the doublet may not be resolved, although knowledge of linewidths and temperature coefficients could help in such a circumstance.

A large scale recrystallisation of furosemide using butanol was performed to produce a quantity of polymorph II suitable for NQR testing. Approximately 65 g of commercial furosemide powder was dissolved in 2 L of hot butanol. The solution was left to cool for 4 hours. The recrystallised furosemide was then recovered using a Buchner funnel and left to dry in air for 36 hours. 54 g of polymorph II was then placed in a cylindrical plastic container, 5 cm diameter by 7 cm height, sample depth 5.5 cm. This sample was used to begin phase II NQR testing.

4.4.3 ^{14}N nuclear quadrupole resonance experiments

An initial cross-relaxation spectrum by David Stephenson on polymorph II showed 2 peaks assigned to ν_0 at 910 kHz and ν_- at 2500 kHz with a weaker dip at 3500 kHz; frequencies which are lower than the corresponding lines in polymorph I (990 kHz, 2620 kHz and 3563 kHz). Assuming a similar lowering in frequency for the ν_+ line, beginning at 3350 kHz a search for the upper line in polymorph II was carried out with intervals of 5 kHz, using a pulse spin locking echo sequence with settings as below:

Event	
90_{eff} Pulse / μs	130
Acquisition	128 points / 10 μs dwell time
Final Delay / ms	50
No. of scans	30000
Frequency / MHz	Variable

Table 4.9: Furosemide phase II PSL pulse sequence settings.

A signal was found at 3422 kHz, 141 kHz below the corresponding polymorph I line at room temperature (figures 4.18, 4.19). As expected from the crystal space group, the signal is a singlet, clearly distinguishing it from the corresponding line in phase I. The 90_{eff} pulse width was established experimentally and the pulse sequence was optimised.

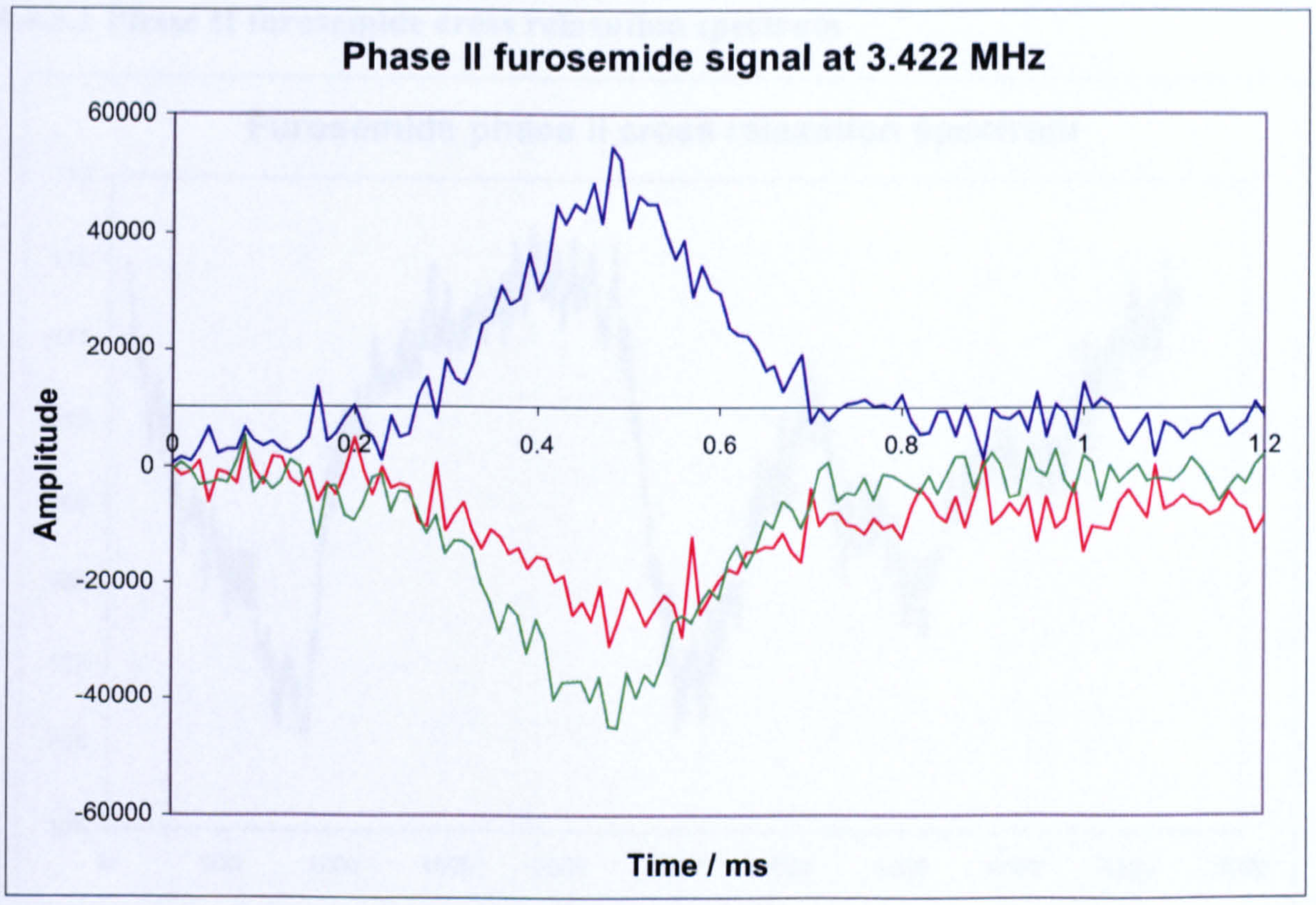

Figure 4.18: 10 summed echoes; ^{14}N signal in furosemide phase II at room temperature, 3.422 MHz.

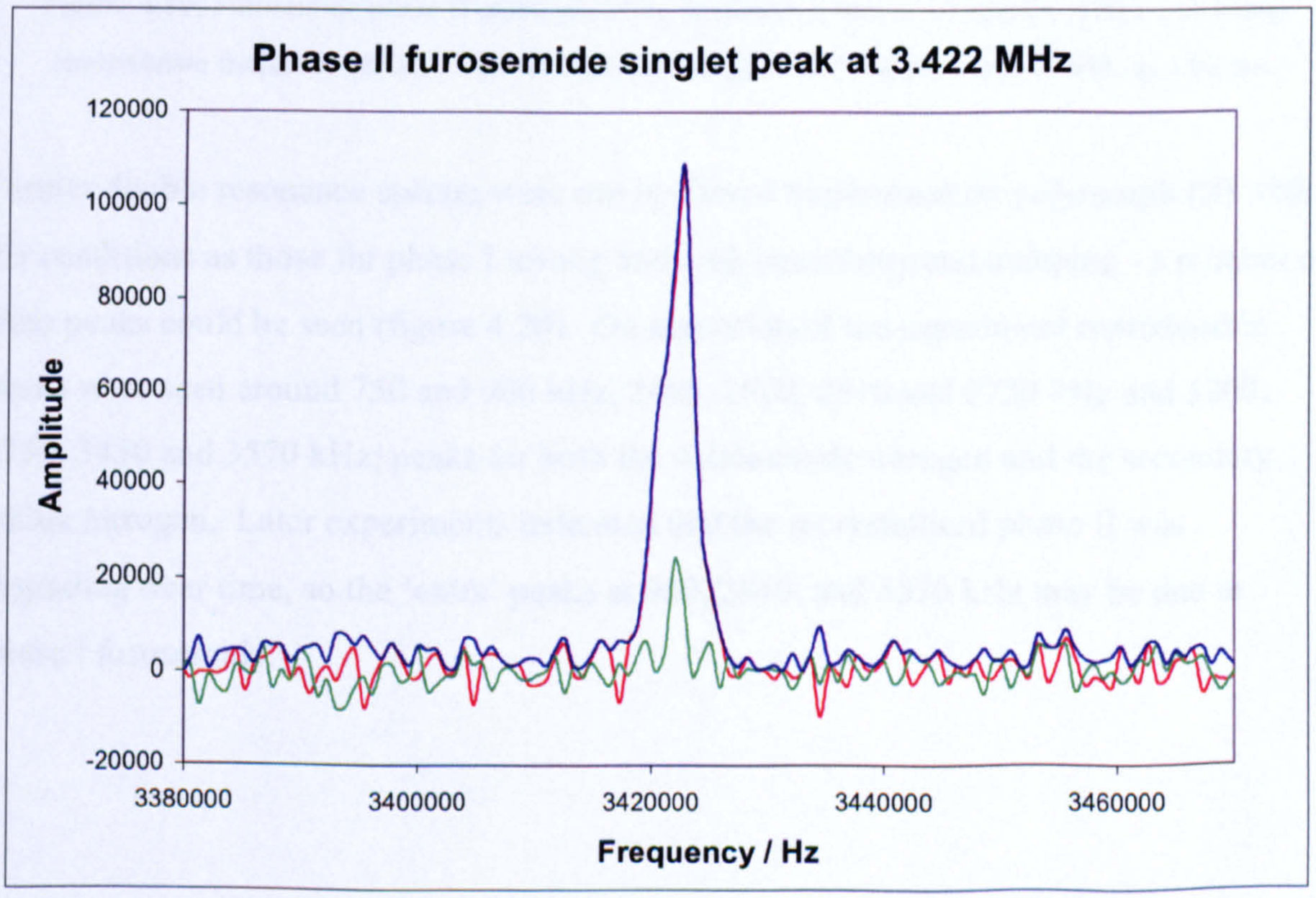

Figure 4.19: Frequency domain ^{14}N singlet signal from room temperature furosemide phase II.

4.4.3.1 Phase II furosemide cross relaxation spectrum

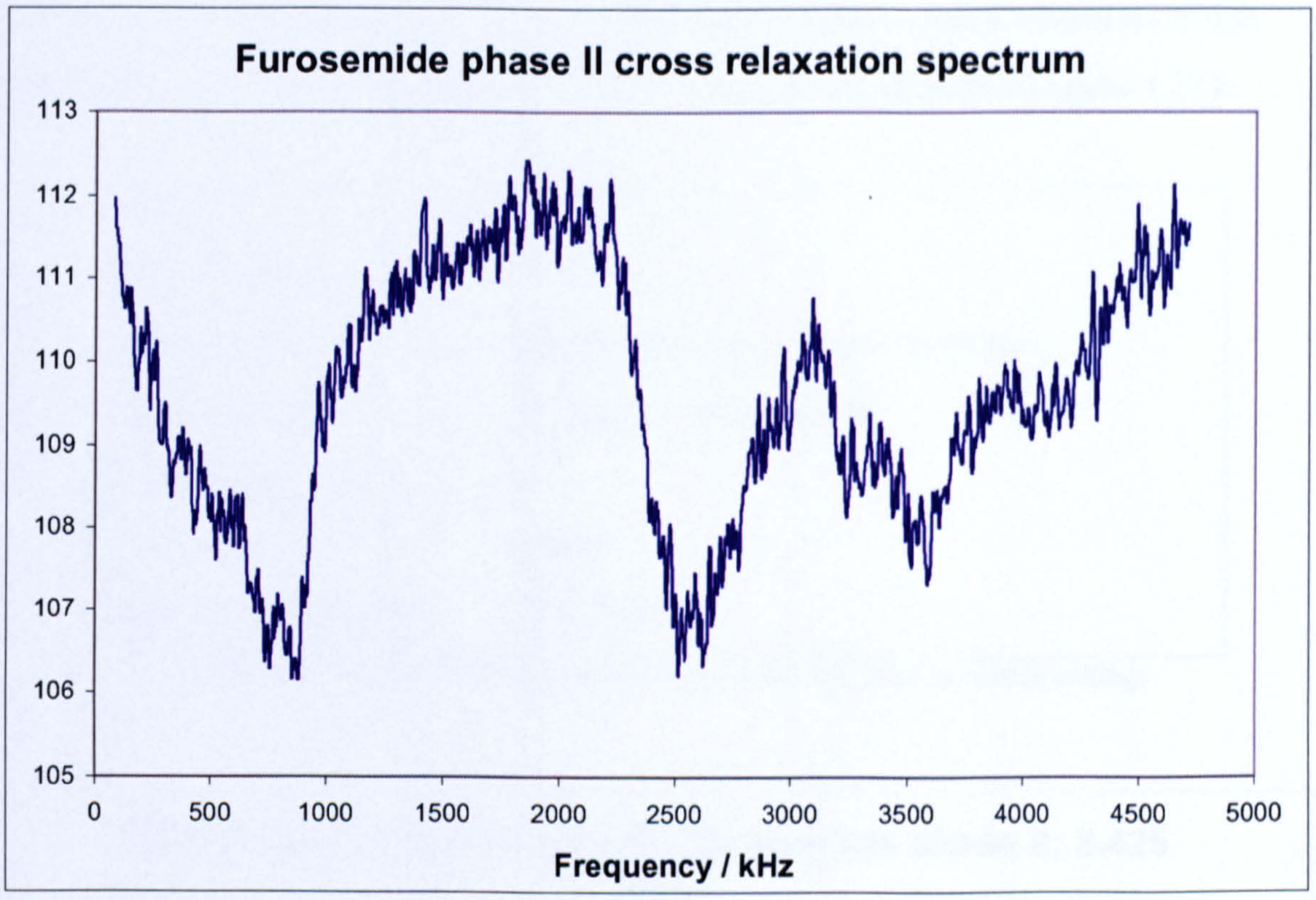

Figure 4.20: Furosemide phase II cross relaxation spectrum, a sum of 16 spectra, with *x* axis being approximate frequency (kHz). Time at high field magnet, $\tau_P = 5$ s, time at low field, $\tau_Q = 80$ ms.

Further double resonance spectra were run by David Stephenson on polymorph (II) with the conditions as those for phase I testing and with smoothing and damping - a number of clear peaks could be seen (figure 4.20). On repetition of the experiment reproducible peaks were seen around 750 and 900 kHz, 2400, 2500, 2610 and 2750 kHz and 3200, 3250, 3450 and 3570 kHz; peaks for both the sulfonamide nitrogen and the secondary amine nitrogen. Later experiments indicated that the recrystallised phase II was degrading over time, so the 'extra' peaks at 900, 2610, and 3570 kHz may be due to phase I furosemide.

4.4.3.2 Characterising the ^{14}N 3.422 MHz signal

4.4.3.2.1 T_1

The spin-lattice relaxation rate, T_1, of the 3.42 MHz signal at room temperature was found using an inversion recovery with pulse spin-locking sequence (figure 4.21).

Event	
90_{eff} Pulse / μs	130
Dead time	Variable 12 points from 1 to 50 ms
Acquisition	128 points / 10 μs dwell
Final delay / ms	50
No. of scans	10000
Excitation frequency	3.422 MHz

Table 4.10: Furosemide phase II inversion recovery pulse sequence settings.

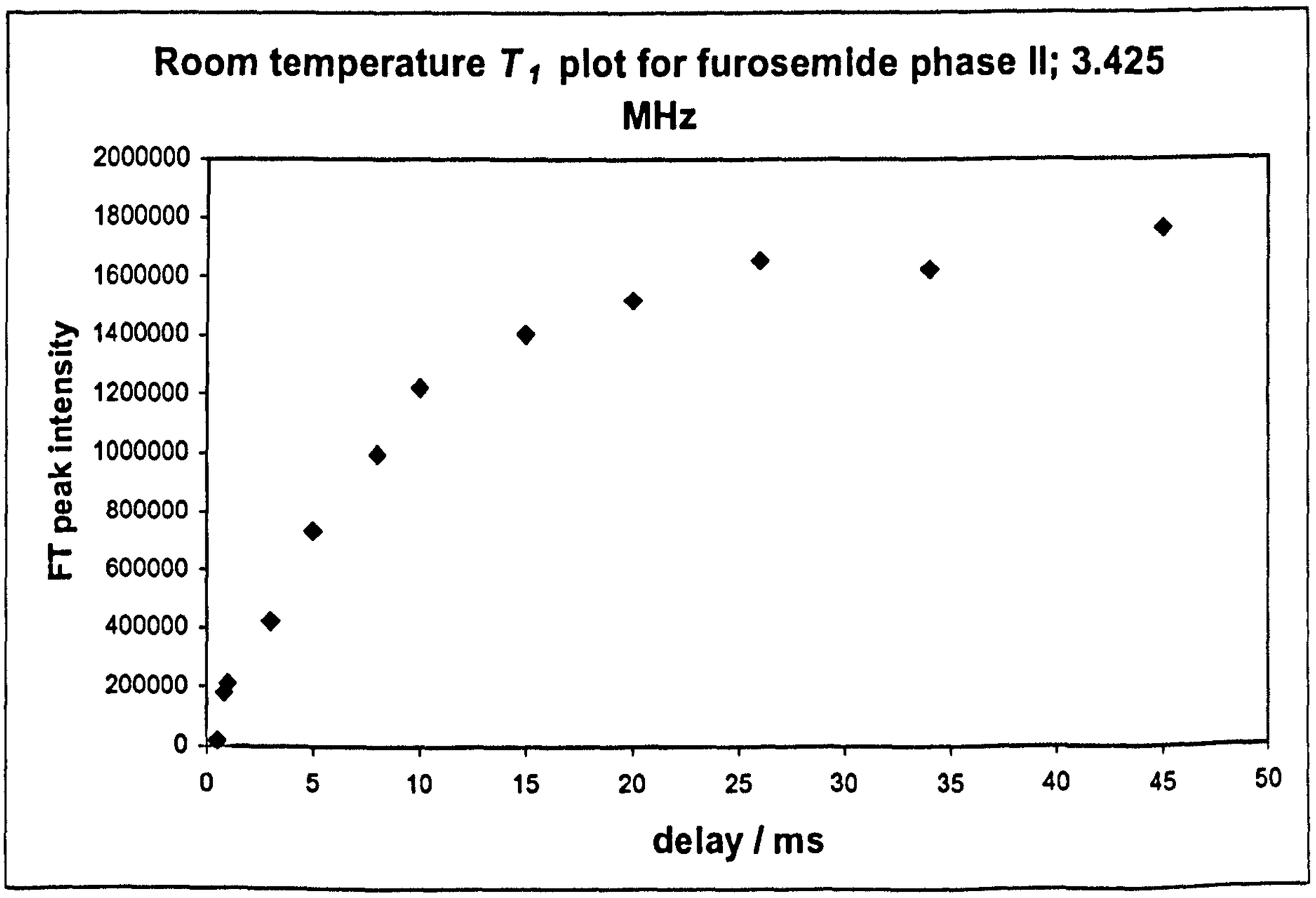

Figure 4.21: T_1 graph from the ^{14}N signal from phase II furosemide at room temperature. $T_1 = 10 \pm 1$ ms; 3.425 MHz.

T_1 was found to be 10 ± 1 ms. This is comparable with the value determined for phase I (7 ms ± 2 ms), indicating that spin-lattice relaxation may occur via the same process in both forms.

Variable temperature work was not carried out on phase II furosemide due to both time restrictions and stability issues.

4.4.3.2.2 T_2

T_2, the spin-spin relaxation time, was found using a Hahn echo sequence. The subsequent pulse sequence settings were used at room temperature:

Event		
Pulse / μs	130	(Phase 0202)
Dead time	Variable - 15 points from 0.2 to 10 ms	
Acquisition	128 points / 10 μs dwell	(Phase 0202)
Final delay / ms	60	
No. of scans	80000	
Excitation frequency	3.563 MHz	

Table 4.11: Furosemide phase II Hahn echo pulse sequence.

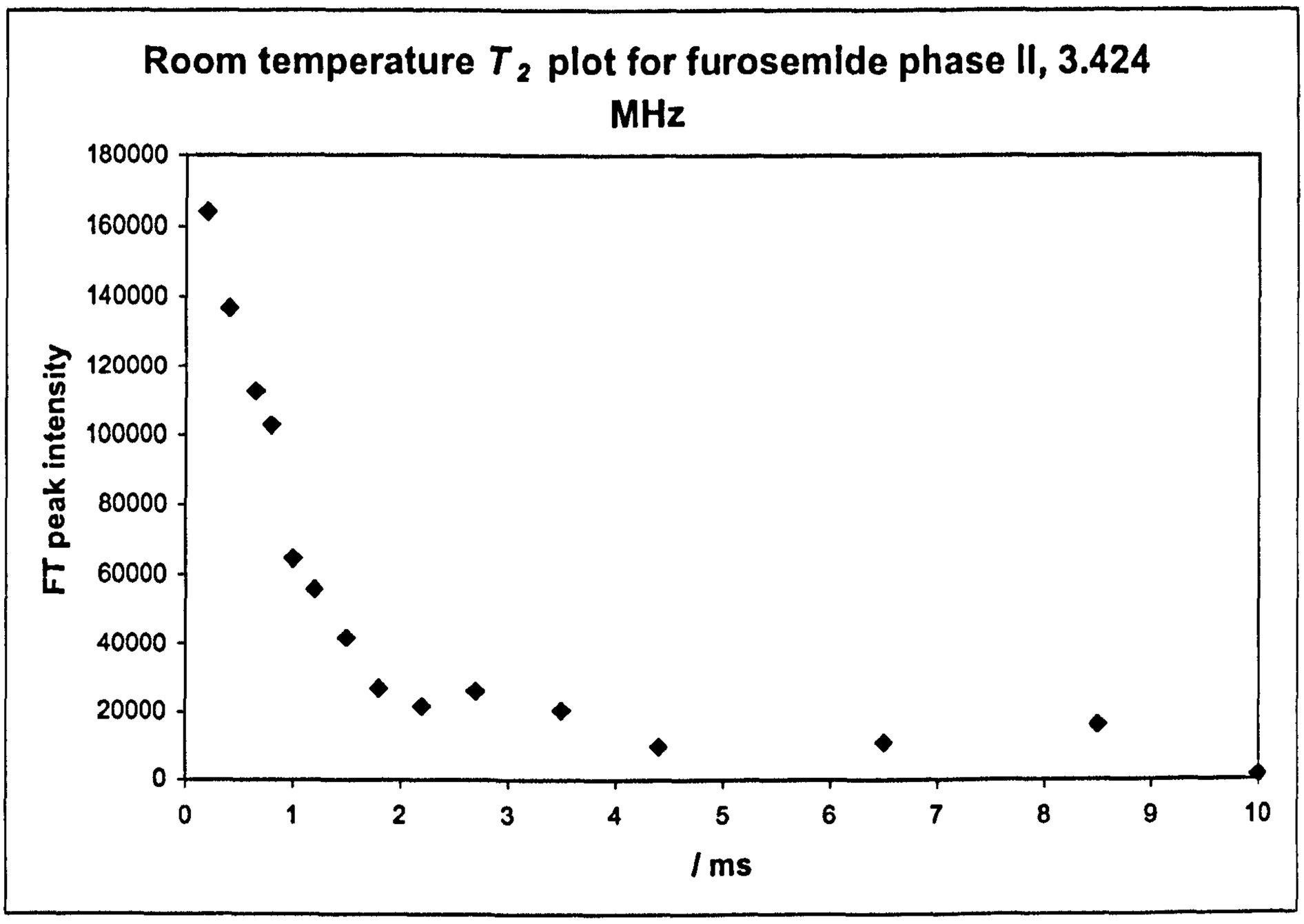

Figure 4.22: Phase II furosemide room temperature T_2 plot; $T_2 = 1.02 \pm 0.08$ ms.

T_2 was found to be short; the mean value over three experiments was 1.02 ± 0.08 ms (figure 4.22). This almost half that of phase I (which was found to be 1.95 ± 0.08 ms). T_2 is a characteristic value of a compound which is determined by dipole-dipole interactions; the different values found for polymorphs I and II indicate the different environments present in the two polymorphs and are another experimental way of distinguishing between them using NQR when observed together with the frequency change.

4.4.3.2.3 T_2e

The experiment was carried out 3 times using the following PSL sequence settings to determine T_2e:

Event	$2\tau = 1.49$ ms
Pulse / μs	110
Acquisition	128 points / 10 μs dwell time
Final Delay / ms	100
No. of scans	5000
Frequency / MHz	3.422

Table 4.12: Furosemide phase II T_2e pulse sequence ($2\tau = 1.49$ ms).

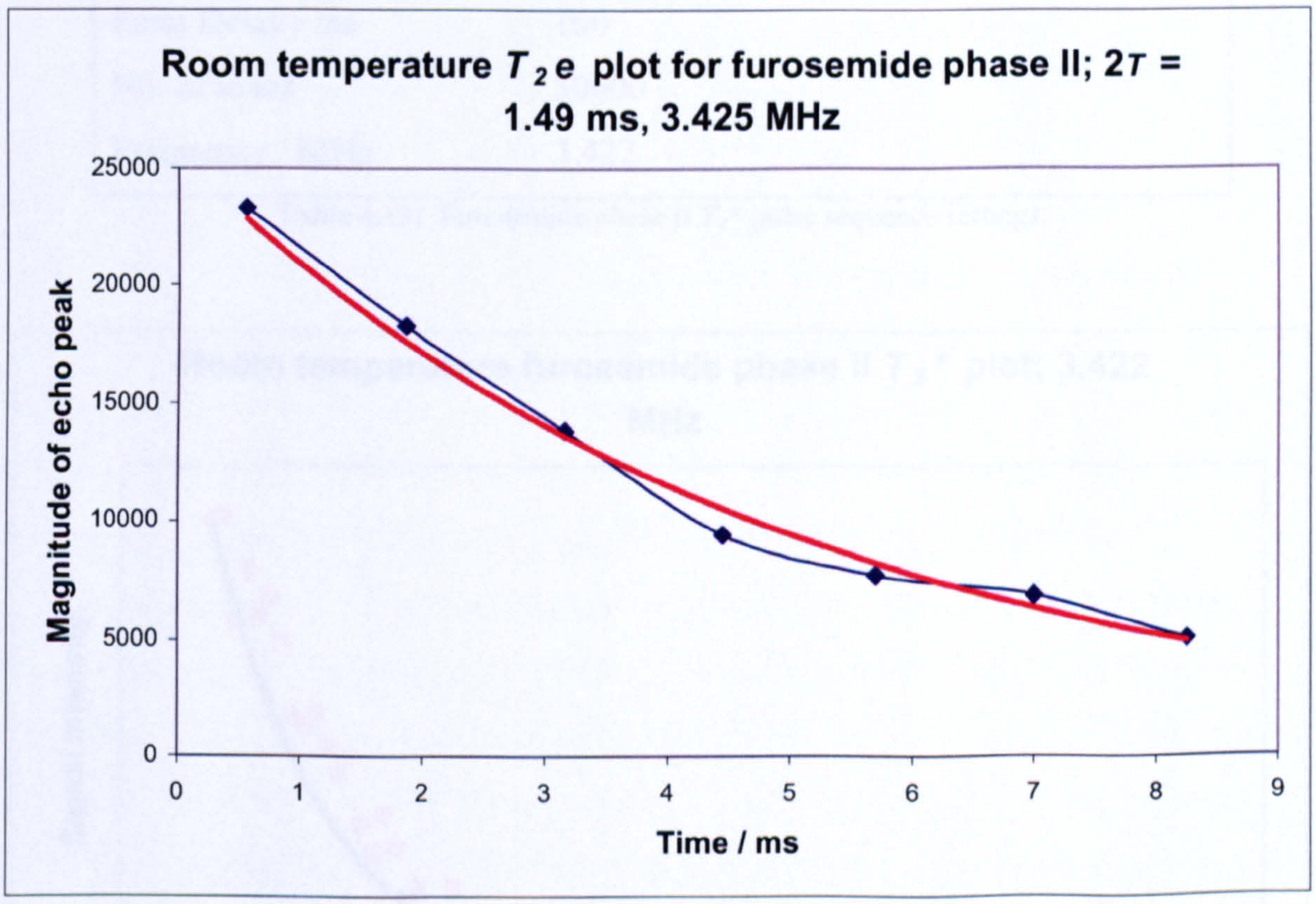

Figure 4.23: Furosemide phase II; 3.425 MHz line echo peak magnitude points for 2τ=1.49 ms; the continuous line is a single exponential fit with $T_2e = 5.5 \pm 1.0$ ms.

Similarly to phase I, only a short echo train could be sustained before the signal was drowned by noise. A good exponential fit ideally requires more points. T_2e was found to be 5.5 ± 1 ms (mean), for a 2τ value of 1.49 ms approximately half that of phase I

furosemide for which a value of 11.30 ± 0.10 ms was determined. The errors are calculated from the T_2e range after 3 experiments.

4.4.3.2.4 T_2*

Again T_2* was calculated at room temperature by fitting half an echo, obtained by a PSL sequence, to an exponential curve with equation (4.1)

The pulse sequence used had the following settings:

Event	
Pulse / μs	50
Acquisition	128 points / 10 μs dwell time
Final Delay / ms	100
No. of scans	30000
Frequency / MHz	3.422

Table 4.13: Furosemide phase II T_2* pulse sequence settings.

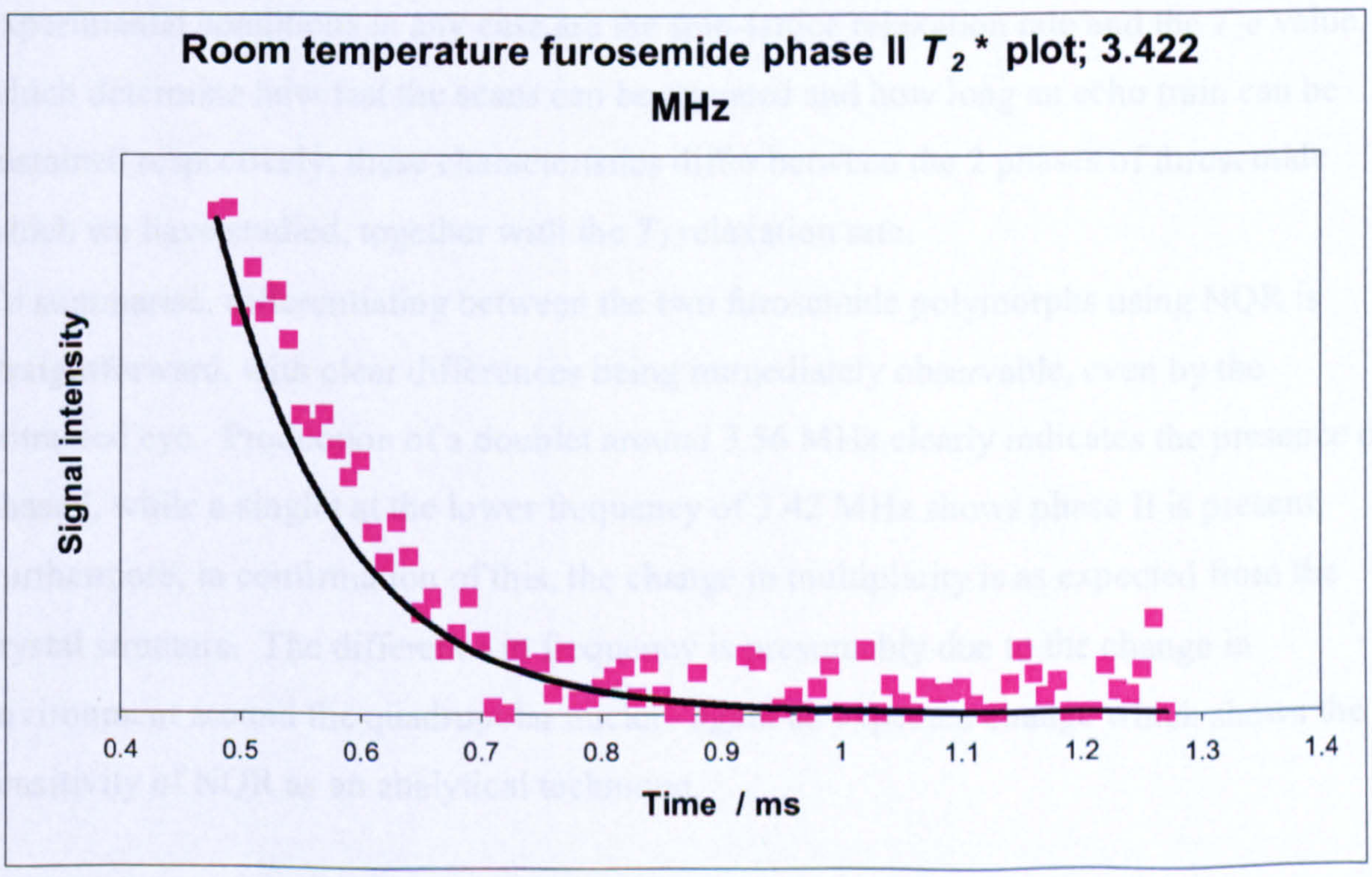

Figure 4.24: T_2* exponential curve for room temperature phase II furosemide; T_2* = 0.11 ± 0.03 ms; 3.422 MHz.

T_2* was found to be 0.11 ± 0.03 ms (mean). The errors are calculated from the results of 3 experiments. This is very similar to the T_2* of phase I (0.10 ± 0.02 ms)

4.4.4 Comparison of phase I and phase II ^{14}N room temperature data

	Phase I furosemide	Phase II furosemide
Frequency	3.5636 and 3.5612 MHz	3.422 MHz
Multiplicity	Doublet	Singlet
T_1	7 ± 2 ms	10 ± 1 ms
T_2e (2 τ = 1.49 ms)	11.30 ± 0.10 ms	5.5 ± 1.0 ms
T_2	1.95 ± 0.32 ms	1.02 ± 0.08 ms
T_2*	0.10 ± 0.02 ms	0.11 ± 0.03 ms
Lorentzian linewidth	3.18 kHz	2.89 kHz

Table 4.14: Furosemide phase I & II; comparison of measured NQR values.

In the case of furosemide the most important factor in identifying a polymorph using NQR is the frequency and the most important values in determining the optimum experimental conditions in any case are the spin-lattice relaxation rate and the T_2e value, which determine how fast the scans can be repeated and how long an echo train can be sustained respectively; these characteristics differ between the 2 phases of furosemide which we have studied, together with the T_2 relaxation rate.

To summarise, differentiating between the two furosemide polymorphs using NQR is straightforward, with clear differences being immediately observable, even by the untrained eye. Production of a doublet around 3.56 MHz clearly indicates the presence of phase I, while a singlet at the lower frequency of 3.42 MHz shows phase II is present. Furthermore, in confirmation of this, the change in multiplicity is as expected from the crystal structure. The difference in frequency is presumably due to the change in environment around the quadrupolar nuclei - again an expected change which shows the sensitivity of NQR as an analytical technique.

4.5 ^{35}Cl furosemide signals

Having shown that ^{14}N NQR can be used to distinguish between furosemide polymorphs, we hoped to similarly characterise and analyse chlorine signals in the various forms of furosemide. Chlorine signals are generally at much higher frequencies than nitrogen signals and are usually stronger, requiring smaller RF coils and therefore smaller volumes of material. Even with fewer nuclei being excited, a peak with a good signal-to-noise ratio can be acquired in a fairly short time in many cases, allowing fast analysis, detection of small amounts and the possibility of single tablet experiments. ^{35}Cl signals have been reported from phase I furosemide at 77 K at a frequency of 36.579 MHz, with no mention of the doublet structure[2] as would have been expected from the crystal structure at room temperature.

4.5.1 Phase I studies: finding the ^{35}Cl signal

The search for the ^{35}Cl line in phase I furosemide at room temperature was begun around the frequency reported by Latosinka using a 3.5 g powder sample, obtained from Sigma and used as received. A PSL echo sequence was used searching downwards in frequency from 36.50 MHz in steps of 0.01 MHz. As discussed above and in chapter 2, a smaller solenoid than those used for ^{14}N work is required, and solenoid C was used together with the NMRkit, a frequency generator and the Amplifier Research amplifier as discussed in chapter 3. Solenoid C was constructed from 2 mm copper wire, supported on PTFE tubing, consisting of 5 turns with a diameter of 15 mm and length of 55 mm with an inductance of approximately 1 μH. The experiments were run at room temperature.

Event	
90_{eff} Pulse / μs	40
Acquisition	64 points / 3 μs dwell time
Final Delay / ms	30
No. of scans	50000
Frequency / MHz	Variable

Table 4.15: Furosemide phase I ^{35}Cl PSL pulse sequence settings.

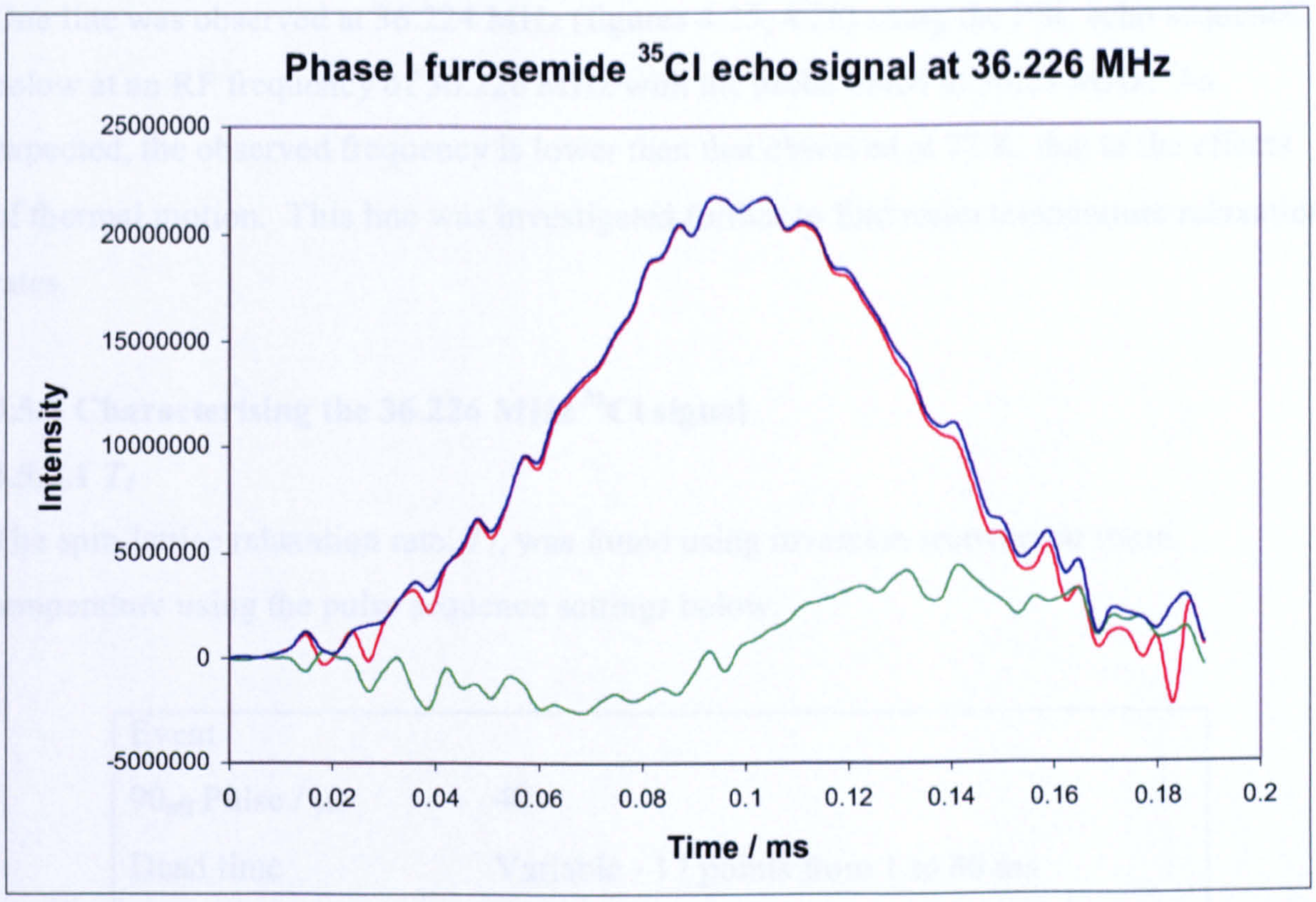

Figure 4.25: Phase I furosemide powder ^{35}Cl room temperature signal in the time domain. 4 summed echoes, 50000 scans; 36.226 MHz.

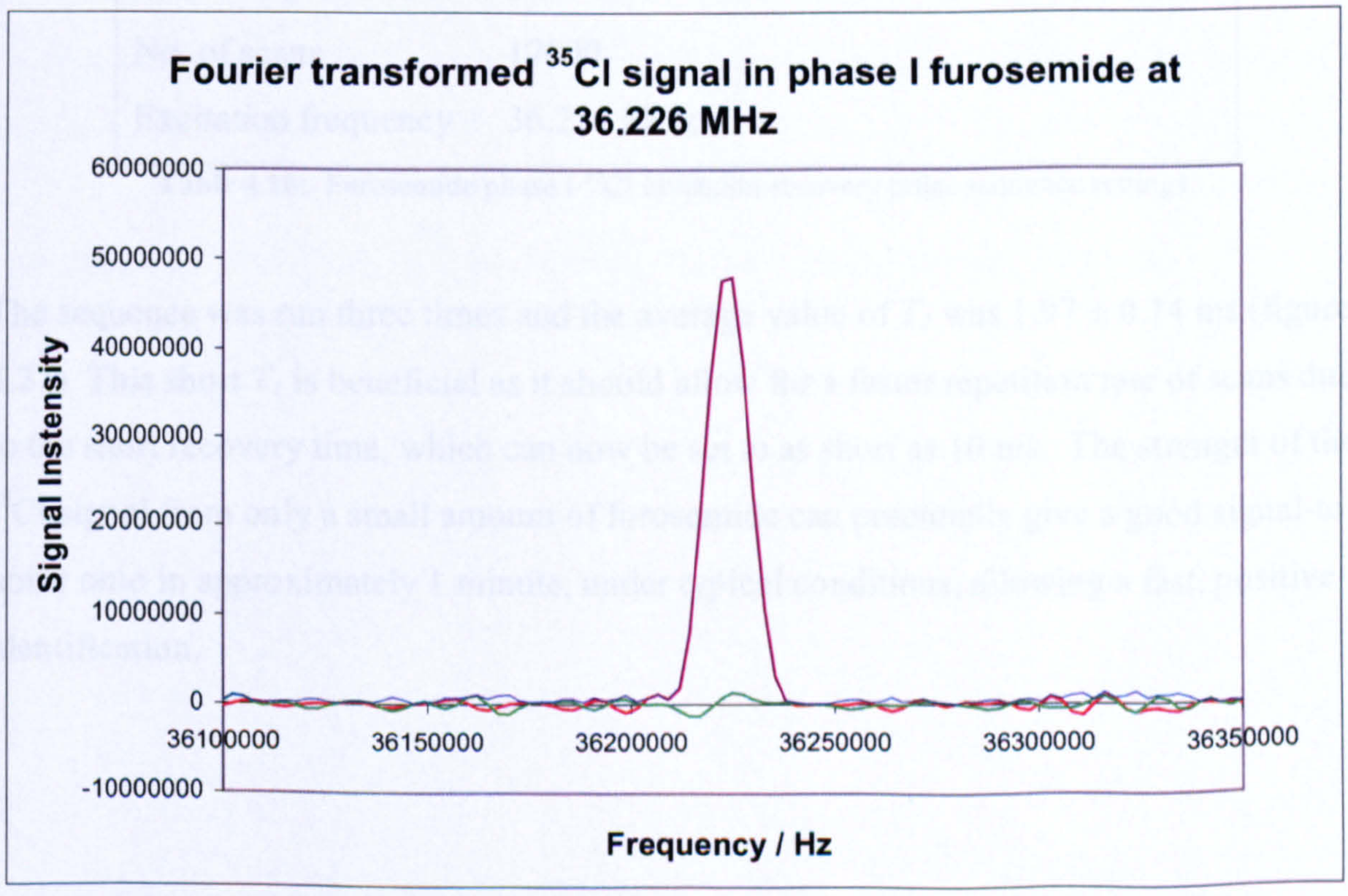

Figure 4.26: Singlet ^{35}Cl peak from phase I furosemide powder; Fourier transformation of figure 4.25, at a frequency 36.2224 MHz, linewidth approximately 10 kHz.

One line was observed at 36.224 MHz (figures 4.25, 4.26) using the PSL echo sequence below at an RF frequency of 36.226 MHz with the probe tuned to 36.23 MHz. As expected, the observed frequency is lower than that observed at 77 K, due to the effects of thermal motion. This line was investigated further to find room temperature relaxation rates.

4.5.2 Characterising the 36.226 MHz ^{35}Cl signal

4.5.2.1 T_1

The spin-lattice relaxation rate, T_1, was found using inversion recovery at room temperature using the pulse sequence settings below.

Event	
90_{eff} Pulse / μs	40
Dead time	Variable - 17 points from 1 to 80 ms
Acquisition	64 points / 3 μs dwell time
Final delay / ms	50
No. of scans	17000
Excitation frequency	36.226 MHz

Table 4.16: Furosemide phase I ^{35}Cl inversion-recovery pulse sequence settings.

The sequence was run three times and the average value of T_1 was 1.97 ± 0.14 ms (figure 4.27). This short T_1 is beneficial as it should allow for a faster repetition rate of scans due to the short recovery time, which can now be set to as short as 10 ms. The strength of the ^{35}Cl signal from only a small amount of furosemide can potentially give a good signal-to-noise ratio in approximately 1 minute, under typical conditions, allowing a fast, positive identification.

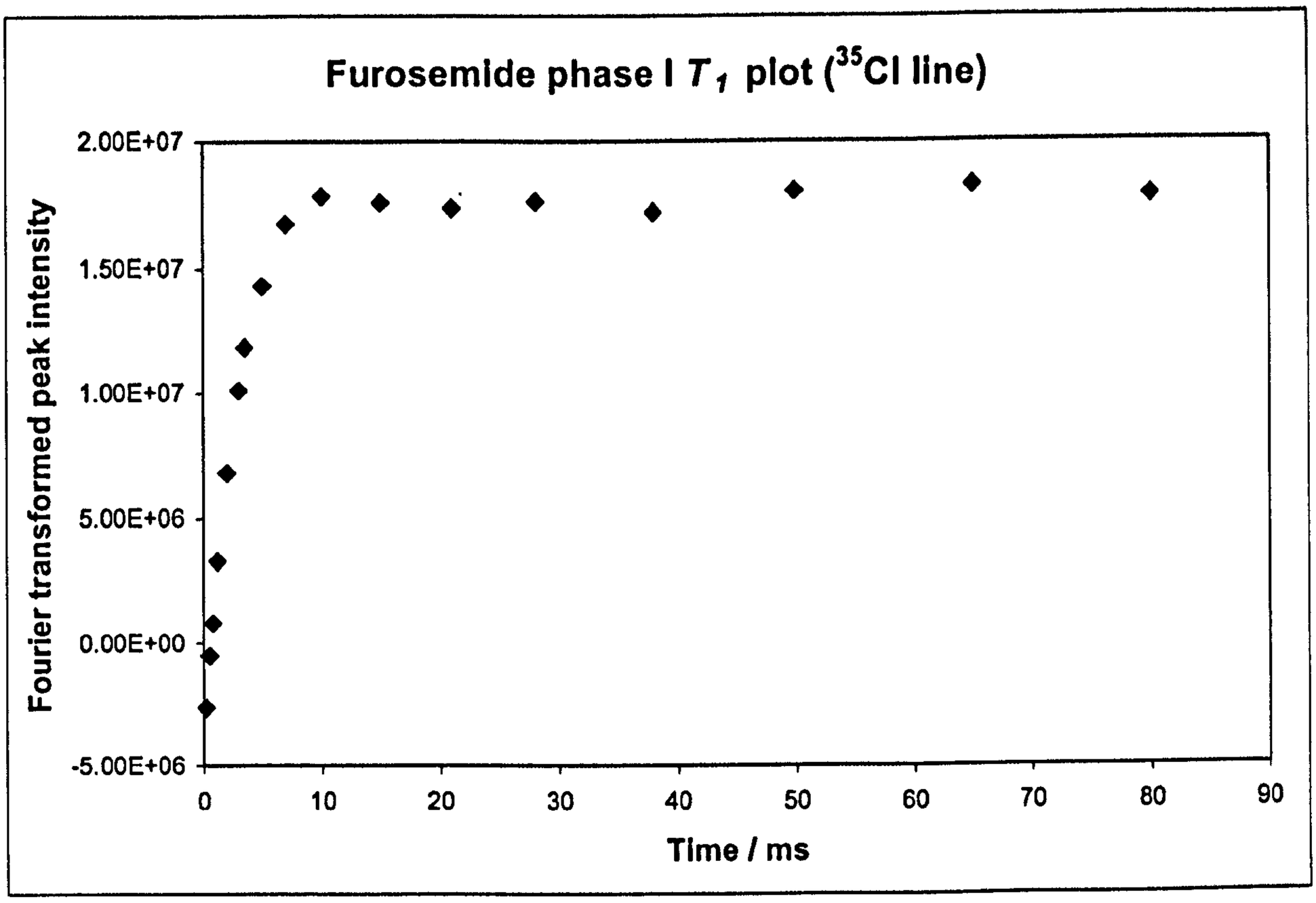

Figure 4.27: Phase I furosemide ^{35}Cl T_1 plot at room temperature. T_1 = 1.99 ± 0.12 ms; 36.226 MHz.

Having determined a short T_1 and a strong signal for ^{35}Cl in furosemide, it was important to find T_2e as the time for which an echo train can be sustained is of great importance experimentally; the longer the time for which the echo train can be maintained the better, allowing fast signal build-up in the addition of the echoes and making the use more viable for real world applications.

4.5.2.2 T_2e

A pulse sequence was set up to monitor the echo train and find the value of T_2e for the ^{35}Cl signal around 36.22 MHz.

Event	$2\tau = 280$ µs
Pulse / µs	40
Acquisition	64 points / 3 µs dwell time
Final Delay / ms	100
No. of scans	100000
Frequency / MHz	36.226

Table 4.17: Furosemide phase I ^{35}Cl T_2e pulse sequence ($2\tau = 280$ µs, 16 sequential echoes).

Only a small number of echoes could be sustained, even with the short 2τ time used. The T_2e average value (over 3 experiments), with $2\tau = 280$ µs, was 0.793 ± 0.018 ms (figure 4.28). The T_2e values and errors were calculated using 'pro Fit', a Macintosh application. Once the scans were complete the resulting series of echoes were separated, phase adjusted and echo Fourier transformed. The data were exported to pro Fit where, after an initial rough fit, with parameters estimated by the user, iterative techniques were used to find the best exponential fit to the T_2e points. The possibility of biexponential behaviour was checked by fitting to a biexponential function but this did not give a significantly better fit than a single exponential. The Levenberg-Marquardt algorithm is used to generate a well fitting function.

Although the pulse lengths and spacings being used in observing the ^{35}Cl line are much shorter than in the previous ^{14}N furosemide work, the number of echoes sustained with a good signal-to-noise ratio is comparable.

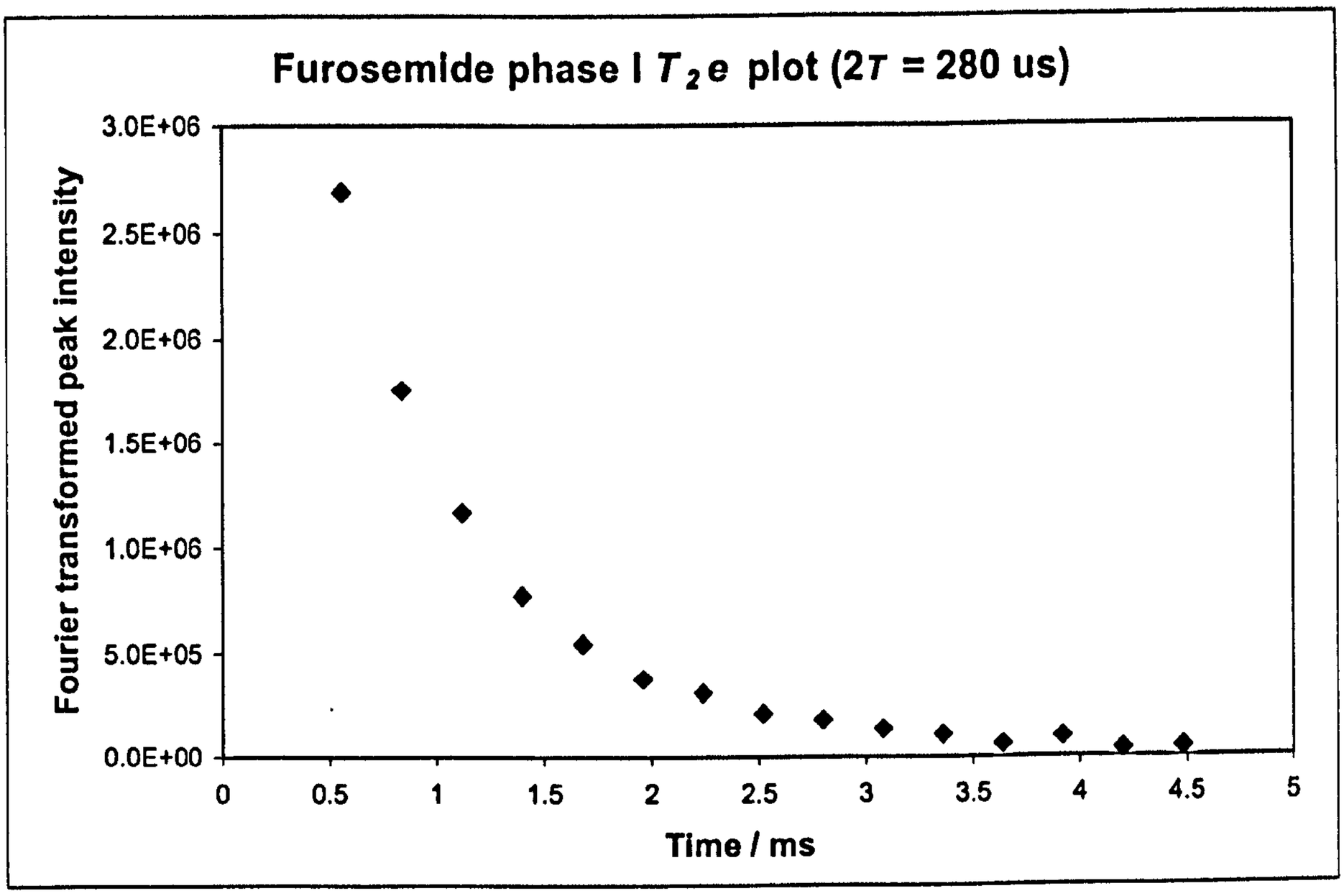

Figure 4.28: Phase I furosemide; ^{35}Cl 36.226 MHz line T_2e plot, where 2 τ = 280 µs; for plot shown T_2e = 0.811 ms.

4.5.2.3 T_2

T_2, the spin-spin relaxation time, was found using a Hahn echo sequence.

Event	
Pulse / µs	40
Dead time	Variable - 21 points from 0.1 to 6.5 ms
Acquisition	64 points / 3 µs dwell time
Final delay / ms	50
No. of scans	50000
Excitation frequency	36.226 MHz

Table 4.18: Furosemide phase I ^{35}Cl Hahn echo pulse sequence.

The T_2 average value (from 3 experiments) was found to be 0.28 ± 0.03 ms (figure 4.29). Like T_1, T_2 for this line in furosemide is quite short, but considerably longer than the T_2^* value quoted below.

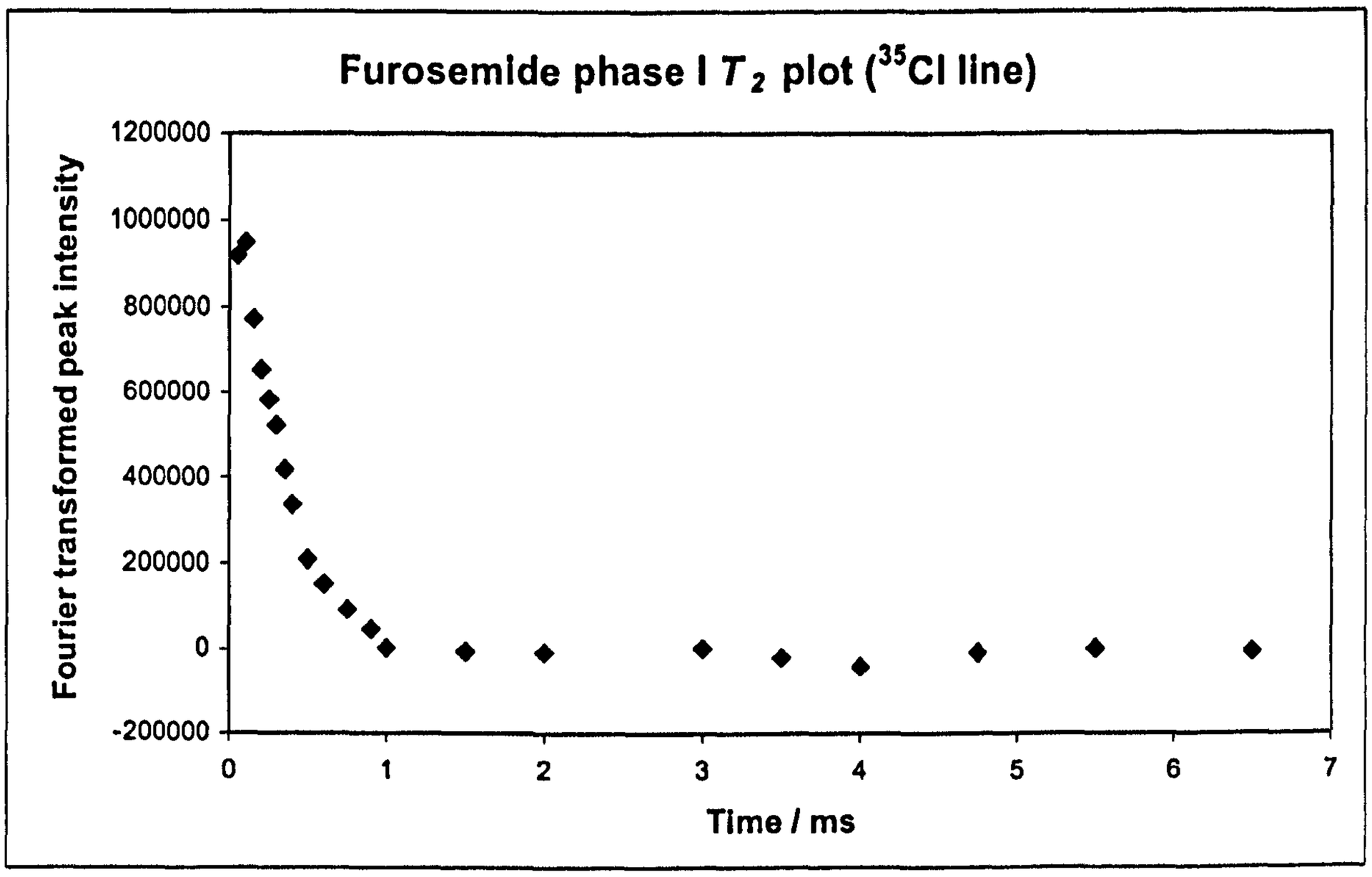

Figure 4.29: Phase I furosemide T_2 plot at room temperature. T_2 = 0.28 ± 0.02 ms; 36.226 MHz.

4.5.2.4 T_2*

T_2*, the spin-phase memory decay time was found by fitting an exponential function to the second half of an echo generated from a PSL sequence as table 4.14 and was found to be 0.0326 ± 0.0023 ms. This is predictably short, considering the T_1 and T_2 values for this ^{35}Cl line.

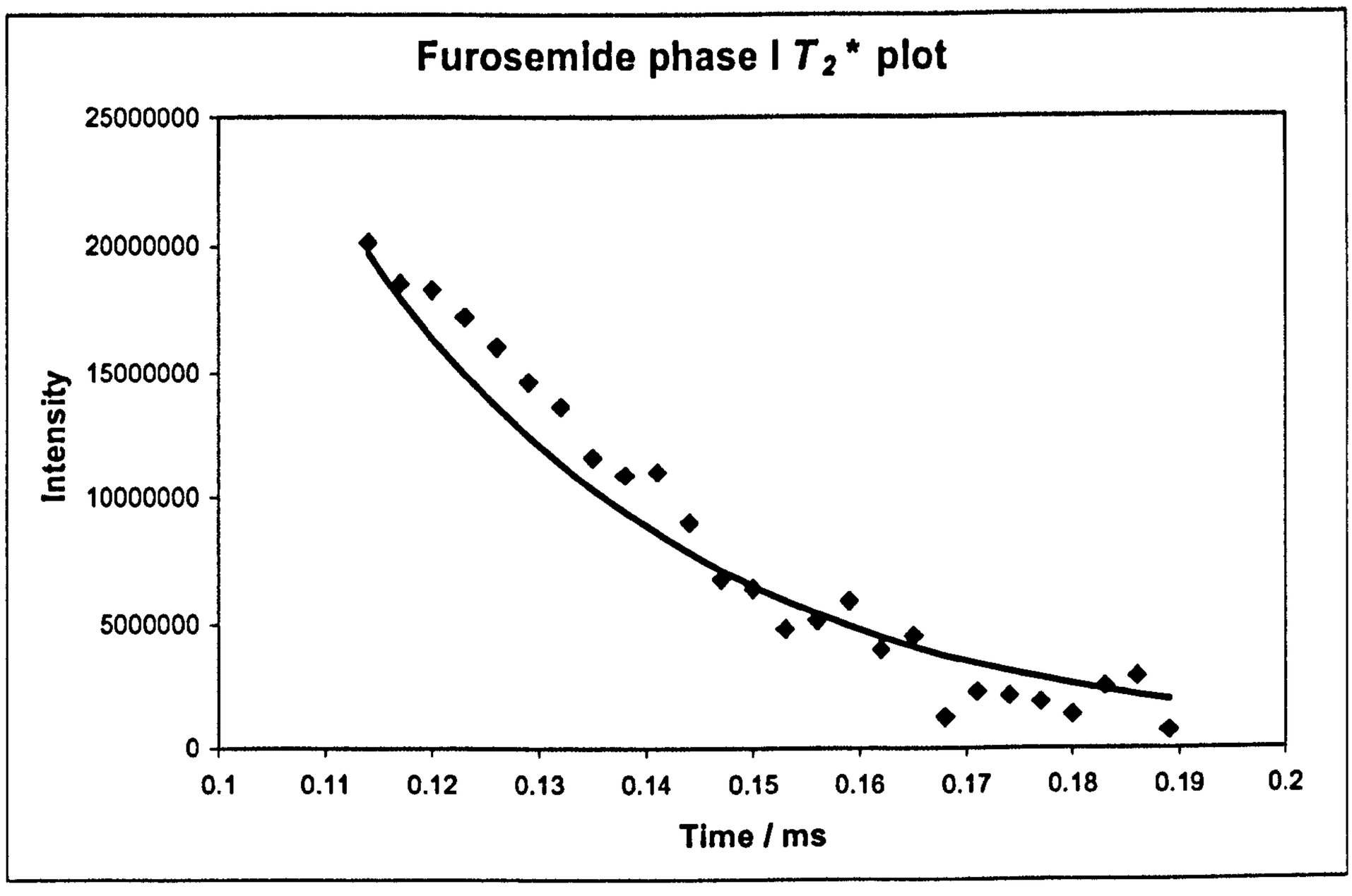

Figure 4.30: Phase I furosemide T_2^* plot at room temperature. $T_2^* = 0.0326 \pm 0.0023$ ms; 36.226 MHz.

4.5.3 Observation of ^{35}Cl signals in furosemide tablets

Further ^{35}Cl work was carried out on 20 mg and 500 mg tablets of furosemide, marketed at Lasix. T_1, T_2, T_2e and T_2^* were found for both using a sample of 80 20 mg tablets and 8 500 mg tablets. Using the same sequences, settings and experimental conditions as for the furosemide powder the signals from each set of tablets were characterized.

4.5.3.1 Characterising ^{35}Cl 36.226 MHz signal from 20 mg tablets

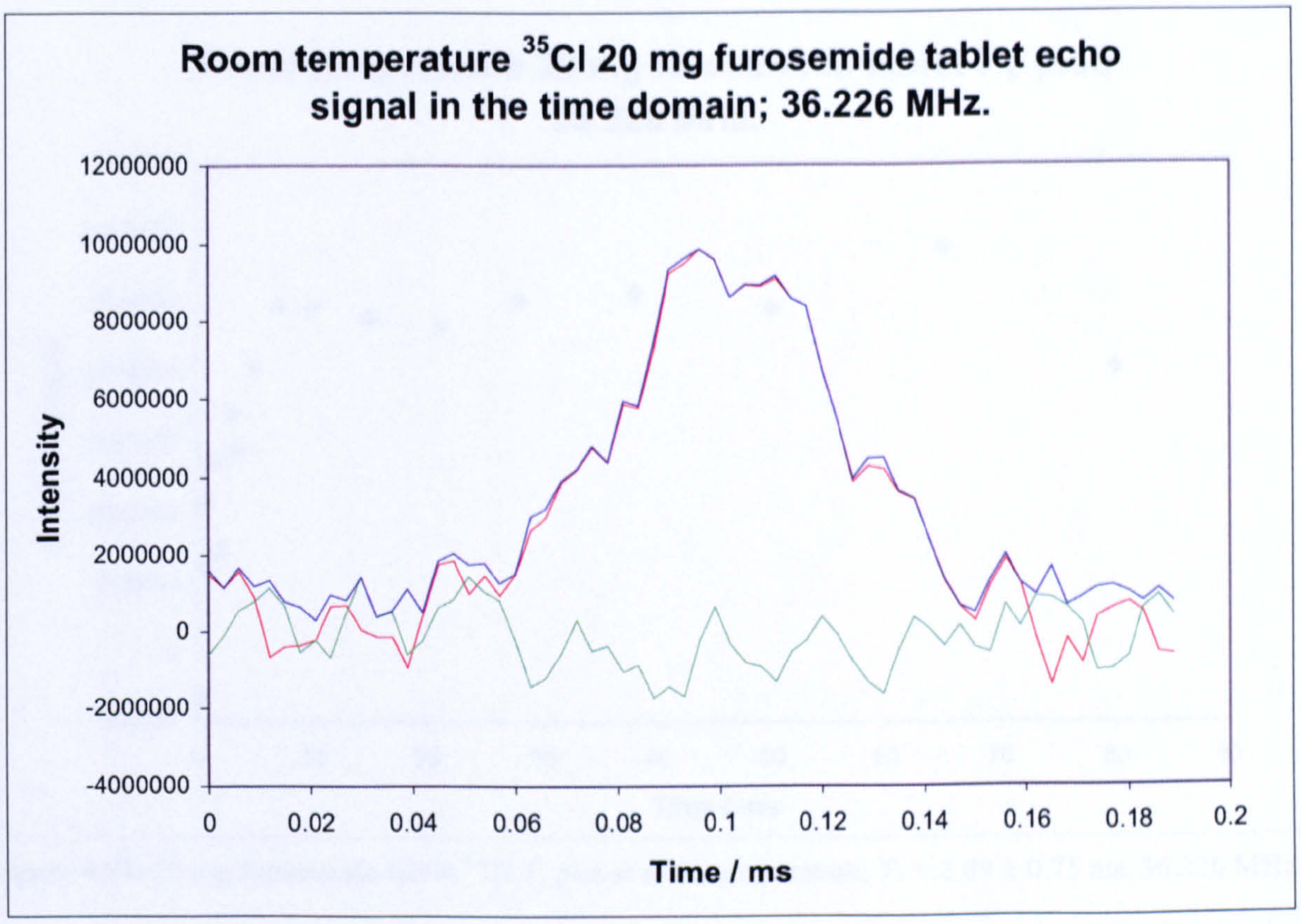

Figure 4.31: 20 mg furosemide tablets ^{35}Cl echo at room temperature; 10000 scans, 36.226 MHz.

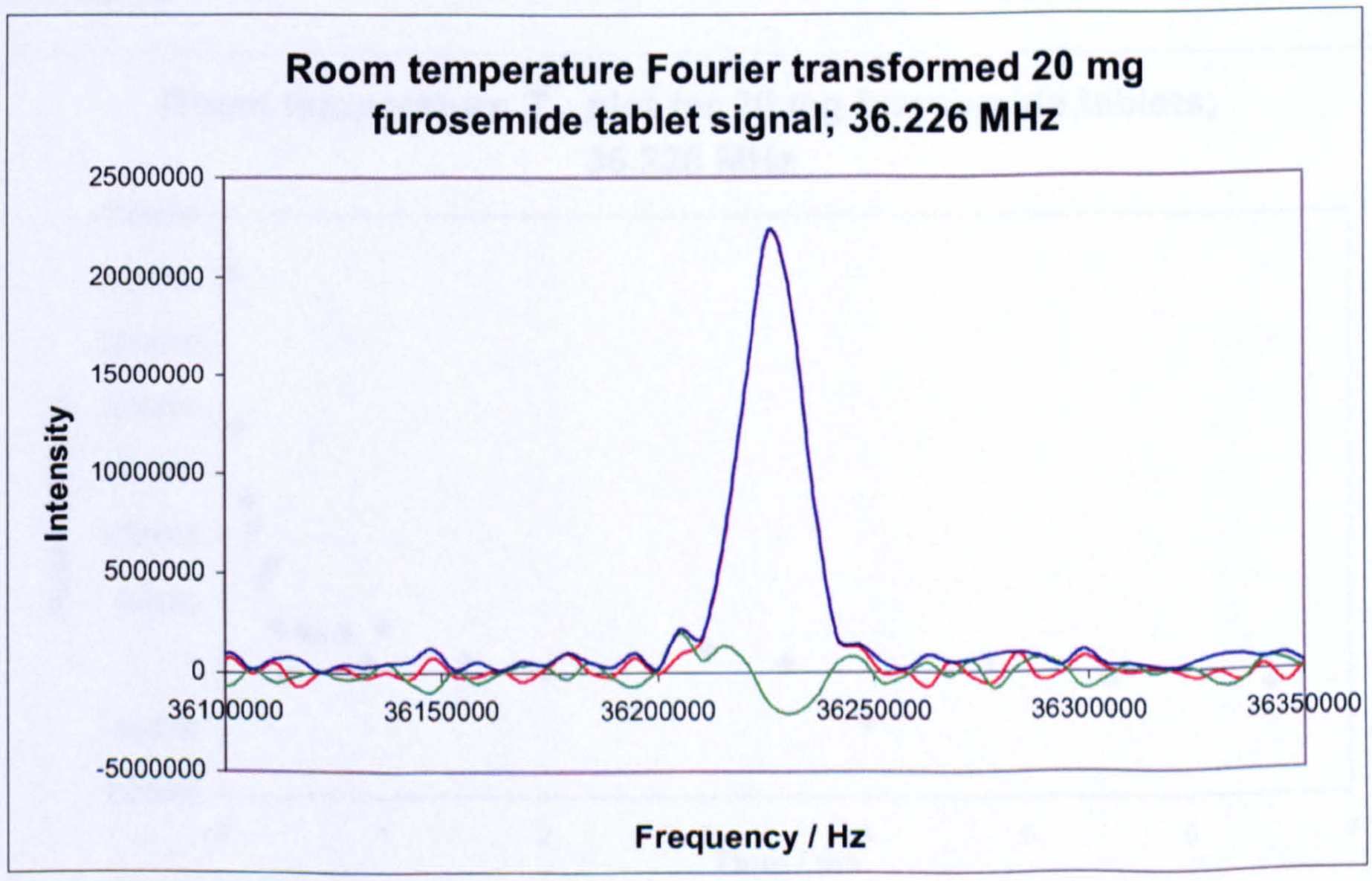

Figure 4.32: 20 mg furosemide tablet ^{35}Cl signal in the frequency domain; Fourier transformation of figure 1; 36.226 MHz.

4.5.3.1.1 T_1

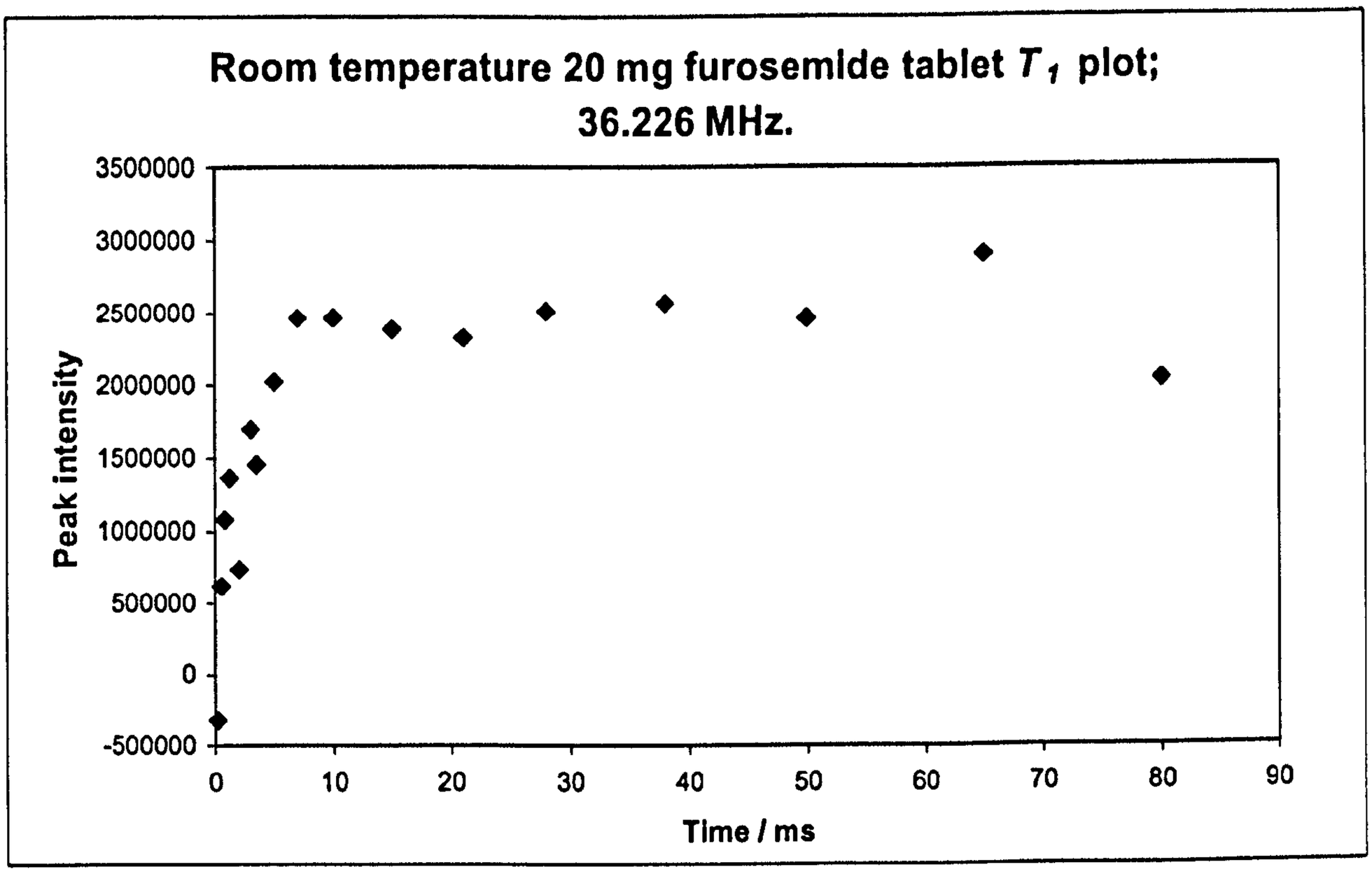

Figure 4.33: 20 mg furosemide tablet ^{35}Cl T_1 plot at room temperature; T_1 = 2.89 ± 0.75 ms, 36.226 MHz.

4.5.3.1.2 T_2

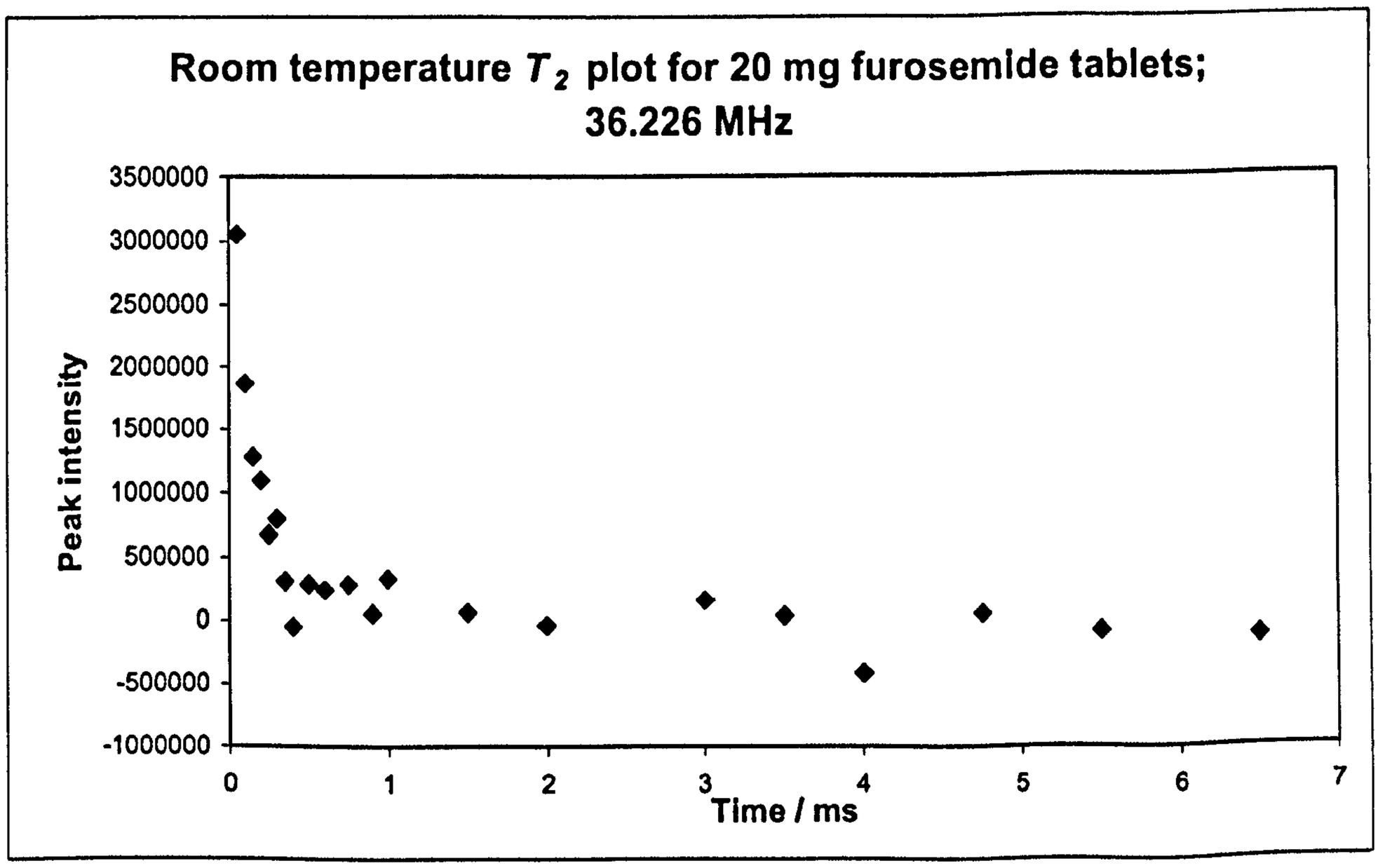

Figure 4.34: 20 mg furosemide tablet ^{35}Cl T_2 plot at room temperature; T_2 = 0.10 ± 0.01 ms, 36.226 MHz.

4.5.3.1.3 T_2e

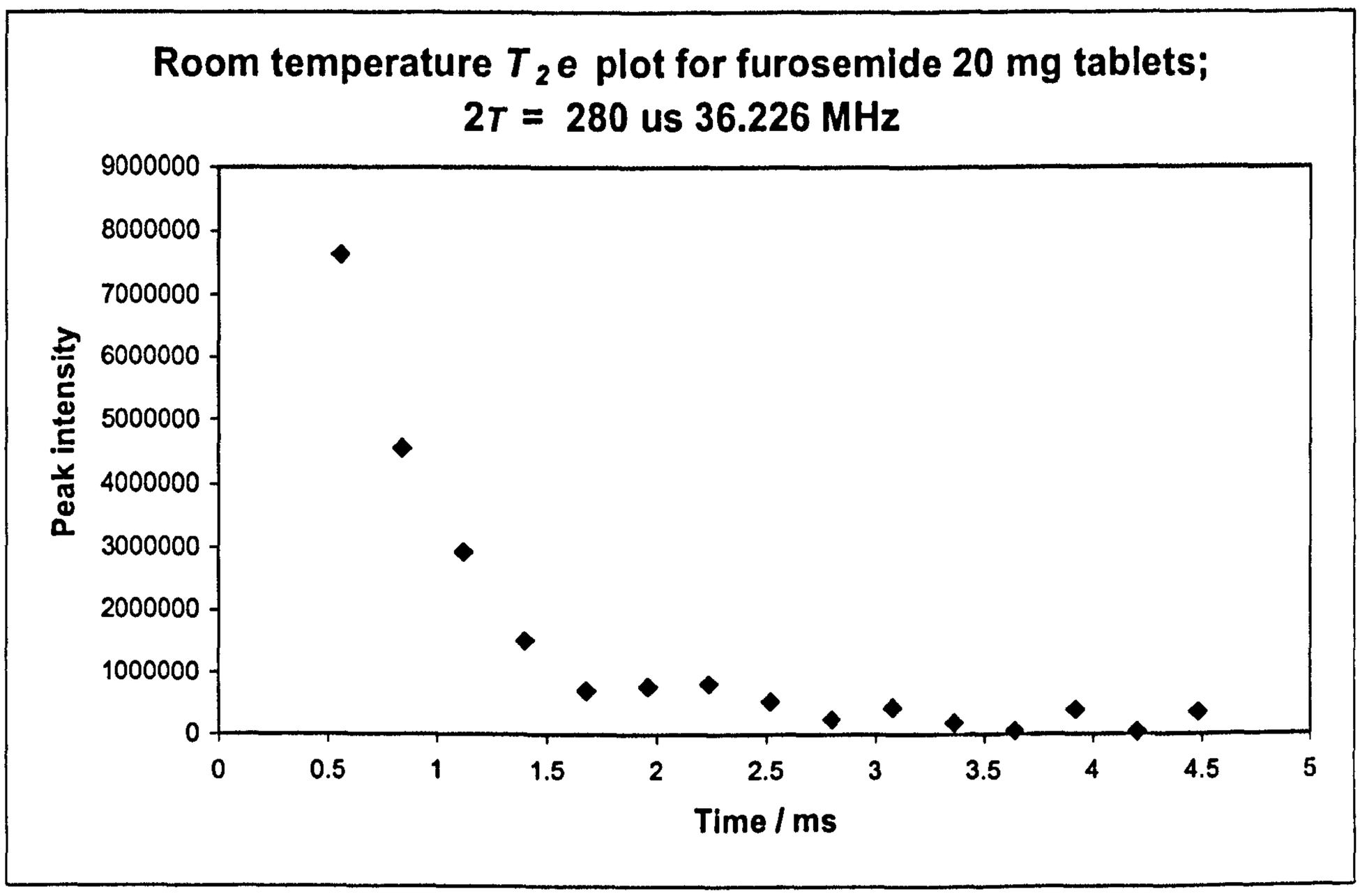

Figure 4.35: 20 mg furosemide tablet ^{35}Cl T_2e plot at room temperature; $T_2e = 0.571 \pm 0.032, 36.226$ MHz.

4.5.3.2 Characterising ^{35}Cl 36.226 MHz signal from 500 mg tablets

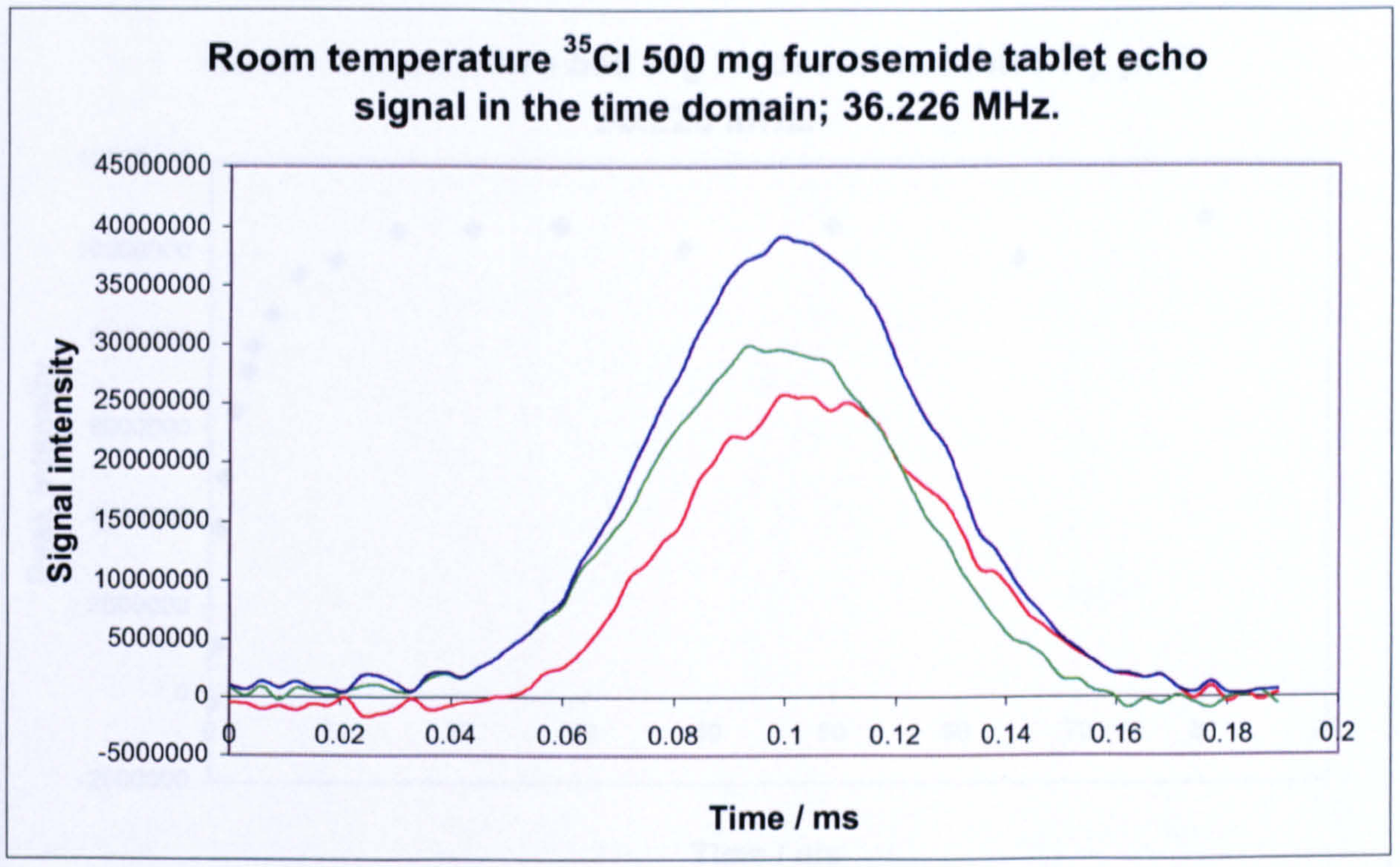

Figure 4.36: 500 mg furosemide tablets ^{35}Cl echo at room temperature; 10000 scans, 36.226 MHz.

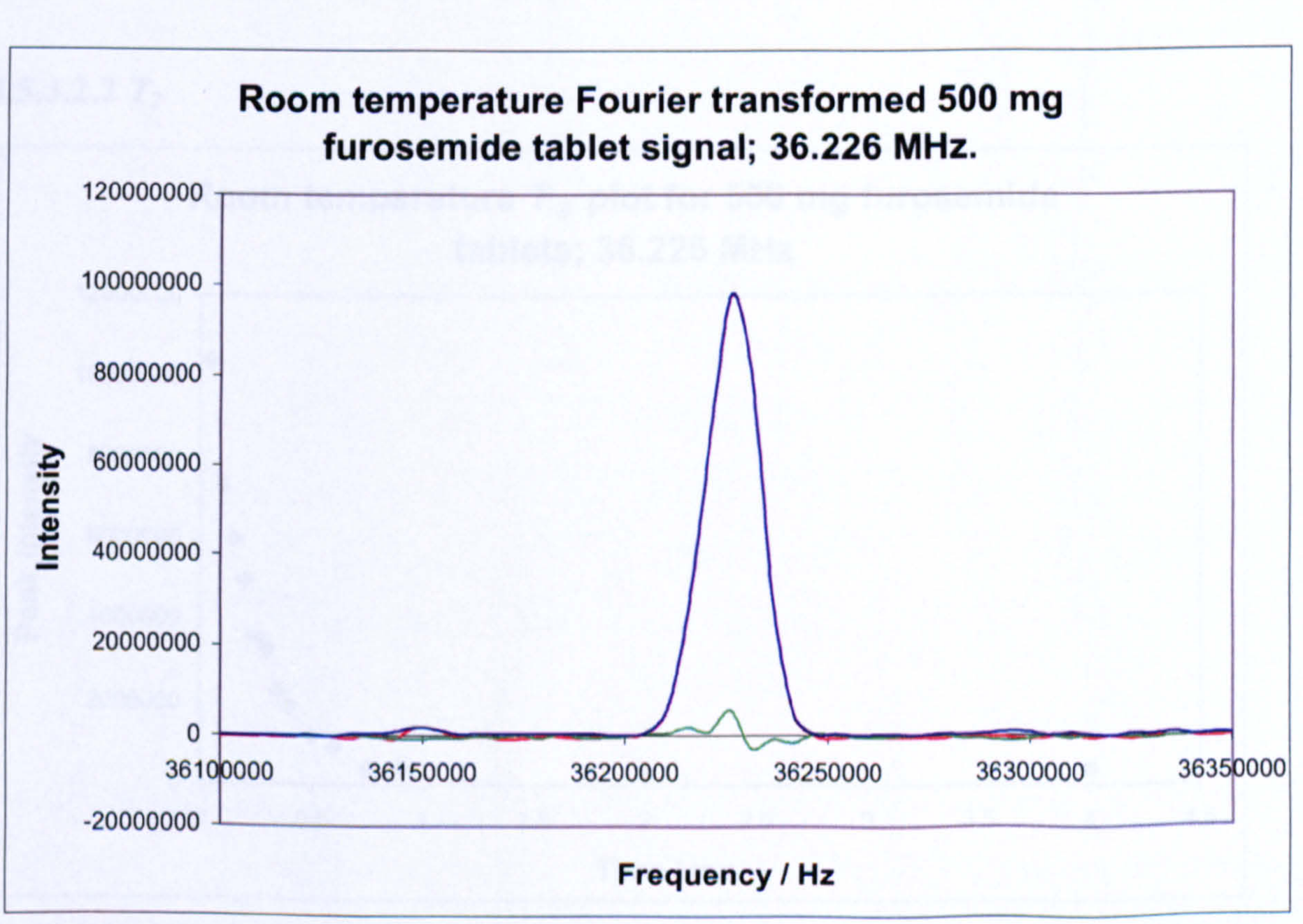

Figure 4.37: 500 mg furosemide tablet ^{35}Cl signal in the frequency domain; Fourier transformation of figure 4.36; 36.226 MHz.

4.5.3.2.1 T_1

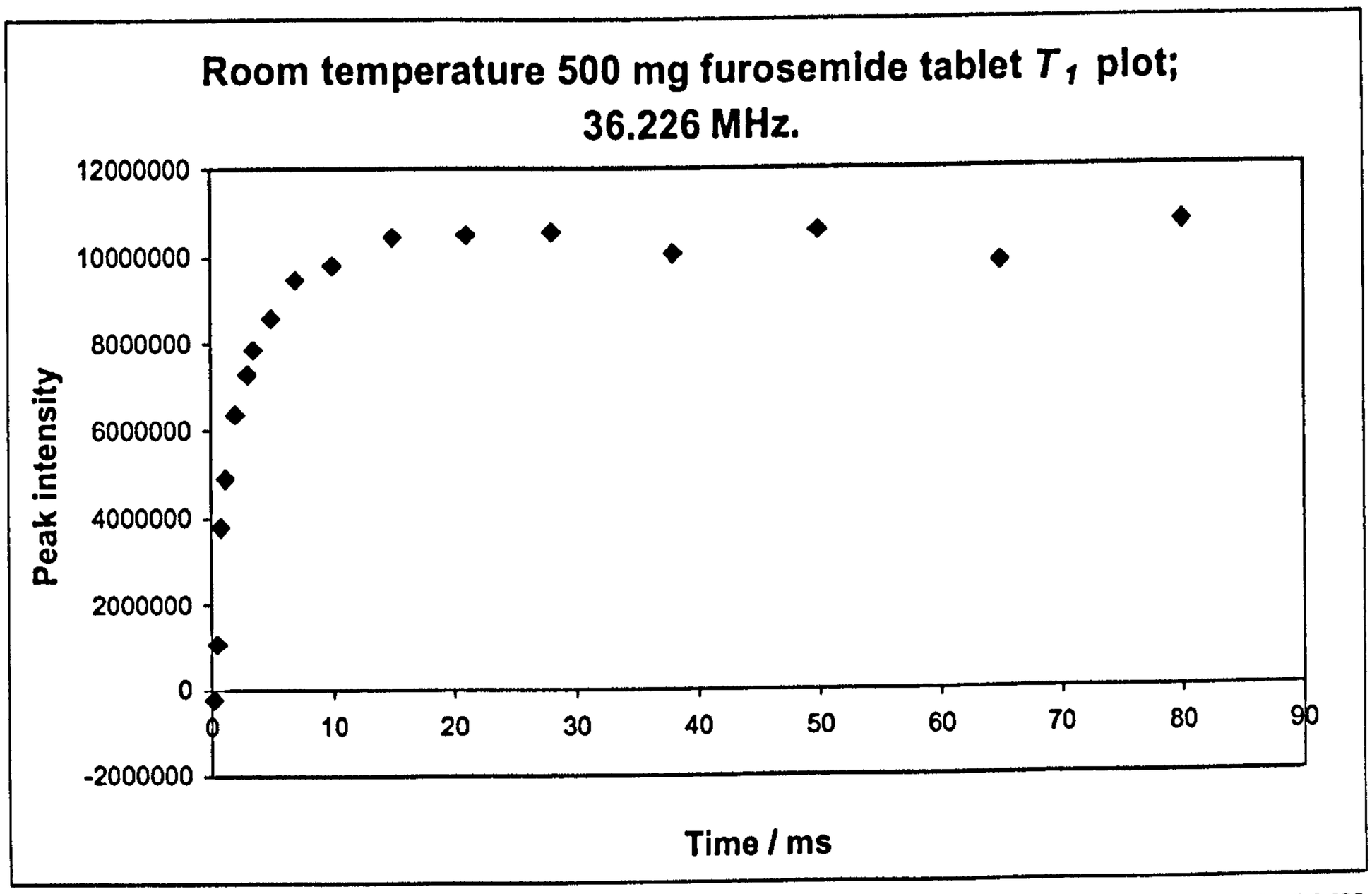

Figure 4.38: 500 mg furosemide tablet ^{35}Cl T_1 plot at room temperature; T_1 = 2.01 ± 0.18 ms, 36.226 MHz.

4.5.3.2.2 T_2

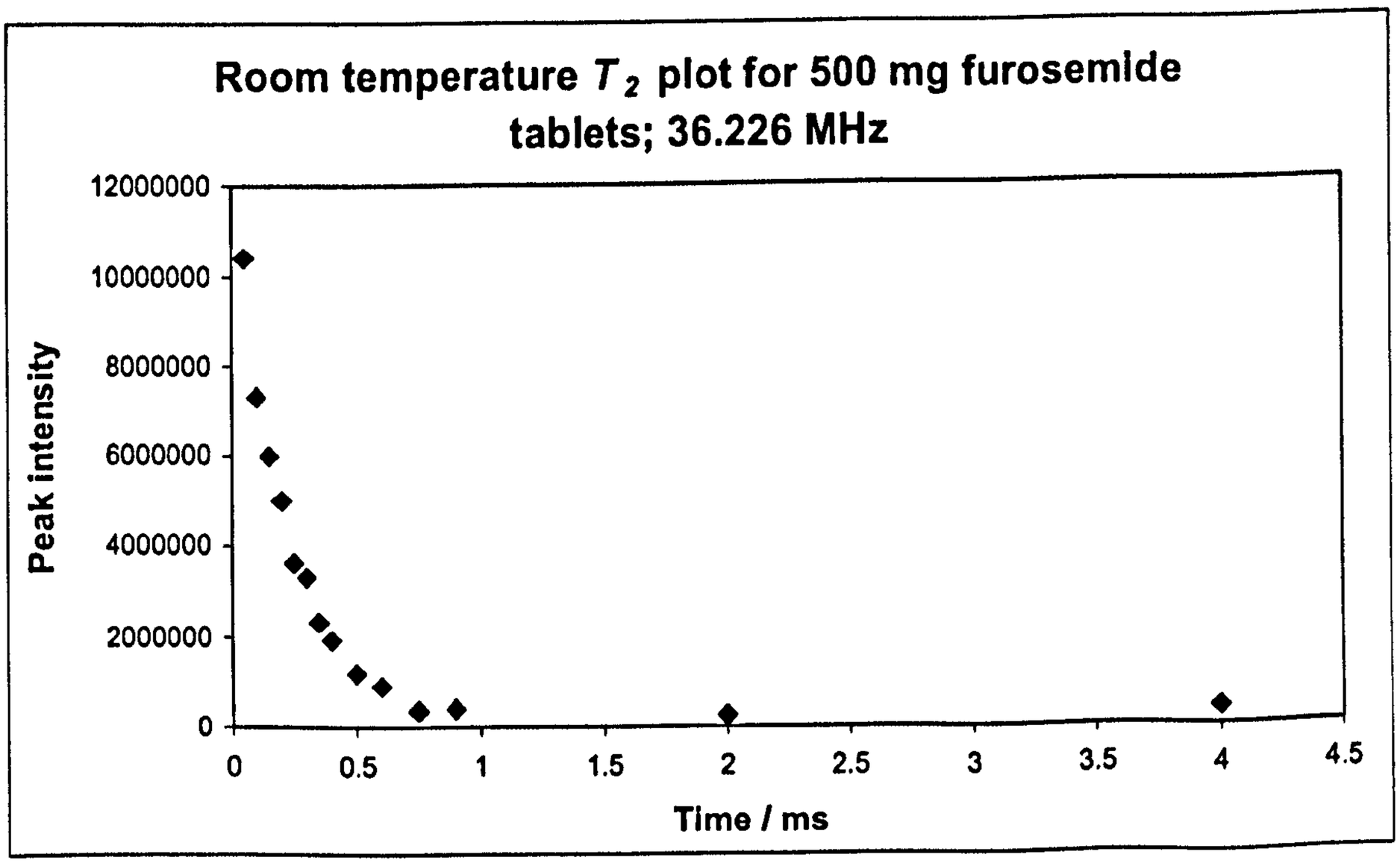

Figure 4.39: 500 mg furosemide tablet ^{35}Cl T_2 plot at room temperature; T_2 = 0.20 ± 0.01 ms, 36.226 MHz.

4.5.3.2.3 T_2e

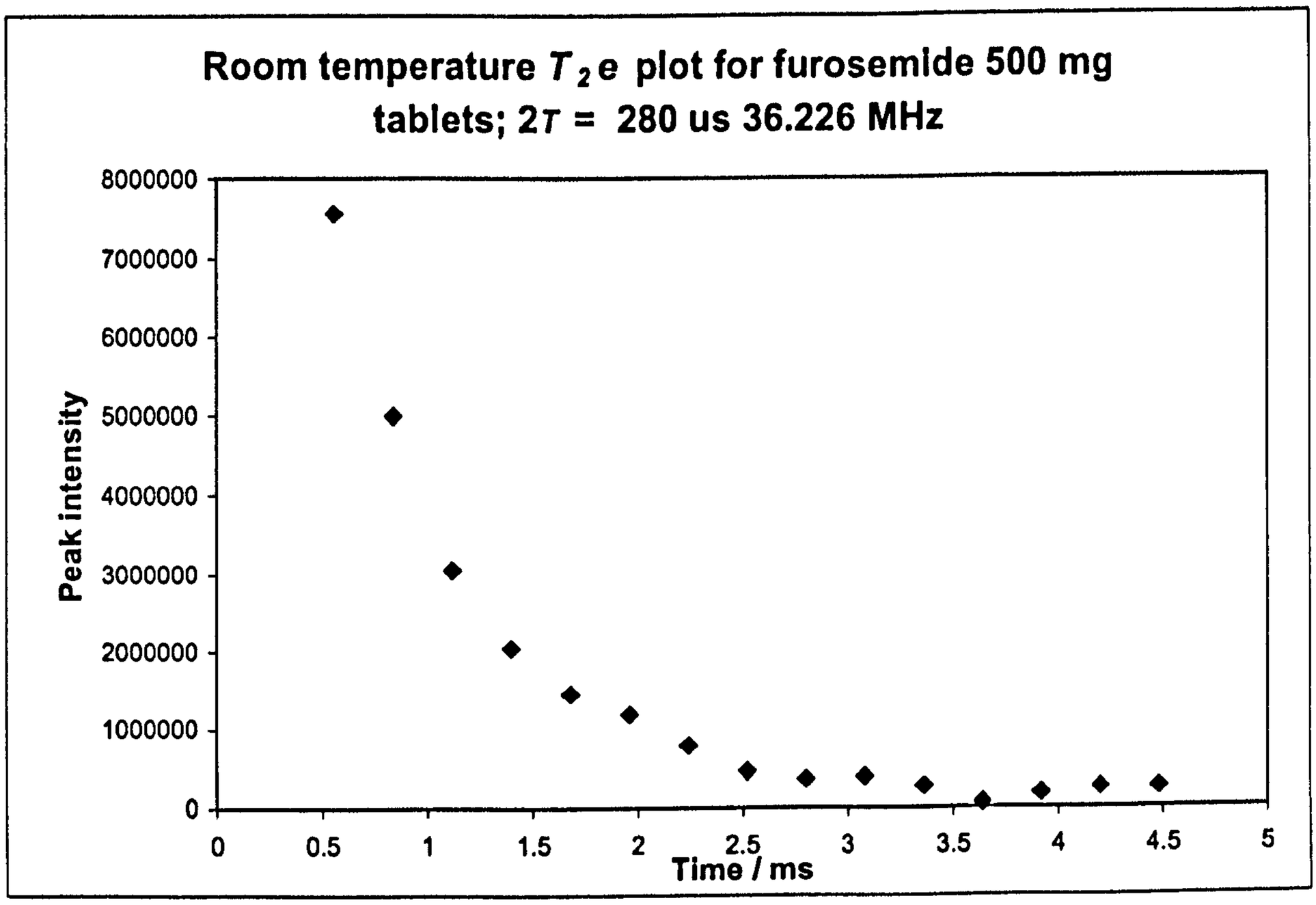

Figure 4.40: 500 mg furosemide tablet ^{35}Cl T_2e plot at room temperature; $T_2e = 0.712 \pm 0.053, 36.226$ MHz.

4.5.4 Summary of results

Sample	3.5 g powder	8x 500 mg tablets	80x 20 mg tablets
T_1 / ms	1.97 ± 0.14	2.09 ± 0.26	2.79 ± 1.06
T_2 / ms	0.28 ± 0.03	0.21 ± 0.01	0.12 ± 0.01
T_2e / ms (2τ = 280μs)	0.793 ± 0.018	0.747 ± 0.043	0.612 ± 0.061
T_2^* / ms	0.0326 ± 0.0023	0.0327 ± 0.0026	0.0285 ± 0.0025

Table 4.19: Comparison of measured ^{35}Cl NQR values from furosemide phase I powder, 500 mg and 20 mg tablets.

Across the range of samples T_2, the spin-spin relaxation rate, varied the most. This relaxation rate depends on dipole-dipole interactions and the differing environments in the tablets formations, which have different percentages of furosemide within them and have undergone compression with the other excipients may be responsible for this range

of results although it is unlikely that compression effects alone would significantly change T_2 values as solids are very resistant to compression. These differences could be investigated further. The errors are largest in the 20 mg tablet samples, as might be expected due to the lower mass of furosemide present in these experiments. The spin-lattice relaxation rate for the 20 mg tablets is much longer than the values found for the powder and 500 mg tablet sample but the larger error does result in T_1 being within the in the same region. The T_2* values were of interest; it was suggested that the linewidths may broaden due to inhomogeneity or compression effects but the powder and 500 mg tablets were in close agreement. Further studies on a range of tablets containing different percentages of API and made with different compression rates could be investigated.

4.5.5 Phase II studies

Using 3 g of phase II furosemide, as prepared earlier, searching was carried out using the same conditions as those for phase I with the same apparatus set-up. The 35 and 39 MHz region was extensively searched using a PSL echo sequence in frequency steps of 0.01 MHz but no signal was observed from the phase II sample. Later tests run on the spectrometer indicated problems in the region, with the apparatus seemingly unable to record certain frequencies.

Unfortunately, we have been unable to show that ^{35}Cl NQR can be used to differentiate between furosemide polymorphs but the promising results achieved in phase I studies indicate that NQR can be used to quickly detect small volumes of phase I furosemide in short amounts of time. We have also characterised the 36.23 MHz line.

Using the information and results gathered so far, we went on to look at ^{35}Cl signals in tablets and the potential for quantitative analysis, as discussed in chapter 5.

4.6 Theoretical calculations

The ^{35}Cl signal should be a doublet, as is the ^{14}N signal in phase I furosemide, of a certain splitting. Theoretical calculations were investigated to see how accurate a prediction

could be given for the ^{35}Cl line already observed, and also as a guide to finding the second line. Also of interest was how closely theoretical calculations could predict the differences between polymorphs.

4.6.1 Frequency prediction

4.6.1.1 Method

Using Gaussian98 (discussed in detail in chapter 7) the quadrupolar coupling constants were calculated for phase I furosemide using the X-ray crystal structure data determined by Lamotte[5]. An orthogonal system must be entered in Gaussian, so the triclinic coordinates were converted using a program ORTH.exe in Fortran. The unit cell dimensions were entered, followed by the triclinic coordinates for each atom individually. The points were then converted via a matrix calculation to the orthogonal system coordinates. The calculation was run on the two adjacent non-equivalent molecules in the crystal structure with a 6-31G* basis set. This allows 2 basis functions per H, 19 basis functions for other atoms and takes into account orbital diffusion, important for the larger chlorine atoms. The quadrupole coupling constant (QCC) and asymmetry parameter, η, were calculated for each ^{14}N and ^{35}Cl atom and the NQR frequencies were predicted (ν_+ and ν_Q respectively) The nuclear electric quadrupole moment is assumed to be –81.65 mB for ^{35}Cl and 20.44 mB for ^{14}N[13].

4.6.1.2 Results

	QCC / MHz	$\eta_{calc.}$	$\nu_{calc.}$ / MHz
Cl(1)	-76.12	0.103	38.12
N(1)	-6.163	0.727	5.792
N(2)	-4.930	0.187	3.962
Cl(51)	-76.39	0.103	38.26
N(51)	-6.926	0.084	5.386
N(52)	-5.544	0.077	4.302

Table 4.20: Predicted NQR data for phase I furosemide, calculated using Gaussian98.

Gaussian predicted ^{35}Cl lines at 38.12 and 38.26 MHz with a splitting of 0.14 MHz between the two lines; typically for ^{35}Cl a second line would be expected within 1 MHz of the first. Accordingly, the frequency range 35.246 to 37.296 MHz was searched in steps of 0.03 MHz. Unfortunately the second line has not yet been found.

4.6.1.3 Discussion

As the work was carried out in the laboratory on a non-thermostatted sample, under conditions where the temperature fluctuated greatly at times, the line may have been 'missed' due to the frequency drifting with temperature. The spectrometer was also found to have problems detecting some frequencies in the 35 to 40 MHz range, which may have led to a lack of detection sensitivity.

The values of 38.12 and 38.26 MHz give a reasonably good prediction for the NQR ^{35}Cl frequency in furosemide. With the ^{35}Cl line already seen at 36.22 MHz, the best calculated theoretical value is within 10% of experimental observations and hence again it has been shown that using Gaussian to restrict the area for a frequency search can be a useful tool. The ^{14}N values calculated were not in such good agreement with the experimentally observed frequencies (doublets around 3.563 and 2.600 MHz). The splittings predicted theoretically for ^{14}N are also much larger than the doublet splitting observed.

4.6.2 Calculating direction cosines

As well as calculating the magnitude and sign of q_{zz}, it is also useful to know the direction of the electric field gradient by calculating the direction cosines. It can be shown that the electric field gradient (EFG) tensor at the origin, due to a charge, e, at point (x, y, z) in molecular coordinates at distance r is

$$\frac{e}{r^5}\begin{bmatrix} 3x^2-r^2 & 3xy & 3zx \\ 3xy & 3y^2-r^2 & 3yz \\ 3zx & 3yz & 3z^2-r^2 \end{bmatrix}$$

The origin is taken as the nucleus under investigation and the EFG tensor calculated over the whole neighbouring charge distribution. Diagonalisation then gives the direction cosines with respect to the molecule axes selected.

4.6.2.1 Method

The values for the field gradient tensor were extracted from the Gaussian results and the direction cosines calculated using Matlab. The field gradient values for the matrix were inputted for each atom and the command **eig** was run. The eigenvectors (direction cosines) and eigenvalues (q_{xx}, q_{yy}, q_{zz}) are produced from this calculation and the eigenvalues are easily verified with the Gaussian-produced values to check the calculation. The position of the maximum principal component (q_{zz}) with respect to a bond within the molecule was then established. Further details are given in chapter 7.

4.6.2.2 Results

Atom	Eigenvectors	w.r.t.	q_{zz}	θ	q_{yy}	θ	q_{xx}	θ
Cl(1)	$\begin{bmatrix} 0.0382 & -0.1691 & -0.9849 \\ 0.9010 & -0.4204 & 0.1071 \\ 0.4322 & 0.8914 & -0.1363 \end{bmatrix}$	C(4)	-3.967	1.68	2.189	88.3	1.778	89.6
N(1)	$\begin{bmatrix} -0.3700 & -0.6978 & -0.6133 \\ -0.8048 & 0.5706 & -0.1636 \\ -0.4641 & -0.4331 & 0.7727 \end{bmatrix}$	S(1)	1.283	82.3	-1.108	28.9	-0.175	62.4
N(2)	$\begin{bmatrix} 0.9973 & -0.0695 & -0.0229 \\ -0.0730 & -0.9697 & -0.2330 \\ 0.0060 & -0.2341 & 0.9722 \end{bmatrix}$	H(2)	1.027	89.1	-0.609	87.3	-0.417	2.83
Cl(51)	$\begin{bmatrix} 0.0357 & -0.1510 & -0.9879 \\ 0.8958 & -0.4334 & 0.0986 \\ 0.4430 & 0.8885 & -0.1198 \end{bmatrix}$	C(54)	-3.982	1.99	2.197	88.0	1.785	89.9
N(51)	$\begin{bmatrix} -0.6987 & 0.6134 & -0.3683 \\ 0.7151 & 0.6153 & -0.3317 \\ -0.0232 & 0.4957 & 0.8685 \end{bmatrix}$	S(51)	1.4422	89.8	-0.782	11.9	-0.661	78.0
N(52)	$\begin{bmatrix} -0.7873 & -0.5826 & 0.2017 \\ -0.6136 & 0.7726 & -0.1633 \\ 0.0607 & 0.2523 & 0.9657 \end{bmatrix}$	H(52)	1.154	89.3	-0.622	50.2	-0.532	39.8

Table 4.21: Calculated eigenvectors, eigenvalues and their angles with respect to bond vectors (Cartesian coordinates) of the quadrupolar nuclei in furosemide.

4.6.2.3 Discussion

The direction cosines are as expected for the chlorine centres, with small angles of q_{zz} (1.68 ° and 1.99 ° for Cl(1) and Cl(51) respectively) relative to the Cl-C bond vector, with q_{yy} and q_{xx} both being at approximately 90 ° to the bond (Cl(1) - 88.3 °, 89.6 ° and Cl(51) – 88.0 ° and 89.9 °). Again, as for the other theoretically calculated parameters, the ^{14}N values were not so consistent. The angles of q_{zz} with respect to the bond vectors for ^{14}N are, as expected, at approximately 90 ° to the bond vectors stated in column 3, in the area of the lone pairs.

4.7 Identification and analysis of polymorphs

As discussed in chapter 1, an important aim of the work was to determine whether nuclear quadrupole resonance could be used to identify different polymorphs of a compound. The NQR results earlier in this chapter show that this can be done with relative ease in the case of furosemide and potentially with other compounds, with an immediate and clear method of distinction, identifiable from observation of the frequency domain signals with a minimum of knowledge or training. Six common analytical techniques (solid-state nuclear magnetic resonance, infrared spectroscopy, X-ray powder diffraction, differential scanning calorimetry, thermogravimetric analysis and microscopy) were used to analyse phases I and II of furosemide and the ease of identification compared to the use of NQR spectra for determination of the polymorph.

4.7.1 Solid-state nuclear magnetic resonance (SSNMR)

4.7.1.1 Introduction

Nuclear magnetic resonance is the spectroscopic technique most closely related to NQR. It has been widely utilised in scientific analysis, from simple one- and two-dimensional spectroscopy used in structure determination to magnetic resonance imaging used medically in a variety of situations. The most basic NMR experiments are ^{1}H NMR scans of solutions, though ^{13}C and many other nuclei with spin $\geq$ ½ are also commonly studied, and a wide range of experimental enhancements exist to improve solution NMR experiments. However, as NQR is a solid-state analytical process it is solid-state NMR which will be discussed in this section with comparison to NQR. Carbon-13 is the most

commonly studied nucleus in solid-state NMR. Like NQR, SSNMR gives us an indication of the environment around the chemically relevant nuclei and is sufficiently sensitive enough that small spatial changes affect the spectra, enabling, for example, identification and differentiation of polymorphs both crystalline[14] and amorphous[15], quantification and the more basic use of determination of structure by analysis of the chemical shift of peaks. SSNMR has the same basic principles as solution NMR but there are some important effects seen in the solid state which are not observed in solution. Simple solid-state NMR spectra contain broad peaks due to dipolar coupling and chemical shift anisotropy stemming from the lack of molecular mobility; in solution rotational molecular movement leads to averaging of positions which is not possible in the solid state. However, both the above factors can be overcome to give high resolution, well resolved spectra.

Dipolar coupling occurs when the magnetic moments of two or more nuclei interact through space and is dependent on the inverse cube of the internuclear distance, the gyromagnetic ratio (making ^{1}H, which has a large gyromagnetic ratio, interactions large) and the dipolar coupling tensor, which in turn is dependent on the molecular orientation[16]. The broadening due to this effect can be reduced by high-power decoupling and magic angle spinning. During high-power decoupling the solid sample is subjected to radiofrequency at the Larmor frequency of the nucleus to be decoupled causing the fast flipping of the spins so averaging the dipolar interaction seen by the nucleus under observation to zero.

The chemical shift interaction is also dependent on the orientation of the nuclei and is highly sensitive. Again, in solution an average orientation is seen due to isotropic motion but in a solid sample it is usually the case that all orientations of the molecule exist and a broad peak, covering the range of chemical shifts produced which can be called the chemical shift anisotropy (CSA) powder pattern, will be observed. This broadening can be overcome by magic angle spinning; in this method the sample is spun at an angle of 54.74 °, the 'magic angle'[17], at a rotation rate greater than the chemical shift anisotropy. This reduces a term in the shielding constant to zero under the spinning conditions, reducing broadening and leading to sharper peaks in the SSNMR spectra.

Having overcome the broadening problems, which lead to featureless spectra making characterisation difficult, other improvements which are not unique to SSNMR can also be made to increase signal to noise, shorten scan times or allow greater chemical insight such as cross polarization, multiple pulse sequences and 2-dimensional experiments. Cross polarization is routinely used in SSNMR experiments as it is a technique which shortens acquisition times; sensitivity and SNR is increased by transferring the higher ^{1}H polarisation to the ^{13}C nuclei. Coupling of the ^{1}H nuclei with the ^{13}C nuclei lessens experimental times which would otherwise be lengthy due to the long spin lattice relaxation time of ^{13}C nuclei.

Dipolar dephasing (also known as non-quaternary suppression) is a technique which is often applied in SSNMR in order to facilitate the assignment of peaks in an SSNMR experiment[18]. Simplification of spectra is achieved as the signals from any nuclei directly bonded to hydrogen are theoretically removed. In reality, signals from methyl groups are usually still observed, due to the reduced C-H dipolar coupling – a result of the internal rotational motion. The signals from nuclei with strong dipolar coupling to hydrogen dephase more rapidly than those with weak coupling and so with the appropriate delay time (40 μs is usually suitable for ^{13}C experiments) only quaternary ^{13}C nuclei signals are observed.

The basic NMR experimental equipment is similar to that used in NQR, though unlike NQR commercial NMR units are widely available which contain the multiple necessary parts housed together. It is a more expensive technique than NQR requiring production of a large magnetic field and also a rotor to facilitate magic angle spinning. Although SSNMR has the advantage that it is a quantitative technique[19] the small and fixed volumes used limit it somewhat in a manner which is not present in NQR analysis. Little sample preparation is required; similarly to NQR polycrystalline solid samples are used without the need for purification or grinding. Single crystals can be studied but this is uncommon. The technique is non-destructive, though it is invasive as samples do need to be removed from their containers and placed in a fixed volume sample tube of the correct dimensions to fit the apparatus.

4.7.1.2 Method

Solid-state ^{13}C NMR experiments were carried out at the EPSRC lab run by Dr. David Apperley at Durham University, with the assistance of Fraser Markwell. Approximately 300 mg of each solid sample was packed into a 7.5 mm ceramic probe. Experiments were run with phase I furosemide (as received from Sigma) and phase II furosemide (recrystallised from butan-1-ol as previously). In order to slow decomposition of the less stable phase II (which had been recrystallised approximately 20 hours prior to the SSNMR run), the experiment was run at -20 C. CP-MAS (cross polarised, with a contact time of 1 ms, magic angle spun, with a spin rate of 4470 Hz) experiments were run in a field of 300 MHz with an acquisition time of 30 ms and the spectra were recorded using a Varian Unity Inova spectrometer. In both cases the recycle time was optimised and found to be 30 ms for phase I and 60 ms for phase II. The phase I spectrum is the result of 250 repetitions, whilst the phase II experiment consisted of 106 repetitions. Initial spectral referencing was with respect to tetramethylsilane, carried out by setting the high frequency from adamantane to 38.4 ppm. A second SSNMR experiment was carried out on phase I with dipolar dephasing in order to identify the methyl groups and quaternary carbons. Conditions were as for the previous phase I experiment with the dephasing delay of 40 μs. With the help of Dr. David Apperley, appropriate literature[20] and with comparison to the SSNMR furosemide spectra obtained by Doherty and York[4] the peaks were assigned.

4.7.1.3 Results

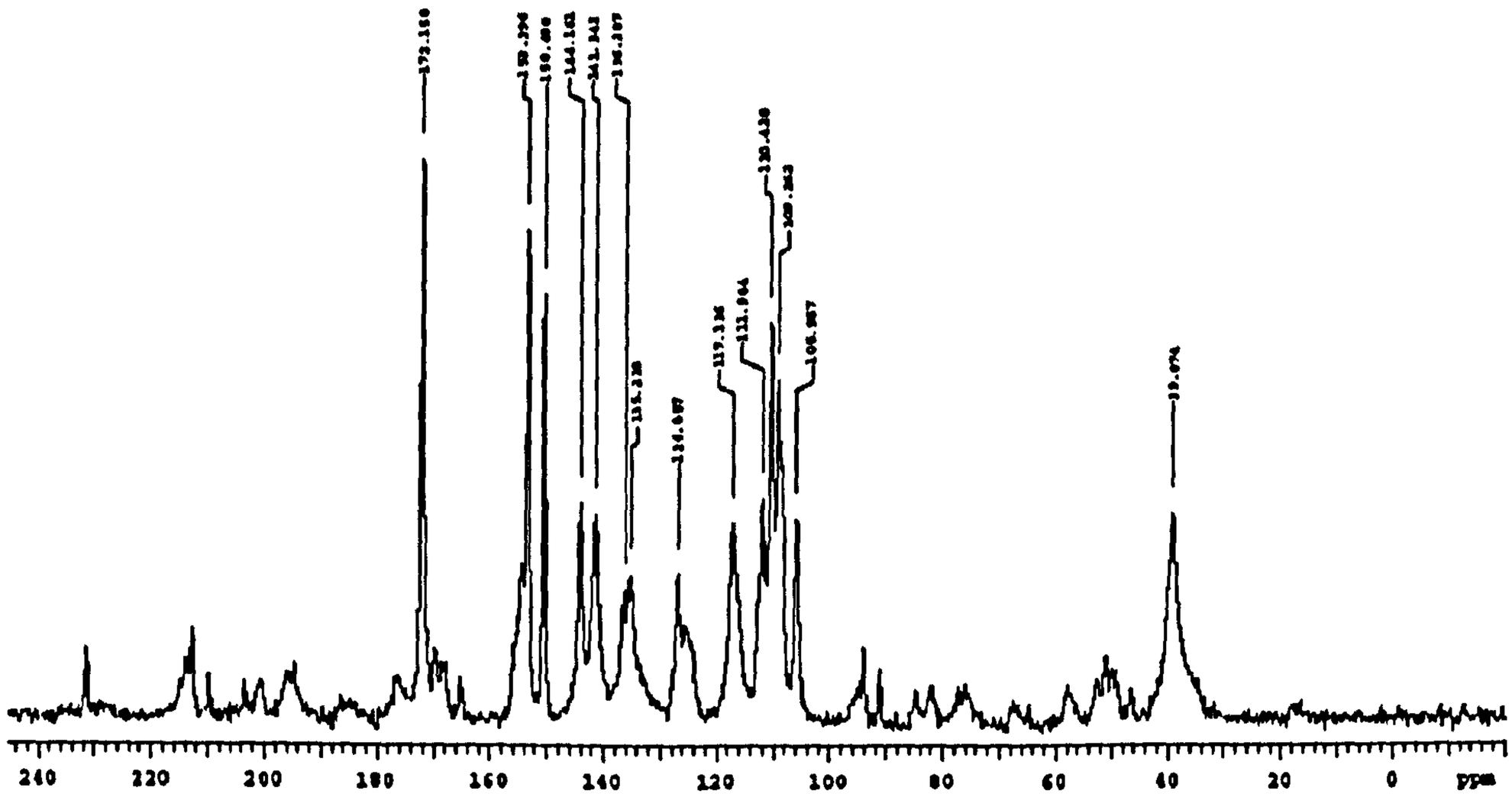

Figure 4.41: Solid-state NMR spectrum from phase I furosemide (room temperature).

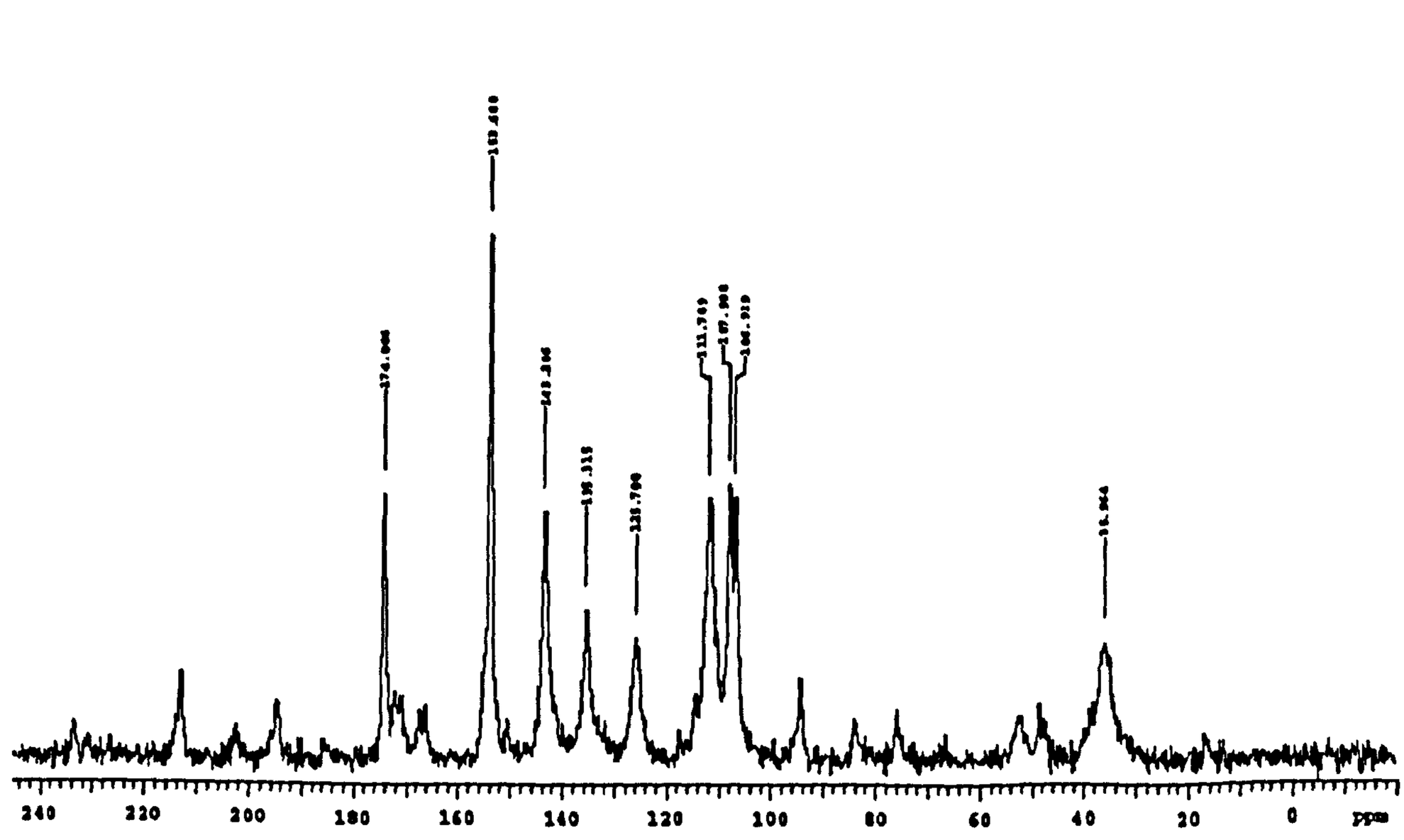

Figure 4.42: Solid-state NMR spectrum from phase II furosemide run at -20 C.

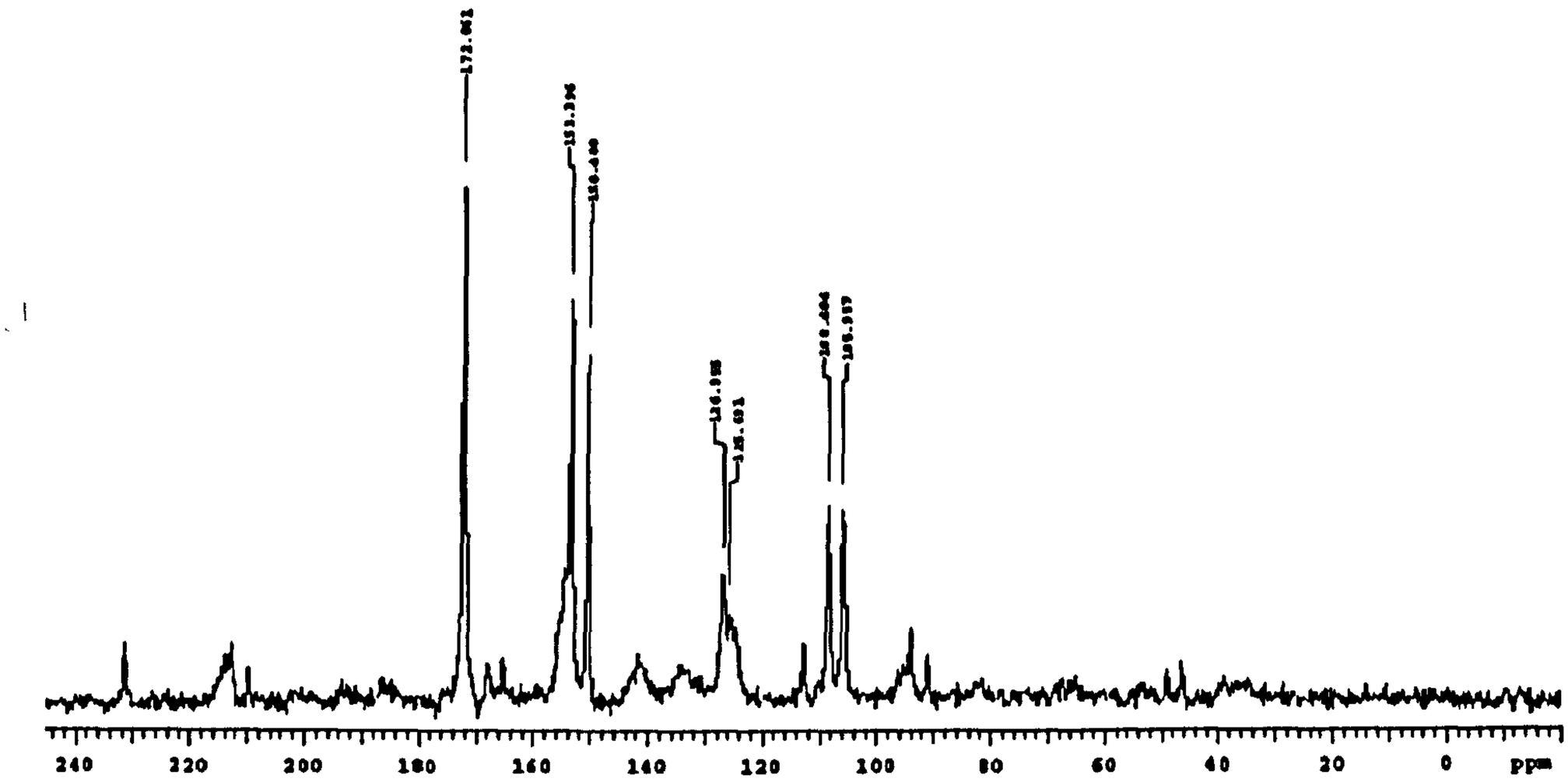

Figure 4.43: Dipolar dephased solid-state NMR spectrum from phase I furosemide (room temperature).

4.7.1.4 Discussion

Phase I		^{13}C	Phase II	
	ppm		ppm	
	172	Q: COOH	174	
	153	Q:Aromatic C-N-	154	May also hide another signal.
	150	Q:Aromatic C-S-		
Furan ring	144	Protonated C	143	
	141			
	135	Protonated aromatic C	135	
	127	Q: C-Cl	126	
	117	Protonated aromatic C		
Furan ring	112	Protonated C	112	
Furan ring	110	Protonated C		
	109	Q: possibly aromatic C-COOH	108	
	106	Q: Possibly furan C	107	
	39	$-CH_2N$	36	

Table 4.22: SSNMR chemical shifts and assignments for phase I and II furosemide. **Q** indicates a quaternary C, as identified by the dipolar dephased spectrum.

There are 12 ^{13}C nuclei in furosemide, from which 12 signals may be expected to be seen. However, the phase I furosemide spectrum (figure 4.41) (run at room temperature) shows 14 labelled peaks and also a number of weaker sidebands which are unlabelled in the spectra while the phase II spectrum (figure 4.42) has only 9 labelled peaks. The peak at 154 in the phase II spectrum may be hiding a peak through overlapping due to broadening caused by residual dipolar coupling between ^{13}C and ^{14}N. There are traces of phase I furosemide in the phase II spectrum (weak signals around 150 and 172 ppm) as may have been expected (in the 20 hours which elapsed between harvesting the crystals and running the experiment some phase II will have decomposed to phase I). Figure 4.43 shows the phase I spectrum obtained with dipolar dephasing with signals only from the quaternary carbons with the same chemical shifts as identified from figure 4.42. The quaternary ^{13}C of the furan ring would be expected to have a chemical shift of around 140 ppm; however, such a peak is not present in the dipolar dephased spectrum. The two peaks at 106 and 108 ppm may be a doublet, as only one quaternary signal (from the aromatic C- COOH) would be expected in this region.

Although the spectra of the two polymorphs show clear differences, they require a more specialised viewing than the corresponding NQR spectra, in which a simple glance at the multiplicity can determine whether phase I or II is present. Another disadvantage of SSNMR is the overlapping of signals – in the case of polymorphs where the less stable form degrades to another form the ^{13}C signals may overlap, and although it could be seen as an advantage that both forms can be seen in the same spectrum, this feature could also be problematic and the specific frequencies that are associated with ^{14}N nuclei and their sensitivity to environmental change mean that such overlapping of frequencies is not a common problem. NQR also has the advantage previously mentioned that a wide range of volumes can be studied, with solenoids built to suit the sample. The SSNMR required a small amount of solid to be placed into a fixed volume tube and the sample needed to be dry – solvent left in the sample could force the lid to be forced from the probe during spinning which could lead to the sample being forced from the probe and into the other equipment. In NQR if the sample has not been fully dried or is even in a slurry a spectrum can be gathered with normal experimental conditions and little further

preparation. Both SSNMR and NQR have the feature that experimental timescales can vary greatly depending on the material under investigation. In the case of furosemide, the SSNMR spectra were accumulated in a number of hours - necessary to enable sharp peaks with good SNR. For NQR, 30 minutes was enough time to give a clear peak to enable identification in the case of both polymorphs, although it should be noted that a much larger sample mass was used (56 g as opposed to 300 mg).

4.7.2 Infrared spectroscopy (IR)

4.7.2.1 Introduction

Absorption IR can give great structural detail of a sample with the molecular vibrational frequencies being highly sensitive to their environment allowing easy identification of different functional groups. IR is a very useful tool in the analytical laboratory and can be used to identify, confirm or differentiate between compounds and also distinguish between polymorphs[21].

The region usually studied is the mid-range 4000 to 400 cm^{-1} and although not all the molecular frequencies in this region can be observed - only vibrational modes that produce a change in the electric dipole moment are IR active - there is usually enough information contained within a scan to uniquely identify the substance either by reference to spectroscopy literature and frequency tables, or in some modern instruments electronically by comparison to a library of previous spectra. Modern instruments use interferometric methods to monitor the whole frequency range at once, and the resulting interferogram then undergoes Fourier transformation to produce the absorption spectrum. A sample requires a little preparation in readiness for an IR scan; a solid sample is ground in a mineral oil mull, or other suspension liquid if required and this suspension is then smeared onto KBr discs before being placed into the cradle in the IR spectrometer so that the IR beam can pass through it. Solids can also be ground with KBr and pressed into discs. Where liquids are being studied they can simply be smeared in a thin layer between KBr discs.

Generally IR scans are fast to run, with a number of scans being run in seconds and these combined to give the spectrum across the range of interest. They are, however, invasive and difficult to quantify and apply to samples in packets or bottles.

4.7.2.2 Method

Furosemide was analysed using IR spectroscopy; various forms of furosemide were recrystallised from different solvents; phase I from acetone, phase II from butanol, and suspected phase I from a 50:50 mixture of ethanol and petroleum ether (40-60) (as used by Lamotte *et al.*[5] in the preparation of furosemide for the X-ray crystal structure determination) and also the Sigma furosemide powder as received.

For each recrystallisation approximately 250 ml of the appropriate solvent, or solvent mixture, was heated and phase I furosemide (Sigma powder) was dissolved to saturation point. The solutions were left to cool overnight and the crystals collected. A small amount (< 1 g) of each sample was ground in a nujol mull. The fine suspension was placed on KBr discs and the IR scan was recorded at room temperature on a Perkin Elmer 1605 FT-IR spectrophotometer. The frequency range was set to 600 to 4000 cm^{-1} with 4 scans being run for each spectrum. The spectra were plotted and analysed in the range 1100 to 4000 cm^{-1}. The fingerprint region was not studied.

4.7.2.3 Results

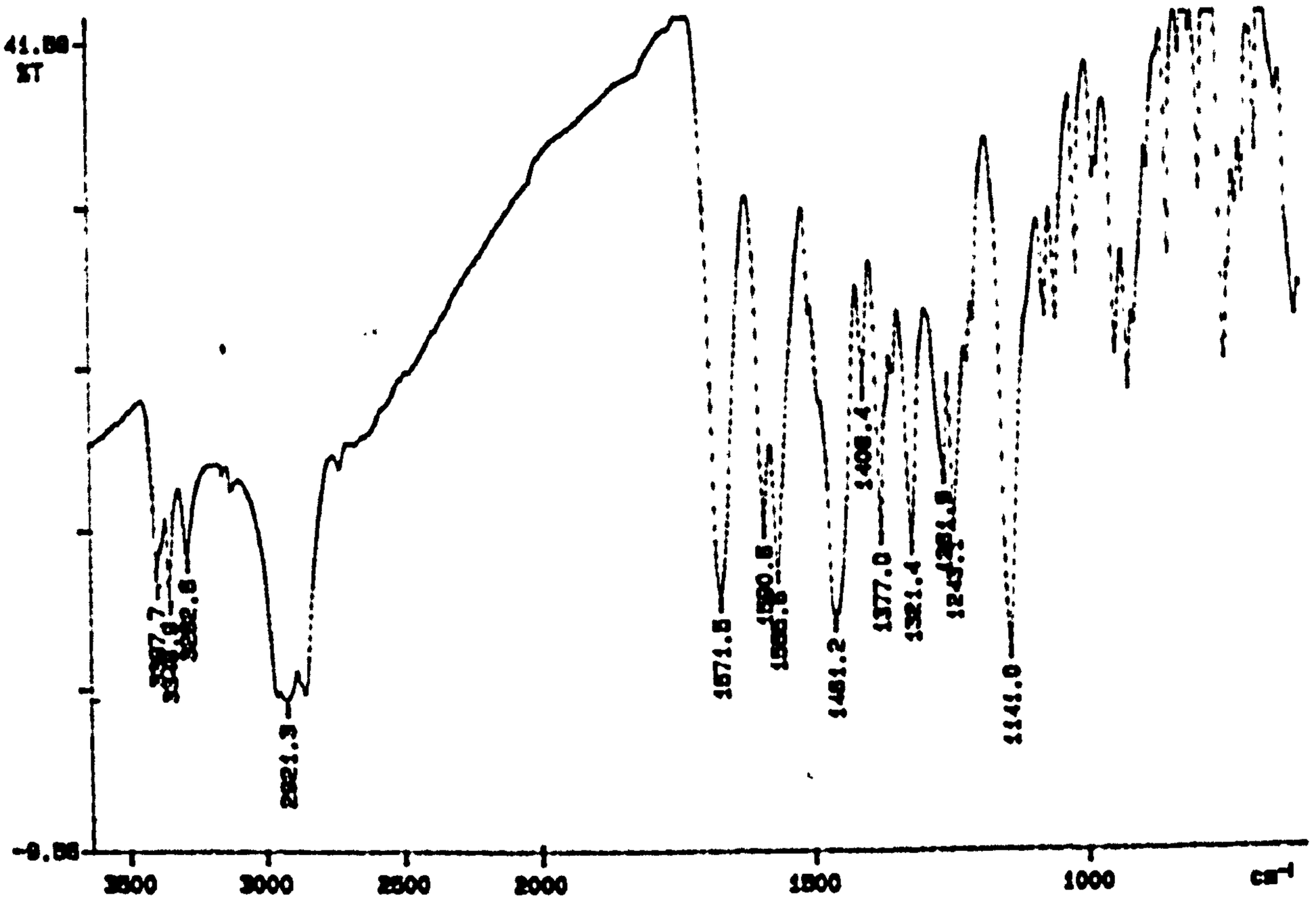

Figure 4.44: IR spectrum of Sigma phase I furosemide powder.

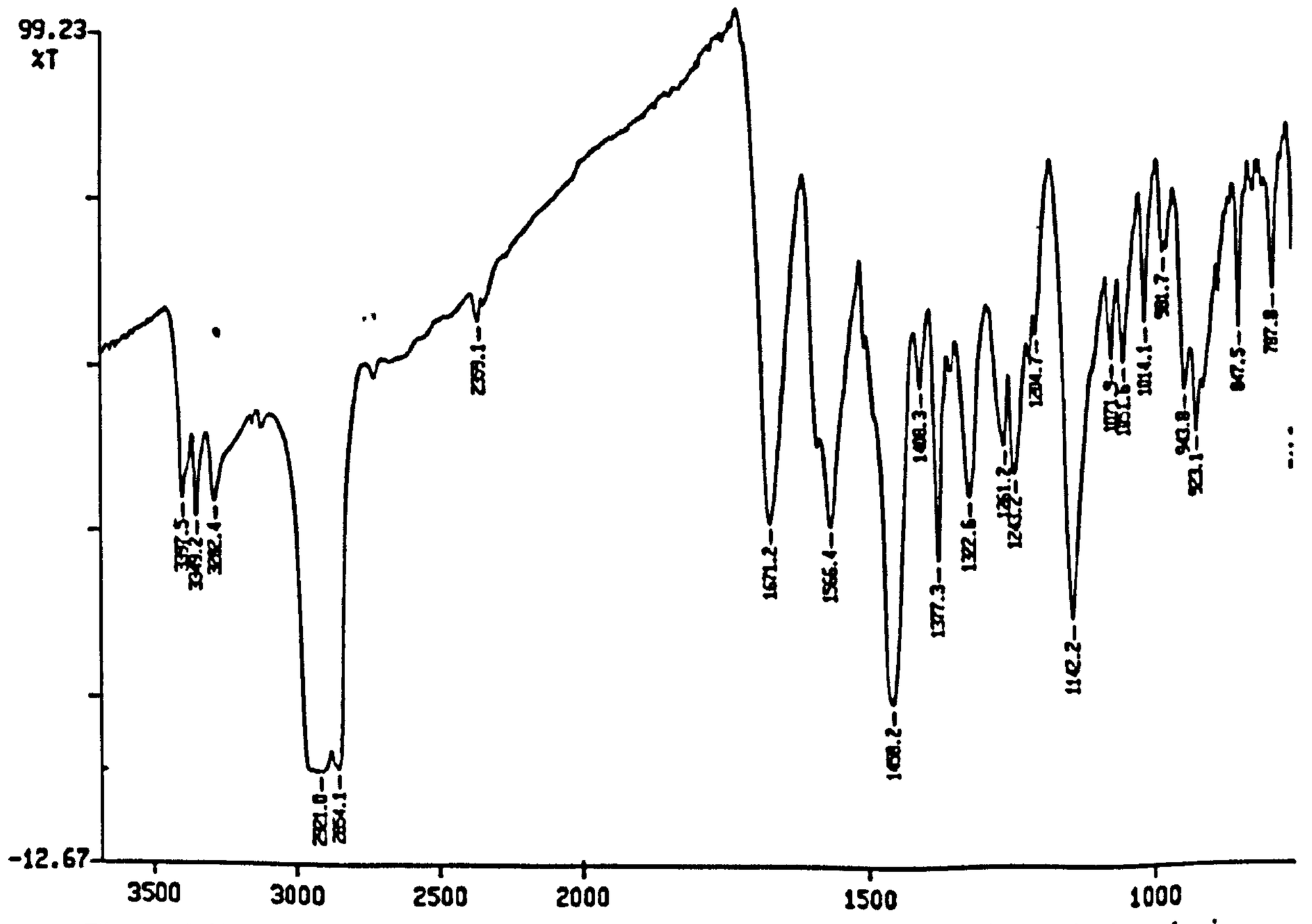

Figure 4.45: IR spectrum of furosemide recrystallised from petroleum ether and ethanol mix.

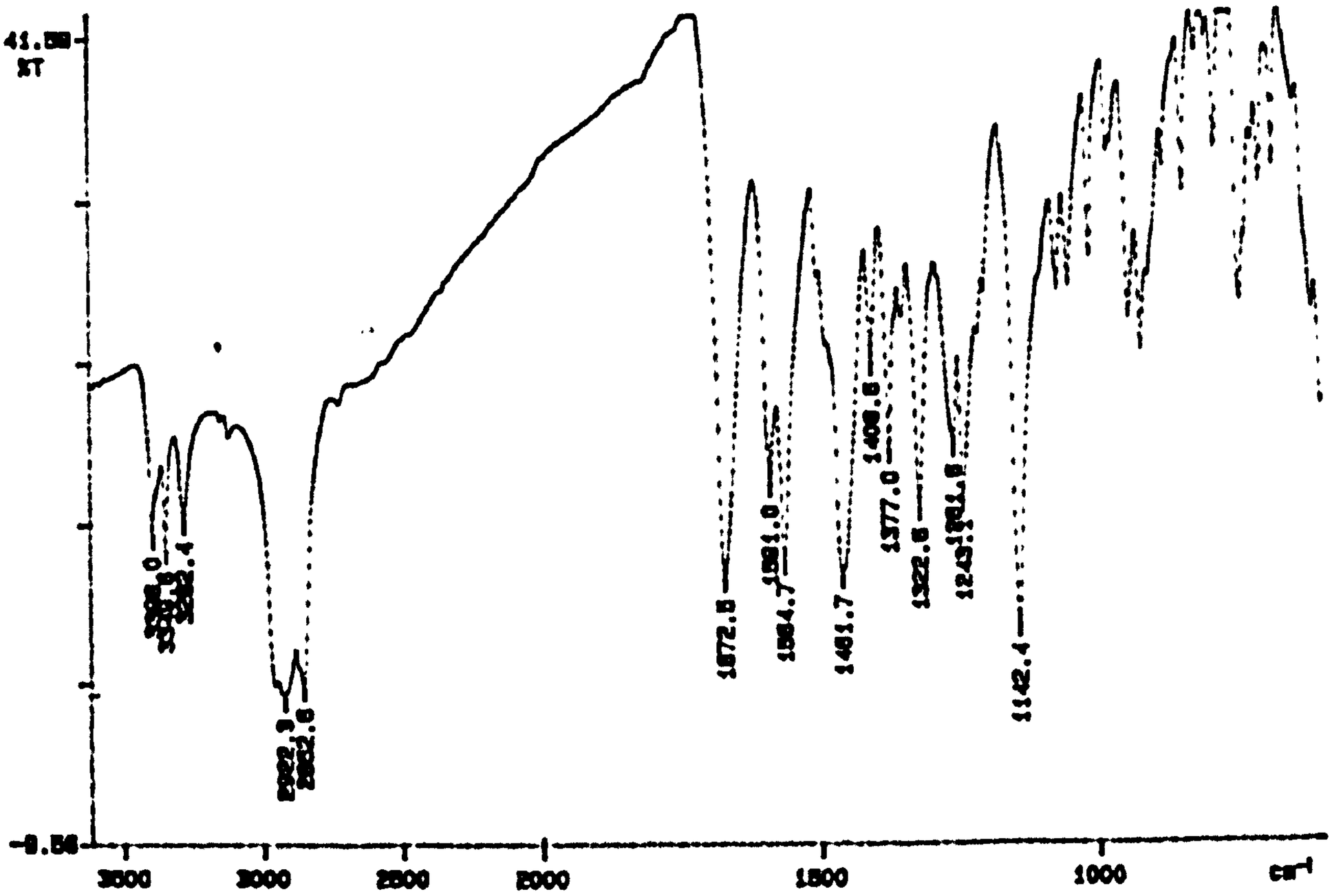

Figure 4.46: IR spectrum of furosemide recrystallised from acetone (pPhase I).

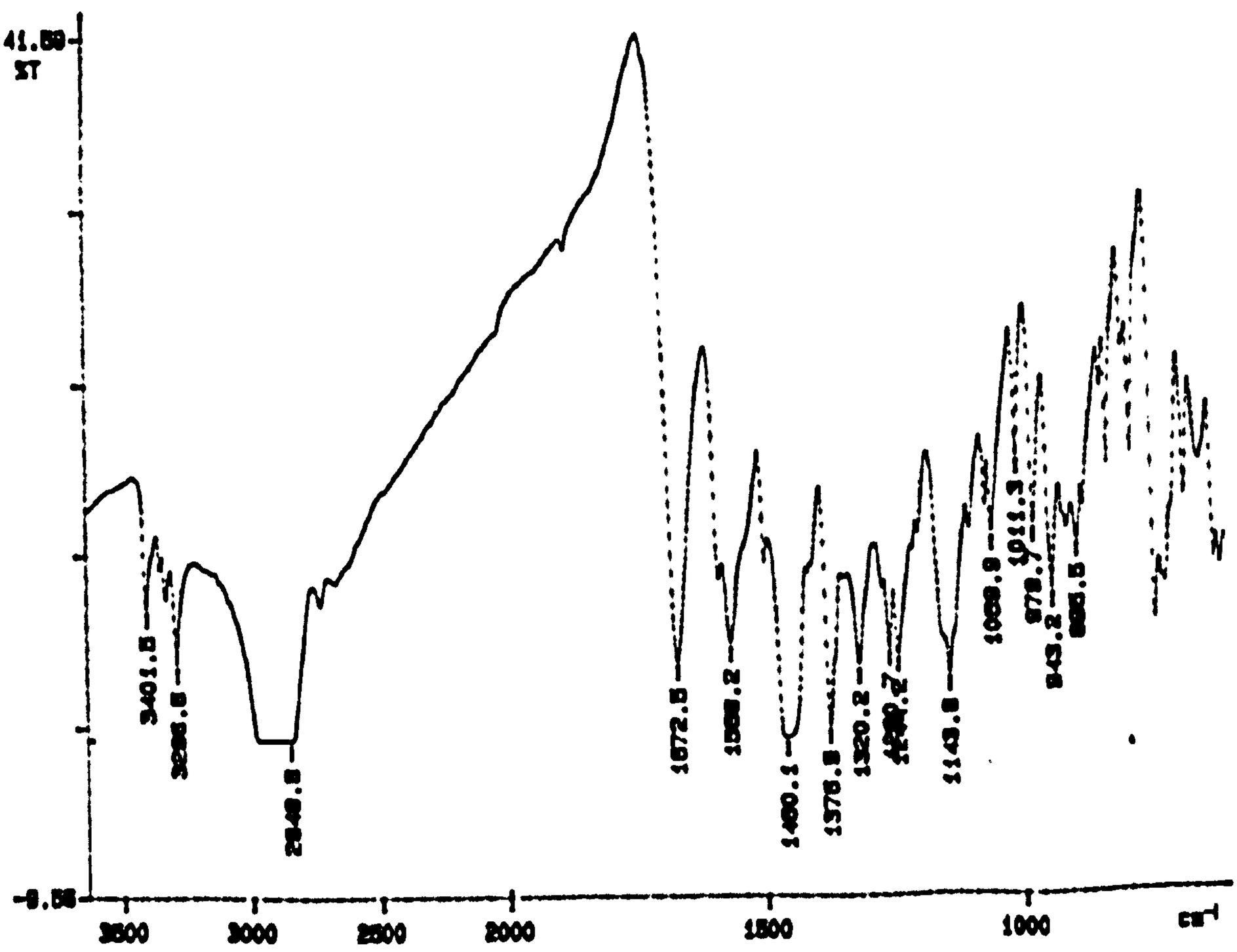

Figure 4.47: IR spectrum of furosemide recrystallised from butanol (phase II).

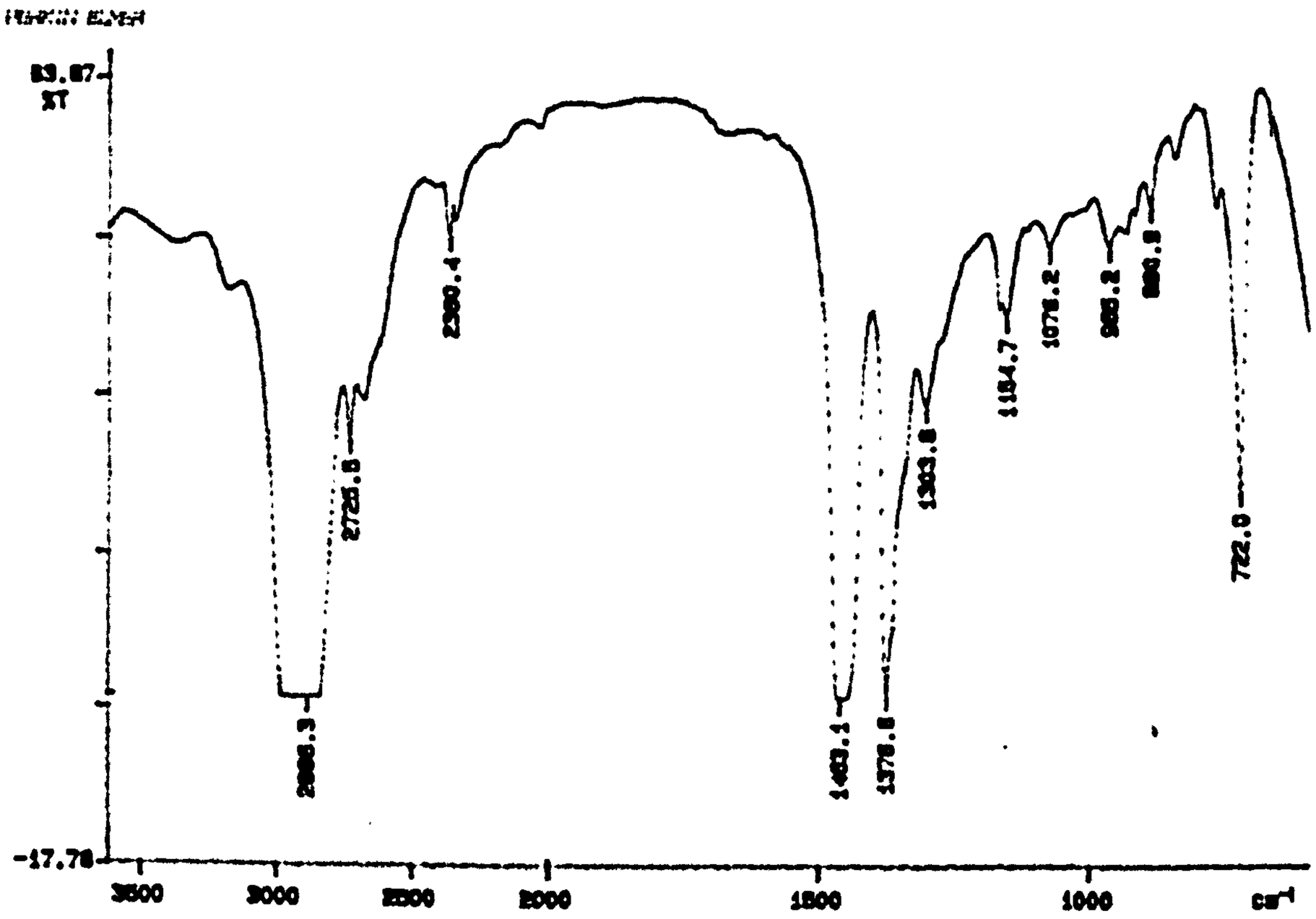

Figure 4.48: IR spectrum of nujol.

4.7.2.4 Discussion

Sample	Sigma powder / cm^{-1}	Phase I; acetone / cm^{-1}	Phase II; butanol/ cm^{-1}	Lamotte; pet. eth. /ethanol / cm^{-1}
Sulfonamide N-H stretch	3397.7	3398.0	3401.5	3397.5
Amine N-H stretch	3348.9	3349.6	Not present	3349.2
Sulfonamide N-H stretch	3282.6	3282.4	3286.6	3282.4
N-H bend	1590.6	1591.0	1588.2	Unmarked
N-H bend	1565.6	1564.7	Unmarked	1566.4
C=O stretch	1671.5	1672.5	1672.5	1671.2
S=O symmetric stretch	1321.4	1322.6	1320.2	1322.6
S=O asymmetric stretch	1141.0	1142.4	1143.8	1142.2

Table 4.23: IR assignments for various furosemide samples in the 1100 – 4000 cm^{-1} region.

The main peaks were assigned with the help of a spectroscopy text (Table 4.23)[22]. The most immediate difference between spectra could be seen in the 3200 to 3400 cm^{-1} region. In the Sigma powder, petroleum ether/ ethanol mix and acetone recrystallisations (figures 4.44, 4.45 and 4.46 respectively), 3 clear peaks, of similar intensities, are seen in this region. However, in the phase II (butanol) (figure 4.47) spectrum there are only 2 strong peaks in the same region, although there is a very weak absorption peak between the two which may be due to a small quantity of phase I due to a polymorphic transformation. In phase II both the sulfonamide N-H stretch vibrations have been shifted to a higher wavenumber and the secondary amine N-H stretch near 3349 cm^{-1} is not observed between the two sulfonamide peaks; it is possible that it is swamped by the lower sulfonamide N-H peak, at 3286.6 cm^{-1}, as secondary amine N-H stretching frequencies are lowered by hydrogen bonding[22]. The Sigma powder, acetone recrystallised and the 'Lamotte' recrystallised forms all have extremely similar vibrational frequencies, confirming that they are all phase I. These results show that IR spectroscopy can be a useful laboratory method of quickly distinguishing between the polymorphs, for example to confirm the phase of a recrystallised sample before further NQR study although the differences are not as immediate as in the NQR spectra and the technique is destructive and invasive.

4.7.3 X-ray powder diffraction (XRPD)

4.7.3.1 Introduction

When an X-ray is beamed at a crystalline sample, the crystals scatter the radiation to produce a diffraction pattern characteristic of that material. A single crystal is usually needed to give a detailed crystallographic structural analysis; more commonly, a polycrystalline sample can be used to give a less detailed spectrum by X-ray powder diffraction, which can nevertheless be used to identify compounds or mixtures of materials.

The arrangement of the crystal lattice and the separation *d(hkl)* of the crystal planes (*hkl*) determine the angles at which diffraction peaks occur, while the electron density distribution within the crystal determines their intensity; the angle and intensity of the lines in the XRPD spectrum together will uniquely identify a compound.

An X-ray tube produces a beam by accelerating electrons towards a metal anode; producing X-rays of a specific wavelength, λ, dependent on the metal used (most often copper), which are then directed onto the sample and the diffracted radiation is subsequently detected. The angle between the sample, the X-ray beam and the detector may be changed to give a wide angular range of the diffraction angle 2θ.

Bragg's equation (4.2) can be applied to calculate the spacing, *d(hkl)*, between the planes of the crystal lattice since the wavelength, λ, and the angle between the sample and the X-ray beam, θ, are known and n is an integer.

$$n\lambda = 2d \sin \theta \qquad (4.2)$$

Little preparation is needed in XRPD; a small amount of the solid sample must be finely ground and is then placed in the sample holder. Modern diffractometers use a detector, such as a scintillation counter connected to a computer or a CCD camera to generate a spectrum electronically which can then be printed out. Spectra of 2θ against intensity are plotted to give a characteristic powder pattern, a 'fingerprint' of the substance under study to be compared with other spectra to determine a difference or with a library of previously studied materials to allow identification. XPRD is routinely used in pharmaceutical analysis in identification but it is not a suitable method for large scale analysis or quantification and the sample preparation inhibits the use of whole 'from the packet' tablets and certainly samples in bottles.

4.7.3.2 Method

Three furosemide samples were analysed by XRPD; 'fresh' phase I, from a newly opened bottle of Sigma purchased furosemide powder, 'old' phase I, the original Sigma powder sample which had been subjected to temperature changes between 0 and 70 °C, and 'fresh' phase II, a sample of furosemide recrystallised from butanol three days before the experiments were run.

A small amount of each sample was placed onto the sample discs, finely ground and evenly spread. They were loaded onto the CuK_α XRPD machine at Merck Sharp and

Dohme, Hoddesdon, model Bruker D8 Advance, and a fast scan was run covering 2θ angles of 3 ° to 40.125 °, with a step value of 0.014 °, at room temperature (298 K).

4.7.3.3 Results

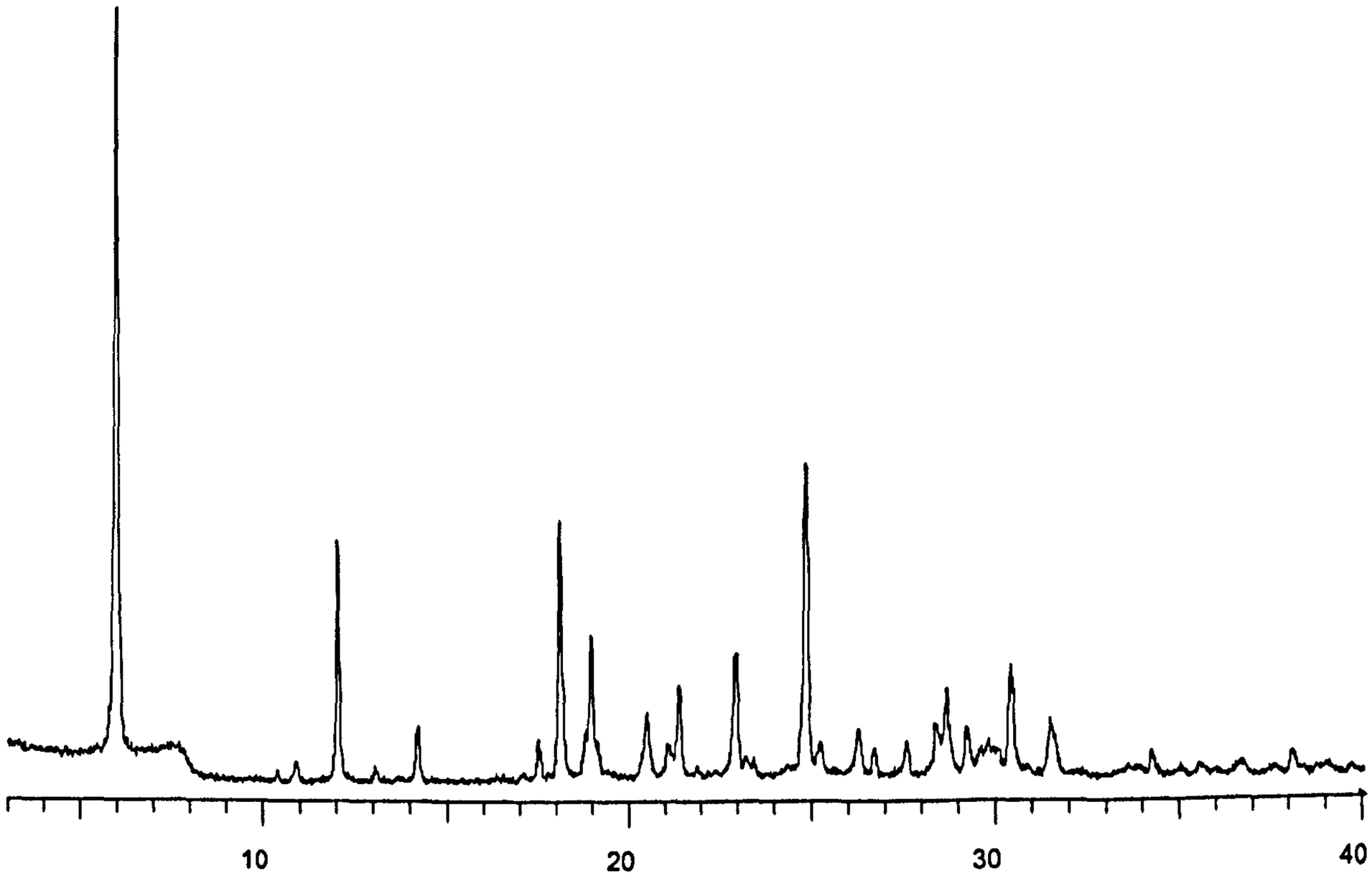

Figure 4.49: XRPD spectrum of fresh phase I furosemide; 2θ = 3 to 40.125 °, room temperature.

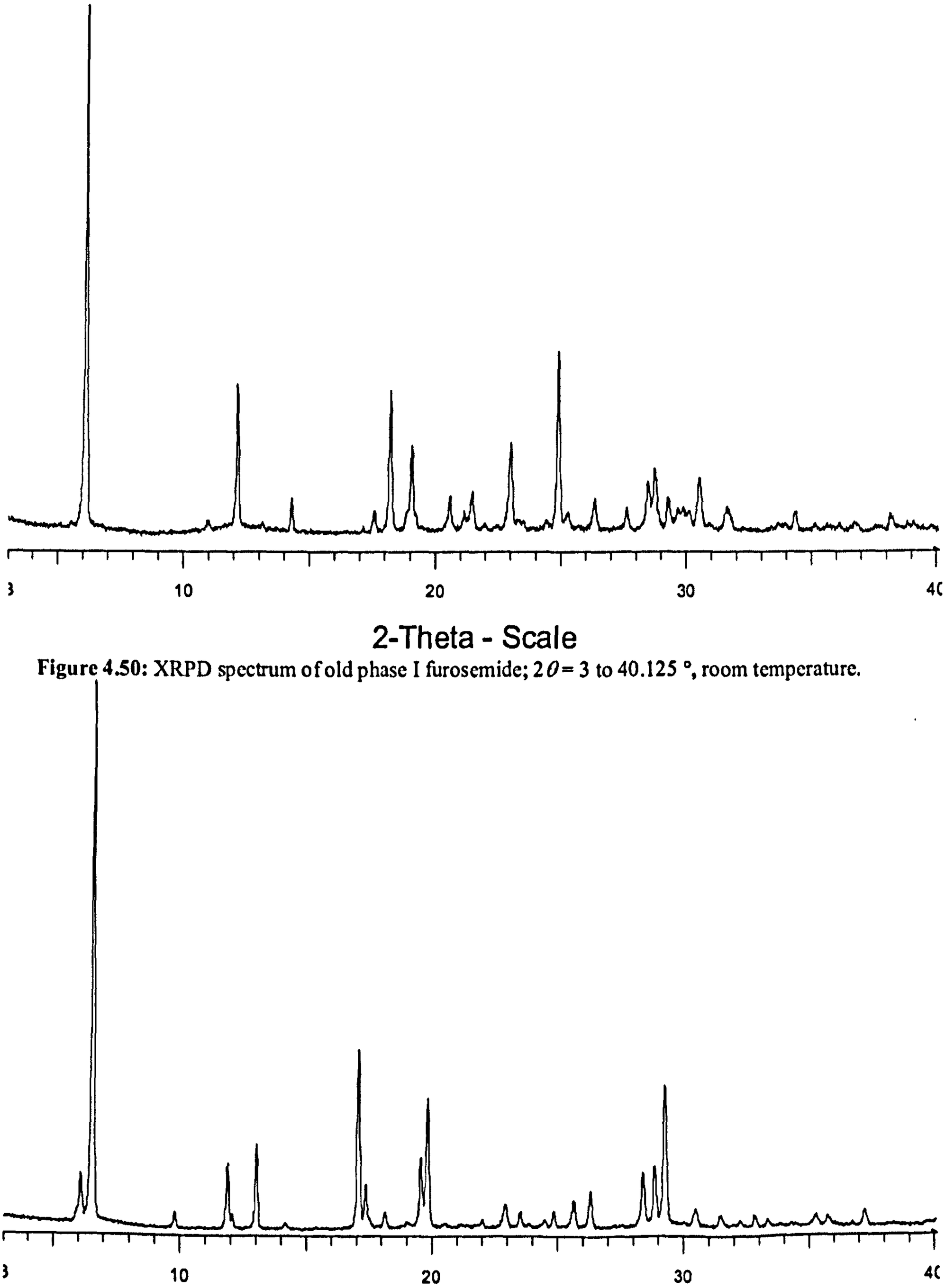

Figure 4.50: XRPD spectrum of old phase I furosemide; $2\theta = 3$ to 40.125 °, room temperature.

Figure 4.51: XRPD spectrum of phase II furosemide; $2\theta = 3$ to 40.125 °, room temperature.

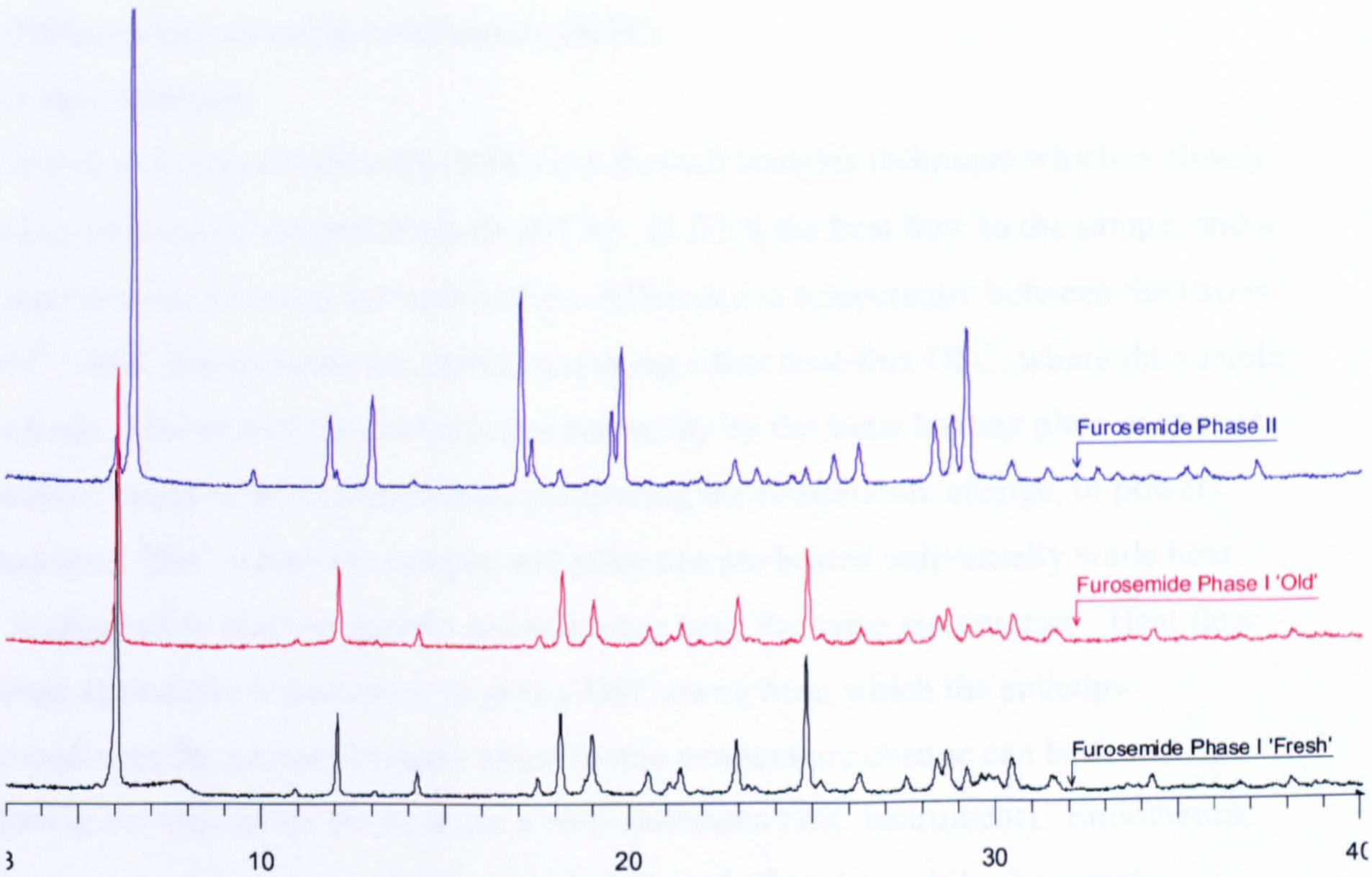

Figure 4.52: Overlay of fresh and old phase I and phase II furosemide XRPD spectra; $2\theta = 3$ to 40.125 °, room temperature.

4.7.3.4 Discussion

Fresh phase I (figure 4.49) and old phase I (figure 4.50) had extremely similar spectra, as expected, with the only difference being a small 'step' at $2\theta = 8$ °. Two further old phase I scans were run, to check whether this was an instrumental fault, and in both the 'step' was still present with no obvious explanation. The main peaks in the phase I spectra are at $2\theta = 6$ °, 12 °, 18 ° and 25 °. Phase II (figure 4.51) had a clearly different spectrum, although there was some evidence of phase I contamination of the sample, with low intensity peaks at $2\theta = 6$ °, 12 °, 18 ° and 25 °. The most intense phase II peaks were at $2\theta = 6.5$ °, 13 °, 17 °, 20 ° and 29 °. Again, we have another clear method of distinguishing between polymorphs in the laboratory, useful for pre-NQR preparation work. The differences are particularly evident in the 'overlay' plot (figure 4.52) but again, to the untrained eye an immediate determination is not as facile as when comparing the NQR spectra for phases I and II of furosemide.

4.7.4 Differential scanning calorimetry (DSC)

4.7.4.1 Introduction

Differential scanning calorimetry (DSC) is a thermal analysis technique which is closely related to differential thermal analysis (DTA). In DTA the heat flow to the sample and a reference remains constant for both and the difference in temperature between the two is plotted[23]. DSC experiments are carried out using either heat-flux DSC, where the sample and reference are heated (or cooled) simultaneously by the same heating plate over a set temperature range with thermocouples monitoring the temperature change, or power-compensated DSC, where the sample and reference are heated individually while heat flow is adjusted so that the sample and reference have the same temperature. Heat flow is plotted against the temperature to give a DSC curve from which the enthalpy associated with the process brought about by the temperature change can be found by integrating the area under the peak (in a well-calibrated DSC instrument). Endothermic reactions, such as melting, are seen as peaks below the baseline while conversely, exothermic processes yield positive peaks above the baseline.

Little preparation is needed prior to a DSC scan - the solid sample is simply placed into a small sample pan, usually aluminium, which is sealed and an empty identical pan is also sealed and used as the reference. A small amount of material is used, less than 100 mg, and the scan time will vary according to the rate at which the temperature is increased and the temperature range.

DSC can be used to confirm melting points, find the enthalpy associated with processes such as phase transitions which may be of particular interest when studying polymorphs, as well as to indicate the purity of compounds (by observation of the lowering of melting points). Differences in the DSC curves from different polymorphs may enable polymorph identification although sample requirements may limit the study of tablets in pharmaceutical analysis and large scale analysis and quantification is not feasible.

4.7.4.2 Method

DSC plots were recorded for 'fresh' phase I, 'old' phase I and 'fresh' phase II using a TA Instruments DSC 2920 modulated DSC machine, at Merck Sharp and Dohme, Hoddesdon, up to 250 °C at a rate of 10 °C min^{-1}. It is important to note that the phase II

sample has continued weight loss due to evaporation of butanol, so the sample size inputted (6.900 mg) is an over estimate.

4.7.4.3 Results

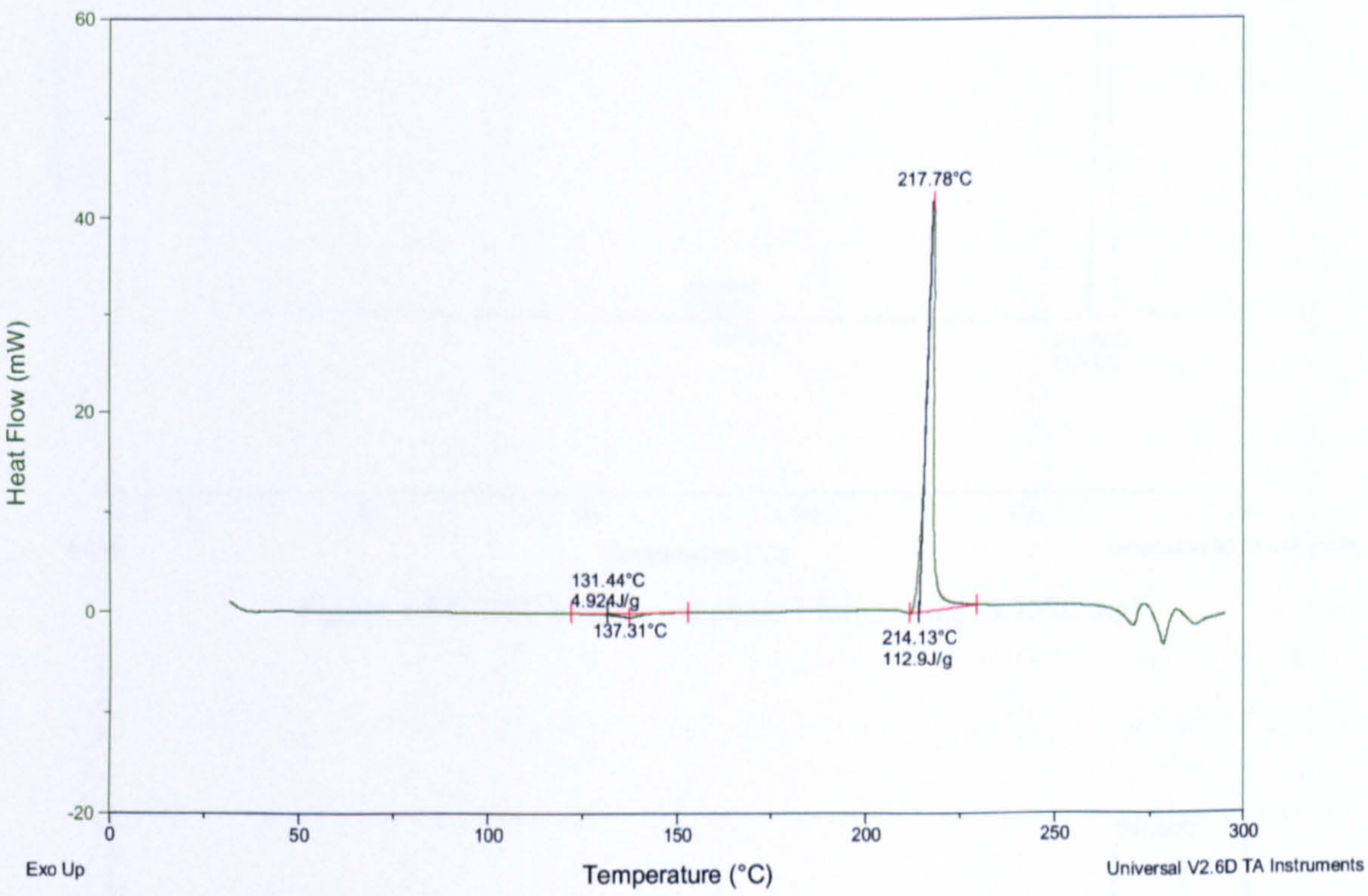

Figure 4.53: DSC plot for fresh phase I furosemide (5.0690 mg).

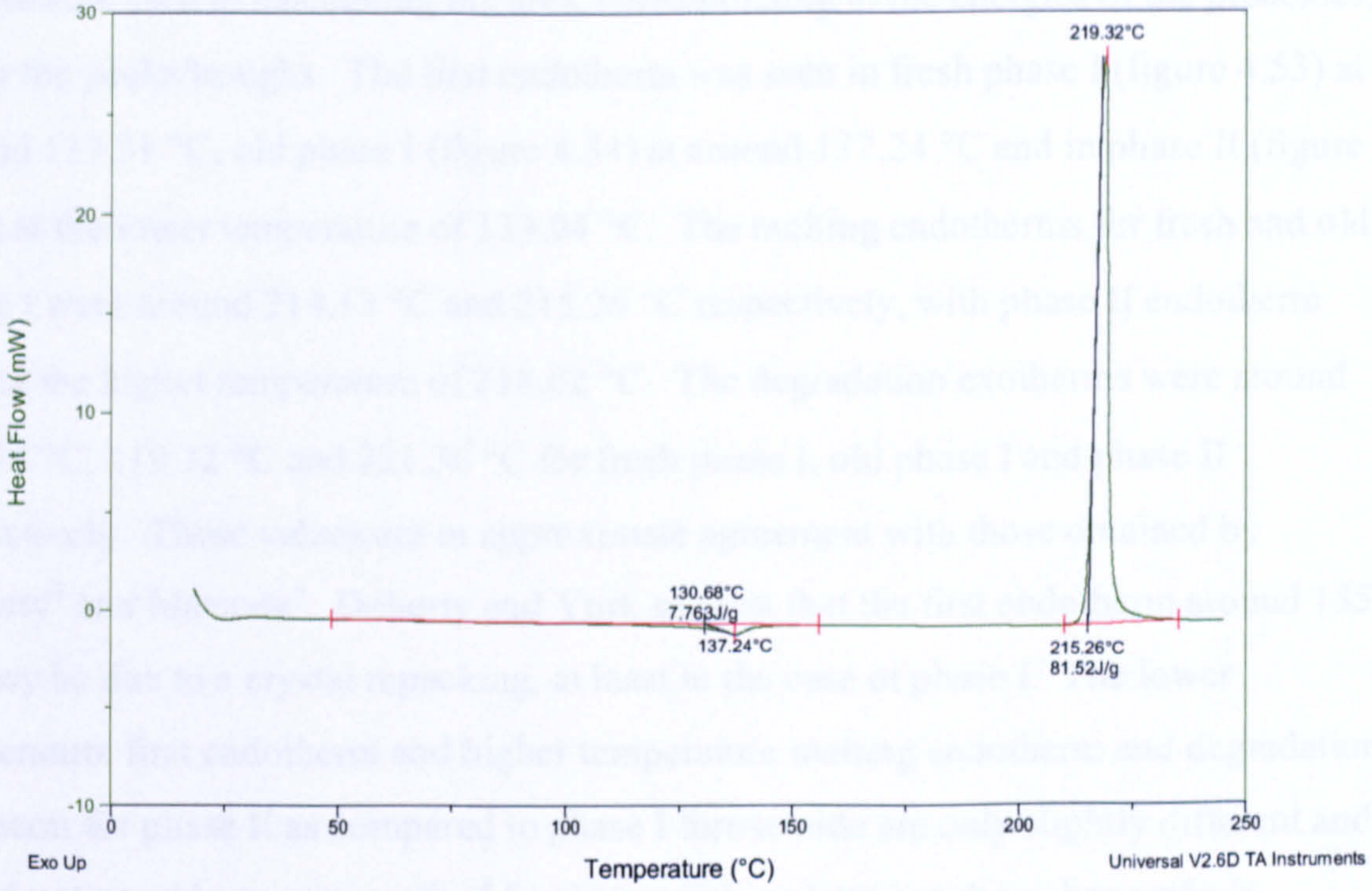

Figure 4.54: DSC plot for old phase I furosemide (6.7590 mg).

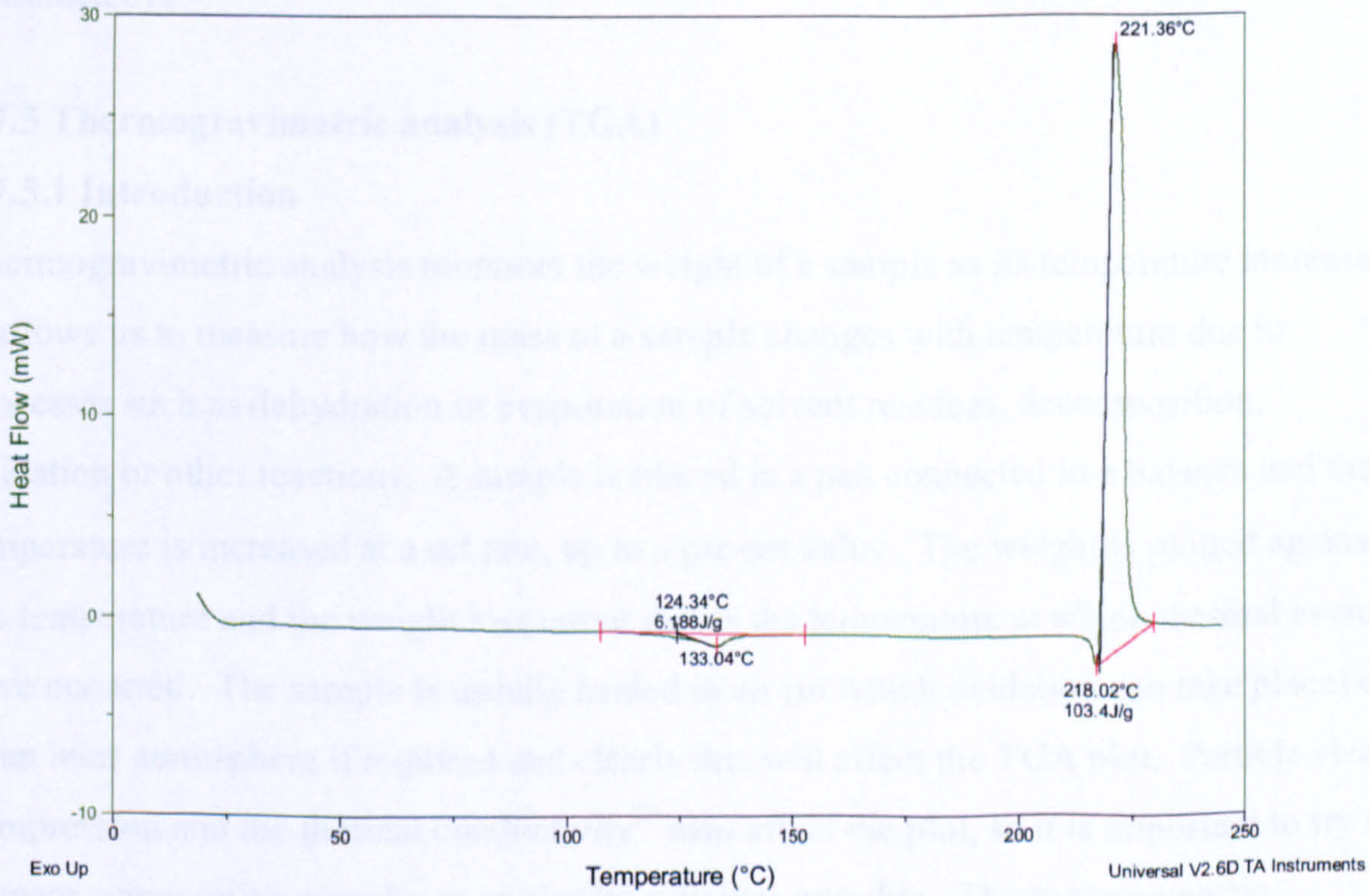

Figure 4.55: DSC plot for phase II furosemide (6.900 mg).

4.7.4.4 Discussion

All three samples gave similar spectra; the green line is the DSC plot and the red lines are the markers used in calculating the area, corresponding to the energies of the processes, under the peaks/troughs. The first endotherm was seen in fresh phase I (figure 4.53) at around 137.31 °C, old phase I (figure 4.54) at around 137.24 °C and in phase II (figure 4.55) at the lower temperature of 133.04 °C. The melting endotherms for fresh and old phase I were around 214.13 °C and 215.26 °C respectively, with phase II endotherm having the higher temperature of 218.02 °C. The degradation exotherms were around 217.78 °C, 219.32 °C and 221.36 °C for fresh phase I, old phase I and phase II respectively. These values are in approximate agreement with those obtained by Doherty[4] and Matsuda[3]. Doherty and York suggest that the first endotherm around 135 °C may be due to a crystal repacking, at least in the case of phase I. The lower temperature first endotherm and higher temperature melting endotherm and degradation exotherm for phase II as compared to phase I furosemide are only slightly different and would not provide an easy method for distinguishing between the polymorphs in comparison to viewing the NQR spectra. On viewing the DSC scans it would not be immediately obvious as to which polymorph produced each scan, particularly to an untrained eye.

4.7.5 Thermogravimetric analysis (TGA)

4.7.5.1 Introduction

Thermogravimetric analysis monitors the weight of a sample as its temperature increases. It allows us to measure how the mass of a sample changes with temperature due to processes such as dehydration or evaporation of solvent residues, decomposition, oxidation or other reactions. A sample is placed in a pan connected to a balance and the temperature is increased at a set rate, up to a pre-set value. The weight is plotted against the temperature and the weight loss curve shows the temperature at which thermal events have occurred. The sample is usually heated in air (in which oxidation can take place) or in an inert atmosphere if required and clearly this will affect the TGA plot. Particle size, compression and the thermal conductivity[23] also affect the plot, so it is important to try to prepare comparative samples in as similar way was possible. Thermogravimetric

analysis can be important in pharmaceutical analysis as it can be used to monitor degradation temperatures in different atmospheres as thermal stability is an important consideration in the storage of drugs. With this technique whole tablets can be studied, as well as small powder samples.

4.7.5.2 Method

Thermogravimetric plots were recorded for fresh phase I, old phase I and fresh phase II using a Hi-Resolutions TGA 250 TA Instruments machine at Merck Sharp and Dohme, Hoddesdon. The temperature was ramped up to 250 °C at a rate of 10 °C min^{-1} under nitrogen at 40 ml min^{-1}.

4.7.5.3 Results

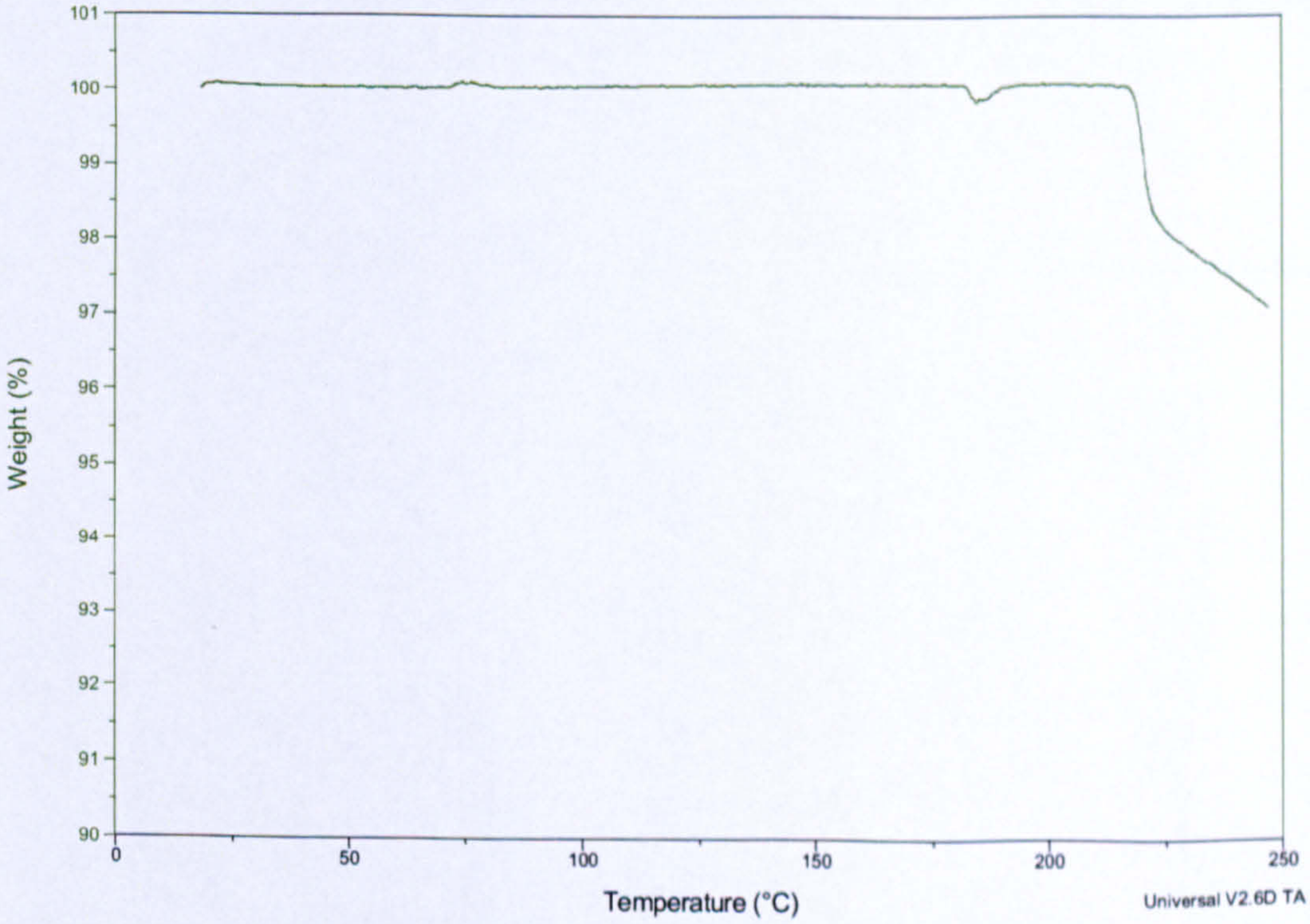

Figure 4.56: Fresh phase I furosemide TGA plot.

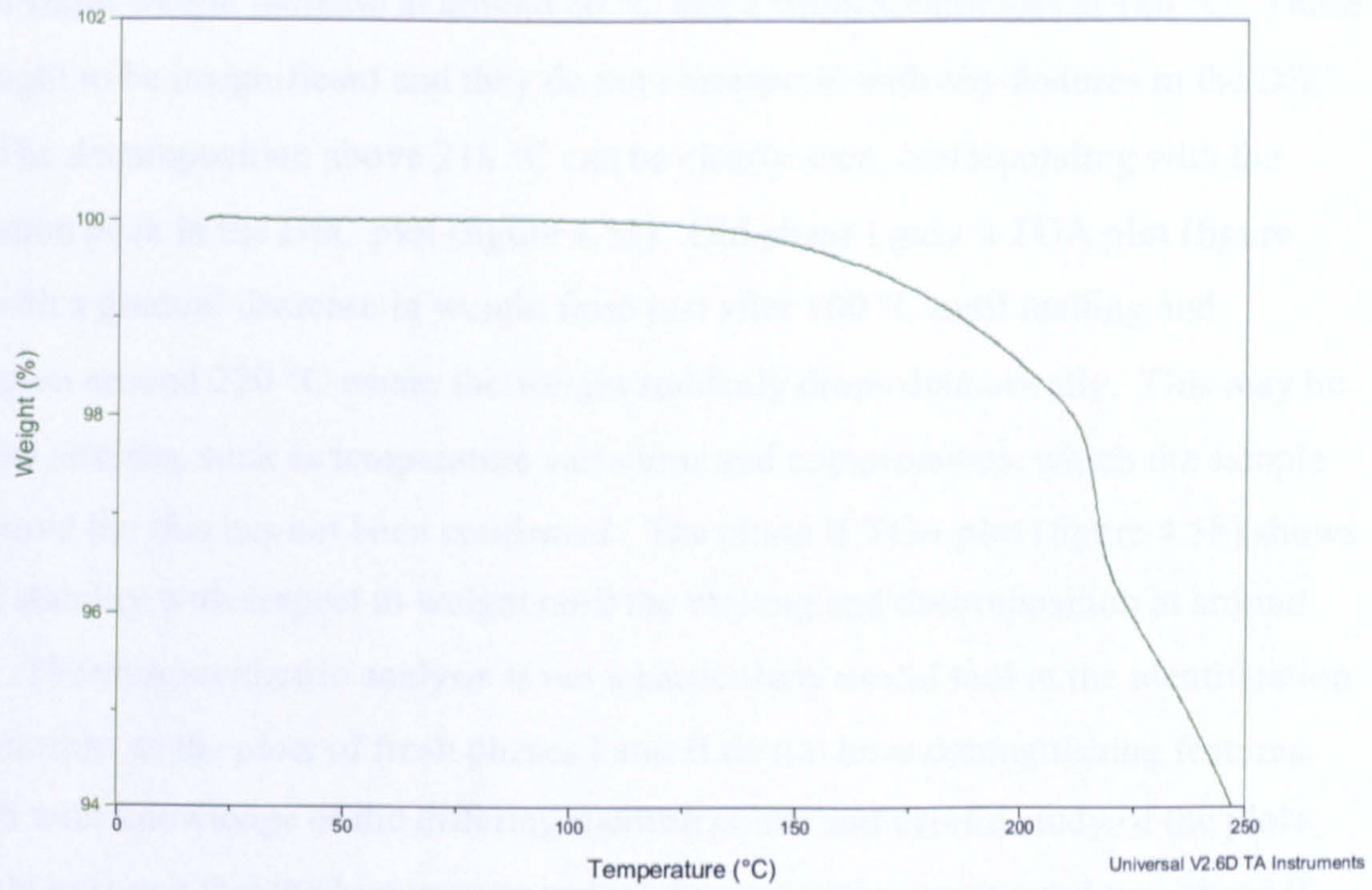

Figure 4.57: Old phase I furosemide TGA plot.

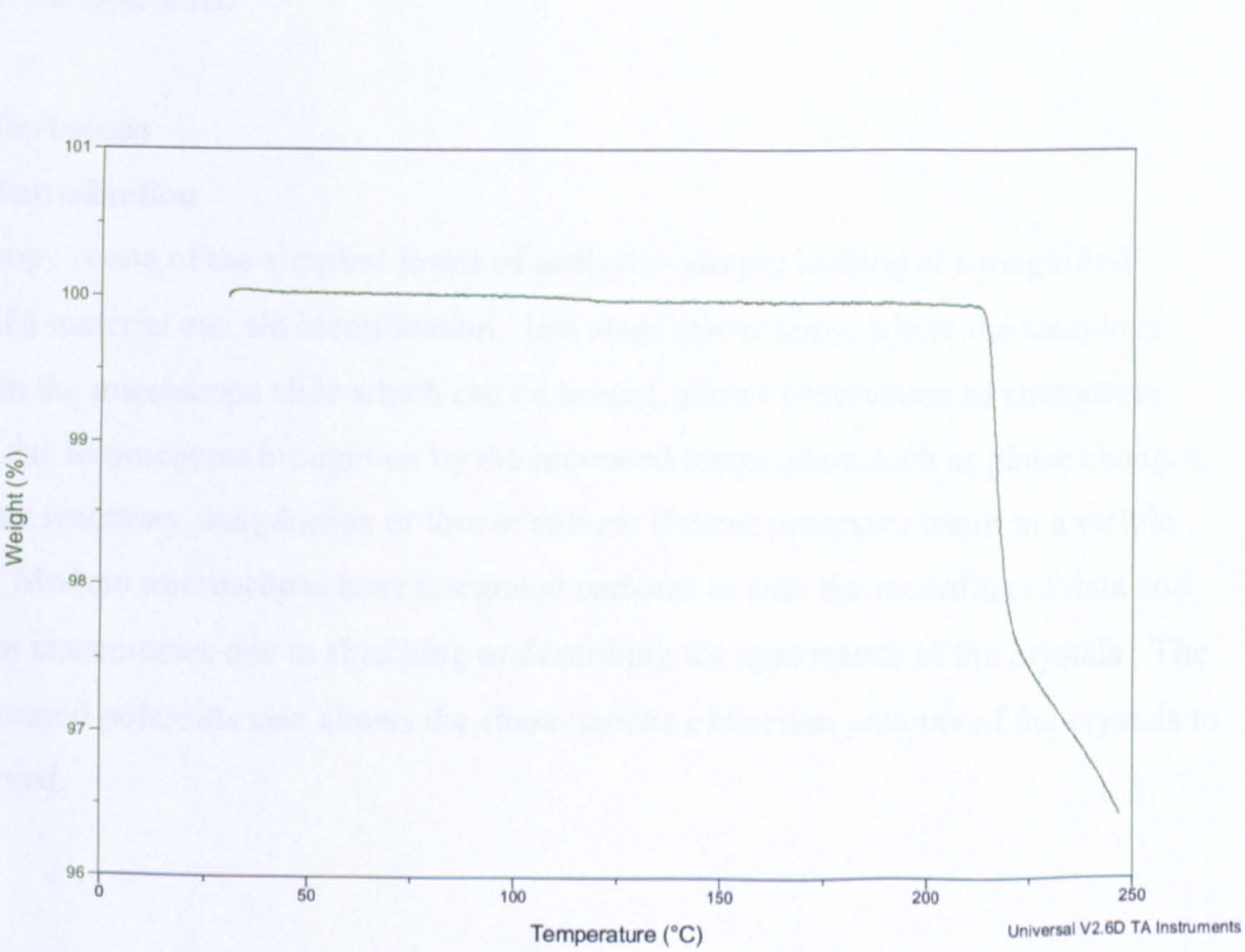

Figure 4.58: Phase II furosemide TGA plot.

4.7.5.4 Discussion

The thermogravimetric temperature vs. weight change plot for fresh phase I, (figure 4.56) shows a slight weight increase at around 80 °C and a slight weight loss at 180 °C. These are thought to be insignificant and they do not correspond with any features in the DSC plots. The decomposition above 218 °C can be clearly seen, corresponding with the degradation peak in the DSC plot (figure 4.53). Old phase I gave a TGA plot (figure 4.57), with a gradual decrease in weight from just after 100 °C until melting and degradation around 220 °C where the weight suddenly drops dramatically. This may be due to the stresses, such as temperature variations and compressions, which the sample has endured but this has not been confirmed. The phase II TGA plot (figure 4.58) shows thermal stability with respect to weight until the melting and decomposition at around 220 °C. Thermogravimetric analysis is not a particularly useful tool in the identification of polymorphs as the plots of fresh phases I and II do not have distinguishing features, although with knowledge of the differing melting points and careful study of the plots one could presume that the higher temperature decomposition compound was phase II, based on the DSC data.

4.7.6 Microscopy

4.7.6.1 Introduction

Microscopy is one of the simplest forms of analysis - simply looking at a magnified image of a material can aid identification. Hot stage microscopy, where the sample is placed on the microscope slide which can be heated, allows observation of changes in crystals due to processes brought on by the increased temperature such as phase changes, solid-state reactions, dehydration or loss of solvent if these processes result in a visible change. Modern microscopes have integrated cameras to ease the recording of data and minimize inaccuracies due to sketching or describing the appearance of the crystals. The use of crossed polaroids also allows the characteristic extinction patterns of the crystals to be observed.

4.7.6.2 Method

Samples of fresh phase I, old phase I and fresh phase II were photographed at twenty times magnification at Merck Sharp and Dohme, Hoddesdon, using a Nikon Eclipse E400 microscope at room temperature. A small amount of each sample was suspended in nujol and examined under the microscope.

4.7.6.3 Results

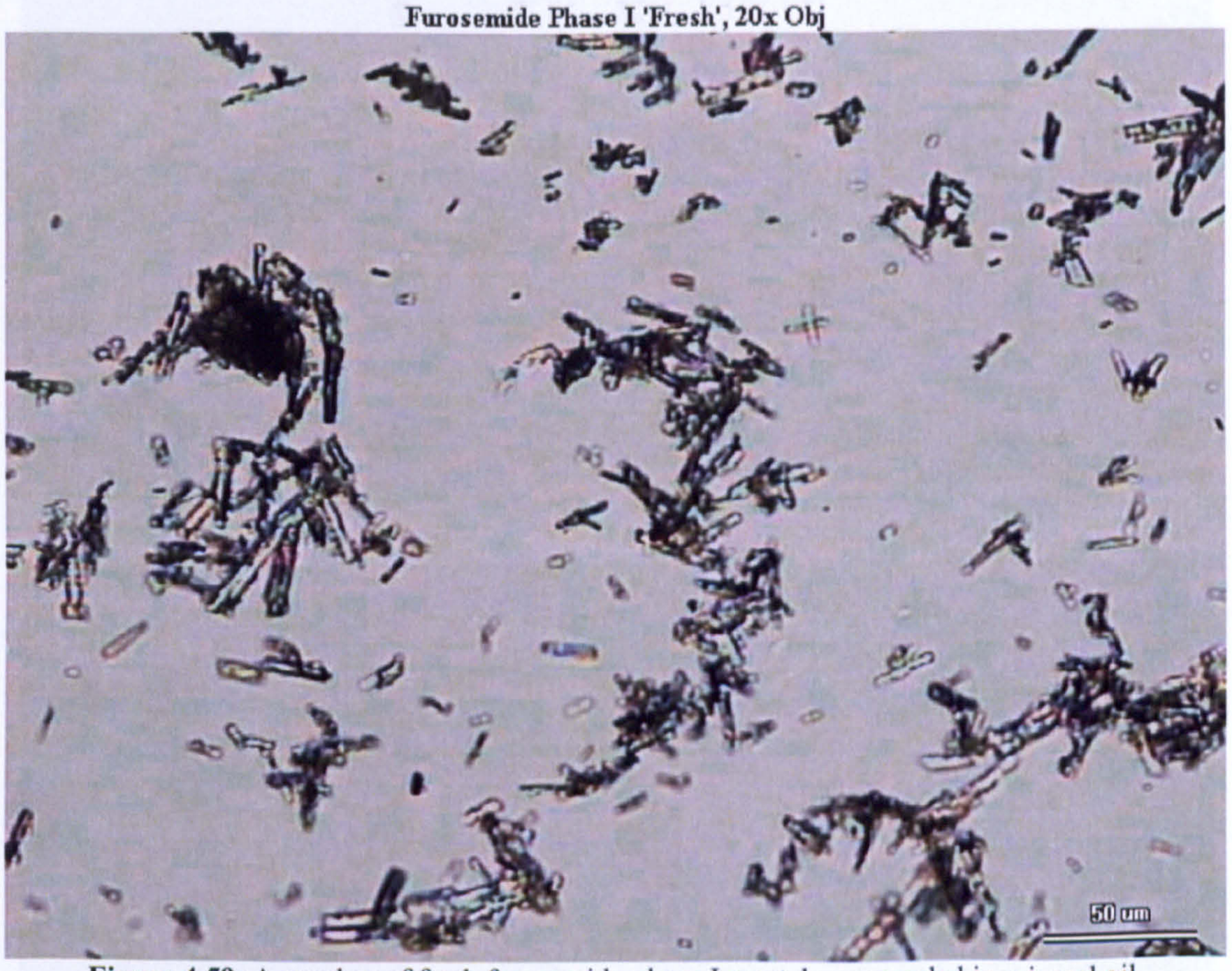

Figure 4.59: A number of fresh furosemide phase I crystals, suspended in mineral oil.

Furosemide Phase I 'Old', 20x Obj

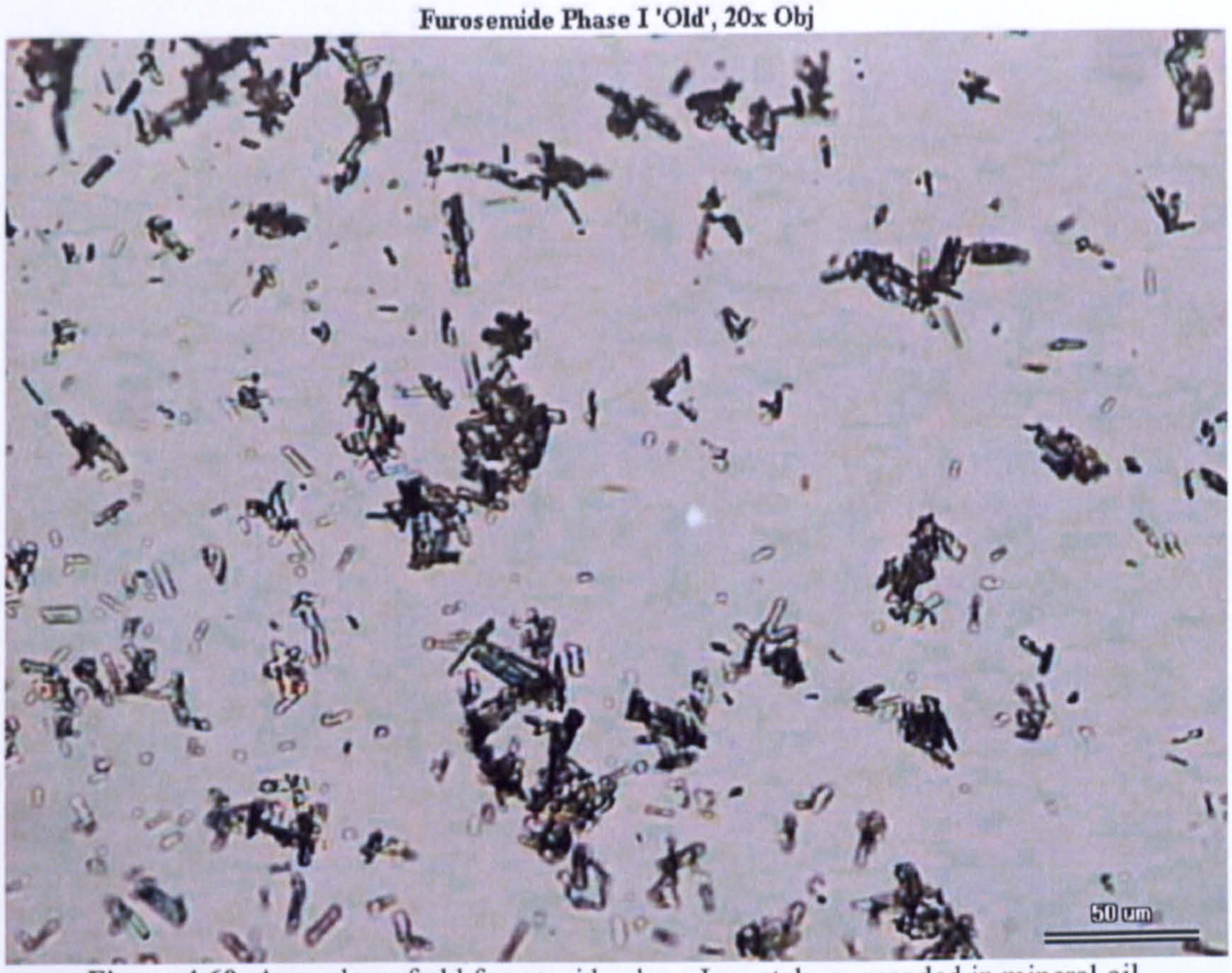

Figure 4.60: A number of old furosemide phase I crystals, suspended in mineral oil.

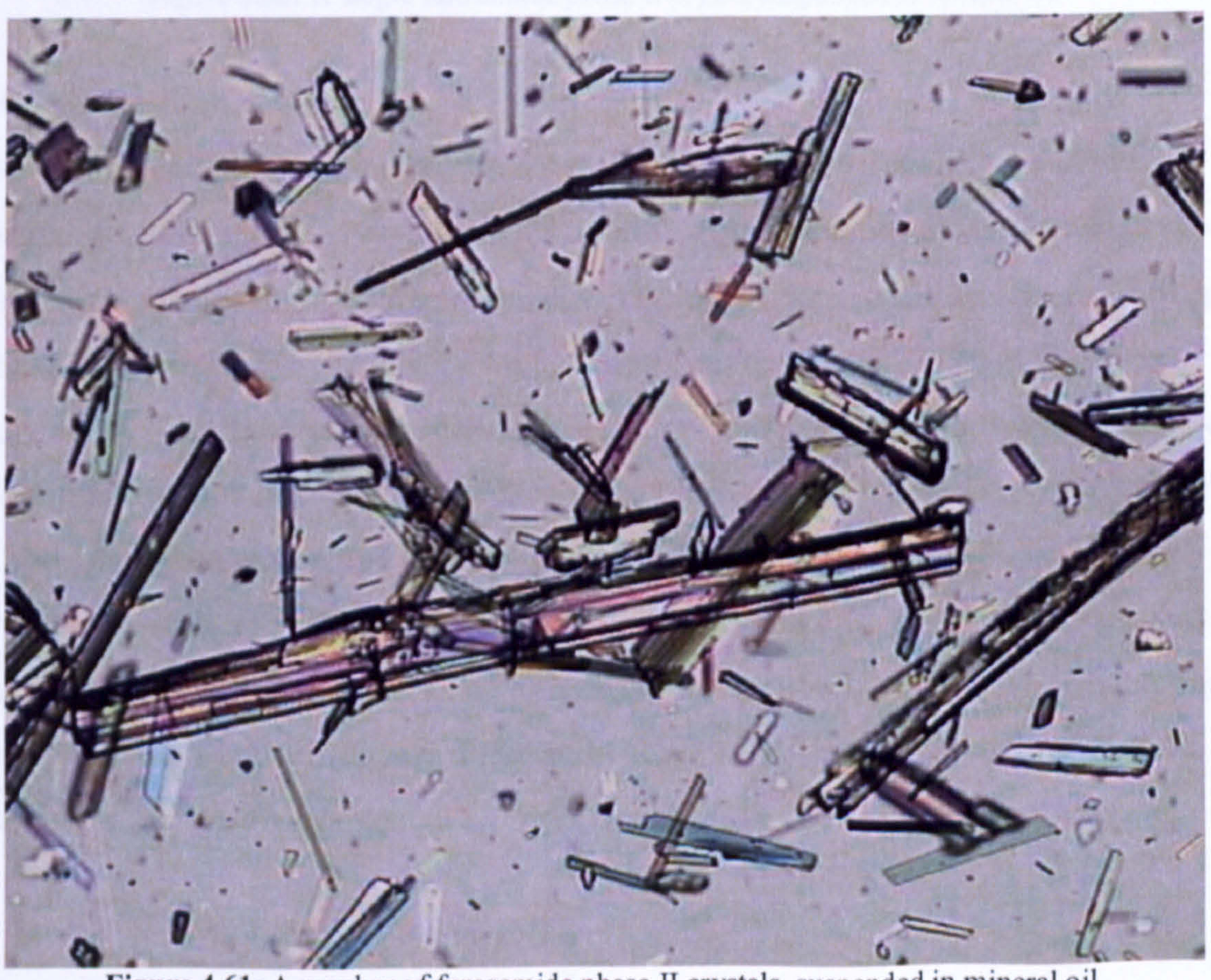

Figure 4.61: A number of furosemide phase II crystals, suspended in mineral oil.

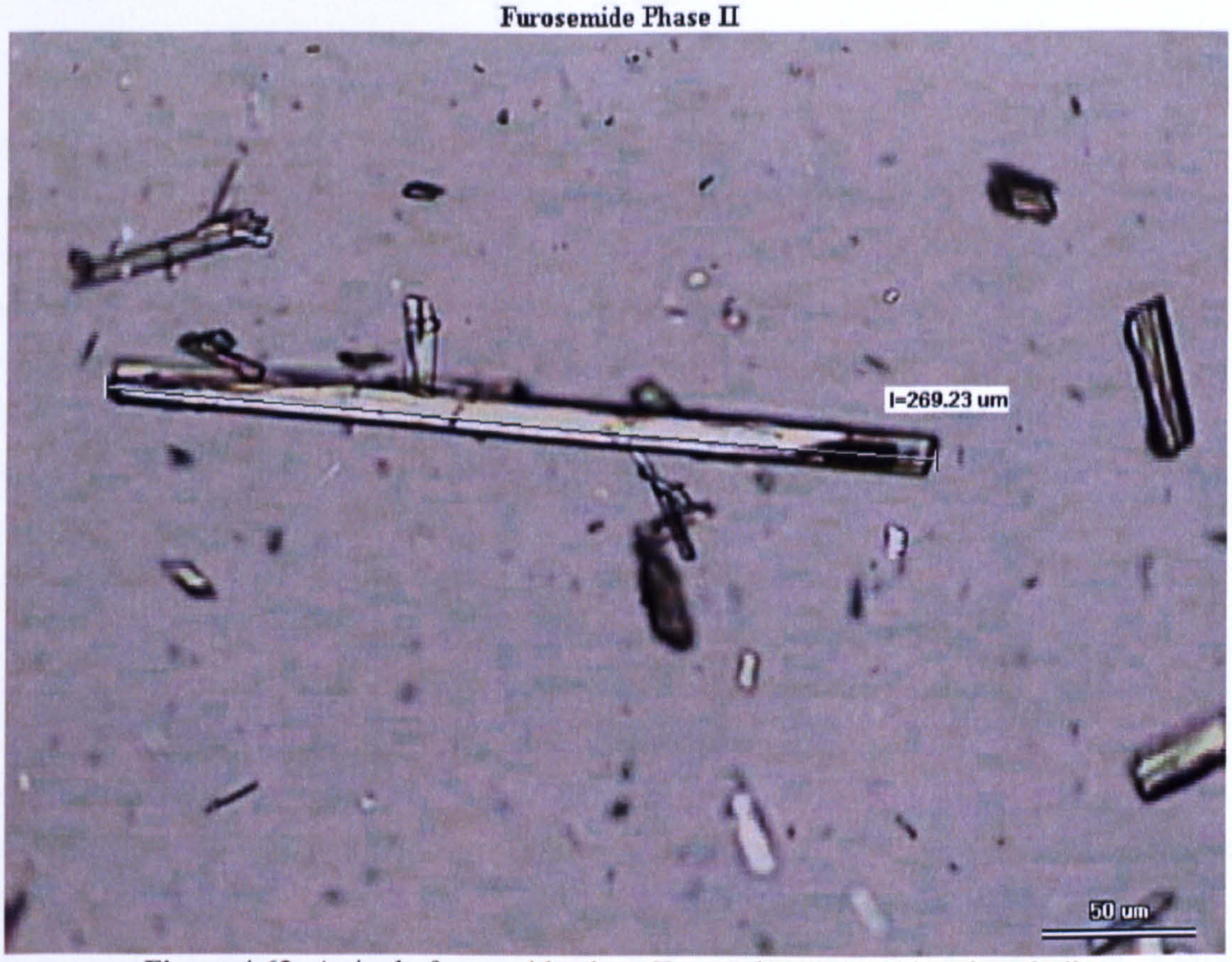

Figure 4.62: A single furosemide phase II crystal suspended in mineral oil.

4.7.6.4 Discussion

Fresh phase I and old phase I (figures. 4.59 and 4.60) are very similar, as would be expected, with the crystals being small (< 20 μm), although the fresh sample does appear to have, on average, slightly longer crystals. The phase II photographs (figures 4.61 and 4.62) show much longer crystals, as we have seen in the previous recrystallisations (figure 4.18). The differences in crystal formation are clearly seen by eye in the case of large crystals, which have undergone slow recrystallisation. If the different polymorphs had both been ground to a fine powder, this would obviously not be the case, and unfortunately such a situation was not studied under the microscope. We can see that in some cases microscopy is a quick and easy way of distinguishing between polymorphs where the crystals are sufficiently different in shape and form but this may not be the situation for many polymorphs.

4.8 References

[1] The Merck Index, **2001**, entry no. 4330.

[2] Latosinska, J. N. *Magn. Reson. Chem.*, **2003**, *41*, 395 - 405.

[3] Matsuda, Y;.Tatsumi, E. *International Journal of Pharmaceutics*, **1990**, *60*, 11 - 26.

[4] Doherty, C.; York, P. *International Journal of Pharmaceutics*, **1988**, *47*, 141 - 155.

[5] Lamotte, J. N.; Campsteyn, H.; Dupont, L.; Vermiere, M. *Acta Crystallogr.* **1978**, *B24*, 1657 - 1661.

[6] Fronckowiak, M.; Hauptman, H. *Am. Cryst. Assoc. Abstracts*, **1976**, *Winter*, 9.

[7] Shin, W.; Jeon, G. S. *Seoul University Journal of Pharmaceutical Sciences*, **1983**, *8*, 45.

[8] Balchin, E. *"Nuclear Quadrupole Resonance: The Detection of Narcotics and Explosives"*, 4th Year Project, March **2002**, King's College London.

[9] Lasix® Tablets 20 mg patient information leaflet, Hocchst Marion Roussel.

[10] Lasix® Tablets 40 mg patient information leaflet, Hoechst Marion Roussel.

[11] Lasix® Tablets 500 mg patient information leaflet, Hocchst Marion Roussel.

[12] Rowe, M. D. King's College London, Personal Communication.

[13] P. Pyykkö, *Mol. Phys.*, **2001**, *99*, 1617.

[14] Atalla, R. H.; Gast, J. C.; Sindorf, D. W.; Bartuska, V. J.; Maciel, G. E. *J. Am. Chem. Soc.*, **1980**, *102*, 3249.

[15] Apperley, D.C.; Forster, A. H.; Fournier, R.; Harris, R. K.; Hodgkinson, P.; Lancaster, R. W.; Rades, T. *Magn. Reson. Chem.* **2005**, *43*, 881 - 892.

[16] Brittain, H. G. *Physical Characterization of Pharmaceutical Solids*, Marcel Dekker, New York. **1995**, pp 94 - 123.

[17] Schmidt-Rohr K. and Spiess, H. W., *Multidimensional Solid State NMR and Polymers*, Academic Press, London. **1994**, pp 35 - 37.

[18] Opella, S. J.; Frey, M. H., *J. Am. Chem. Soc.* **1979**, 101, 5854 - 5856.

[19] Harris, R.K. *Analyst*, **1985**, *110*, 649 - 655.

[20] Wehrli, F. W.; Wirthlin, T. *Interpretation of Carbon-13 NMR Spectra*, Heyden & Son Ltd., London. **1976.**

[21] Simmons, D. L.; Ranz, R. J., Gyanchandani, N. D.; Picotte, P. *Can. J. Pharm. Sci.*, **1972**, *7*, 121.

[22] Pretsch, E.; Buhlmann, P.; Affolter, C. *"Structure and Determination of Organic Compounds"*, Springer, **2000**, 3rd Edition.

[23] Bryn, S. R.; Pfeiffer, R. R.; Stowell, F. G. *Solid State Chemistry of Drugs*, 2nd ed.; SSCI Inc.: West Lafayette, IN, **1999**; pp 45 - 139.

5 Quantification

5.1 Introduction

An analytical technique which allows for quantification of substances is highly desirable in the pharmaceutical industry. Although some methods of analysis currently used do allow for quantification, including X-ray crystallography[1] and solid-state NMR[2], they are not applicable to the study of bulk samples in the non-invasive, non-destructive manner of which NQR is capable.

NQR has been shown to give a reasonably linear dependence of peak intensity on sample weight from ^{63}Cu in Cu_2O and ^{209}Bi in $BiCl_3$[3] and has long been suggested as a quantitative analytical technique[4] but in the areas in which NQR has been utilized so far quantification has not been considered a major need – a 'yes/no' determination has been more important. Even more importantly, no quantitative work has yet been published on the key nucleus, ^{14}N although some quantitative NQR work has been published on the ^{35}Cl signal in a mixture of amorphous and crystalline chlorpropamide[5]. The study of this nucleus in pharmaceutical samples is therefore an ideal area in which to explore its quantitative nature, as it is readily applicable to topics such as the confirmation of the number of tablets in a bottle or weight of API in a tablet, allowing determination of both quantity and strength.

5.2 ^{14}N studies

5.2.1 Furosemide

Initially PSL sequences at 3.563 MHz were to be used to study 500 mg tablets of furosemide to see if a linear response would be obtained with respect to the number of tablets/mass of furosemide. The experiment was designed and initial experiments carried out to determine the optimum conditions. As the RF field is less homogeneous at the edges of the solenoid, efforts were to be made to keep the tablets as central as possible, especially at small volumes. This was done by wrapping tissue paper around the tablets to make a column of the diameter of the neck of the container.

Initial tests indicated that a large number of scans would have to be run to allow detection of the smaller numbers of tablets with a satisfactory signal to noise ratio, meaning the experiments would last approximately 24 hours. It was decided to postpone ^{14}N studies

on furosemide and move to quantitative measurements using a substance with a stronger signal, so as to achieve a large set of data with sufficient experimental repeats in a shorter time.

5.2.2 Triazole

5.2.2.1 Introduction

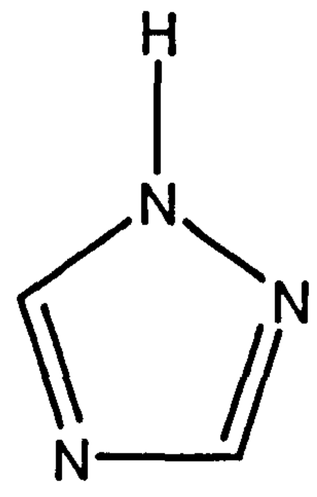

8

1,2,4-Triazole (**8**), an anti-fungal material, was chosen as a substance with a number of strong ^{14}N singlet signals[6,7,8,9], including one with an NQR frequency (3.787 MHz) close to that of furosemide (3.563 MHz). This allowed a number of measurements for each mass to be taken in the same day, minimizing machine drift and allowing a full set of quantitative results to be acquired in a shorter timescale. Also, the singlet makes area measurements easier and more accurate as there are not overlap issues.

5.2.2.2 Initial experiments

The variable pitch solenoid (figure 3.5) was tuned to 3.787 MHz and an RF excitation frequency of 3.786 MHz was used. Triazole gave strong signals, with a long FID. A Bessel plot was carried out to determine to 90_{eff} pulse before each set of experiments. The following sequence was applied and T_2* was calculated by fitting an exponential curve to the real data (figure 5.1), using ProFit.

Event		
90_{eff} Pulse / μs	80	(Phase 20)
Acquisition	1024 points / 10 μs dwell	(Phase 02)
Final delay / ms	800	
No. of scans	1000	
Excitation frequency	3.786 MHz	

Table 5.1: Pulse sequence settings to yield triazole FID.

The time domain signal was then baseline corrected, phase adjusted and Fourier transformed to give a singlet peak at 3,786,758 Hz, with a linewidth of 322 Hz (figure 5.2) at room temperature.

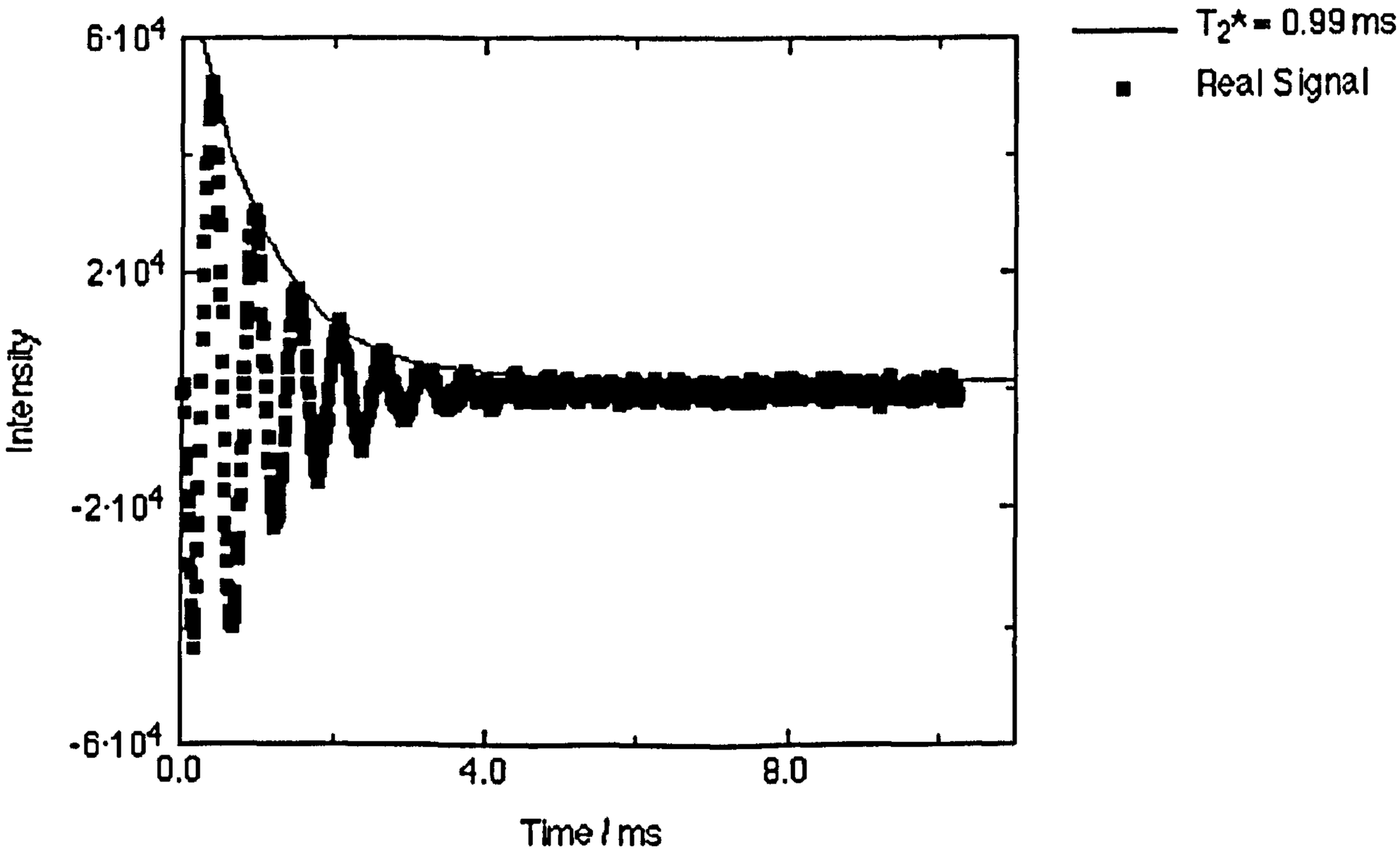

Figure 5.1: Time domain ^{14}N triazole signal with exponential fit. $T_2^* = 0.99 \pm 0.02$ ms.

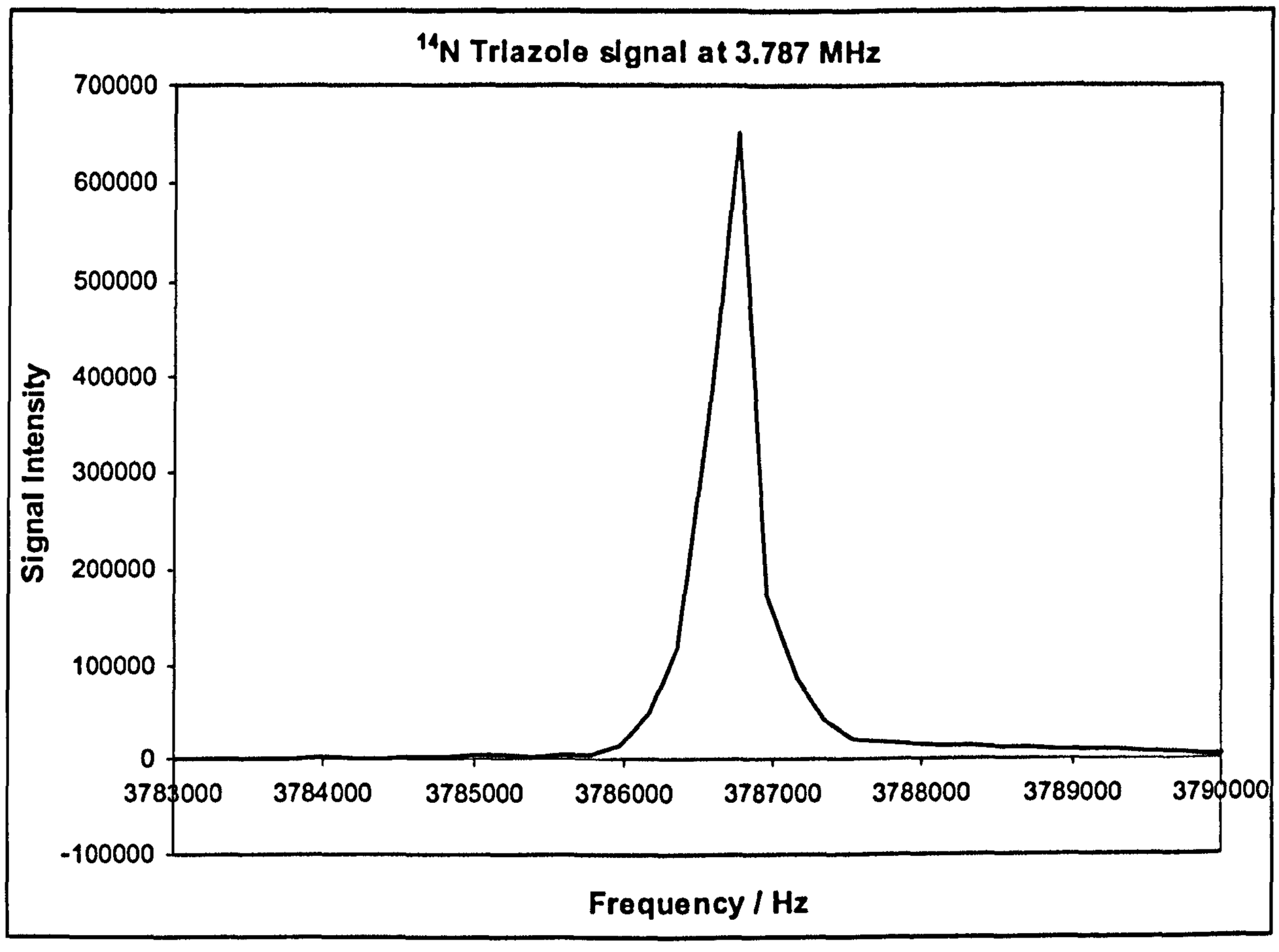

Figure 5.2: Fourier transformed peak from ^{14}N triazole signal. Linewidth = 322 Hz, Frequency = 3,786,758 Hz.

An inversion-recovery sequence was used to find the spin-lattice relaxation time, with the *Q*-damper on, allowing a short total dead time of 50 μs and an enhanced T_1 plot (figure 5.3), with good negative intensity values fitted to a single exponential recovery:

Event		
90_{eff} Pulse / μs	80	(Phase 20)
Dead time	Variable - 15 points from 1 to 2000 ms	
Acquisition	256 points / 20 μs dwell (Phase 02)	
Final delay / ms	50	
No. of scans	100	
Excitation frequency	3.786 MHz	

Table 5.2: Inversion recovery settings to yield triazole T_1.

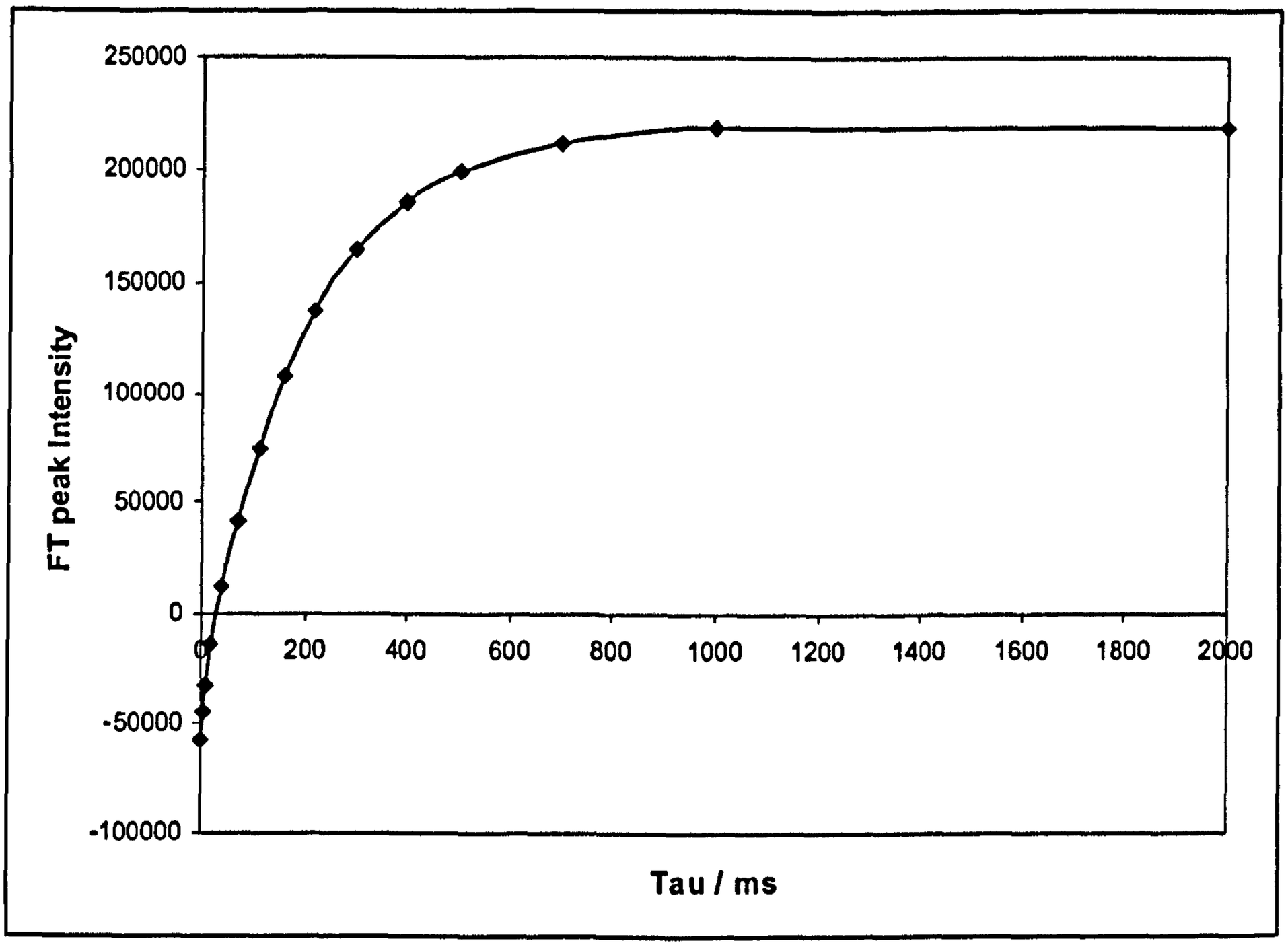

Figure 5.3: T_1 inversion recovery plot for ^{14}N triazole signal at 3.787 MHz, $T_1 = 177 \pm 6$ ms.

T_2 and T_2e measurements were attempted but achieving echoes was unsuccessful; this may be due to the long, strong FID, which could be masking the echo. Although phase tables were used to attempt to filter out any FID contribution, a clear echo still could not be seen (figure 5.4); compare this to the echoes seen using a similar sequence in furosemide (figure 5.5).

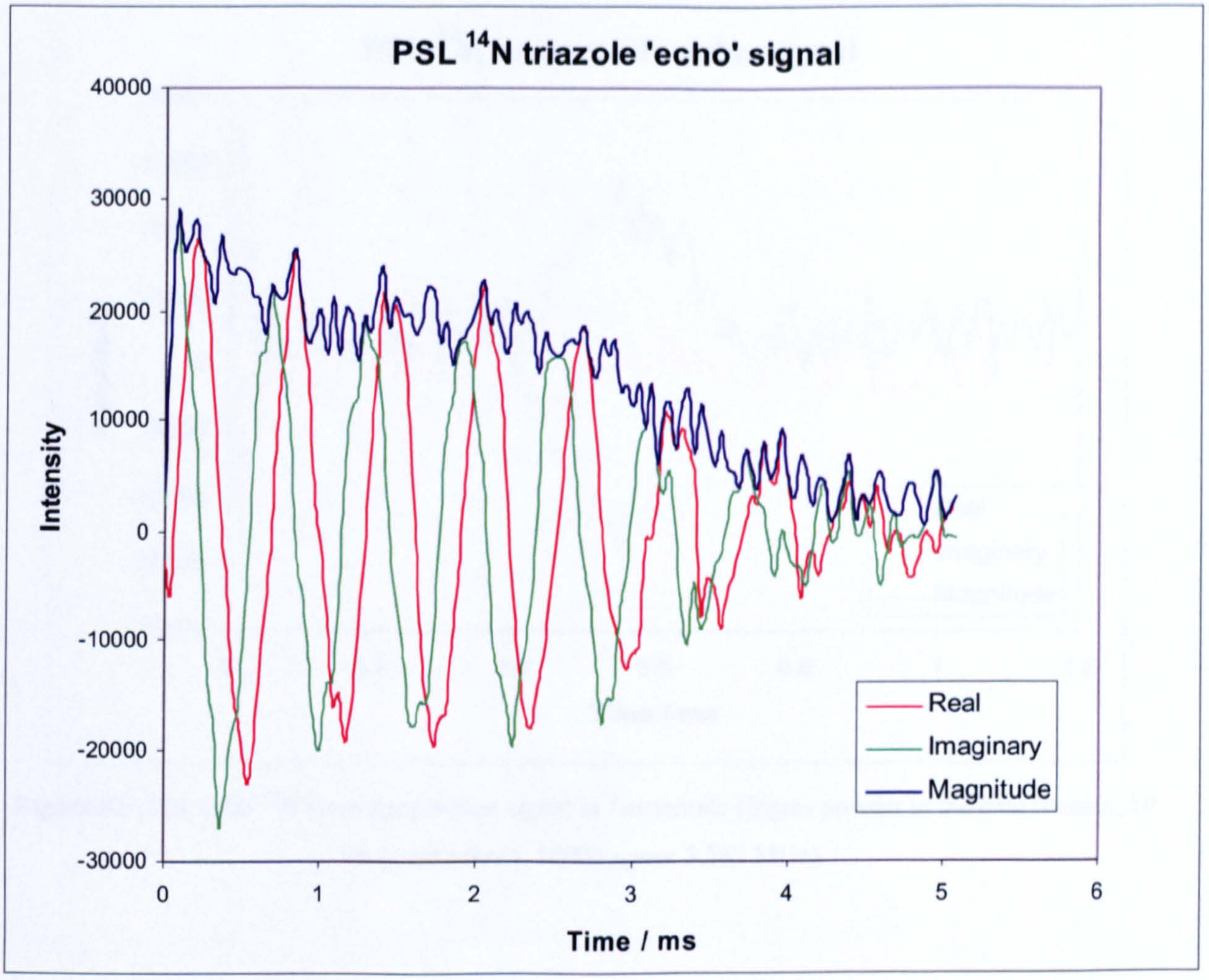

Figure 5.4: Attempted PSL echo ^{14}N signal in triazole at 3.787 MHz.

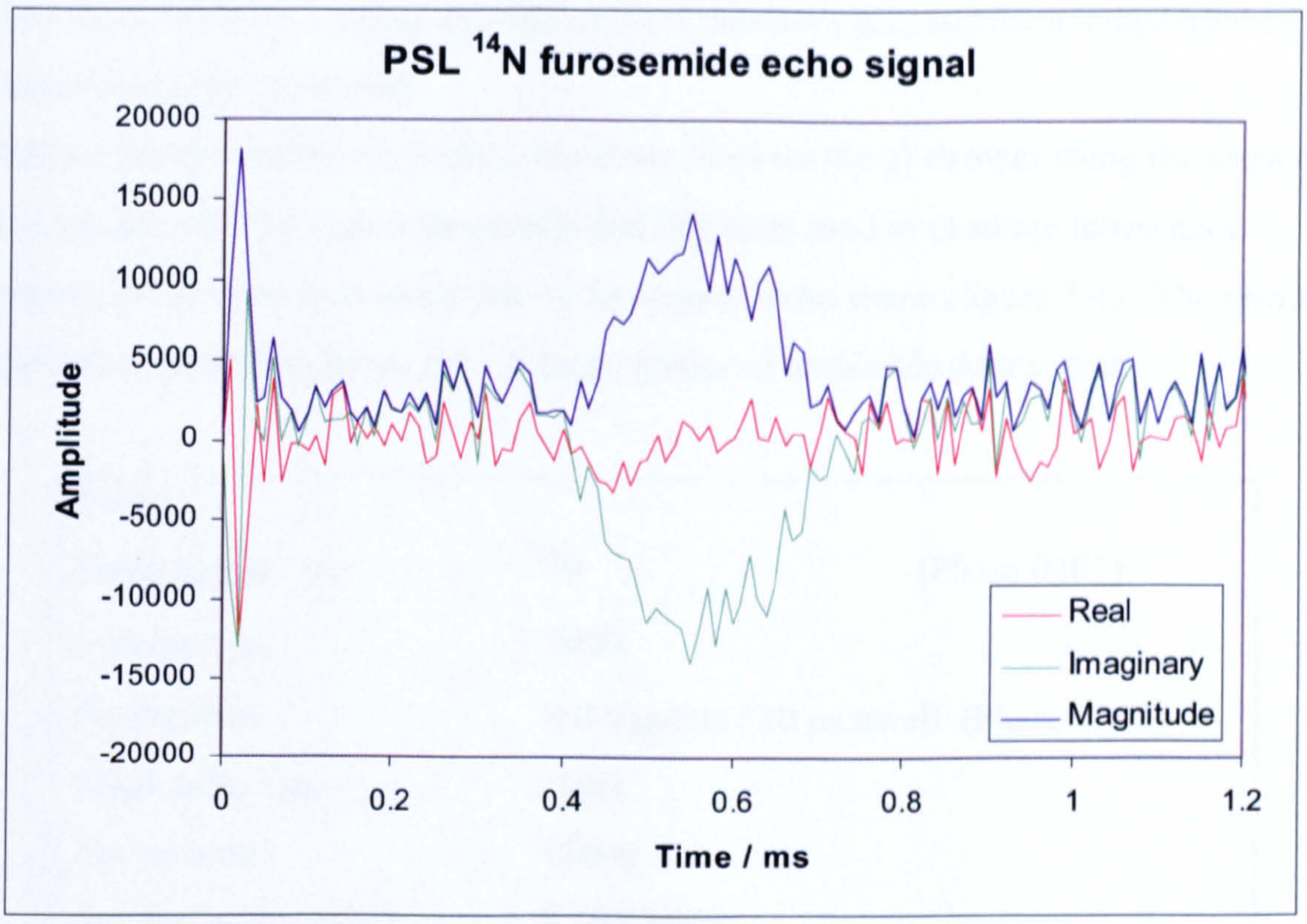

Figure 5.5: PSL echo ^{14}N room temperature signal in furosemide (Sigma powder in the time domain; 10 summed echoes, 10000 scans; 3.562 MHz).

5.2.2.3 Quantitative experiments

For ease of handling 5 g packets of triazole were made up using clingfilm and sticky tape. The samples were placed as centrally as possible in the container to be examined, with respect to both length and diameter, to ensure field homogeneity - also maximized by use of a solenoid of variable pitch. However, this became more difficult with larger masses; although the packages were packed in as small a space as possible, some triazole was inevitably close to the edges of the solenoid as the filling factor increased. 100.42 g of 99.5 % 1,2,4-1H-Triazole from Acros Organics was used as a standardisation sample prior to every quantitative run (simple FID, 100 μs pulse, 250 scans, 900 ms between scans, which is greater than $5T_1$ to ensure full recovery). For temperature stabilization, the required number of packets were placed in the container and put within the oil coil for at least 12 hours, with the standardization sample being placed in the canister but outside the oil coil for the same period. The experimental sample was then taken out and the standard sample placed within the RF coil. Three test runs were carried out at the

beginning of each day, taking approximately 3 minutes each, and the average used as the standardization measurement.

Initially a number of PSL sequences were run (without the *Q*-damper using the sequence below) as this was the type of sequence that had been used to examine furosemide. However, these were abandoned due to the strange echo shape (figure 5.4). The results achieved are plotted in figure 5.6. A large scatter of unreliable data is seen.

Event		
Pulse length / μs	70	(Phase 0202)
τ delay / μs	3000	
Acquisition	1024 points / 10 μs dwell	(Phase 0202)
Final delay / ms	1000	
No. of scans	15000	
Excitation frequency	3.786 MHz	

Table 5.3: PSL sequence settings for quantification of triazole.

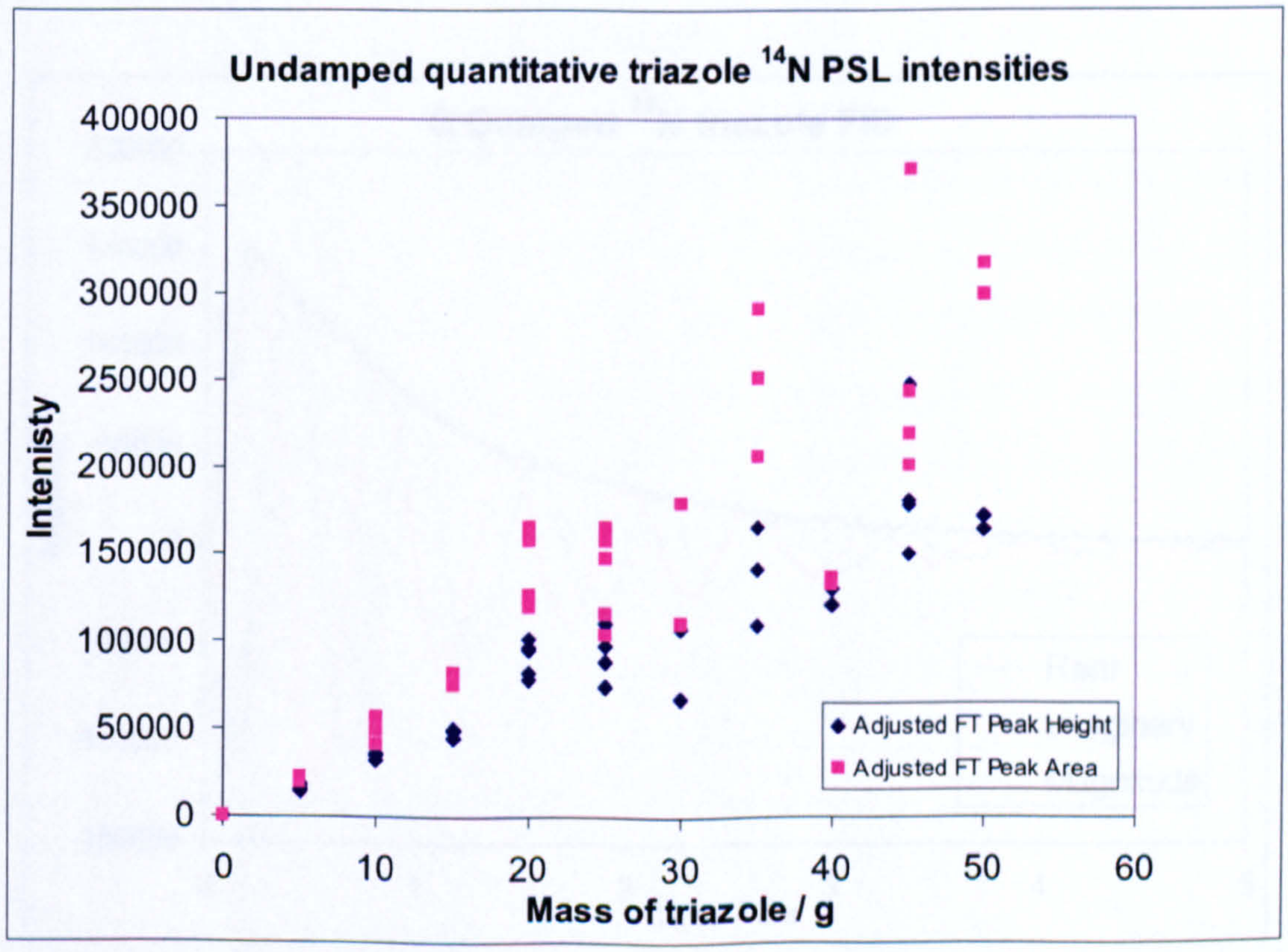

Figure 5.6: The standardized ^{14}N signal echo Fourier transformed peak heights and integrated areas for varying mass of triazole using PSL sequences.

The experiments were continued using FIDs only and the *Q*-damper was tuned and adjusted to 3.79 MHz. A number of measurements was recorded and plotted in the quantitative analysis; these were signal-to-noise ratio, peak height, peak area and maximum FID intensity. The oil bath as set to 298 K and was constant to within ± 0.1 K; this was the assumed temperature of the sample. The following settings were used in the quantitative measurements:

Event		
90_{eff} Pulse / μs	80	(Phase 20)
Acquisition	512 points / 10 μs dwell	(Phase 02)
Final delay / ms	900	
No. of scans	2000	
Excitation frequency	3.786 MHz	

Table 5.4: FID pulse sequence settings for quantification of triazole.

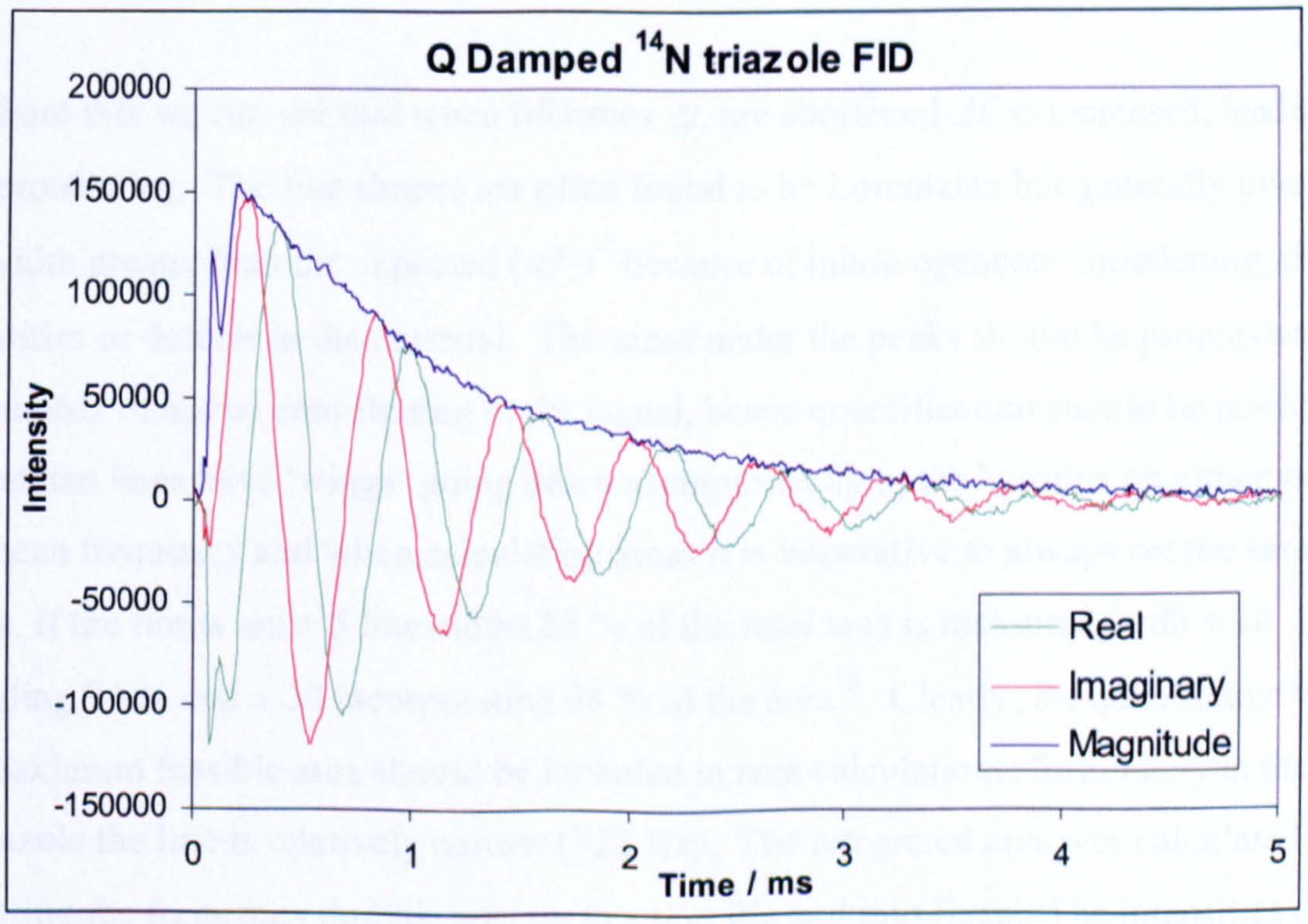

Figure 5.7: A *Q*-damped ^{14}N triazole (70 g) FID off resonance signal.
The rise and *Q* damping 'blip' can be seen at the beginning of the spectrum.

In each *Q*-damped FID there is a 'rise' and spike in each time domain spectrum before the FID (figure 5.7); this region was not included in the Fourier transformation and its contribution was not counted in the area measurements or peak heights. To remove the rise region the time domain spectra were shifted left by 20 points (0.2 ms) for each data set before baseline correcting and carrying out the Fourier transformation. The same process was carried out for the standardization plots.

Baseline correction is of utmost importance when dealing with quantitative experiments as a fluctuating or offset baseline will make false contributions to the integrated area. Badly defined baselines can also be a serious systematic error. Ensuring there is no breakthrough also achieves a more accurate integration result, as the first FID points determine the baseline and an incorrect point can lead to a d.c. offset and a number of incorrect points will greatly affect the baseline and lead to 'bowing' or 'rolling'[10]. A twisted baseline can also be due to badly adjusted phases[11].

The Heisenberg uncertainty principle states that

$$\Delta E.\Delta t \geq h/2\pi \qquad (5.1)$$

and from this we can see that when lifetimes Δt, are shortened ΔE is increased, leading to line broadening. The line shapes are often found to be Lorentzian but generally give a linewidth greater than the expected $(\pi T_2)^{-1}$ because of inhomogeneous broadening, due to impurities or defects in the material. The areas under the peaks should be proportional to the number of nuclei contributing to the signal, hence quantification should be possible. Lorentzian lines have 'wings' going down asymptotically to the baseline on either side of the mean frequency and when calculating areas it is imperative to always set the same limits. If the limits are ± 5 linewidths 85 % of the total area is measured, with ± 10 including 94 % and ± 30 incorporating 98 % of the area[12]. Clearly, for quantitative work the maximum feasible area should be included in area calculations; fortunately in the case of triazole the line is relatively narrow (322 Hz). The integrated area was calculated by exporting the frequency domain spectra to a text file and into Excel. The intensities of all the real points between 3800039 Hz and 3772500 Hz (a range of ± 50 linewidths) were added together (as all the frequency increments are equal) to give the rectangular

integration value including greater than 98 % of the area. The Fourier transformed peak intensity, the integrated area and the standardization adjusted peak intensities and areas (in arbitrary units) were all plotted against mass of triazole (figures 5.8 – 5.12). Statistical analysis for all sets of data for both regression with an intercept (table 5.5) and regression through the origin (table 5.6) was carried out in order to determine whether quantitative analysis and prediction of mass from signal intensity could be achieved.

5.2.2.4 Results and discussion

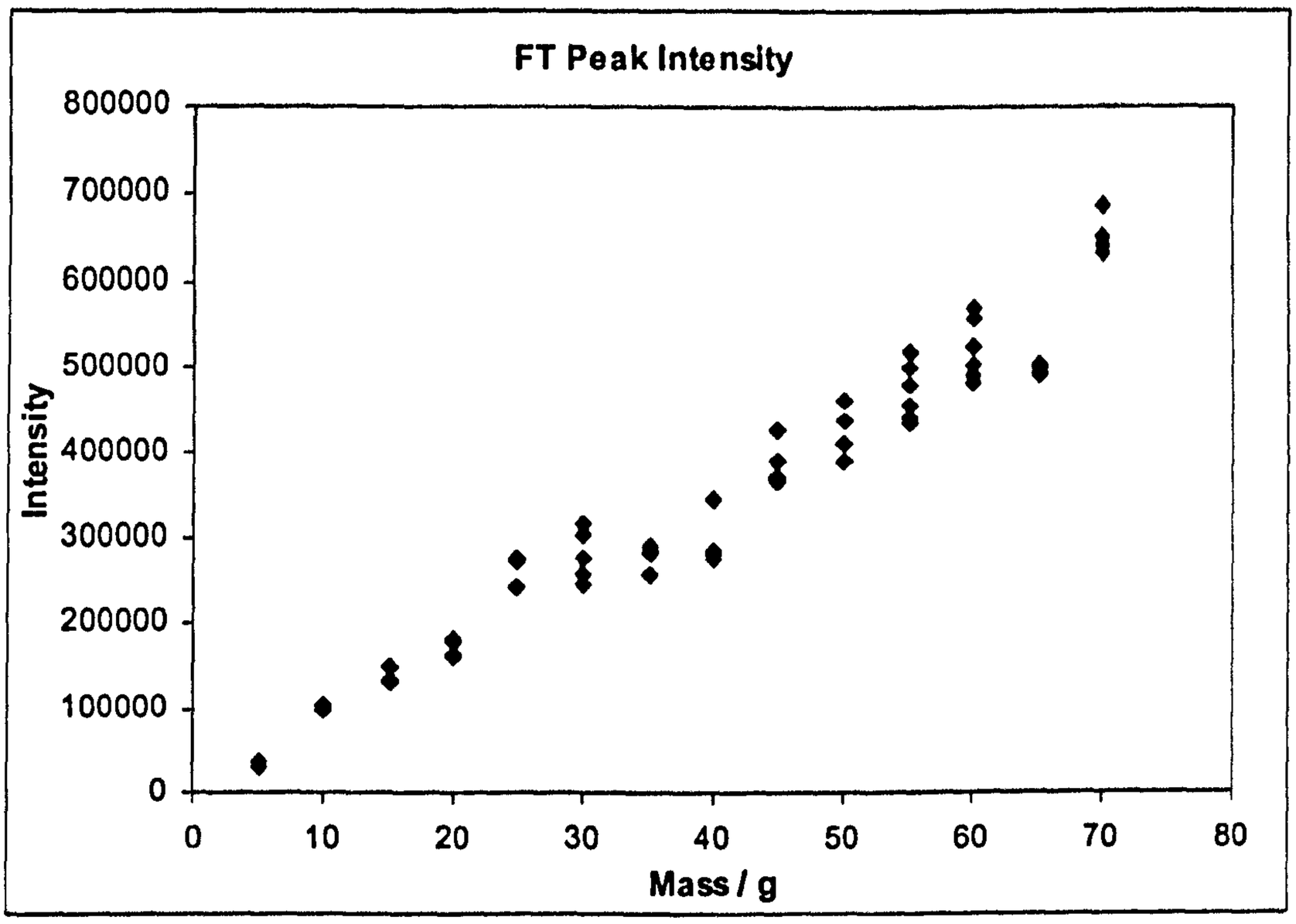

Figure 5.8: Variation of the ^{14}N triazole Fourier transformed peak intensity with varying mass. $y = 8370.2x + 8008.5$, $R^2 = 0.9569$. Assuming no blank signal (i.e. regression through the origin) $y = 8538.6x$, $R^2 = 0.9564$.

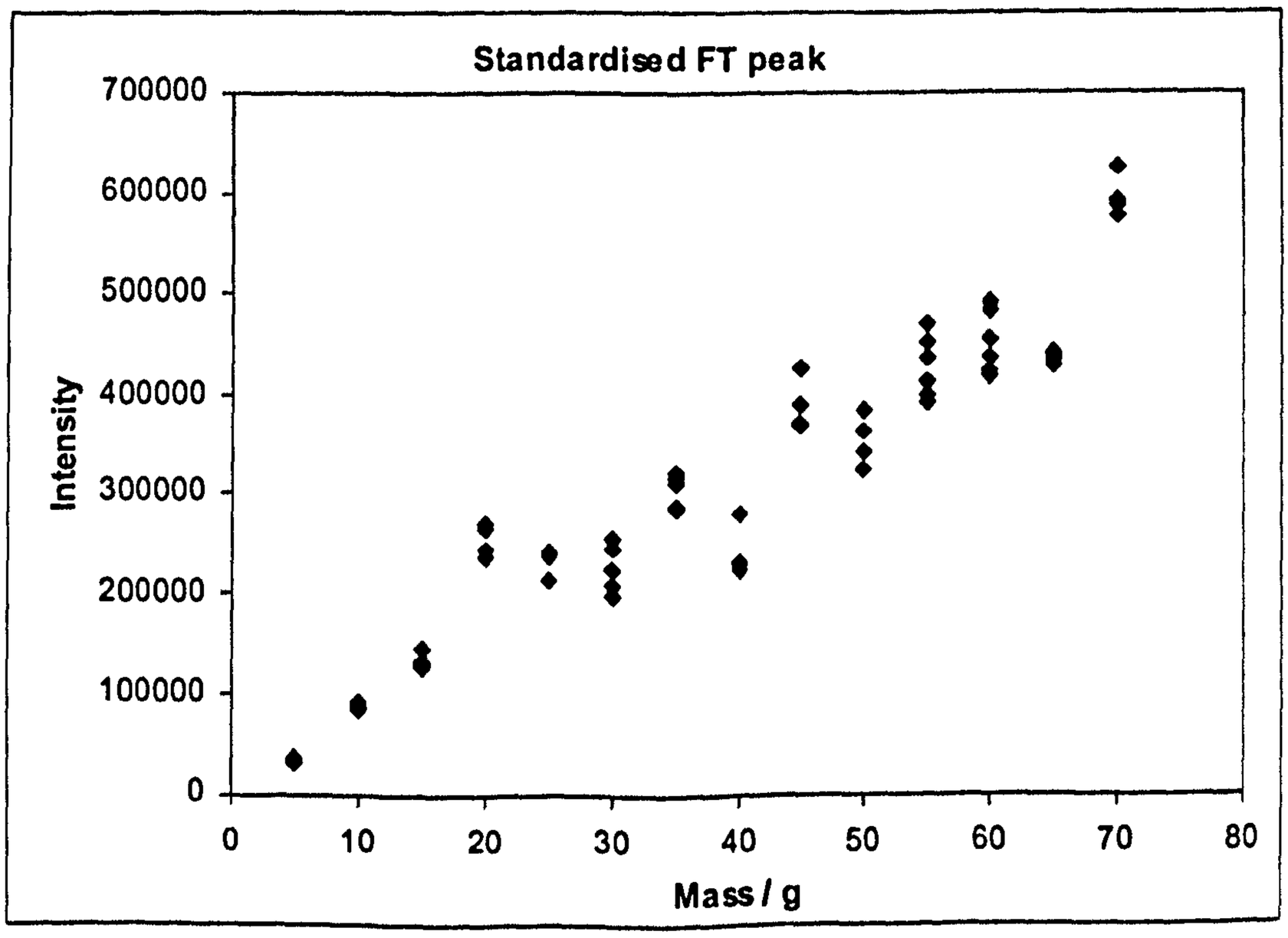

Figure 5.9: Variation of the ^{14}N triazole standardized Fourier transformed peak intensity with varying mass. $y = 7079.8x + 30533$, $R^2 = 0.9074$. Assuming no blank signal $y = 7721.8x$, $R^2 = 0.8978$.

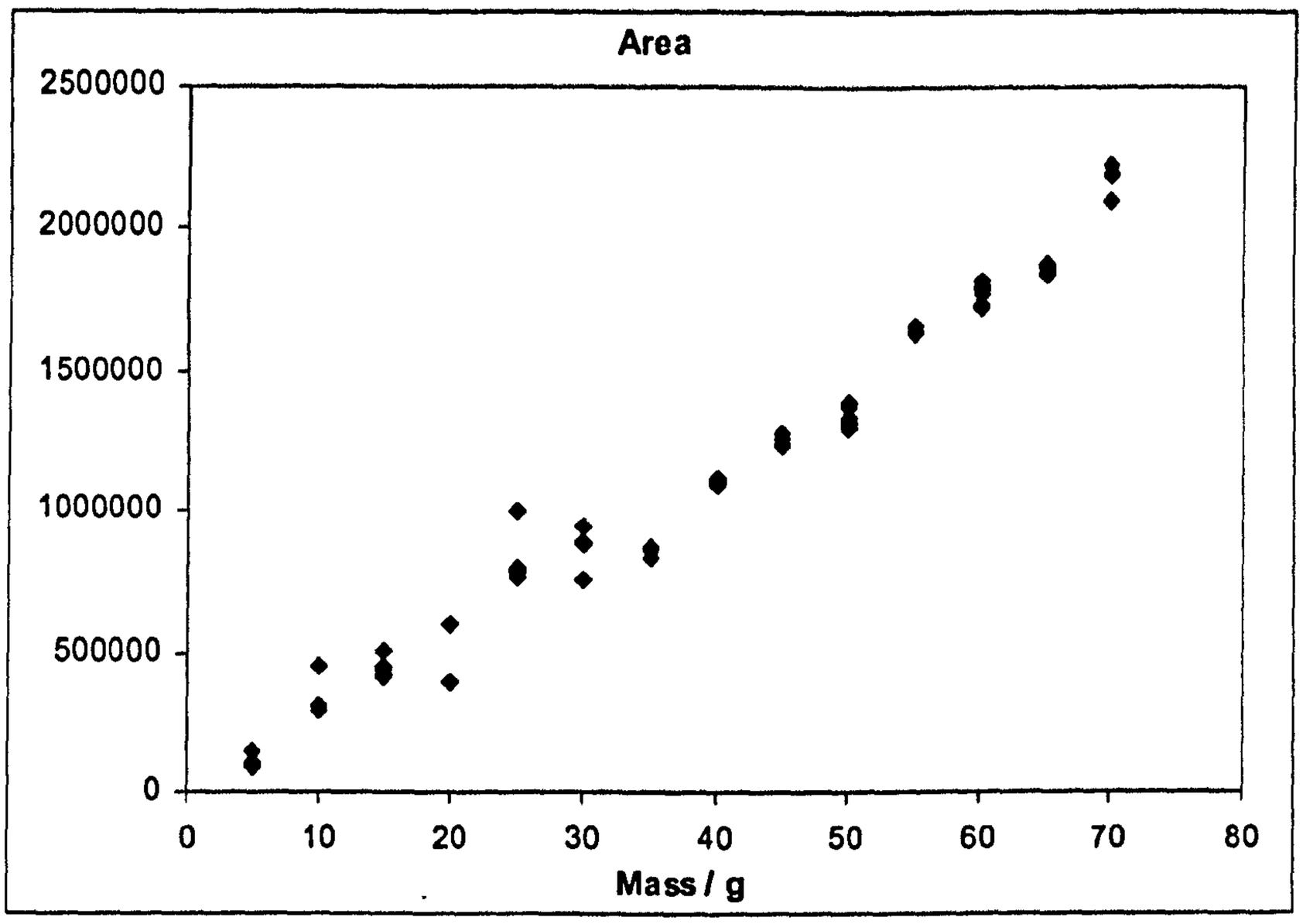

Figure 5.10: Variation of the ^{14}N triazole integrated area with varying mass. $y = 29570x - 24713 R^2 = 0.9800$. Assuming no blank signal $y = 29061x$, $R^2 = 0.9797$.

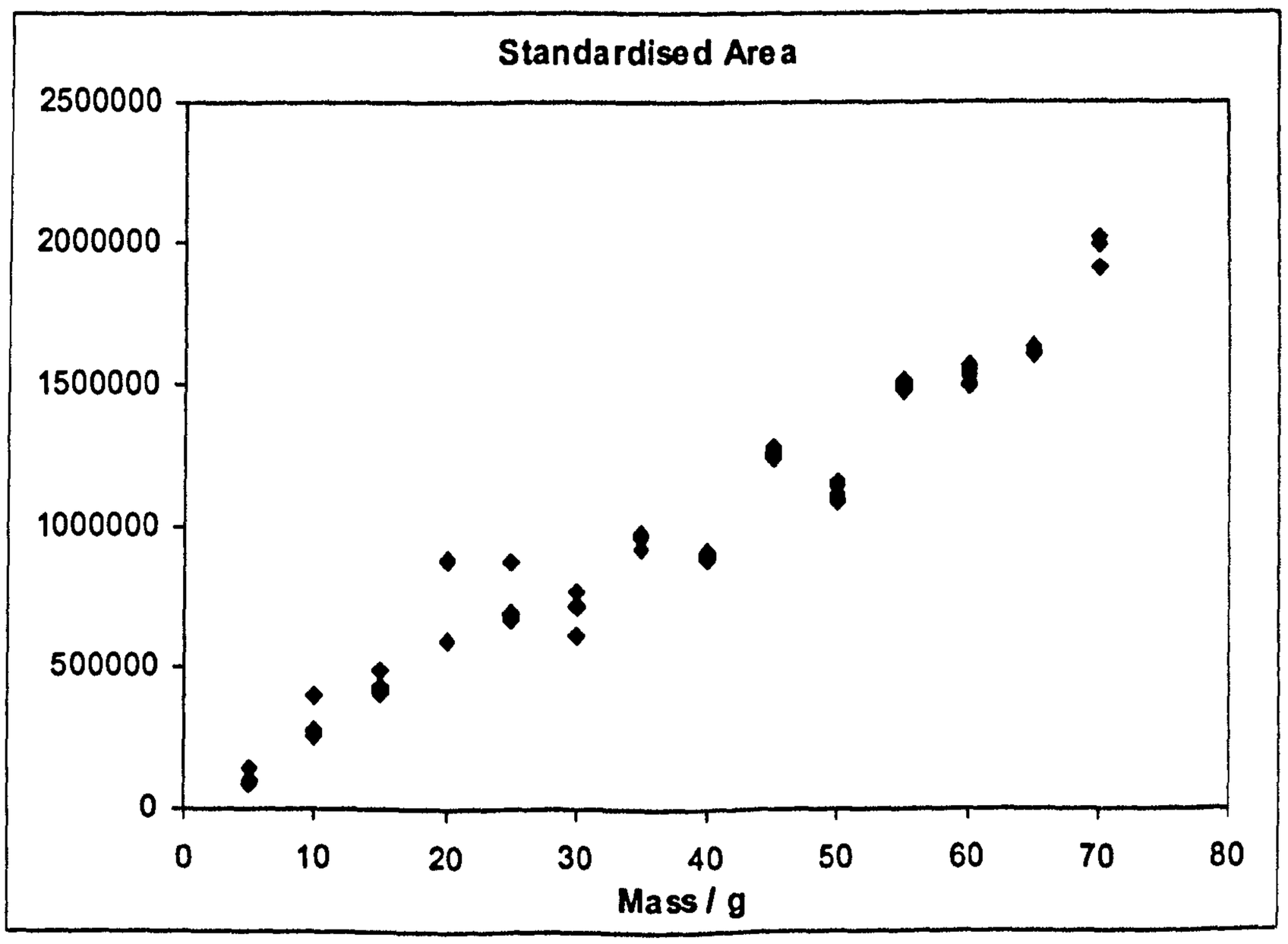

Figure 5.11: Variation of the ^{14}N triazole standardized integrated area with varying mass. $y = 25304x + 43993$, $R^2 = 0.9493$. Assuming no blank signal: $y = 26210x$, $R^2 = 0.9477$.

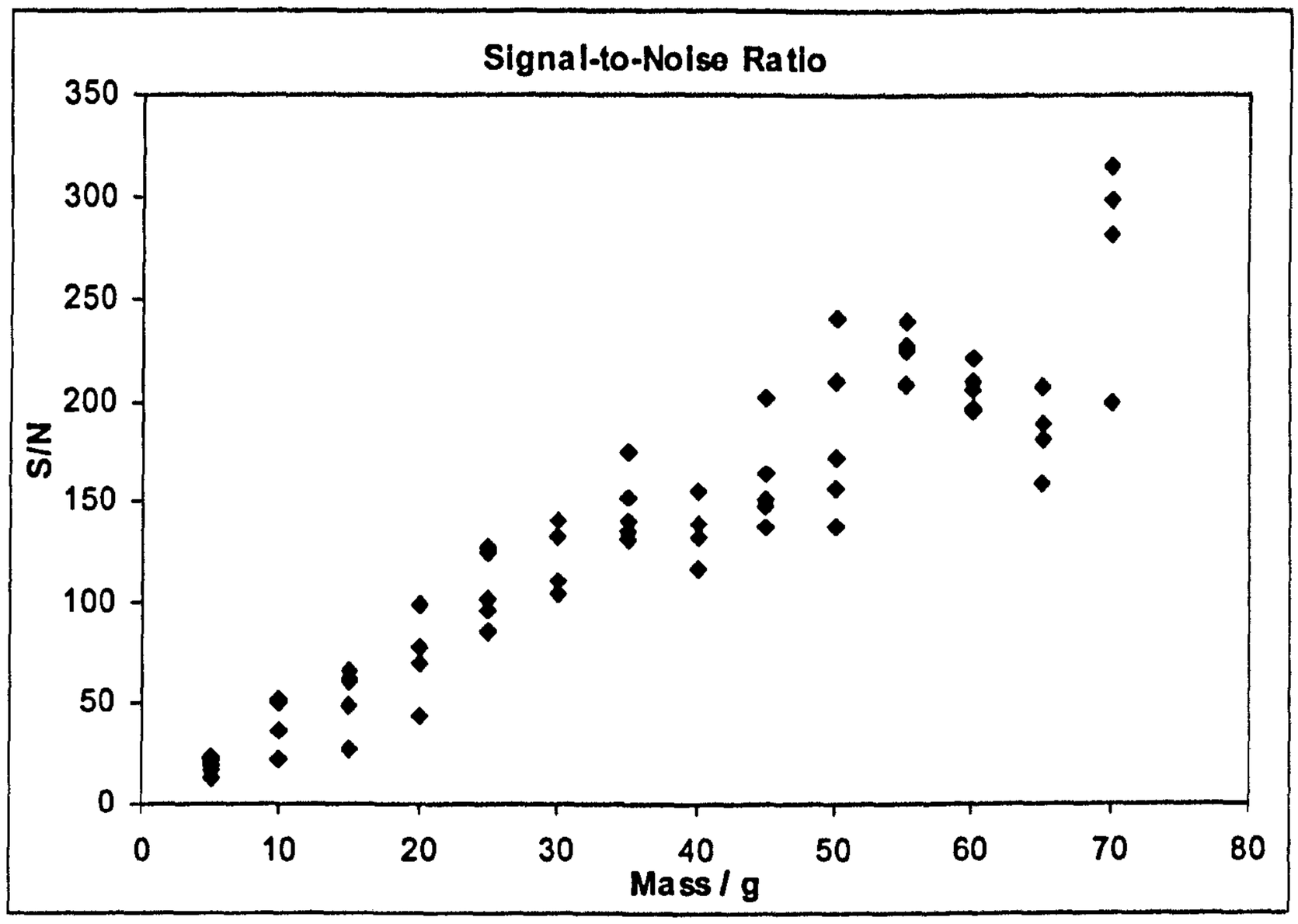

Figure 5.12: Variation of the ^{14}N triazole signal-to-noise ratio with varying mass.

Using Excel, least squares fits were applied to the data to give a straight line equation of the form

$$y = bx + a \tag{5.2}$$

(where in the above cases y is intensity and x is mass in grams) and the coefficients of determination, R^2, for both offset and non-offset assumptions. The errors of the intercept a and the gradient b were defined[13] as

$$S_a = S_{y/x}\left[\frac{\sum_{i=1}^{n} x_i^2}{n\sum_{i=1}^{n}(x_i - \bar{x})^2}\right]^{1/2} \tag{5.3}$$

$$S_b = \frac{S_{y/x}}{\left[\sum_{i=1}^{n}(x_i - \bar{x})^2\right]^{1/2}} \tag{5.4}$$

where the bar notation indicated the mean value of x and the residual standard deviation is defined as

$$S_{y/x} = \left[\frac{\sum_{i=1}^{n} (y_i - \hat{y}_i)^2}{n-2} \right]^{1/2} \tag{5.5}$$

where $\hat{y}_i$ are the fitted y values.

The confidence limits were calculated as

$$a \pm t.s_a \tag{5.6}$$

$$b \pm t.s_b \tag{5.7}$$

for the intercept and gradient respectively, where t is the two tailed t-distribution for 95 % confidence at n-2 degrees of freedom taken from statistics tables[14]. In the case of the gradient and intercept in these results $n = 70$, $t = 1.994$.

With all the same settings as previously a known mass of triazole (50 g) was placed in the probe, with 5 sets of data being collected. The mean y_0 values for FT peak intensity, standardized peak intensity, integrated area and standardized integrated area were recorded and the predicted mass, x_0, was calculated using the appropriate values of a and b. The error in x_0 is defined as follows[15,16]

$$S_{x_0} \cong \frac{S_{y/x}}{b} \left[\frac{1}{m} + \frac{1}{n} + \frac{(y_0 - \bar{y})^2}{b^2 \sum_i (x_i - \bar{x})^2} \right]^{1/2} \tag{5.8}$$

where m is the number of readings (in this case 5), with confidence limits

$$x_0 \pm t.S_{x0} \tag{5.9}$$

with a t value of 3.182. The same calculations were then carried out for a least squares fitting but with zero offset assumed.

Regression with an intercept	FT peak intensity	Standardised FT peak intensity	Integrated area	Standardised integrated area
Gradient	8370	7080	29570	25303
Standard deviation	215	274	515	714
Confidence interval	± 429	± 547	± 1028	± 1424
Intercept	8009	9216	-24713	43993
Standard deviation	9216	11737	22548	31244
Confidence interval	± 18377	± 23403	± 44961	± 62301
Confidence coefficient, r	0.9782	0.9526	0.9899	0.9743
y_0	398540	375851	1473077	1389215
Predicted mass x_0 / g	**46.66**	**48.78**	**50.65**	**53.16**
Standard deviation	2.00	3.03	1.38	2.25
Confidence interval	± 6.38	± 9.64	± 4.40	± 7.17

Table 5.5: Statistics relating to the quantification of triazole calculated assuming a regression with an intercept.

Regression through the origin	FT peak intensity	Standardised FT peak intensity	Integrated area	Standardised integrated area
Gradient	8539	7722	29061	26210
Standard deviation	217	288	539	765
Confidence interval	± 432	± 574	± 1074	± 1524
Confidence coefficient, *r*	0.9780	0.9475	0.9898	0.9735
y_0	398540	375851	1473077	1389215
Predicted mass x_0 / g	**46.68**	**48.67**	**49.76**	**53.00**
Standard deviation	1.98	2.91	1.44	3.23
Confidence interval	± 6.29	± 9.27	± 4.59	± 10.27

Table 5.6: Statistics relating to the quantification of triazole calculated assuming a zero offset (regression through the origin).

As foreseen, the integrated area has predicted the mass of triazole most closely and with smaller errors in both the offset and non-offset data sets. Unexpectedly, standardisation did not improve the errors in any case but did improve the predicted mass from the Fourier transformed peak intensity. A more useful standardization set up would be to have two thermostatted probes under the same conditions, attached to the same spectrometer, whereby a single standardization run could be performed before each quantitative measurement, instead of a number of runs before the whole set of standardization runs. If there is machine drift across the day, this is not currently picked up. A slight inflection in slope near a mass of 30 to 40 g is visible in figures 5.8 to 5.10, which may be due to the filling factor, as the 5 g packets were packed into the sample containers centrally along the length of the solenoid at first but above masses of 40 g the triazole packets were placed further towards the edges of the container. Use of a variable pitch solenoid should have minimised this affect by providing a more homogenous field.

Overall, the results are good for quantitative prediction, with errors of less than ± 5 % in both integrated area predictions, showing that the ^{14}N singlet FID signals at 3.787 MHz in triazole can be used to estimate quantity to within this error. Ensuring a true integrated area value by baseline correction and *Q*-damping to inhibit breakthrough are useful, and possibly essential, techniques. In cases, such as furosemide, where the signal is weaker or there is a doublet, further work must be carried out to see if similarly accurate quantitative analysis can be achieved.

The confidence limits of the intercepts in all cases show that it is acceptable for the line to regress through the origin, as would be expected in this analysis, where a zero mass should give a zero signal. The errors in the non-offset data were only slightly greater for the gradients than in the offset data, with the errors in predicted mass being slightly greater for the area values and slightly less for the Fourier transformed values.

Accuracy could be increased in a number of ways: increasing the number of calibration runs (*n*), the number of test runs (*m*) or simply the number of scans in each experiment would all give more accurate results but increase the time taken. Signal processing techniques and greater optimization of the pulse sequences could lessen the time taken to achieve signals with acceptable signal-to-noise ratios. Zero time resolution methods[17] could also produce even better results: their disadvantage is that their success relies on having suitable values for the relaxation times.

5.2.3 Mixed samples

Having demonstrated the ability to quantify samples of a single material, the next challenge was to see if similar results could be generated using mixed samples. A number of combinations of samples were looked into, with a view to finding a suitable system to which signal processing techniques could be applied. Ideally, the ^{14}N frequencies of each material should be in close proximity; the single frequency used to excite the samples would be placed at the midpoint between the two NQR frequencies. It is important that the nuclei in both samples experience the same field and receive similar amounts of energy for the work to allow quantitative analysis. The sinc function determines the range over which the RF pulse will be effective and the two NQR frequencies should lie at points of the same magnitude along either side of the function.

5.2.3.1 Sulfapyridine

Initially, a sulfapyridine combination was suggested as suitable for the work; it is a well-studied material with a number of ^{14}N NQR frequencies[18] across a range of polymorphs and solvates. The solvate form recrystallised from acetone, SPA, with one ^{14}N frequency at 2.895 MHz and the polymorph obtained from Sigma (which can also be recrystallised from ethanol), SPE, with one ^{14}N frequency at 2.923 MHz were suggested as suitable samples for a mixed-material investigation, with NQR frequencies in reasonable proximity to each other. Although a standard set up with the previously used solenoids would not cover such a frequency range, damping of the NQR coil with a 10 Ohm resistor allowed observation of frequencies up to 70 kHz greater or lesser than the incident central frequency, allowing up to a 140 kHz range to be studied.

Using SPA and SPE as the binary system would demonstrate the ability to observe two forms of one drug within a single RF frequency experiment but it was decided that although of interest, this combination would not be suitable as a model for quantitative work, due to the fairly rapid solvent loss and decomposition over time of the SPA polymorph making precise quantification impractical, particularly as the weak ^{14}N signals were being studied (a better choice would be the higher frequency and more sensitive ^{35}Cl NQR signals). As triazole is known to have strong FID signals at a number of frequencies (including those at around 3.793, 2.503, 2.405, 2.257 and 2.114[5,6,7,8]) and already shown to give a linear response, a second material with a ^{14}N frequency in close proximity needed to be found.

5.2.3.2 Histidine and triazole

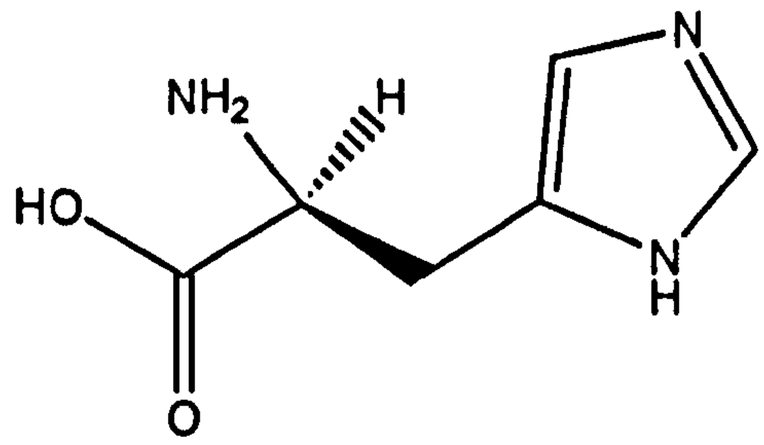

9

L-Histidine, an amino acid with reported ^{14}N NQR frequencies around 2.41 and 2.63 MHz at 77 K[19] was chosen as a potential partner to triazole for quantitative analysis. The lower frequency line of histidine was studied, together with a triazole ^{14}N signal around 2.40 MHz in order to see if a histidine/triazole mixed sample could be shown to give a linear response with respect to the mass of each material.

5.2.3.2.1 ^{14}N preliminary studies

An initial room temperature FID sequence was run to establish the triazole signal in the region using the pulse sequence as that in table 5.4. Approximately 80 g of triazole was irradiated at 2.400 MHz; a strong FID signal was obtained which on Fourier transformation showed a ^{14}N singlet peak at 2.402 MHz.

The same pulse sequence was used to study approximately 80 g of histidine (again at 2.400 MHz) but no signal was observed. A PSL sequence was then used (table 5.7) to produce the echo seen in figure 5.13. After Fourier transformation and baseline correction this yielded a singlet peak at 2.390 MHz (figure 5.14).

Event		
Pulse length / μs	70	(Phase 0202)
τ delay / μs	800	
Acquisition	128 points / 10 μs dwell	(Phase 0202)
Final delay / ms	4000	
No. of scans	15000	
Excitation frequency	2.400 MHz	

Table 5.7: PSL pulse sequence for preliminary studies of histidine.

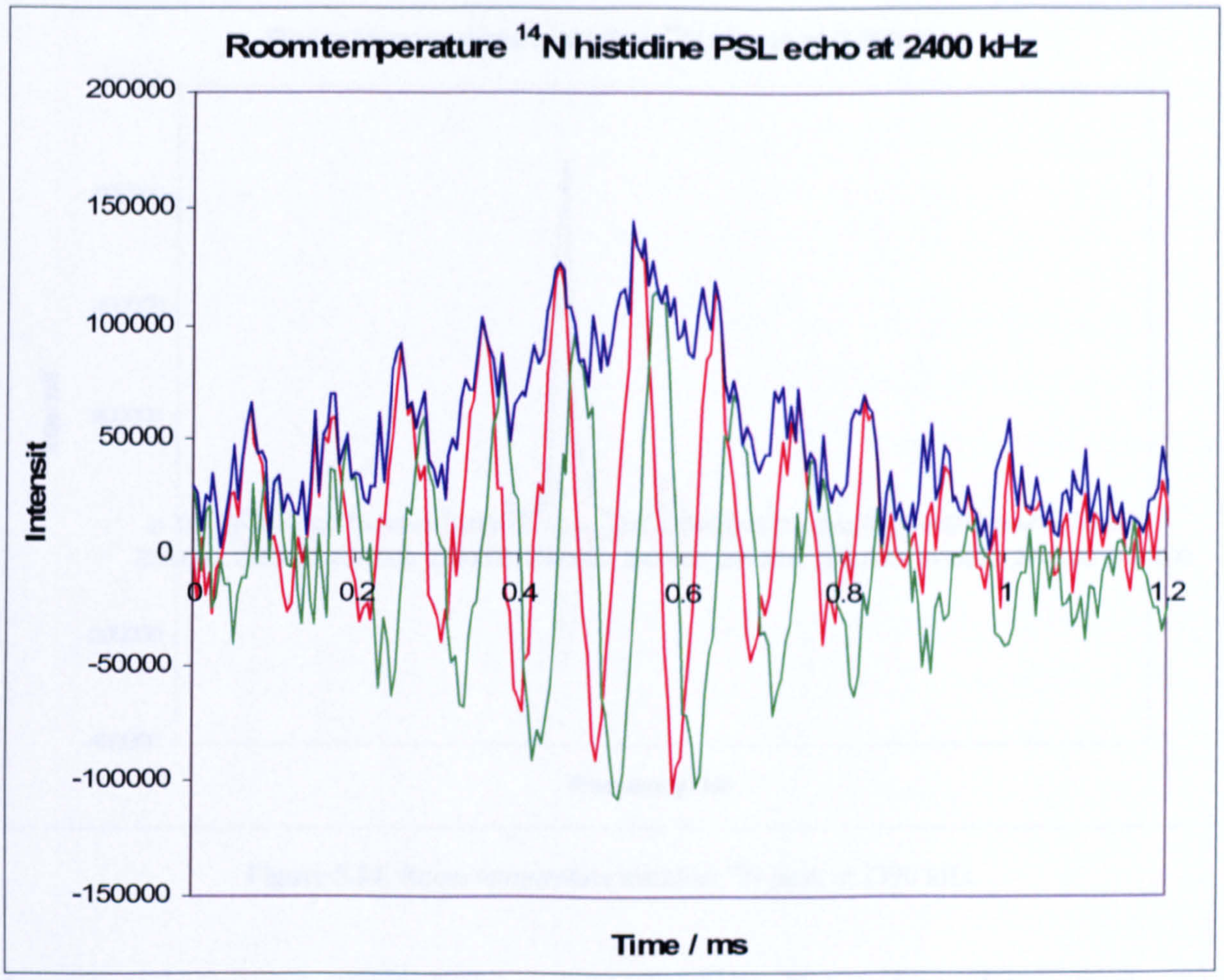

Figure 5.13: Room temperature histidine PSL ^{14}N echo at 2400 kHz.

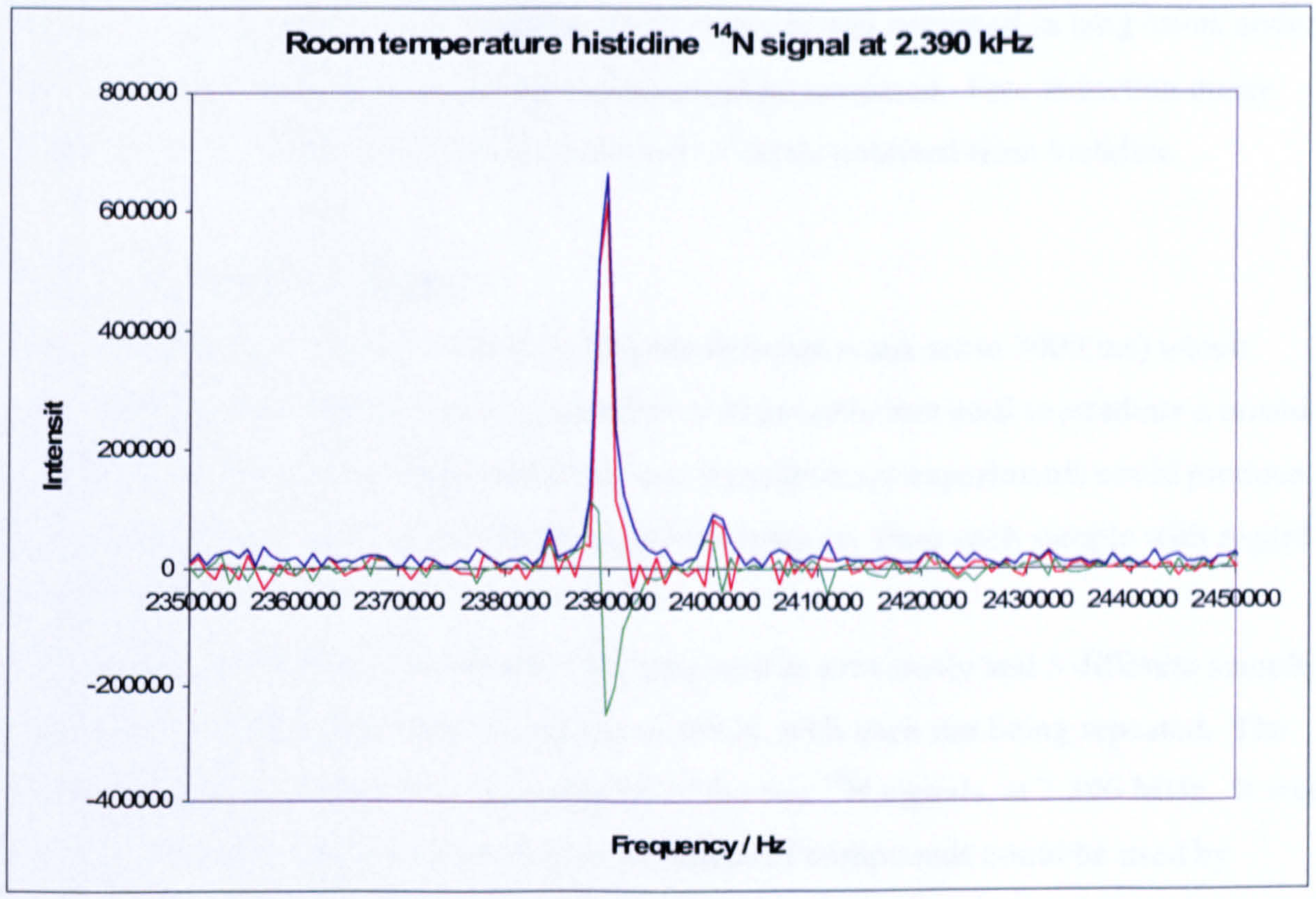

Figure 5.14: Room temperature histidine ^{14}N peak at 2390 kHz.

A steady state sequence (Table 5.8) was used to estimate T_1 in order to determine the recycle time between scans; the experiment which gave the best fit found T_1 to be 446.9 ± 38.8 ms.

Event		
90_{eff} Pulse / μs	70	(Phase 0202)
Acquisition	512 points / 5 μs dwell	(Phase 0202)
Dead time	Variable - 14 points from 1 to 3000 ms	
Final delay / ms	20	
No. of scans	5000	
Excitation frequency	2.400 MHz	

Table 5.8: Steady state sequence settings for determination of histidine T_1 value.

Using a PSL sequence echoes could be easily obtained and sustained in long trains under the conditions of table 5.7 at least 32 echoes could be sustained. Free induction decay signals with sufficient SNR however were not so easily obtained from histidine.

5.2.3.2.2 Quantitative studies

The PSL sequence (Table 5.7 except with time between scans set to 3000 ms) which successfully produced large peaks in histidine was nevertheless used to irradiate a mixed sample of triazole and histidine in order to see if preliminary experiments could produce a linear response in the Fourier transformed peak intensity from each sample with regard to their mass.

5 g packages of histidine and triazole were prepared as previously and 5 different sample combination experiments were carried out at 298 K, with each run being repeated. The excitation frequency was set to the midpoint of the two ^{14}N signals, at 2.396 MHz. It was hoped that the data recorded from this combination of compounds could be used by Samuel Somasundaram at King's College London in a modeling process. Signal processing using approximative maximum likelihood (AML) algorithms[20] (see chapter 8 for further details) has been shown to enhance NQR spectra in single material studies and it was hoped that the mixed system investigated here would be suitable for this method of modeling.

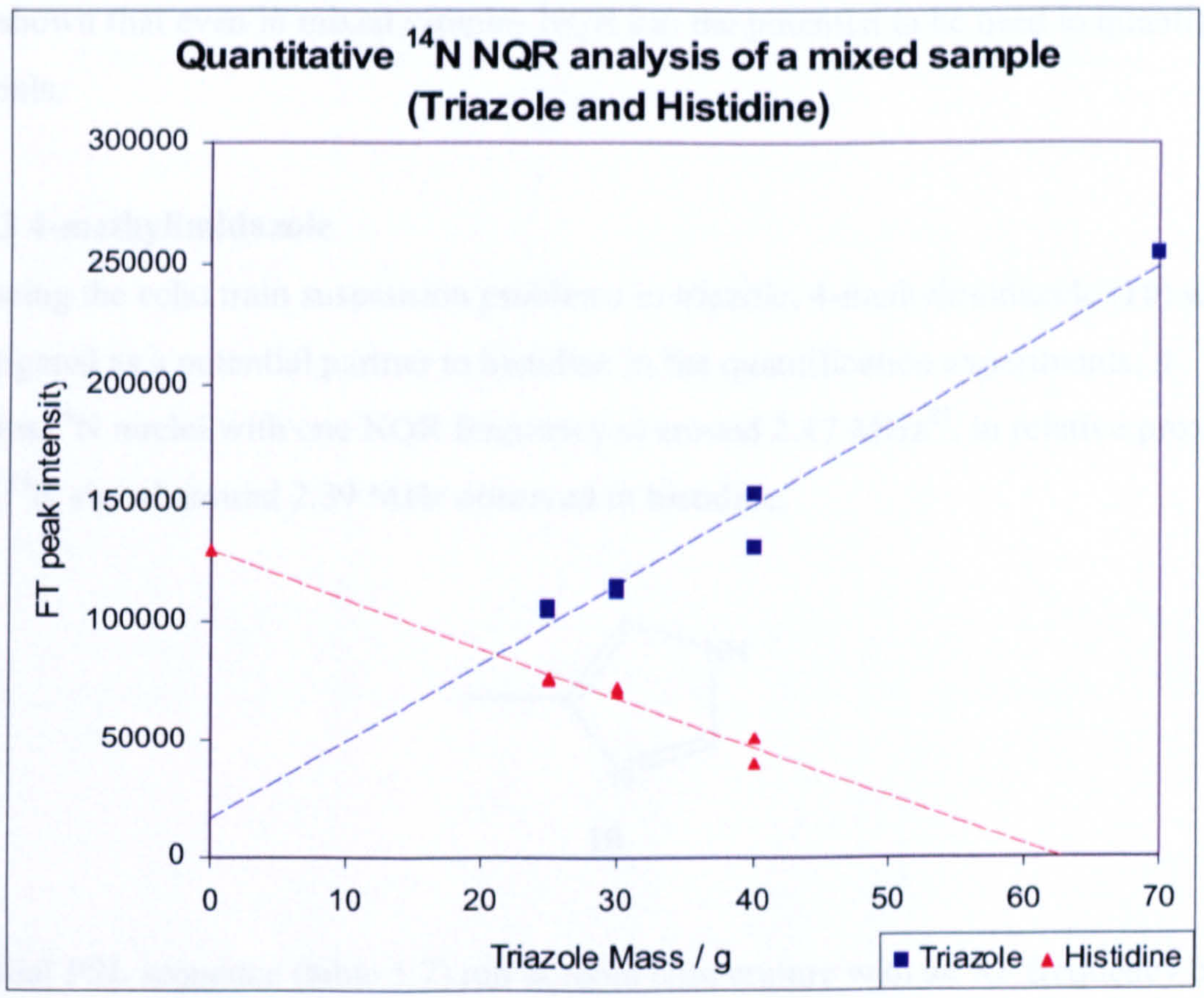

Figure 5.15: Peak intensities of the triazole and histidine ^{14}N peaks at 2.402 and 2.390 MHz respectively against varying mass of triazole; total mass = 70 g.

Plotting the Fourier transformed peak intensity against the triazole mass gave an approximately linear response from the small number of data points recorded. For both the triazole and histidine lines (fitted using least squares regression with Excel) there appears to be an offset. Further experimental combinations to give 7 to 10 points of the graph and possibly the plotting of the integrated area may give a more persuasive linear equation for prediction of mass with regard to the ^{14}N NQR signal. Although these initial results look quite promising (with some discrepancy in the 40 g triazole runs) they were not continued: triazole did not sustain an echo train effectively, as is required by the model which was potentially going to be used if the results were put through for signal processing and so another material was looked into which could meet the necessary conditions. However, this set of results could be expanded in future and the results analysed more thoroughly, as the earlier triazole quantitative experiments were, and they

have shown that even in mixed samples NQR has the potential to be used to quantify materials.

5.2.3.3 4-methylimidazole

Following the echo train suspension problems in triazole, 4-methylimidazole (**10**) was investigated as a potential partner to histidine in the quantification experiments; it contains ^{14}N nuclei with one NQR frequency at around 2.47 MHz[21], in relative proximity to the ^{14}N signal around 2.39 MHz observed in histidine.

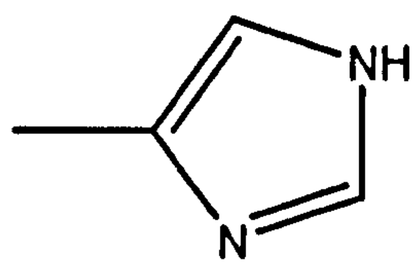

10

An initial PSL sequence (table 5.7) run at room temperature with an RF frequency of 2.470 MHz on approximately 50 g of 4-methylimidazole was found to yield an echo, with Fourier transformation producing a doublet signal with peaks at 2.467 and 2.469 MHz.

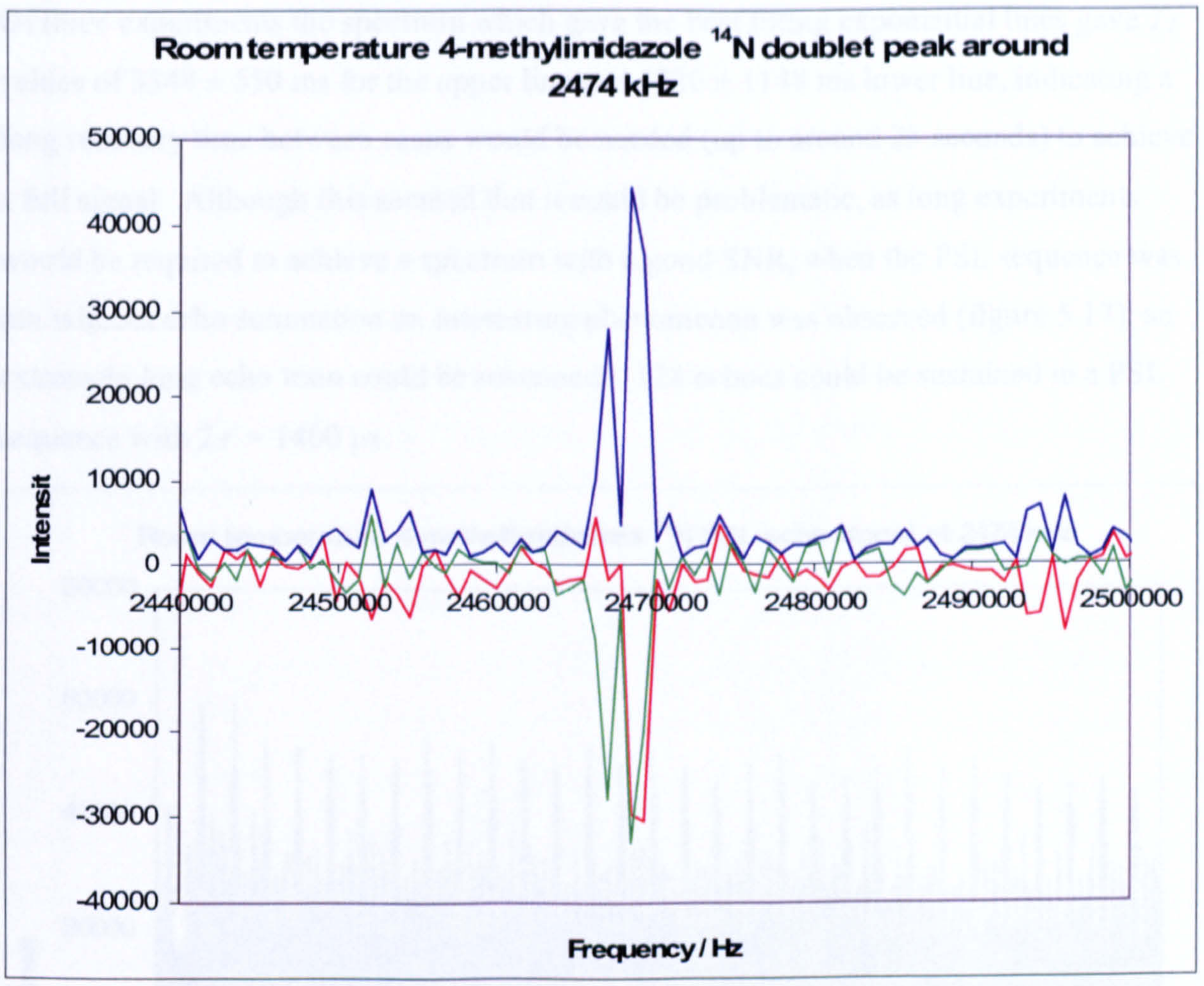

Figure 5.16: Room temperature 4-methylimidazole ^{14}N doublet peak (2.467 and 2.469 MHz).

An inversion recovery sequence was then run to estimate the value of the spin-lattice relaxation rate, in order to determine the recovery time necessary between scans.

Event		
90_{eff} Pulse / μs	80	(Phase 20)
Dead time	Variable - 14 points from 1 to 8000 ms	
Acquisition	128 points / 10 μs dwell	(Phase 0202)
Final delay / ms	8000	
No. of scans	750	
Excitation frequency	2.464 MHz	

Table 5.9: Inversion recovery pulse sequence settings used to find methylimidazole T_1 value.

Of three experiments the spectrum which gave the best fitting exponential lines gave T_1 values of 3348 ± 550 ms for the upper line and 4220 ± 1148 ms lower line, indicating a long recovery time between scans would be needed (up to around 25 seconds) to achieve a full signal. Although this seemed that it could be problematic, as long experiments would be required to achieve a spectrum with a good SNR, when the PSL sequence was run without echo summation an interesting phenomenon was observed (figure 5.17); an extremely long echo train could be sustained – 128 echoes could be sustained in a PSL sequence with 2τ = 1400 μs.

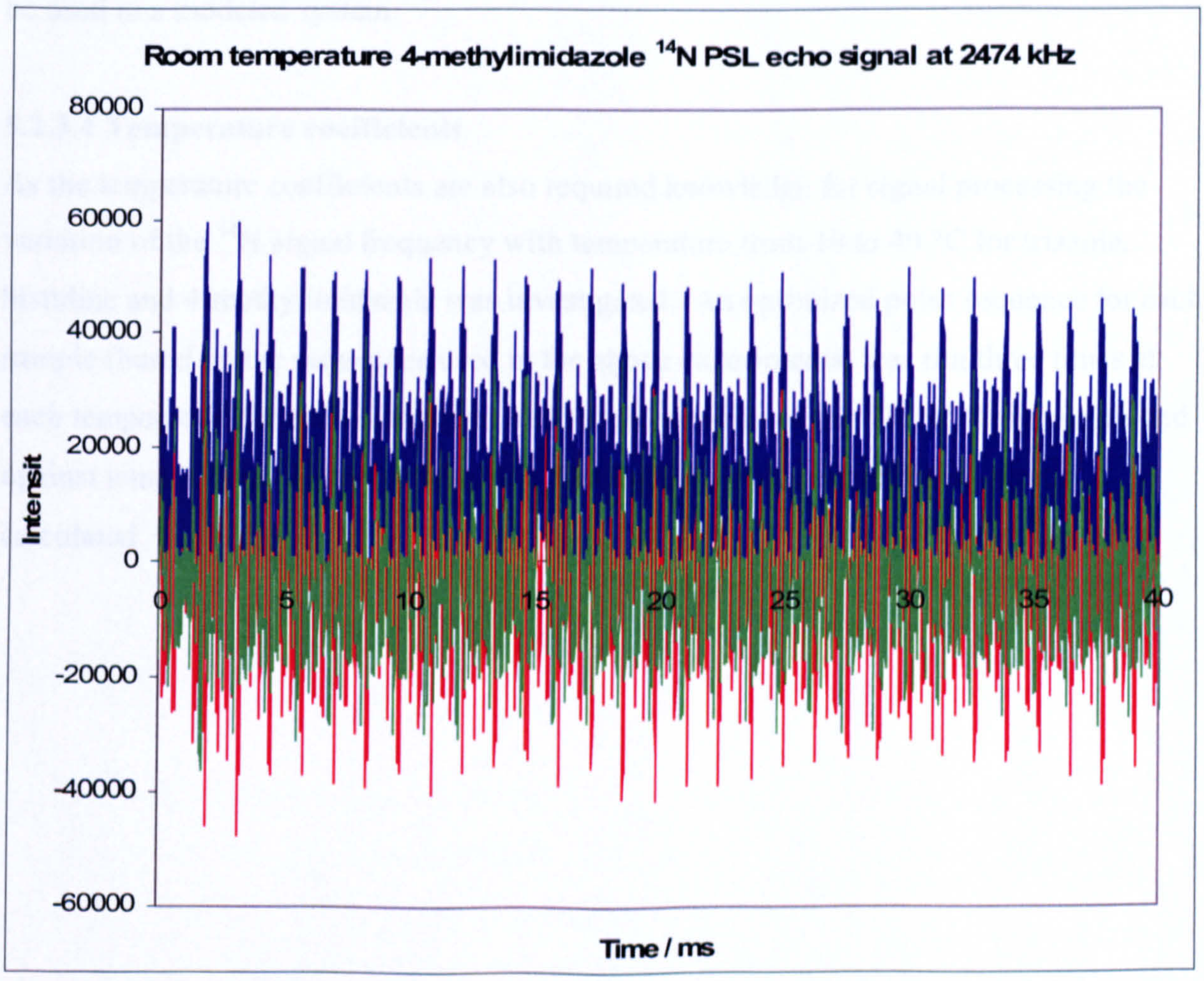

Figure 5.17: Room temperature 4-methylimidazole ^{14}N echo train;
32 echoes at 2474 kHz with 2τ = 1400 μs.

This is a feature which has been observed previously using echo sequences in the study of sodium nitrite[22]; summing of echoes in a PSL echo train is particularly useful in cases of materials that have a long spin-lattice relaxation rate as the need to wait $5T_1$ for

recovery is lessened as the signal is built up via summation. In mixed samples it is beneficial but the extent is somewhat dependent of the NQR characteristics of the other sample present in the combination. Although 4-methylimidazole has a somewhat lengthy spin lattice relaxation rate, it's ability to sustain echo trains and the NQR frequency in close proximity to that of histidine mean that there is potential for use of a histidine/4-methylimidazole mixed sample set of experiments using AML algorithms in signal processing. Having established the frequencies, recovery times and echo characteristics, the variation of frequency with temperature was also required if the combination was to be used in a modeled system.

5.2.3.4 Temperature coefficients

As the temperature coefficients are also required knowledge for signal processing the variation of the ^{14}N signal frequency with temperature from 10 to 40 °C for triazole, histidine and 4-methylimidazole was investigated. An optimized pulse sequence for each sample (based on the sequences used in the above experiments) was run three times at each temperature for each compound and the frequencies of the ^{14}N NQR signals plotted against temperature. From the resulting data the temperature coefficients were calculated.

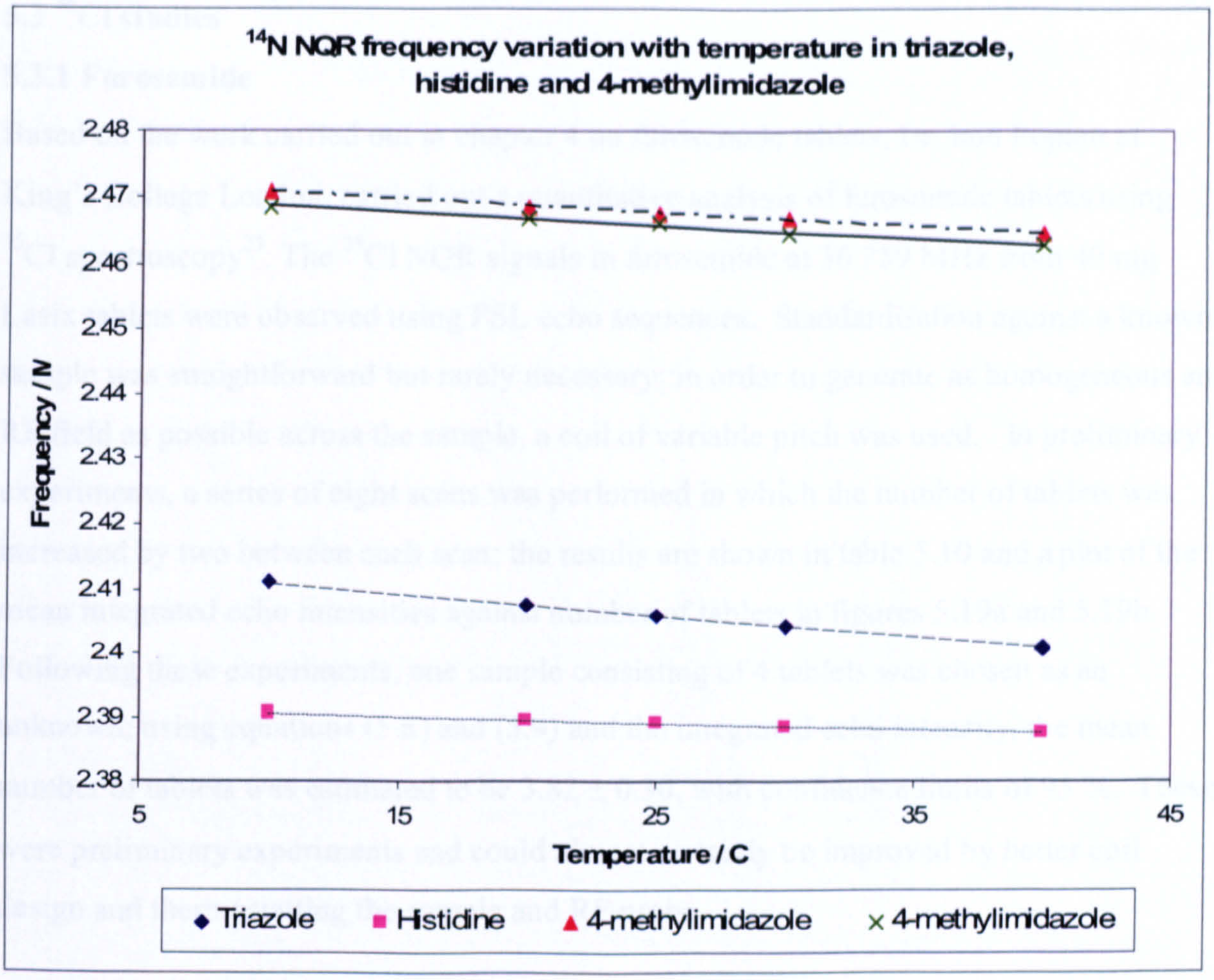

Figure 5.18: Frequency variation with temperature from 10 to 40 °C for ^{14}N signals in triazole, histidine and 4-methylimidazole.

A least squares fit using the Excel program gave linear equations of

$y = -3.37*10^{-4}x + 2.41$ (triazole)

$y = -1.01*10\text{-}^{4}x + 2.39$ (histidine)

$y = -2.06*10^{-4}x + 2.47$ (4-methylimidazole upper line)

$y = -1.91*10^{-4}x + 2.47$ (4-methylimidazole lower line).

from which temperature coefficients of each peak can be seen as the gradient value. These were recorded for future use in signal processing algorithms.

5.3 ^{35}Cl studies

5.3.1 Furosemide

Based on the work carried out in chapter 4 on furosemide tablets, Dr. Iain Poplett at King's College London, carried out a quantitative analysis of furosemide tablets using ^{35}Cl spectroscopy[23]. The ^{35}Cl NQR signals in furosemide at 36.759 MHz from 40 mg Lasix tablets were observed using PSL echo sequences. Standardisation against a known sample was straightforward but rarely necessary; in order to generate as homogeneous an RF field as possible across the sample, a coil of variable pitch was used. In preliminary experiments, a series of eight scans was performed in which the number of tablets was increased by two between each scan; the results are shown in table 5.10 and a plot of the mean integrated echo intensities against number of tablets in figures 5.19a and 5.19b. Following these experiments, one sample consisting of 4 tablets was chosen as an unknown; using equations (5.8) and (5.9) and the integrated echo intensity, the mean number of tablets was estimated to be 3.82 ± 0.30, with confidence limits of 95 %. These were preliminary experiments and could almost certainly be improved by better coil design and thermostatting the sample and RF probe.

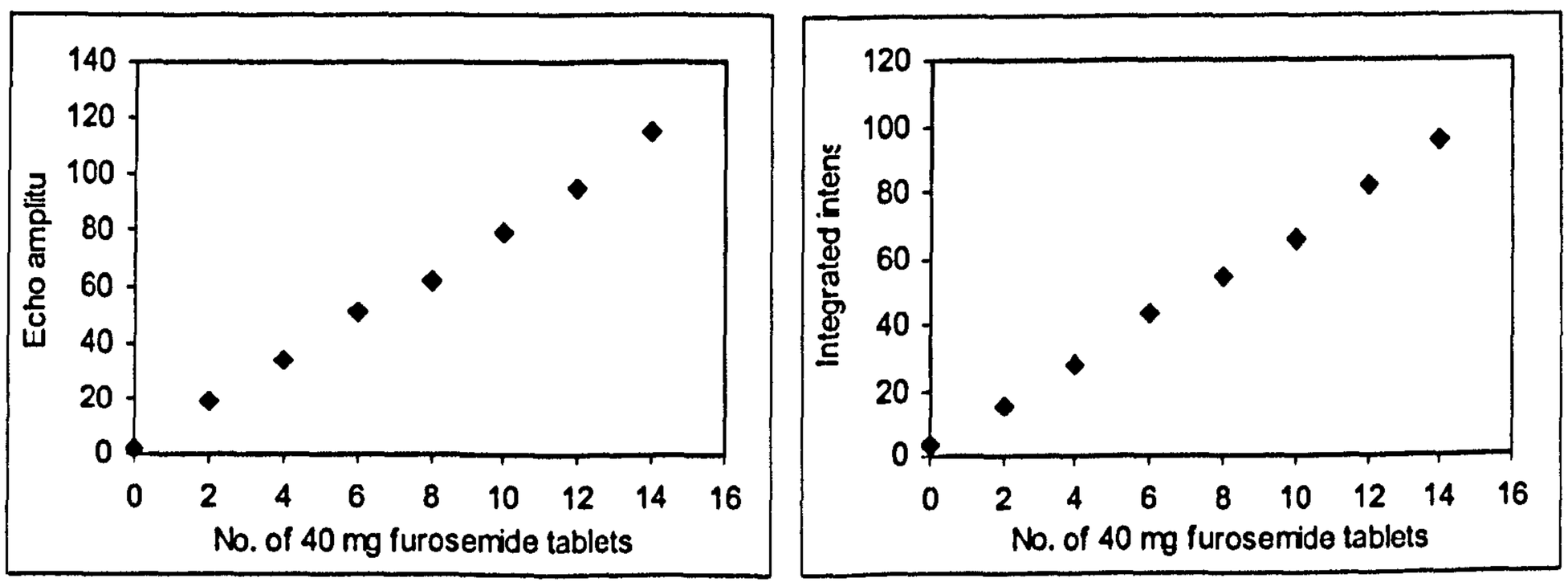

Figure 5.19a and 5.19b. Variation of the ^{35}Cl signal intensity in furosemide from different numbers of 40 mg tablets; in (a) echo amplitude is plotted against the number of tablets, in (b) the integrated intensity is plotted on the *y* axis.

No. of 40 mg tablets	Mean echo amplitude	Mean integrated intensity	Mean SNR
0	1.9	3.6	1.7
2	18.9	15.6	4.3
4	33.9	27.8	8.5
6	51.2	43.4	12.2
8	62.3	54.3	10.8
10	78.9	65.4	14.7
12	95.1	81.6	19.6
14	115.0	95.5	24.0

Table 5.10: Measurements obtained in quantitative analysis of furosemide tablets using ^{35}Cl NQR.

5.4 Summary

We have demonstrated that NQR can be used to quantify powder and tablets by using both ^{14}N and ^{35}Cl detection with estimation of mass within reasonable errors. The triazole ^{14}N experimental results underwent a vigorous analysis, and the ability to estimate mass from signal response was demonstrated and shown to have reasonable errors. Dr. Iain Poplett's work showed that similarly, the number of tablets within a solenoid could be estimated from the ^{35}Cl signal integrated echo intensity. The quantification of tablets within a bottle or packet would be of particular interest in the pharmaceutical industry in the area of quality control in bottling tablets. Single material studies have shown that linear responses with regard to mass can be achieved using both free induction decays and pulse spin locked echo signals under suitable conditions, with *Q*-damping and the use of a solenoid of variable pitch being important instrumental inclusions in the experiments. The foundations have been set for work with signal processing algorithms which could bring shorter experimental times and smaller errors in estimation.

5.5 References

[1] Bugay, D.E.; Newman, A. W.; Findlay, W. P. *J. Pharm. Biomed. Anal.*, **1995**, *15*, 49 - 61.

[2] Harris, R. K.; Kenwright, A. M.; Say, B. J.; Yeung, R. R.; Fletton, R. A.: Lancaster, R. W.; Hardgrove Jr., G. L. *Spectrochem. Acta*, **1990**, *46A*, 927 - 935.

[3] Schultz, H. D.; Karr, C. *Anal. Chem.* **1969**, *41*, 661 - 664.

[4] Hacobian, S. *Aust. J. Chem.* **1962**, *15*, 21 - 33.

[5] Perez, S.C.; Cerioni, L.; Wolfenson, A. E.; Faudone, S.; Cuffini, S. L., *Int. J. Pharm.*, **2005**, *298*, 143 - 152.

[6] Palmer, M. H.; Stephenson D.; Smith, J. A. S. *Chem. Phys.*, **1985**, *97*, *1*, 103 - 111.

[7] Schempp, E.; Bray, P. J., *Phys. Lett. A*, **1967**, *25, 6*, 414 - 415.

[8] Guibe, L.; Lucken, E. A. C., *Mol. Phys.*, **1968**, *14*, *1*, 73 - 77.

[9] Stephenson, D.; Smith, J. A. S., *Proc. Roy. Soc. London A*, **1988**, *416*, 149 - 178.

[10] Freeman, R. *A Handbook of Nuclear Magnetic Resonance*, 2nd Edition. Addison Wesley Longman Ltd, **1997**, pp 116 – 117.

[11] *Modern NMR Spectroscopy, 2nd Edition*, Sanders & Hunter, Oxford University Press, **1993**, pp 45 - 46.

[12] Kemp, W. *NMR in Chemistry: A Multinuclear Introduction*, Macmillan, **1986**, pp 27 - 28.

[13] Miller, J. N. *Spectroscopy International*, **1991**, *3*, 45 - 47.

[14] *Statistical Methods For Engineers and Scientists 3rd Edition*. Betrea, R.M.; Boullion, T. L.; Duran, B. S. Marcel Dekker, **1995**.

[15] Adams, M. J. *Chemometrics in Analytical Spectroscopy*, The Royal Society of Chemistry, **1995**, pp 155 - 163.

[16] Miller, J. N. *Spectroscopy International*, **1994**, *4*, 41 - 43.

[17] Singh, M. A.; Armstrong, R. L. *J. Magn. Reson.*, **1988**, *78*, 538 - 554.

[18] Subbarao, S. N.; Bray, P. J. *Org. Magn. Reson.* **1981**, *15*, 307 - 310.

[19] Hunt, M. J.; Mackay, A. L.; Edmonds, D. T., *Chem. Phys. Lett.*, **1975**, *34, 3*, 473 - 475.

[20] Somasundaram, S.; Jaokbsson, A.; Smith, J. A. S.; Althoefer, K. A. *SPIE Proc.*, **2006**, *6217*, pp 62172D.

[21] Garcia, M. L. S.; Smith, J. A. S.; Bavin, P. M. G.; Banellin, C. R., *J. Chem. Soc., Perkin Trans 2*, **1983**, 9, 1391 - 1399.

[22] Rudakov, T.N.; Belyakov, A. V. *J. Phys.D: Appl. Phys.* **1998**, *31*, 1251 - 1256.

[23] Balchin, E.; Malcolme-Lawes, D. J.; Poplett, I. J. F.; Rowe, M. D.; Smith, J. A. S.; Pearce, G. E. S.; Wren, S. A. C. *Anal. Chem.* **2005**, *77*, 3925 - 3930.

6 ^{14}N quadrupole resonance in other compounds

6.1 Chloroquine diphosphate

Chloroquine diphosphate (protonated at the amine nitrogens) (11) is primarily used as an anti-malarial treatment; it exhibits polymorphism[1] and this characteristic has been studied using the 'standard' methods of DSC, TA, IR, XRPD and electron microscopy. It is a pharmaceutically well studied compound and is of interest in this work because it contains four quadrupolar sites, which gives it great potential for use as a candidate for the study of transitional behaviour and polymorphic effects by both ^{14}N and ^{35}Cl NQR analysis. Work was carried out on a sample of chloroquine diphosphate in the hope of establishing one or some of its NQR frequencies.

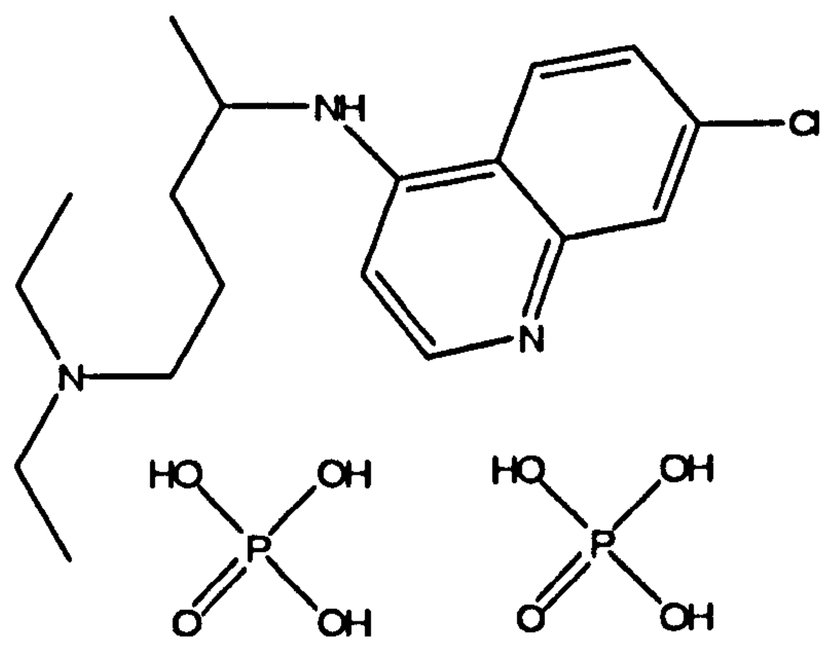

11

6.1.1 ^{14}N studies

Using the standard ^{14}N experimental apparatus room temperature frequency searching was begun. An NQR solenoid consisting of 35 turns, length 7 cm, diameter 5.5 cm, made previously by Dr. Michael Rowe, with an inductance of 46 μH was placed into the temperature controlled probe but with no oil flow through (see chapter 3). A simple FID pulse sequence was used with the settings below to search for the room temperature ^{14}N signals from the protonated amine groups between 1.000 and 1.100 MHz (this frequency range was selected based on work that found diethyl ammonium chloride and dimethyl ammonium chloride to have protonated ^{14}N frequencies at 1.0395 and 1.250 MHz respectively[2]:

Event		
Pulse / μs	60	(Phase 20)
Acquisition	512 points / 10 μs dwell	(Phase 02)
Final delay / ms	1000	
No. of scans	50000	
Excitation frequency	1.000 to 1.100 in 10 kHz steps	

Table 6.1: FID pulse sequence settings in searching for chloroquine signal.

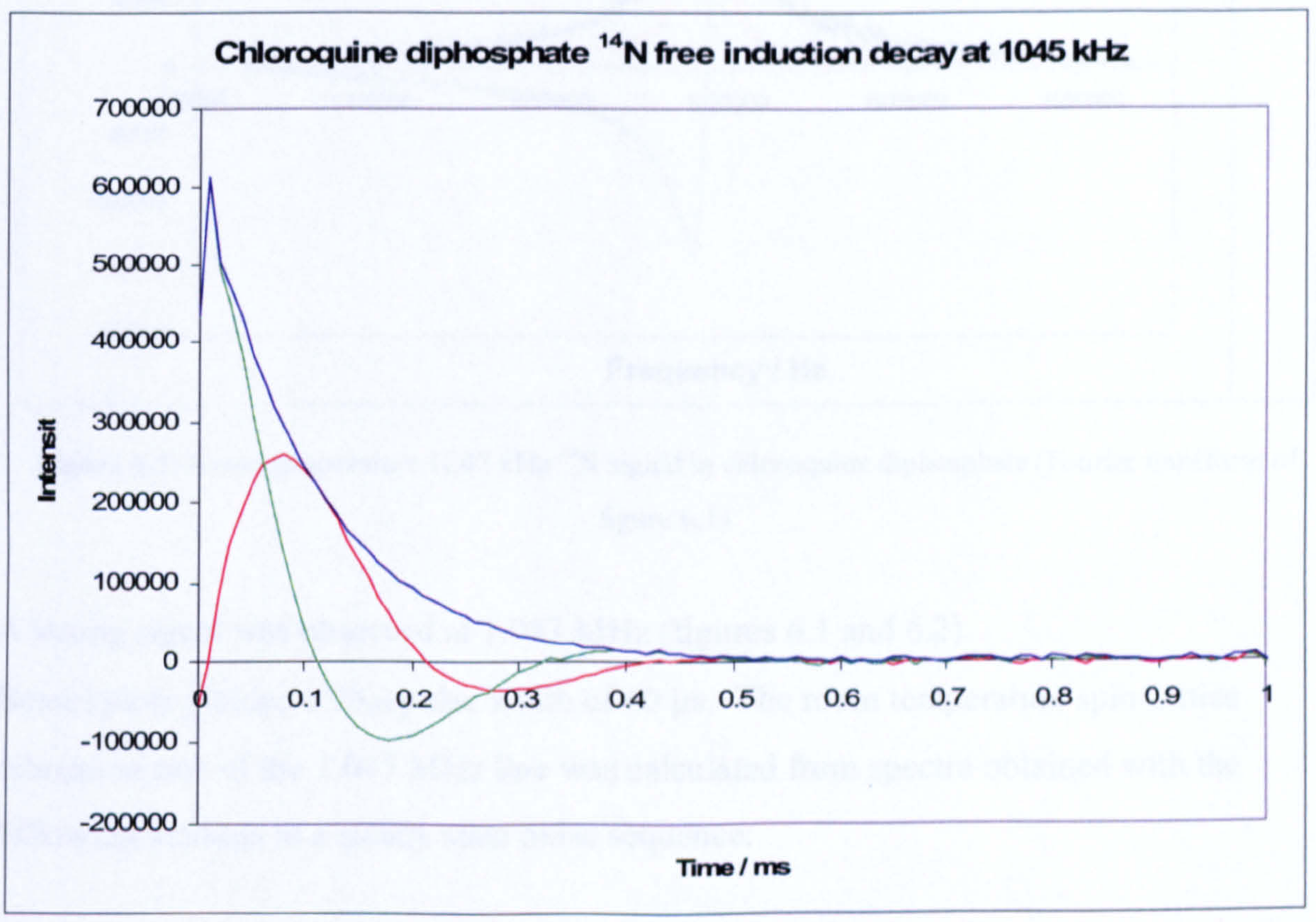

Figure 6.1: Room temperature ^{14}N free induction decay in chloroquine diphosphate following irradiation at 1045 kHz.

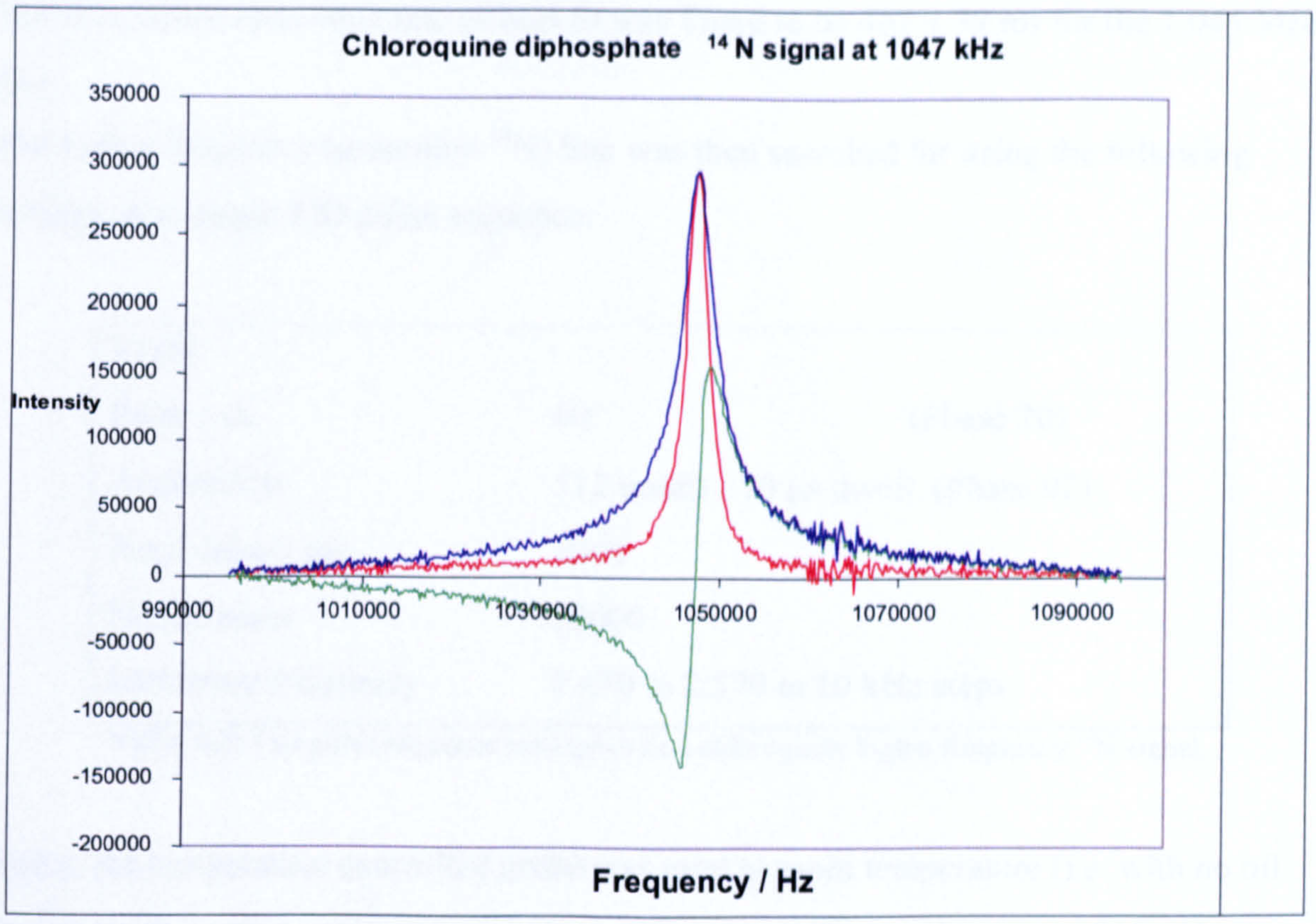

Figure 6.2: Room temperature 1047 kHz ^{14}N signal in chloroquine diphosphate (Fourier transform of figure 6.1).

A strong signal was observed at 1.047 MHz (figures 6.1 and 6.2).

Bessel plots yielded a 90_{eff} pulse width of 60 μs. The room temperature spin-lattice relaxation rate of the 1.047 MHz line was calculated from spectra obtained with the following settings in a steady state pulse sequence:

Event		
90eff Pulse / μs	60	(Phase 0202)
Acquisition	512 points / 5 μs dwell	(Phase 0202)
Dead time / μs	Variable - 14 points from 1 to 2500 ms	
Final delay / ms	20	
No. of scans	12000	
Excitation frequency	1.045 MHz	

Table 6.2: Steady state pulse sequence settings to determine chloroquine T_1 value.

The spin lattice relaxation rate of best fit was found to be 467 ± 79 ms for the 1.045 MHz line.

The higher frequency (quinoline ^{14}N) line was then searched for using the following settings in a simple FID pulse sequence:

Event		
Pulse / μs	60	(Phase 20)
Acquisition	512 points / 10 μs dwell	(Phase 02)
Final delay / ms	1000	
No. of scans	50000	
Excitation frequency	2.470 to 2.570 in 10 kHz steps	

Table 6.3: FID pulse sequence settings to find chloroquine higher frequency ^{14}N signal.

Again, the temperature controlled probe was used at room temperature (i.e. with no oil flow through) with a solenoid consisting of 24 turns, with an inductance of 19 μH.

Following the observation of a very weak FID signal around 2.530 MHz, a PSL sequence with the following settings was run.

Event		
90_{eff} pulse length / μs	130	(Phase 0202)
τ delay / μs	580	
Acquisition	128 points / 10 μs dwell	(Phase 0202)
Final delay / ms	1000	
No. of scans	15000	
Excitation frequency	2.540 MHz	

Table 6.4: PSL sequence settings to observe chloroquine higher frequency ^{14}N signal.

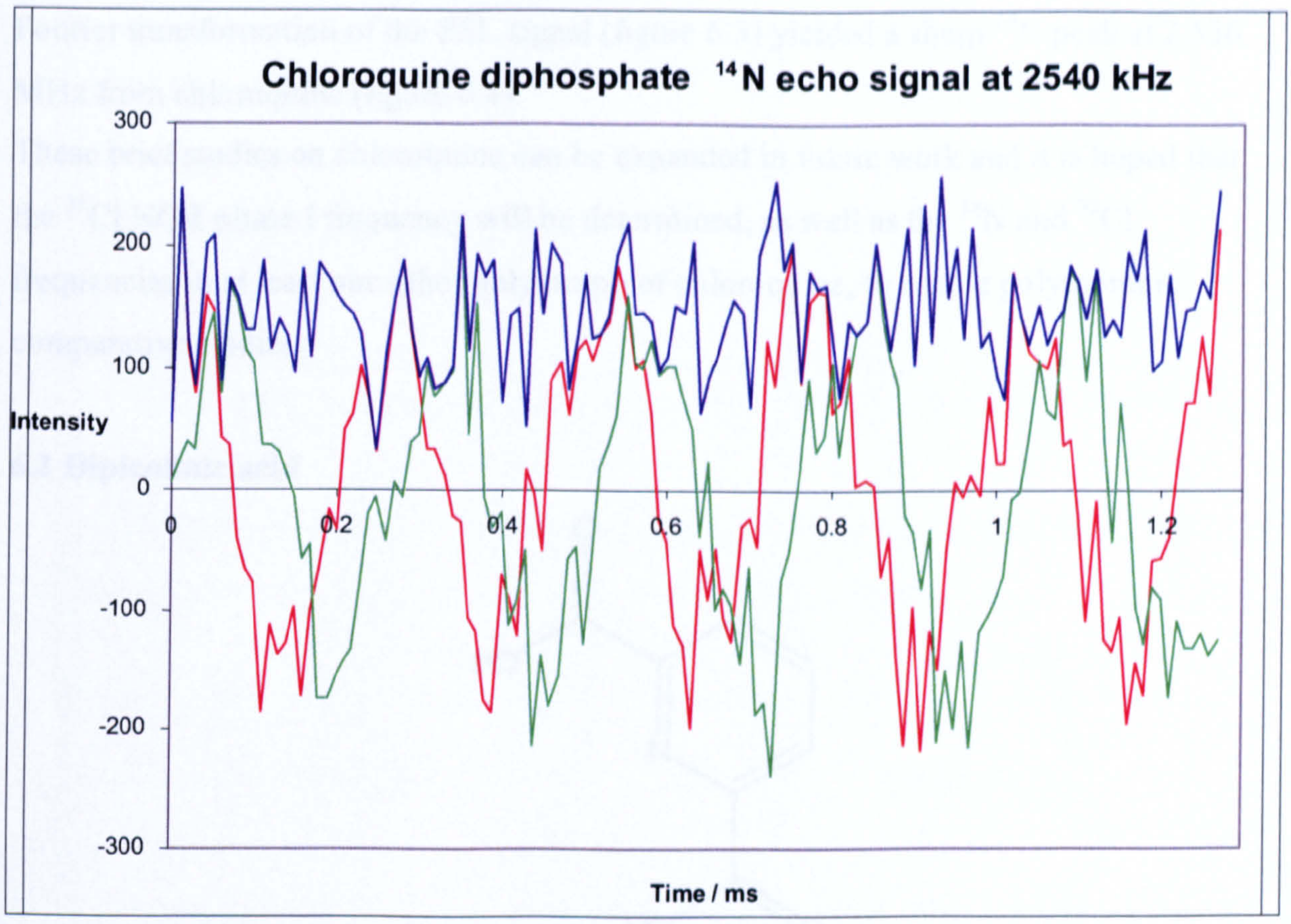

Figure 6.3: Room temperature ^{14}N PSL single summed echo in chloroquine diphosphate following irradiation at 2540 kHz.

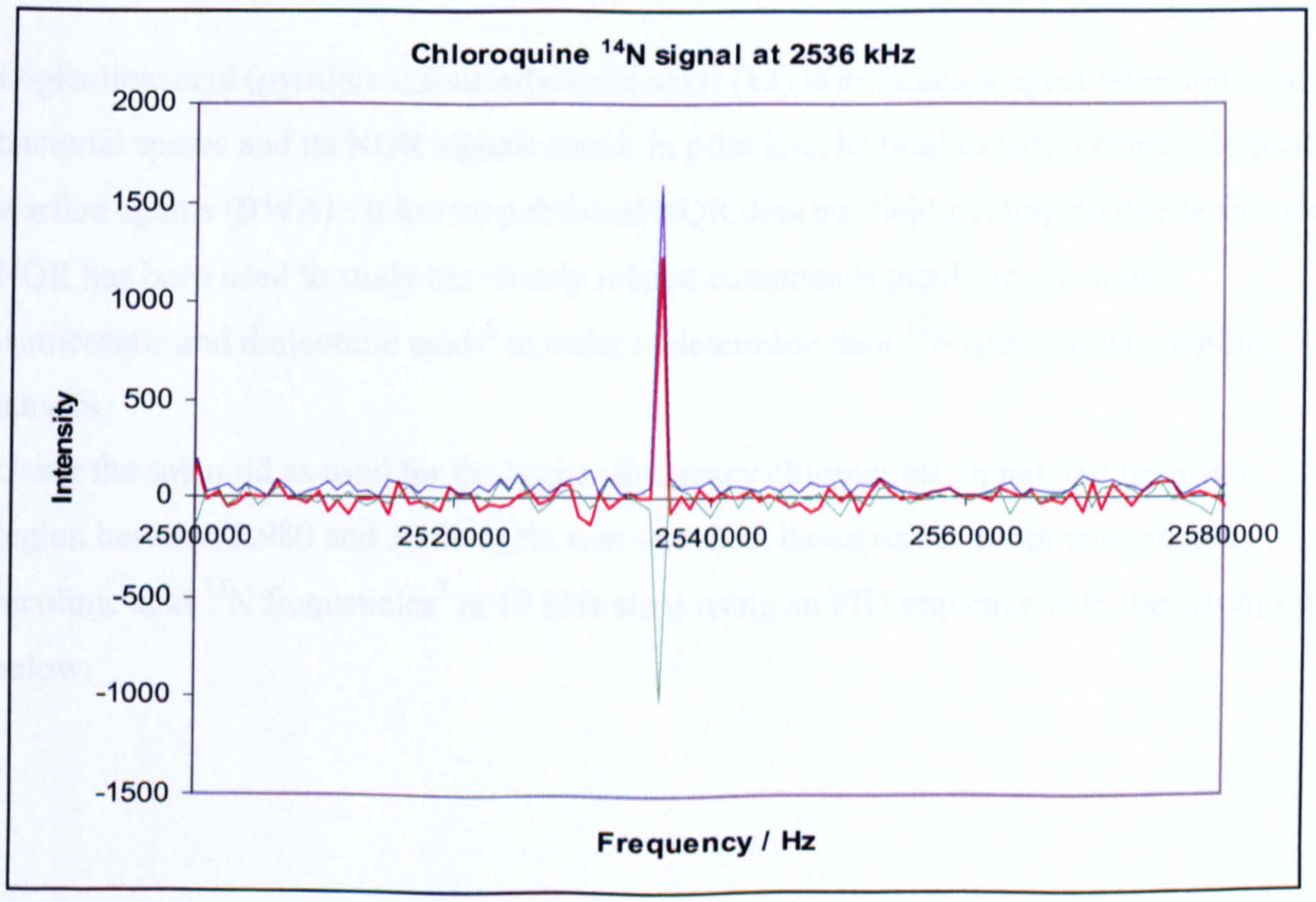

Figure 6.4: Room temperature ^{14}N Fourier transformed chloroquine diphosphate signal at 2536 kHz.

Fourier transformation of the PSL signal (figure 6.3) yielded a sharp ^{14}N peak at 2.536 MHz from chloroquine (figure 6.4).

These brief studies on chloroquine can be expanded in future work and it is hoped that the ^{35}Cl NQR phase I frequency will be determined, as well as the ^{14}N and ^{35}Cl frequencies in at least one other polymorph of chloroquine, to enable polymorphic comparative studies.

6.2 Dipicolinic acid

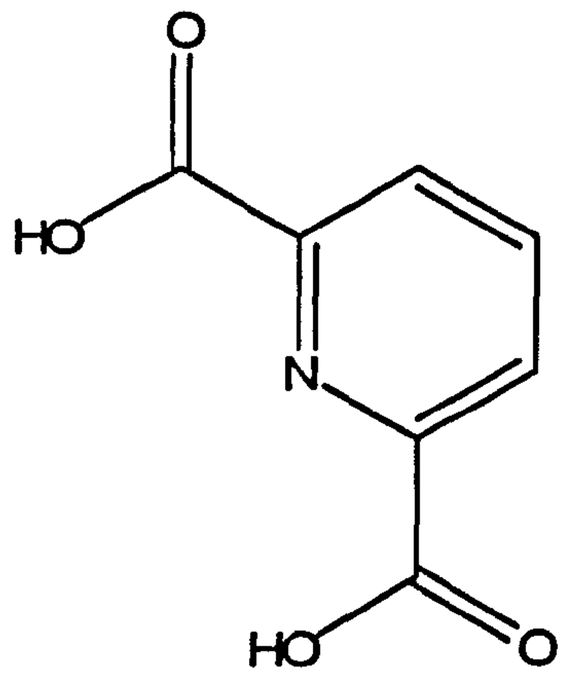

12

Dipicolinic acid (pyridine-2,6-dicarboxylic acid) (**12**) is a chelating agent often found in bacterial spores and its NQR signals could, in principle, be used to detect bacteriological warfare agents (BWA). It has no published NQR data but field-cycling double resonance NQR has been used to study the closely related compounds picolinic, nicotinic, isonicotinic and dinicotinic acids[3] in order to determine their ^{14}N quadrupole coupling tensors.

Using the solenoid as used for the higher frequency chloroquine signal, the frequency region between 2.980 and 3.160 MHz was searched, based on the room temperature picolinic acid ^{14}N frequencies[3] in 10 kHz steps using an FID sequence with the settings as below:

Event		
Pulse / μs	60	(Phase 20)
Acquisition	512 points / 10 μs dwell	(Phase 02)
Final delay / ms	1000	
No. of scans	50000	
Excitation frequency	2.980 to 3.160 in 10 kHz steps	

Table 6.5: FID sequence settings to observe dipicolinic acid ^{14}N signal.

A signal was observed around 3.145 MHz but it appeared to have a rather fast decay time leading to a PSL sequence to be used with the following settings:

Event		
90_{eff} pulse length / μs	80	(Phase 0202)
τ delay / μs	3000	
Acquisition	512 points / 10 μs dwell	(Phase 0202)
Final delay / ms	6000	
No. of scans	5000	
Excitation frequency	3.145 MHz	

Table 6.6: PSL sequence settings to observe dipicolinic acid ^{14}N signal.

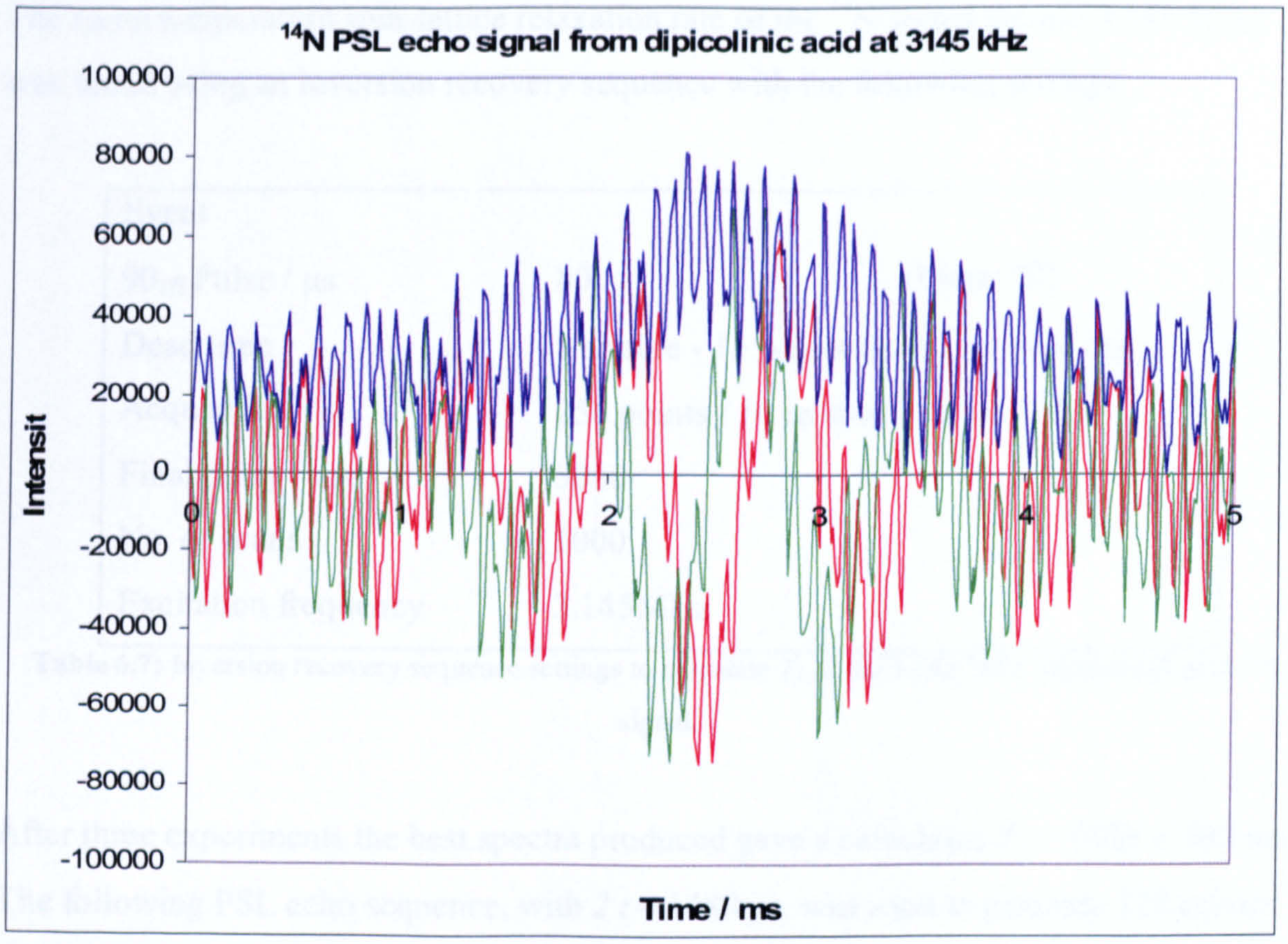

Figure 6.5: Dipicolinic acid ^{14}N signal; 32 summed PSL echoes at 3145 kHz.

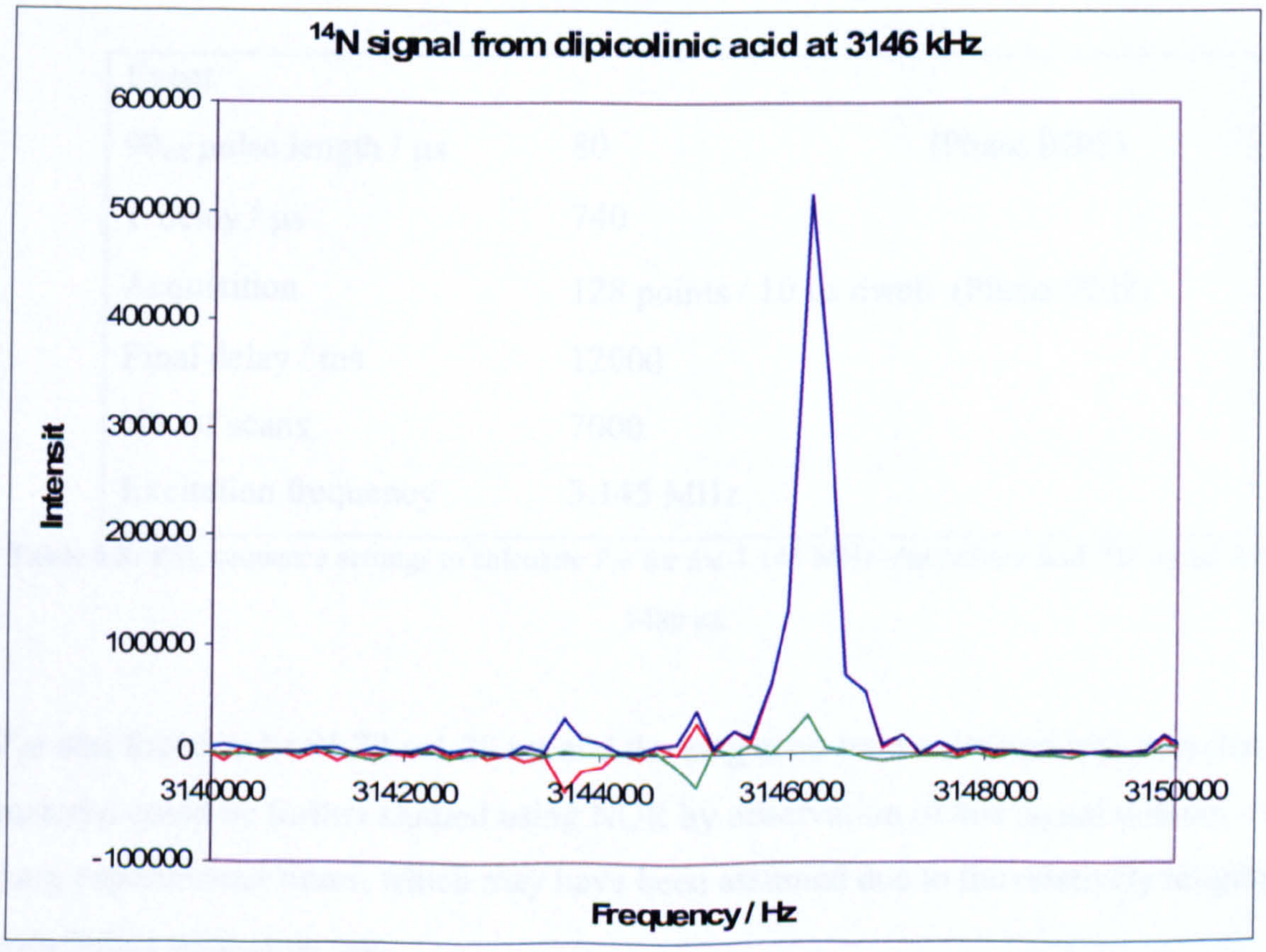

Figure 6.6: Dipicolinic acid ^{14}N signal at 3146 kHz (Fourier transform of figure 6.5).

The room temperature spin-lattice relaxation rate of the ^{14}N signal around 3.145 MHz was found using an inversion recovery sequence with the following settings:

Event		
90_{eff} Pulse / μs	80	(Phase 20)
Dead time	Variable - 15 points from 1 to 5000 ms	
Acquisition	256 points / 10 μs dwell	(Phase 02)
Final delay / ms	5000	
No. of scans	1000	
Excitation frequency	3.145MHz	

Table 6.7: Inversion recovery sequence settings to calculate T_1 of the 3.145 MHz dipicolinic acid ^{14}N signal.

After three experiments the best spectra produced gave a calculated $T_1 = 1336 \pm 307$ ms. The following PSL echo sequence, with $2\tau = 1480$ μs, was used to generate 128 echoes and the T_2e value found under these conditions.

Event		
90_{eff} pulse length / μs	80	(Phase 0202)
τ delay / μs	740	
Acquisition	128 points / 10 μs dwell	(Phase 0202)
Final delay / ms	12000	
No. of scans	7000	
Excitation frequency	3.145 MHz	

Table 6.8: PSL sequence settings to calculate T_2e for the 3.145 MHz dipicolinic acid ^{14}N signal with $2\tau = 1480$ μs.

T_2e was found to be 91.72 ± 1.28 ms and the long echo train sustained indicates that this material could be further studied using NQR by observation of this signal without overly long experimental times, which may have been assumed due to the relatively lengthy spin-lattice relaxation rate.

A simple FID pulse sequence was used with the settings below to search for the room temperature higher frequency ν_+ ^{14}N signal, again based on the room temperature picolinic acid data[3].

Event		
Pulse / μs	60	(Phase 20)
Acquisition	512 points / 10 μs dwell	(Phase 02)
Final delay / ms	1000	
No. of scans	10000	
Excitation frequency	3.600 to 3.760 in 10 kHz steps	

Table 6.9: FID sequence settings to observe higher frequency dipicolinic acid ^{14}N signal.

An FID was observed following irradiation at 3.750 MHz, and Fourier transformation gave a peak at 3.756 MH (figure 6.7).

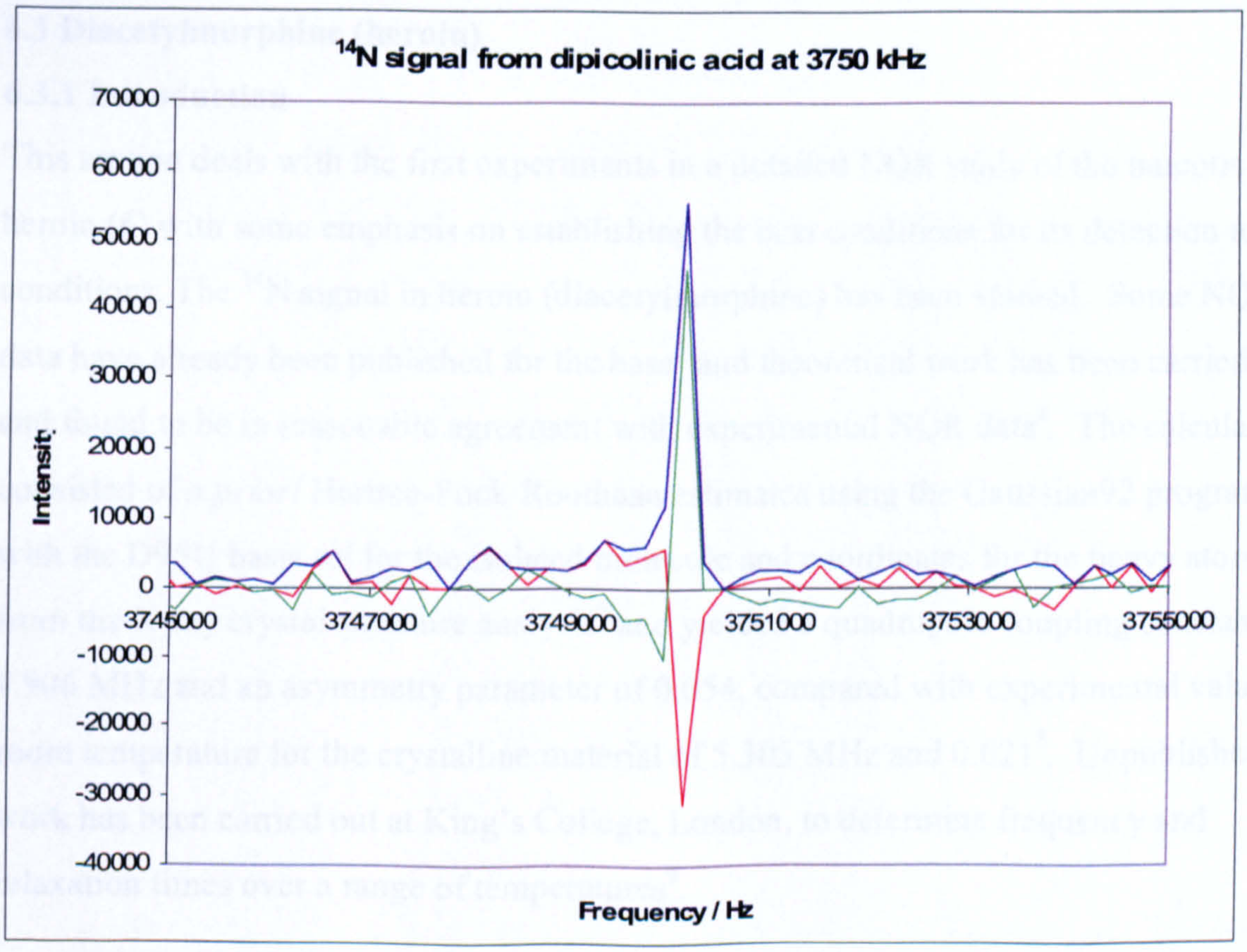

Figure 6.7: Dipicolinic acid ^{14}N signal at 3756 kHz (RF radiation at 3750 kHz).

It can be assumed that the signal at 3756 kHz is the ν_+ line, with ν_- being equal to 3146 kHz. ν_0 can be calculated to be 610 kHz.

$$\frac{e^2qQ}{h} = \frac{2}{3}(\nu_+ + \nu_-) \qquad (6.1)$$

$$\eta = 2\frac{(\nu_+ - \nu_-)}{(\nu_+ + \nu_-)} \qquad (6.2)$$

From the above equations the quadrupole coupling constant, e^2qQ/h, can be calculated to be 4601 kHz and η, the asymmetry parameter, to be 0.177. Seliger *et al*[3]. calculated the quadrupole coupling constant for picolinic acid to be 4159 kHz, with an asymmetry parameter of 0.347. The QCC is of a similar magnitude to that of dipicolinic acid, whilst pyridine has a QCC value of 4584 kHz[4], which is very close to that of dipicoline acid.

6.3 Diacetylmorphine (heroin)

6.3.1 Introduction

This section deals with the first experiments in a detailed NQR study of the narcotic heroin (**6**) with some emphasis on establishing the best conditions for its detection in real conditions. The ^{14}N signal in heroin (diacetylmorphine) has been studied. Some NQR data have already been published for the base[5] and theoretical work has been carried out and found to be in reasonable agreement with experimental NQR data[6]. The calculation consisted of *a priori* Hartree-Fock-Roothaan estimates using the Gaussian92 program with the D95U basis set for the isolated molecule and coordinates for the heavy atoms from the X-ray crystal structure analysis[7] and yielded a quadrupole coupling constant of −4.906 MHz and an asymmetry parameter of 0.054, compared with experimental values at room temperature for the crystalline material of 5.305 MHz and 0.021[8]. Unpublished work has been carried out at King's College, London, to determine frequency and relaxation times over a range of temperatures[9].

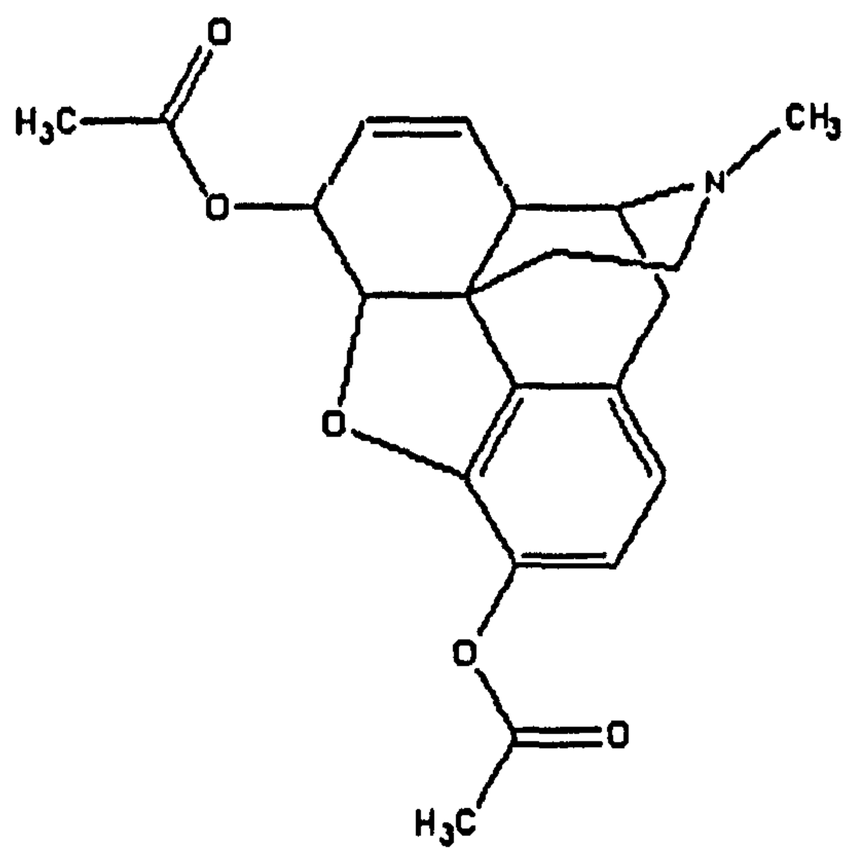

6

It should be noted that the literature reports the existence of two different polymorphic forms of heroin base. The first known form, which is presumably the most common, is orthorhombic with space group $P2_12_12_1$ and $Z = 4$[7]. Its hexagonal crystals can be prepared from an aqueous solution of the hydrochloride by adding sodium acetate. X-ray crystal structures have been published for both polymorphs[7,10]; in both, the nitrogen ring is in the "chair" form. There is only one type of nitrogen in the unit cell of the orthorhombic form, which contains 4 identical molecules, whereas the monoclinic form has two different molecules in the repeat unit and therefore two different types of nitrogen in the crystal. Therefore only one set of three ^{14}N transitions should be observed for the orthorhombic form but in the case of the monoclinic form each line should be split into a doublet. It seems that all NQR experiments carried out so far have been on the more common orthorhombic form, as no doublets have been reported.

The experiments were carried out on a 66 g sample of the orthorhombic form supplied by DSTL at Fort Halstead. Its purity was checked by elemental analysis;

Element	Calculated %	Found %
C	68.9	68.11
H	5.46	6.24
N	3.83	3.71

Previous ^{14}N data for this material are summarized in table 6.8. The present experiments were designed to check these values of frequencies and relaxation times, and in particular check the values of T_2e, the multipulse echo decay time in a pulsed spin locking (PSL) sequence and its dependence on pulse spacing. Maintaining the echo train is important commercially, as the greater the number of echoes that can be summed, the better signal to noise ratio can be achieved in a given time.

	ν /kHz	e^2qQ/h /kHz	η	$\Delta\nu_{1/2}$ /kHz	T_2* /ms	T_1 /ms	T_2 /ms	T_2e /ms	Ref.
ν_+	4007	5305	0.021	7.7	0.26 ± 0.05	524 ± 150	6 ± 3	11 ± 2*	[8,11]
ν_-	3951			6.7	0.30 ± 0.05	396 ±300	10 ± 3	16 ± 2*	
ν_+	4006.0	5304	0.021	9.1	-	-	-	-	[12]
ν_-	3950.2			7.8	-	-	-	-	
ν_+	4025	5317	0.028	Several kHz	-	<1000	> 0.1	-	[13]
ν_-	3950				-	400		-	
ν_+	4026	5317	0.029	-	-	-	-	-	[5]
ν_-	3950			-	-	-	-	-	

Table 6.10: Previous room temperature data for heroin base. Results for T_2e (denoted by *) were obtained on resonance with 2τ=1.1 ms.

6.3.2 ^{14}N T_2e experiments

T_2e values were calculated for the 66 g sample of heroin at further values of 2τ. The decaying echo trains were obtained by means of pulsed spin locking sequences at resonance frequencies of 3.951 and 4.007 MHz, values which agree with previous results obtained at King's College[8, 11, 12] but not with work by Grechishkin and Ya Sinyavski[5] and Garroway[13]. The 90_{eff} pulse widths were optimised and the experiments run on resonance at room temperature, with the following settings on the Tecmag Libra Spectrometer.

Event	2τ = 1.74 ms	2τ = 0.8 ms
90_{eff} Pulse / μs	100	50
Acquisition	128 points / 10 μs dwell	128 points / 5 μs dwell
Final Delay / ms	2000	2000
No. of scans	30000	30000
Frequency / MHz	3.951 / 4.007	3.951 / 4.007

Table 6.11: PSL sequence settings used to find T_2e at two values of 2τ.

The magnitude at the peak of each echo was plotted and fitted to an exponential curve using Excel (figures 6.7 and 6.8) and the errors represent the range of values obtained over 3 experiments.

The results in table 6.12 show that the change in a single exponential T_2e with 2τ between 0.8 and 1.74 ms for both heroin lines appears to be insignificant.

ν_+ : 4.007 MHz		ν_- : 3.951 MHz	
2τ / ms	T_2e / ms	2τ / ms	T_2e / ms
0.8	18 ± 2	0.8	15.5 ± 1
1.1	11 ± 2*	1.1	16 ± 2*
1.74	13.5 ± 1	1.74	13.5 ± 1

Table 6.12: T_2e values for various 2τ spacings. Results denoted by * previously obtained[8, 11].

However there is some evidence in figures 6.8 and 6.9 that the decays are actually biexponential, although approximately 100 points or more would be needed to give a confident fit. This feature is being further studied.

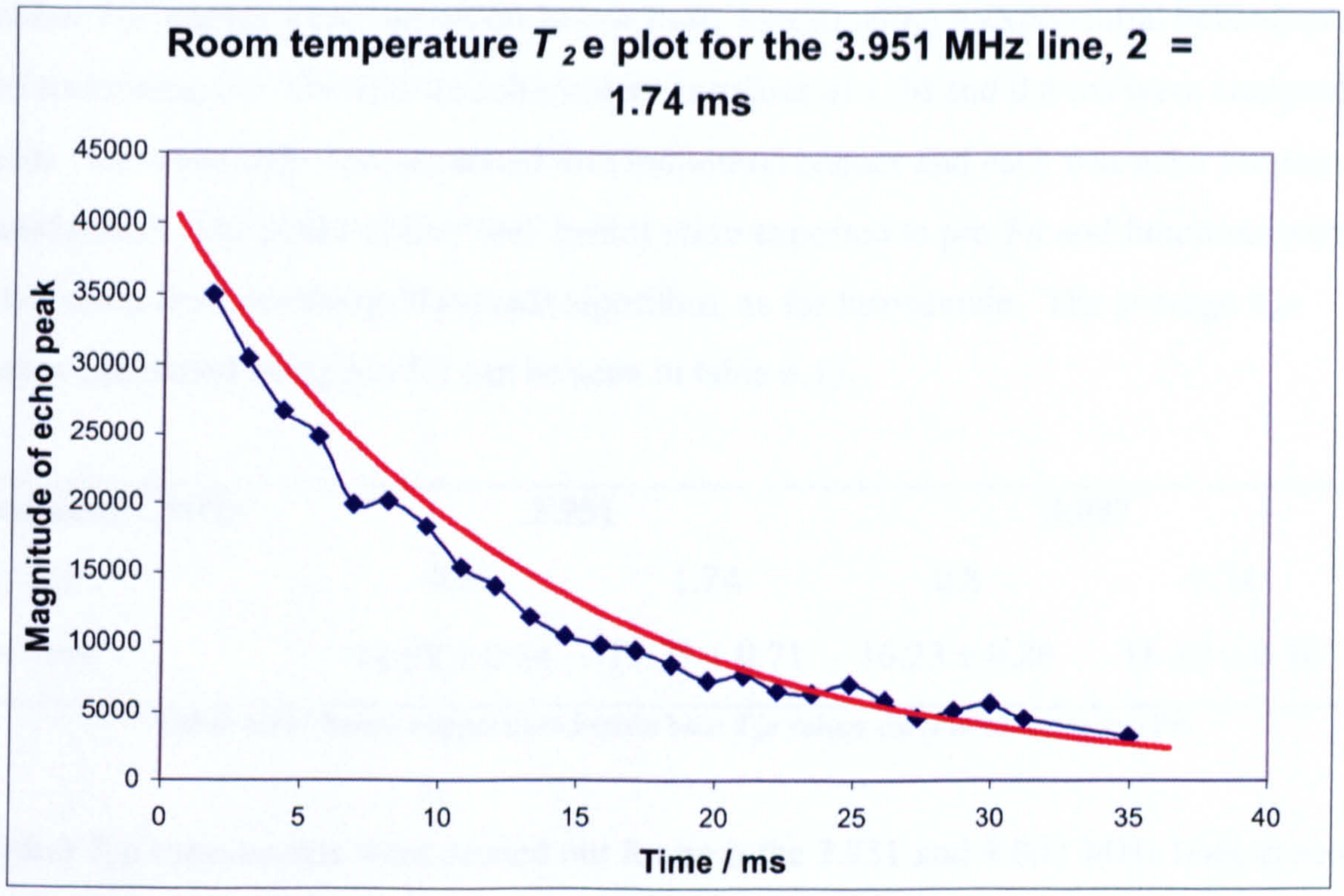

Figure 6.8: ν_- line data points for 2τ=1.74 ms; the continuous line is a single exponential fit with T_2e = 13.5 ± 1.0 ms.

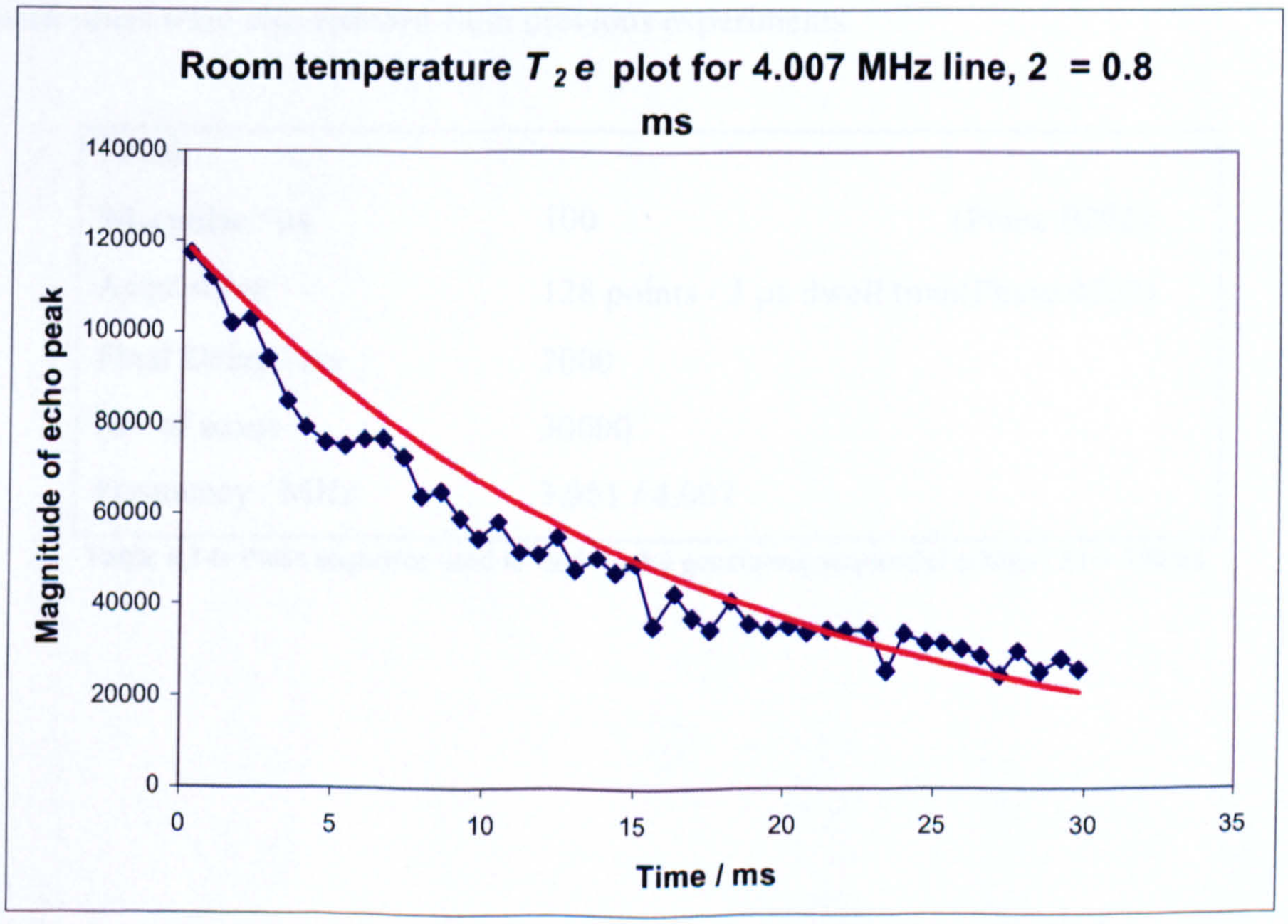

Figure 6.9: ν_+ line data points for 2τ= 0.8 ms; the continuous line is a single exponential fit with T_2e = 18 ± 2 ms.

Further T_2e studies were carried on heroin base, investigating biexponential behaviour and shortening 2τ. The spectra achieved at 2τ values of 1.74 and 0.8 ms were analysed again. The echo train was separated into individual echoes and each was echo Fourier transformed. The peaks of the 'real' points were exported to pro Fit and functions were fitted using the Levenburg-Marquadt algorithm, as for furosemide. The average T_2e values calculated using pro Fit can be seen in table 6.13.

Frequency / MHz	**3.951**		**4.007**	
2τ / ms	0.8	1.74	0.8	1.74
T_2e / ms	14.98 ± 0.44	15.33 ± 0.71	16.23 ± 0.26	16.10 ± 0.46

Table 6.13: Room temperature heroin base T_2e values calculated using pro Fit.

Further T_2e experiments were carried out for both the 3.951 and 4.007 MHz lines at room temperature, with a 2τ value of 550 μs, using the sequence in table 6.14. In order to achieve short 2τ values, Q-damping was necessary to enable shorter dead times. The dwell times were also reduced from previous experiments.

Event		
90_{eff} pulse / μs	100	(Phase 0202)
Acquisition	128 points / 3 μs dwell time	(Phase 0202)
Final Delay / ms	2000	
No. of scans	30000	
Frequency / MHz	3.951 / 4.007	

Table 6.14: Pulse sequence used to find T_2e by generating sequential echoes; 2τ = 550 μs.

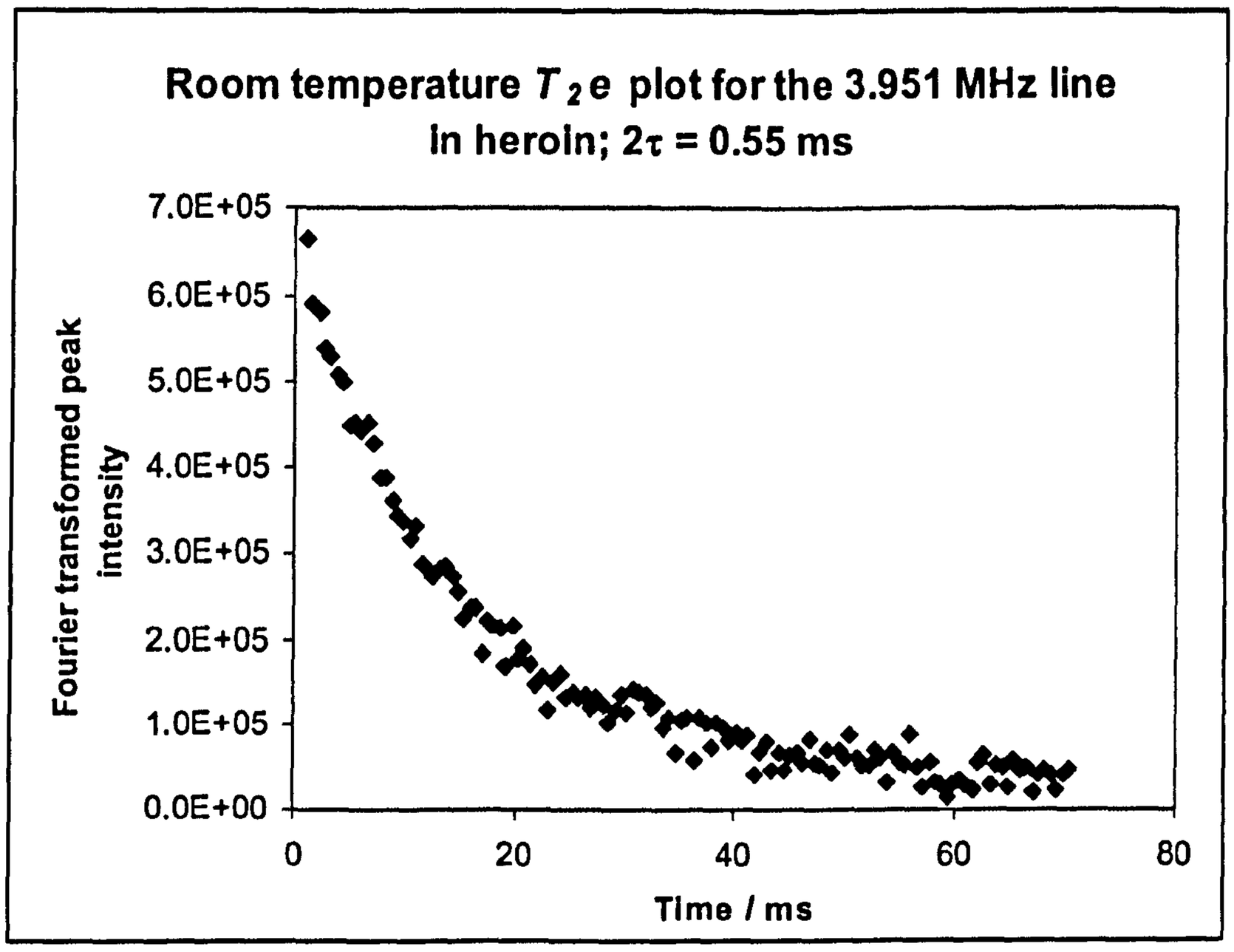

Figure 6.10: Heroin base; ^{14}N 3.951 MHz T_2e plot, where $2\tau = 550$ μs; $T_2e = 18.52 \pm 0.31$ ms.

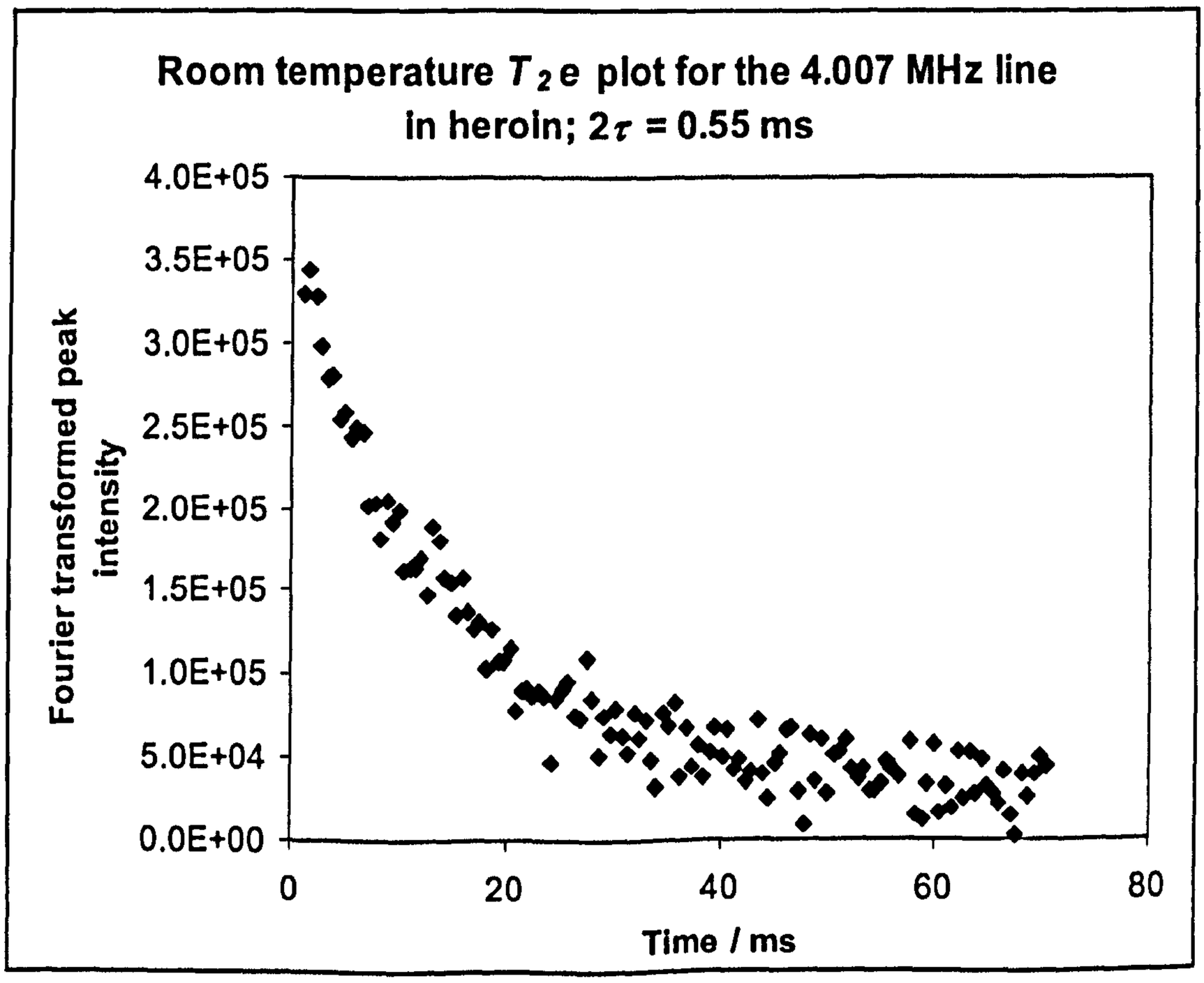

Figure 6.11: Heroin base; ^{14}N 4.007 MHz T_2e plot, where $2\tau = 550$ μs; $T_2e = 20.77 \pm 0.65$ ms.

The T_2e average value (over 3 experiments), with $2\tau = 550$ μs, was 18.30 ± 0.42 ms for the 3.951 MHz line and 20.32 ± 0.61 for the 4.007 MHz line. The usual trend of increased T_2e with decreasing 2τ was observed and the data for each line was plotted (figures 6.12 and 6.13).

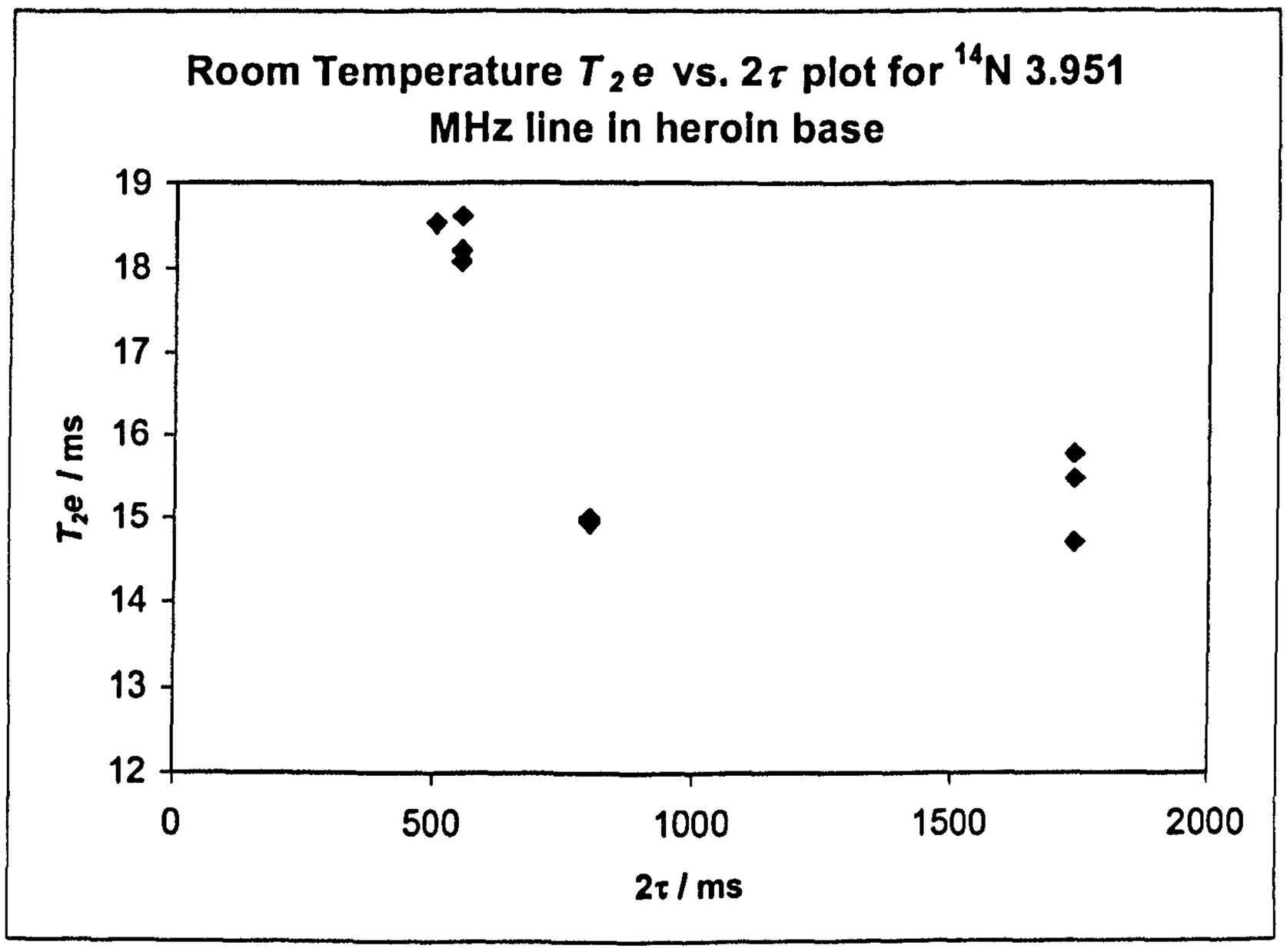

Figure 6.12: Heroin base ^{14}N 3.951 MHz room temperature T_2e vs. 2τ plot.

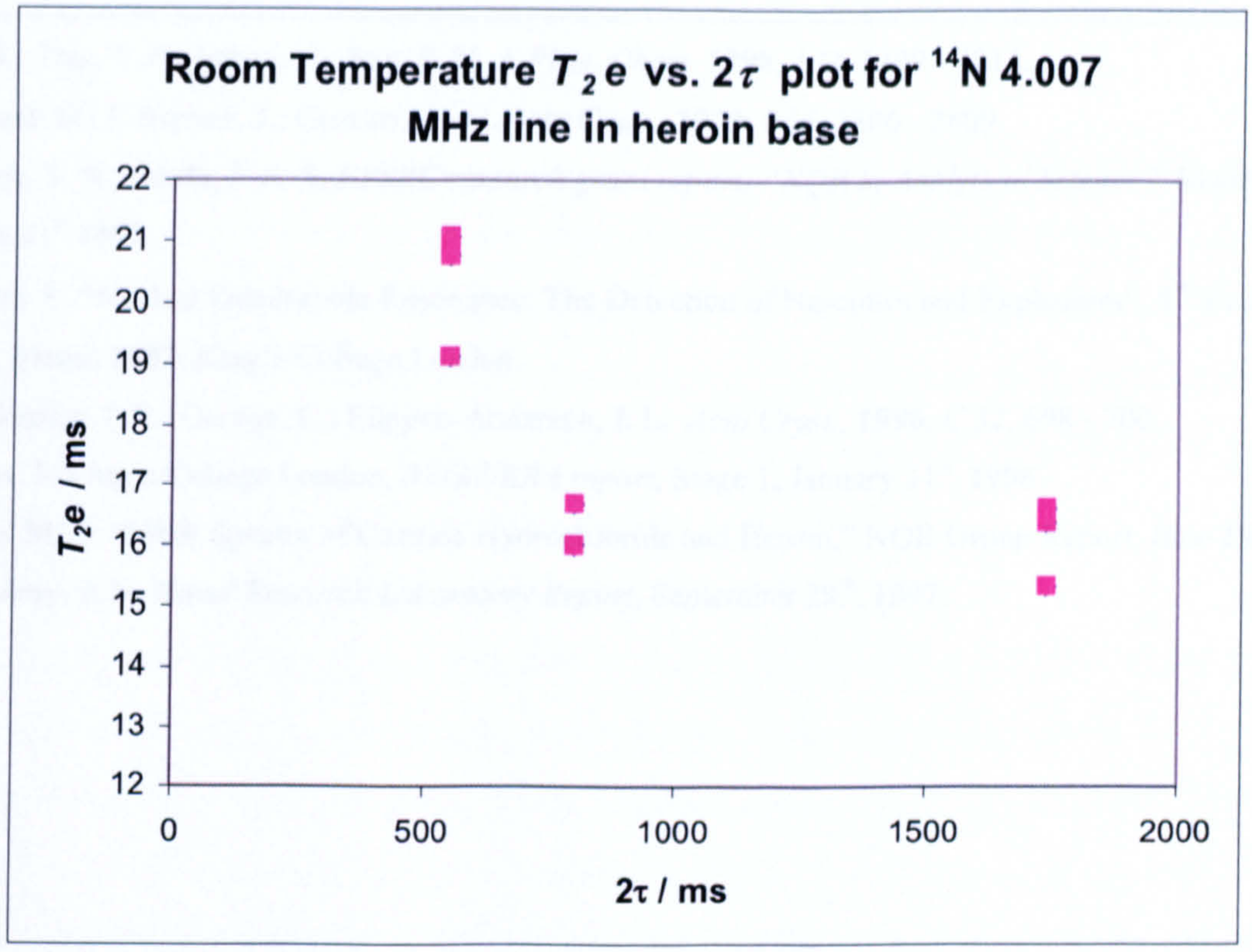

Figure 6.13: Heroin base ^{14}N 4.007 MHz room temperature T_2e vs. 2τ plot.

These results demonstrate the need to optimise pulse sequences in NQR, particularly in real life situations, such as in a search by Customs and Excise for narcotics, in order to decrease the experimental time needed to give spectra with a good SNR. Decreasing the time between pulses in an echo train will help to sustain a longer echo train, allowing a greater number to be summed, thus decreasing the number of scans necessary to achieve a good final yes/no result. The real increases are clearly observed when 2τ vales are below 0.5 ms, emphasizing the need to improve Q-damping performance in order to minimise dead times.

6.4 References

[1] Bjerga Bjåen A.-K.; Nord K.; Furuseth S.; Ågren T.; Tønnesen H. H.; Karlsen J.; *Int. J. Pharm.*, **1993**, *92*, 183 - 189.

[2] Edmonds, D. T.; Hunt, M. J.; Mackay, A. L., *J. Magn. Reson.*, **1973**, *9*, 66 - 74.

[3] Seliger, J.; Žagar, V.; Zidanšek, A.; Blinc, R., *Chem. Phys.*, **2006**, *331*, 131 - 136.

[4] N.S. Kim, J.P. Bray, *Org. Magn. Reson.* **1981**, *15*, 370.

[5] Grechishkin, V. S.; Ya Sinyavski, N. *Physics Uspekhi*, **1997**, *40 (4)*, 393 - 406.

[6] Pati, R.; Das, T. P.; Sahoo, N.; Ray, S. N. *J. Phys. Chem.* 1998, *102*, 3209 - 3214.

[7] Canfield, D.; J. Barrick, J.; Giessen, B. C. *Acta Cryst.*, 1979, *B35*, 2806 - 2809.

[8] Mallion, S. N.; Smith, J. A .S. *EPSRC research grant report; "NQR in Analytical Science"*, March 1st- October 31st 1997.

[9] Balchin, E. "Nuclear Quadrupole Resonance: The Detection of Narcotics and Explosives", 4th Year Project, March 2002, King's College London.

[10] Deschamps, J. R.; George, C.; Flippen-Anderson, J. L. *Acta Cryst.*, 1996, *C 52*, 698 - 700.

[11] Barras, J. King's College London, *BTG/DERA report*, Stage 1, January 31st, 1996.

[12] Rowe, M. D. "NQR Spectra of Cocaine Hydrochloride and Heroin," NQR Group Report, June 2001.

[13] Garroway, A.N. *Naval Research Laboratory Report*, September 29th, 1997.

7 The theoretical calculation of quadrupolar parameters

7.1 Introduction and theory of Gaussian calculations

One of the major hurdles in commencing NQR experiments is the determination of the NQR frequencies of previously uncharacterised materials. Although resonant frequencies can be predicted somewhat by comparison with nuclei in similar environments or functional groups or by approximate, semi-empirical theories such as that of Townes and Dailey,[1] the highly sensitive nature of NQR which advantageously allows for unique identification may prove a hindrance in initial experiments.

The objective of this chapter was to see how closely *ab initio* theoretical calculations of the quadrupole tensor matched experimental values in the solid state, given the X-ray or neutron crystal structure. By inputting the atomic coordinates of a system the electric field gradient and eigenvalues can be calculated, from which the quadrupole coupling constant, asymmetry parameter, NQR frequency and direction cosines can be calculated. The electric field gradient (EFG) is a second rank tensor which can be represented by a traceless matrix. The eigenvalues are the characteristic values of the matrix and define three mutually perpendicular directions which give the principal axes of the tensor with respect to the molecule-based axes used in the calculation.

Gaussian 98™ [2] is a program that calculates semi empirical and *ab initio* molecular orbitals, which can then be used to predict molecular properties and reactions. Mathematical approximations are used to solve the Schrödinger equation, in this case, from the known structural information[3]. The atomic coordinates of a system are inputted, e.g. from the X-ray crystal structure analysis, along with the overall charge and multiplicity. The 'instructions' as to which model to use to calculate the molecular orbitals and what to predict are set by the operator at the beginning of a command file. In this case the program was told specifically to generate quadrupolar data and the electric field gradients. The self consistent field (SCF) Hartree-Fock (HF) method was used in all calculations. SCF theory uses first principles (*ab initio*) to solve the Schrödinger equation in an iterative manner. In the Hartree-Fock method a molecular orbital

approximation is used to solve the equation and a basis set, which must be specified by the user, represents the molecular orbitals.

As discussed in chapter 2, the quadrupole coupling constant, defined as e^2qQ/h in MHz, can be calculated as follows[4]:

$$\text{QCC (MHz)} = -234.9647Qq \tag{7.1}$$

where Q is the nuclear electric quadrupole moment in Barn (10^{-28} m^2) and q is q_{zz}, the maximum principal component of the electric field gradient at the nucleus in atomic units. A negative sign is present in equation (7.1), unlike in the referenced literature, as the Gaussian programme produces q values with the opposite sign.

The asymmetry parameter, η, a measure of axial symmetry, was calculated as follows:

$$\eta = \frac{q_{yy} - q_{xx}}{q_{zz}} \tag{7.2}$$

where q_{yy} and q_{xx} are the two remaining principal components of the electric field gradient, where $q_{zz} \geq q_{yy} \geq q_{xx}$.

For ^{35}Cl, a spin-$^3/_2$ nucleus, the quadrupole resonance frequency can then be calculated from the equation

$$\nu_Q = \frac{1}{2}QCC\left(1 + \frac{\eta^2}{3}\right)^{1/2} \tag{7.3}$$

The nuclear electric quadrupole moment for ^{35}Cl is assumed to be –81.65 mB[5].

For a nucleus with spin $I = 1$, such as ^{14}N, the following equations are used

$$\nu_x = \frac{3}{4}QCC\left(1 + \frac{\eta}{3}\right) \tag{7.4}$$

$$\nu_y = \frac{3}{4}QCC\left(1 - \frac{\eta}{3}\right) \tag{7.5}$$

$$\nu_z = \frac{1}{2} QCC\eta \qquad (7.6)$$

The nuclear electric quadrupole moment for ^{14}N is assumed to be 20.44 mB[5].
Using the above equations simultaneously, the asymmetry parameter can be calculated from the observed NQR frequencies in solids.

7.2 Heroin hydrochloride monohydrate

As well as security applications regarding explosives, another main area of interest in NQR is in the detection of narcotics, and many materials such as ecstasy (MDMA hydrochloride)[6], cocaine base[7], cocaine hydrochloride[7] and heroin base[8,9] and have already been studied. ^{14}N signals have been reported using pure NQR in cocaine, cocaine hydrochloride and heroin, but the pure, zero-field NQR ^{14}N frequencies in heroin hydrochloride monohydrate have yet to be observed using this method.
Little NQR work has been published on heroin hydrochloride monohydrate; a double resonance experiment conducted at 20 K gave just one broad response near 1.08 MHz, assigned to ^{14}N. No other signals were detected[10]. In this chapter more detailed cross relaxation and double resonance by level crossing spectra have been obtained and the experimental characteristic values found compared with those predicted theoretically. Much of the work in this chapter was included in the published article 'The unusual solid state structure of heroin hydrochloride monohydrate and its selective detection using NQR spectroscopy'[11].

7.2.1 Double resonance measurements

7.2.1.1 Cross relaxation

7.2.1.1.1 Method

A room temperature cross relaxation spectrum was obtained by David Stephenson at the University of the West Indies. A high field (20.10 MHz) residence time of 10 s was used with 0.07 s in low field; the baseline corrected spectrum is shown in figure 7.1.

7.2.1.1.2 Results

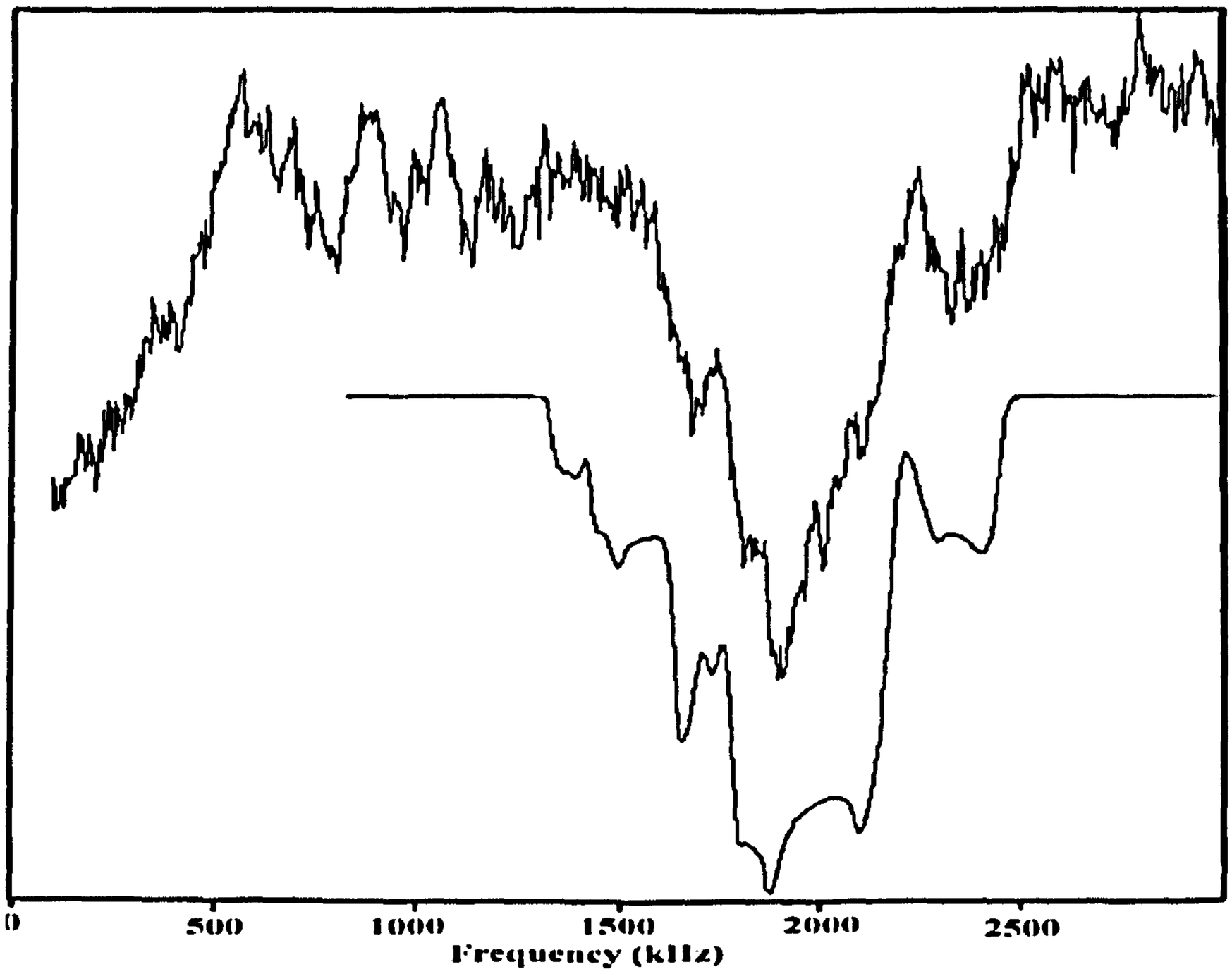

Figure 7.1: Cross relaxation spectrum of heroin hydrochloride monohydrate.

A clear broad peak just below 2000 kHz can be seen, assigned to overlapping ^{35}Cl and ^{37}Cl lines broadened by the applied magnetic field. A fit to the observed line shape shown by the lower curve in the figure, gives a ^{35}Cl quadrupole coupling constant of 3.81 MHz and asymmetry parameter of 0.4, predicting a zero-field frequency of 1.950 MHz.

7.2.1.2 Level crossing

7.2.1.2.1 Method

Double resonance by level crossing (DRLC) experiments were carried out at Dr. Anthony Horsewill's laboratory at the University of Nottingham. The applied magnetic field of a superconducting solenoid, continuously powered by a fast switching power supply rated at 15 V and 160 A so that the magnetic field was proportional to the instantaneous current, was switched at a rate of 8 T s^{-1} from the observation field, B_{nm}, of 0.627 T (corresponding to a ^{1}H NMR frequency of 26.7 MHz) to zero field, where it was irradiated by a frequency-swept radiofrequency with a B_1 field of about 0.2 mT. The 90 °

pulse employed to record the signal had a duration of 1 μs and the total dead-time was 4 μs. The sample temperature was 4.2 K. The NMR sequence used in the DRLC experiments is shown in figure 7.2 as discussed in chapter 3.

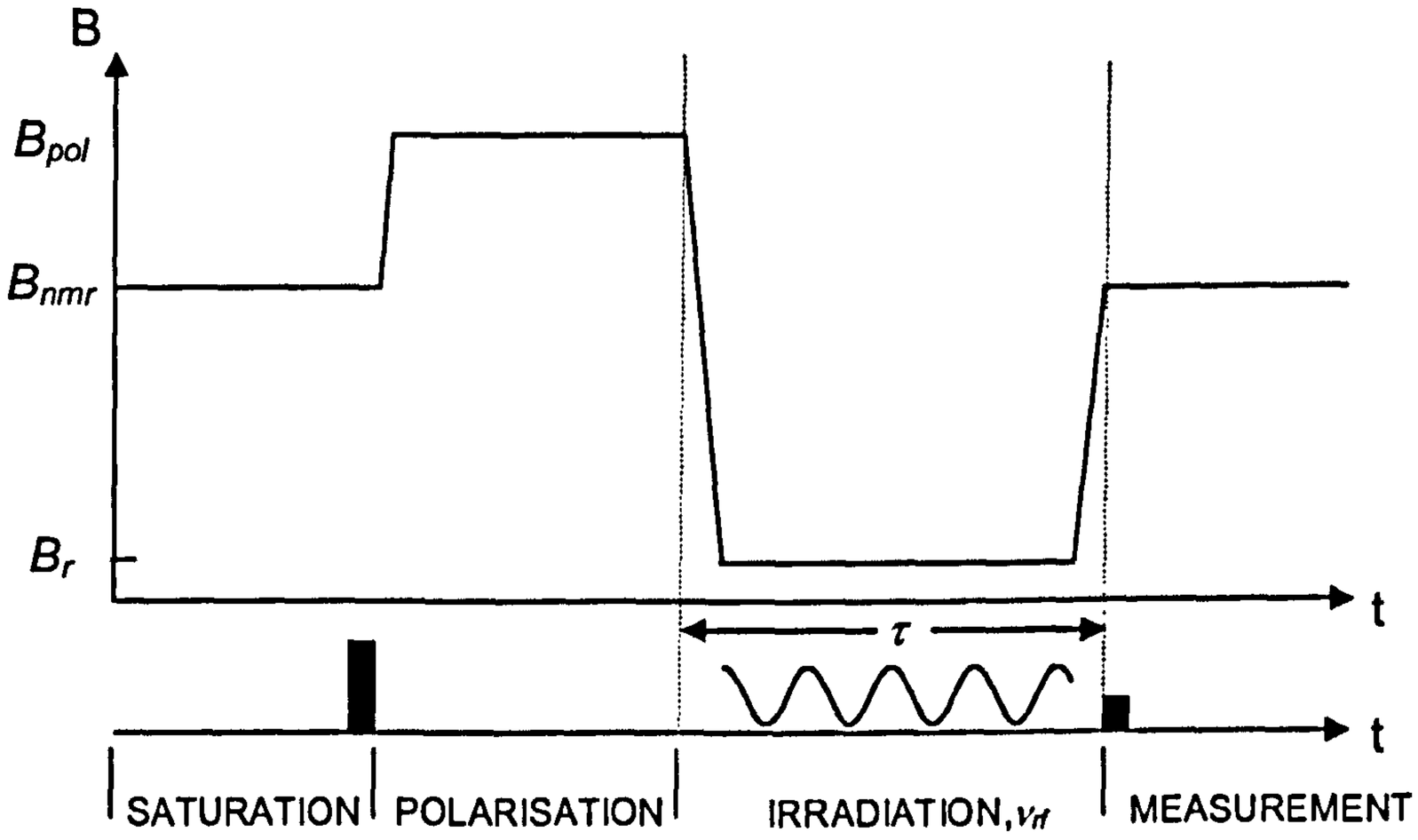

Figure 7.2: NMR sequence used in DRLC experiments.

7.2.1.2.2 Results

Areas of interest could be seen in the low resolution spectrum (figure 7.3). Higher resolution spectra were produced for these regions and clear, well resolved doublets were observed near 0.957 and 1.035 MHz (figure 7.4), assigned to ν_- and ν_+ for ^{14}N; there was also a broad apparent doublet, near 1.965 MHz (figure 7.5), assigned to ^{35}Cl, in good agreement with the CR experiments (figure 7.1) at room temperature.

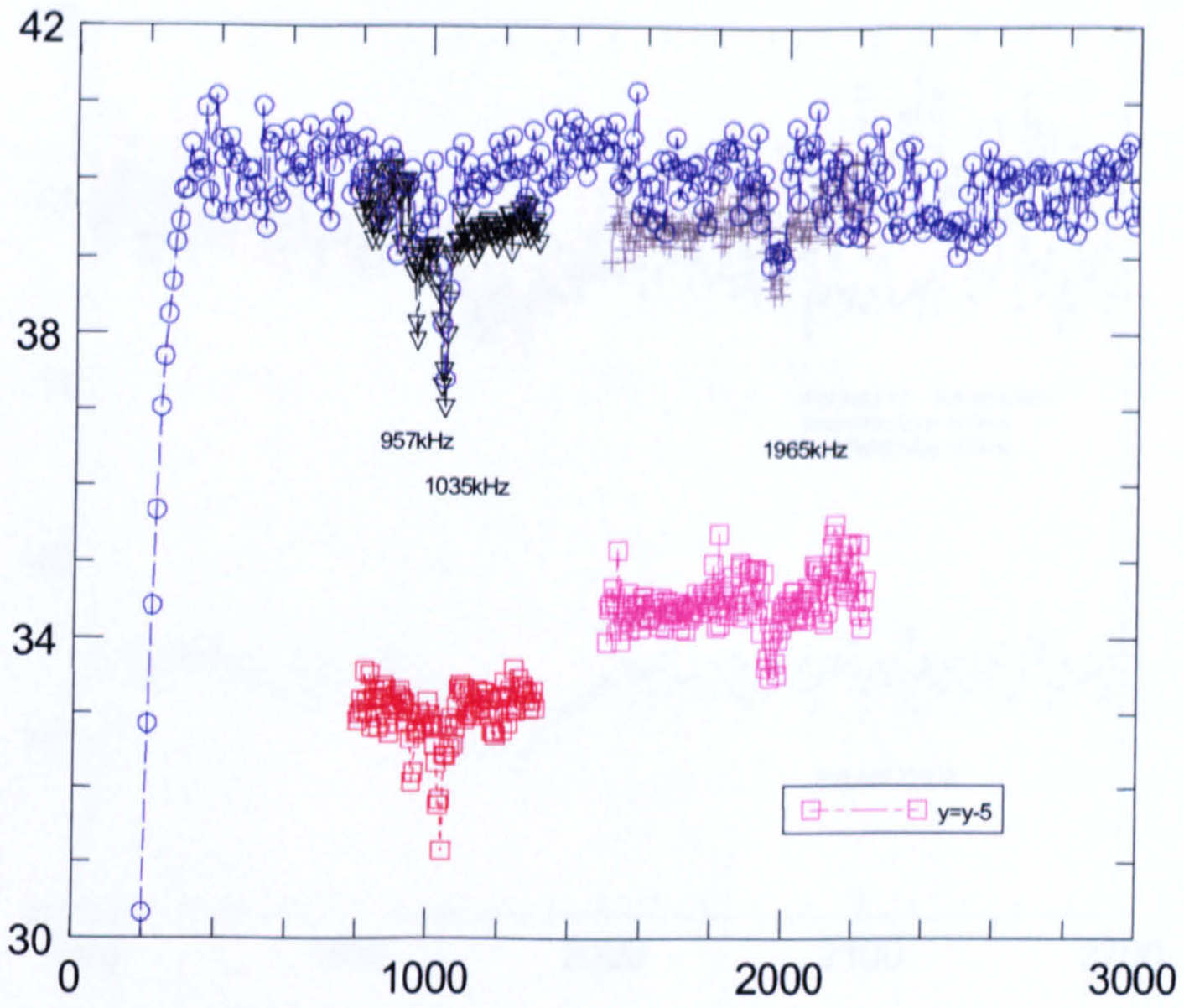

Figure 7.3: Zero field level crossing spectrum of heroin hydrochloride monohydrate.

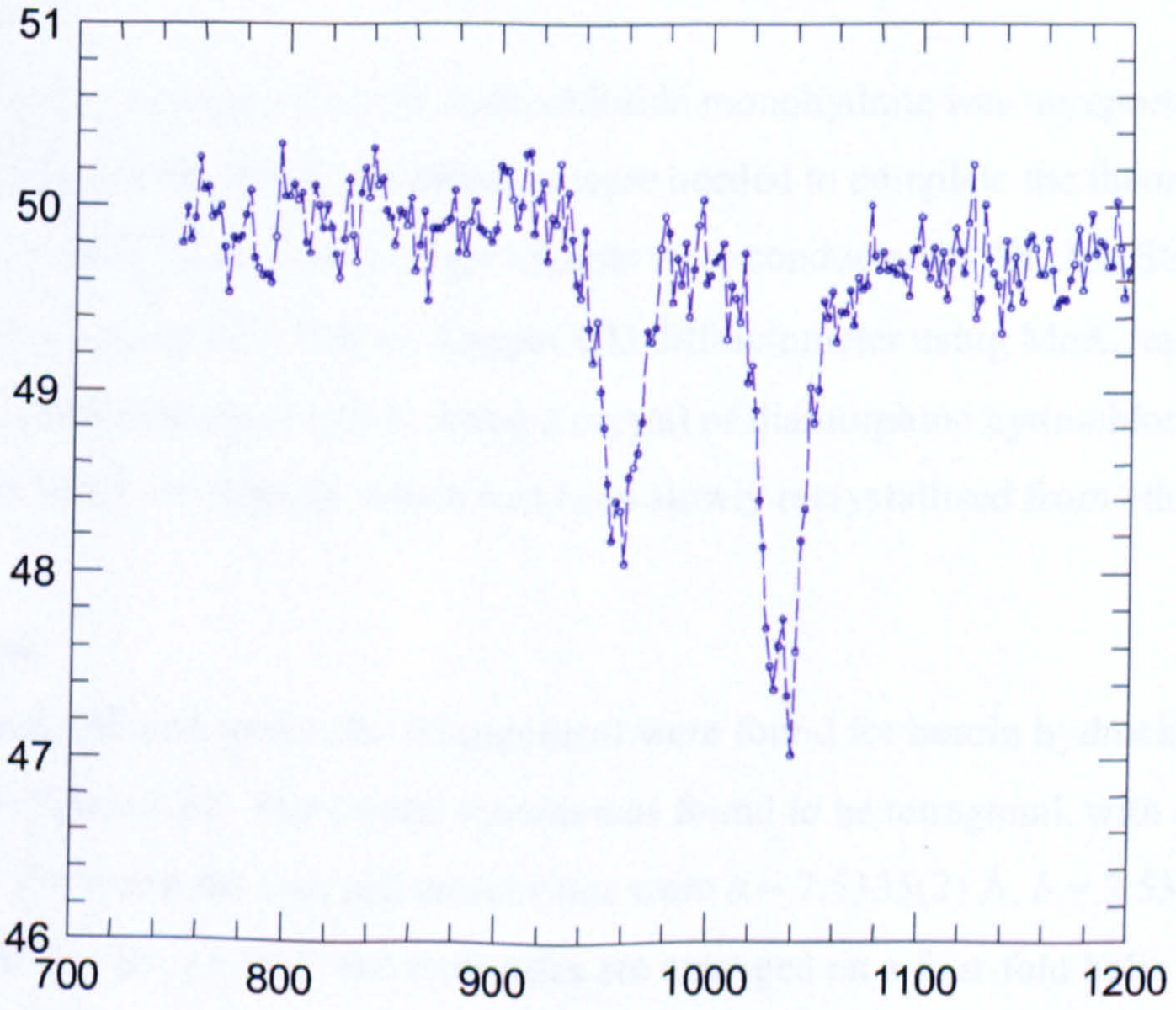

Figure 7.4: Higher resolution level crossing spectrum across the ^{14}N signal region.

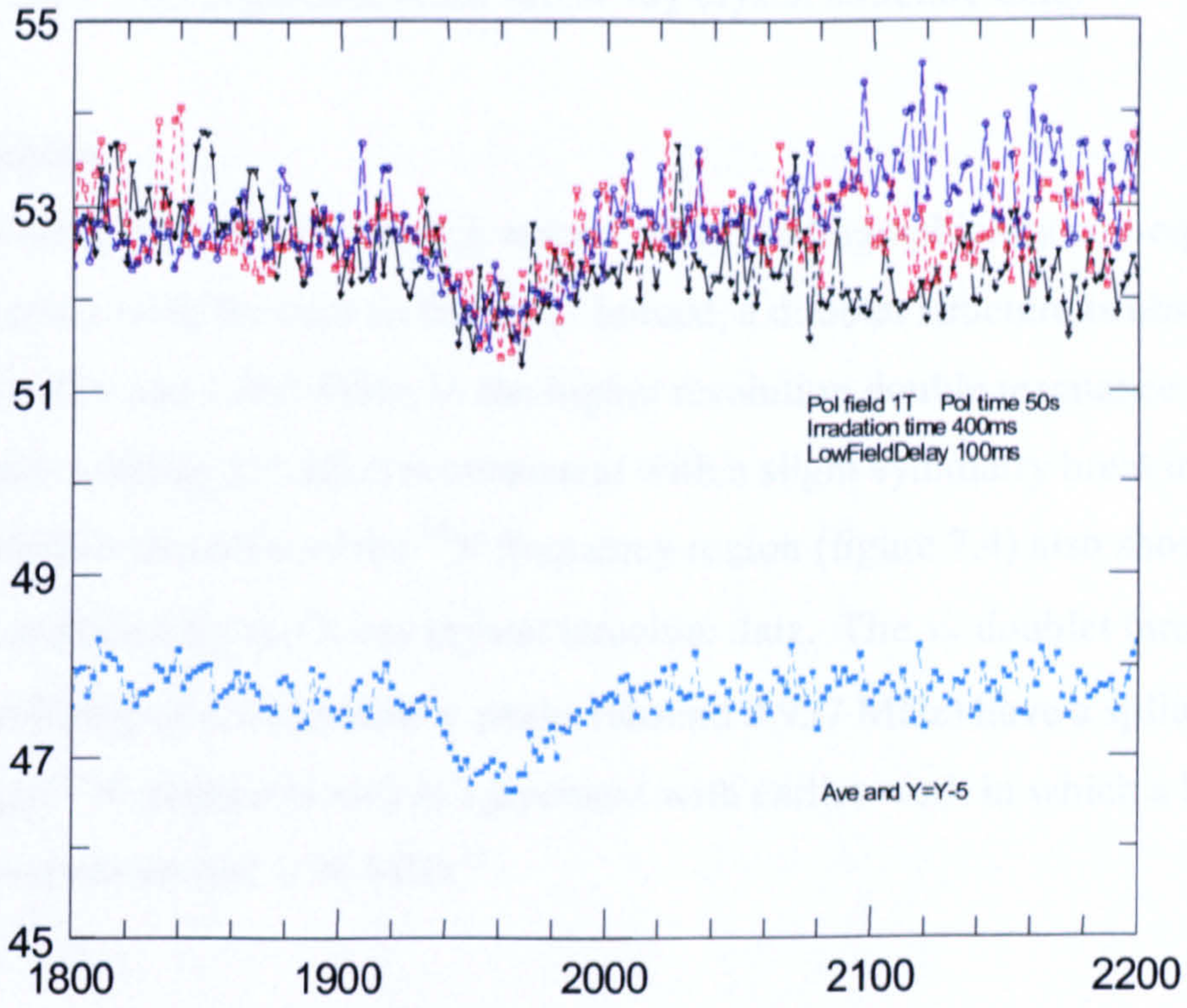

Figure 7.5: Higher resolution level crossing spectrum of ^{35}Cl region.

7.2.2 X-ray crystallography

7.2.2.1 Method

The X-ray crystal structure of heroin hydrochloride monohydrate was unreported prior to our experiments. As the atomic coordinates were needed to complete the theoretical calculations, X-ray crystal structure experiments were conducted by Dr. Jon Steed at King's College London on a Nonius KappaCCD diffractometer using MoK_α radiation with a sample temperature of 120 K, using a crystal of diamorphine hydrochloride BP, obtained from Macfarlen-Smith, which had been slowly recrystallised from ethanol.

7.2.2.2 Results

An unusual unit cell and molecular arrangement were found for heroin hydrochloride monohydrate (figure 7.6). The crystal system was found to be tetragonal, with a $P4_1$ space group. $Z = 8$ and the unit cell dimensions were $a = 7.5335(2)$ Å, $b = 7.5335(2)$ Å, $c = 71.976(4)$ Å, $\alpha = \beta = \gamma = 90$ °; the molecules are arranged on a four-fold helix of pitch

72.0 Å with its axis parallel to the *c* axis, requiring a total of eight molecules in order to complete one turn. (See Appendix A for full X-ray crystal structure data)

7.2.2.3 Discussion

Having the space group $P4_1$, the two Cl^- anions are crystallographically non-equivalent; they should yield a peak for each in the ^{35}Cl. Indeed, a doublet structure is observed, with peaks at 1.950 and 1.965 MHz, in the higher resolution double resonance spectra (figure 7.5); this splitting (15 kHz) is consistent with a slight symmetry breaking.

The high resolution spectrum of the ^{14}N frequency region (figure 7.4) also shows doublet structures, as predicted by the X-ray crystal structure data. The ν_+ doublet (around 1.035) has a splitting of 6.5 kHz and ν_- peaks (around 0.957 MHz) have a splitting of 5.7 kHz. The upper ^{14}N doublet is also in agreement with earlier work in which a broad signal was observed around 1.08 MHz[10].

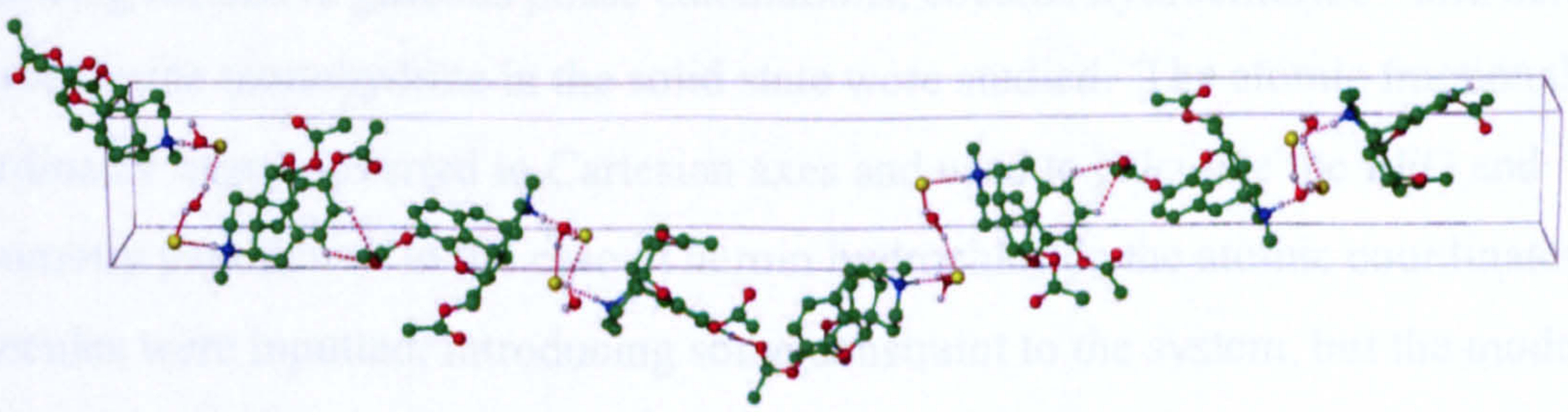

Figure 7.6: Heroin hydrochloride monohydrate helix.

7.2.3 Quadrupole coupling constants and frequency prediction

7.2.3.1 Dichlorine monoxide as a sample material

An initial simple test model was used as a trial to see how closely theoretical predictions agreed with practical values and also to become familiar with the methods needed in using the Gaussian98 programme. Using the bond lengths and angles for dichlorine monoxide in the gas phase derived from microwave spectroscopy[12] the asymmetry parameter and QCC were calculated, running the Gaussian programme with a basis set of 3-21G, and compared to known literature values in the gas phase[13] of 0.06 and -140 MHz respectively. With the eigenvalues, q_{zz}, q_{yy} and q_{xx}, generated by the Gaussian program, the theoretical values for Cl_2O were found to be 0.031 and –114 MHz for the asymmetry parameter and the QCC respectively. Compared with the microwave values above, this is rather poor agreement, corresponding to a 20 % error in the QCC; however, there are limitations to the accuracy in the model used, for example the neglect of the effects of molecular vibrations. The larger the basis set used, the more accurate the model and the better the prediction, although the computer cost is greater.

7.2.3.2 Heroin hydrochloride and cocaine hydrochloride preliminary calculations

Following the above gaseous phase calculations, cocaine hydrochloride[14] and heroin hydrochloride monohydrate in the solid state were studied. The atomic fractional coordinates were converted to Cartesian axes and used to calculate the EFG and asymmetry parameter. In the case of heroin hydrochloride the atomic coordinates for two molecules were inputted, introducing some constraint to the system, but the model was still fairly approximate as it neglected the effects of the polarisation of the medium which could influence the charge distribution around the quadrupolar nuclei, the so-called Lorentz field. In the case of cocaine hydrochloride, only one molecule was used in the calculation.

7.2.3.2.1 Method

A simple basis set was used above to study the simple compound dichlorine monoxide. However, there are a number of basis sets available for use in the Gaussian98™ programme. The STO-3G basis set is an example of a minimal basis set, using fixed size

atomic-type orbitals. It can be used for elements up to Xe but such a simple basis set would not be expected to give accurate results for larger compounds. Split valence basis sets increase the number of basis functions by having more than one size of basis function for each orbital. 3-21G, 6-21G and 6-31G are examples of split valence basis sets, with polarization functions (d), (d) and (3df, 3pd) respectively. The allowance for polarization into extra orbitals increases the accuracy of the model, as in reality, such restrictions on electron location are not present. The three mentioned basis sets were used to carry out calculations for heroin hydrochloride monohydrate to observe the effect on the accuracy of prediction, whilst only the 6-31G basis set was used for cocaine hydrochloride. In all cases the calculated frequency is the single allowed transition in ^{35}Cl or the ν_+ transition in ^{14}N, calculated using equations (7.3) and (7.4) respectively. Note that the theoretical calculations give the sign of the quadrupole components, information that is not usually available from pure NQR experiments.

7.2.3.2.2 Results

Compound	Basis Set	Nucleus	η (calc.)	QCC/MHz (calc.)	Freq./MHz (calc.)
HerHCl	3-21G	N(1)	0.07	-1.708	1.320
		Cl(2)	0.65	6.559	3.500
		N(2)	0.17	-1.761	1.408
		Cl(1)	0.99	5.666	3.260
	6-21G	N(1)	0.07	-1.709	1.322
		Cl(2)	0.43	5.845	3.011
		N(2)	0.17	-1.765	1.411
		Cl(1)	0.83	-5.216	2.893
	6-31G	N(1)	0.11	-1.652	1.295
		Cl(2)	0.36	5.776	2.950
		N(2)	0.21	-1.716	1.388
		Cl(1)	0.92	-4.017	2.275
CocHCl	6-31G	N	0.37	-1.668	1.417
		Cl	0.31	-8.739	4.438

Table 7.1: Summary of the results from a Gaussian 98 calculation of the quadrupole parameters in heroin hydrochloride monohydrate and cocaine hydrochloride.

7.2.3.2.3 Discussion

The cocaine hydrochloride experimental values ($\eta = 0.263$, QCC = 1.18 MHz, $\nu_+ = 0.961$ MHz for the nitrogen and $\eta = 0.2$, QCC = 5.02 MHz, $\nu_Q = 2.531$ MHz for chlorine) were found by Yesinowski[7]; they are not in good agreement with the calculated theoretical values. This may be because only one molecule is present in the calculation and the hydrogen positions are not well known.

In the case of heroin hydrochloride monohydrate, N(1) and Cl(2) should be the nuclei with more reliable values; they have the most accurately known environment in the Gaussian system as the two water molecules involved in hydrogen bonding to Cl(2) are included in the calculation and the amine N(1) hydrogen is also hydrogen bonded to Cl(2). However, as we see from Table 7.1, the calculated frequencies for the ν_+ line of the N(1) nuclei, ranging from 1.295 to 1.320 MHz, are not in good agreement with the experimental value of 1.035 MHz, found by DRLC by Anthony Horsewill. The experimental asymmetry parameter for ^{14}N in heroin hydrochloride monohydrate was calculated, using the ν_+ and ν_- values of 1.035 and 0.957 MHz (figure. 7.4) to be 0.116, in reasonable agreement with the low asymmetry parameter calculated at the highest basis set (0.11). The QCC was calculated to be 1.341 MHz; again, in rather poor agreement with the Gaussian values for N(1) and N(2) which range between 1.65 and 1.77 MHz across all 3 basis sets used.

The calculated values of the QCC and the ν_Q frequency for ^{35}Cl are in rather poor agreement with the experimental values; however, as the basis set increases, allowing for greater polarization, the theoretical value tends towards the experimental. As the chlorine is a large anion it was necessary to run a calculation with a larger basis set which includes diffuse functions, as this will allow for electrons being far from the nucleus. This, and other improvements in the model, are discussed in the next section.

7.2.3.3 Heroin hydrochloride monohydrate; the final calculations

One important problem is that the X-ray crystal structure analysis, as expected, gives too short a value for the N-H bond length; consequently the coordinates of the hydrogen atoms involved in the hydrogen bonds were altered to give more realistic bond distances,

based on known hydrogen bond data. A spreadsheet was set up to generate altered atomic coordinates, corresponding to the change in bond length, with the only required input being original coordinates of both atoms and the desired bond length. The hydrogen was positioned at the same angle relative to the heteroatom it was classically bonded to previously.

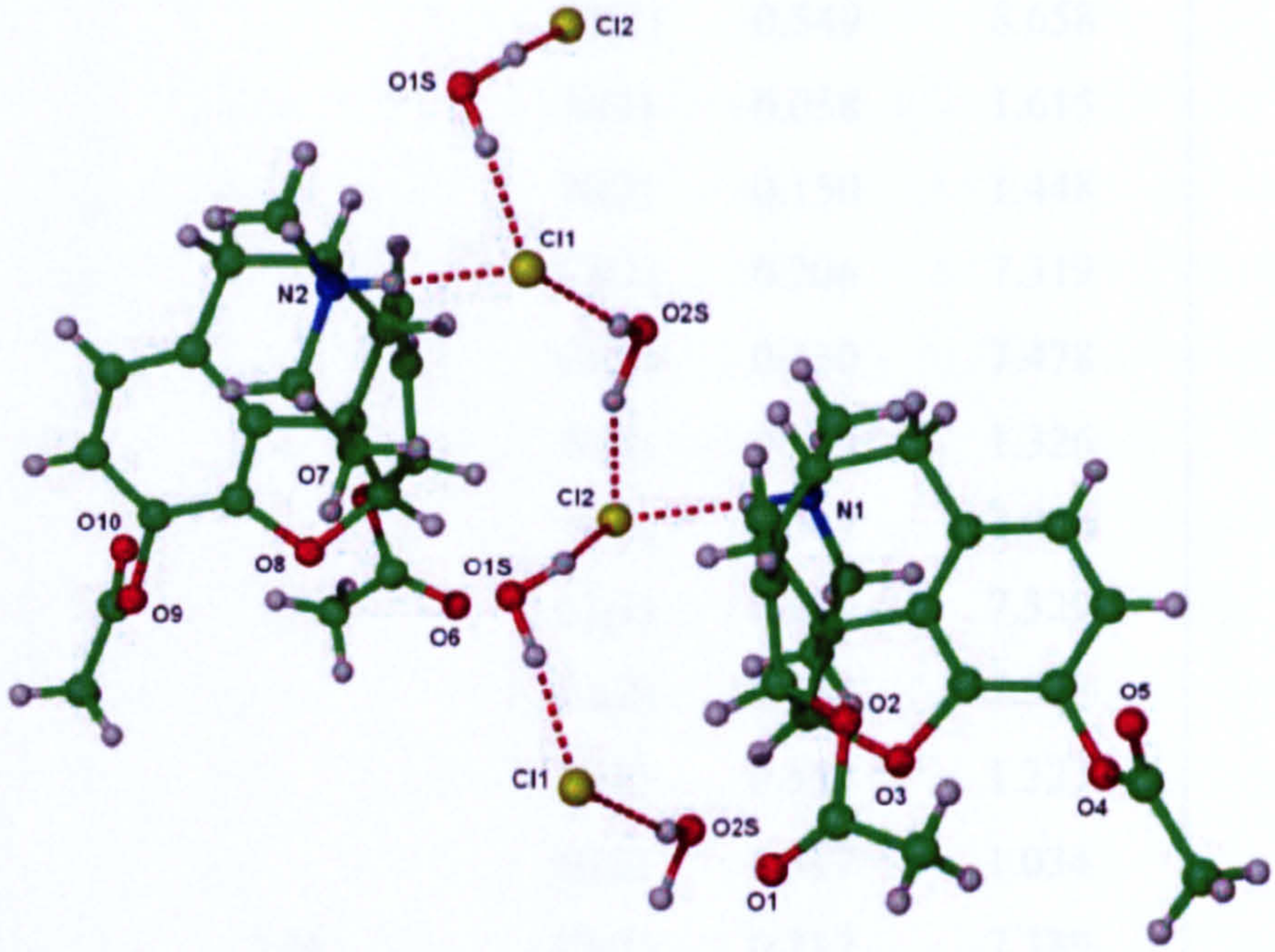

Figure 7.7: X-ray crystal structure of heroin hydrochloride monohydrate.

7.2.3.3.1 Method

The coordinates for both of the main morphine cations were entered, together with the central Cl(1) and Cl(2) anions and the water molecules immediately hydrogen bonded to the central Cl(1) and Cl(2). This was done so that the environment around the quadrupolar nuclei was as 'true' as possible. The two 'outer' Chlorine atoms were not included in the calculation, neither was the water molecule lowermost in figure 7.7.

Using a lower basis set, the effect of changing the bond length on the quadrupole coupling constant (QCC) and asymmetry parameter, η, was investigated. The X-ray crystal structure indicated that one of the O(2S)-H bonds was significantly longer than the others and so this was taken into account by using a simple basis set, STO-G, to calculate the effect of changing the bond length on QCC and η.

O-H Bond length (Å)	Atom	η_{calc}	QCC_{calc} (MHz)
0.98	Cl(1)	0.199	5.123
	Cl(2)	0.549	8.658
	N(1)	0.058	1.615
	N(2)	0.150	1.448
1	Cl(1)	0.206	7.319
	Cl(2)	0.450	7.478
	N(1)	0.553	1.326
	N(2)	0.317	1.033
1.02	Cl(1)	0.209	7.329
	Cl(2)	0.512	7.338
	N(1)	0.555	1.323
	N(2)	0.317	1.034
1.04	Cl(1)	0.212	7.339
	Cl(2)	0.581	7.189
	N(1)	0.557	1.319
	N(2)	0.316	1.036
1.06	Cl(1)	0.215	7.349
	Cl(2)	0.658	7.032
	N(1)	0.561	1.314
	N(2)	0.315	1.037
1.1	Cl(1)	0.222	7.393
	Cl(2)	0.567	6.699
	N(1)	0.838	1.305
	N(2)	0.315	1.039

Table 7.2: Comparison of η and QCC values for heroin hydrochloride monohydrate with varying O(2S)-H bond lengths, calculated using Gaussian98™.

The 1.02 Å calculation gave similar QCC values for Cl(1) and Cl(2) in the STO-G calculations (table 7.2). The coordinates were adjusted accordingly. The bond length was changed so that the HÔH angle was the same as the crystal structure suggested, i.e. the bond was lengthened or shortened along the same line as the bond. The N-H bond lengths were set to 1.017 Å, based on known hydrogen bond data[15].

Finally, since Gaussian98™ is intended for gaseous calculations, the introduction of constraints in the system is desirable. The calculations were run with the basis set 6-31+G*, a polarised basis set, allowing orbitals to change size by adding orbitals with extra angular momentum, i.e., adding d functions. 6-31+G* also includes diffuse functions, allowing greater occupancy of space by the orbitals, important in this case because of the large chlorine anions, where the electrons are not close to the nucleus. 19 basis functions are used per first row atom and 2 are used per hydrogen. The theoretical calculations were run on the two non-equivalent molecules and the quadrupole coupling constant (QCC) and asymmetry parameter, η, were calculated for each ^{14}N and ^{35}Cl atom from which the NQR frequencies were predicted (ν_+ and ν_Q respectively).

It was decided to run two calculations, one with all O-H lengths set at 0.98 Å and another with all O-H bond lengths set to 0.98 Å except the O(2S)-H bond, which was set to 1.02 Å.

7.2.3.3.2 Results

Atom	η	QCC (MHz)	ν_+ / ν_Q (MHz)
Cl (1)	0.311	-4.076	2.070
Cl (2)	0.827	5.388	2.990
N (1)	0.098	-1.575	1.230
N (2)	0.142	-1.399	1.110

Table 7.3: Theoretical NQR values for heroin hydrochloride calculated using Gaussian98, where all O-H bond lengths = 0.98 Å; O(2S)-H bond length = 0.98 Å.

Atom	η	QCC (MHz)	ν_+ / ν_Q (MHz)
Cl (1)	0.338	-4.123	2.100
Cl (2)	0.677	5.311	2.851
N (1)	0.146	-1.560	1.219
N (2)	0.126	-1.460	1.113

Table 7.4: Theoretical NQR values for heroin hydrochloride calculated using Gaussian98, where all O-H bond lengths = 0.98 Å except O(2S)-H bond length = 1.02 Å.

7.2.3.3.3 Discussion

The room temperature double resonance spectra of the heroin hydrochloride monohydrate (figures 7.3, 7.4, 7.5) show clear minima which allow comparison with the theoretical calculated values. The dip at 1965 kHz is assigned to Cl and this frequency is in good agreement with the predicted ν_Q frequency for Cl(1), 2070 kHz with the O(2S)- H bond length = 0.98 Å and 2100 kHz with the O(2S)- H bond length = 1.02 Å, found using the Gaussian98™ program.

The asymmetry parameter was estimated by David Stephenson to be around 0.4 and this is in good agreement with the values of 0.311 and 0.338 obtained theoretically. The ^{14}N dips at 957 and 1035 kHz in figure 7.4 are in reasonable agreement with the theoretical values of 1230 / 1219 and 1110 / 1113 kHz for N(1) and N(2) respectively. The low asymmetry parameters of 0.098 / 0.146 and 0.142 / 0.126 are also what would be expected for the nitrogen sites in heroin hydrochloride, having an approximately trigonal axial environment.

The higher resolution spectra, obtained by frequency stepping in smaller amounts, show resolved doublets for the ^{14}N lines (figure 7.4) and the ^{35}Cl line (figure 7.5) with a splitting of 7, 9 and 20 kHz for the signals around 957, 1035 and 1965 kHz respectively. As mentioned earlier; this may be due to the slight differences in environment The doublet structure seen in the level crossing spectra may be attributable to dipolar interactions between the quadrupolar and hydrogen nuclei. It is possible to calculate quantum mechanically a theoretical value for this splitting and this could be investigated in further studies. Dr. Horsewill reported that he was not able to switch to exactly zero

field in the double resonance experiments; there is a possibility that the doublet structure is due to Zeeman splitting by this small field.

The theoretical NQR values for Cl (2) are quite different to those for Cl(1) in both calculations. With QCCs of 5.388 MHz (0.98 Å) and 5.311 MHz (1.02 Å) and η having values of 0.827 and 0.677, the predicted ν_Q frequencies are 2.99 and 2.851 MHz in comparison with the observed doublet at 1.965 MHz. This region could be further studied by cross relaxation to see if there are any additional quadrupolar features, although there are no obvious features in this region in figure 7.3. However, as the scan was only run to 3 MHz, which is very close to the predicted frequencies, a further experiment covering a slightly higher range may prove useful.

7.2.3.3.4 Conclusion

For ^{14}N, the two sets of results are in reasonable agreement, bearing in mind that thermal motion effects have been neglected and the experimental assignment for the observed doublets has been made to optimize the agreement between the asymmetry parameters rather than the quadrupole coupling constants. The predicted NQR frequencies are sufficiently close to experiment, bearing in mind the neglect of temperature effects, to be used as preliminary estimates when frequency searching for unknown resonances.

For ^{35}Cl, the agreement is less satisfactory, largely because the electric field gradients at this ion are governed by the positions of hydrogen-bonded hydrogen atoms, which are imprecisely located in the X-ray crystal structure analysis. The main uncertainty lies in the position of the O(2S)-H(2S1) hydrogen atom, which strongly affects the electric field gradient at Cl(2); the X-ray value for the Cl(2)···H(2S1) bond length (1.16 Å) is anomalously long and suggests that the H coordinates are unreliable. The quadrupole parameters at Cl(1) are better reproduced and predict an NQR frequency of 2.071 MHz compared with mean values of 1.965 and 1.950 MHz from experiment at 4.2 K and room temperature respectively, which should be regarded as unexpectedly good agreement.

7.2.4 Direction cosines

7.2.4.1 Method

As well as calculating the magnitude of q_{zz}, it is also useful to know the direction of the electric field gradient by calculating the direction cosines. It can be shown that the electric field gradient at the origin, due to a charge, e, at point (x, y, z) at distance r is

$$\frac{e}{r^5}\begin{bmatrix} 3x^2-r^2 & 3xy & 3zx \\ 3xy & 3y^2-r^2 & 3yz \\ 3zx & 3yz & 3z^2-r^2 \end{bmatrix}$$

The values for the field gradient tensor were extracted from the Gaussian results and the directional cosines calculated using Matlab. The field gradient values for the matrix are inputted for each atom and the command **eig** is run. The eigenvectors (direction cosines) and eigenvalues (q_{xx}, q_{yy}, q_{zz}) are out put. The eigenvalues can be easily verified with the Gaussian-produced values to check the calculation. The position of the maximum principal component (q_{zz}) with respect to a bond within the molecule or along a vector can then be established.

7.2.4.2 Results

Atom	Eigenvectors	w.r.t.	q_{zz}	θ	q_{yy}	θ	q_{xx}	θ
Cl(1)	$\begin{bmatrix} 0.9921 & -0.0046 & 0.1256 \\ 0.0818 & -0.7826 & 0.6171 \\ -0.0955 & 0.6225 & 0.7768 \end{bmatrix}$	H(2)	-0.212	23.3	0.139	86.4	0.073	68.4
Cl(2)	$\begin{bmatrix} 0.9889 & 0.1322 & 0.0676 \\ 0.1418 & -0.7061 & -0.6938 \\ 0.0440 & -0.6957 & 0.7170 \end{bmatrix}$	H(1)	0.281	70.3	-0.257	20.2	0.024	85.8
N(1)	$\begin{bmatrix} 0.0186 & -0.4676 & -0.8838 \\ -0.8877 & 0.3991 & -0.2298 \\ -0.4601 & -0.7888 & 0.4076 \end{bmatrix}$	H(1)	0.328	2.86	-0.180	90.0	-0.148	87.1
N(2)	$\begin{bmatrix} 0.3731 & -0.1176 & -0.9203 \\ -0.7274 & -0.6528 & -0.2115 \\ 0.5759 & -0.7483 & 0.3292 \end{bmatrix}$	H(2)	0.291	2.79	-1.166	65.1	-0.125	87.2

Table 7.5: Calculated eigenvectors, eigenvalues and their angles with respect to bonds (Cartesian coordinates) of the quadrupolar nuclei in heroin hydrochloride monohydrate.

7.2.4.3 Discussion

The direction cosine results for heroin hydrochloride were as expected for ^{14}N, with a small angle between the N-H bond and the maximum principal component of the electric field gradient (2.86 ° and 2.79 ° for N(1) and N(2) respectively). This is chemically predictable, as the asymmetry parameter of ^{14}N is low, and q_z would be expected to be close to the N-H bond. The ^{35}Cl results are less consistent, as seen for previous calculations.

7.2.4.4 Conclusion

The objective of the present work was to find a good theoretical model to give reliable NQR frequencies in the solid state, so reducing the time taken in searching for unknown

frequencies. Further work needs to be done on refining the theoretical models used; although they so far have yielded values with rather larger than expected errors; a neutron structure analysis is needed rather than X-rays to achieve reliable hydrogen coordinates. In cases where the NQR frequencies are unknown values within 25 % may be helpful in providing a starting point from which to search for signals experimentally.

7.3 References

[1] Townes, C. H.; Dailey, B. P. *J. Chem. Phys.* **1952**, 20, 35 - 40.

[2] Frisch, M. J.; Trucks, G. W.; Schlegel, H. B.; Scuseria, G. E.; Robb, M. A.; Cheeseman, J. R.; Montgomery, Jr., J. A.; Vreven, T.; Kudin, K. N.; Burant, J. C.; Millam, J. M.; Iyengar, S. S.; Tomasi, J.; Barone, V.; Mennucci, B.; Cossi, M.; Scalmani, G.; Rega, N.; Petersson, G. A.; Nakatsuji, H.; Hada, M.; Ehara, M.; Toyota, K.; Fukuda, R.; Hasegawa, J.; Ishida, M.; Nakajima, T.; Honda, Y.; Kitao, O.; Nakai, H.; Klene, M.; Li, X.; Knox, J. E.; Hratchian, H. P.; Cross, J. B.; Adamo, C.; Jaramillo, J.; Gomperts, R.; Stratmann, R. E.; Yazyev, O.; Austin, A. J.; Cammi, R.; Pomelli, C.; Ochterski, J. W.; Ayala, P. Y.; Morokuma, K.; Voth, G. A.; Salvador, P.; Dannenberg, J. J.; Zakrzewski, V. G.; Dapprich, S.; Daniels, A. D.; Strain, M. C.; Farkas, O.; Malick, D. K.; Rabuck, A. D.; Raghavachari, K.; Foresman, J. B.; Ortiz, J. V.; Cui, Q.; Baboul, A. G.; Clifford, S.; Cioslowski, J.; Stefanov, B. B.; Liu, G.; Liashenko, A.; Piskorz, P.; Komaromi, I.; Martin, R. L.; Fox, D. J.; Keith, T.; Al-Laham, M. A.; Peng, C. Y.; Nanayakkara, A.; Challacombe, M.; Gill, P. M. W.; Johnson, B.; Chen, W.; Wong, M. W.; Gonzalez, C.; Pople, J. A. Gaussian 01, Development Version (Revision B.01), Gaussian, Inc., Pittsburgh, PA, **2003**.

[3] Foresman, J. B.; Frisch, A. *Exploring Chemistry with Electronic Structure Methods*, **Second Edition**, Gaussian, Inc.

[4] Cohen, E. R.; Taylor, B. N. *J. Phys. Chem, Ref. Data*, **1988**, *96*, 92.

[5] P. Pyykkö, *Mol. Phys.*, **2001**, *99*, 1617 - 1629.

[6] Rowe, M. D.; Smith, J. A. S. Unpublished results.

[7] Yesinowski, J. P.; Buess, M. L.; Garroway, A. N.; Ziegeweid, M.; Pines, A. *Anal. Chem.* **1995**, *67*, 2256 - 2263.

[8] Balchin, E. *"Nuclear Quadrupole Resonance: The Detection of Narcotics and Explosives"*, 4th Year Project, March **2002**, King's College London.

[9] Grechishkin, V. S.; Ya Sinyavski, N. *Physics Uspekhi*, **1997**, *40 (4)*, 393 - 406.

[10] Emery, E.F.; McGrath, K.; Yesnowski, J. P.; Miller, J. B.; Butler, L. G. *"^{14}N NQR and NMR of Heroin Hydrochloride"*, 38th ENC (Poster Session), Orlando, FL, March 23 - 27, **1997**.

[11] Balchin, E.; Bearpark, M.; Malcolme-Lawes, D. J.; Rowe, M. D.; Smith, J. A. S.; Steed, J. W.; Wu, W.; Horsewill, A. J.; Stephenson, D. *N. J. Chem.* **2004**, *28*, 1309 - 1314.

[12] Herberich, G. E.; Jackson, R. H.; Millen, D. J. *J. Chem. Soc.*, **1966**, *A*, 336.

[13] Downs, A. J.; Adams, C. J. *The Chemistry of Chlorine, Bromine, Iodine and Astatine,* Pergamon Press.

[14] Gabe, E. J.; Barnes, W. H. Acta Cryst., 1963, 16, 796 - 801.

[15] Demaison, J.; Margules, L.; Boggs, J. E. *Chem. Phys.*, **2000**, *260*, 65 - 81.

8 Future perspectives and summary

8.1 Future perspectives

NQR analysis has potential for use at all stages of manufacture. During synthesis of the API the formation of the solid NQR-sensitive product could be monitored, with quantification being especially useful at this stage. Once formed, crystal quality and compression effects could be assessed by linewidth measurements; changes in the ^{14}N linewidths across the furosemide tablet and powder experiments indicate there may be the possibility of determining experimental conditions and from this, point of manufacture or batch.

Post-production, the mass of API within a single tablet can be monitored and on packaging the total mass can be estimated, from which the number of tablets contained within a container calculated, allowing quality control checking of strength and amount. Degradation of the active pharmaceutical ingredient, or indeed any NQR-sensitive component of a formulation, could be easily monitored over time, provided that the experimental time is suitably rapid compared to the degradation timescale. Such experiments could be carried out *in situ* or otherwise. Long term degradation in response to the storage environment could also be monitored to observe the effects of temperature, humidity or air on the sample material, even whilst still sealed in their original packaging. Turnover from one polymorph to another could be monitored in a stirred slurry, although again the experimental time would need to be suitably short in comparison to the turnover timescale. If NQR were to become a more commonly used analytical technique in pharmaceutical industry such an instrument could be used in hospitals, to check medicines and by retailers in checking shelf life and specifically designed instrumentation would be required. Commercially, a pulsed NQR spectrometer could be made having a 'Yes/No' capability based on an AML algorithm with suitable software providing real time operation; with little sample preparation needed it would be easy to use, portable, and suitable for use in the end stages of manufacture and quality control. In the research and development stages, NQR spectrometers which allowed automated frequency searching could be made to allow for faster initial characterisation of materials. Exploiting the tendency for signal strength to increase with increasing frequency for example ^{35}Cl in organic compounds giving signals around 20 – 36 MHz, as in

furosemide, ^{127}I giving signals around 300 - 600 MHz[1] as in thyroxins, higher frequency work up to 300 MHz or more, could be carried out; for example pharmaceutical solids containing $^{79,81}Br$ nuclei may give signals in the higher frequency region between 80 and 300 MHz[2] which should have low acquisition times to give a good signal-to-noise ratios. Work in this frequency region needs a complete redesign of the RF probe, using, for example, transmission line designs[3] or series tuned high-frequency RF coils[4] or a butterfly-capacitor[5]circuit in loop gap resonators[6] in order to study the large volumes of medicine containers or even small numbers of tablets.

General improvements in coil design, electronics, pulse sequences and all areas of NQR experimentation could increase field homogeneity and signal-to-noise ratios or decrease the time needed to achieve a result.

More radical changes in experimental apparatus, such as multiple coils for multiplexing[7] – allowing three dimensional, independent, orthogonal RF fields to be produced - could allow a number of materials to be detected simultaneously in cases where the frequency separations were too large to allow analysis such as that carried out in chapter 5 on mixed samples. Two techniques which can be easily added to current NQR apparatus and experiments and are being looked into at King's College are polarisation-enhanced NQR and signal processing using approximative maximum likelihood (AML) algorithms and are discussed in more detail below.

8.1.1 Polarization-enhanced nuclear quadrupole resonance

A technique known as polarization-enhancement is more complicated than pure zero-field NQR, requiring more instrumentation and a switched d.c. magnetic field, but the increase in sensitivity achieved can greatly reduce the time taken to acquire a signal with sufficient SNR. It is particularly suited to low radiofrequency ^{14}N signals, which are inherently weak, so may overcome the problems associated with the timescales in ^{14}N work which are not so prevalent in ^{35}Cl experiments. Like many techniques used in NQR, it was first applied to NMR[8] and subsequently adapted with advancements in NMR happening more rapidly due to its more prevalent use and study. It is a double-resonance technique, similar to those described in chapter 3. However, unlike previous methods

where the effects of quadrupolar nuclei on the spin-½ nuclei were being measured, the quadrupolar nuclei are themselves measured directly.

Application of a magnetic field polarises the protons, or any other magnetic nuclei in the sample, at a frequency ν_P; the field is then switched off or the sample moved to zero field. In an adiabatic process the collapsing proton levels energy levels cross the quadrupolar levels when $\nu_P = \nu_Q$, so transferring the proton polarisation to the quadrupolar nuclei, whereupon an enhanced NQR signal at a frequency ν_Q ($\nu_P >> \nu_Q$) may be observed in zero field with an intensity increased by a factor of approximately (ν_P/ν_Q). Luznik *et. al*[9] have suggested the approximate equation (8.1) can be used to estimate the enhancement factor,

$$F = \frac{\nu_P}{\nu_Q} \cdot \frac{N_P}{N_P + N_Q} \qquad (8.1)$$

They recorded the experimental enhancement and compared this to the calculated theoretical enhancement of the ^{14}N signal for a number of materials; good agreement was observed. The magnetic fields required are not necessarily homogeneous, provided that the entire sample experiences roughly the same polarising field; the more critical factors are the values of the proton and ^{14}N spin-lattice relaxation times; both T_1 values must be sufficiently long to allow movement of the sample to zero field whilst maintaining a level of polarization. Movement of the sample from high to zero field cannot usually be accomplished in times less than 50 to 100 ms, depending on the transfer distance but fast, automated switching of an electromagnet can be conducted in considerably shorter times. Work carried out by Dr. Iain Poplett at King's College London on ammonium nitrate demonstrated the increase in intensity achieved by use of PE-NQR in comparison to zero-field NQR.

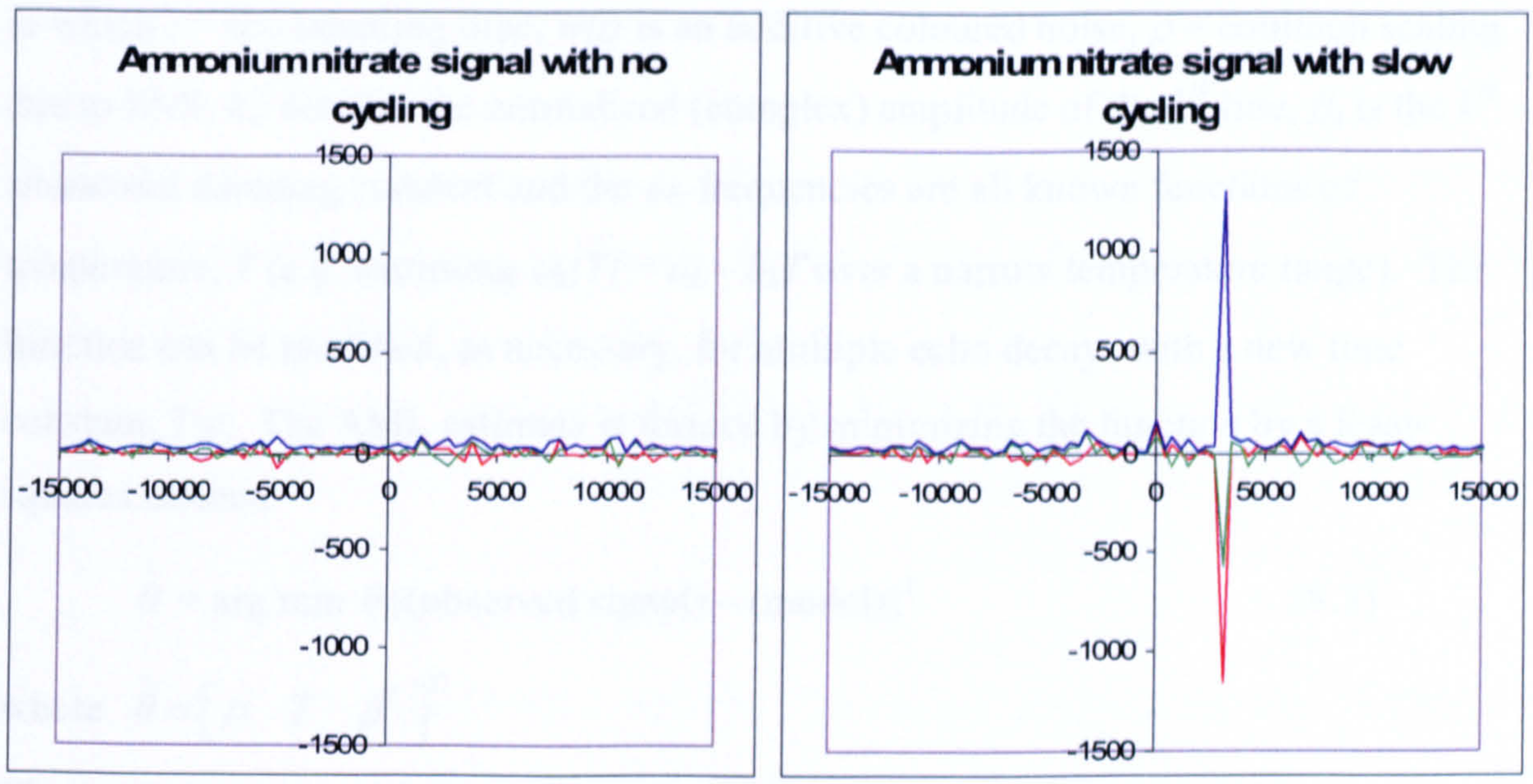

Figure 8.1: (a) - ^{14}N averaged NQR signal from NH_4NO_3 at 423 kHz from one multiple-pulse sequence and (b) – as a but following application of a magnetic field of 0.47 T. In both figures the *x* axis represents *Δfrequency* from the RF input in Hz and the *y* axis is signal intensity.

Pre-polarisation in a magnetic field of 0.47 T dramatically enhanced the ^{14}N NQR signal at 0.423 MHz from crystalline NH_4NO_3; a single multiple-pulse sequence yields a signal drowned in noise under normal zero-field conditions (figure 8.1a) in comparison with the strong signal seen after a single multiple pulse sequence using PE-NQR (figure 8.1b). Although most PE-NQR work has been carried out using explosives[10,11], the technique can be readily applied to pharmaceutical analysis.

8.1.2 Signal Processing

Signal processing techniques such as applying approximative maximum likelihood (AML) algorithms to NQR data can help to reduce the time needed to identify a compound by enhancing NQR spectra[12]. A model based algorithm is used, exploiting the maximum amount of prior knowledge about the signal and in which a *d*-line spectrum is modelled as a sum of *d* exponentially-damped sinusoids.

The model signal

$$y_{FID}(t) = \rho \sum_{k=1}^{d} k_k^f e^{-\beta_k t + i\omega_k(T)t} T + w(t) \qquad (8.2)$$

in which t = the sampling time, $w(t)$ is an additive coloured noise, ρ = common scaling due to SNR, k_k^f denotes the normalized (complex) amplitude of the k^{th} line, β_k is the k^{th} sinusoidal damping constant and the ω_k frequencies are all known functions of temperature, T (e.g. assuming $\omega_k(T) = a_k - b_k T$ over a narrow temperature range). The function can be modified, as necessary, for multiple echo decays with a new time constant, T_2e. The AML estimate is formed by minimizing the function by a least-squares method

$$\hat{\theta} = \arg\min \theta \,\|(\text{observed signal}) - (\text{model})\|^2 \qquad (8.3)$$

where $\hat{\theta} = \left[\rho \quad T \quad \beta^T\right]^T$

The output is a test statistic S or a generalised likelihood ratio test (GRLT) and a signal is deemed to be present only if $S > \gamma$ where γ is a pre-determined threshold value reflecting the acceptable probability of a false alarm. In principle this technique is capable of being modified to determine the ratio of polymorphic forms in a sample – a method of quantitative analysis. As shown in chapter 5, the temperature coefficients must be known for each line in the spectrum and ideally both lines will have similar behaviour with regards to echo trains, NQR frequencies and spin-lattice relaxation rates which will minimise 'wasted' time in recovery time . A long echo train is also desirable, such as in the case of 4-methylimidazole. Applying AML algorithms of this kind to NQR signals can hopefully generate faster detection times and a more automated analysis suitable for commercial and industrial use.

8.2 Summary

The work presented in this thesis has shown that pulsed nuclear quadrupole resonance is well suited to the analysis of pharmaceutical solids. As a non-invasive and non-destructive solid state analytical method it can be applied in the determination of polymorphs; its highly sensitive nature results in frequency shifts for even small positional changes of nuclei within the crystal structure as was demonstrated in the theoretical calculations. In the case of furosemide the polymorphic change brought a change in the crystal lattice which resulted in differing peak multiplicities as well as a

frequency shift, which allowed for immediate and obvious differentiation between the two phases studied.

Quantification of single samples of both tablets and volumes of bulk powder has been demonstrated using ^{35}Cl and ^{14}N signals and the potential to measure mixed samples in a quantitative manner has been observed.

A wide range of volumes can be analysed without the need for sample preparation, from single tablets to large masses of solids, having the advantage that NQR solenoids can be designed specifically for the sample to be studied, with probe modifications being relatively cheap and easy to carry out.

We have shown that pulsed nuclear quadrupole resonance spectroscopy is an analytical technique with great potential for future use in the pharmaceutical industry, complementing its use in security applications and providing a flexible, sensitive, non-destructive and non-invasive method of analysis across a wide range of materials.

8.3 References

[1] Shishkin, V. A.; Balicheva, T. G.; Petrova, G. A.; Potapov, A. G.; Cheburina, L. A. *J. Mol. Struct.* **1982**, *83*, 349 - 352.

[2] Hadipour, N. L.; Javadian, S. *J. Mol. Struct.*, **2000**, *525*, 129 - 134.

[3] Das, T. P.; Hahn, E. L."*Nuclear Quadrupole Resonance Spectroscopy*," Academic Press, **1958**.

[4] Cook, B.; Lowe, I. J. *J. Magn. Reson.*, **1982**, *49*, 346 - 349.

[5] Butcher, P. M.; Smith, J. A. S.; Turner, C. J. *J. Phys. E: Sci. Instrum.*, **1979**, *12*, 484 - 489.

[6] Mrse, A. A.; Lee, Y.; Bryant, P. L.; Fronczek, F. R.; Simeral, L. S.; Butler, L. G. *Chem. Mater.*, **1998**, *10*, 1291 - 1300.

[7] Peshkovsky, A.S.; Cerioni, L.; Osan, T.M.; Avdievich, N.I.; Pusiol, D.J. *Solid State Nucl. Magn. Res.*, **2006**, *30*, 75 - 80; Ching-Ming-Li, European Patent number EP1416291A2, **2004**.

[8] Bendall, M. R.; Doddrell, D. M.; Pegg, D.T.; *J. Am. Chem. Soc.*, **1981**, *103*, 4603 - 4605.

[9] Luznik, J.; Pirnat, J.; Trontelj, Z., *Solid State Comm.*, **2002**, *121*, 653 - 656.

[10] Luznik, J.; Pirnat, J.; Jazbinšek, V.; Apih, T.; Gregorovic, A.; Blinc, R.; Seliger, J.; Trontelj, Z. *App. Phys. Lett.*, **2006**, *89*, 123509 - 123511.

[11] Rudakov, T. N.; Hayes, P.A. *J. Magn. Res.*, **2006**, *183*, 96 - 101.

[12] Somasundaram, S.; Jakobsson, A.; Smith, J. A. S.; Althoefer, K. A. *SPIE Proc.*, **2006**, *6217*, pp 62172D.

9 Appendices

9.1 Heroin hydrochloride crystal structure data

	x	*y*	*z*	*U(eq)*
Cl(1)	-5653(5)	9729(6)	8120(1)	41(1)
O(1S)	629(14)	9213(13)	8303(2)	58(4)
O(1)	5960(15)	10081(14)	7589(2)	42(3)
N(1)	-759(16)	3540(17)	7983(2)	31(3)
C(1)	5760(20)	9600(20)	7256(3)	49(6)
Cl(2)	-650(5)	5282(6)	8372(1)	40(1)
O(2)	3414(14)	8977(13)	7464(1)	32(3)
N(2)	-5769(15)	11372(17)	8508(2)	37(4)
C(2)	5150(20)	9640(20)	7453(4)	44(6)
O(3)	4479(13)	5937(12)	7599(2)	36(3)
C(3)	2671(18)	8711(18)	7649(2)	26(4)
O(4)	5070(13)	3998(14)	7246(2)	40(3)
C(4)	720(20)	8890(20)	7631(2)	39(5)
O(5)	4017(15)	5831(16)	7025(2)	51(3)
C(5)	-470(20)	7933(19)	7718(2)	30(4)
O(6)	910(15)	4908(14)	8902(2)	47(3)
C(6)	90(20)	6441(19)	7841(2)	27(4)
O(7)	-1557(15)	6057(13)	9027(2)	40(3)
C(7)	-1290(20)	4930(20)	7837(2)	36(5)
O(8)	-575(12)	9074(13)	8896(2)	33(3)
C(8)	-2160(19)	2190(20)	8012(2)	47(5)
O(9)	57(13)	11030(14)	9245(2)	40(3)
C(9)	1042(17)	2870(19)	7957(2)	26(4)
O(10)	-959(16)	9192(16)	9469(2)	52(3)
C(10)	2408(19)	4290(19)	7936(2)	29(4)
C(11)	1870(20)	5620(20)	7783(2)	30(4)

O(2S)	-4373(14)	5779(13)	8195(2)	58(4)
C(12)	3387(17)	6956(18)	7737(2)	30(4)
C(13)	3200(20)	4820(20)	7505(2)	37(4)
C(14)	1700(20)	4745(19)	7600(2)	23(4)
C(15)	230(20)	3930(20)	7541(2)	24(4)
C(16)	-1556(18)	4089(19)	7642(2)	29(4)
C(17)	340(20)	3116(19)	7361(2)	38(5)
C(18)	1950(20)	3110(18)	7266(2)	43(5)
C(19)	3400(20)	3989(19)	7340(2)	28(4)
C(20)	5180(30)	4910(20)	7077(3)	41(5)
C(21)	6970(20)	4592(18)	6987(2)	55(6)
C(22)	840(20)	5440(20)	9229(3)	60(6)
C(23)	100(30)	5450(20)	9035(3)	42(5)
C(24)	-2280(20)	6290(20)	8846(2)	34(4)
C(25)	-4254(19)	6055(18)	8865(2)	24(4)
C(26)	-5400(20)	7040(20)	8775(2)	46(5)
C(27)	-4940(20)	8590(20)	8655(2)	34(5)
C(28)	-6330(20)	10059(19)	8659(2)	27(4)
C(29)	-7129(18)	12839(17)	8476(2)	32(4)
C(30)	-3928(17)	12230(20)	8542(2)	43(5)
C(31)	-2590(20)	10705(18)	8559(2)	30(4)
C(32)	-3160(20)	9370(20)	8705(2)	35(5)
C(33)	-1632(18)	8101(19)	8760(2)	29(4)
C(34)	-1790(20)	10127(19)	8986(2)	37(5)
C(35)	-3350(20)	10257(19)	8890(2)	33(5)
C(36)	-4870(20)	11130(20)	8967(3)	38(5)
C(37)	-6554(19)	10940(20)	8851(2)	40(5)
C(38)	-4640(20)	11978(19)	9128(2)	32(4)
C(39)	-3040(20)	11897(19)	9224(2)	31(4)
C(40)	-1630(20)	10970(20)	9153(2)	43(5)
C(41)	190(30)	10140(20)	9407(3)	41(5)

C(42)	1910(20)	10420(18)	9508(3)	71(7)

Table 9.1: Atomic coordinates (x 10^4) and equivalent isotropic displacement parameters ($Å^2$x 10^3) for heroin hydrochloride monohydrate. *U(eq)* is defined as one third of the trace of the orthogonalized U^{ij} tensor.

O(1)-C(2)	1.20(2)
N(1)-C(9)	1.459(15)
N(1)-C(8)	1.483(17)
N(1)-C(7)	1.536(18)
C(1)-C(2)	1.49(3)
O(2)-C(2)	1.399(18)
O(2)-C(3)	1.455(16)
N(2)-C(29)	1.525(16)
N(2)-C(28)	1.529(18)
N(2)-C(30)	1.551(16)
O(3)-C(13)	1.448(18)
O(3)-C(12)	1.502(16)
C(3)-C(4)	1.485(17)
C(3)-C(12)	1.564(19)
O(4)-C(20)	1.39(2)
O(4)-C(19)	1.429(16)
C(4)-C(5)	1.31(2)
O(5)-C(20)	1.178(17)
C(5)-C(6)	1.495(19)
O(6)-C(23)	1.20(2)
C(6)-C(11)	1.531(19)
C(6)-C(7)	1.55(2)
O(7)-C(23)	1.33(2)
O(7)-C(24)	1.427(16)
C(7)-C(16)	1.55(2)

O(8)-C(34)	1.375(18)
O(8)-C(33)	1.461(16)
O(9)-C(41)	1.35(2)
O(9)-C(40)	1.433(17)
C(9)-C(10)	1.493(17)
O(10)-C(41)	1.212(19)
C(10)-C(11)	1.546(18)
C(11)-C(14)	1.47(2)
C(11)-C(12)	1.558(18)
C(13)-C(14)	1.33(2)
C(13)-C(19)	1.349(19)
C(14)-C(15)	1.335(19)
C(15)-C(17)	1.43(2)
C(15)-C(16)	1.535(19)
C(17)-C(18)	1.395(19)
C(18)-C(19)	1.383(19)
C(20)-C(21)	1.52(2)
C(22)-C(23)	1.51(2)
C(24)-C(25)	1.502(17)
C(24)-C(33)	1.574(19)
C(25)-C(26)	1.312(19)
C(26)-C(27)	1.49(2)
C(27)-C(32)	1.51(2)
C(27)-C(28)	1.52(2)
C(28)-C(37)	1.54(2)
C(30)-C(31)	1.537(17)
C(31)-C(32)	1.52(2)
C(32)-C(35)	1.50(2)
C(32)-C(33)	1.546(18)
C(34)-C(35)	1.36(2)
C(34)-C(40)	1.37(2)

C(35)-C(36)	1.43(2)
C(36)-C(38)	1.33(2)
C(36)-C(37)	1.53(2)
C(38)-C(39)	1.391(19)
C(39)-C(40)	1.372(19)
C(41)-C(42)	1.50(2)

C(9)-N(1)-C(8)	116.2(12)
C(9)-N(1)-C(7)	113.2(12)
C(8)-N(1)-C(7)	112.4(12)
C(2)-O(2)-C(3)	117.5(14)
C(29)-N(2)-C(28)	113.1(12)
C(29)-N(2)-C(30)	108.7(11)
C(28)-N(2)-C(30)	114.1(12)
O(1)-C(2)-O(2)	122(2)
O(1)-C(2)-C(1)	128.5(18)
O(2)-C(2)-C(1)	109.7(18)
C(13)-O(3)-C(12)	104.1(11)
O(2)-C(3)-C(4)	106.9(12)
O(2)-C(3)-C(12)	110.9(11)
C(4)-C(3)-C(12)	117.1(12)
C(20)-O(4)-C(19)	117.8(13)
C(5)-C(4)-C(3)	126.0(16)
C(4)-C(5)-C(6)	120.2(15)
C(5)-C(6)-C(11)	112.8(14)
C(5)-C(6)-C(7)	110.4(13)
C(11)-C(6)-C(7)	106.7(12)
C(23)-O(7)-C(24)	116.2(13)
N(1)-C(7)-C(6)	108.1(13)
N(1)-C(7)-C(16)	112.0(13)
C(6)-C(7)-C(16)	113.9(14)

C(34)-O(8)-C(33)	103.9(11)
C(41)-O(9)-C(40)	116.7(14)
N(1)-C(9)-C(10)	114.0(12)
C(9)-C(10)-C(11)	110.9(12)
C(14)-C(11)-C(6)	110.5(13)
C(14)-C(11)-C(10)	111.5(12)
C(6)-C(11)-C(10)	107.2(13)
C(14)-C(11)-C(12)	99.6(12)
C(6)-C(11)-C(12)	116.1(13)
C(10)-C(11)-C(12)	111.9(12)
O(3)-C(12)-C(11)	102.2(11)
O(3)-C(12)-C(3)	110.5(12)
C(11)-C(12)-C(3)	112.1(11)
C(14)-C(13)-C(19)	122.1(16)
C(14)-C(13)-O(3)	110.4(15)
C(19)-C(13)-O(3)	127.4(16)
C(13)-C(14)-C(15)	124.0(16)
C(13)-C(14)-C(11)	111.7(14)
C(15)-C(14)-C(11)	124.3(15)
C(14)-C(15)-C(17)	116.2(14)
C(14)-C(15)-C(16)	122.5(15)
C(17)-C(15)-C(16)	120.6(15)
C(15)-C(16)-C(7)	110.4(13)
C(18)-C(17)-C(15)	119.4(15)
C(19)-C(18)-C(17)	120.0(16)
C(13)-C(19)-C(18)	118.1(15)
C(13)-C(19)-O(4)	120.9(15)
C(18)-C(19)-O(4)	120.9(14)
O(5)-C(20)-O(4)	121.7(18)
O(5)-C(20)-C(21)	128.0(17)
O(4)-C(20)-C(21)	110.2(14)

O(6)-C(23)-O(7)	123.9(17)
O(6)-C(23)-C(22)	123.1(19)
O(7)-C(23)-C(22)	112.9(17)
O(7)-C(24)-C(25)	106.1(12)
O(7)-C(24)-C(33)	110.4(12)
C(25)-C(24)-C(33)	116.7(12)
C(26)-C(25)-C(24)	122.4(14)
C(25)-C(26)-C(27)	125.3(15)
C(26)-C(27)-C(32)	112.0(14)
C(26)-C(27)-C(28)	113.6(13)
C(32)-C(27)-C(28)	108.8(14)
C(27)-C(28)-N(2)	105.5(12)
C(27)-C(28)-C(37)	113.8(13)
N(2)-C(28)-C(37)	112.9(13)
C(31)-C(30)-N(2)	106.6(12)
C(32)-C(31)-C(30)	111.5(13)
C(35)-C(32)-C(27)	107.4(15)
C(35)-C(32)-C(31)	110.4(13)
C(27)-C(32)-C(31)	110.2(14)
C(35)-C(32)-C(33)	97.0(13)
C(27)-C(32)-C(33)	118.8(14)
C(31)-C(32)-C(33)	112.1(13)
O(8)-C(33)-C(32)	105.4(11)
O(8)-C(33)-C(24)	109.9(12)
C(32)-C(33)-C(24)	113.7(12)
C(35)-C(34)-C(40)	119.3(16)
C(35)-C(34)-O(8)	112.3(15)
C(40)-C(34)-O(8)	128.4(17)
C(34)-C(35)-C(36)	121.7(17)
C(34)-C(35)-C(32)	109.4(15)
C(36)-C(35)-C(32)	128.9(16)

C(38)-C(36)-C(35)	116.9(16)
C(38)-C(36)-C(37)	128.8(15)
C(35)-C(36)-C(37)	114.2(16)
C(36)-C(37)-C(28)	116.1(14)
C(36)-C(38)-C(39)	121.6(15)
C(40)-C(39)-C(38)	120.4(15)
C(34)-C(40)-C(39)	119.7(15)
C(34)-C(40)-O(9)	120.0(17)
C(39)-C(40)-O(9)	120.0(16)
O(10)-C(41)-O(9)	123.9(18)
O(10)-C(41)-C(42)	121.4(19)
O(9)-C(41)-C(42)	114.7(16)

Table 9.2: Bond lengths (Å) and angles (°) of heroin hydrochloride.

	U^{11}	U^{22}	U^{33}	U^{23}	U^{13}	U^{12}
Cl(1)	39(3)	45(3)	40(3)	-1(2)	-1(2)	-4(2)
O(1S)	59(9)	52(9)	64(10)	-13(6)	7(7)	-11(6)
O(1)	30(8)	43(9)	53(10)	-8(6)	-9(7)	-15(6)
N(1)	39(9)	30(9)	24(8)	6(6)	1(6)	-13(7)
C(1)	64(15)	28(12)	56(16)	5(10)	37(11)	-2(9)
Cl(2)	43(3)	39(3)	37(3)	-3(2)	-2(2)	4(2)
O(2)	34(7)	38(7)	25(7)	7(5)	5(5)	2(6)
N(2)	37(7)	33(7)	41(8)	4(6)	-16(6)	18(6)
C(2)	12(13)	11(12)	110(20)	5(12)	-11(12)	4(9)
O(3)	38(8)	33(8)	37(8)	-1(5)	-5(6)	4(6)
C(3)	29(11)	8(9)	40(11)	-8(7)	0(8)	-10(8)
O(4)	44(8)	45(8)	30(8)	13(6)	3(5)	11(6)
C(4)	27(11)	26(11)	62(13)	-2(9)	-12(9)	16(9)
O(5)	35(9)	65(9)	53(9)	20(7)	-3(6)	1(6)

C(5)	32(8)	22(8)	36(8)	-6(7)	2(7)	12(7)
O(6)	40(8)	45(9)	56(11)	0(7)	-9(8)	1(7)
C(6)	33(11)	3(10)	46(12)	0(8)	-13(8)	-2(8)
O(7)	28(8)	33(7)	58(9)	-7(6)	-8(6)	4(6)
C(7)	13(10)	54(13)	40(13)	18(10)	9(8)	9(9)
O(8)	27(7)	34(8)	38(8)	-4(5)	-2(6)	5(5)
C(8)	45(12)	65(13)	31(10)	-5(9)	18(8)	-31(10)
O(9)	34(8)	49(8)	36(9)	15(6)	2(6)	-9(6)
C(9)	18(10)	47(12)	14(10)	11(8)	7(7)	-7(9)
O(10)	52(9)	46(9)	58(9)	10(7)	-1(7)	0(6)
C(10)	8(10)	58(13)	22(10)	-9(8)	-9(7)	1(8)
C(11)	21(11)	55(12)	13(10)	7(8)	-2(7)	13(9)
O(2S)	38(8)	48(8)	89(11)	-18(6)	-23(7)	9(6)
C(12)	23(8)	27(8)	39(8)	-8(6)	-1(6)	-18(7)
C(13)	18(12)	62(13)	31(12)	0(9)	-13(9)	20(9)
C(14)	19(11)	24(11)	27(11)	-13(7)	4(9)	-10(8)
C(15)	26(11)	27(11)	17(10)	2(8)	6(7)	12(9)
C(16)	31(11)	10(10)	45(13)	0(8)	-1(8)	2(8)
C(17)	39(13)	40(13)	36(12)	3(9)	-3(8)	-9(9)
C(18)	50(13)	19(11)	59(13)	-11(8)	1(10)	-12(10)
C(19)	38(13)	27(11)	18(10)	0(8)	13(9)	7(9)
C(20)	49(14)	34(13)	40(15)	3(10)	-25(11)	-4(10)
C(21)	42(14)	80(15)	42(12)	12(11)	15(10)	30(10)
C(22)	66(15)	64(14)	49(16)	-7(11)	-14(11)	18(11)
C(23)	60(16)	47(14)	18(12)	14(10)	-3(10)	-12(11)
C(24)	56(13)	29(11)	18(10)	3(7)	-11(8)	10(9)
C(25)	26(8)	29(8)	15(7)	7(6)	3(6)	-7(7)
C(26)	34(12)	41(12)	63(13)	10(10)	1(9)	-11(10)
C(27)	22(11)	56(14)	26(11)	1(9)	-2(8)	1(9)
C(28)	46(12)	21(11)	14(10)	-1(7)	4(8)	6(8)
C(29)	35(11)	7(9)	53(11)	-7(7)	-6(8)	9(8)

C(30)	10(10)	49(13)	69(14)	7(10)	-2(8)	-6(9)
C(31)	38(12)	9(10)	42(12)	-10(8)	-16(8)	8(8)
C(32)	26(12)	29(12)	50(14)	2(9)	-12(9)	10(9)
C(33)	34(11)	27(10)	27(9)	-12(7)	14(8)	5(9)
C(34)	66(15)	22(11)	24(11)	-4(8)	-13(10)	18(10)
C(35)	58(14)	13(11)	27(12)	11(8)	-6(10)	-13(9)
C(36)	33(12)	32(12)	49(13)	-11(9)	26(10)	12(9)
C(37)	25(11)	63(13)	31(12)	11(9)	9(9)	-3(9)
C(38)	32(12)	28(12)	37(12)	-2(9)	2(8)	1(8)
C(39)	47(13)	34(11)	12(9)	-4(7)	2(8)	-14(10)
C(40)	36(14)	39(12)	54(13)	18(10)	-31(11)	-7(10)
C(41)	42(14)	19(12)	60(17)	-6(10)	10(11)	6(10)
C(42)	55(15)	71(16)	88(17)	22(13)	-32(13)	-21(11)

Table 9.3: Anisotropic displacement parameters ($Å^2 x\ 10^3$) for heroin hydrochloride monohydrate. The anisotropic displacement factor exponent takes the form: $-2\pi^2[\ h^2\ a^{*2}U^{11} + ... + 2\ h\ k\ a^*\ b^*\ U^{12}]$.

	x	*y*	*z*	*U(eq)*
H(1S1)	1840	9198	8253	87
H(1)	-715	4168	8094	37
H(1A)	6434	8512	7234	74
H(1B)	6512	10635	7232	74
H(1C)	4725	9632	7173	74
H(2)	-5685	10732	8398	44
H(3)	3094	9714	7728	31
H(4)	289	9787	7550	46
H(5)	-1700	8187	7702	36
H(6)	199	6891	7971	33
H(7)	-2459	5443	7876	43

H(8A)	-1843	1443	8119	71
H(8B)	-2266	1443	7901	71
H(8C)	-3294	2779	8037	71
H(9A)	1067	2102	7846	32
H(9B)	1358	2125	8066	32
H(10A)	3563	3745	7903	35
H(10B)	2551	4927	8055	35
H(12)	4099	7220	7851	36
H(16A)	-2095	2897	7655	34
H(16B)	-2374	4835	7568	34
H(17)	-684	2585	7307	46
H(18)	2058	2502	7151	51
H(21A)	7917	4839	7077	82
H(21B)	7104	5379	6879	82
H(21C)	7054	3353	6946	82
H(22A)	2140	5408	9224	90
H(22B)	404	4393	9296	90
H(22C)	459	6516	9295	90
H(24)	-1828	5312	8765	41
H(25)	-4686	5158	8946	28
H(26)	-6620	6740	8786	56
H(27)	-4862	8148	8524	41
H(28)	-7499	9534	8622	32
H(29A)	-7221	13578	8587	48
H(29B)	-8288	12307	8448	48
H(29C)	-6753	13573	8370	48
H(30A)	-3608	13020	8437	51
H(30B)	-3944	12949	8657	51
H(31A)	-2477	10099	8437	36
H(31B)	-1410	11191	8592	36
H(33)	-886	7850	8648	35

H(37A)	-7066	12136	8832	48
H(37B)	-7425	10238	8923	48
H(38)	-5592	12656	9178	39
H(39)	-2927	12490	9340	37
H(42A)	2094	9452	9597	107
H(42B)	1875	11555	9575	107
H(42C)	2895	10436	9419	107
H(2S1)	-3062	5988	8277	107
H(2S2)	-4489	6940	8150	107
H(1S2)	76	8223	8243	107

Table 9.4: Hydrogen coordinates (x 10^4) and isotropic displacement parameters ($Å^2$x 10^3) for heroin hydrochloride monohydrate.

D-H...A	d(D-H)	d(H...A)	d(D...A)	<(DHA)
O(1S)-H(1S1)...Cl(1)#1	0.98	2.15	3.119(11)	167.5
N(1)-H(1)...Cl(2)	0.93	2.17	3.095(14)	172.1
N(2)-H(2)...Cl(1)	0.93	2.14	3.056(15)	169.0
O(2S)-H(2S1)...Cl(2)	1.16	2.01	3.103(11)	154.9
O(2S)-H(2S2)...Cl(1)	0.94	2.29	3.174(11)	158.1
O(1S)-H(1S2)...Cl(2)	0.96	2.46	3.153(11)	128.9

Table 9.5: Hydrogen bonds for heroin hydrochloride monohydrate (Å and °).

Cl	-3.71377	1.61812	-0.91933
O	1.01939	1.22972	0.39733
H	1.93102	1.21842	0.03817
O	5.03548	1.88345	-4.73983
N	-0.02666	-3.04416	-1.90792

H	0.00634	-2.57104	-1.10798
C	4.88154	1.52295	-7.13520
H	5.39242	0.70199	-7.29470
H	5.45088	2.30118	-7.31017
H	4.10483	1.54554	-7.73238
Cl	0.05581	-1.73148	0.89317
O	3.11751	1.05236	-5.63910
N	-3.80082	2.85588	1.87320
H	-3.73775	2.37444	1.08002
C	4.42132	1.55348	-5.72259
O	3.91954	-1.23853	-4.66850
C	2.55767	0.85141	-4.31150
H	2.87638	1.60705	-3.73929
O	4.36469	-2.69915	-7.21300
C	1.08448	0.98846	-4.43796
H	0.76257	1.66202	-5.02550
O	3.57110	-1.31821	-8.80080
C	0.18829	0.26562	-3.81357
H	-0.73558	0.45659	-3.92535
O	1.23048	-2.01304	4.71101
C	0.61443	-0.85869	-2.92581
H	0.69510	-0.51921	-1.98868
O	-0.62750	-1.14786	5.60833
C	-0.42978	-1.99757	-2.95813
H	-1.30743	-1.61000	-2.67613
O	0.11231	1.12506	4.66480
C	-1.08168	-4.06380	-1.69365
H	-0.84337	-4.62400	-0.92567
H	-1.16224	-4.62370	-2.49388
H	-1.93670	-3.61761	-1.51968
O	0.58783	2.59838	7.17374

C	1.32985	-3.54887	-2.09067
H	1.34891	-4.12730	-2.89385
H	1.56854	-4.11007	-1.31081
O	-0.17742	1.21383	8.79141
C	2.35903	-2.47869	-2.24506
H	3.22912	-2.88928	-2.47841
H	2.46706	-1.99876	-1.38595
C	1.95137	-1.47502	-3.34759
O	-2.74888	-1.35705	-0.38073
C	3.09695	-0.47078	-3.67278
H	3.63335	-0.27173	-2.85268
C	2.95652	-2.08016	-5.34795
C	1.82421	-2.13621	-4.65957
C	0.71914	-2.74971	-5.08978
C	-0.62711	-2.63051	-4.36289
H	-1.03343	-3.52828	-4.26802
H	-1.24339	-2.06853	-4.89630
C	0.79890	-3.36365	-6.38412
H	0.03005	-3.76321	-6.77359
C	2.01605	-3.36815	-7.06480
H	2.09532	-3.82592	-7.89347
C	3.10754	-2.70607	-6.53319
C	4.44499	-2.01307	-8.42436
C	5.79791	-2.25150	-9.07510
H	6.50933	-2.06530	-8.42731
H	5.89726	-1.65840	-9.84891
H	5.85935	-3.18449	-9.36862
C	1.17838	-1.61139	7.06441
H	2.15730	-1.63703	7.02591
H	0.84942	-2.40157	7.54169
H	0.89109	-0.80179	7.53600

C	0.62088	-1.60186	5.66484
C	-1.17535	-0.96905	4.30326
H	-0.83215	-1.70884	3.72457
C	-2.65932	-1.14952	4.44498
H	-2.98471	-1.82474	5.02864
C	-3.52306	-0.40825	3.79166
H	-4.44228	-0.63359	3.87392
C	-3.17815	0.75805	2.93147
H	-3.11768	0.42751	1.98966
C	-4.22436	1.86685	2.95932
H	-5.10407	1.47169	2.69481
C	-4.82560	3.96105	1.63913
H	-4.89441	4.51816	2.44246
H	-5.69852	3.56099	1.44329
H	-4.54231	4.51410	0.88137
C	-2.41406	3.50619	2.11569
H	-2.17293	4.09743	1.35915
H	-2.42576	4.04465	2.94637
C	-1.40462	2.35381	2.23819
H	-1.32077	1.89746	1.36361
H	-0.51669	2.72022	2.47780
C	-1.83356	1.34737	3.29092
C	-0.68398	0.39174	3.68419
H	-0.12232	0.20322	2.87857
C	-0.80652	1.91848	5.30992
C	-1.97959	2.01632	4.62190
C	-3.12340	2.67174	5.17569
C	-4.39191	2.53001	4.34069
H	-4.77762	3.43192	4.20703
H	-5.04815	2.00182	4.86079
C	-2.95099	3.31315	6.33364

H	-3.66752	3.82358	6.69215
C	-1.74671	3.25190	7.02792
H	-1.65961	3.69870	7.86177
C	-0.68436	2.55071	6.51646
C	0.69133	1.93001	8.34379
C	1.98683	2.13941	9.07377
H	2.12250	1.41013	9.71422
H	1.95736	2.99374	9.55299
H	2.72607	2.15102	8.43052
H	-1.76147	-1.20012	0.20702
H	-2.83657	-0.48232	-0.70060
H	0.60255	0.48370	-0.03338
Cl*	3.81973	1.61812	-0.91933
H	4.69693	-0.48232	-0.70060
O	4.78462	-1.35705	-0.38073
H	5.77203	-1.20012	0.20702
H*	-5.60248	1.21842	0.03817
O*	-6.51411	1.22972	0.39733
H*	-6.93095	0.48370	-0.03338
Cl*	-7.47769	-1.73148	0.89317

Table 9.6: Heroin hydrochloride monohydrate coordinates used for theoretical calculation; starred (*) atoms not included in calculation.

PAPER

NJC
www.rsc.org/njc

The unusual solid state structure of heroin hydrochloride monohydrate and its selective detection using NQR spectroscopy

Elizabeth Balchin,[a] David J. Malcolme-Lawes,[a] Michael D. Rowe,[a] John A. S. Smith,*[a] Michael J. Bearpark,[b] Jonathan W. Steed,[c] Weimin Wu,[d] Anthony J. Horsewill[d] and David Stephenson[e]

[a] *Department of Chemistry, King's College London, The Strand, London, WC2R 2LS UK*
[b] *Department of Chemistry, Imperial College London, South Kensington Campus, London, SW7 2AZ UK*
[c] *Department of Chemistry, University of Durham, South Road, Durham, DH1 3LS UK*
[d] *School of Physics and Astronomy, University of Nottingham, Nottingham, NG7 2RD UK*
[e] *Chemistry Department, University of the West Indies, St. Augustine, Trinidad, West Indies*

Received (in Montpellier, France) 5th February 2004, Accepted 16th June 2004
First published as an Advance Article on the web 4th October 2004

Heroin hydrochloride monohydrate, the normal crystalline form of this material, has been studied by X-ray crystallography, nuclear quadrupole resonance spectroscopy, and theoretical calculations. The X-ray data at 120 K could be refined in either of the two space groups $P4_1$ or $P4_12_12$ with the latter higher symmetry form being the more likely, but for the NQR spectra at 4.2 K the doublet structure suggests that a slight symmetry breaking has ocurrred, which lowers the symmetry to $P4_1$. The crystals have the unusual unit cell dimensions of $a = b = 7.5335(2)$ Å, $c = 71.976(4)$ Å, with $Z = 8$ (and $Z' = 2$ in $P4_1$); the molecules are arranged on a four-fold helix of pitch 72.0 Å with its axis parallel to the c axis, requiring a total of eight molecules in order to complete one turn. As in the free base the nitrogen ring system of the N-protonated heroin molecule has a chair conformation; in $P4_1$ the N–H hydrogen is bonded to a Cl^- with N–H···Cl distances of 3.056(15) and 3.095(14) Å and each Cl^- ion is also hydrogen bonded to two water molecules. ^{14}N and ^{35}Cl quadrupole resonance frequencies have been observed in both the pure material and material from a drugs seizure by two double resonance techniques; in cross-relaxation spectra, a broad $^{35,37}Cl$ resonance is found near 1.95 MHz at room temperature and an analysis of the line shape predicts an average quadrupole coupling constant for the two ions of 3.817 MHz and an asymmetry parameter of 0.4. In double resonance by level crossing experiments, ^{14}N doublets are observed near 0.965 and 1.035 MHz at 4.2 K, predicting a mean quadrupole coupling constant of 1.333 MHz and an asymmetry parameter of 0.158. A doublet ^{35}Cl signal is also observed at 1.965 MHz. The doublet patterns observed are consistent with a $P4_1$ space group at 4.2 K. The similarity of the NQR data from the pure sample and the seizure confirms that the illicit sample is of the helical monohydrate, suggesting that these methods can be used to detect the narcotic in real situations. Theoretical calculations with Gaussian at the HF/6-31+G* level for two molecules at the configurations they adopt in the solid state are in reasonable agreement with these conclusions for ^{14}N and one of the ^{35}Cl ions.

Introduction

Heroin (diacetylmorphine, **1**) is a class A drug, closely related to morphine and codeine, and derived from the opium poppy.

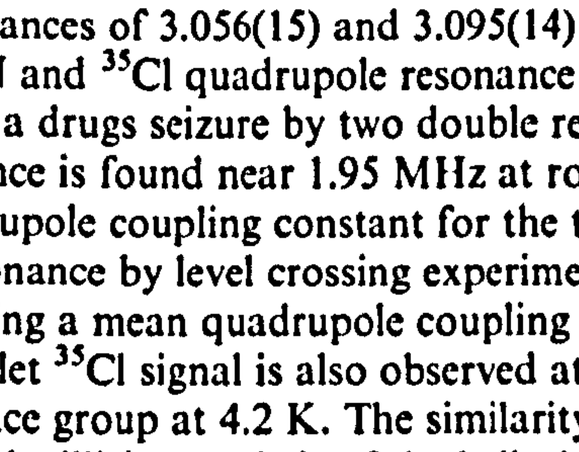

1

It is produced by acetylation of morphine extracted from poppy latex, followed by treatment with HCl to give the hydrochloride, which is recrystallised from ethanol and diethyl ether to give heroin hydrochloride monohydrate. The monohydrate can be dried to give an anhydrous form. While simple colorimetric tests exist to detect the presence of drugs such as heroin hydrochloride, a simple quantitative, portable and non-destructive method for selectively identifying heroin in the presence of closely related compounds such as acetylcodeine is highly desirable. The ratio of acetylcodeine to heroin is, for example, often used as an indication of the origin of illicit drugs. In this paper, we have determined the unusual crystal structure of heroin hydrochloride monohydrate and from this result calculated the ^{14}N and ^{35}Cl nuclear quadrupole resonance (NQR) frequencies using Gaussian (method: HF/6-31+G*). Using these values as a guide, we then detected both ^{14}N and ^{35}Cl quadrupole resonance signals by double resonance and cross-relaxation techniques. Signals have been observed at identical frequencies in a sample of illicit heroin hydrochloride monohydrate taken from a drug seizure.

Experimental

Materials

A sample of diamorphine hydrochloride BP was obtained from Macfarlen-Smith and used in the double resonance NQR experiments. The loss on drying was stated to be 3.7%,

DOI: 10.1039/b401797h

compared to 4.3% expected for the pure monohydrate. For the X-ray studies, a sample was recrystallised from ethanol as in the common illicit production process. The sample of illicit heroin hydrochloride was obtained from the Forensic Science Service in the UK; its purity was estimated to be 85% as base, or 97.5% as the hydrochloride monohydrate.

X-Ray crystallography

The X-ray measurements were conducted on a Nonius ^{Kappa}CCD diffractometer using MoK_α radiation and a sample temperature of 120 K. Approximate unit cell dimensions were determined by the Nonius Collect program from 20 index frames of width 0.5° in ϕ using a Nonius ^{Kappa}CCD diffractometer, with a detector-to-crystal distance of 60 mm. The Collect program was then used to calculate a data collection strategy to 99.5% completeness for θ = 25° using a combination of 0.3° ϕ and ω scans of 120 s deg^{-1} exposure time. Crystals were indexed using the DENZO-SMN package and positional data were refined along with diffractometer constants to give the final unit cell parameters. Integration and scaling (DENZO-SMN, Scalepack) resulted in unique data sets corrected for Lorentz and polarisation effects and for the effects of crystal decay and absorption by a combination of averaging of equivalent reflections and an overall volume and scaling correction. Structures were solved using SHELXS-97[1] and developed *via* alternating least squares cycles and difference Fourier synthesis (SHELXL-97[2]) with the aid of the program XSeed[3] as an interface to the SHELX programs, from which the figures were prepared. All non-hydrogen atoms were modelled anisotropically, while hydrogen atoms were placed in calculated positions, assigned an isotropic thermal parameter 1.2 times that of the parent atom (1.5 for terminal atoms) and allowed to ride. Acidic protons were located on the final difference Fourier map and included as riding atoms with fixed isotopic thermal parameters as described above.

Because of extensive twinning there was some difficulty in establishing the correct space group for the crystal at 120 K; the X-ray data could be refined in either $P4_1$ or $P4_12_12$ with some preference for the latter. The problem lies in the lack of a firm absence condition for the 2_1 screw axis in the (0k0) reflections, the average intensity of which was 1.9 times the standard uncertainty. The refinement in either space group proved essentially identical with two apparently independent but highly correlated molecules, so there are no strong crystallographic grounds to assign a symmetry lower than $P4_12_12$ at 120 K. Collection of a further data set at 30 K gave no further evidence for a phase change to $P4_1$. However, the doublet structure of the NQR spectra taken at 4.2 K (see Fig. 8 below) suggests that $P4_1$ is the correct space group, at least at 4.2 K, implying that slight symmetry breaking occurs between 30 and 4.2 K, lowering the symmetry to $P4_1$. It is this latter structure that has been used in the theoretical calculations of the NQR parameters and for which X-ray structural data are reported in the remainder of the paper.

Crystal data for $C_{21}H_{26}ClNO_6$:† M = 423.88, 0.30 × 0.25 × 0.10 mm^3, tetragonal, space group $P4_1$ (No. 76), a = b = 7.5335(2), c = 71.976(4) Å, U = 4084.9(3) Å^3, Z = 8, D_c = 1.378 g cm^{-3}, F_{000} = 1792, 3475 unique reflections. Final GoF = 1.024, R_1 = 0.0726, wR_2 = 0.1011, R indices based on 1729 reflections with $I > 2\sigma(I)$ (refinement on F^2), 530 parameters, 25 restraints (on displacement parameters). LP and absorption corrections applied, μ = 0.225 mm^{-1}. Absolute structure parameter: −0.22(19).[4] In $P4_12_12$ (No. 92) the crystal data are much the same except there were 2808 unique reflections (R_{int} = 0.0854). Final GoF = 1.000, R_1 = 0.0778, wR_2 = 0.0943, R indices based on 1328 reflections with $I > 2\sigma(I)$ (refinement on F^2), 273 parameters, 0 restraints, LP and absorption corrections applied. Absolute structure parameter: −0.3(2).[4]

† CCDC reference number 242245. See http://www.rsc.org/suppdata/nj/b4/b401797h/ for crystallographic data in .cif or other electronic format.

NQR measurements

Double resonance by level crossing (DRLC) experiments[5] were performed at 4.2 K by means of the magnetic field cycle illustrated in Fig. 1. The polarising field B_{pol} was typically 0.8 to 1 T with a polarisation time of 30 to 60 s; the NMR observation field B_{nmr} was 0.627 T (^{1}H frequency of 26.7 MHz) and the residual field B_{res} lay between 1.5 and 2.0 mT. The magnetic field was provided by a superconducting solenoid of low inductance (L = 0.023 H) continuously powered by a fast switching power supply rated at 15 V and 160 A so that the magnetic field was proportional to the instantaneous current. The maximum field-ramping rate of the system was 10 T s^{-1}, but in these experiments the system was routinely operated at 8 T s^{-1}. The superconducting magnet system incorporated a variable temperature helium cryostat for the sample. Sample temperatures, measured by a calibrated Cernox resistance thermometer, were stable to within 0.05 K. The ^{1}H NMR signal was detected by an NMR coil tuned to 26.7 MHz. The 90° pulse employed to record the signal had a duration of 1 μs and the total dead-time was 4 μs. The broadband secondary rf irradiation used to drive the quadrupolar transitions was provided by a pair of Helmholtz coils comprising approximately 8 turns. The secondary rf field amplitude at the sample was approximately 0.2 mT, with irradiation times of typically 400 ms.

Cross-relaxation (CR) NQR spectra were recorded at room temperature using pneumatic transfer of the sample from high field to the cross-relaxation field.[6] In these experiments, B_{nmr} in Fig. 1 was set to equal to B_{pol}, both being supplied by a permanent magnet of 0.472 T field (^{1}H NMR frequency of 20.10 MHz). The sample was polarised in high field for 10 s, after which the ^{1}H NMR signal was recorded by means of a 90° pulse, and then transferred to the cross-relaxation field B_{res} for approximately 70 ms. No rf radiation was applied in this experiment, but the CR spectrum was obtained by stepping B_{res} between successive ^{1}H NMR signals from 0 to 3000 kHz in steps of 4.58 kHz. The spectrum was scanned twice and the two data sets added. The spectrum was corrected for a frequency offset caused by the stray field from the permanent magnet. The curved base line typical of cross-relaxation spectra was eliminated by applying a manual polynomial correction. The data were smoothed using a damping algorithm; a new smoothed point is calculated from the raw data by allowing it to change the previous point in the smoothed data set by 20% of their difference. This is quite a severe smoothing but does not affect the line shape because of its broadness (for chlorine) compared to the frequency step used.

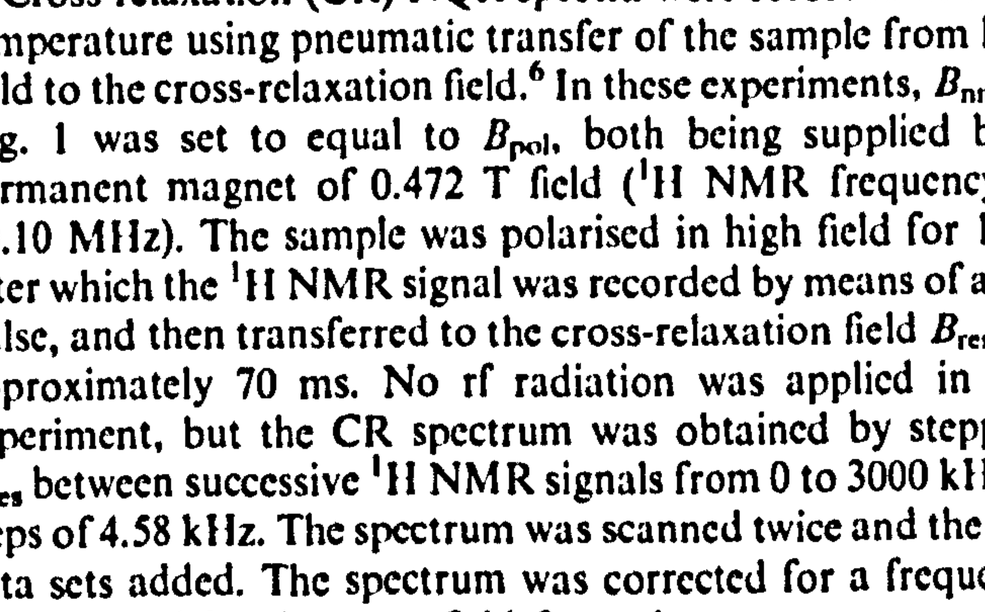

Fig. 1 Magnetic field cycle in the double resonance experiments.

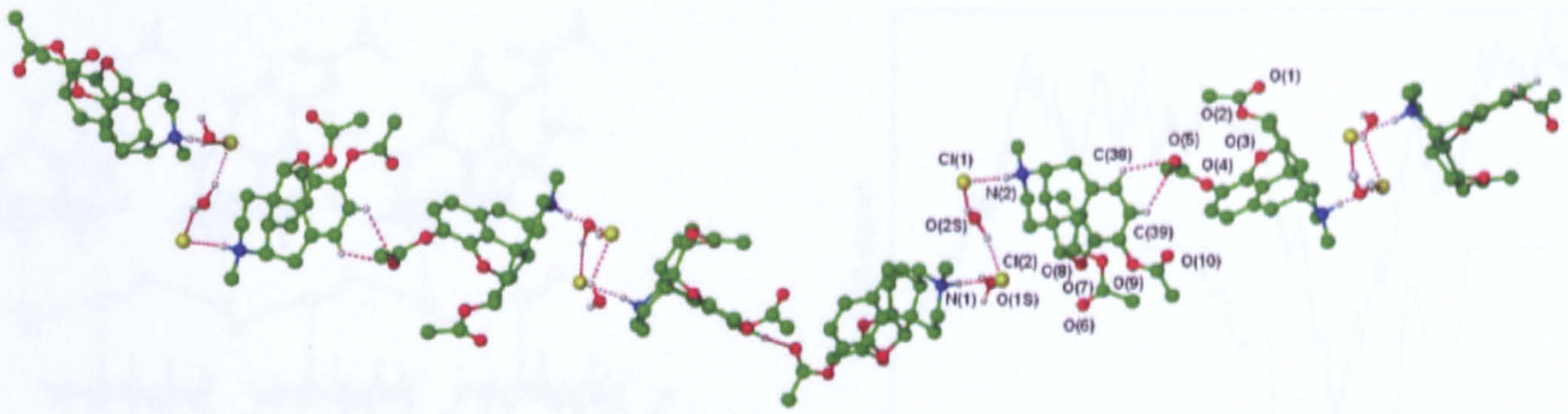

Fig. 2 Helical crystal packing along the *c* axis in heroin hydrochloride monohydrate showing labelling of the atoms (in $P4_1$).

Results and discussion

X-Ray crystal structure

Surprisingly, no details of the X-ray crystal structure of heroin hydrochloride monohydrate have been reported previously, despite the fact that it is readily crystallised. In fact, the structure determination proved challenging with even relatively large crystals showing weak scattering, partially because the compound displays a highly asymmetric plate-type morphology with extensive twinning and there is a long crystallographic *c* axis (Fig. 2) and hence potential problems of peak overlap in the detector.

The water and chlorine ions form an infinite hydrogen-bonded chain perpendicular to the 4_1 helical axis (*c* axis) with each water molecule hydrogen bonding to both chlorine ions. Hydrogen bond distances and angles are given in Table 1. The chlorine ions also form short, charge-assisted hydrogen bonds to the NH groups of the heroin cations (Fig. 3) with the interaction N(1)···Cl(2) being significantly longer than its symmetry independent counterpart in $P4_1$, N(2)···Cl(1) (Table 1). However, the D–H distances in Table 1 are subject to considerable unspecified errors; most are too short, as expected from X-ray measurements, but O(2S)–H(2S1) is anomalously long.

The most remarkable feature of the structure is the four-fold helix of pitch 72.0 Å, which requires a total of eight molecules in order to complete one turn (and hence one repeat of the crystallographic *c* axis). The molecules stack in face-to-face pairs interacting *via* the water/anion layers as described above. Each pair then propagates the helix to the neighbouring pair *via* a series of CH···O interactions[7] involving the ester carbonyl atoms O(5) and O(10) (Fig. 4). We have previously reported several helical structures brought about by weak hydrogen-bonding interactions and shown that in one case at least, helical packing of a resolved chiral compound necessitates a $Z = 2$ structure.[8,9]

Nuclear quadrupole resonance spectra

The asymmetric hydrogen bonding around each chlorine ion in the X-ray crystal structure leads to a non-zero quadrupole interaction at this nucleus and a finite nuclear quadrupole resonance (NQR) frequency, clearly shown in DRLC spectra near 1.965 MHz (Fig. 5) and as a broad dip near 1.9 MHz in the CR spectrum (Fig. 6). Since Cl(1) and Cl(2) are crystallographically non-equivalent in $P4_1$, two ^{35}Cl frequencies are expected and these are apparently resolved in DRLC spectra collected with smaller frequency steps (Fig. 7) at frequencies of 1.950 and 1.965 MHz, consistent with a slight symmetry breaking, reducing the space group symmetry to $P4_1$ at the lower temperature of 4.2 K used for the NQR experiments. No other signals assignable to ^{35}Cl were observed in frequency sweeps up to 4 MHz and none for ^{37}Cl. An almost identical ^{35,37}Cl CR spectrum was observed from a sample of street heroin hydrochloride monohydrate under the same experimental conditions, suggesting that in the solid state both had the same structure. This material also had the same ^{1}H NMR spectrum in solution as the pure material.

For a spin 3/2 nucleus such as ^{35}Cl and ^{37}Cl, the single frequency observed for each nucleus is given by the equation

$$\nu_Q = \frac{1}{2}\left(\frac{e^2qQ}{h}\right)\left(1+\frac{\eta^2}{3}\right)^{1/2} \qquad (1)$$

where

$$\left(\frac{e^2qQ}{h}\right)$$

is the nuclear quadrupole coupling constant (NQCC) in frequency units, q being the maximum principal component of the electric field gradient, Q the nuclear electric quadrupole moment and η the asymmetry parameter. From the two DRLC ^{35}Cl frequencies, which were excited in low or zero magnetic fields, it is impossible to deduce the quadrupole coupling constants and asymmetry parameters separately from eqn. (1). However, in CR spectra, the dips are generated in a non-zero magnetic field, and the Zeeman broadening of the observed

Table 1 Hydrogen bonds in heroin hydrochloride monohydrate

D–H···A	*d*(D–H)/Å	*d*(H···A)/Å	*d*(D···A)/Å	∠DHA/°
O(1S)–H(1S1)···Cl(1)	0.98	2.15	3.119(11)	167.5
N(1)–H(1)···Cl(2)	0.93	2.17	3.095(14)	172.1
N(2)–H(2)···Cl(1)	0.93	2.14	3.056(15)	169.0
O(2S)–H(2S1)···Cl(2)	1.16	2.01	3.103(11)	154.9
O(2S)–H(2S2)···Cl(1)	0.94	2.29	3.174(11)	158.1
O(1S)–H(1S2)···Cl(2)	0.96	2.46	3.153(11)	128.9

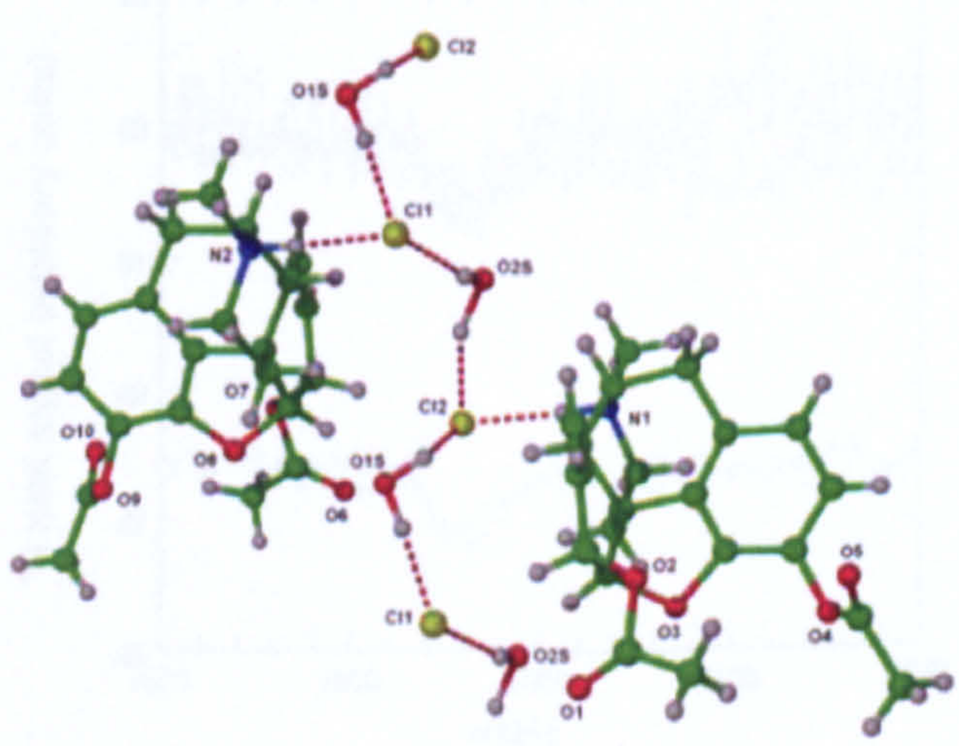

Fig. 3 Projection of two independent molecules on the *ab* plane, showing the N–H···Cl$^-$ and Cl$^-$···OH$_2$ hydrogen bonding.

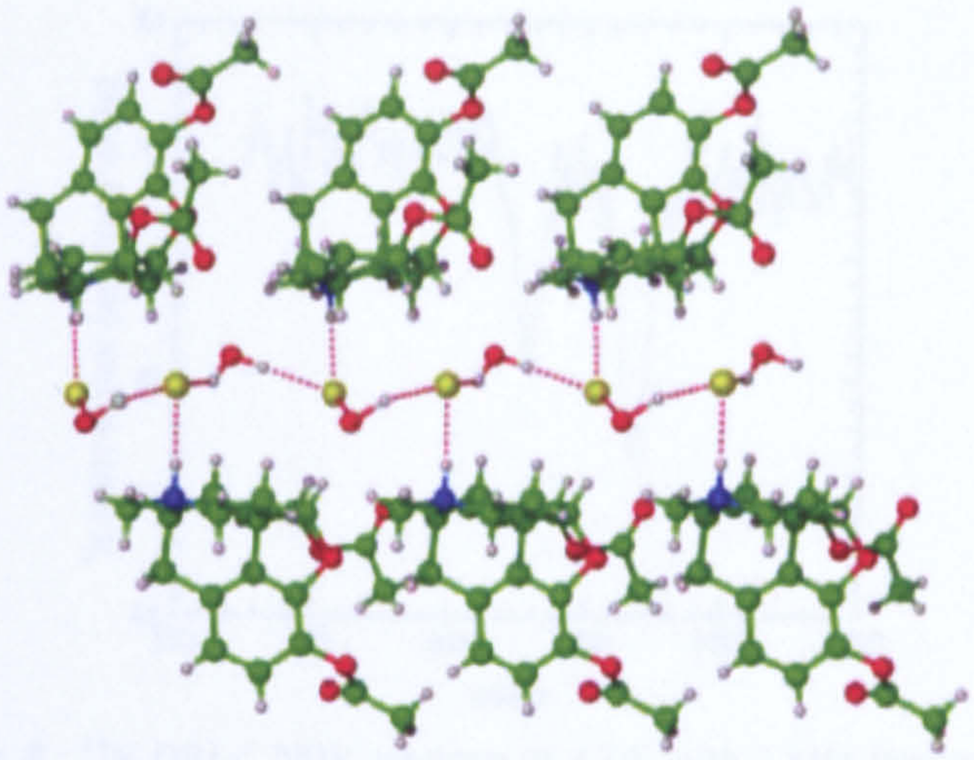

Fig. 4 Aryl and methyl CH···O interactions between the helices. Aryl C···O 3.270 Å, CH_3 C···O 3.200 Å.

lines allows both quantities to be estimated by building up simulated spectra in much the same way as the experiment. The proton frequency is incremented (usually in 10 kHz steps) from low frequency to a point where the proton Zeeman splitting exceeds any quadrupole splitting. At each proton frequency, the Zeeman interaction for the chlorine can be obtained from its gyromagnetic ratio (compared to that of protons). The Zeeman interaction and quadrupole interaction of the chlorine are then used to calculate the energies and wavefunctions of the quadrupole levels. This is repeated for 400 crystal orientations. The proton frequency is then incremented. During this cycle, data relevant to building up the final spectrum are stored for later use. Data is stored on the following basis: cross relaxation only occurs efficiently when the splitting of the proton Zeeman levels is of a similar magnitude to the splitting of a pair of quadrupole levels. As the frequency mismatch increases the efficiency is assumed to decrease as a Gaussian function with a time constant of approximately 50 μs so only splittings that have a mismatch of less than 70 kHz need to be stored.

Energy exchange between the two systems is facilitated by dipolar coupling between the two nuclei. This energy exchange is only allowed if the change in quantum number for the quadrupolar nuclei is ±1 or zero (from inspection of the dipolar Hamiltonian). The transition probability for the energy exchange between the two pairs of levels is calculated on this basis and stored so that when the program ends a large amount of data has been stored in the format: proton frequency, frequency mismatch, transition probability. This contains all the information necessary to build up a cross-relaxation spectrum as a histogram of block size 10 kHz.

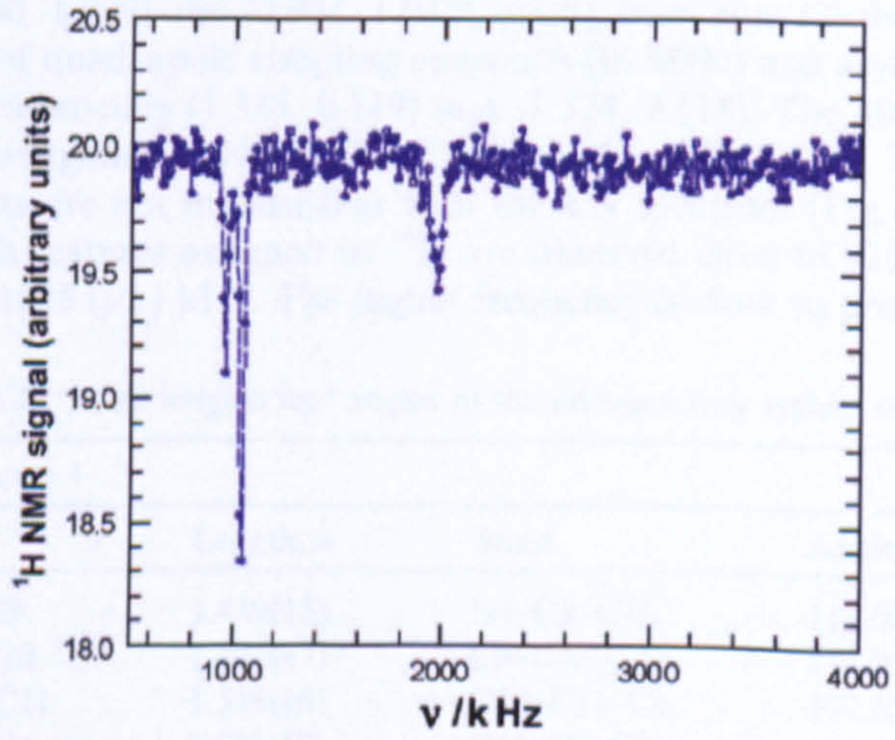

Fig. 5 Double resonance by level crossing (DRLC) spectrum of heroin hydrochloride monohydrate at 4.2 K; experimental conditions are given in the text.

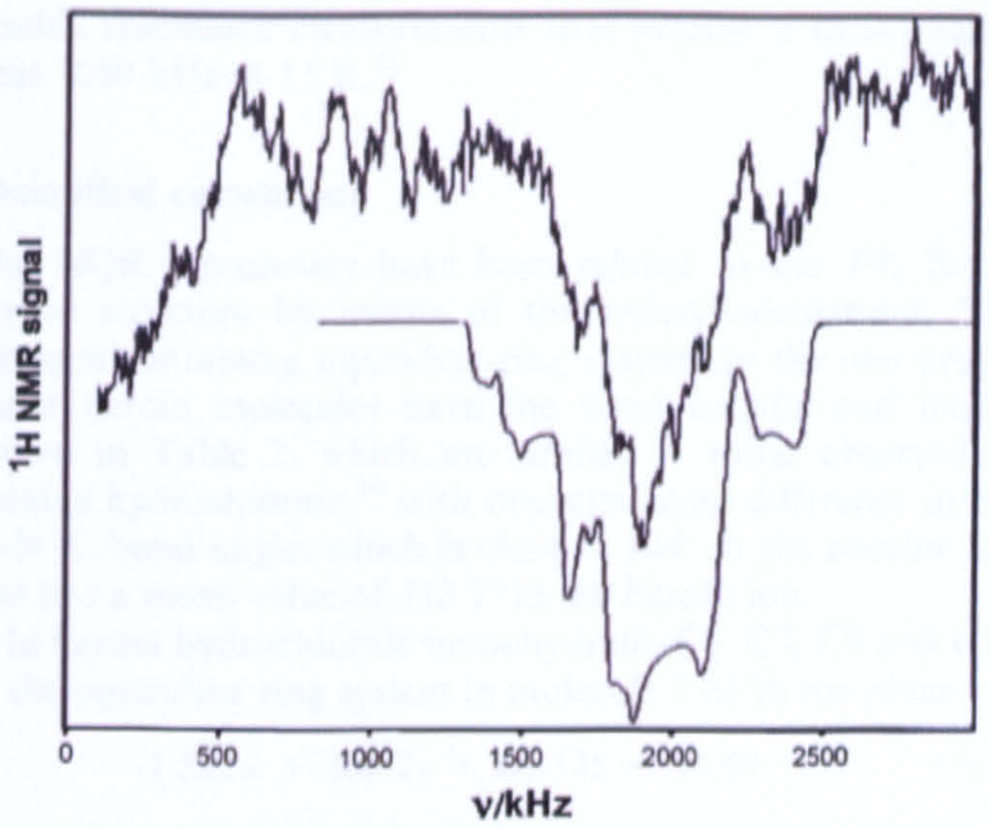

Fig. 6 Cross-relaxation (CR) spectrum of pure heroin hydrochloride monohydrate at room temperature with a residence time in high field of 10 s and in low field of 70 ms. The lower curve is a theoretical fit for a ^{35}Cl quadrupole coupling constant of 3.817 MHz and asymmetry parameter of 0.4.

The chlorine cross-relaxation spectrum is further complicated by overlapping contributions from the two chlorine isotopes, 35 and 37. The line shape for each isotope is calculated separately and the two added, in proportion to their natural abundances, to give the final spectrum. The lower abundance ^{37}Cl contributes quite significantly to the line shape because of its smaller gyromagnetic ratio. Also, ^{37}Cl has a smaller quadrupole interaction, by a factor of 1.269, which causes the cross-relaxation condition to be realized at lower fields, also reducing the Zeeman broadening and hence increasing its relative intensity.

Inspection of the experimental spectrum suggested a zero field resonance frequency of around 2000 kHz (for ^{35}Cl). Refinement of this value was achieved by calculating a series of cross-relaxation spectra using this value and an asymmetry parameter of 0.0 to 1.0 in steps of 0.2. The best fit was with η = 0.4 (lower line in Fig. 6). The fit was further improved by offsetting the two spectra by 50 kHz, suggesting that the ^{35}Cl NQR lines in zero field should be seen around 1950 kHz, in good agreement with the DRLC values. Combining the DRLC frequencies of 1.950 and 1.965 MHz at 4.2 K with the CR estimate of the asymmetry parameter (assumed to be the same for both lines) gives quadrupole coupling constants of 3.801 and 3.830 MHz.

The ^{35}Cl frequencies lie between two values previously published in hydrochlorides, *viz.* ^{35}Cl/^{37}Cl frequencies at

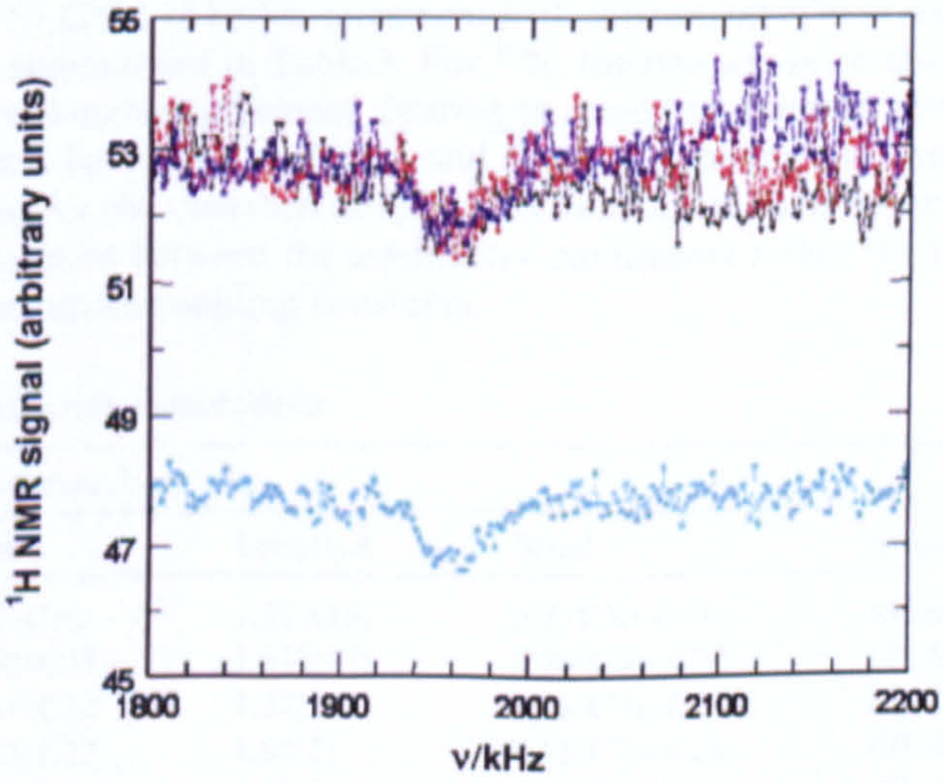

Fig. 7 The ^{35}Cl DRLC spectrum at 4.2 K with frequency steps of 2 kHz; the lower spectrum is an average of the upper spectra.

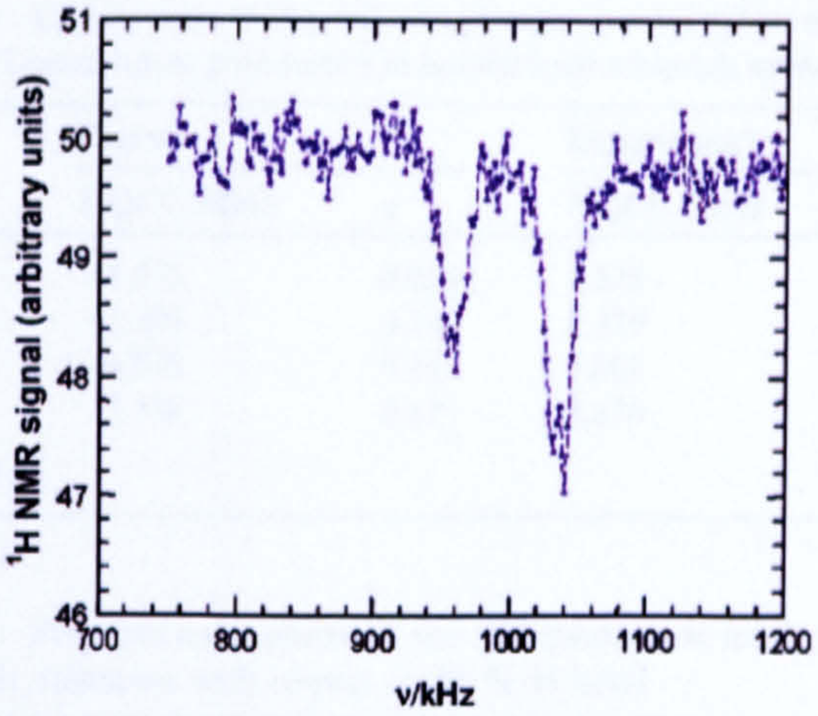

Fig. 8 ^{14}N DRLC NQR spectrum at 4.2 K with 2 kHz frequency steps.

1.215/0.860 MHz for decylamine hydrochloride[10] and 5.524/4.366 MHz for pyridine hydrochloride;[11] they are lower than the corresponding frequencies of 2.53/1.99 MHz reported for cocaine hydrochloride near 295 K[12,13] and the ^{35}Cl frequency of 2.712 MHz observed in ecstasy (MDMA hydrochloride)[13] at similar temperatures. These differences reflect important changes in the hydrogen bonding; in cocaine hydrochloride,[14] for example, the Cl^- ion is hydrogen bonded to just one N–H group with an N–H···Cl bond length of 3.06(9) Å, and the same is true in pyridine hydrochloride, where the hydrogen bond length is shorter at 2.95 Å.[15] In contrast, in heroin hydrochloride monohydrate, the Cl^- ion is hydrogen bonded not only to NH, with hydrogen bond lengths of 3.065(15) and 3.095(14) Å, but also to two O–H groups from two neighbouring water molecules. It is clear from these results that CR and NQR measurements of the ^{35}Cl signals provide a means of detecting these drugs and of distinguishing between them.

The ^{14}N DRLC spectrum is readily assigned if the observed doublets near 0.957 and 1.035 MHz, shown under higher resolution in Fig. 8, are assigned to ν_- and ν_+, respectively; for spin 1 nuclei; these are related to the quadrupole coupling constant and asymmetry parameter by the equation

$$\nu_\pm = \frac{3}{4}\left(\frac{e^2qQ}{h}\right)\left(1 \pm \frac{\eta^2}{3}\right)^{1/2} \qquad (2)$$

Note that once again the doublet structure predicted by the X-ray crystal structure analysis in $P4_1$ is clearly resolved, with splittings of 6.5 kHz for ν_+ and 5.7 kHz for ν_-. It is impossible from these measurements alone to say which component of each doublet goes with the other; on the rather arbitrary basis of intensities, we pair off the frequencies (in MHz at 4.2 K) as (0.960, 1.039) and (0.954, 1.032), giving from eqn. (2) the two sets of quadrupole coupling constants (in MHz) and asymmetry parameters (1.333, 0.119) and (1.324, 0.118). The alternative assignment gives (1.328, 0.108) and (1.329, 0.128). These results are not inconsistent with the CR spectrum (Fig. 6) in which features assigned to ^{14}N are observed close to 926 (ν_-) and 1085 (ν_+) kHz. The higher frequency is close to previous double resonance measurements that located a broad signal near 1080 kHz at 15 K.[16]

Theoretical calculations

The NQR parameters have been related to the $P4_1$ X-ray crystal structure by means of theoretical calculations. The nitrogen-containing piperidine ring systems in the two protonated heroin molecules have the bond lengths and angles shown in Table 2, which are similar to those observed in cocaine hydrochloride,[14] with one significant difference in the C–N–C bond angle, which is close to 104° in the cocaine ion and has a mean value of 113.7° in the heroin ion.

In heroin hydrochloride monohydrate, C6, C7, C9 and C10 in the piperidine ring system in molecule 1 lie in the plane

$$-1.522x + 1.812y + 68.33z = 54.69 \qquad (3)$$

with an rms deviation of 0.048 Å, with N1 lying at 0.617 Å and C11 at −0.772 Å from this plane; in molecule 2, C27, C28, C30 and C31 lie in the plane

$$1.543x + 1.705y + 68.54z = 60.06 \qquad (4)$$

with an rms deviation of 0.031 Å, N2 lying at −0.693 Å and C32 at 0.719 Å from this plane. Both conformations are therefore chair, as in cocaine hydrochloride[14] and the free bases.[17–19]

The molecular dimensions for both molecules from the X-ray crystal structure analysis have been used to calculate the quadrupole parameters for both ^{14}N and ^{35}Cl using Gaussian[20] (HF/6-31+G*), with three corrections. Both N–H bond lengths have been lengthened from 0.93 to 1.04 Å, one of the O–H bond lengths [O(2S)–H(2S1)···Cl(2)] shortened from 1.16 to 0.98 Å and the others set to the same value, to be more consistent with acceptable values. Nuclear electric quadrupole moments of +20.44(3) mB for ^{14}N and −81.65(80) mB for ^{35}Cl were used[21] and the quadrupole coupling constants calculated using the equation.[22]

$$\text{NQCC (in MHz)} = 234.9647Qq \qquad (5)$$

where Q is the nuclear electric quadrupole moment in Barn (10^{-28} m^2) and q is q_{zz}, the maximum principal component, in atomic units (from Gaussian).

To simulate the effects of the solid state, the calculations for heroin hydrochloride monohydrate were performed for the two hydrogen-bonded molecules in the $P4_1$ structure shown in Fig. 3, each chlorine ion, Cl(1) and Cl(2), being hydrogen bonded to one N–H group and two water molecules, O(1S) and O(2S). Several different basis sets were used in the calculations, the general conclusion being that the larger split sets with the inclusion of polarization (*e.g.*, 3d functions for Cl) such as 6-31+G* gave better agreement with experiment. These results are summarised in Table 3. For ^{14}N, the two sets of results are in reasonable agreement, bearing in mind that thermal motion effects have been neglected and that the experimental assignment for the observed doublets has been made to optimise the agreement between the asymmetry parameters rather than the quadrupole coupling constants.

Table 2 Bond lengths and angles in the nitrogen ring system of heroin hydrochloride monohydrate

Molecule 1				Molecule 2			
Bond	Length/Å	Bond	Angle/°	Bond	Length/Å	Bond	Angle/°
N1–C9	1.459(15)	N1–C9–C10	114.0(12)	N2–C30	1.551(16)	N2–C30–C31	106.6(12)
C9–C10	1.493(17)	C9–C10–C11	110.9(12)	C30–C31	1.537(17)	C30–C31–C32	111.5(13)
C10–C11	1.546(18)	C10–C11–C6	107.2(13)	C31–C32	1.52(2)	C31–C32–C27	110.2(14)
C11–C6	1.531(19)	C11–C6–C7	106.7(12)	C32–C27	1.51(2)	C32–C27–C28	108.8(14)
C6–C7	1.55(2)	C6–C7–N1	108.1(13)	C27–C28	1.52(2)	C27–C28–N2	105.5(12)
C7–N1	1.536(18)	C7–N1–C9	113.2(12)	C28–N2	1.529(18)	C28–N2–C30	114.1(12)

Table 3 Comparison of theoretical and experimental values of the ^{14}N and ^{35}Cl quadrupole parameters in heroin hydrochloride monohydrate

	Theory		Experiment[a]	
Atom	NQCC/MHz	η	NQCC/MHz	η
N(1)	−1.575	0.098	1.328	0.108
N(2)	−1.399	0.142	1.329	0.128
Cl(1)	−4.076	0.311	3.801	0.4
Cl(2)	5.388	0.827	3.830	0.4

[a] At 4.2 K.

Table 4 Principal components of the ^{14}N quadrupole tensor in MHz and their directions with respect to the N–H bond

N atom & bond	$e^2q_{zz}Q/h$	θ/°	$e^2q_{yy}Q/h$	θ/°	$e^2q_{xx}Q/h$	θ/°
N(1)–H(1)	−1.575	2.86	0.865	90.0	0.710	87.1
N(2)–H(2)	−1.399	2.79	0.799	90.0	0.600	87.2

The predicted NQR frequencies (ν_+ at 1.220 and 1.099 MHz, ν_- at 1.142 and 1.000 MHz) were sufficiently close to experiment (doublets close to 1.035 and 0.957 MHz), bearing in mind the neglect of temperature effects, to be used as preliminary estimates when frequency searching for unknown resonances. For ^{35}Cl, the agreement is less satisfactory, largely because the electric field gradients at this ion are governed by the positions of hydrogen-bonded hydrogen atoms, which are imprecisely located in the X-ray crystal structure analysis. The main uncertainty lies in the position of the O(2S)–H(2S1) hydrogen atom, which strongly affects the electric field gradient at Cl(2); the X-ray value for the O(2S)···H(2S1) bond length (1.16 Å) is anomalously long and suggests that the H coordinates are unreliable. The quadrupole parameters at Cl(1) are better reproduced and predict an NQR frequency of 2.071 MHz compared with mean values of 1.965 and 1.950 MHz from experiment at 4.2 K and room temperature, respectively, which should be regarded as unexpectedly good agreement.

As well as calculating the magnitude of q_{zz}, it is also useful to know the direction of the electric field gradient by calculating the direction cosines. It can be shown that the electric field gradient at the origin, due to a charge e at point (x, y, z) distance r away is

$$\frac{e}{r^5}\begin{bmatrix} 3x^2 - r^2 & 3xy & 3zx \\ 3xy & 3y^2 - r^2 & 3yz \\ 3zx & 3yz & 3z^2 - r^2 \end{bmatrix}$$

The values for the field gradient tensor were extracted from the Gaussian results and the direction cosines calculated. The eigenvalues were compared with the Gaussian-produced values to check the calculation. The position of the maximum principal component (q_{zz}) with respect to a bond within the molecule was then established (Table 4).

The direction cosine results for heroin hydrochloride monohydrate were as expected for ^{14}N, with a small angle between the N–H bond and the maximum principal component of the electric field gradient. This is chemically predictable, as the asymmetry parameter of ^{14}N is low, and q_{zz} would therefore be expected to be close to the N–H bond.

Conclusions

The X-ray crystal structure analysis of heroin hydrochloride monohydrate reveals an unusual structure in which eight molecules form a four-fold helix of pitch 72 Å, the repeat unit containing just one independent molecule at 120 K. There is no evidence for a space group of lower symmetry than $P4_12_12$ at 120 or 30 K, whereas the doublet structure of the NQR spectra recorded at 4.2 K implies two independent molecules more consistent with the space group $P4_1$ at this lower temperature. A sample of the same material from a drug seizure is shown to have the same ^{35}Cl spectrum. A theoretical calculation for a hydrogen-bonded pair of molecules with the dimensions found from the X-ray analysis gives good agreement for the ^{14}N quadrupole parameters but less so for ^{35}Cl, whose quadrupole parameters depend sensitively on the imprecisely located hydrogen atoms in the two water molecules to which they are hydrogen bonded. The unique structure of heroin hydrochloride hydrate is reflected in the NQR data and hence suggests that NQR cross-relaxation methods could form the basis for a sensitive method for the selective detection of this material in the presence of other closely related compounds.

Acknowledgements

This work has been supported by grants from the Royal Society and EPSRC (AJH) and from Quantum Magnetics, Merck Sharp and Dohme, AstraZeneca, DSTL and a DTA award (EB, MDR, DJM-L and JASS).

References

1 G. M. Sheldrick, *SHELXS-97, Program for solution of crystal structures*, University of Göttingen, Germany, 1997.
2 G. M. Sheldrick, *SHELXL-97, Program for refinement of crystal structures*, University of Göttingen, Germany, 1997.
3 L. J. Barbour, *XSeed*, University of Missouri-Columbia, Columbia, MO, 1999.
4 H. D. Flack, *Acta Crystallogr., Sect. A*, 1983, **39**, 876.
5 D. T. Edmonds, *Phys. Rep.*, 1977, **29**, 233.
6 D. Stephenson and J. A. S. Smith, *Proc. R. Soc. London, Ser. A*, 1988, **416**, 149.
7 G. R. Desiraju, *Acc. Chem. Res.*, 1996, **29**, 441.
8 I. Forristal, J. Lowman, K. Afarinkia and J. W. Steed, *CrystEngComm*, 2001, **53**.
9 S. E. Gibson (née Thomas), H. Ibrahim and J. W. Steed, *J. Am. Chem. Soc.*, 2002, **124**, 5109.
10 J. Seliger, V. Zagar, R. Blinc and G. Chapuis, *J. Chem. Phys.*, 1983, **78**, 2661.
11 G. V. Rubenacker and T. L. Brown, *Inorg. Chem.*, 1980, **19**, 392.
12 J. P. Yesinowski, M. L. Buess, A. N. Garroway, M. Ziegeweid and A. Pines, *Anal. Chem.*, 1995, **67**, 2256.
13 M. D. Rowe and J. A. S. Smith, unpublished results.
14 E. J. Gabe and W. H. Barnes, *Acta Crystallogr.*, 1963, **16**, 796.
15 C. Rerat, *Acta Crystallogr.*, 1962, **15**, 427.
16 E. F. Emery and L. G. Butler, *Abs. Pap. Am. Chem. Soc.*, 1996, **211**(1), A087.
17 R. J. Hrynchuk, R. J. Barton and B. E. Robertson, *Can. J. Chem.*, 1983, **61**, 481.
18 D. Canfield, J. Barrick and B. C. Giessen, *Acta Crystallogr., Sect. B*, 1979, **35**, 2806.
19 J. R. Deschamps, C. George and J. L. Flippen-Anderson, *Acta Crystallogr., Sect. C*, 1996, **52**, 698.
20 M. J. Frisch, G. W. Trucks, H. B. Schlegel, G. E. Scuseria, M. A. Robb, J. R. Cheeseman, J. A. Montgomery, Jr., T. Vreven, K. N. Kudin, J. C. Burant, J. M. Millam, S. S. Iyengar, J. Tomasi, V. Barone, B. Mennucci, M. Cossi, G. Scalmani, N. Rega, G. A. Petersson, H. Nakatsuji, M. Hada, M. Ehara, K. Toyota, R. Fukuda, J. Hasegawa, M. Ishida, T. Nakajima, Y. Honda, O. Kitao, H. Nakai, M. Klene, X. Li, J. E. Knox, H. P. Hratchian, J. B. Cross, C. Adamo, J. Jaramillo, R. Gomperts, R. E. Stratmann, O. Yazyev, A. J. Austin, R. Cammi, C. Pomelli, J. W. Ochterski, P. Y. Ayala, K. Morokuma, G. A. Voth, P. Salvador, J. J. Dannenberg, V. G. Zakrzewski, S. Dapprich, A. D. Daniels, M. C. Strain, O. Farkas, D. K. Malick, A. D. Rabuck, K. Raghavachari, J. B. Foresman, J. V. Ortiz, Q. Cui, A. G. Baboul, S. Clifford, J. Cioslowski, B. B. Stefanov, G. Liu, A. Liashenko, P. Piskorz, I. Komaromi, R. L. Martin, D. J. Fox, T. Keith, M. A. Al-Laham, C. Y. Peng, A. Nanayakkara, M. Challacombe, P. M. W. Gill, B. Johnson, W. Chen, M. W. Wong, C. Gonzalez and J. A. Pople, *Gaussian 01, Development Version (Revision B.01)*, Gaussian, Inc., Pittsburgh, PA, 2003.
21 P. Pyykkö, *Mol. Phys.*, 2001, **99**, 1617.
22 E. R. Cohen and B. N. Taylor, *J. Phys. Chem. Ref. Data.*, 1998, **96**, 92.1

Anal. Chem. 2005, *77*, 3925–3930

Perspectives

Potential of Nuclear Quadrupole Resonance in Pharmaceutical Analysis

Elizabeth Balchin,[†] David J. Malcolme-Lawes,[†] Iain J. F. Poplett,[†] Michael D. Rowe,[†] John A. S. Smith,*[,†] Gareth E. S. Pearce,[‡] and Stephen A. C. Wren[§]

Chemistry Department, King's College, Strand, London WC2R 2LS, United Kingdom, Merck, Sharp and Dohme, Hertford Road, Hoddesdon, Hertfordshire EN11 9BU, United Kingdom, and AstraZeneca, Silk Road Business Park, Charter Way, Macclesfield, Cheshire SK10 2NA, United Kingdom

Nuclear quadrupole resonance is a radio frequency (rf) spectroscopic technique, closely related to NMR, which can be used to detect signals from solids containing nuclei with spin quantum number >1/2. It is nondestructive, highly specific and noninvasive, requires no static magnetic field, and as such is currently used in the detection of explosives and narcotics. Recent technological advances in pulsed NQR methods have shortened detection times, eliminated spurious signals, and enhanced the sensitivity of detection of ^{14}N frequencies, which lie in the low rf range of 0.4–6 MHz, encouraging a wider range of "real world" applications. This Perspective highlights some of the advantages of NQR, the applications in which it could be used, such as the quantification of pharmaceuticals and the identification of polymorphs. Other roles could include detection, analysis, and quality control of pharmaceuticals at all stages of manufacture. Finally, recent advances which enhance even further the sensitivity of detection will be discussed.

PHARMACEUTICAL ANALYSIS

Organic chemical analysis is a key part of the identification, development, and quality assurance of new pharmaceuticals. For example, analytical methods play a critical role in supporting the scale-up of the synthetic route, development of the manufacture of the final dosage form, assessment of stability, and control of quality and consistency of the commercial product.[1–3]

Because of the important role of chemical analysis, there is continued interest in the refinement of existing analytical techniques and the development of new ones. The objectives of these refinement and development exercises typically include improving the speed and quality of decision-making. This can be achieved by finding ways of generating the same information more quickly or by generating additional useful information within the same time span. Products and processes need to be characterized more quickly and more fully, with the ultimate aim of decreasing development times, reducing manufacturing costs, and increasing the quality and safety of the final product.

Development in analytical chemistry proceeds not only by experimentation and application, but also by theoretical investigation. This theoretical investigation should include not only a better understanding of the physicochemical processes that underpin existing analytical methodologies, but also the identification of other physical phenomena which could form the basis of new analytical methodologies.

In this paper, we propose that recent advances in the technique of pulsed nuclear quadrupole resonance (NQR) have established it as a valuable technique in pharmaceutical analysis.

Most pharmaceuticals are marketed as solid dosage forms, for example, oral tablets, but the majority of the organic chemical analysis techniques used are solution-based. As a result, for example, HPLC, electrospray MS, and solution NMR are widely used in assessing the quantity of active agent, chemical purity, and the identification of both active agent and impurities. While such approaches enable tight control of the quality and consistency of the dosage form, they inevitably require time and effort in sample preparation and are inherently destructive in nature. Other important information, such as the polymorphic form of the active agent, is lost by solution-based methods, and so solid-state techniques such as IR, powder XRD, and solid-state NMR are used, as well.[4]

An additional area of interest in pharmaceutical analysis is that of moving the analysis closer to the process it is being used to control. Most control strategies rely on end-point testing in which the manufactured material is sampled and the samples are brought to the laboratory for testing. End-point testing imposes limits on the time scale in which process changes can be made. There is increasing interest in taking analysis from the laboratory and into the manufacturing and raw material receipt environments. Tech-

* Corresponding author. E-mail: John.Smith@kcl.ac.uk.
† King's College.
‡ Merck, Sharp and Dohme.
§ AstraZeneca.

(1) Gorog, S. *Trends Anal. Chem.* 2003, *20*, 407–415.
(2) Lewen, N. S.; Schenkenberger, M. M. *Encyclopedia of Spectroscopy and Spectrometry*; Lindon, J. C., Tranter, G. E., Holmes, J. L., Eds.; Academic Press: London, 2000, pp 1791–1800.
(3) Ohanessian, L.; Streeter, A. J. *Handbook of Pharmaceutical Analysis*; Marcel Dekker Inc.: New York, 2001.
(4) Bryn, S. R.; Pfeiffer, R. R.; Stowell, F. G. *Solid State Chemistry of Drugs*, 2nd ed.; SSCI Inc.: West Lafayette, IN, 1999; pp 45–139.

10.1021/ac0503658 CCC: $30.25
Published on Web 05/27/2005

niques such as near-IR (NIR) have made significant impacts here, but because NIR is a secondary technique, a significant calibration exercise is required before data can be interpreted in a meaningful way. Such at-line testing can also be improved by the addition of noninvasive techniques to the analytical armory so that pharmaceutical formulations can be analyzed without removal from their packaging. The development of noninvasive techniques may also prove useful in other environments, for example, hospitals, and in the detection of counterfeit products.

Such considerations lead to the conclusion that there is still benefit in developing new techniques for pharmaceutical analysis, and NQR is an example of a technique that may well hold promise in answering some of the challenges detailed above.

THE BASIC PRINCIPLES OF NQR

Nuclear quadrupole resonance (NQR) is a technique in radio frequency (rf) spectroscopy in which the signals arise from the interaction of the electric quadrupole moment of the quadrupolar nuclei in the sample with the electric field gradient (EFG) of their surroundings;[5] rf radiation excites transitions between the energy levels generated by this interaction at frequencies that are characteristic of a given material and can be used, therefore, not only to identify it but also to estimate quantity. The method is noninvasive, and signals are seen only in solids, so suspensions of materials and mixtures with other substances are eligible. Unlike the closely related technique of nuclear magnetic resonance (NMR), no static magnetic field is necessary, so remote materials and large volumes—at the moment, the record is 8000 L^6—can be examined. The most commonly distributed quadrupolar nucleus in pharmaceuticals is ^{14}N, a spin-1 nucleus, which will be the main subject of this review. In addition, there are many other quadrupolar nuclei that are commonly found in medicines, such as ^{23}Na, ^{35}Cl, and ^{79}Br, that are equally amenable to the same methods and to which some reference will be made.

There are three allowed transitions in the general case for a spin-1 nucleus such as ^{14}N, one frequency (ν_x or ν_+) being the sum of the other two (ν_y or ν_-, ν_z or ν_0), the vast majority of which lie at the rather low radio frequencies between 0.2 and 6 MHz. These frequencies are related to quantities known as the quadrupole coupling constant and asymmetry parameter by eq 1, where (e^2qQ/h) is the nuclear quadrupole coupling constant (NQCC); e is the charge on the electron, h is Planck's constant, $q = q_{zz}$ is the maximum principal component of the electric field gradient tensor, and Q is the nuclear electric quadrupole moment. η is the asymmetry parameter defined as the difference between the other two components (q_{xx} and q_{yy}) of the electric field gradient tensor divided by q; it is a positive number lying between 0 and 1.

$$\nu_x = 3/4\frac{(e^2qQ)}{h}(1 + \eta/3)$$

$$\nu_y = 3/4\frac{(e^2qQ)}{h}(1 - \eta/3)$$

$$\nu_z = 1/2\frac{(e^2qQ)}{h}\eta \qquad (1)$$

Spin-3/2 nuclei, such as ^{23}Na, ^{35}Cl, and ^{79}Br, have two doubly degenerate levels, transitions between which give rise to just one frequency equal to

$$\nu_Q = 1/2\frac{(e^2qQ)}{h}\left(1 + \frac{\eta^2}{3}\right)^{1/2} \qquad (2)$$

Despite the low radio frequencies characteristic of ^{14}N signals, recent advances in pulsed NQR spectroscopy have significantly improved their sensitivity of detection.[6] In pulsed NQR, the ^{14}N nuclei are subject to bursts of rf radiation at or near their NQR frequency, and the resulting transient signals are monitored in the quiescent periods between pulses. The signals are generated by the interaction of the nuclear magnetic moment with the magnetic component B_1 of the rf field. They can be of two types: free induction decays (FID) and echoes. A FID is the decaying signal observed immediately following a pulse, whereas an echo is a regenerated signal with maximum intensity between rf pulses in a multiple-pulse train. The rf radiation can be generated in a number of ways: a conventional solenoid or bird-cage coil can be used to detect signals from samples dispensed in bottles, whereas tablets in blister packs could be studied by a planar single turn or spiral of copper wire or ribbon, which can also function as a receiver of the signals from the sample. Alternatively, separate transmit and receive antennae may be used. Note, however, that the samples need not be removed from their container. ^{14}N signals are usually very weak, and many responses must be accumulated to achieve an acceptable signal-to-noise ratio (SNR). For this purpose, extended trains of pulses have been developed in which the observed responses between pulses are averaged to enhance the SNR. The use of short, high-power rf pulses with active damping during the probe ring-down means that fast multiple-pulse sequences can be used to average many responses in times as short as a minute or less.[6] One example is known as pulsed spin locking (PSL) and can be represented by

$$\alpha_{0^\circ} - (\tau - \alpha_{90^\circ} - \tau -)_n$$

where α represents the pulse width, selected to optimize the signal; the subscripts denote the rf phase; τ determines the pulse spacing, which is 2τ after the first two pulses; and n determines the number of pulses in the train whose optimum value depends on the relaxation times of the material. The entire pulse sequence is repeated, often several hundred times, for further signal-averaging, depending on the quantity of material in the sample and, in the case of remote detection, its distance from the antenna. The problems posed by spurious signals, such as those observed from piezoelectric materials, have been largely eliminated by cycling the phases of the rf pulses and signals[7,8] before processing, which can be in the time domain or frequency domain after Fourier transformation. Since the pulse sequence repetition time is limited by the need to wait for the nuclear spins to recover their equilibrium magnetization and this time is determined by

(5) Smith, J. A. S. *Chem. Soc. Rev.* **1986**, *15*, 225–260.
(6) Barras, J.; Gaskell, M. J.; Hunt, N.; Jenkinson, R. I.; Pedder, D. A. G.; Shilstone, G. N.; Smith, J. A. S. *Appl. Magn. Res.* **2004**, *25*, 411–437.
(7) Smith, J. A. S.; Peirson, N. F. U.S. Patent 6,208,136 B1, March 27, 2001.
(8) Peirson, N. F.; Barras, J.; Smith, J. A. S. U.K. Patent GB98/03099, October 15th, 1998.

the spin–lattice relaxation time T_1, this is an important parameter that needs to be measured before any analytical measurements should be undertaken.

In pharmaceutical analysis, the important quantities determined by experiment are the nuclear quadrupole coupling constants (NQCC) and asymmetry parameters, which function in much the same way as the chemical shift or, rather, the chemical shift anisotropy in NMR, since they also contain information on the asymmetry through the two other components of the EFG tensor, q_{xx} and q_{yy}. Because Laplace's equation holds,

$$q_{xx} + q_{yy} + q_{zz} = 0 \qquad (3)$$

there are only two independent parameters that define this tensor; unfortunately the direction cosines of these tensor components are not usually derived in measurements on powders; a single crystal would be needed.

SELECTIVITY AND IDENTIFICATION

A knowledge of the two parameters, NQCC and η, can often be used to identify a material through published lists of NQR frequencies[9] or those in related compounds. As an example, consider the antihypertensive drug Atenolol, which has the structure 1 with two different kinds of nitrogen atoms, one amine, and the other amide.

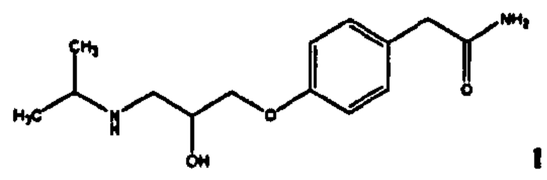

1

At room temperature, the NQR frequencies, NQCC and η, are determined as[10], I 0.47, 2.98, 3.50 MHz: NQCC = 4.32 MHz, η = 0.241, II 0.65, 1.60, 2.14 MHz: NQCC = 2.493 MHz, η = 0.433 in which the frequencies have been combined according to eq 1 so that the largest is close to the sum of the other two. A comparison of these with the listed parameters[9] for Me_2NH at 77 K (4.65 MHz, 0.169) and acetamide (2.526 MHz, 0.375) leads us to assign I to the amine group and II to the amide. These comparisons are rarely exact, or even nearly so, first, because NQR frequencies in solids are averages over all molecular and torsional modes within the molecules and so are temperature-dependent, and second, there are solid-state effects, just as in solid-state NMR, which can be rather large in the presence of hydrogen bonding to the atom containing the quadrupolar nucleus. An important difference from NMR, however, is the much greater spectral range that is obtained in NQR. There are large differences in the frequencies of nuclei in different chemical functional groups and even within the same functional group. Although this may be a disadvantage in the design of the instrument and location of the signal, it has one important consequence in pharmaceutical analysis in that NQR is likely to be a highly selective technique. It is a relatively easy matter to distinguish between different chemical species and different polymorphs; even if by coincidence the frequencies are the same, this is only likely to be true at a single temperature and in any case, the relaxation times are almost certain to be different.

(9) *NQR Database*. Japan Association of International Chemical Information (JAICA): Nakai Building, 6-25-4 Henkomagome, Bunkyo-ku, Tokyo 113, Japan.

(10) NQR Group, King's College London, and the Josef Stefan Institute, Ljubljana, unpublished results.

Table 1. Comparison of Theoretical and Experimental Values of the ^{14}N Quadrupole Parameters in Heroin Hydrochloride Monohydrate

	theory		experiment[a,13]	
atom	QCC (MHz)	η	QCC (MHz)	η
N(1)	−1.575	0.098	1.328	0.108
N(2)	−1.399	0.142	1.329	0.128

[a] At 4.2 K.

FREQUENCY PREDICTION

Theoretical calculations, for example, by Gaussian at the HF/6-31+G* level, can now be used to check experimental values of quadrupole coupling constants in cases for which an accurate structure for the molecule is available. Strictly speaking, such programs predict NQCC for a rigid molecule in the gas phase, but some allowance can be made for solid-state effects and hydrogen bonding by including a cluster of molecules at the configuration they adopt in the solid state. Recent examples include Gaussian calculations of the narcotics heroin and cocaine[11,12] and heroin hydrochloride monohydrate,[13] for which X-ray crystal structures and experimental frequencies[13,14] are available. In the case of the latter, two hydrogen-bonded molecules were used in the calculation, a total of 110 atoms, and NQCC and asymmetry parameters were predicted to within 15% of the experimental values, as shown in Table 1 for the two protonated nitrogen atoms, N(1) and N(2) in the two different protonated heroin cations in the unit cell. Note that the calculation gives the sign of the NQCC as well as their direction cosines with respect to the axial system used, information not usually available from NQR experiments.

APPLICATIONS OF NQR TO PHARMACEUTICAL ANALYSIS

Although several early papers have emphasized the importance of NQR in both qualitative[15] and quantitative[16,17] analysis and in the detection of explosives,[18] it has only recently been realized that new developments in pulsed rf spectroscopy,[19] some of which we have already referred to, and new methods of improving the signal-to-noise ratio (SNR)[20] suggest the possibility of a much wider application of NQR techniques, particularly at the low radio

(11) Pati, R.; Das, T. P.; Sahoo, N.; Ray, S. N. *J. Phys. Chem.* **1997**, *101*, 6101–6106.

(12) Pati, R.; Das, T. P.; Sahoo, N.; Ray, S. N. *J. Phys. Chem.* **1998**, *102*, 3209–3214.

(13) Balchin, E.; Bearpark, M.; Malcolme-Lawes, D. J.; Rowe, M. D.; Smith, J. A. S.; Steed, J. W.; Wu, W.; Horsewill, A. J.; Stephenson, D. *N. J. Chem.* **2004**, *28*, 1309–1314.

(14) Yesinowski, J. P.; Buess, M. L.; Garroway, A. N.; Ziegeweid, M.; Pines, A. *Anal. Chem.* **1995**, *34*, 2256–2263.

(15) Brame, E. G. *Anal. Chem.* **1967**, *39*, 918–921.

(16) Schultz, H. D.; Karr, C. *Anal. Chem.* **1969**, *41*, 661–664.

(17) Hacobian, S. *Aust. J. Chem.* **1962**, *15*, 21–33.

(18) Peirson, N. F.; Rowe, M. D.; Smith, J. A. S. *Proceeding of a Joint Workshop on Research on Demining Technologies*; European Commission, JRC, Ispra, Italy, July 2000, pp 91–93; see also <http://www.nqrconsultancy.co.uk>.

(19) Suits, B. H.; Garroway, A. N.; Miller, J. B.; Sauer, K. L. *Solid State Nucl. Magn. Reson.* **2003**, *24*, 123–126.

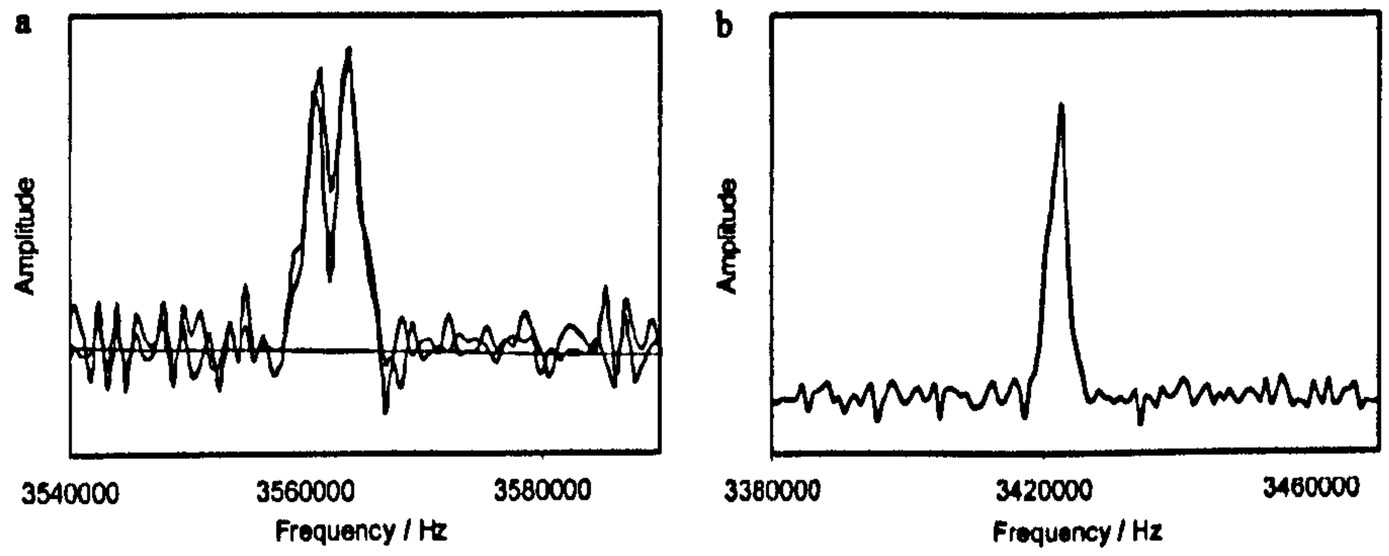

Figure 1. a. Doublet peak from phase I furosemide (Sigma powder) with frequencies 3.564 and 3.561 MHz, splitting ~2.35 kHz and line width ~1.6 kHz for both lines. b. ^{14}N singlet signal at 3.422 MHz from room temperature phase II furosemide with line width ~3 kHz.

frequencies typical of ^{14}N. We illustrate these comments by recent NQR studies of two well-known medicines, furosemide (**2**) and sulfapyridine (**3**).

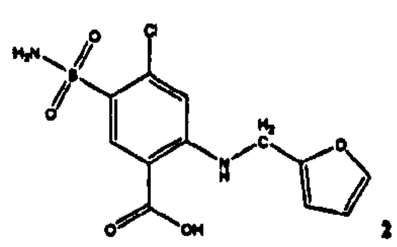

2

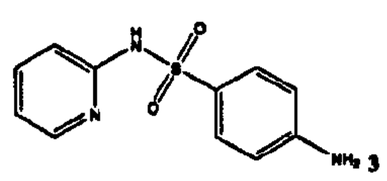

3

POLYMORPHISM

An important aspect of pharmaceutical development is the identification and selection of the appropriate polymorphic form, because this can have significant effects on the stability, processability, and bioavailability of a pharmaceutical formulation.

As an important example, furosemide (**2**) has at least two polymorphs, for both of which X-ray crystal structures have been published,[21,22] enabling comparisons to be made with the expected point symmetry of the molecules in the solid state and providing an additional check on the polymorphic form. The crystal contains two quadrupolar nuclei, ^{14}N and ^{35}Cl, and signals from both nuclei have been detected. In this example, both polycrystalline furosemide, as supplied by Sigma, and tablets of differing size marketed as Lasix (Hoechst-Marion-Roussel) were studied and compared. Both gave rise to very similar ^{14}N NQR spectra: near 3.65 MHz, a clear doublet is seen, assigned to the sulfonamide nitrogen, with peaks at 3.564 and 3.561 MHz at room temperature (Figure 1a) and with line widths close to 1.6 kHz.

The doublet structure is predicted from the crystal structure analysis of form I.[21] In comparison with this, recrystallization of this sample from *n*-butanol gives the metastable form II when the line frequency shifts to 3.422 MHz. The change of 0.141 MHz is easily observed when line widths are only a few kilo-Hertz or less. In addition, the line is now a singlet (Figure 1b), in agreement with the prediction of the point symmetry of the molecule in this form.[22]

For furosemide, ^{35}Cl signals have been detected at 77 K;[23] only one frequency is reported, at 36.759 MHz, which appears to correspond to the line at 36.266 MHz at room temperature, an indication of the temperature effects for this nucleus to which we have already referred. Notably, this line has a very short spin–lattice relaxation of 2 ms at room temperature, a value not untypical of the higher frequencies observed for ^{35}Cl nuclei in organic compounds. As a consequence, strong signals can be obtained in a few seconds.

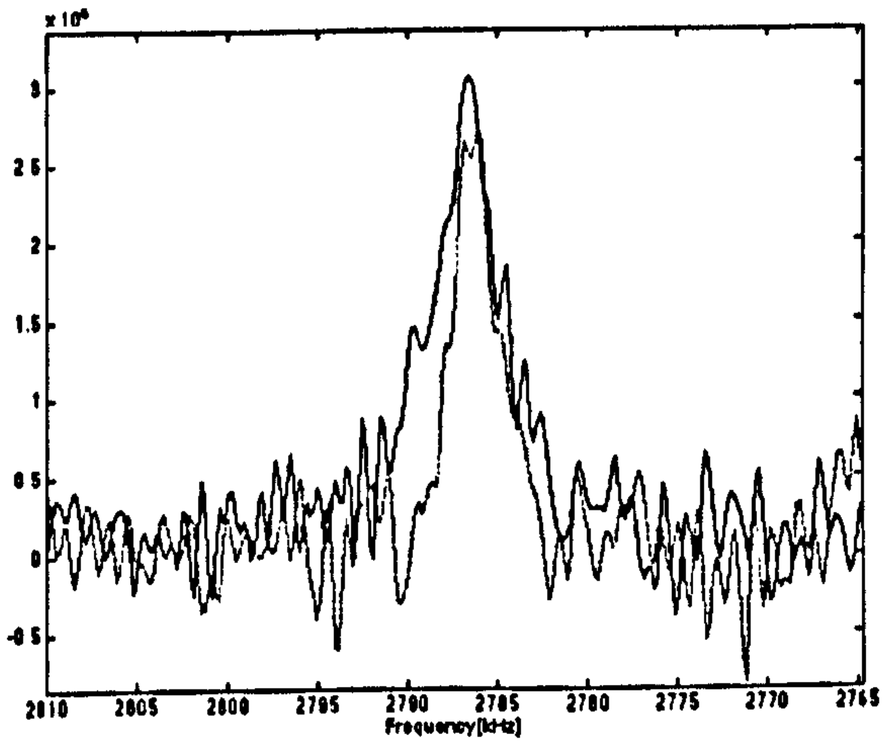

Figure 2. Comparison of the line widths for the 2.787 MHz line of sulfapyridine at room temperature for the powder sample as supplied by Sigma, and recrystallized from ethanol – • – •.

Another rather different example is the bacteriocide sulfapyridine (**3**), which also exists in different morphological forms. In this case, the NQR spectra of material as supplied by Sigma can be compared with material prepared by recrystallization from solvents such as ethanol and acetone (Table 2). Consider the 2.807 MHz line at 77 K, which has been tentatively assigned as ν_+ of the $-NH_2$ group.[24] At room-temperature, its frequency falls to 2.787 MHz, and signals at this frequency can be seen in both the sample from Sigma and that recrystallized from ethanol, indicating that they both consist of the same morphological form. However, their line widths are different, as shown in Figure 2, that of the recrystallized sample (2.5 kHz) being significantly less than that of the raw sample (4.0 kHz). The reason seems to be that, in general, NQR lines are inhomogeneously broadened, due in part to defects and crystalline imperfections but also to the presence

(20) Jakobsson, A.; Mossberg, M.; Rowe, M. D.; Smith, J. A. S. *IEEE International Conference on Acoustics, Speech and Signal Processing*, Philadelphia, March 19–23, 2005; Vol. IV, pp 653–656.
(21) Lamotte, J. N.; Campsteyn, H.; Dupont, L.; Vermiere, M. *Acta Crystallogr.* **1978**, *B24*, 1657–1661.
(22) Fronckowiak, M.; Hauptmann, H. *Am. Cryst. Assoc. Abstracts* **1976**, 9.
(23) Latosinska, J. N. *Magn. Reson. Chem.* **2003**, *41*, 395–405.
(24) Subbarao, S. N.; Bray, P. J. *Org. Magn. Reson.* **1981**, *15*, 307–310.

Table 2. ^{14}N NQR Parameters of Sulfapyridine (Sigma) at ~25 °C

Sigma powder			from ethanol		from acetone		
ν, MHz	$\Delta\nu_{1/2}$, kHz	T_1, s	ν, MHz	$\Delta\nu_{1/2}$, kHz	ν, MHz	$\Delta\nu_{1/2}$, kHz	T_1, s
			1.480 ± 0.001	1.8 ± 0.2			
2.284 ± 0.001	5.0 ± 0.5	1.0 ± 0.1	2.283 ± 0.001	3.0 ± 0.2			
2.393 ± 0.001	3.5 ± 0.5	1.4 ± 0.1	2.392 ± 0.001	1.8 ± 0.2			
2.787 ± 0.001	4.0 ± 0.4	0.65 ± 0.5	2.786 ± 0.001	2.5 ± 0.3	2.895 ± 0.001	2.8 ± 0.3	
2.924 ± 0.001	3.8 ± 0.4	0.70 ± 0.5	2.923 ± 0.001	2.5 ± 0.3	3.060 ± 0.001	1.0 ± 0.1	0.01 ± 0.001

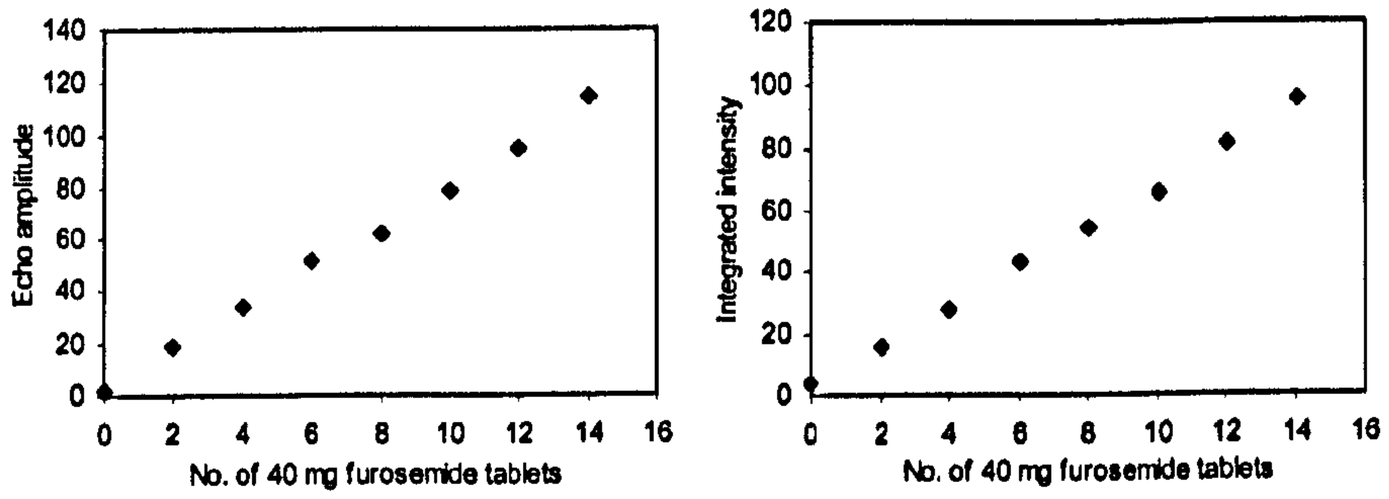

Figure 3. Variation of the ^{35}Cl echo amplitude and integrated echo intensity for furosemide from different numbers of 40-mg tablets.

of impurities or even strain in the material, factors alleviated by recrystallization. This line-broadening suggests a possible role for the technique in quality control.

Table 2 lists some of the NQR parameters at 25 °C of the three different samples of this drug examined; it is clear that the sample as supplied has the same frequencies and spin–lattice relaxation times as that recrystallized from ethanol, as expected, but different line widths, as we have indicated. It is also clear that recrystallization from acetone has produced a different form, which subsequent analysis has shown to be an acetone solvate. Both frequencies and relaxation times are now different, a convincing illustration of the solid-state effects to which we have already referred.

QUANTIFICATION USING ^{35}CL

Previous NQR experiments on inorganic compounds containing quadrupolar nuclei, such as ^{63}Cu in Cu_2O and ^{209}Bi in $BiCl_3$, showed that there was a reasonably linear dependence of peak signal intensity on sample weight.[16] These experiments were performed on a variable-frequency oscillator spectrometer, but there is reason to suppose that an equal or even better performance could be obtained from modern pulsed rf spectrometers. The ^{35}Cl NQR signals in furosemide at 36.266 MHz provides an example. For these experiments, actual tablets were used, and fast echo sequences were averaged over several scans. Standardization against a known sample was straightforward but rarely necessary; however, tablets in a dispensing bottle are best examined in an rf probe with as homogeneous an rf field as possible across the sample, for example, by the use of a coil of variable pitch.[25] In preliminary experiments, a series of eight scans was performed in which the number of tablets was increased by two between scans; the results are shown as plots of the echo amplitude and mean integrated echo intensities against number of tablets in Figure 3. Following these experiments, one sample consisting of four tablets was chosen as an unknown; from the integrated echo intensity, the mean number of tablets was estimated to be 3.82 ± 0.30, with confidence limits of 95%. These are preliminary experiments and could almost certainly be improved by better coil design and thermostating the sample and rf probe; they are now being extended to a study of the ^{14}N signal near 3.56 MHz.

IMPROVING NQR SENSITIVITY

A serious disadvantage of NQR methods involving ^{14}N has always been the relative weakness of signals detected at such low frequencies, in comparison with many hundreds of MHz common in modern NMR spectrometers. Again, recent advances in experimental techniques suggest that this problem could be considerably reduced in several ways. First, the use of cryogenic rf coils, as has already been introduced in high-field NMR, would certainly be an advantage in improving SNR, particularly at the low NQR frequencies characteristic of ^{14}N at which sample losses are minimal. Another development would exploit some of the recent signal enhancement methods developed for NQR spectroscopy,[26,27] of which the most promising is polarization-enhanced NQR (PE-NQR). In this method, the sample, containing both ^{1}H and quadrupolar nuclei, is polarized for a sufficient time in high field, say, at a frequency ν_H of 40 MHz. The field is then switched off or the sample is ejected. As its value falls, level crossing occurs between the ^{1}H levels and the quadrupolar levels (provided the latter lie at less than 40 MHz), whereupon the latter rapidly reach the same spin temperature as the former. A conventional pulsed NQR experiment in zero field would then be predicted to give a signal whose intensity was enhanced by a factor close to the ratio of the two frequencies, ν_H/ν_Q.

Unfortunately, little experimental work has so far been undertaken to check these predictions; one recent example is a PE-NQR study of *p*-nitrobenzoic acid[27] in which the protons were polarized in a magnetic field of 0.2 T (ν_H = 8.5 MHz), and an observed enhancement factor of 7 could be compared with a prediction of 7.4. The success of the method depends critically

(25) Leifer, M. C. *J. Magn. Reson.* 1993, *A105*, 1–6.

(26) Blanz, M.; Rayner, T. J.; Smith, J. A. S. *Meas. Sci. Technol.* 1993, *4*, 48–59.
(27) Blinc, R.; Apih, T.; Seliger, J. *Appl. Magn. Reson.* 2004, *25*, 523–534.

on the spin–lattice relaxation times of both the quadrupolar nuclei and the protons: if these are too short, it may be difficult to cycle the applied magnetic field quickly enough to capture the enhanced NQR signal. As an example of the potential advantages, the NQR signals in Figure 1 were obtained by Fourier transformation of the averaged signal from 16 PSL sequences with $\tau = 1$ ms and a repeat time of 1.5 s, in a total acquisition time of 25 s. In a successful PE-NQR experiment with a polarizing field of 0.5 T, only one PSL sequence would have been needed to achieve the same SNR in a time <0.1 s. This speed of data capture implies that the method could be used to examine signals from single tablets in a blister pack or larger samples on a production line or even within a chemical reactor. The polarizing field need not be homogeneous, provided that the entire sample experiences roughly the same polarizing field.

SUMMARY

Recent advances in instrumentation have shown that NQR shows excellent potential in the field of pharmaceutical analysis due to its simplicity, high selectivity, linear response (in certain situations), and also because it is a noninvasive technique. The high selectivity means that NQR is capable of distinguishing between very similar chemical environments, such as those occurring in different polymorphic forms. The relationship between line width and crystalline perfection indicates roles for NQR for quality control purposes and in the monitoring of, for example, recrystallization processes. The noninvasive and nondestructive nature of the technology allows analysis of the active pharmaceutical compound in situ within a formulation and within its packaging, lending itself to the "black-box" deployment of the technology in the manufacturing process, and possibly in clinical environments. Its quantitative and noninvasive nature will allow the accurate identification and quantification of tablets contained within a closed bottle. Although there are problems with NQR sensitivity (in particular, for ^{14}N), further improvements in techniques and instrumentation may help to address them.

Received for review March 2, 2005. Accepted April 12, 2005.

AC0503658